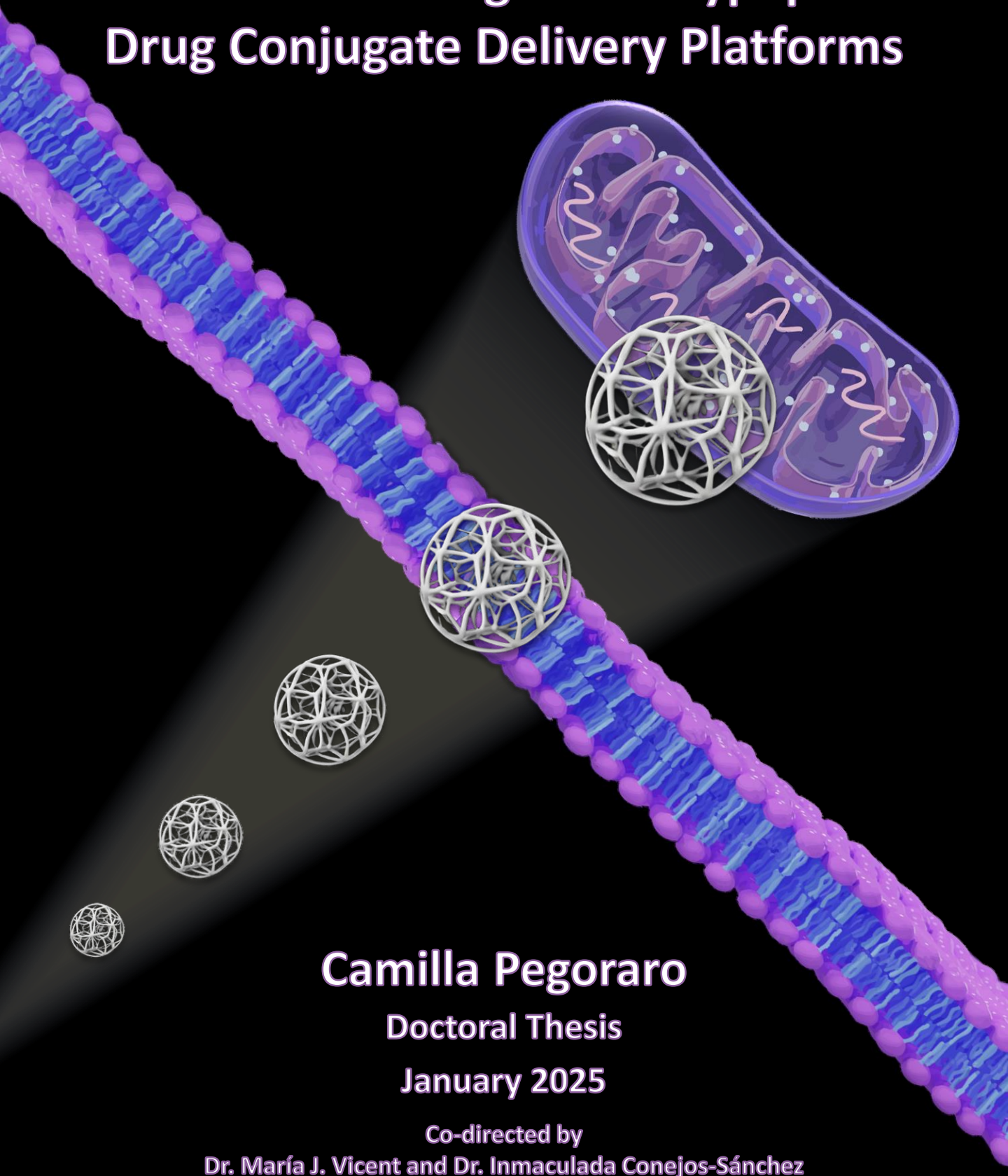
VALENCIA BIOMEDICAL RESEARCH FOUNDATION
CENTRO DE INVESTIGACIÓN PRÍNCIPE FELIPE

Polymer Therapeutics Laboratory

VNIVERSITAT DE VALÈNCIA

Doctoral Program in Biomedicine and Biotechnology

Mitochondria Targeted Polypeptide-Drug Conjugate Delivery Platforms



Camilla Pegoraro

Doctoral Thesis

January 2025

Co-directed by
Dr. María J. Vicent and Dr. Inmaculada Conejos-Sánchez

VNIVERSITAT DE VALÈNCIA

Faculty of Biological Sciences

Doctoral Program in Biomedicine and Biotechnology

VALENCIA BIOMEDICAL RESEARCH FOUNDATION
CENTRO DE INVESTIGACIÓN PRÍNCIPE FELIPE

Polymer Therapeutics Laboratory

MITOCHONDRIA TARGETED POLYPEPTIDE-DRUG CONJUGATE DELIVERY PLATFORMS

Camilla Pegoraro

Doctoral Thesis

January 2025

Co-directed by

Dr. María J. Vicent and Dr. Inmaculada Conejos-Sánchez

Dr. María J. Vicent, Ph.D. in Chemistry and Head of the Polymer Therapeutics Laboratory at the Centro de Investigación Príncipe Felipe (Valencia, Spain), and Dr. Inmaculada Conejos-Sánchez, Ph.D. in Polymer Chemistry and Senior Researcher of the same laboratory

CERTIFY that the present work

"**MITOCHONDRIA TARGETED POLYPEPTIDE-DRUG CONJUGATE DELIVERY PLATFORMS**"

has been developed by Camilla Pegoraro under their supervision in the Centro de Investigación Príncipe Felipe (CIPF) in Valencia as a thesis project to obtain a Ph.D. degree in Biomedicine and Biotechnology from the University of Valencia, Faculty of Biological Sciences.

Dr. María J. Vicent

Dr. Inmaculada Conejos-Sánchez

A mamma Elisabetta,

A Papà Marco,

A Riccardo

In the darkest times,

hope is something you give yourself.

That is the meaning of inner strength.

Table of Contents

ACKNOWLEDGMENTS 9

LIST OF ABBREVIATIONS 19

ABSTRACT 23

RESUMEN 25

1 GENERAL INTRODUCTION 29

1.1 Mitochondrial Biology and Structure 30

1.1.1 Mitochondrial Bioenergetics 32

1.1.2 Mitochondrial Functions Beyond Energy Production 35

1.1.3 Mitochondrial Genetics and Primary Mitochondrial Diseases 37

1.1.4 Mitochondrial Dysfunction in Secondary Mitochondrial Disease 39

1.1.5 Mitochondrial Involvement in Triple-Negative Breast Cancer 44

1.2 Therapeutic Potential of Nanomedicine 48

1.2.1 Intracellular Delivery in Nanomedicine 49

1.2.1.1 Biological Barriers 49

1.2.1.2 Endosomal Escape vs. Direct Plasma Membrane Permeation 57

1.2.2 Polymer Therapeutics as Nanomedicines 61

1.2.2.1 Polypeptide-based Polymer Therapeutics 63

1.3 Subcellular Targeting with Polymer Therapeutics: Mitochondria in the Spotlight 65

1.3.1 Unique Features of Mitochondria for Targeting 66

1.3.2 Challenges in Mitochondrial Targeting 69

1.3.3 Mitochondrial Targeting using Polymer Therapeutics 70

1.3.3.1 Smart Materials 71

1.3.3.2 Hierarchical Targeting 73

1.3.3.3 Specific Mitochondrial Targeting Localization 74

1.3.3.4 Inherent Mitochondria-Targeting Polymeric Carriers 75

1.4 Manuscript I: Review 77

2 OBJECTIVES 113

3 PUBLICATIONS 115

3.1 Manuscript II 116

3.1.1 Scientific Article I: Introduction and Background 116

3.2 Manuscript III 136

3.2.1 Scientific Article II: Introduction and Background 136

3.3 Manuscript IV 147
3.3.1 Scientific Article III: Introduction and Background 147
4 FINAL DISCUSSION AND REMARKS 160
5 REFERENCES 178
6 ANNEXES 209
6.1 Annex 1: Thesis Summary in Spanish 210
6.2 Annex 2: Supplementary Material of Manuscript II 224
6.3 Annex 3: Supplementary Material of Manuscript III 299
6.4 Annex 4: Supplementary Material of Manuscript IV 337

ACKNOWLEDGMENTS

It honestly feels surreal to reach the end of this PhD— a journey, an adventure, a roller coaster, a nightmare, and a dream, all wrapped into these incredible four years. When I first applied for this position, driven by the hope of contributing even the tiniest fraction toward improving patients' lives, I could never have imagined the path ahead or how intense it would be. Every time I tried to explain my work to family and friends, I found it frustrating to reduce it to "just doing some experiments trying to target mitochondria." It was so much more than that. It was a true challenge—the kind that pushes you beyond your comfort zone and forces you to discover what you're truly capable of. This journey was filled with joy, luck, laughs, travel, and collaborations that turned into friendships. But it was also a test of resilience: accepting failure, managing projects and time, thinking critically, facing frustration, enduring sleepless nights, summoning patience, and—most of all—writing, rewriting, editing, correcting, and writing all over again. A PhD is not just about professional growth; it is, above all, an intense journey of personal transformation—one that is hard to compare to any early-stage work experience. I won't deny that there were moments when I felt like giving up. But I was fortunate enough to be surrounded by people who reminded me of my worth and reassured me that, eventually, I would make it.

For that, and for being part of this incredible journey, I owe my deepest thanks to all of you.

First, I want to express my deepest gratitude to my supervisors, **Maria Jesús and Inmaculada**. **MJ**, thank you for giving me the opportunity to be part of this ambitious lab and for pushing me beyond what I ever thought I was capable of. Your trust and the passion you instill in young scientists are truly inspiring. This lab shapes you in so many ways—not just through experiments, but also through the seminars, travels, and networking opportunities you encourage us to pursue. Your dedication leaves a lasting impact, and I feel incredibly fortunate to have been part of this journey under your guidance. **Inma**, I honestly struggle to put into words how grateful I am to have had you as my supervisor, mentor, and friend. In *"only four months ejejeje"*—and beyond—we accomplished so much together, and I could never have done it without you. Your support, patience, laughs, celebrations, and sensitivity have been the pillars of my PhD. I know it hasn't always been easy, and we've navigated dark moments together, but please remember: you are special, and you are worth so much. As you know, I have a tattoo that says, *"mai s'apagarà la nostra llum"*. Well… this couldn't be truer for you. You are a star, and your light will never fade. I truly hope to have you in my life for many, many years to come.

Next, a huge thank you to all the members of the **Polymer Therapeutics Lab**—you are incredible people, each bringing something unique that makes this team so special. To the new lab members, I wish you all the best—I have no doubt you'll take the lab to even greater heights! To the *old crew*—**Inma, Ana, Maria Medel, Esther Masia, Snezana, Stuart, Amina, Maria Ibáñez, Paz, Inés, Toni, Justine, Tetiana, Paula, Esther**

Martínez, Zaida, and Karolina—I honestly owe you so much. I'll never forget all the laughs, the joy, the endless meetings, the Spanish lessons, the dancing, the weddings, the shared frustrations, the long lab days, the lunches, the travels, the tears, the knowledge, and every unforgettable moment we went through together. You made this journey what it was, and I'm so grateful to have shared it with you. Thank you, **Stu**, for all the tips, help, sharp comments, and much-needed mental support during this long writing process. It definitely wasn't easy, but it was worth it—and it wouldn't have been the same without you. Gracias a **Toni** por su actitud relajada y positiva en el laboratorio, a **Inés**, mi amiga mito, por compartir momentos difíciles y aventuras en el hospital La Fe, y a **Paz**, por haber sido un apoyo desde mis primeros días en Valencia, por ayudarme con la gestión de la tesis, y por enseñarme todo lo que sé de español. Una mención especial va para algunas personas a las que tengo la suerte de llamar amigas. E grazie, **Alessio**, perché anche senza condividere il laboratorio, i tuoi consigli, la tua passione e il tuo cinismo sono stati preziosi in questi anni. **María Medel**, nuestra referente en el laboratorio de química, has sido una ayuda inestimable, no solo en la práctica del laboratorio, sino también a nivel personal. Tu optimismo, tu generosidad (especialmente haciéndonos probar todos los dulces existentes en la Tierra), tus palabras de consuelo y tu paciencia han sido insustituibles. Si un día en el lab se sentía más ligero, era gracias a ti. **Esther Masiá**, al principio casi me intimidaban tu disciplina, tu control y tu infinito conocimiento de biología. Pero con el tiempo aprendí a conocerte, y te convertiste en mi guía y en el apoyo más valioso que podría haber tenido. Contigo compartí la alegría de los experimentos exitosos y la frustración de los que no lo fueron, risas, lágrimas, canciones, cotilleos en la cell culture room, carreras por las escaleras entre el lab y el flow cytometry, y horas extra analizando datos. Te estoy profundamente agradecida. Tu fortaleza y tu espíritu de "nunca rendirse" son una fuente de inspiración. Has sido una verdadera mentora. **Snežana**, fuiste mi primera amiga en el laboratorio y la persona que más eché de menos cuando te fuiste. Eres la persona más talentosa que he conocido, con una pasión desbordante por la ciencia, una organización impresionante y una mentalidad ganadora como nunca había visto antes. Gracias por ser una amiga con mayúsculas, dentro y fuera del lab, por creer en mí, por entender lo que significa estar lejos de la familia, por levantarme en los peores momentos del doctorado, y por celebrar conmigo cada éxito (y hay que decirlo, somos unas compañeras de fiesta top) con una sinceridad absoluta. Estoy segura de que harás grandes cosas y no veo la hora de estar allí para verlo. **Maria Ibáñez**, mi compañera de despacho durante años. Gracias por compartirlo todo: tu bondad, tu generosidad y tu disposición han sido fundamentales para mí. Eres una persona increíblemente talentosa y con una creatividad enorme. Créetelo, porque vales muchísimo, y estoy segura de que terminarás el doctorado de la mejor manera posible. **Amina**, fuiste el mejor descubrimiento de mis últimos años en Valencia. Al principio no entendía tu reserva y tu cara (ajajajaj), y jamás habría imaginado que te convertirías en uno de mis pilares, una hermana para mí. Podría escribir mucho más, pero espero que ya lo sepas. Gracias por todas las risas, las discusiones, las lágrimas, las fiestas y borracheras, las confesiones, el deporte (próximas campeonas de

pádel), tu esfuerzo por aprender italiano para que pudiera expresarme como en casa, y tu atención a los detalles. Eres una crack dentro y fuera del lab, y espero que compartamos muchas más experiencias juntas.

Todos los experimentos de estos años no habrían sido posibles sin la ayuda del personal técnico altamente cualificado del **CIPF**. Quiero agradecer especialmente a **Mario** por todas las fotos tomadas en el TEM a lo largo de estos años y por hacer que las horas de análisis fueran más divertidas con nuestros blind-guessing games. A **Alberto**, por haberme contagiado su pasión por el mundo de la microscopía confocal y por todas las recomendaciones musicales. Y a **Alicia**, gracias por tu disposición, tu entusiasmo ante cada idea loca que te proponía, por haber analizado incontables datos conmigo, por tu amabilidad y por haber confiado en mí. Y gracias, **Domingo**, por todas las charlas durante las largas horas de mediciones.

Thank you to all the collaborators I've had over the years, especially the colleagues at **La Fe Hospital** for their help with the Seahorse experiments, Prof. **Pavels Arsenyan** and colleagues from the **Latvian Institute of Organic Synthesis** for the cardiolipin studies, for their efficiency, and for providing valuable feedback. A big thanks to Prof. **Petra Schwille** and all my colleagues at the **Max Planck Institute of Biochemistry**—especially **Sveto, Adrian, Nishu, and Henry**—for making my experience in Munich truly unique, for being such a close-knit group in such a short time, and for making science both interdisciplinary and fun. I am also grateful to Prof. **Ben Feringa** and all my colleagues at the **University of Groningen**—true chemistry geniuses—for their help with my experiments whenever I needed it. And a special thanks to my colleagues at **Curapath**, especially **Aroa**, for assisting me with experiments, for their advice, and for making me feel like an integral part of the patent-writing process.

I can't go without thanking all my colleagues from **ITN BIOMOLMACS**—**Adrien, Ainoa, Ke, Roberto, Jonas, Yuechi, Alex, Clémence, Sebastian, Noemi, Yusuf, Maria, Beatriz, and Ekaterina**. Over these years, I've had the incredible fortune of being part of a group of 15 young researchers—some of the most brilliant people I've ever met. Sharing this international and intercultural adventure with you all, traveling across Europe to meet up, or spending months collaborating together, has been an incredibly stimulating, fun, and productive experience. Among this amazing group, there are a few people I want to mention especially. **Ekaterina**, my colleague in Valencia—thank you for being such an efficient and reliable collaborator and for sharing this journey as a true team from the very beginning. **Alex**, you were the first person from the consortium I had a video call with during Covid, and I knew right away you'd become a friend. Thank you for bringing your creativity and initiative to the table, making everything feel lighter and more enjoyable. **Noemi**, my Italian partner-in-crime—thank you for sharing the joys and struggles of the PhD, and for your honesty in all our conversations during the meetings. **Ainoa**, thank you for welcoming me in Groningen, making me feel at ease, and recognizing my value in a world full of top-tier chemists, where I often felt out of place. You are truly an inspiration—I've never met someone with such an interdisciplinary mind, passion for details, and goal-oriented drive. I have no doubt you'll achieve incredible things, and I hope to be there to witness them.

Maria, my *amiga ehhhhh*, the sunshine of our consortium. Having you in the group was a true privilege, and our time together in Munich only confirmed it. Thank you for supporting and understanding me, for your empathy and wisdom, for sharing the struggles, and for your ever-present smile. Traveling across Europe with you always felt like being at home. **Yusuf**, *"ragazzo giovane eeeee"*, from the very first day in Munich, I knew you'd be more than just a science colleague—you'd be a true friend. Thank you for all the deep conversations, for your understanding and non-judgmental attitude, for your humor, for the endless laughs, for your curiosity, and most of all, for opening the doors of your home in India to me. You are a one-of-a-kind person, and I owe you so much for helping me get through this PhD.

Mi doctorado en Valencia no solo estuvo marcado por el laboratorio, sino también por las grandes personas que conocí fuera de él, especialmente gracias al vóley playa, mi gran pasión y mi vía de escape durante todos estos años.

Quiero agradecer a mis "compañeras de equipo" de tantos años en la Malva: **Ursula, Kamile, Laura, Blanquita, Raquel, Rakel, Sara C., Sara S., Violeta, Blanca y Cristina**. Pongo "compañeras de equipo" entre comillas porque, aunque el vóley playa no es un deporte de equipo en el mismo sentido que el voleibol, con vosotras siempre me sentí parte de un verdadero equipo. Gracias por levantarme el ánimo cuando llegaba corriendo al entrenamiento frustrada porque un experimento no salía, por las birritas post-entreno para ponernos al día, por las pachangas del fin de semana, por los torneos por toda la Comunidad Valenciana, y por motivarme a mejorar cuando más dudaba de mí misma. Gracias en especial a **Ursu**, mi primera (y única ajjaja) compañera más "fija" de torneos. Gracias por compartir victorias y (muchas) derrotas, por tu sabiduría y por el cariño y la atención que siempre tienes para todas. Gracias **Kami**, fuiste un verdadero descubrimiento para mí! Gracias por compartir conmigo la incapacidad de cantar correctamente las letras de las canciones en español, por hacerme sentir que siempre estás ahí y por tu honestidad. Y sobre todo, gracias por incluirme en tu newsletter de amigos cercanos—me encanta cómo eres capaz de expresar tan bien cosas que yo también pienso pero que nunca sé cómo decir. Gracias **Lau**, mi bonica del corazón. Gracias por tu atención y empatía cuando estaba de bajón, por mostrarme que es posible compaginar 4,000 cosas a la vez y aun así estar siempre para los demás, por tus dibujos preciosos y por las risas y confesiones con una birrita en mano. Gracias **Blanquita**, porque contigo entendí el verdadero valor de escuchar. Gracias por buscarme incluso cuando yo intentaba estar a mi aire, por convencerme de hacer cosas nuevas (longboard o pintura, que aún tenemos pendiente), por compartir tu vulnerabilidad conmigo y, sobre todo, por estar siempre ahí.

La Malva no es solo un lugar aleatorio de entrenamiento, sino una verdadera comunidad de amigos insustituibles que me acogieron desde mis primeros días en Valencia, cuando el confinamiento no hizo nada fácil mi llegada a la ciudad ni mi vida social. Sin embargo, las personas que conocí fueron especiales y, durante todos estos años, han sido mi familia.

Gracias a todos los amigos de "Una Buena Mezcla", un nombre que representa perfectamente a este grupo. Gracias, **Justine**, fuiste una de las primeras personas que conocí en Valencia y has sido una amiga, no solo en el lab, sino sobre todo fuera. Gracias por por abrirme siempre las puertas de tu casa con comida belga y cócteles increíbles, por las fiestas y los mini viajes que compartimos. Aunque nuestras vidas hayan tomado caminos distintos, me alegra muchísimo seguir teniéndote en mi círculo de amigos. Gracias, **Val**, por tu honestidad y tu personalidad tan envolvente, por nuestras charlas y por compartir tantos cambios. Gracias, **Jorge**, por tus consejos desde lo alto de tu experiencia (eres un mentor espacial), por tu positividad, por los pádel improvisados y por haberme hecho conocer a la increíble **Vanesa**. Gracias, **Giada**, aunque no vivas en Valencia, para mí eres parte de mi familia valenciana. Gracias por tu sonrisa y tu risa contagiosa, por tu bondad y por estar ahí cuando me sentía mal, por tu cercanía y por siempre hacerme sentir importante. Gracias, **Carlos**, por tu generosidad, las micas espaciales, las frases hechas y los dichos murcianos, y por todas las noches compartidas. Y gracias, **Andrea**, ha sido un placer conocerte poco a poco; valoro muchísimo tu sentido del humor y tu gran corazón. Gracias, **Jorghino**, la cuota joven del grupo, un torbellino de experiencias, emociones, energía e infinitas responsabilidades. Gracias por estar siempre presente en el grupo y por unirnos a todos con tu sensibilidad y tu forma de ser. Gracias, **Simla**, por la calma y serenidad que transmites y por las mañanas de yoga, un espacio de recarga en todos los sentidos. Gracias, **Mati**, por las risas cuando no entendía nada de tu acento argentino, por las pachangas en la playa y por hacerme los días más ligeros cada vez que te veía. Gracias, **Giulia**, mi amiga romana. Gracias porque contigo se pueden compartir momentos de extrema vulnerabilidad y sinceridad en los momentos difíciles, pero también de pura ligereza e ironía. No es casualidad que nuestro grupo trashvalenciano siempre haya producido auténticas joyas. Y gracias por compartir conmigo la pasión imparable por el deporte en todos sus sentidos y por la bandera azzurra. Gracias, **Ale**, porque probablemente, si no hubiera sido por ti y por haberme introducido en este mundo, me habría perdido muchas de las experiencias que viví. Gracias por tu sabiduría, por nuestras rutas en bicicleta hablando de la vida, por tu risa inconfundible, por los mil eventos en la playa y por ser una pieza clave del trashvalenciano. Y gracias a ambas por hacerme conocer a **Noe** y **Glenny**, dos personas increíbles. Gracias a los chamos **Marisol**, **Luna** y **Marco** por vuestra bromas y risas dentro y fuera de la playa. Gracias, **Manu**, mi alemanU favorito. Gracias por tu ironía germano-uruguaya, por nuestras noches de cine con el chamo, por tu determinación y humildad, y por esas noches que recargan el corazón. Gracias, **Alonso**, el papi-chamo, mi primer amigo en Valencia. Gracias por hacerme sentir en casa desde el primer día, por tu lado divertido y a veces despistado, pero al mismo tiempo por estar siempre ahí y por tener mil detalles conmigo. Gracias por ser tú mismo, sin importar el contexto, por organizar siempre planes para que todos estemos bien (tipo ramen night), por las noches de cine y las pachangas de los domingos, por tu generosidad y por haberme mostrado, poco a poco, tu lado más vulnerable. Y gracias a las dos personas que han sido el pilar de mi vida en Valencia. Gracias, **Giuseppe**, mi compi del mixto, mi amigo perezoso (ajajajaj). Gracias porque contigo puedo hablar de todo, por tu inteligencia emocional, por los torneos jugados juntos, por las

noches compartiendo tu pasión por la comida, por tu curiosidad, los mini viajes y experiencias juntos, y por tus palabras siempre acertadas en el momento justo. Gracias, **Ellie**, por haber sido como una hermana para mí. Gracias por tu inteligencia emocional y tu capacidad de analizar las cosas, por tu escucha atenta, por estar siempre ahí y por haber sabido tomar las riendas de nuestra amistad en los momentos más difíciles. Gracias por tu sinceridad, por tu forma de incluir a todos, por haber intentado siempre hacerme ver mi valor cuando yo no lo veía, por las birritas en la terraza, por las noches de baile, por las confesiones más íntimas y vergonzosas. Eres una amiga insustituible y una mamá increíble. Y gracias por haber traído al mundo a **Indi**, nuestra alegría desde hace un año y medio.

Valencia è stata una città che ho amato, una città perfetta sulla carta. Non nego, però, che questi anni siano stati anche colmi di malinconia per il mio paese, la mia casa e tutte le persone che la rendono speciale. Tornare da voi è sempre stato il mio porto sicuro, e in tutti questi anni mi siete mancati moltissimo.

Grazie alle mie compagne di squadra dell'Arcella Volley—**Sofia, Francesca R., Marta, Francesca S.** (Simonaaa) e **Veronica**. Con voi ho vissuto degli anni sportivi pazzeschi, fatti di vittorie, sconfitte, pianti, abbracci, bullismo (ahahah), pizzate e feste ignoranti. Ma soprattutto, con voi ho imparato cosa significa davvero essere una squadra: dove una manca, l'altra c'è, dove una è giù, l'altra compensa, e dove problemi e debolezze si trasformavano sempre in scherzi e momenti di leggerezza. Grazie per esserci sempre state, nonostante le nostre vite abbiano preso strade diverse. Un grazie speciale a **Franci Rigon**, la mia piccola bomber. Grazie per la tua attenzione costante, per avermi sempre fatto sentire che c'eri, per avermi fatto morire dal ridere (nonostante tu sia una bulla), per aver divorato valanghe di tramezzini e per la polenta in faccia per migliorare la pelle. Grazie, **Sofi**, alias 42chiliinpancapiana avventuriera. Sei un'amica accogliente, non giudicante e super responsabile (meno male che ci sei tu!). Grazie per aver sempre saputo trovare le parole giuste e per avermi difesa dalla Rigon.

Grazie **Giulia**, ho la fortuna di averti come amica dai tempi delle medie e di non averti mai persa, nonostante viaggi, cambi di vita e chilometri di distanza. Grazie per le chiacchierate oneste, per avermi messa in discussione aiutandomi a crescere, per aver condiviso con me le nostre paturnie da drama queens, e per ammettere senza problemi che siamo entrambe pessime col telefono, ma che ci vogliamo bene lo stesso.

Grazie agli amici di "Persone Simpatiche"— **Alessia, Chiara, Marco, Alice, Elia, Rod, Enrico, Andrea e Kevin**. Grazie perché ogni volta che tornavo a casa e vi vedevo, era come fare un salto indietro ai tempi spensierati dell'università in Casa Dori. Anche se non sono stata molto presente, vi ringrazio perché ogni volta che ci siamo visti mi avete sempre fatto sentire accolta. Grazie soprattutto ad **Alice** per la sua dolcezza, semplicità e attenzione. Un grazie speciale a **Marco**, il mio brate. Dall'Erasmus come divorati in UK sei diventato per me un amico insostituibile. Grazie per avermi fatto scoprire Madrid, per rendere persino le conferenze divertenti, per lo scambio di idee e confessioni, e per essere un compagno di festa pazzesco. E grazie soprattutto per

avermi fatto conoscere **Maria** e **Sergio**, due belle persone che hanno reso ancora più speciale il mio tempo a Valencia.

Grazie agli amici di "Eccoli"— **Alessandro, Riccardo, Nicolò, Sara e Francesco**. Ci siamo conosciuti meglio negli ultimi anni e sono estremamente felice di avervi nella mia vita. Grazie per le gite in montagna, i Capodanni insieme, le sfangate di cibo e le nottate di giochi. Come vi ho detto, sapere di tornare a casa e avere piani con voi rendeva il rientro ancora più speciale.

Grazie ai miei amici di "Rimpianto e Rancore"— **Nicolò** ed **Elena**. Grazie **Nic**, per le serate a casa tua, per le tue risate ciniche, per esserti aperto con me, per essere il mio medico di fiducia, per i tuoi racconti tragicomici sull'ospedale e per fare sempre i salti mortali per riuscire a vederci ogni volta che tornavo. Grazie **Ele**, per averci capite fin dai primi giorni nella squadra dell'Absolut, per la tua gentilezza e spontaneità, per avermi fatto apprezzare un pochino i gatti, per le risate a casa di Nic, e per non avermi mai giudicata ma sempre ascoltata.

Grazie **Alice** e **Sara**, le mie compagne delle elementari e non solo. Grazie per essere cresciute insieme, e perché, nonostante strade, vite e luoghi diversi, riusciamo sempre a ritagliarci dei momenti di leggerezza e aggiornamenti

Grazie ai miei amici e compagni dell'università, per aver sempre cercato di incastrare agende impossibili pur di aggiornarci e vederci. Grazie soprattutto a **Pier**, perché, nonostante ci sentiamo pochissimo, so che non cambia nulla dai tempi dell'università. Grazie **Matteo** Bru, per avermi fatto sentire la tua vicinanza e per aver sempre trovato parole di supporto per questa mia avventura. Grazie **Valentina**, per aver condiviso con me le CRS Conference, per farmi sempre morire dal ridere con le tue imitazioni leggendarie, e per aver diviso con me gioie e dolori del dottorato. Grazie **Martina**, la mia sister e coinquilina dell'Erasmus, ormai bruxellese d'eccellenza. Grazie per esserci sempre stata, anche a distanza, per farmi ridere con la tua vita incasinata, e per raccontarci i drammi per poi riderci su—perché con te ho scoperto cosa significa vivere e condividere tutto con qualcuno.

Grazie a **Jacopo** Lonzi, il fratello che non ho mai avuto. Grazie perché, come un vero fratello, riesci sempre a farmi girare le scatole, e spesso siamo in disaccordo, ma so che su di te posso sempre contare. Grazie per aver continuato a chiamarmi anche quando non rispondevo mai, per gli aggiornamenti sulla vita, per il classico "quando torni, Milli?", per avermi sempre supportata, anche da lontano, per esserti aperto con me su questioni difficili e per mostrarmi la tua forza d'animo. Grazie **Riccardo**, Richi Piri, un'amicizia positiva fin da quando ero piccola, per la tua gentilezza e accoglienza, per far stare sempre tutti bene con il tuo modo di fare spontaneo, e per le nostre cene di aggiornamento ogni tanto. E grazie a entrambi per avermi fatto conoscere **Michela** e **Giorgia**, due persone davvero speciali.

Grazie alle mie amiche di "Tondo e Pungente"**, Chiara e Alessia**. Grazie **Chiara**, ti ho conosciuta poco a poco, e ora sei per me un'amicizia fondamentale. Grazie per aver condiviso con me i dolori del dottorato e delle situazioni difficili, per aver sempre trovato il lato positivo e la grinta per andare avanti. Grazie per le avventure di questi anni, tra camping, furgonetas e feste, per le parole di conforto, per le tue iniziative sociali, per essere sempre così accogliente e per il tuo ottimismo contagioso. Sei una fonte di ispirazione. Grazie **Alessia**, la mia cuz fin dai tempi dell'asilo. Grazie per essere stata un'amicizia vera e stabile per tanti anni (nonostante il mio rapporto pessimo col telefono), per essere una persona su cui so di poter sempre contare, per aver capito e accettato tutte le fasi della mia vita (ovviamente tutto documentato dalle foto ahah), per credere in me più di quanto lo faccia io, per esserti fidata di me, per la tua ambizione coinvolgente, per la tua intraprendenza, per avermi coinvolto nei tuoi mille progetti, per le ubriacature epiche, e per aver condiviso con me alcuni dei momenti più belli della mia vita, come l'Interrail. Sono fiera di essere tua amica e sono sicura che farai grandi cose—e spero di essere lì per vederle.

Grazie alle mie BFF, **Sara, Gaia e Alessia**. Faccio fatica a descrivere cosa siete per me, ma, come mi dice sempre Richi, siete una delle mie fortune più grandi dai tempi dell'Olympia Volley a 11 anni. Stare a Valencia senza di voi non è stato facile, ma vi ringrazio perché con voi so cos'è la vera amicizia—quella che ti sostiene nei momenti difficili, ma soprattutto quella che gioisce sinceramente per te nei successi. Grazie **Sara**, per essere una persona super interessante, piena di idee a volte bizzarre, per aver sempre saputo capire e accettare le nostre differenze ridendoci su, per le serate di giochi a casa tua, per il tuo modo di fare spontaneo e accogliente che fa sentire sempre tutti a casa, per la tua onestà e visione del mondo, e per cercare ogni volta di capire quando sarei tornata, per rimetterci tutte nell'ovile. Grazie **Gaia**, per avere un'anima così gentile, per la tua sensibilità, per le nostre emozioni a specchio, per la tua precisione e ambizione, per condividere con me quelle mille sensazioni difficili da spiegare, per cercare sempre di fare le cose più carine e curate quando noi siamo delle cialtrone, per quei tuoi due lati caratteriali—uno timido e l'altro sfrontato—che mi fanno sempre troppo ridere. Grazie **Alessia**, il mio pitio, il mio punto di riferimento da quando sono piccola, la mia sorella di vita. Grazie per la tua esuberanza, per aver fatto con te le peggiori e migliori cazzate della mia vita, per i pianti prima di ogni partenza, per avermi fatto sentire che le mie gioie erano anche le tue, per la tua intelligenza emotiva fuori dal comune, per sapere sempre trovare le parole giuste, per essere il mio supporto costante, per avermi insegnato che va bene non essere sempre al 100%, per essere un mix perfetto tra pazzia e responsabilità, per conoscermi come pochi al mondo e per credere sempre nel mio futuro. Non so come esprimere quanto sono grata per la nostra amicizia, mi sei mancata infinitamente in questi anni. E grazie a tutte e tre per avermi fatto conoscere Leonardo (il **Marez**), Filippo (**Pippo**) e Lorenzo (**Lollo**)—quando torno e siamo tutti insieme, mi sento in famiglia.

Grazie alla famiglia di Riccardo—**Luisa, Pasquale** e **Lorenzo e** nonna **Teresa**—per avermi sempre fatto sentire a casa, per esservi presi cura della Camillina quando eravamo insieme, per i pranzi e le cene buonissime

condivisi, per aver sempre supportato me e Riccardo nelle nostre decisioni, e per aver gioito con noi in ogni passo del nostro percorso.

Grazie ai miei cugini, **Francesco** e **Gianluca**, perché in questi anni lontano da casa ho forse capito ancora di più il valore della famiglia e quanto per me siete importanti. Grazie per darci l'appuntamento ogni volta che tornavo, per avermi resa partecipe dei vostri cambiamenti di vita, per capirci nonostante le differenze. Sono fiera di voi. E grazie per aver organizzato i ritrovi con **Marione** e **Paglia**, i miei cugini acquisiti.

Grazie a mio zio **Alberto**, per la sua generosità e bontà, a mia zia **Antonella**, per la sua curiosità e disponibilità, e a **Walter**, ormai per me una persona di famiglia e un riferimento. Grazie per prenderti cura dei miei genitori mentre non ci sono e per essere un vero amico.

Grazie ai miei nonni, **Elsa** e **Vinicio**, che ho la fortuna di avere ancora con me. Grazie nonno, per le tue preoccupazioni affettuose, per darmi sempre il cioccolatino o la paghetta quando tornavo a casa, come quando ero piccola, e per le tue battute che mi fanno sempre sorridere. Grazie nonna, per avermi cresciuta con i tuoi sorrisi, per la tua forza d'animo impressionante, per essere quasi più in forma di me, per essere la mia fan numero uno e per ascoltarmi sempre con entusiasmo. Grazie per trovare sempre il lato positivo, per i nostri pranzi insieme, per aver capito perché volessi andare via. So che questi anni non sono stati semplici, ma sono felice che li abbiamo affrontati insieme. Grazie anche ai miei nonni **Primo** e **Claudia**, che, anche se non ci sono più, sento continuamente riflessi nel mio carattere.

Grazie **Riccardo**, il mio compagno di vita. Se mi avessero detto che in cinque anni e mezzo avrei condiviso così tanto con una persona, non ci avrei mai creduto—dall'appartamentino durante il Covid a Padova alla nostra vita a Valencia. Non mi bastano le parole per ringraziarti per questa incredibile avventura insieme. Grazie per avermi accompagnata nei momenti più bui e per avermi tenuta per mano, per essere stato il mio fan numero uno, per avermi sfidata, sapendo che potevo fare meglio, per esserci persi e ritrovati, per i mille viaggi dentro e fuori dall'Europa (nonostante la tua passione per i videogiochi e per le cose comode eheheh), per la tua generosità e bontà d'animo, per la tua stranezza e per il fatto di essere sempre te stesso, fregandotene del giudizio degli altri. Grazie per aver cercato di tirarmi su di morale quando mi vedevi giù, conoscendo alla perfezione il mio amore per l'horchata o l'IKEA, per esserti messo in gioco anche fuori dalla tua comfort zone, per aver cucinato piatti buonissimi, per aver condiviso con me gioie e paure per il futuro, per aver giocato in squadra, per esserti messo in discussione, anche quando non era facile, e per avermi mostrato l'amore vero nelle piccole cose. Sei una persona bellissima, e sono fiera di te e di tutto ciò che abbiamo vissuto insieme, con la speranza di vivere tante altre avventure ancora.

Grazie alla mia mamma **Betty** e al mio papà **Marco**. So che non è stato facile accettare la mia decisione, ma vi ringrazio per aver sempre supportato ogni mia scelta. Questa tesi la dedico a voi. Grazie papà, per la tua bontà e i tuoi consigli preziosi, per la tua finezza, per le tue battute, per le nostre camminate, anche in silenzio,

per la tua pazienza infinita, per la tua stima incondizionata, per la tua curiosità, per avermi insegnato il valore della correttezza e della professionalità, per la tua umiltà e per i tuoi abbracci sicuri. Grazie mamma, perché sei una forza della natura. Grazie per le chiamate infinite, per il tuo entusiasmo e la tua forza d'animo, per il tuo ottimismo contagioso, per aver fatto di tutto per farmi sentire la tua vicinanza anche a distanza, per le tue ricette buonissime, per il tuo modo di farti in quattro pur di vedere felici le persone che ami, per la tua capacità multitasking, che spero prima o poi di acquisire, per la tua voglia di imparare e per il coraggio di affrontare tutto senza paura. Ho una gran fortuna ad avervi come genitori. Grazie per avermi insegnato tanto, per i sacrifici a cui forse non sempre sono stata abbastanza riconoscente, per aver sofferto con me e gioito con me sempre. Stando lontano si imparano tante cose, e sicuramente una delle più importanti è il valore delle persone e della famiglia. Grazie per tutto quello che avete fatto per me.

This thesis marks the end of an intense and beautiful chapter, but also the beginning of new adventures. I carry with me everything I have experienced, every lesson learned, and, most importantly, the value of the people who have walked this path with me. Thank you to all of you, near or far, for being a part of it.

LIST OF ABBREVIATIONS

Abbreviation	Name
ACC	Acetyl-CoA carboxylase
ADP	Adenosine diphosphate
AKT	Protein Kinase B
ALD5	Aldehyde dehydrogenase 5
ALDH2	Aldehyde dehydrogenase 2
Ananan	Ala-asn-ala-asn-ala-asn-miniPEG-Lys
ANT	Adenine nucleotide translocator
ASOs	Antisense oligonucleotides
ATP	Adenosine triphosphate
AuNPs	Gold nanoparticles
Bak	Bcl-2 homologous antagonist/killer
Bax	Bcl-2-associated X protein
BL1	Basal-like 1
BL2	Basal-like 2
CAT	Catalase
CI-IV	Complex I-IV
CL	Cardiolipin
CLIC	Clathrin-independent carriers
CME	Clathrin-mediated endocytosis
CPMs	Cell-penetrating motifs
CPPs	Cell-penetrating peptides
CPT1A	Carnitine palmitoyltransferase 1A
cRGD	Cyclic Arg-Gly-Asp
CV	ATP synthase (Complex V)
CVME	Caveolae-mediated endocytosis
Cy5	Cyanine5
DA	Dimethylmaleic anhydride
DLCs	Delocalized lipophilic cations
D-Nal	D-naphthylalanine
DOX	Doxorubicin
DQA	Dequalinium
Drp1	Dynamin-like protein
ECM	Extracellular matrix
EPR	Enhanced permeability and retention
ER	Endoplasmic reticulum
ETC	Electron transport chain
EVs	Extracellular vesicles
F16	(E)-4-(1H-indol-3-ylvinyl)-N-methylpyridineiodide
F6P	Fructose-6-phosphate
F-actin	Filamentous actin
FADH2	Reduced flavin adenine dinucleotide
FAO	Fatty acid oxidation
FASN	Fatty acid synthase

Fe-S	Iron-sulfur
FITC	Fluorescein Isothiocyanate
GA	Glycyrrhetinic acid
GEEC	GPI-anchored protein-enriched early endosomal compartments
GFLG	Glycyl-phenylalanyl-leucyl-glycine
GLUTs	Glucose transporters
GPI	Glycosylphosphatidylinositol
GPx	Glutathione peroxidase
GR	Glutathione reductase
GSH	Glutathione
HIF-1α	Hypoxia-inducible factor-1α
HKII	Hexokinase II
hMT1A	Human metallothionein 1A
HPMA	N-(2-hydroxypropyl) methacrylamide
IBM	Inner boundary membrane
IGF-1R	Anti-insulin growth factor 1 receptor
IM	Immunomodulatory
IMM	Inner mitochondrial membrane
IMS	Intermembrane space
IONPs	Oxide nanoparticles
LAR	Luminal androgen receptor
LDH	Lactate dehydrogenase
LNPs	Lipid nanoparticles
Loni	Lonidamine
M	Mesenchymal
MAMs	Mitochondria-associated membranes
MCT1	Monocarboxylate transporter 1
MCTs	Monocarboxylate transporters
MCU	Mitochondrial calcium uniporter
MDR	Multidrug resistance
Mfn1/Mfn2	Mitofusin 1 and 2
MICOS	Contact site and cristae organizing system
MM	Molecular Motor
MMP	Mitochondrial membrane potential
MMP-9/2	Matrix metalloproteinase 9/2
MOMP	Mitochondrial outer membrane permeabilization
MPC	Pyruvate carrier
MPPs	Mitochondrial penetrating peptides
mPTP	Mitochondrial permeability transition pore
Msp1	Mitochondrial Sorting Protein 1
mt-CPOs	Mitochondrial-targeting cell-penetrating oligomers
mtDNA	Mitochondrial DNA
MT-ND4	NADH dehydrogenase subunit 4
mTOR	Mammalian target of rapamycin
MTS	Mitochondrial targeting sequence
MT-TL1	Mitochondrially Encoded tRNA-Leu (UUA/G)
Mw	Molecular Weight

NCA-ROP	N-carboxyanhydride ring-opening polymerization
NADH	Reduced nicotinamide adenine dinucleotide
nDNA	Nuclear DNA
NF-κB	Nuclear factor-κB
NMR	Nuclear magnetic resonance
NO	Nitric oxide
OCR	Oxygen consumption rate
OMM	Outer mitochondrial membrane
OPA1	Optic atrophy type 1
OPDEA	Poly[2-(N-oxide-N,N-diethylamino)ethyl methacrylate]
OXPHOS	Oxidative phosphorylation
PAMAM	Poly(amidoamine)
Parg	Poly-L-arginine
Parkin	RBR E3 ubiquitin-protein ligase
PAS	Penetration-accelerating segment
PBA	polybutyl acrylate
PBAE	Poly(β-amino ester)
PBLG	Poly(γ-benzyl-l-glutamate)
PDI	Polydispersity Index
PCL	poly ε-caprolactone
PDH	Pyruvate dehydrogenase
PDH	Pyruvate dehydrogenase
pDNA-Luc	Plasmid DNA coding luciferase
PE	Phosphatidylethanolamine
PEG	Polyethylene glycol
PEI	Polyethyleneimine
PEP	Phosphoenolpyruvate
PGA	Poly-L-glutamic acid
PGC-1α	Peroxisome Proliferator-Activated Receptor Gamma Coactivator 1α
Phis	Poly-L-histidine
PI3K	Phosphoinositide 3-kinase
PINK1	PTEN-induced kinase 1
PKM2	Pyruvate kinase muscle isozyme 2
PLGA	Poly(lactic-co-glycolic acid)
PLL	Poly-L-lysine
PLL-Gua	Guanidinium-functionalized poly(L-lysine)
PLO	Poly-L-ornithine
PLO_n-PLP_m	Poly-L-ornithine–poly-L-proline
PMDs	Primary mitochondrial diseases
P-MM	Polypeptide-conjugated molecular motor
PSar	Polysarcosine
PTX	Paclitaxel
R8	Octaarginine
RES	Reticuloendothelial system
ROS	Reactive oxygen species
rRNAs	ribosomal RNAs

siRNA	Small interfering RNA
SLC1A5	Solute carrier family 1 member 5
SMDs	Secondary mitochondrial diseases
SNCs	Silica nanocapsules
SOD	Superoxide dismutase
SRC	Spare respiratory capacity
SS	Szeto-Schiller
TCA	Tricarboxylic acid
TEG	Tetra(ethylene glycol)
TIM	Translocase of the IMM complex
TDL	Total drug loading
TME	Tumor microenvironment
TMV	Tobacco mosaic virus
TNBC	Triple-negative breast cancer
TOM	Translocase of the OMM complex
TPP	Triphenylphosphonium
tRNAs	transfer RNAs
TRV3	Trivalent compound
TSPO	Translocator protein
Ub	Ubiquitin
UV-Vis	UV-visible
VDACs	Voltage-dependent anion channels
VLC-3	$PSar_{100}$-b-PGA_{15}
α-CD	α-cyclodextrin
α-KG	α-ketoglutarate
α-TOS	α-tocopherol succinate

ABSTRACT

The dysfunction of mitochondria - key organelles involved in cellular energy production, apoptosis, and metabolism – represents a hallmark of diseases such as cancer; therefore, targeting mitochondria presents a promising strategy to enhance therapeutic precision, particularly in cancer treatments where dysfunctional mitochondria support tumor growth, survival, and resistance to therapy. Importantly, achieving efficient and specific mitochondrial delivery remains a significant challenge in advancing cancer therapies.

Presented as a compendium of scientific articles, this Ph.D. thesis focuses on the rational design of polymer therapeutics for mitochondrial targeting; specifically, we selected polypeptide-based nanocarriers due to their biodegradability and ability to be fine-tuned to specific purposes. We designed these nanocarriers to promote efficient mitochondrial targeting, address critical challenges in cellular uptake and target specificity, and integrate them into advanced delivery systems and multimodal therapies. This research demonstrates the potential of these mitochondrially-targeted platforms in treating aggressive cancers such as triple-negative breast cancer (TNBC), which represents our model system. To provide a comprehensive overview of the challenges and recent advancements in mitochondrial targeting for therapeutic applications using nanomedicine, we published a review, which forms an annex to the introduction of this thesis.

The first article introduced poly-L-ornithine–poly-L-proline (PLO_n-PLP_m) diblock copolymers designed for mitochondrial targeting. These polypeptide-based nanocarriers overcame limitations associated with traditional mitochondrial-targeting strategies by utilizing an energy-independent uptake mechanism (bypassing endosomal pathways) and enabling efficient mitochondrial accumulation even under conditions of membrane depolarization. At a specific n:m ratio (1:3), these polypeptide-based nanocarriers - referred to as mitochondrial targeting cell-penetrating oligomers (mt-CPOs) - induced mitochondrial dysfunction (including mitochondrial depolarization, reactive oxygen species generation, and disruption of oxidative phosphorylation) and significant anti-tumorigenic effects in MDA-MB-231 TNBC cells at sub-IC_{50} concentrations (>IC_{15}). Physical studies in membrane models, including small unilamellar vesicles and mitoplasts, revealed and validated cardiolipin-specific interactions, unveiling the localized membrane remodeling and patch formation crucial for efficient mitochondrial targeting. Furthermore, the functionalization of PLO_6-PLP_{22} with polyglutamic acid (PGA) demonstrated the translational potential of mt-CPOs, highlighting their versatility as mitochondrial targeting moieties for larger drug delivery systems at sub-IC_{15}

concentrations. Conjugation of PLO_6-PLP_{22} to Lonidamine and α-tocopherol succinate, selected for their mitochondria-dependent mechanisms of action, maintained mitochondrial targeting and enhanced synergistic anti-tumor activity in MDA-MB-231 cells.

In the second article, we extended the application of mitochondrial targeting polypeptide-based nanocarriers by conjugating light-responsive molecular motors (MMs) to a previously developed PGA-functionalized PLO_6-PLP_{22} nanocarrier (P). P-MM conjugates maintained rotational capacity and light-induced supramolecular reorganization, transitioning from micellar structures to elongated worm-like assemblies. These structural changes enhanced cellular uptake while preserving mitochondrial localization in MDA-MB-231 cells, showing a direct correlation between light-induced structural changes and improved biological performance. Incorporating a PGA carrier then ensured minimal cytotoxicity, enhancing the biocompatibility and biological efficacy of MMs.

The third article introduced C-TRV3-A, a polypeptide-based nanoconjugate that integrates mitochondrial targeting with non-viral gene delivery. C-TRV3-A comprises a functionalized poly-L-ornithine backbone and TRV3 conjugated via a redox-sensitive disulfide linker (TRV3 incorporates triphenylphosphonium for mitochondrial targeting, Cy5 dye as a model drug, and Atto488 for imaging). This multifaceted design supported efficient mitochondrial localization following endosomal escape and selective release of TRV3 under reducing environments, optimizing trafficking within TNBC cells. In vitro evaluations of C-TRV3-A formulated in polyplexes with plasmid DNA-Luciferase and a polyanionic polypeptide (VLC-3) demonstrated elevated transfection efficiency in conventional 2D monolayer cultures and advanced 3D spheroid cultures of TNBC cells with minimal cytotoxicity. C-TRV3-A-based polyplexes also exhibited stability in complex biological media, including human plasma, and revealed promise in non-viral gene delivery and mitochondrial-targeted gene therapy.

These studies provide novel and effective strategies to advance mitochondrial-targeted therapeutics, utilizing polypeptide-based nanocarriers with inherent mitochondrial tropism, functionalizing them with specific targeting moieties, incorporating light-responsive features, and designing multifunctional systems for mitochondrial targeting and non-viral gene therapy. These findings contribute to the growing field of precision nanomedicine, offering promising platforms for advanced cancer therapies with potential applications in multimodal therapeutic strategies and the hope of advancing to preclinical/clinical settings.

RESUMEN

La disfunción de la mitocondria – orgánulo clave involucrado en la producción de energía celular, la apoptosis y el metabolismo celular – representa una característica distintiva en enfermedades como el cáncer. Por este motivo, el uso de estrategias terapéuticas dirigidas a mitocondria representa un enfoque prometedor para mejorar la precisión terapéutica, especialmente en tratamientos contra el cáncer, donde esta disfuncionalidad favorece el crecimiento tumoral, la supervivencia y la resistencia a la terapia. Es importante destacar que conseguir un transporte de fármacos eficiente y específico a las mitocondrias constituye un desafío significativo en el desarrollo de terapias anticancerígenas avanzadas.

Presentada como un compendio de artículos científicos, esta tesis doctoral se centra en el diseño racional de terapias poliméricas dirigidas a mitocondria. En particular, hemos seleccionado nanotransportadores basados en polipéptidos debido a su biodegradabilidad y versatilidad, así como su capacidad de ser diseñados para fines específicos. Diseñamos estos nanotransportadores para promover un transporte mitocondrial eficiente, abordar desafíos críticos en la internalización celular y la especificidad del objetivo, e integrarlos en sistemas avanzados de transporte de fármacos y nanoterapias multimodales. Esta investigación demuestra el potencial de estas plataformas dirigidas a mitocondria en el tratamiento de cánceres agresivos, como el cáncer de mama triple negativo (TNBC, por sus siglas en inglés), el cual se ha utilizado en esta tesis como nuestro sistema modelo. Para proporcionar una visión integral de los desafíos y avances recientes en el transporte a mitocondria con aplicaciones terapéuticas en nanomedicina, publicamos una revisión que se incluye como anexo en la introducción de esta tesis.

El primer artículo describe copolímeros dibloque de poli-L-ornitina–poli-L-prolina (PLO_n-PLP_m) diseñados para dirigirse a las mitocondrias. Estos nanotransportadores basados en polipéptidos superaron las limitaciones asociadas con las estrategias tradicionales de direccionamiento mitocondrial al utilizar un mecanismo de internalización celular independiente de la energía (evitando las vías endosomales) y permitir una acumulación mitocondrial eficiente incluso en condiciones de despolarización de la membrana. A una relación específica de n:m (1:3), estos nanotransportadores polipeptídicos – denominados oligómeros penetrantes de células dirigidos a mitocondrias (mt-CPOs) – indujeron disfunción mitocondrial (incluyendo despolarización mitocondrial, generación de especies reactivas de oxígeno y alteración de la fosforilación oxidativa) y efectos antitumorales significativos en células TNBC MDA-MB-231 a concentraciones sub-IC_{50}

(>IC_{15}). Estudios físicos realizados en modelos de membranas, incluyendo vesículas unilamelares pequeñas y mitoplastos, desvelaron y validaron las interacciones específicas con la cardiolipina, revelando la remodelación localizada de la membrana y la formación de parches, cruciales para una especificidad a mitocondria eficiente. Además, la funcionalización de ácido poliglutámico (PGA) con PLO_6-PLP_{22} demostró el potencial traslacional de los mt-CPOs, resaltando su versatilidad como componentes de sistemas de administración de fármacos a concentraciones sub-IC_{15}. La conjugación de los fármacos a Lonidamina y succinato de α-tocoferol, seleccionados por sus mecanismos de acción dependientes de la mitocondria, a PLO_6- PLP_{22} mantuvo la especificidad mitocondrial y mejoró la actividad antitumoral sinérgica en células MDA-MB-231.

En el segundo artículo, se ha extendido la aplicación de los nanotransportadores polipeptídicos dirigidos a mitocondria al conjugarlos con motores moleculares (MMs) fotoactivados en un nanotransportador, PLO6-PLP22, previamente funcionalizado con PGA (P). Los conjugados P-MM conservaron la capacidad de rotación y la reorganización supramolecular inducida por la luz, facilitando la transición de estructuras micelares a ensamblajes elongados tipo gusano. Estos cambios estructurales mejoraron la captación celular mientras se preservaba la localización mitocondrial en células MDA-MB-231, mostrando una correlación directa entre las modificaciones estructurales inducidas por la luz y el mejor desempeño biológico. La incorporación de un transportador PGA aseguró una citotoxicidad mínima, mejorando la biocompatibilidad y eficacia biológica de los MMs.

Por último, el tercer artículo presenta C-TRV3-A, un nanoconjugado polipeptídico que integra la orientación mitocondrial con la capacidad de transfección génica, utilizándose como vector no viral. C-TRV3-A está compuesto por una estructura de poli-L-ornitina funcionalizada y TRV3 conjugado mediante un enlace disulfuro sensible al entorno redox. TRV3 está formado por tres componentes: trifenílfosfonio para la orientación mitocondrial, una sondafluorescente, Cy5, como fármaco modelo y otra sonda, Atto488, para imagen. Este diseño multifuncional permitió una localización mitocondrial eficiente tras el escape endosomal y la liberación selectiva de TRV3 en ambientes reductores, optimizando su tráfico dentro de células TNBC. La evaluación in vitro de poliplejos formados por C-TRV3-A , ADN plasmídico-Luciferasa y un polipéptido polianiónico (VLC-3), demostró una elevada eficiencia de transfección tanto en cultivos convencionales 2D en monocapa como en cultivos avanzados 3D de esferoides TNBC con una citotoxicidad mínima. Los poliplejos basados en C-TRV3-A también mostraron estabilidad en medios biológicos complejos,

incluyendo plasma humano, y demostraron su potencial como vectores no virales con aplicación en terapia génica dirigida a mitocondria.

Estos estudios proporcionan estrategias novedosas y efectivas para el desarrollo de terapias dirigidas a mitocondria, utilizando nanotransportadores polipeptídicos con tropismo mitocondrial inherente, funcionalizándolos con elementos de direccionamiento específicos, incorporando características fotoactivas y diseñando sistemas multifuncionales para un transporte específico a mitocondria incluyendo la capacidad de actuar como vector no viral. Estos hallazgos contribuyen al campo emergente de la nanomedicina de precisión, ofreciendo plataformas prometedoras para terapias avanzadas contra el cáncer, con aplicaciones potenciales en estrategias terapéuticas multimodales y la posibilidad de avanzar hacia estudios preclínicos e incluso clínicos.

1 GENERAL INTRODUCTION

This general introduction serves to provide additional context and an overview that complements the review titled "*Unlocking the Mitochondria for Nanomedicine-based Treatments: Overcoming Biological Barriers, Improving Designs, and Selecting Verification Techniques*," authored by Pegoraro et al. and published in Advanced Drug Delivery Reviews[1]. Attached as an Annex in Section 1.4, this review comprehensively examines the challenges and advancements in targeting mitochondria for therapeutic purposes using nanomedicine.

In this introduction, I aim to outline and update the key themes and findings discussed in the review, emphasizing the significance of mitochondrial biology in nanomedicine. By providing this additional context, I hope to enhance the reader's understanding of the complexities of mitochondrial targeting and the innovative strategies proposed to overcome existing barriers.

1.1 Mitochondrial Biology and Structure

Mitochondria are highly dynamic, multifunctional organelles that play essential roles in cellular bioenergetics and homeostasis. Mitochondria are the primary site of adenosine triphosphate (ATP) synthesis, functioning as critical regulators of cellular signaling, biosynthetic pathways, and overall cellular maintenance[2] (**Figure 1.1**). The presence of circular mitochondrial DNA (mtDNA), which highlights their endosymbiotic origin and allows for the synthesis of essential proteins within the mitochondrial matrix[3], represents a defining feature of mitochondria.

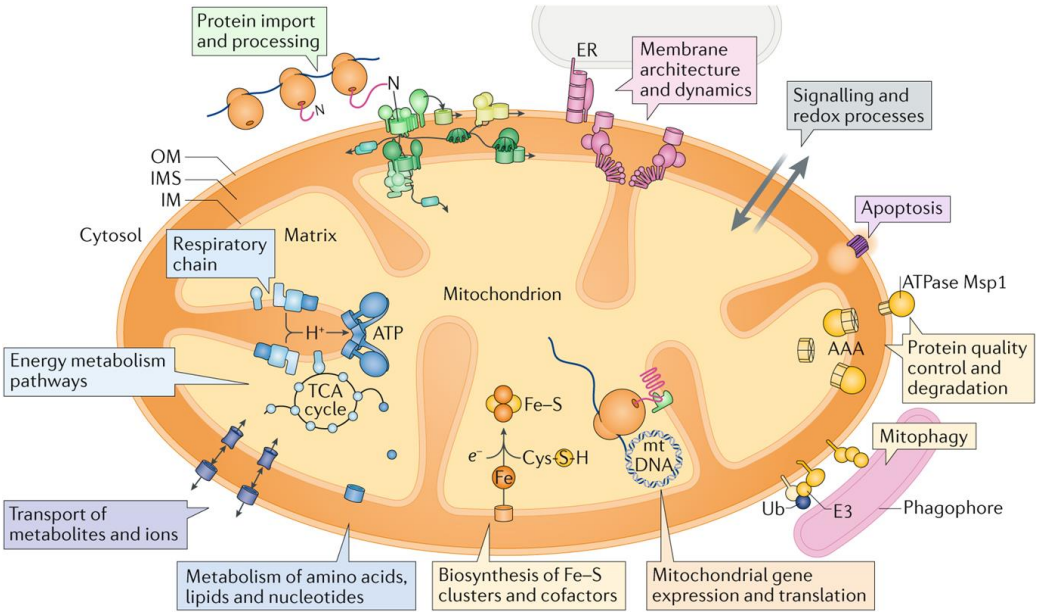


Figure 1.1. An Overview of Mitochondrial Function. The mitochondrion demonstrates multiple essential roles: energy metabolism via pathways such as the tricarboxylic acid (TCA) cycle, transport of metabolites and ions, biosynthesis of amino acids, lipids, and nucleotides, and iron-sulfur (Fe-S) cluster formation. Other critical processes include mitochondrial gene expression, protein import and processing, interactions with the endoplasmic reticulum (ER), membrane architecture and dynamics, and pathways related to mitophagy, apoptosis, and protein quality control, which involves Ubiquitin (Ub), Mitochondrial Sorting Protein 1 (Msp1), and ATPases associated with diverse cellular activities (AAA). Mitochondrial DNA (mtDNA) is present in the matrix. OM: Outer membrane; IMS: intermembrane space; IM: Inner membrane. Sections 1.1.1-1.1.5 describe these features (Reproduced from Pfanner et al.[4])

The mitochondrial matrix represents the site where critical metabolic processes occur, including the tricarboxylic acid (TCA) cycle, mtDNA replication, and mitochondrial protein synthesis. These processes occur in space enclosed by a dual-membrane system comprised of the outer mitochondrial membrane (OMM) and the inner mitochondrial membrane (IMM)[5] (**Figure 1.2**). The OMM functions as a selective barrier that mediates interactions between mitochondria and the cytosol while facilitating signaling processes that extend beyond the mitochondrion[6]. The lipid composition of the OMM resembles that of eukaryotic plasma membranes, allowing for the passage of ions and small molecules (less than 6 kDa) through voltage-dependent anion channels (VDACs)

and protein import pores formed by the translocase of the OMM complex (TOM complex) and the sorting and assembly machinery complex[7–9].

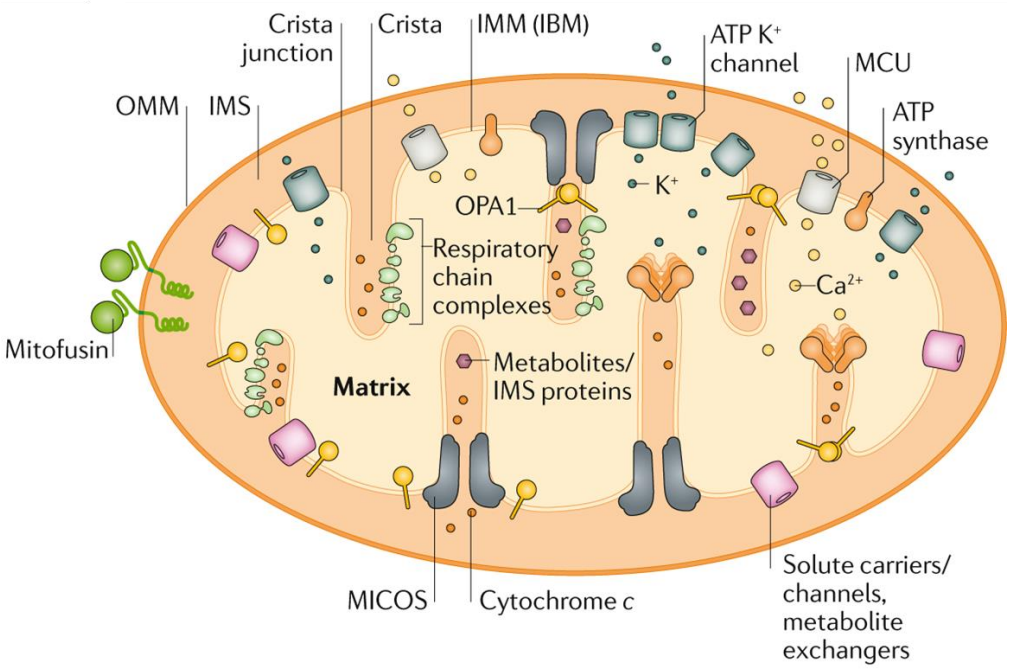


Figure 1.2. The structure and components of the mitochondria. A schematic illustration of mitochondrial structure: two membranes enclosing the matrix. The outer mitochondrial membrane (OMM) acts as a diffusion barrier and mediates signal transduction, while the inner mitochondrial membrane (IMM) includes the inner boundary membrane (IBM) and mitochondrial cristae. The IBM contains transport channels for metabolites and ions, such as the mitochondrial calcium uniporter (MCU), whereas cristae are invaginations that facilitate oxidative phosphorylation and mitochondrial DNA maintenance. Cristae junctions connect to the IBM, preventing content leakage into the intermembrane space (IMS). Cristae formation is regulated by proteins such as the mitochondrial contact site and cristae organizing system (MICOS) and optic atrophy type 1 (OPA1), which maintain structural integrity and facilitate ATP synthase organization. Mitofusins and cytochrome c, essential components for the mitochondrial dynamics and apoptosis, will be discussed in section 1.1.2. (Reproduced from Giacomello et al.[2])

Recent advances in imaging have revealed how OMM-associated proteins interact with other organelles, such as the endoplasmic reticulum (ER), to form mitochondria-associated membranes (MAMs). These contact sites remain crucial for calcium signaling and lipid transfer, which are essential to energy balance maintenance and cellular homeostasis.

In contrast, the IMM is organized into two specialized subdomains: the inner boundary membrane (IBM) and the cristae[3]. The IBM aligns parallel to the OMM and supports the exchange of ions, ATP, adenosine diphosphate (ADP), and small metabolites between the cytosol and mitochondrial matrix through various transport channels. These include the translocase of the inner membrane (TIM) complex, the adenine nucleotide translocator (ANT), and the mitochondrial calcium uniporter (MCU)[2]. Cristae - folded structures within the IMM – are critical for energy production; they house respiratory chain complexes and ATP synthase and support optimized

oxidative phosphorylation (OXPHOS). Cryo-electron tomography studies have provided high-resolution images illustrating how the IMM's structure facilitates these processes by supporting the precise organization of ATP synthase dimers, enhancing proton efficiency and production[10,11].

Cristae junctions—narrow clefts connecting cristae to the IBM—maintain compartmentalization within cristae, preventing diffusion into the intermembrane space (IMS)[12]. The integrity and organization of cristae are dynamically regulated in response to various signals, including energy demands and apoptotic cues. Key membrane-shaping protein complexes, such as the mitochondrial contact site and cristae organizing system (MICOS) and fusion protein optic atrophy type 1 (OPA1), play vital roles in mediating structural interactions between the IMM and OMM[13].

The IMM differs from the OMM in permeability, shape, protein-to-lipid ratio (higher in proteins), and lipid composition[14]. The IMM is particularly rich in cardiolipin (CL), a unique phospholipid synthesized within mitochondria that constitutes 15-20% of total mitochondrial phospholipids[15]. CL has a distinctive conical shape characterized by a double glycerophosphate backbone with three glycerol moieties and four fatty acyl chains, rather than the typical two fatty acyl side chains found in most phospholipids[16]. This unique structure allows CL to exert lateral pressure within the membrane, promoting negative curvature that favors non-bilayer structures such as hexagonal phases, thereby facilitating cristae formation[17].

The intricate structure of mitochondria supports organization but directly influences their multifaceted functions. The extensive surface area provided by cristae enhances ATP synthesis through OXPHOS by accommodating high densities of ATP synthase complexes[18]. Furthermore, specific transport channels within both membranes facilitate critical metabolic exchanges necessary for maintaining cellular energy balance. The following sections will explore how these structural features enable mitochondria to perform essential roles in energy production, calcium signaling, apoptosis regulation, and overall cellular homeostasis.

1.1.1 Mitochondrial Bioenergetics

Mitochondria are commonly known as the “powerhouse of the cell” due to their role in energy production. The conversion of ATP to ADP represents the primary source of cellular energy. Cells must utilize nutrients to regenerate ATP molecules to sustain energy production[19] (**Figure 1.3**).

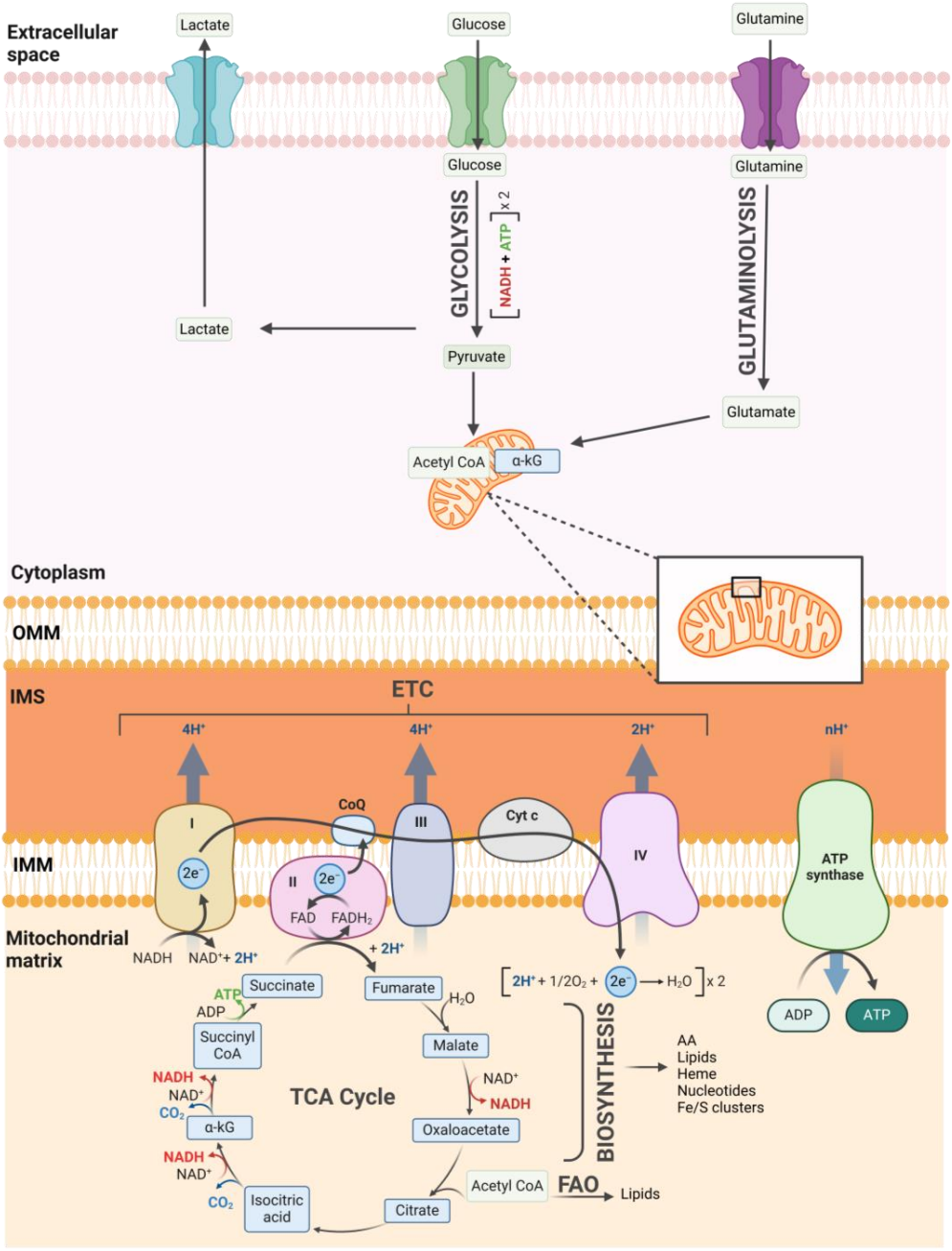


Figure 1.3. Mitochondrial bioenergetics. Schematic representation of mitochondrial bioenergetics and its integration with cellular metabolism. Glucose is transported into the cell via glucose transporters (green, GLUTs) and metabolized through glycolysis to generate pyruvate. Pyruvate is either exported as lactate through monocarboxylate transporters (blue, MCTs) or imported into mitochondria via the mitochondrial pyruvate carrier (MPC) for conversion to acetyl-CoA. Glutamine, imported via the solute carrier family 1 member 5 (purple, SLC1A5) transporter, undergoes glutaminolysis to form glutamate, which enters the tricarboxylic acid (TCA) cycle as α-ketoglutarate (α-KG). Within the mitochondrial matrix, the TCA cycle produces reduced nicotinamide adenine dinucleotide (NADH) and reduced flavin adenine dinucleotide ($FADH_2$), which transfer electrons to the electron transport chain (ETC) located in the inner mitochondrial membrane (IMM). Electron transfer through complexes I-IV drives proton (H^+) translocation into the intermembrane space (IMS), generating a proton motive force that powers ATP synthesis via the F1F0 ATP synthase. Fatty acid oxidation (FAO) provides additional acetyl-CoA for the TCA cycle, linking lipid metabolism to mitochondrial bioenergetics. Mitochondria also supports biosynthetic pathways, including the production of amino acids, lipids, heme, nucleotides, and iron-sulfur (Fe/S) clusters, highlighting their essential role in energy metabolism and cellular homeostasis. *Figure created with Biorender.*

The energy production process begins with glycolysis, which occurs in the cytosol and does not require oxygen. One glucose molecule becomes metabolized into two pyruvate molecules during glycolysis, yielding a net gain of two ATP molecules[20]. Pyruvate then enters the mitochondria through the mitochondrial pyruvate carrier (MPC), where it undergoes decarboxylation and oxidation by pyruvate dehydrogenase (PDH) to form acetyl-CoA[21]. Recent studies have explored how regulatory mechanisms such as phosphorylation control PDH activity, linking it to the cell's metabolic state and demands[22]. Subsequently, acetyl-CoA enters the TCA cycle in the mitochondrial matrix in a process that requires oxygen, comprising a series of enzymatic reactions that generate three molecules of reduced nicotinamide adenine dinucleotide (NADH), one molecule of reduced flavin adenine dinucleotide ($FADH_2$), and one molecule of guanosine triphosphate per cycle[23]. The production of two acetyl-CoA molecules for each glucose molecule leads to the release of carbon dioxide and the generation of electron carriers (NADH and $FADH_2$), which remain crucial for oxidative phosphorylation, donating electrons to the electron transport chain (ETC)[23]. NADH and $FADH_2$ molecules are oxidized by complex I (CI) and complex II (CII), transferred to coenzyme ubiquinone (Q), followed by complex III (CIII), cytochrome c, and complex IV (CIV). This process transfers electrons to molecular oxygen, facilitating ATP synthesis via ATP synthase (complex V). Mitochondria exploit this electrochemical gradient to pump protons from the matrix to the IMS, with complex V (CV) using this generated proton motive force to produce ATP coupled to water generation[24]. The complete oxidation of one glucose molecule can yield 30 ATP molecules. The proton gradient established during respiration powers ATP synthase leads to higher proton concentrations (pH 6.8–7.4) in the IMS than in the mitochondrial matrix (pH 7.5–8.2)[25] and a highly negative polarized (approximately ranging from - 108 to - 180 mV) IMM. The resulting charge difference is known as the mitochondrial membrane potential (MMP)[26].

Evaluating mitochondrial bioenergetics typically involves measuring specific parameters, such as basal respiration - the oxygen consumption rate (OCR) necessary for the maintenance of basic ATP production under standard conditions. ATP-coupled respiration measures the fraction of OCR directly utilized for ATP synthesis, offering insights into the efficiency of OXPHOS. The spare respiratory capacity (SRC) reflects the difference between basal and maximum respiration rates, highlighting the mitochondria's ability to meet increased energy demands or stress, indicating metabolic flexibility and resilience. Proton leak, where protons re-enter the mitochondrial matrix without contributing to ATP synthesis, represents a critical metric that impacts mitochondrial efficiency and regulates heat production and reactive oxygen species (ROS) generation[27,28].

The ETC inherently produces unpaired electrons through complexes I, II, and III, which subsequently interact with oxygen to generate ROS within the IMM. The superoxide anion represents the predominant ROS in mitochondria and reacts with protons to yield hydrogen peroxide or hydroxyl radicals[29]. Mitochondria serve as the primary source of ROS in cells, which can function as signaling molecules at lower concentrations; for example, ROS activate transcription factors such as nuclear factor-κB (NF-κB) and hypoxia-inducible factor-1α (HIF-1α) to drive cellular responses to oxidative stress and hypoxia, highlighting the mitochondria's role in sensing and responding to environmental changes[30]. Recent evidence suggests that controlled ROS production plays a role in adaptive responses, such as increasing mitochondrial biogenesis and resilience, in scenarios like endurance training and metabolic stress[31].

Cristae shape and dynamics remain vital for mitochondrial bioenergetics, particularly in regulating OXPHOS efficiency. Cristae curvature affects the ETC complex and ATP synthase distribution; ETC complexes primarily reside in regions displaying low curvature, while ATP synthase displays enrichment in regions displaying high curvature[32]. This spatial organization supports optimal ATP production, especially in energy-demanding tissues like the heart and skeletal muscle with greater cristae curvature. Changes in cristae morphology can impact the assembly and stability of respiratory supercomplexes[33], which are essential for efficient electron transfer. For example, cristae widening can destabilize respiratory supercomplexes and reduce OXPHOS efficiency[34]. Proteins such as OPA1 maintain cristae structure by regulating junctions and supporting ATP synthase organization[35]. Additionally, alterations in cristae morphology can influence mitochondrial ROS production, impacting cellular signaling related to energy metabolism[36]. CL, enriched in the highly curved and negative cristae regions, also plays a crucial role in preserving the integrity of the MICOS complex and stabilizing ATP synthase dimerization and functionality[37–39].

1.1.2 Mitochondrial Functions Beyond Energy Production

Mitochondrial dynamics, encompassing fusion and fission, further complement cristae structure in maintaining mitochondrial function and cellular homeostasis[2]. Mitochondrial fusion, driven by the coordinated actions of the OMM GTPases Mitofusin 1 and 2 (Mfn1/Mfn2) and OPA1 in the IMM, allows mitochondria to merge and exchange contents[40]. This process remains critical for maintaining mitochondrial integrity by diluting damaged components, distributing mtDNA evenly, and ensuring a homogenous population of functional mitochondria. Fusion also synergizes with cristae remodeling by OPA1, enhancing respiratory efficiency under increased energy demands

and providing a rapid adaptive response to fluctuating cellular conditions[41]. Conversely, mitochondrial fission, predominantly regulated by dynamin-like protein (Drp1), segments mitochondria, allowing the isolation of damaged or dysfunctional parts. This process remains essential for quality control by facilitating the selective autophagic removal of defective mitochondria through mitophagy[40]. The combination of fission and subsequent mitophagy prevents the accumulation of damaged mitochondria, which could otherwise disrupt cristae organization, prompt excessive ROS production, and impair cellular signaling pathways related to energy homeostasis[42]. Notably, PTEN-induced kinase 1 (PINK1) and RBR E3 ubiquitin-protein ligase (Parkin) play crucial roles in tagging damaged mitochondria for mitophagy by promoting the ubiquitination of outer membrane proteins, signaling their sequestration by autophagosomes[41,42].

Beyond their role in dynamics and quality control, mitochondria play an integral role in the biosynthesis of essential cellular building blocks. The involvement of mitochondria in the synthesis of purine nucleotides, amino acids, glucose, heme, urea, fatty acids, and cholesterol underscores their multifunctional nature[43]. Fatty acid β-oxidation (FAO) within the mitochondrial matrix generates acetyl-CoA, a critical metabolite that feeds into the TCA cycle[44]. This cycle produces NADH and $FADH_2$, yielding intermediates such as citrate, α-ketoglutarate, succinyl-CoA, fumarate, and malate[23]. These intermediates extend mitochondrial influence beyond ATP production by contributing to biosynthetic pathways and metabolic signaling. For example, α-ketoglutarate participates in amino acid synthesis and functions as a cofactor in dioxygenase reactions that modulate gene activity[45]. Succinate can inhibit prolyl hydroxylases from stabilizing HIF-1α under normoxic conditions, promoting angiogenesis and metabolic adaptation[45]. Additionally, pyruvate from glycolysis enters the mitochondria and becomes converted to acetyl-CoA or utilized in gluconeogenesis, thereby linking glycolytic and mitochondrial metabolism[46]. Mitochondria synthesize heme by converting glycine and succinyl-CoA into 5-aminolevulinic acid as the first step in heme production, which remains crucial for hemoproteins such as cytochromes[47]. Mitochondria also assemble iron-sulfur (Fe/S) clusters, essential for the function of enzymes in the ETC and DNA repair[48]. The production of acetyl-CoA also connects mitochondrial metabolism to nuclear gene regulation through histone acetylation. Acetyl-CoA availability directly influences histone acetylation, modulating chromatin structure and gene expression[49], which establishes a connection between mitochondrial metabolic state and nuclear transcriptional control, demonstrating the organelle's role as a bridge between cellular energy metabolism and epigenetic regulation.

Mitochondria also serve as regulatory hubs for apoptotic pathways, facilitated by releasing cytochrome c from the IMS into the cytosol, which initiates caspase-dependent apoptosis[50]. Mitochondrial outer membrane permeabilization (MOMP), mediated by the pro-apoptotic Bcl-2-associated protein X (Bax) and homologous antagonist/killer (Bak)[51], enables the release of apoptogenic factors via the opening of the mitochondrial permeability transition pore (mPTP)[52,53]. ROS can activate transcription factors such as NF-κB[54], which drive cellular responses to oxidative stress, including the activation of apoptotic pathways.

Mitochondria represent essential regulators of intracellular calcium (Ca^{2+}) signaling, playing a crucial role in cellular metabolism and homeostasis[55]. Under resting conditions, mitochondrial Ca^{2+} concentrations remain similar to the cytosol (100–200 nM); however, during stimulation with Ca^{2+}-modulating agents, mitochondria accumulate Ca^{2+} levels 10- to 20-fold higher than the cytosol[56]. Ca^{2+} uptake occurs through OMM VDACs facilitated by the IMM MCU. The electrochemical gradient established by the MMP provides the driving force for Ca^{2+} uptake. Ca^{2+} stimulates critical metabolic enzymes in ATP production once inside the matrix, linking Ca^{2+} signaling to energy metabolism[56,57]. The proximity of mitochondria to the ER further enhances Ca^{2+} transfer efficiency, reinforcing the role of MAMs in rapid signaling[58]. Mitochondria also buffer excess cytosolic Ca^{2+} through a complex system of antiporters, which extrude Ca^{2+} back into the cytosol to maintain cellular homeostasis. Of note, excessive mitochondrial Ca^{2+} influx can increase ROS production and may trigger apoptotic pathways via the mPTP[59], underscoring the importance of tight regulation for cellular function and survival.

1.1.3 Mitochondrial Genetics and Primary Mitochondrial Diseases

The circular mitochondrial genome, discovered in 1963, evolved from formerly free-living prokaryotes according to the endosymbiotic theory[60]. mtDNA is physically distinct from nuclear DNA (nDNA), exhibits specific modes of regulation concerning copy number, replication, transcription, and translation, and is inherited exclusively from the mother. Human spermatozoa lack functional mtDNA due to mechanisms such as mitophagy and ubiquitination that prevent paternal transmission. 95% of human mtDNA encodes 13 proteins, 22 transfer RNAs (tRNAs), and 2 ribosomal RNAs (rRNAs) essential for OXPHOS and production ATP production[61]; however, nuclear genes encode most mitochondrial proteins— around 1,500 distinct types[62]. These proteins contain mitochondrial targeting sequences (MTSs), short peptide motifs typically located at their N-termini characterized by their hydrophobic nature and positive charge, allowing them to interact effectively

with the mitochondrial import machinery[63]. Upon entering the mitochondrial environment, MTSs adopt an alpha-helical conformation crucial for recognition by the TOM complex[64], which itself facilitates the initial import of precursor proteins into the IMS. Following this step, the TIM complex mediates the translocation of proteins into the mitochondrial matrix or the insertion into the IMM[65]. After import, MTSs undergo cleavage by mitochondrial processing peptidases, allowing for proper protein folding and function. The approximately 16.5 kilobase-long mitochondrial genome varies significantly in copy number across different cell types—ranging from over 100,000 copies in mature oocytes to none in erythrocytes[66]. This variability leads to heteroplasmy, where genetic variants exist at different frequencies within individual cells and even within single mitochondria[67]. Over time, common groups of germline mtDNA variations, known as mtDNA haplotypes, have evolved through gradual mutations in matrilineal lineages[68]. These haplotypes are instrumental in tracing human migrations and may influence disease risk and severity[69]. The high mutation rate of mtDNA contributes to this influence by inducing functional impairments in mitochondrial processes (particularly OXPHOS), which can compromise cellular energy production[70]. Moreover, mtDNA copy number variability can exacerbate the effects of pathogenic mutations[71]. The non-Mendelian inheritance of mtDNA results in maternal lineage-specific diseases that may present variably among siblings due to differences in heteroplasmy levels[72]. Emerging research strategies have focused on capturing mitochondrial genetic variation at the single-cell level to address these complexities[66].

Primary mitochondrial diseases (PMDs) represent a diverse and genetically intricate group of multisystem disorders that arise from impaired mitochondrial function due to mutations in mtDNA/nDNA[73]. Said mutations can disrupt genes encoding essential components, including proteins involved in mitochondrial transport, metabolic enzymes, assembly factors, signaling pathways, and those critical for mitochondrial fusion and fission. PMDs may also originate from mutations in genes coding for structural RNAs, such as tRNAs and rRNAs, or those impacting non-coding regions, such as the mtDNA D-loop, which plays a crucial role in regulating mtDNA replication and transcription. The impairment of OXPHOS represents a central feature of mitochondrial diseases[74]. Clinically, PMDs manifest across various tissues, with the most significant impact observed in organs with high energy demands, such as the brain, heart, and skeletal muscles[75]. Prominent examples include mitochondrial encephalomyopathy with lactic acidosis and stroke-like episodes (MELAS), characterized by stroke-like episodes, seizures, and lactic acidosis due to a mutation in the mitochondrially encoded tRNA-Leu (UUA/G) (*MT-TL1)* gene[76], and Leigh Syndrome, a severe neurodegenerative disorder defined by bilateral lesions in the brainstem and basal ganglia,

resulting in progressive neurological decline[77]. Classifying mitochondrial disorders into PMDs, which stem from germline mutations in mtDNA/nDNA, and secondary mitochondrial diseases (SMDs), where external factors disrupt mitochondrial function without direct genetic mutations, remains essential to delineate their pathophysiology[73]. This distinction enhances our understanding of the diverse mechanisms underlying mitochondrial dysfunction and supports the development of targeted diagnostic and therapeutic strategies, facilitating a more comprehensive approach to managing these complex disorders.

1.1.4 Mitochondrial Dysfunction in Secondary Mitochondrial Disease

SMDs encompass a variety of disorders characterized by mitochondrial dysfunction resulting from external stressors, such as environmental toxins, chronic inflammation, and metabolic imbalances[78]. SMDs can also arise from systemic conditions—health issues that affect the entire body but do not primarily involve mitochondrial dysfunction. In these cases, primary disease processes induce mitochondrial impairment as a secondary effect[79]. This dual role of mitochondrial dysfunction—acting as a consequence of other pathologies and contributing to disease progression—distinguishes SMDs from PMDs, which are exclusively caused by genetic mutations in mtDNA/nDNA[78]. Although the specific molecular mechanisms involved may vary according to the disease context, common mitochondrial functions and behavior observed across these conditions include impaired bioenergetics, reduced mitochondrial biogenesis, increased oxidative stress, reduced mitochondrial biogenesis, disrupted Ca^{2+} homeostasis, and alterations in mitochondrial dynamics along with quality control processes[80,81].

The pathophysiology of SMDs —such as in neurodegenerative disorders, cardiovascular and kidney diseases, metabolic disorders, and cancer—is thus multifactorial, with mitochondrial dysfunctions playing a central role. In **Table 1.1**, examples of SMDs and related mitochondrial dysfunctions are detailed.

Table 1.1. Examples of Secondary Mitochondrial Diseases and Associated Mitochondrial Dysfunctions

Disease/Condition	Mitochondrial Dysfunction(s)	Key Mitochondrial Pathway or Component Affected	Pathophysiology and Clinical Relevance	Ref.
Ischemia-Reperfusion Injury	Excessive ROS production, Ca^{2+} influx, mPTP opening	OXPHOS, MMP	Reperfusion causes a surge in ROS and Ca^{2+}, leading to mPTP opening, ATP depletion, and necrotic cell death, contributing to tissue damage and organ dysfunction	82,83
Heart Failure	Hypoxia, metabolic switch to glycolysis, impaired OXPHOS	HIF-1α, ATP synthesis, mitochondrial biogenesis	Chronic hypoxia leads to HIF-1α accumulation, reduced OXPHOS, and glycolysis dependency, thereby impairing myocardial efficiency and contractile function and worsening heart failure	84,85
Alzheimer's Disease	Impaired OXPHOS, excessive ROS production, mtDNA damage	Mitochondrial dynamics, mitophagy, ETC complex I-IV	Oxidative stress, mtDNA mutations, and impaired mitophagy lead to neuroinflammation, damaged mitochondria accumulation, and neuronal death, accelerating cognitive decline	86–88
Parkinson's Disease	Reduced complex I activity, ROS-induced oxidative stress, disrupted mitophagy	ETC Complex I, PINK1/Parkin pathway	Dysfunctional mitophagy due to PINK1/Parkin pathway impairment causes accumulation of damaged mitochondria, ROS production, and dopaminergic neuronal loss	89,90
Diabetic Nephropathy	Reduced mitochondrial biogenesis, increased ROS production, and altered Ca^{2+} handling	PGC-1α, ATP synthesis, MCU	Hyperglycemia upregulates ROS, reduces PGC-1α expression, disrupts Ca^{2+} handling, and leads to mitochondrial damage, promoting renal injury	91,92
Chronic Obstructive Pulmonary Disease	Impaired OXPHOS, increased mitochondrial ROS, dysregulated mitophagy	Respiratory chain complexes, PINK1/Parkin pathway	Oxidative stress impairs OXPHOS and increases ROS, contributing to lung tissue damage, inflammation, and emphysema	93,94
Obesity	Altered mitochondrial biogenesis, impaired FAO, increased ROS	PGC-1α, FAO, ATP synthase	Excess nutrients overwhelm FAO capacity, causing lipid accumulation and oxidative stress in adipose tissue and liver, contributing to metabolic syndrome	95,96
Amyotrophic Lateral Sclerosis	Impaired mitochondrial trafficking, increased ROS, disrupted ATP production	Mitochondrial motor proteins (e.g., kinesin), ETC complexes	Mitochondrial mislocalization and oxidative stress impair ATP supply to neurons, leading to motor neuron degeneration and muscle weakness.	97,98
Non-Alcoholic Fatty Liver Disease	Impaired FAO, oxidative stress, mtDNA mutations	FAO enzymes, ETC complexes, mtDNA repair enzymes	Excessive fat intake overwhelms mitochondrial FAO capacity, leading to ROS accumulation, mtDNA damage, and hepatic inflammation	99,100

Disease/Condition	Mitochondrial Dysfunction(s)	Key Mitochondrial Pathway or Component Affected	Pathophysiology and Clinical Relevance	Ref.
Huntington's Disease	Defective mitophagy, altered Ca^{2+} handling, mitochondrial fragmentation	PINK1/Parkin pathway, MCU, Drp1-mediated fission	Mutant huntingtin protein disrupts Ca^{2+} homeostasis and mitophagy, leading to mitochondrial fragmentation, ROS production, and neuronal death	101
Fibromyalgia	Impaired ATP production, oxidative stress, increased apoptosis	ETC complexes, ATP synthase, Bcl-2 family	Mitochondrial dysfunction and oxidative stress contribute to chronic fatigue and muscle pain, with increased apoptosis observed in muscle biopsies	102
Chronic Kidney Disease	Impaired mitochondrial dynamics, oxidative stress, mtDNA damage	mPTP, mitochondrial fusion/fission	Increased mPTP opening, ROS-induced lipid peroxidation, and mtDNA damage reduced ATP generation, leading to cell injury, nephron damage, and fibrosis	103
Cancer	Warburg effect, metabolic plasticity, apoptotic resistance	AKT/mTOR pathway, Bcl-2 family proteins, MMP	Cancer cells alternate between glycolysis and OXPHOS, activate survival pathways, and suppress apoptosis, supporting growth and chemoresistance	104,105

ROS: Reactive oxygen species; mPTP: Mitochondrial permeability transition pore; OXPHOS: Oxidative phosphorylation; MMP: Mitochondrial membrane potential; ATP: Adenosine triphosphate; HIF-1α: Hypoxia-inducible factor-1α; mtDNA: Mitochondrial DNA; ETC: Electron transport chain; PINK1: PTEN-induced kinase 1; Parkin: RBR E3 ubiquitin-protein ligase; PGC-1α: Peroxisome Proliferator-Activated Receptor Gamma Coactivator 1α; MCU: Mitochondrial calcium uniporter; FAO: Fatty acid oxidation; Drp1: Dynamin-like protein; AKT: Protein Kinase B; mTOR: mammalian target of rapamycin.

Generally, impaired OXPHOS serves as a core feature, leading to decreased ATP synthesis and elevated ROS production. Under normal conditions, mitochondrial antioxidant defenses—both enzymatic (e.g., superoxide dismutase, catalase, glutathione reductase, and glutathione peroxidase and non-enzymatic (e.g., vitamin E, vitamin C, glutathione (GSH), carotenoids, and flavonoids)—control ROS levels to prevent oxidative damage[81]. However, non-scavenged ROS can cause oxidative damage to critical mitochondrial components, including proteins, lipids, and mtDNA, when antioxidant defenses become overwhelmed, creating a vicious cycle of mitochondrial and cellular dysfunction[106]. Excessive ROS production represents a hallmark across SMDs. The sudden reintroduction of oxygen after hypoxia triggers a surge in ROS and Ca^{2+} influx in ischemia-reperfusion injury[82]. This cascading effect opens the mPTP, leading to loss of MMP, ATP depletion, and, ultimately, cell death, which significantly contributes to tissue/organ damage[83]. Hypoxia represents another common feature in SMDs. In cardiovascular diseases (e.g., heart failure), hypoxia leads to HIF-1α accumulation, which prompts the expression of genes that switch cardiomyocyte metabolism from OXPHOS to glycolysis, forcing cells to rely on anaerobic respiration. This metabolic shift disrupts MMP and depletes ATP, impairing contractile function. Switching to anaerobic glycolysis also results in cellular acidification thanks to the accumulation of protons. Cardiomyocyte damage has been linked to hypoxia severity; while HIF-1α protects against oxidative damage and promotes mitophagy in acute hypoxia, prolonged exposure increases ROS levels and cell death, which reduces cardiac efficiency[84]. In neurodegenerative diseases (e.g., Alzheimer's and Parkinson's disease), mitochondrial dysfunction manifests through compromised OXPHOS efficiency, excessive ROS production, and iron-induced lipid peroxidation[107]. Accumulation of damaged mitochondria—resulting from disrupted fission-fusion balance and defective mitophagy—further aggravates neuroinflammation and neuronal apoptosis, accelerating disease progression[108,109]. Impairing the PINK/Parkin-dependent or -independent mitophagy pathway represents a critical mechanism in Alzheimer's pathology[86]. In diabetic nephropathy, reduced mitochondrial biogenesis due to the downregulation of peroxisome proliferator-activated receptor gamma coactivator 1-alpha (PGC-1α), a crucial regulator of mitochondrial health, prompts mitochondrial dysfunction. Hyperglycemia contributes to this dysfunction by increasing ROS production and inhibiting PGC-1α expression, leading to diminished ATP synthesis and exacerbating the renal damage commonly associated with diabetic kidney disease[91].

In cancer biology, the role of mitochondrial dysfunction is particularly compelling and multifaceted[110]. Although cancer cells rely on glycolysis even in the presence of oxygen—a

phenomenon termed the Warburg effect[111,112]—recent studies revealed that the implication of metabolic reprogramming remains ununiform across cancer types. Many tumors exhibit metabolic plasticity, alternating between glycolysis and OXPHOS to adapt to fluctuating environmental/cellular conditions[113], which allows them to optimize energy production, enhance biosynthetic pathways, and sustain rapid proliferation[114]. Mitochondria remains essential for supporting these adaptive strategies undergoing significant changes in biogenesis, OXPHOS capacity, and dynamic behavior. The frequent upregulation of mitochondrial fission in cancer facilitates cell division by ensuring the distribution of mitochondria to daughter cells during mitosis. Proteins such as Drp1 regulate this process, with overexpression/overactivation linked to aggressive tumor behavior and poor prognosis in certain cancers[115]. Conversely, enhanced mitochondrial fusion can protect cancer cells from stress-induced mitochondrial damage, maintaining the MMP and promoting survival[116,117]. A critical aspect of mitochondrial reprogramming in cancer involves ROS generation. While excessive ROS can cause oxidative damage, moderate levels signal molecules to activate pro-survival/proliferative pathways[118,119]. Mitochondrial ROS activate AKT/mTOR (AKT: Protein Kinase B; mTOR: mammalian target of rapamycin) signaling to promote cell growth and survival[120]. Additionally, ROS stabilize HIF-1α to help tumor cells adapt to hypoxic conditions by inducing the expression of genes that support angiogenesis, glucose uptake, and glycolysis[121]. This dual role of ROS in cancer illustrates how mitochondrial dysfunction simultaneously supports cellular damage and tumor progression. Mitochondrial reprogramming is also linked to alterations in MMP and apoptotic resistance. In many cancers, the balance between pro-apoptotic and anti-apoptotic proteins at the mitochondrial membrane shifts to favor survival. The Bcl-2 family of proteins, including anti-apoptotic members like Bcl-2 and Bcl-xL, modulate MOMP to inhibit cytochrome c release and prevent apoptosis[122]. This mechanism provides cancer cells with a significant survival advantage, allowing them to evade programmed cell death under conditions that typically trigger apoptosis. Mitochondria also support cancer cell survival through MAMs, which facilitate interactions with the ER for Ca^{2+} signaling and lipid transfer. Altered MAMs in cancer can disrupt Ca^{2+} regulation, enhancing apoptotic resistance and metabolic flexibility[123].

Mitochondrial adaptations are especially pronounced in aggressive cancers such as triple-negative breast cancer (TNBC), where metabolic flexibility, apoptotic resistance, and ROS signaling enhance tumor invasiveness and treatment resistance[124–126]. Understanding these mitochondrial changes remains vital to the development of targeted therapies that disrupt cancer cell survival

pathways. The following section will explore mitochondrial mechanisms specific to TNBC, examining their roles in tumor growth and metastasis.

1.1.5 Mitochondrial Involvement in Triple-Negative Breast Cancer

Breast cancer - a heterogeneous group of diseases that involves malignant growth within breast tissue - carries a high potential for metastasis. Among molecular subtypes, the absence of estrogen, progesterone, and HER2 receptors distinguishes TNBC, making it challenging to treat due to the lack of targeted therapeutic options[127]. TNBC accounts for approximately 10-15% of all breast cancer cases and is known for its aggressive behavior, high recurrence rates, and poor prognosis[128]. This subtype predominantly affects younger women and is more prevalent in African American populations[129]. TNBC tumors often originate in the milk ducts and display a propensity for early and widespread metastasis, with frequent dissemination to the brain, liver, and lungs, where metastasis significantly diminishes patient survival outcomes[130]. Molecular profiling has revealed the non-uniform nature of TNBC; instead, this cancer type displays considerable heterogeneity, which has led to the classification of TNBC into six transcriptional subtypes: basal-like 1 (BL1), basal-like 2 (BL2), immunomodulatory (IM), luminal androgen receptor (LAR), mesenchymal (M), and mesenchymal stem-like (MSL)[131] (**Figure 1.4**). Each subtype exhibits unique pathway activations that reflect distinct biological behaviors and treatment responses. For example, the BL1 and BL2 subtypes associate with cell proliferation and DNA repair pathways, the IM subtype displays an enrichment in immune signaling pathways, and the M and MSL subtypes associate with epithelial-mesenchymal transition and cell motility. LAR subtypes are hormonally regulated, reflecting a reliance on androgen receptor signaling. EMT, in particular, becomes highly upregulated in TNBC compared to other breast cancer subtypes, facilitating cell detachment, motility, and invasion[132]. These characteristics enable TNBC cells to penetrate nearby tissues, intravasate into lymphatic and blood vessels, and establish secondary metastatic sites[133].

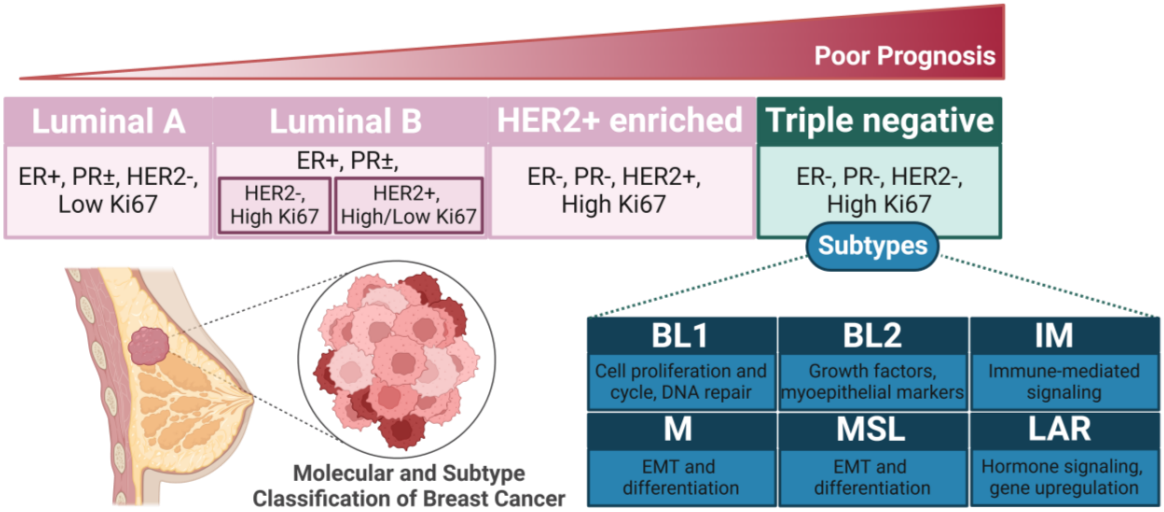


Figure 1.4 Molecular and Subtype Classification of Breast Cancer. Schematic representation of breast cancer subtypes according to the immunohistochemical detection of estrogen receptor (ER), progesterone receptor (PR), human epithelial receptor 2 (HER2), and the proliferation marker Ki67 expression and Triple negative subtypes classification in basal-like 1 (BL1), basal-like 2 (BL2), immunomodulatory (IM), mesenchymal (M), mesenchymal stem-like (MSL) and luminal androgen receptor (LAR). *Figure created with Biorender* and Adapted from Boix-Montesinos et al[134].

In addition to molecular complexity, distinct metabolic alterations that significantly contribute to aggressivity and treatment resistance characterize TNBC[135]. TNBC cells exhibit a marked preference for glycolysis, even in sufficient oxygen[136], driven by increased glucose uptake facilitated by the upregulation of glucose transporters such as GLUT1[137]. This metabolic shift allows TNBC cells to rapidly generate ATP and essential biosynthetic intermediates like phosphoenolpyruvate (PEP) and fructose-6-phosphate (F6P) , which remain critical to the nucleotide and amino acid synthesis necessary for tumor growth and proliferation[138]. Furthermore, TNBC cells rely on glutaminolysis as a complementary metabolic pathway to glycolysis, providing anaplerotic substrates that fuel the TCA cycle in situations of limited glucose[139]. The conversion of glutamine to α-ketoglutarate supports OXPHOS and essential biosynthetic pathways critical for TNBC cell proliferation[140]. Recent studies highlighted metabolic heterogeneity among breast cancer subtypes; they revealed that MDA-MB-231 (TNBC) cells primarily rely on glycolysis, exhibiting elevated lactate dehydrogenase (LDH) activity that converts pyruvate to lactate instead of entering the TCA cycle. This mechanism supports increased NADH levels, which may inhibit pyruvate dehydrogenase (PDH) activity. In contrast, MCF-7 (Luminal A) cells depend more on mitochondrial respiration and possess higher levels of monocarboxylate transporter 1 (MCT1) for lactate uptake due to lower lactate production[135]. The lactate produced from glycolysis in TNBC cells contributes to the acidification of the tumor microenvironment (TME), promoting invasion and immune evasion[141]. Lactate uptake by neighboring cancer-associated fibroblasts leads to the production of metabolites such as glutamine,

which further fuels TNBC cells; this cooperative metabolic exchange sustains tumor survival and growth within the TME[142]. Enhanced expression of glycolytic enzymes, particularly pyruvate kinase muscle isozyme 2 (PKM2), catalyzes pyruvate formation, favoring conversion to lactate rather than the implication of the TCA cycle[143]. Despite this reliance on glycolysis, TNBC cells demonstrate significant metabolic plasticity, allowing them to dynamically switch between glycolysis and OXPHOS in response to environmental fluctuations such as nutrient availability or hypoxia[144].

In TNBC, lipid metabolism reprogramming supports rapid proliferation and survival, involving increased de novo fatty acid synthesis and enhanced lipid uptake. Essential enzymes such as fatty acid synthase (FASN) and acetyl-CoA carboxylase (ACC) become upregulated, elevating fatty acid levels that become incorporated into the complex lipids needed for membrane biosynthesis, energy storage, and signaling[126]. In addition to synthesis, TNBC cells utilize FAO as an alternative energy source, especially under metabolic stress when glycolysis is limited. Recent findings underscore the role of PKM2 in mediating this shift, modulating carnitine transport essential for FAO, thereby enabling TNBC cells to maintain energy production under glycolytic inhibition[145]. Increased expression of carnitine palmitoyltransferase 1A (CPT1A) further underscores TNBC's reliance on FAO to meet energy demands[146]. In parallel, TNBC cells exploit lipophagy – the breakdown of lipid droplets to release fatty acids for mitochondrial β-oxidation – to sustain energy levels under nutrient deprivation[147].

CL, the unique phospholipid of the IMM, plays a multifaceted role in TNBC, balancing metabolic resilience and susceptibility to apoptosis. Rawling et al. reported that targeting CL depletion selectively induces apoptosis in TNBC cells by facilitating cytochrome c release, thereby sensitizing cells to mitochondrial stress[148]. Hardy et al. further explored how exposure to saturated fatty acids such as palmitate reduced CL content, thereby destabilizing mitochondrial membrane potential, disrupting ATP synthesis, and triggering cell death pathways[149]. Terao et al. demonstrated that all-trans retinoic acid reduces CL levels by downregulating nuclear genes encoding mitochondrial proteins, leading to decreased mitochondrial number and functionality, thereby altering energy dynamics in TNBC cells[150].

Imbalanced mitochondrial dynamics also represents an important factor leading to TNBC progression, with mitochondrial fission playing a complex role in TNBC. Humphries et al. demonstrated that enforcing mitochondrial fission in TNBC increased intracellular ROS levels, reduced cell migration, and formed actin-rich migratory structures[151,152]. Conversely, Wang et al.

reported that moderate Drp1-mediated fission may aid TNBC cells under metabolic or therapeutic stress by supporting mitophagy and ROS management[153]. Controlled fission allows TNBC cells to maintain bioenergetic efficiency and resist apoptosis through the selective removal of damaged mitochondria, especially in response to chemotherapy[154]. Controversy regarding controlled mitochondrial fission reflects mitochondrial ROS's context-dependent role in TNBC. While high ROS levels can inflict damage[155,156], controlled ROS production stabilizes HIF-1α, enhancing the expression of genes involved in glucose uptake, angiogenesis, and adaptation to hypoxic conditions[157]. Additionally, TNBC cells utilize mitochondrial ROS to activate PI3K/AKT (PI3K: phosphoinositide 3-kinase) signaling, supporting cell survival, proliferation, and metastasis under oxidative stress[158]. In addition to fission, regulated mitophagy - mainly through the PINK1/Parkin pathway - remains crucial to mitochondrial quality control in TNBC. This process selectively clears damaged mitochondria to prevent the accumulation of dysfunctional organelles that impair cellular metabolism and energy production. Maintaining mitochondrial quality through mitophagy allows TNBC cells to sustain bioenergetic efficiency, especially under conditions of high oxidative stress. For example, upregulated PINK1/Parkin signaling in TNBC promotes survival by preserving mitochondrial integrity even in the presence of elevated ROS levels[159,160].

Elevated MMP in TNBC cells plays a crucial role in their resistance to apoptosis and metabolic resilience[161]. Enhanced MMP boosts the electrochemical gradient necessary for ATP production, enabling TNBC cells to survive stressful conditions such as hypoxia and nutrient deprivation. Crucially, heightened MMP delays MOMP, a critical step in apoptosis, thereby inhibiting the release of pro-apoptotic factors like cytochrome c. Anti-apoptotic proteins from the Bcl-2 family, including Bcl-2 and Bcl-xL, play a central role in preventing the activation of pro-apoptotic proteins such as Bax and Bak. MOMP inhibition preserves the MMP and effectively allows TNBC cells to evade apoptosis[162].

Understanding these intricate mechanisms of mitochondrial and metabolic reprogramming in TNBC highlights the urgent need for multi-targeted therapeutic strategies. Such approaches could disrupt the resilience and adaptability of cancer cells within hostile microenvironments, ultimately improving treatment outcomes for patients with this aggressive subtype of breast cancer. Targeting various aspects of TNBC metabolism and mitochondrial function may enhance the effectiveness of existing therapies and aid the development of novel treatment options to overcome the challenges posed by this heterogeneous disease. Thus, we chose TNBC as a model disease in this thesis.

1.2 Therapeutic Potential of Nanomedicine

Nanomedicine applies nanotechnology to medicine by integrating nano- and bio-materials at the nanometer scale to develop advanced, scalable drug delivery systems and medical devices[163]. This field leverages the unique properties of nanomaterials, such as their size (5–200 nm), large specific surface area, and surface functionalization flexibility, to enhance therapeutic efficacy[164–166]. These features contribute to reduced toxicity, improved bioavailability, and enhanced pharmacokinetics[166]. Since the approval of the first nanomedicine, Doxil[167], in 1995, over a hundred nanomedicine products have been approved by regulatory agencies worldwide[168], including innovations like Moderna's COVID-19 vaccine SpikeVax in 2021[169]. These nanoscale systems have revolutionized treatments for various conditions, including cancer, cardiovascular and neurodegenerative diseases, and inflammatory disorders[170].

In cancer therapy, nanomedicines exploit the enhanced permeability and retention (EPR) effect — a phenomenon in which abnormal tumor vasculature and impaired lymphatic drainage allow nanomedicines to accumulate in tumors[171,172] — and mechanisms such as transcytosis and active cell targeting to facilitate selective tissue accumulation[173,174]. However, challenges remain; a 2021 update to the "Nano-Tumor Database" reported that only 0.67% of the injected dose of nanomedicines reaches the tumor site[175], highlighting the need for improved strategies to overcome the insufficient delivery of nanomedicine. Recent efforts have focused on engineering nanomedicines with tailored physicochemical properties to improve their interaction with biological barriers, therefore, enabling enhanced tissue/cellular uptake and organelle targeting[176]. Subcellular targeting, particularly of mitochondria, has emerged as a promising precision strategy, offering enhanced specificity, minimized resistance, and reduced off-target effects[177]; however, targeting organelles requires fine-tuned control over cellular entry and organelle-specific localization. Addressing these challenges remains essential to unlocking nanomedicine's full therapeutic potential.

The following section will discuss intracellular delivery approaches in nanomedicine, focusing on strategies to navigate biological barriers and enable precise subcellular targeting.

1.2.1 Intracellular Delivery in Nanomedicine

1.2.1.1 Biological Barriers

Nanomedicines encounter complex biological barriers that influence their therapeutic effectiveness, ranging from systemic clearance mechanisms to tissue-specific and cellular barriers (**Figure 1.5**). The first line of defense against nanomedicine after administration is the reticuloendothelial system (RES), which comprises phagocytic cells (predominantly macrophages in the liver and spleen) that detect and clear foreign particles from the bloodstream[178]. Rapid clearance mechanisms pose a significant challenge to maintaining therapeutic concentrations of nanomedicines in circulation long enough to reach the target tissues. The formation of the protein corona represents a critical factor in this process, which occurs when proteins from the bloodstream, such as serum albumin, immunoglobulins, and complement components, adsorb onto the surface of nanoparticles[179]. This corona profoundly alters the nanoparticles' biological identity, influencing their interactions with immune cells, ultimately affecting their pharmacokinetics and biodistribution, and reducing specific targeting[180,181].

To counteract RES clearance and the effects of the protein corona, nanomedicines are often coated with polyethylene glycol (PEG) in a process known as PEGylation, which promotes a 'stealth' effect that reduces immune recognition and extends circulation time. Although widely used, PEGylation can prompt an "accelerated blood clearance" phenomenon upon repeated administration, as anti-PEG antibodies form and trigger more rapid clearance with subsequent doses[182]. Additionally, PEG's non-biodegradable nature can lead to accumulation in lysosomes and liver of normal tissues, posing long-term risks such as macromolecular syndrome[183]. These limitations have prompted research into alternative stealth materials, such as hydrophilic polymers (e.g., poly(2-oxazoline) or polysarcosine (PSar)) and biodegradable zwitterionic polymers (including zwitterionic polypeptides) that help the nanosystems to evade immune detection without inducing the accelerated blood clearance response[184–186]. Banskota et al. demonstrated that zwitterionic polypeptides, composed of multiple repeats of a five-amino-acid motif containing a cationic-anionic residue pair derived from elastin-like polypeptides rich in lysine and glutamic acid, extended the half-life of the commonly employed chemotherapeutic paclitaxel (PTX) by 17 times compared to free PTX and 1.6 times compared to a “non-stealth” control in mice with aggressive prostate or colon cancer[187].

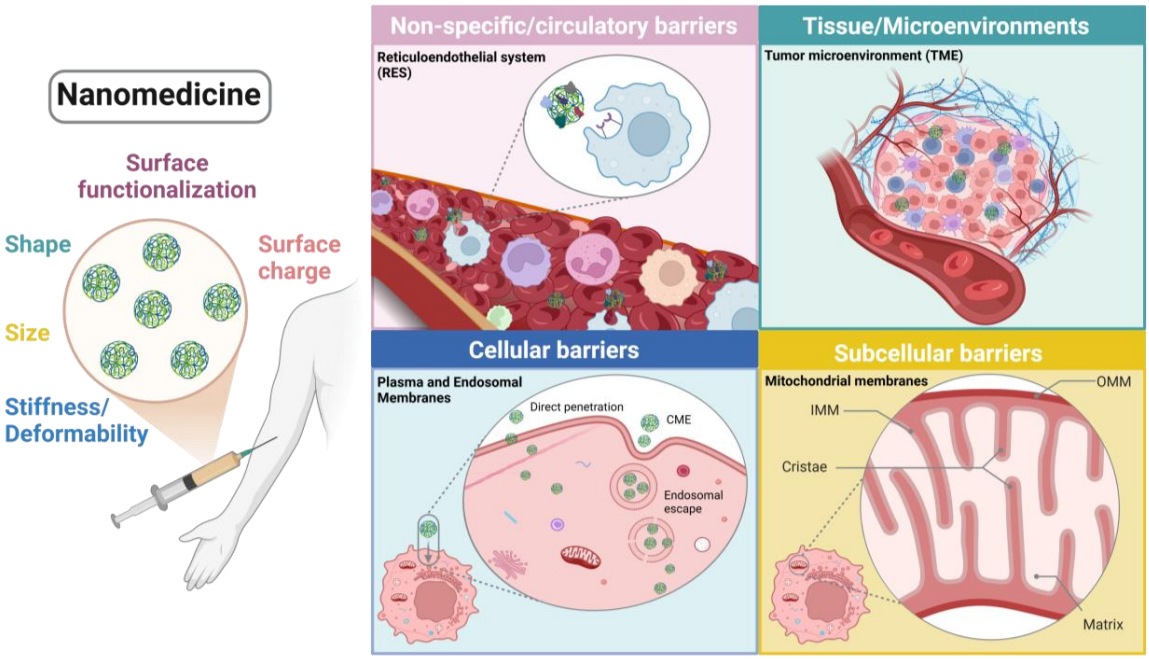


Figure 1.5. Biological Barriers in Nanomedicine Delivery. The figure illustrates the significant barriers nanomedicines encounter during systemic delivery, from circulation to subcellular localization. On the left, nanomedicine properties such as size, shape, surface charge, stiffness/deformability, and surface functionalization are depicted as critical factors influencing their ability to overcome these barriers. On the right, biological barriers are highlighted, including clearance by the reticuloendothelial system (RES), penetration within the tumor microenvironment (TME), and obstacles at the cellular and subcellular levels. Cellular barriers include the plasma and endosomal membranes, which regulate nanomedicine uptake through mechanisms such as clathrin-mediated endocytosis (followed by endosomal escape) and direct penetration. Subcellular barriers involve crossing mitochondrial membranes, including the outer mitochondrial membrane (OMM) and inner mitochondrial membrane (IMM), to reach the matrix and cristae. *Figure created with Biorender*.

Additionally, biomimetic strategies have emerged as a novel approach to evading RES detection[188]. Shielding nanomedicines with isolated membrane proteins or native plasma membranes created particles that appear as "self" to the immune system, thereby avoiding phagocytic clearance. Li et al. developed biomimetic nanovaccines by coating porous silicon-gold nanocomposites with cancer plasma membranes derived from 4T1 murine breast cancer cells[189]. The membrane coating enabled immune evasion, prolonged circulation, and tumor-specific targeting. Treatment with these nanoparticles supported combined photothermal therapy and immunomodulation; near-infrared irradiation ablated tumor cells via heat generation by the nanoparticle, which also enhanced antitumor immunity through weak immunostimulatory effects. In 4T1 tumor-bearing mice, this approach significantly reduced tumor growth and lung metastasis. Despite their potential, scaling up biomimetic nanoparticles remains challenging due to the need for precise control over membrane coatings to preserve biological activity and surface marker integrity.

At the tissue level, particularly within the TME, nanomedicines face barriers limiting their effectiveness. The TME is characterized by irregular vasculature, elevated interstitial pressure, and a dense extracellular matrix (ECM), which impedes nanoparticle penetration. Although the EPR effect theoretically promotes nanomedicine accumulation in tumors, the TME features often counteract this advantage by preventing effective extravasation and retention[190]. The TME, while presenting a significant physiological barrier, also offers distinct characteristics that can be leveraged in the design of stimuli-responsive nanomedicines, enabling cargo release in response to disease-specific triggers such as protease activity (e.g., matrix metalloproteinases, overexpressed in tumors), altered acidic pH, redox balance (e.g., high GSH levels) and hypoxia[191]. Dual-responsive nanopharmaceuticals offer a multi-targeted approach, combining stable systemic circulation with selective release in the TME through a multi-stimuli-triggered approach. Gao et al. designed a nanoplatform leveraging dual-stimuli responsiveness to target normoxic tumor cells and hypoxic cancer stem cells[192]. This system integrated a thioketal-bearing ROS-responsive prodrug, activated by photodynamic-induced ROS in normoxic environments, and an acid-responsive polymer for enhanced drug release in the acidic TME. A hypoxia-responsive prodrug targeted cancer stem cells via nitroreductase activation under hypoxic conditions, with tumor targeting further enhanced by the matrix metalloproteinase 2 (MMP-2)-mediated removal of PEG, which facilitated deep tissue penetration. This platform demonstrated significantly higher tumor inhibition in breast and head-neck cancer models than in non-stimuli-responsive controls or single-stimulus-responsive systems.

Modifying nanomedicine properties such as size, shape, stiffness/deformability and surface charge can impact tumor penetration and retention. Smaller nanosystems (< 100 nm) penetrate tumors more effectively[193], surface charges can be optimized with switchable mechanisms to improve interactions with the TME[194,195], and non-spherical nanomedicines (e.g., rods or filaments) have demonstrated superior ECM penetration compared to spherical particles[196]. The stiffness/ deformability of nanomedicines can significantly influence their ability to penetrate tumors. For example, Deng et al. demonstrated that core–shell nanoparticles made from amphipathic PEG-b-(poly ε-caprolactone (PCL)-g-polybutyl acrylate (PBA)) (PEG–(PCL-g-PBA)) (PEC-B), which shared identical chemical composition, size, and surface properties but differed in rigidity, exhibited varying penetration behaviors in 4T1 tumor-bearing mice[197]. PCL, a semi-crystalline polymer, and PBA, an amorphous polymer with a low glass transition temperature, allowed the crystalline structure of the nanoparticle core to be adjusted by altering the CL-to-BA ratio. This change in crystallinity correlated with rigidity. Enhanced tumor penetration observed from PEC-B_{30} to PEC-B_{120} (as PBA content

increased) was attributed to the nanoparticles' softer and more flexible structure. The physicochemical properties of nanomedicines can be dynamically controlled in response to specific stimuli. Xu et al. developed dual-responsive nanoparticles composed of a poly(lactic-co-glycolic acid) (PLGA) core loaded with the chemotherapeutic doxorubicin (DOX), coated with a pH-sensitive poly(β-amino ester) polymer (PBAE) and stabilized with a matrix metalloproteinase 9 (MMP-9)-cleavable PEG corona[198]. These nanoparticles transformed from spherical into elongated rod-like shapes in response to acidic pH and MMP-9 overexpression in the TME, enhancing penetration and retention. This shape-shifting behavior facilitated prolonged drug retention, with ~3.7% retained tumor drug concentrations of the injected dose at 96 hours - 2.6 times higher than non-transformable spherical nanoparticles.

At the cellular level, nanomedicines face complex challenges related to uptake, intracellular trafficking, and subcellular targeting, significantly influencing therapeutic outcomes. Nanomedicine internalize through diverse mechanisms, including clathrin-mediated endocytosis (CME), caveolae-mediated endocytosis (CVME), macropinocytosis, and less-characterized pathways like clathrin-independent carriers (CLIC) and glycosylphosphatidylinositol (GPI)-anchored protein-enriched early endosomal compartments (GEEC)[199]. Each pathway offers distinct advantages and limitations, influenced by nanosystems properties, cellular microenvironments, and cell-dependent endocytic machinery[200].

CME, the most extensively characterized pathway, involves the formation of clathrin-coated pits, which internalize nanomedicines and transport them through early and late endosomes to lysosomes. While this process accommodates a broad range of sizes and surface chemistries, making CME a widely utilized mechanism[201], not all internalized cargo follows this degradative route—some, like the transferrin receptor, are recycled back to the plasma membrane[202,203]. However, for nanomedicines requiring cytosolic delivery, lysosomal trafficking can limit therapeutic efficacy when the endosomal/lysosomal compartment is not the intended target. Endosomal escape or alternative uptake strategies, such as CVME, have been explored to reduce lysosomal degradation. However, the intracellular trafficking of nanomedicines internalized via CVME remains poorly understood and highly debated, with evidence suggesting it may depend on cell type and nanomedicine composition[204–206]. While some studies propose that this pathway bypasses lysosomal degradation[207], facilitating cargo delivery to the ER or Golgi apparatus—similar to certain viruses[207]—more recent findings indicate that caveolin-1-positive vesicles are often directed to endolysosomes for degradation[208–210]. The extent to which CVME enhances cytosolic delivery

remains uncertain and requires further investigation. This pathway relies on plasma membrane invaginations coated with caveolin, forming small caveolae (50–80 nm)[211]. Nanomedicines designed with caveolin-targeting ligands or optimized for specific sizes/surface properties remain more likely to exploit CVME[212]; however, this mechanism depends significantly on specific cellular conditions (e.g., the presence of lipid rafts and sufficient caveolin expression), thereby limiting applicability in specific cell types[200,213].

Macropinocytosis represents another significant uptake pathway, particularly in cancer cells, where the upregulation of this actin-driven mechanism meets increased metabolic demands[214]. This process engulfs extracellular fluid and particles into large vesicles (macropinosomes, 0.2–5 μm), providing a route for internalizing larger nanomedicines or therapeutic systems with high payloads[211]. Advances in engineering nanomedicine with surface modifications that selectively activate macropinocytosis in the TME hold promise but require further refinement to improve specificity and therapeutic outcomes[215,216].

Emerging clathrin-independent pathways, including CLIC and GEEC, have gained attention as alternative mechanisms for cellular internalization. These pathways often associate with the presence of lipid raft microdomains and function independently of traditional proteins like clathrin or caveolin[217]. While less studied, CLIC and GEEC are instrumental in cells lacking caveolae or exhibiting non-standard endocytic behaviors. By leveraging such mechanisms, nanomedicines may overcome limitations posed by more conventional uptake pathways[200]; however, their variability across different cell types and limited characterization underscores the need for further research to fully exploit their potential. Direct plasma membrane permeation, while bypassing endocytic pathways entirely, provides an alternative approach for cytosolic delivery (discussed in the next section).

Nanomedicine physicochemical properties - including size, shape, surface charge, stiffness/deformability, and surface functionalization - represent critical determinants of cellular uptake, directly influencing their interactions with cellular membranes and internalization mechanisms; however, these properties are not static. Their dynamic and context-dependent effects vary with cell type, microenvironmental conditions, and biological components such as the protein corona. Understanding these interdependencies remains crucial to optimizing nanomedicine design to overcome delivery barriers and improve therapeutic efficacy.

Nanomedicine size significantly influences the mechanism and efficiency of cellular uptake, often in a cell-type-dependent manner[218]. Smaller nanosystems (<50 nm) typically utilize CVME, compatible with the vesicle size range, while larger analogues predominantly rely on CME, which accommodates nanomedicines up to approximately 200 nm, where macropinocytosis can also occur[219,220]. Notably, uptake mechanisms rarely show exclusivity, with multiple pathways often involved. The protein corona further modulates these size-dependent uptake patterns[221]; for example, Zhang et al. demonstrated that iron oxide nanoparticles (IONPs) exhibited higher internalization levels in J774A.1 macrophages after 6 h compared to IONPs coated with extracellular protein coronas (IONP@LS)[221]. Their findings revealed macropinocytosis as the primary pathway for "naked" IONPs, while IONP@LS primarily became internalized via CVME and micropinocytosis. Energy constraints add another layer of complexity; ultra-small nanosystems often fail to induce sufficient membrane curvature for wrapping during endocytosis, limiting their uptake efficiency, while larger nanomedicines face slower receptor diffusion kinetics, which hinders their internalization. Theoretical modeling, supported by experimental data, identified 25-50 nm as an optimal size range that achieves maximal uptake rates and the highest internalization efficiency[218].

The shape of nanomedicines also plays a critical role in cellular uptake. Rod-shaped nanosystems display enhanced penetration through multicomponent lipid bilayers in simulations compared to spherical or disc-shaped particles, likely due to their anisotropic geometry and increased surface area[222]. Experimental studies have corroborated these findings, revealing that helical rod-shaped nanoparticles obtained from the self-assembly of poly(γ-benzyl-l-glutamate)-block-PEG (PBLG(fluorescein Isothiocyanate, FITC)-b-PEG) block copolymers with PBLG or polystyrene homopolymers achieve higher internalization rates than smooth or striped spherical counterparts of similar size[223]. Nanomedicine shape also influences uptake mechanisms; for instance, Liu et al. compared rod-like bio-nanoparticles derived from tobacco mosaic virus (TMV) and demonstrated that their aspect ratio (length-to-width ratio) influenced internalization pathways in different cell lines[224]. TMV4 and TMV8 became internalized via microtubule transport in HeLa cells and clathrin-mediated uptake in HUVECs, whereas TMV17 utilized caveolae-mediated pathways and microtubule transport in both cell types. Notably, unlike most nanomedicines, macropinocytosis did not contribute to the internalization of any TMV nano-rods, regardless of their aspect ratio or cell type. Interestingly, contrasting evidence suggests that spherical nanosystems often outperform rod-shaped particles in cellular uptake, particularly in cancer cells[225]. Theoretical models further elucidated the energetic requirements of shape-mediated uptake, with simulations

revealing that rod-shaped nanoparticles required more significant membrane-wrapping energy than spherical particles, which may reduce cellular internalization efficiency in some contexts[226]. The discrepancies in the literature reflect how the effectiveness of non-spherical shaped nanomedicines varies depending on the preclinical context and experimental conditions.

Surface charge plays a pivotal role in determining the cellular uptake of nanomedicines, primarily through electrostatic interactions with the negatively charged phospholipid bilayer of plasma membranes. Positively charged nanosystems typically exhibit enhanced cellular uptake due to their strong electrostatic attraction to the plasma membrane; however, high cationic charge densities pose significant challenges: they disrupt membrane integrity and induce cytotoxicity, which has been harnessed to promote cancer cell death and inhibit metastasis, as demonstrated with guanidinium-functionalized polycarbonates[227]. Additionally, positively charged nanomedicines interact non-specifically with anionic biological surfaces, including mucosal membranes, the ECM, or blood proteins, and accelerate protein corona formation[228]. While some studies have shown that anionic nanomedicines achieve efficient cellular uptake[229], they generally display lower cell adhesion or uptake and aggregate when their negative charge density is too high[230]. However, certain anionic materials, such as the polypeptide poly-L-glutamic acid (PGA), exhibit remarkable stealth properties that prevent aggregation while achieving efficient cellular uptake, even at low surface charge. This performance can be further enhanced through strategic modifications to polymer architecture, such as transitioning from linear designs to star-shaped or crosslinked structures[231–234]. To address the limitations associated with static surface charges – whether positive or negative – dynamic charge-switching nanoparticles have been developed as a complementary strategy. These nanoparticles maintain a neutral/slightly negative charge during systemic circulation, reducing off-target interactions and improving stability, but shift to a positive charge in response to acidic or enzymatic conditions in the TME, thereby enhancing tumor-specific uptake[230]. Zhang et al. reported that poly(histidine)-based nanoparticles initially exhibited an anionic surface charge, minimizing interactions with serum proteins and enhancing stability in circulation[235]. Upon reaching the acidic TME, the protonation of imidazole groups reversed the surface charge, thereby significantly enhancing cellular uptake. This adaptive strategy effectively balances biocompatibility with therapeutic efficacy by minimizing systemic toxicity while enhancing site-specific delivery[230]. In addition to influencing uptake efficiency, surface charge can modulate the internalization mechanism; for example, Olivieri et al. demonstrated that amine-functionalized polystyrene nanoparticles preferentially utilized macropinocytosis as their primary internalization pathway in

Chinese hamster ovary cells, whereas anionic nanoparticles became internalized through clathrin-mediated and lipid raft-dependent mechanisms[236]. These findings emphasize the need for tailored surface modifications to optimize cellular uptake for specific applications.

Stiffness, or nanomedicine deformability, plays a significant and cell-type-dependent role in cellular uptake, influencing interactions with cancer cells and macrophages. Hui et al. investigated silica nanocapsules (SNCs) with tunable elasticities to evaluate the effects of nanoparticle stiffness on uptake mechanisms[237]. In SKOV3 cancer cells, stiff SNCs demonstrated higher CME internalization than soft SNCs due to their ability to maintain spherical shapes and facilitate efficient membrane wrapping and receptor binding. In RAW264.7 macrophages, stiff SNCs were preferentially internalized via actin-dependent phagocytosis and macropinocytosis, as their structural integrity facilitated recognition and engulfment. In contrast, soft SNCs deformed during uptake in both cell types, increasing energy demands for membrane wrapping and reducing uptake efficiency. Interestingly, nonspecific uptake pathways in cancer cells were less influenced by nanosystem stiffness, with both stiff and soft SNCs showing similar behavior. Nanomedicine deformability can also influence the bio-nano interface and cellular trafficking of therapeutic molecules. Vicente-Ruiz et al. developed a polymer conjugate by linking anti-insulin growth factor 1 receptor (IGF-1R) antibody (AVE1642) to PGA, enhancing the antibody's hinge flexibility[238]. While it remains unclear whether this flexibility or PGA-IGF-1R interactions alter receptor binding, PGA-AVE1642 showed enhanced membrane binding, delaying energy-dependent uptake and reducing IGF-1R internalization. PGA-AVE1642 predominantly colocalized with caveolin-1, bypassing early endosomes and directly targeting lysosomes, unlike AVE1642, which internalized via clathrin-mediated endocytosis and localized to early endosomes. These changes modulated cellular trafficking, inhibited MAPK and PI3K signaling, and reduced receptor recycling and nuclear translocation, enhancing antitumor efficacy in an orthotopic prostate cancer mouse model.

These physicochemical properties display interdependence and dynamically interact with biological systems, highlighting the complexity of nanomedicine design; moreover, they influence cellular uptake mechanism and play critical roles in determining the subcellular fate of nanomedicines, dictating whether they remain confined within endosomal compartments or successfully bypass them to deliver their payload directly into the cytosol.

1.2.1.2 Endosomal Escape vs. Direct Plasma Membrane Permeation

Efficient intracellular delivery of nanomedicines hinges on overcoming biological barriers, particularly ensuring escape from endosomal compartments or bypassing endocytosis altogether via direct plasma membrane permeation (**Figure 1.6**). Nanomedicines internalized through CME or macropinocytosis often traffic to late endosomes and lysosomes, where the acidic microenvironment and enzymatic activity degrade their payloads, which requires the development of effective endosomal escape strategies.

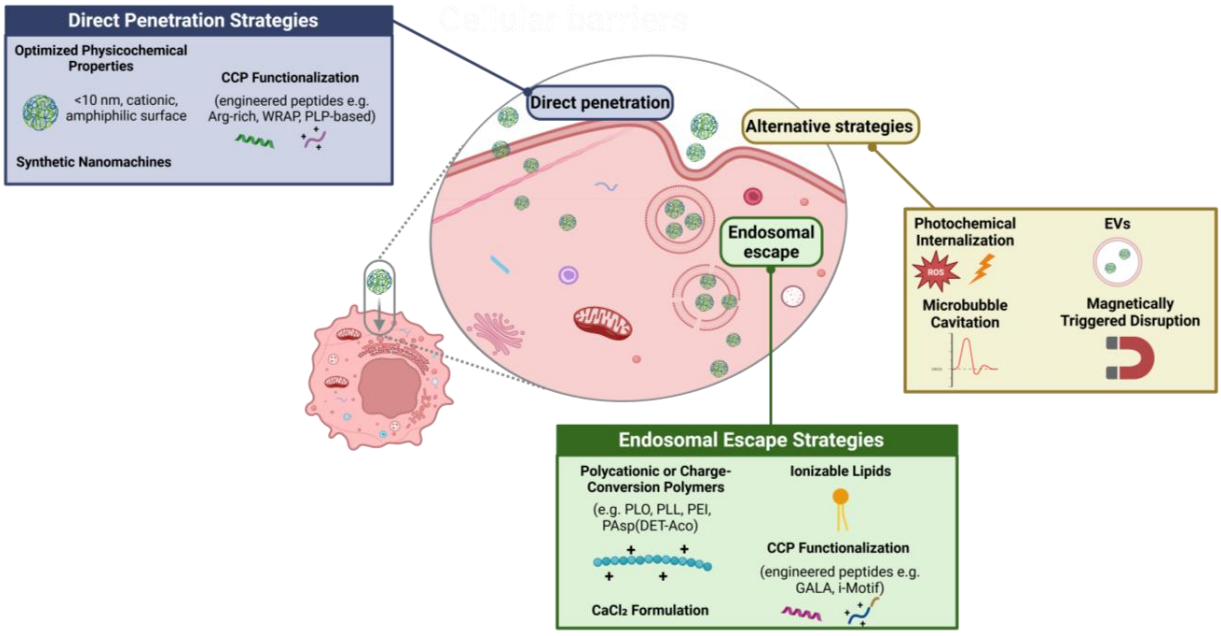


Figure 1.6 Strategies for overcoming cellular barriers in nanomedicine delivery. The main approaches include endosomal escape strategies (polycationic or charge-conversion polymers such as poly(L-ornithine) (PLO), poly(L-lysine) (PLL), polyethylenimine (PEI), poly(aspartic acid) (PAsp(DET-Aco)), ionizable lipids, cell-penetrating peptide (CCP) functionalization (e.g., GALA, i-Motif), calcium chloride ($CaCl_2$) formulation), alternative strategies (photochemical internalization, microbubble cavitation, extracellular vesicles (EVs), magnetically-triggered disruption), and direct penetration strategies (optimized physicochemical properties, CCP functionalization, synthetic nanomachines). *Figure created with Biorender*.

Lipid nanoparticles (LNPs) frequently employ ionizable lipids that remain neutral at physiological pH but acquire a positive charge in acidic endosomes; this charge shift destabilizes the membrane, forming non-bilamellar hexagonal structures that facilitate vesicle disruption and promote cytosolic release[239]. The payload (e.g., RNA species), the cell-dependent release profiles of LNPs, and the lack of methods to study their endosomal escape mechanisms remain critical bottlenecks in RNA-based therapeutics[240]. The approval of groundbreaking therapeutics such as the first small interfering RNA (siRNA) drug, Onpattro (Alnylam, 2018)[241], and the SARS-CoV-2 vaccines Spikevax (Moderna)[169] and Comirnaty (Pfizer/BioNTech)[242], which utilize three distinct ionizable

lipids, highlighted the profound impact of minor chemical modifications on the biological performance of these lipids. The extensive structural diversity of ionizable lipids spurred a focus on high-throughput synthesis strategies to accelerate the discovery of novel candidates for RNA delivery. Li et al. recently employed this approach combined with a four-component reaction and machine learning to evaluate the transfection efficiency of LNPs formulated with a library of 584 ionizable lipids[243]. This method led to the identification of lipids 119-23, which outperformed benchmark lipids in transfecting muscle and immune cells.

Most polymer-based formulations rely on the proton sponge mechanism for endosomal escape, where polycationic polymers like polyethyleneimine (PEI) and polypeptides such as poly-L-lysine (PLL) or poly-L-ornithine (PLO) buffer acidic environments, causing osmotic swelling and vesicle rupture[244–252]. Of note, the role of buffering capacity remains under debate, as factors like polymer conformation, geometry, and acid degradability influence escape, which may involve additional mechanisms such as membrane destabilization or nanoparticle swelling[253]. Stimuli-responsive materials have emerged to address the toxicity of polycationic polymers and enhance therapeutic efficacy; for example, Dirisala et al. developed PLO-based mRNA polyplexes coated with charge-conversion polymers such as poly{N-[N'-(2-aminoethyl)-2-aminoethyl]aspartamide} modified with cis-aconitic acid PAsp(DET-Aco), which reverses charges in acidic pH to produce cationic PAsp(DET), improving RNA delivery and endosomal escape via pH-triggered cleavage of cis-aconitylamide bonds[254]. Similarly, Mixich et al. designed PEG–poly(glycerol) (PEG–PG) block copolymers modified with phenylalanine (Phe) (PEG–PG(Phe)) micelles with phenylalanine-modified biodegradable ester bonds, enabling pH-selective endosomal destabilization and enhanced protein expression in vivo[255].

Beyond polycationic polymers, alternative strategies for improving endosomal escape have been explored. Park et al. developed spherical nucleic acids encapsulated in PLGA nanoparticles salted with $CaCl_2$, where calcium influx triggers proton accumulation, enhancing escape[256]. These formulations significantly improved gene silencing (8–18-fold) and reduced late endosome accumulation in U87-MG glioblastoma cells compared to NaCl-salted counterparts. Peptide-functionalized nanocarriers also represent a promising approach, with lytic peptides (e.g., M-lycotoxin or KLA) and cell-penetrating peptides (CPPs) key players. CPPs are classified as non-amphipathic cationic (e.g., arginine-rich), primary amphipathic (e.g., MPG and penetratin), or secondary amphipathic peptides that adopt α-helical or β-sheet structures upon membrane

interaction; however, the low efficiency of CPPs and toxicity of lytic peptides requires peptide engineering[257].

To address these limitations, Li et al. designed GALA, a pH-sensitive peptide composed of repeating glutamic acid-alanine-leucine-alanine (EALA) units, to mimic viral peptides[258]. GALA enhances endosomal escape by forming α-helices at acidic pH, destabilizing membranes. Hagino et al. demonstrated the utility of cholesterol-GALA-coated LNPs, which improved endosomal escape and transfection efficiency in a metastatic lung cancer model[259]. Research has also accelerated the development of stimuli-responsive CPPs[260]. Narum et al. developed DELVR, a pH-sensitive delivery system for antisense oligonucleotides (ASOs), which uses gold nanoparticles (AuNPs) with a pH-responsive i-Motif DNA hybridized to ASOs and CPPs[261]. Acidification triggers i-Motif folding, which released ASOs and activates CPPs to enhance endosomal disruption, significantly improving ASO efficacy. Wang et al. proposed a modular approach to rationalize CPP design, adjusting transition pH (pH_o) to optimize CPPs[262]. Their design incorporated three components: a hydrophilic histidine network (modulating pH responsiveness), a hydrophobic leucine module (for self-assembly), and a lysine module (for nucleic acid binding). Encouragingly, their approach increased transfection efficiency 9-fold in 293T and HeLa cells compared to unoptimized peptides.

Several alternative strategies have been proposed and investigated to overcome the limitations and controversies of lipid- and polymer-based endosomal escape mechanisms. These include i) photochemical internalization, which uses photosensitizers to generate ROS or heat upon light exposure to destabilize endosomal membranes[263]; ii) extracellular vesicles (EVs), naturally occurring nanoparticles with fusogenic properties that enable intracellular delivery through endosomal fusion[264–266]; iii) microbubble cavitation, where ultrasound-induced bubbles create mechanical forces to disrupt endosomes[267]; and iv) magnetically triggered disruption, utilizing magnetic fields to generate local heat or mechanical stress to facilitate endosomal escape[268]. For example, porphyrin derivatives have been used as photosensitizers in siRNA-loaded formulations to induce photochemical internalization, significantly enhancing cytosolic delivery and therapeutic efficacy in preclinical cancer models such as breast and prostate cancer[269,270]. While these methods show considerable promise, combining multiple mechanisms within a single formulation has emerged as the most effective strategy to improve intracellular delivery, optimize efficiency, and advance nanomedicine into clinical applications.

Despite advancements in endosomal escape strategies, inefficiencies, payload degradation, and reliance on endocytic uptake remain significant challenges. These limitations highlight the potential of bypassing endocytosis altogether via direct plasma membrane permeation, an energy-independent process that eliminates the need for vesicular trafficking and subsequent escape mechanisms. Direct permeation can be broadly categorized into membrane fusion, typically employed in lipid-based materials or engineered EVs[271], and direct membrane penetration, which relies on critical physicochemical properties such as compact size (<10 nm), cationic charge, and amphiphilic surface patterns[272,273]. These properties reduce the energy barrier for membrane insertion, facilitating efficient lipid bilayer translocation[274]. Ray et al. demonstrated that polyacrylate-coated quantum dots switched from energy-dependent endocytosis to energy-independent direct membrane penetration after amphiphilic sodium linoleate became electrostatically bound to their surface[275]. Among strategies for direct permeation, CPPs - previously discussed for their role in endosomal escape - have shown promise; however, the precise mechanisms by which CPPs interact with membranes remain partially defined, with proposed models including inverted micelle formation, pore formation, carpet-like interactions, and vesicle budding-and-collapse mechanisms[276–278]. The sequence, secondary structure adaptability, concentration, and cell type all influence the effectiveness of CPPs[279–281]. Beyond arginine-rich CPPs, commonly used for energy-independent delivery of peptides or nanoparticles[282,283], innovative designs have expanded applications. Deshayes et al. developed a family of tryptophan-arginine-rich amphipathic peptides (WRAP) that form stable peptide-based nanoparticles in the presence of siRNA, facilitating direct translocation and payload release[284]. Additionally, the introduction of proline residues into CPPs enhances membrane penetration by promoting the formation of a polyproline type II helical structure[285].

Inspired by the precise and responsive behavior of biological molecular machines like proteins, dynamic synthetic nanomachines offer innovative strategies for overcoming cellular barriers. These systems mimic natural processes, where conformational changes enable biological molecules to interact with and penetrate membranes. Jeong et al. designed a synthetic nanomachine based on AuNPs functionalized with stimuli-responsive molecular ligands[286]. This design integrates a hydrophobic alkanethiol core, a hydrophilic tetra(ethylene glycol) unit, and a hydrophobic alkyl end group, which the nanomachine buries to maintain solubility when folded in aqueous conditions. The alkyl groups unfold upon contact with lipid bilayers, enabling direct penetration and apoptosis induction by mimicking biological toxins. The authors enhanced

selectivity by functionalizing the system with C6-dimethyl maleic anhydride latches, neutralizing surface charge, and sterically blocking alkyl group exposure, reducing cytotoxicity. In the acidic TME, the latches cleave, exposing the alkyl groups and activating cytotoxicity. Xia et al. developed a biomimicry assembly for cytosolic protein delivery inspired by filamentous actin (F-actin), which promotes membrane fusion by increasing membrane tension[287]. Cationic liposomes, as the backbone, supported the incorporation of NIR cyanine dyes to mimic F-actin. These dyes self-assemble within the lipid bilayer through π–π interactions, enhancing membrane fusion and bypassing endocytosis. This platform efficiently delivered proteins like FITC-labeled bovine serum albumin and enhanced green fluorescent protein, maintaining bioactivity as shown by β-galactosidase assays. Furthermore, DNase I delivery demonstrated anti-tumor efficacy, underscoring the therapeutic potential of this rapid and efficient system for protein delivery.

Endosomal escape and direct plasma membrane permeation offer distinct strategies for intracellular delivery, each with unique advantages and challenges. While endosomal escape remains essential to overcoming vesicular barriers, direct permeation bypasses these barriers and offers a promising alternative. Of note, combining elements from both approaches and further optimizing their mechanisms could pave the way for more efficient and versatile nanodelivery systems.

1.2.2 Polymer Therapeutics as Nanomedicines

Polymer therapeutics comprise a versatile and evolving family of nanomedicines designed to address the inherent limitations of conventional small-molecule drugs. This category includes polymeric drugs, polymer-drug conjugates, polymer-protein conjugates, polymeric micelles with covalently bound drugs, and polyplexes for non-viral gene delivery (**Figure 1.7**). Recent innovations have extended the scope of polymer therapeutics to include self-assembling polymer systems and hybrid nanosystems that incorporate inorganic or lipidic components[288], expanding their applicability in tackling complex biomedical challenges.

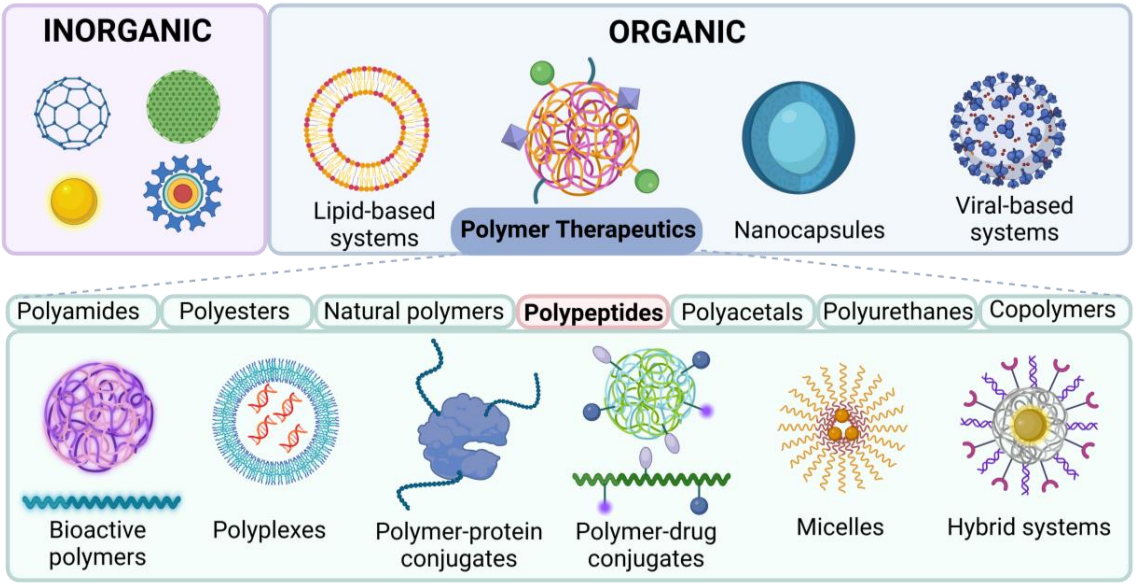


Figure 1.7. Types of nanomedicines and the position of polymer therapeutics in the field. *Figure created with Biorender* and Adapted from Melnyk and Đorđević et al.[249]

A defining feature of polymer therapeutics is the ability to fine-tune physicochemical properties to achieve optimal therapeutic performance. Molecular attributes such as size, architecture, charge, deformability and hydrophobicity can be precisely adjusted to enhance drug solubility, prolong systemic circulation, and improve targeted delivery. Beyond passive mechanisms (EPR effect), rational design enables the incorporation of active targeting moieties, such as antibodies, peptides, or small molecules, to facilitate selective interaction with disease-specific biomarkers.

Stimuli-responsive polymer therapeutics, in particular ***polymer conjugates***, significantly advance payload release in response to specific biological or environmental triggers, such as pH, redox potential, enzymatic activity, or temperature[289]. Acid-labile linkers have been employed to release drugs in the acidic TME or endosomal compartments, while disulfide bonds represent a commonly utilized linking chemistry for redox-sensitive drug release in intracellular environments rich in GSH[290]. This level of control over drug release enhances therapeutic efficacy and minimizes off-target effects, a critical consideration for clinical translation.

Polymer-drug conjugates have emerged as a cornerstone of polymer therapeutics, offering numerous advantages such as improved pharmacokinetics and pharmacodynamics, extended circulation half-life, reduced systemic toxicity, the ability to overcome drug resistance mechanisms like p-glycoprotein-mediated multidrug resistance (MDR), controlled drug release, combination therapy, and modulation of cellular signaling[289,291]. Among the approximately 30 marketed polymer

conjugates (predominantly polymer-protein conjugates[292,293]) a PEGylated conjugate of naloxone for opioid-induced constipation (Movantik®)[294] represents a milestone as the first marketed polymer-drug conjugate, although its rational significantly differs from most of those encountered in clinical stages, looking at systemic delivery[289,295,296]. In this line, although the withdrawal of blockbusters such as polyglutamic acid-PTX (Opaxio)[297] highlights the complexities of development, advances in polymer chemistry, conjugation strategies, and rational design continue to drive innovation.

Integrating self-assembling and hybrid systems has further expanded the potential of polymer therapeutics; for example, combining polymers with AuNPs or lipid components has enabled the development of theranostic systems that offer simultaneous therapy and diagnostics[298] and improve therapeutic precision[299] and provide real-time feedback on treatment efficacy.

As polymer therapeutics evolve, their success will depend on addressing key challenges such as manufacturing scalability, regulatory approval, and patient-specific therapy design. Advances in synthetic polymer chemistry and a deeper understanding of disease biology will drive the development of the next-generation polymer-based nanomedicines. These systems will address systemic and intracellular barriers and enable precise subcellular targeting, aligning with the demands of personalized medicine and emerging therapeutic paradigms.

1.2.2.1 Polypeptide-based Polymer Therapeutics

Polypeptide-based polymer therapeutics represent an evolving class of nanomedicines, offering unmatched versatility and adaptability in drug delivery systems. Derived from synthetic analogs of natural proteins, polypeptides exhibit biocompatibility, biodegradability, and structural precision, making them highly suitable for addressing the limitations of traditional drug delivery platforms. The development of advanced polymerization techniques, particularly N-carboxyanhydride ring-opening polymerization (NCA-ROP), has enabled the production of polypeptides with controlled molecular weight (Mw), narrow polydispersity (PDI), and precise functional side chains. These characteristics allow for fine-tuning fundamental physicochemical properties such as size, charge, hydrophobicity, and architecture, which are critical for optimizing drug solubility, biodistribution, and cellular uptake[300]. For example, linear, star-shaped, micellar, and dendritic architectures can be tailored to specific applications[301]; moreover, post-synthetic modifications permit the attachment of bioresponsive linkers, targeting moieties and imaging agents, thereby enhancing therapeutic potential.

A defining feature of polypeptide therapeutics is their ability to incorporate bioresponsive linkers, allowing controlled drug release in response to environmental or biological triggers. pH-sensitive linkers, such as hydrazones, orthoesters, and cis-aconityl bonds, exploit the acidic TME and intracellular compartments to enable targeted drug release. Similarly, redox-responsive disulfide linkers leverage the elevated GSH levels in tumor cells to achieve site-specific drug delivery. Protease-cleavable linkers, designed to respond to enzymes overexpressed in the TME, such as glycyl-phenylalanyl-leucyl-glycine or valine-citrulline, further enhance precision in drug delivery[249]. These linkers, combined with the self-assembling capabilities of polypeptide carriers, create multivalent delivery platforms that enhance therapeutic efficacy and minimize off-target effects. By self-assembling into nanoscale structures, polypeptides further improve circulation times and passive targeting via the EPR effect, particularly in tumors or sites of inflammation.

Charge modulation plays a critical role in optimizing polypeptide-based therapeutics. Neutral or slightly negative charges reduce non-specific interactions and improve circulation times, while shielded positive charges enhance cellular uptake. PEGylation or the use of PSar can overcome the limitations of charge-mediated immune clearance, with PSar emerging as a safer and equally effective alternative to PEG. PSar coatings minimize hypersensitivity reactions and long-term accumulation risks, further enhancing the clinical viability of polypeptide systems[302]. Bayraktutan et al. developed pSar-PBAE polyplexes as an alternative to PEG for steric stabilization[303]; among the tested polyplexes, 50%-pSar formulations revealed superior self-amplifying mRNA expression in colorectal cancer cells monolayers and organoids, driven by efficient uptake and endosomal escape, highlighting pSar's potential for intratumoral gene delivery and its promise as a PEG alternative for immunotherapy applications.

Polypeptide-based nanocarriers have also proven effective in enabling combination therapies; their multivalency allows for the conjugation of multiple therapeutic agents, offering precise control over drug ratios, synergistic effects, and tailored release profiles. PGA-based combination nanoconjugates have demonstrated enhanced efficacy in 3D breast cancer models compared to single-drug conjugates or free drugs[231], while PLL or PLO have shown promise in gene delivery applications, eventually combined with chemotherapeutic agents, enhancing intracellular delivery and therapeutic outcomes through synergistic drug treatment[304]. Polypeptide carriers have shown the ability to overcome MDR, a significant challenge in cancer therapy, by facilitating intracellular drug delivery mechanisms that circumvent efflux pathways. Yang et al. demonstrated that nanoparticles obtained from the self-assembly of a negatively charged pH-sensitive polypeptide

PEG-b-poly(L-lysine)-graft-cyclohexene-1,2-dicarboxylic anhydride and a cationic anticancer polypeptide guanidinium-functionalized poly(L-lysine) (PLL-Gua) exhibited similar in vitro anticancer efficacy and induced morphological changes in MCF-7 and resistant MCF-7/ADR (breast cancer cells lines), demonstrating their ability to bypass drug resistance mechanisms[305].

Recent advances in crosslinking strategies have expanded the stability and functionality of polypeptide systems. Crosslinked structures, such as those employing bioresponsive disulfides or azide-alkyne click chemistry[234,306], enhance serum half-lives and control drug release kinetics under physiological conditions. These advancements, combined with the rational design of linkers targeting subcellular compartments, highlight the adaptability of polypeptides in addressing complex therapeutic challenges. Furthermore, incorporating advanced analytical tools has improved our understanding of the interactions between polypeptides and the bio-nano interface, paving the way for more efficient and predictable drug delivery outcomes.

Polypeptide-based polymer therapeutics have emerged as a pivotal element in nanomedicine, providing a platform for the rational design of nanomedicines tailored to specific therapeutic needs. Their ability to integrate tunable physicochemical properties, bioresponsive linkers, and multivalent architectures underscores their potential to address the unmet needs of precision medicine, such as precise subcellular targeting. As research advances, these systems are expected to set new benchmarks in targeted drug delivery, reinforcing their role in the next generation of biocompatible and effective therapeutic strategies.

1.3 Subcellular Targeting with Polymer Therapeutics: Mitochondria in the Spotlight

Polymer therapeutics have become increasingly sophisticated in their ability to navigate through or past biological barriers, offering versatile platforms for addressing complex therapeutic challenges. Recent advancements emphasize the modular design of polymer-based systems - incorporating bioresponsive linkers and targeting moieties - and their inherent tropism for specific subcellular organelles, such as mitochondria, lysosomes, and the nucleus. These organelles play pivotal roles in cellular function and disease progression, making them critical therapeutic targets. Mitochondria have emerged as a particularly compelling focus due to their central role in energy production, apoptosis, ROS production/signaling, and the pathogenesis of primary and secondary

mitochondria diseases. This section explores the strategies and innovations in polymer therapeutics aimed at achieving effective mitochondria targeting and its distinctive features for targeting.

1.3.1 Unique Features of Mitochondria for Targeting

Mitochondria possess distinctive features that set them apart from other organelles, making them compelling targets for precision drug delivery. The MMP represents among the most critical characteristics for targeting, as the highly negative charge attracts positively-charged molecules; however, the cationic charge must be distributed over a hydrophobic surface to effectively cross the membrane and reduce activation energy, as the IMM remains impermeable to polar molecules. Delocalized lipophilic cations (DLCs) - among the first mitochondriotropic compounds developed - exhibit a strong affinity for mitochondria, rapidly cross mitochondrial membranes without requiring specific import mechanisms, and accumulate in the mitochondrial matrix. Their accumulation follows the Nernst equation, which predicts a ten-fold increase in DLC concentration for every 61.5 mV rise in MMP. DLC accumulation has particular relevance in cancer cells, where elevated metabolic activity leads to an MMP of approximately 60 mV higher than in normal cells[307].

Triphenylphosphonium (TPP), a positively charged phosphorus ion linked to three lipophilic phenyl groups, represents the most widely studied DLC. TPP-based conjugates such as mitoQ (ubiquinone-TPP) and SkQ1 (plastoquinone-TPP) display anti-oxidant and anti-inflammatory activity and have progressed to clinical trials for indications such as multiple sclerosis-related fatigue (Phase 1/2, NCT03166800) and dry eye syndrome (Phase III, NCT03764735). Additional DLCs include dequalinium (DQA), a dicationic amphiphilic molecule that self-assembles into vesicles ("DQAsomes") for gene delivery and cancer therapy; the fluorescent dye rhodamine 123; the rhodacyanine derivative MTK-077; the cytotoxic compound (E)-4-(1H-indol-3-ylvinyl)-N-methylpyridineiodide (F16); guanidine and biguanidine derivatives; and iridium(III) complexes. We direct the reader to a review by Wang et al., which provides a more detailed discussion on DLCs[308].

The concentration-dependent toxicity of DLCs poses challenges and opportunities, as their accumulation in cancer cells induces selective mitochondrial dysfunction and apoptosis[309]. Kubi et al. designed non-peptidic cell-penetrating motifs (CPMs) with enhanced safety and efficacy for mitochondrial targeting[310]. The authors built CPMs on a benzene scaffold decorated with guanidinium groups and hydrophobic aromatic residues, such as D-phenylalanine or D-naphthylalanine (D-Nal). When conjugated with the D-peptide sequence (ala-asn-ala-asn-ala-asn-

miniPEG-Ly; ananan), CPM3 improved mitochondrial colocalization efficiency by 1300-fold compared to TPP-ananan; furthermore, CPM3 (CPM functionalized with D-Nal) supported a 35-fold increase in mitochondrial disruption and apoptosis induction relative to the free drug when linked to geldanamycin, while remaining non-toxic in HeLa cells at equivalent doses.

The presence of the TOM/TIM complex can also be exploited for mitochondrial targeting. This protein import machinery facilitates the translocation of 99% of mitochondrial proteins from the cytosol to the IMM. Amphiphilic α-helical MTSs have been employed in gene delivery applications; for example, Yu et al. demonstrated enhanced mitochondrial delivery of plasmid DNA encoding the NADH dehydrogenase subunit 4 (*MT-ND4*) using an MTS-modified adeno-associated virus, which restored optic atrophy in a mouse model of Leber's hereditary optic neuropathy[311]. The problematic preparation process for MTS-installed adeno-associated viruses and the reduced loading capacity prompted Yoshinaga et al. to develop a mitochondria-targeting gene delivery system using a synthetic peptide derived from the 32 N-terminal residues of the mitoNEET protein - an OMM protein involved in ROS sensing and biogenesis regulation - fused with arginine-histidine or lysine-histidine repeats[312]. This design facilitated polyplex formation, plasmid encapsulation, and mitochondrial targeting via natural mitoNEET recognition pathways and successfully delivered a large mtDNA plasmid (16.7 kbp) into HeLa ρ0 cells (lacking mtDNA), enabling the expression of multiple genes and restoring mitochondrial energy production. Of note, limitations such as the lack of a universal MTS sequence and the inability of MTSs to cross the plasma membrane without additional carriers have constrained their broader application. Combining MTSs with CPPs significantly enhances mitochondrial targeting; for example, Klimpel et al. reported that conjugating the sC18 CPP to an aldehyde dehydrogenase 5 (ALD5) MTS supported robust mitochondrial localization with enhanced cytotoxicity when linked to chlorambucil, a DNA alkylating agent[313]. Kang et al. employed an in silico approach to design a cell-penetrating artificial mitochondria-targeting peptide by screening optimal CPP and MTS combinations. The HIV-1 TAT fused with the MTS of aldehyde dehydrogenase 2 (ALDH2) represented the most effective combination and facilitated efficient delivery of the protein human metallothionein 1A (hMT1A) into mitochondria after crossing the plasma membrane, reducing mitochondrial damage in a Parkinson's disease mouse model[314].

Affinity-driven targeting represents another promising approach to target mitochondria, exploiting the unique lipid composition of mitochondria. Szeto-Schiller (SS) peptides selectively accumulate in the IMM by interacting with CL[315], which remains essential for mitochondrial processes such as cristae stability, protein import, and apoptosis. These peptides, characterized by

alternating aromatic and cationic residues, facilitate mitochondrial targeting and exhibit bioactivity; for example, Cerrato et al. revealed that modifications to SS-31, which inhibits cytochrome c/CL peroxidase activity, reduce ROS production and have progressed to Phase III trials for primary mitochondrial myopathy (NCT03323749), such as substituting lysine with ornithine or fusion with CPP such as PepFect14[316], further enhances mitochondrial uptake and ROS scavenging[317]. Shin et al. introduced CMP3013, a cyclohexylalanine-containing α-helical amphipathic peptide designed to overcome the affinity of SS peptides for CL[318]. Incorporating hydrophobic cyclohexylalanine and four positive charges in an α-helical structure of CMP3013 (compared to the β-sheet of SS peptides) demonstrated more robust and more selective binding to CL in the IMM. CMP3013 bound effectively to remodel CL, rescuing cristae integrity, boosting MMP, reducing ROS, and enhancing ATP production at nanomolar concentrations. In a mouse model of acute kidney injury, <1 mg/kg CMP3013 improved mitochondrial function, reduced nephrotoxic markers, and enhanced survival, demonstrating superior efficacy and selectivity compared to traditional SS peptides.

Mitochondrial penetrating peptides (MPPs) represent another innovative approach to target mitochondria, as these biodegradable and tunable peptides leverage positive charge and lipophilicity to cross mitochondrial membranes. Kelley et al. established a conceptual framework for MPP design, emphasizing the importance of charge-dependent lipophilicity. Their studies revealed that MPPs must meet a specific threshold of charges and lipophilicity (LogP) for effective mitochondrial localization[319,320]. MPPs have been employed to deliver small molecules, fluorescent dyes, theranostics, and anti-Plasmodium therapeutic agents; for example, Xiao et al. designed MTP3, a mitochondria-penetrating peptide composed of three positively charged arginines and two alternating D- and vL-naphthylalanines, which facilitated the delivery of DOX by exploiting a self-immolative disulfide linker cleaved in the presence of elevated GSH levels in cervical and lung cancer cells[321]. DOX release induced mitochondrial depolarization and reduced MMP to trigger apoptosis. Additionally, the Chmielewski research group identified a class of cationic amphiphilic polyproline helices that directly permeate the plasma membrane and colocalize with mitochondria[322,323]; meanwhile, modifications such as elongation or dimerization enhanced their targeting efficiency[324,325]. Recent studies focused on the self-assembly properties of MPPs; for example, Jeena et al. developed a novel approach using heterochiral assembly of amphiphilic MMPs to target cancer cell mitochondria[326]. They designed a mitochondria-penetrating tripeptide, Mito-FF, and an enantiomer, Mito-ff, which self-assembled into superfibrils within mitochondria when co-administered. These superfibrils exhibited enhanced interaction with mitochondrial membranes,

increasing penetration and causing significant mitochondrial disruption, leading to apoptosis in prostate, cervix, and colon cancer cells by collapsing MMP and generating ROS.

Alternative approaches have targeted OMM receptors, such as translocator protein (TSPO), galectin-3, and hexokinase II (HKII), which all become overexpressed in cancer cells. Woldetsadik et al. developed a hexokinase II-derived CPP (pHK-PAS) by coupling the N-terminal 15 amino acids of HKII, responsible for mitochondrial binding to a penetration-accelerating segment (PAS)[327]. This peptide effectively disrupted the association between HKII and OMM VDAC, which remains critical for cancer cell survival. In HeLa cancer cells, pHK-PAS depolarized the MMP, inhibited mitochondrial respiration, depleted intracellular ATP levels, and triggered cytochrome c release, leading to apoptosis. Importantly, these effects displayed selectivity to cancer cells, with assays in non-cancerous HEK293 cells reporting significantly lower cytotoxicity.

Cysteine-rich peptides, such as roseltide rT1, display high specificity for the OMM[328], and intrinsically disordered N-terminal domains from endoplasmic reticulum signaling proteins such as hormone somatostatin and amyloid precursor proteins have been shown to target the mitochondrial matrix[329]; however, their potential as delivery vehicles remains underexplored.

Mitochondrial targeting strategies harness unique features such as MMP, lipid composition, and protein import machinery to achieve precise therapeutic delivery. Innovations in peptides, nanostructures, and receptor-specific approaches present exciting opportunities for tackling mitochondrial dysfunction and related diseases.

1.3.2 Challenges in Mitochondrial Targeting

Mitochondrial targeting poses challenges that hinder the clinical translation of concepts with promising in vitro findings. Mitochondria-targeting molecules such as CPPs and MPPs suffer from physiological instability, including rapid proteolytic degradation and hepatic and renal clearance. These issues reduce systemic stability, limit bioavailability, and narrow their therapeutic window. The lack of selectivity between healthy and diseased tissues also represents a critical barrier. Targeting strategies that rely on features like MMP or CL interactions may inadvertently affect healthy cells with similar mitochondrial characteristics. Furthermore, the heterogeneity of mitochondrial features across cell types and disease states complicates the design of effective targeting molecules. For example, cancer cell mitochondria often exhibit elevated MMP or altered CL content, but the significant variation in these traits across tumor types and during progression

limits the universal applicability of many approaches. Toxicity represents another significant concern, especially for cationic molecules such as TPP, as they non-specifically accumulate and induce off-target effects.

Encouragingly, ongoing advances in nanomedicine have begun to address these challenges. In particular, polymer conjugates offer enhanced systemic stability and targeted release of bioactive molecules by tailor-designed synthesis and the incorporation of bioresponsive linkers that specifically undergo cleavage in the mitochondrial microenvironment. Rationally designed polymers support the ability to modulate size, charge, and surface chemistry to optimize delivery while minimizing non-specific interactions; they also allow for precise conjugation of targeting moieties, which enables improved mitochondrial specificity through interactions with unique features such as the TOM/TIM complex or CL[330].

1.3.3 Mitochondrial Targeting using Polymer Therapeutics

Crossing multiple biological barriers requires the precise customization of mitochondria-targeting polymer therapeutics, considering each stage of their in vivo journey. Cancer cell mitochondria offer distinctive features - such as enhanced mitochondrial depolarization, elevated ROS and GSH levels, abnormal ATP production, increased OCR, and upregulated anti-apoptotic signaling - that make them prime therapeutic targets. Drugs and targeting molecules such as TPP, with inherent mitochondrial toxicity, further amplify the therapeutic potential of these approaches. This section focuses on polymer therapeutics that primarily target mitochondria in cancer models while also highlighting emerging targeting molecules and their applications in other mitochondria-related diseases.

Polymer-based materials, especially polypeptides, serve as versatile platforms for designing mitochondria-targeting nanomedicines due to their inherent biodegradability, multivalency (facilitating combination therapies), and tunable responsiveness to specific stimuli. These systems frequently integrate mitochondria-targeting molecules, such as DLCs or MPPs, within smart materials or hierarchical targeting strategies. Challenges such as the intrinsic toxicity of DLCs, the physiological instability of MPPs, and the complexity of multi-level targeting designs have driven efforts to develop polymeric carriers modified with novel mitochondria-specific ligands or exhibiting intrinsic mitochondrial tropism (**Figure 1.8**). For a broader discussion of alternative approaches using nanomedicine to mitochondrial targeting, including lipid and hybrid materials, their specific

stimuli-triggered drug release, and state-of-the-art to evaluate mitochondrial targeting with nanomedicine, please refer to the review: "*Unlocking the Mitochondria for Nanomedicine-based Treatments: Overcoming Biological Barriers, Improving Designs, and Selecting Verification Techniques*," authored by Pegoraro et al. and published in Advanced Drug Delivery Reviews[1] and attached as an Annex in Section 1.4.

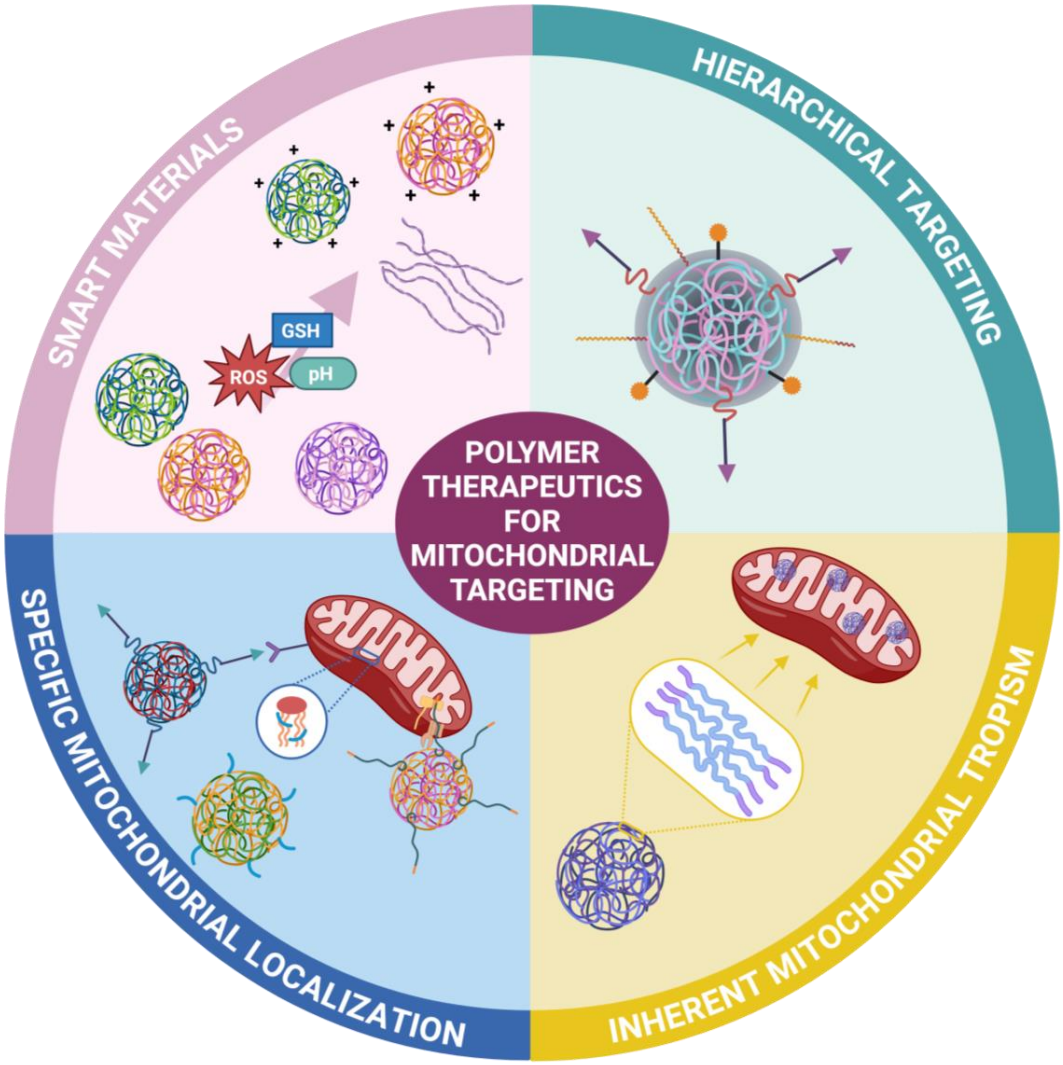


Figure 1.8. Mitochondrial Targeting using Polymer Therapeutics. The figure illustrates four critical strategies in polymer-based therapeutics for mitochondrial targeting. These include i) stimuli-responsive smart materials activated by elevated levels of reactive oxygen species (ROS) or glutathione (GSH) or acidic pH; ii) hierarchical systems designed to overcome sequential biological barriers; iii) polymeric nanocarriers functionalized with targeting moieties for precise mitochondrial localization; and iv) polymeric materials with inherent mitochondrial tropism that naturally interact with mitochondrial membranes or specific lipids like cardiolipin. *Figure created with Biorender*.

1.3.3.1 Smart Materials

Innovative smart materials with dynamic properties adapt to specific stimuli or microenvironments to enhance mitochondria-targeted therapeutic outcomes. Charge-reversal

materials represent a notable example: they initially possess a neutral or negative charge during administration to evade immune detection (stealth properties) but conversion to a positive charge under specific conditions (such as the acidic pH found in lysosomes/TME) to improve cell internalization.

Deng et al. developed α-cyclodextrin (α-CD)-based nanocarriers for breast cancer treatment and incorporated three functional elements: DOX conjugated via a pH-sensitive hydrazone linker; nitric oxide (NO) precursors for GSH-triggered NO release; and an acid-sensitive dimethylmaleic anhydride (DA)-modified PEG layer linked to an MPP[331]. The resultant α-CD-DOX-DA nanoparticles exhibited charge-reversal properties, displaying stability at pH 7.4 but undergoing charge reversal at pH 6.5 in the acidic TME to enhance mitochondrial localization. NO release amplifies the effects of DOX within the mitochondria by increasing membrane permeabilization, reducing ATP levels, and disrupting mitochondrial respiration. Compared to control nanoparticles containing a succinic anhydride linker that does not respond to acidic pH, α-CD-DOX-DA nanoparticles significantly improved therapeutic outcomes in 4T1 and drug-resistant MCF-7/DOX in vivo breast cancer models, overcoming drug resistance and metastasis through enhanced retention and targeted action.

Yang et al. employed the Pt(IV) prodrug OxPt-CDM and the mitochondrial-targeting cytotoxic peptide (FKLAK) as building blocks for the polymerization of a polymeric dual-drug nanoparticle for combination therapy[332]. Specifically, the two anhydride groups of OxPt-CDM reacted with FKLAK amino groups to form acid-labile amide bonds. The authors constructed this nanoparticle via polymerization at an emulsion interface, resulting in amphiphilic cross-linked polymers that self-assembled into nanoparticles with nearly 100% drug-loading efficiency. The amide bonds remained stable under neutral conditions but hydrolyzed under the acidic conditions of the TME, enabling the controlled release of OxPt-CDM and FKLAK. OxPt-CDM became reduced to its active form by the high intracellular GSH levels encountered in lung cancer cells, while FKLAK enhanced Pt accumulation by inhibiting drug efflux, effectively facilitating combination chemotherapy in vivo.

Smart materials can respond to stimuli or microenvironments by altering charge-based properties, enabling structural disassembly, and undergoing morphological changes. Song et al. introduced a coupling-induced assembly strategy to construct artificial shells on mitochondria for enhanced sonodynamic therapy[333]. Their peptide-porphyrin conjugate (TCPP-GGDFDFDYCGDKDRDK, named P1) combined mitochondria-targeting and oxidation-responsive modules (CGDKDRDK), a self-assembling module (FFY), and a porphyrin-based sonosensitizer

(TCPP). In the oxidative mitochondrial environment of tumor cells, the thiol group of P1 formed covalent disulfide bonds, transforming peptide-porphyrin conjugate nanoparticles into stable nanofibers through the ordered stacking of FFY dimers. This transformation increased mitochondrial binding via multivalent interactions, thereby enhancing mitochondrial targeting. The system generated ROS upon ultrasound irradiation, causing the loss of MMP and apoptosis. This approach supported the stabilization of self-assembled materials under physiological conditions and demonstrated a novel strategy for achieving dynamic morphological transitions to amplify therapeutic outcomes in a HeLa cell subcutaneous tumor model.

Despite the successes of these examples, the charge-reversal strategy remains constrained by challenges such as low conversion efficiency and reliance on heterogeneous stimuli (e.g., tumor pH variability and resistance mechanisms), which can increase the risk of off-target toxicity.

1.3.3.2 Hierarchical Targeting

Hierarchical targeting employs a multi-stage approach integrating a range of targeting elements and responsive release mechanisms to ensure the precise delivery of therapeutic agents to their intended subcellular destinations. Compared to charge-reversal strategies, hierarchical targeting offers improved specificity, enhanced therapeutic efficacy, and reduced off-target effects.

Ma et al. developed a mitochondria-targeted PTX delivery system using a TPP-poly(amidoamine)(PAMAM) dendrimer-PTX nanoconjugate[334]. The authors linked a TPP moiety to PAMAM via an amide bond and attached PTX through a disulfide bond. They achieved active targeting by conjugating glucose-PEG moieties via an MMP2-responsive GPLGIAGQ peptide linker, exploiting the overexpression of GLUT1 proteins in MCF7/ADR cells. In vivo experiments revealed that MMP2 overexpression in the TME triggered the detachment of the PEG layer, exposing the TPP moieties after nanoconjugate accumulation in the tumor. This mechanism supported mitochondrial targeting through direct cell penetration and the release of PTX following GSH-induced cleavage of the disulfide linker. The nanoconjugate significantly improved tumor growth inhibition compared to free PTX; furthermore, the authors observed the downregulation of efflux pump transporters due to ATP deprivation, which protected PTX from being pumped out of cells.

Liu et al. developed a mitochondria-targeting delivery system (GNPs-P-Dox-GA) to overcome MDR by enhancing ROS generation[335]. They conjugated DOX with glycyrrhetinic acid (GA), which functioned as both a tumor-targeting ligand (targeting protein kinase Cα) and a mitochondrial-

targeting agent (targeting serine hydroxy-methyltransferase 2, a mitochondrial protein involved in the serine/glycine biosynthesis pathway) to form GA-Dox. The authors then grafted the conjugate onto an N-(2-hydroxypropyl) methacrylamide (HPMA) copolymer backbone via a pH-sensitive hydrazone linker (P-Dox-GA) and attached the entire construct onto gelatin nanoparticles. The nanoparticles remained stable in circulation but underwent MMP2-mediated degradation in the TME, releasing P-Dox-GA, which displayed improved tumor penetration. The acidic microenvironment within tumor cell lysosomes hydrolyzed the hydrazone linker to release GA-Dox, which targeted mitochondria to induce ROS generation, leading to mitochondrial damage and the suppression of P-glycoprotein activity. This mechanism prompted robust in vitro and in vivo antitumor efficacy, with a tumor growth inhibition rate 1.75 times greater than free DOX in a HepG2/adriamycin (HepG2/ADR) mouse model. Overall, these findings demonstrated that hierarchical targeting effectively addressed MDR in cancer therapy.

While offering enhanced specificity, hierarchical targeting systems face limitations due to their reliance on multiple sequential steps (e.g., tissue penetration, cell uptake, and subcellular localization) that must display/retain efficient activity. Variability in biological conditions (e.g., tumor heterogeneity, microenvironmental factors, or receptor expression) can also hinder their activity. Finally, the complex design and manufacturing processes associated with hierarchical targeting systems prompt additional challenges when considering scalability and clinical translation.

1.3.3.3 Specific Mitochondrial Targeting Localization

Due to their proven efficacy, DLCs are widely used mitochondria-targeting molecules in nanomedicine; however, they still suffer from significant limitations. Their dependence on MMP for accumulation reduces retention after treatment-induced mitochondrial depolarization. While they tend to accumulate in cancer cell mitochondria due to the higher MMP, this behavior also remains inconsistent due to tumor cell heterogeneity. Additionally, DLCs exhibit concentration-dependent toxicity, which can be beneficial in designing cancer therapies but may limit their application in non-cancer diseases. Furthermore, DLCs like TPP lack specificity and accumulate in various mitochondrial compartments, including the mitochondrial matrix and IMM, and, as such, lack a precise targeting mechanism.

To improve specificity, mitochondria-targeting moieties that bind specific molecular targets independently of the MMP offer significant advantages, especially when the targets exhibit pathological alterations. Sharma et al. developed a PAMAM dendrimer conjugated to a TSPO

targeting ligand (D-DPA) for glioblastoma treatment[336]. TSPO, upregulated in neuroinflammation and cancer, plays a role in cholesterol transport for steroidogenesis; in glioblastoma, TSPO overexpression in tumor-associated macrophages correlates with poor prognosis. D-DPA successfully targeted tumor-associated macrophages, colocalized with mitochondria, and enhanced proinflammatory cytokine production while reducing cytotoxicity in non-cancer cells compared to a conventional TSPO ligand. Zhang et al. employed SS-31 for mitochondrial targeting as a component of an ischemic stroke treatment[337]. SS-31 targets CL in the IMM independently of MMP, reducing mitochondrial ROS production and inhibiting mPTP formation. The authors conjugated SS-31 to chitosan via a ROS-sensitive crosslinker to create multifunctional nanoparticles encapsulating the antioxidant Puerarin. In vivo studies in a stroke mouse model demonstrated that these nanoparticles significantly reduced infarct size, mitigated oxidative stress and inflammation, and restored mitochondrial function.

In a related study, Li et al. developed a mitochondrial-targeted drug delivery system (P-D-R8MTS) to suppress breast cancer metastasis[338]. Their system incorporated HPMA copolymers modified with a hybrid peptide (R8MTS) – which combines the CPP octaarginine (R8) for cell penetration and the ALD5 MTS for mitochondrial targeting - and DOX via a pH-sensitive hydrazone linker (P-D-R8MTS). In 4T1 and MDA-MB-231 breast cancer cells, P-D-R8MTS demonstrated enhanced cellular uptake, mitochondrial co-localization, and ROS generation, effectively inhibiting cancer cell migration and invasion. In vivo, P-D-R8MTS reduced tumor growth by 86.8% in 4T1 tumor-bearing mice and completely prevented lung metastases.

These studies underscore the potential of mitochondria-targeting strategies to overcome the limitations of DLCs and improve the precision and efficacy of polymer-based therapeutics. By incorporating specific targeting mechanisms that do not rely on MMP, these approaches enhance selective mitochondrial accumulation and activity in pathological contexts.

1.3.3.4 Inherent Mitochondria-Targeting Polymeric Carriers

Polymeric carriers with intrinsic mitochondrial tropism present a safer and cost-effective alternative due to their reduced need for complex functionalization. This reduced complexity lowers production costs and facilitates more straightforward clinical translation, making them a promising platform for targeted therapies. Geng et al. demonstrated the mitochondrial colocalization of zwitterionic poly[2-(N-oxide-N,N-diethylamino)ethyl methacrylate] (OPDEA) following internalization via micropinocytosis in HepG2 cells in vitro and also in vivo[339]. Jin et al. expanded

upon this concept by designing an amphiphilic block polymer combining OPDEA with dichloroacetate to induce mitochondrially-mediated pyroptosis through oxidative stress activation in osteosarcoma models[340].

OPDEA displays significant mitochondrial affinity through an unknown mechanism; however, additional properties can be fine-tuned to enhance the targeting efficiency of polymers. Liu et al. reported that fluorinated phosphatidylethanolamine (PE)-PEG derivatives self-assembled into fluoroamphiphiles, exhibiting enhanced cellular uptake and novel mitochondria-targeting properties[341]. Among the various PEGm-Fn derivatives evaluated, PEG2k-F7 displayed the highest internalization levels in ovarian (HeLa and NCI/ADR-RES) and breast cancer cells due to optimal hydrophilicity-to-hydrophobicity balance. This derivative targeted mitochondria in a potential-independent manner through CL binding, which they validated in isolated mitochondria and mitochondria-like liposomes. When loaded with the anti-cancer drug vitamin E succinate, PEG2k-F7 micelles significantly reduced tumor size in a 4T1 mouse model, outperforming the free drug.

Polymeric carriers can also incorporate targeting moieties directly in their structure. Zhang et al. developed nanoparticles using a near-infrared Changsha Red monomer, a DLC copolymerized with dimethylacrylamide[342]. Functionalized with a cyclic Arg-Gly-Asp (cRGD) peptide to target integrins overexpressed by melanoma cells, these nanoparticles displayed mitochondria-targeting properties without additional functionalization. In melanoma models, these nanoparticles combined mild photothermal therapy and immunotherapy to enhance mitochondrial damage and inhibit primary and metastatic tumors.

Cohen-Erez et al. fabricated polypeptide-based nanoparticles by coassembling poly-γ-glutamic acid (γ-PGA) with the β-sheet peptide PFK to form negatively charged PoP-NPs[343]. They developed enhanced formulations (C-LND-mPoP-NPs) to minimize cytotoxicity while maintaining mitochondrial targeting via electrostatic interactions with the negatively charged mitochondrial membrane. Loaded with the OMM inhibitor lonidamine (LND), these nanoparticles demonstrated enhanced therapeutic efficacy in TNBC models, significantly inhibiting tumor growth compared to the free drug.

Polypeptide-based polymer therapeutics with mitochondrial targeting properties remain a relatively unexplored area, despite their considerable promise in nanomedicine, as highlighted in section 1.2.2.1. This thesis investigates this innovative approach, demonstrating its clear potential and feasibility. To provide a broader context for this work, the review authored by Pegoraro et al.

[1]has been included in section 1.4, offering a comprehensive overview of of alternative nanomedicine strategies for mitochondrial targeting, including lipid and hybrid materials, stimuli-responsive drug release, and advancements in evaluating mitochondrial targeting.

1.4 Manuscript I: Review

In the following section, a review on advancements in mitochondria-targeted nanomedicines is presented to conclude Chapter 1. This review focuses on overcoming biological barriers, optimizing design strategies, and validating precision-targeting approaches, providing a comprehensive foundation for the thesis.

Reference[1]: Pegoraro, C., Domingo-Ortí, I., Conejos-Sánchez, I., & Vicent, M. J. (2024). Unlocking the mitochondria for nanomedicine-based treatments: Overcoming biological barriers, improving designs, and selecting verification techniques. Advanced Drug Delivery Reviews, 207, 115195. DOI: 10.1016/j.addr.2024.115195&#8203.

Advanced Drug Delivery Reviews 207 (2024) 115195

Contents lists available at ScienceDirect

Advanced Drug Delivery Reviews

journal homepage: www.elsevier.com/locate/adr

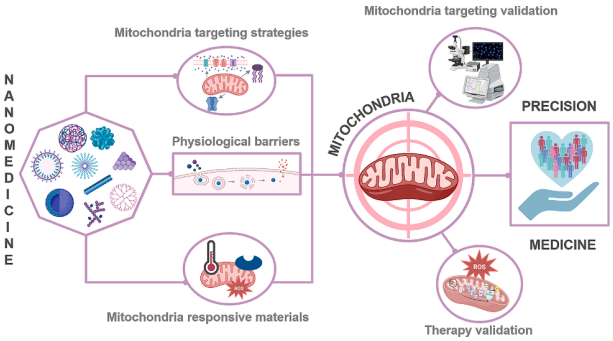
Unlocking the Mitochondria for Nanomedicine-based Treatments: Overcoming Biological Barriers, Improving Designs, and Selecting Verification Techniques

Camilla Pegoraro, Inés Domingo-Ortí, Inmaculada Conejos-Sánchez *, María J. Vicent *

Polymer Therapeutics Laboratory and CIBERONC, Príncipe Felipe Research Center, Av. Eduardo Primo Yúfera 3, E-46012 Valencia, Spain

GRAPHICAL ABSTRACT

Advancements in Mitochondria-Targeted Nanomedicines for Precision Therapeutic Delivery. Unveiling biological barriers, nanomedicine rational design, and validation techniques for subcellular precision.



Abbreviations: Aco, Cis-aconitic acid; AIF, Anti-apoptosis-inducing factor; AKI, Acute kidney injury; ATP, Adenosine triphosphate; B6, Vitamin B6; Bax, Bcl-2-associated X protein; Bcl-2, B-cell lymphoma-2; Ber, Berberine; BSA, Bovine serum albumin; C, Chitosan; C6, Coumarin 6; CA, Free cinnamaldehyde; CAFs, Cancer-associated fibroblasts; CAMP, Cell penetrating artificial mitochondria-targeting peptide; CD, Cyclodextrin; Cela, Celastro; CHEMS, Cholesteryl hemisuccinate; CLEM, Correlative light-electron microscopy; CLSM, Confocal laser scanning microscopy; CME, Clathrin-mediated endocytosis; CNM, Cinnamaldehyde; COVID-19, Coronavirus disease 2019; CPEGT, C18-PEG2k-TPP; CPP, Cell-penetrating peptide; CPT, Camptothecin; CQ, Chloroquine; cRGD, Cyclic Arg-Gly-Asp; CS, Chondroitin sulfate; CSMA, Changsha Red-based polymer; CSOSA, Polycationic glycolipid polymer; Cur, Curcumin; CVME, Caveolae-mediated endocytosis; Cyt-C, Cytochrome *C*; DA, Dimethylmaleic anhydride; DCFH-DA, 2′,7 -dichlorofluorescein diacetate; DF, Dual function; DHE, Dihydroethidium; DLC, Delocalized lipophilic cation; Dlin-MC3-DMA, Dilinoleylmethyl-4-dimethylaminobutyrate; DLPE, 1,2-dilauroyl-*sn*-glycero-3-phosphoethanolamine; DMA, Dimethylacrylamide; Dmt, 2,6-dimethyl-L-tyrosine; DOPAP, 1,2-dioleoyl-3-dimethylammonium propane; DOPE, Dioleoylphosphatidylethanolamine; DOTAP, 1,2-dioleoyl-3-trimethylammonium propane; DOX, Doxorubicin; DP, Polymer dendron; DPA, 5,7-dimethylpyrazolo[1,5-α]pyrimidin-3-ylacetamide; DQA, Dequalinium; DSPE, 1,2-distearoyl-*sn*-glycero-3-phosphoethanolamine; dsRNA, Double-stranded RNA; DSSP, DLPE-SS-mPEG4K; ECAR, Extracellular acidification rate; ECM, Extracellular matrix; EELS, Electron energy loss spectroscopy; EFTEM, Energy-filtered transmission electron microscopy; EMA, European medicines agency; EPC, Egg yolk phosphatidyl choline; EPR, Enhanced permeability and retention; ESI-MS, Electrospray ionization-mass spectrometry; ETC, Electron transport chain; EV, Extracellular vesicle; FA, Folic acid; FAD, Flavin adenine dinucleotide; Fc, Fenton organocatalyzed ferrocene; FCCP, Carbonyl cyanide-p-trifluoromethoxyphenylhydrazone; FDA, Food and drug administration; FITC, Fluorescein; Fn, Fluorocarbon segments.

* Corresponding authors.

E-mail addresses: cpegoraro@cipf.es (C. Pegoraro), idomingo@cipf.es (I. Domingo-Ortí), iconejos@cipf.es (I. Conejos-Sánchez), mjvicent@cipf.es, mjvicent@gmail.com (M.J. Vicent).

https://doi.org/10.1016/j.addr.2024.115195
Received 24 October 2023; Received in revised form 13 January 2024; Accepted 2 February 2024
Available online 5 February 2024
0169-409X/© 2024 The Author(s). Published by Elsevier B.V. This is an open access article under the CC BY-NC license (http://creativecommons.org/licenses/by-nc/4.0/).

ARTICLE INFO

Keywords:
Intracellular delivery
Subcellular targeting
Stimuli-responsive nanomedicine
Mitochondrially targeted precision nanomedicines
Mitochondrial activity and metabolism
Physico-chemical characterization

ABSTRACT

Enhanced targeting approaches will support the treatment of diseases associated with dysfunctional mitochondria, which play critical roles in energy generation and cell survival. Obstacles to mitochondria-specific targeting include the presence of distinct biological barriers and the need to pass through (or avoid) various cell internalization mechanisms. A range of studies have reported the design of mitochondrially-targeted nanomedicines that navigate the complex routes required to influence mitochondrial function; nonetheless, a significant journey lies ahead before mitochondrially-targeted nanomedicines become suitable for clinical use. Moving swiftly forward will require safety studies, *in vivo* assays confirming effectiveness, and methodologies to validate mitochondria-targeted nanomedicines' subcellular location/activity. From a nanomedicine standpoint, we describe the biological routes involved (from administration to arrival within the mitochondria), the features influencing rational design, and the techniques used to identify/validate successful targeting. Overall, rationally-designed mitochondria-targeted-based nanomedicines hold great promise for precise subcellular therapeutic delivery.

1. Introduction

1.1. Unleashing the Power Within: The Significance of Intracellular Delivery

Subcellular targeting of bioactive compounds has emerged as a promising frontier in precision medicine, offering opportunities for improved therapeutic outcomes and personalized treatments. By specifically targeting subcellular compartments or organelles where disease-related processes occur, therapeutically-relevant molecules can accumulate at higher concentrations at an intended site, thereby enhancing specificity and efficacy. Targeted delivery approaches also enable the administration of lower therapeutic doses, thereby minimizing unwanted off-target toxicities in non-targeted tissues and enhancing the overall safety profile of a given therapeutic strategy [1]. Subcellular targeting of bioactive molecules also holds significant potential regarding therapeutic resistance by overcoming associated mechanisms in complex diseases such as cancer [2,3]. Additionally, multivalent approaches to the simultaneous/sequential delivery of various agents to distinct intracellular compartments can leverage synergistic effects and improve the likelihood of successful treatment outcomes [4]. Furthermore, subcellular targeting strategies support real-time monitoring of treatment responses at the subcellular level; imaging techniques or tracking specific subcellular biomarkers or metabolites can dynamically assess therapeutic efficacy [5]. Said monitoring capabilities can provide valuable insights into subcellular changes occurring during disease development/treatment schedules and allow for timely adjustments in therapeutic strategies.

Despite advancements in subcellular drug delivery strategies through the development of multiple nanomedicine-based approaches, key biological barriers remain significant, often impeding progress beyond preclinical stages [6,7]. This review aims to provide an overview of the physiological barriers that hinder efficient intracellular delivery, focusing on the mitochondrion as the final target. Mitochondria play crucial roles in cellular metabolism, function, and regulation and influence redox status, cell growth, signaling, and ion homeostasis. Due to their involvement in cell death/survival, the pathogenesis/progression of various diseases (including genetic disorders, neurodegeneration, cardiovascular diseases, diabetes, and cancer) critically involve mitochondria-associated processes [8]. Therefore, given the apparent

fNDs, Fluorescent nanodiamonds; FRET, Förster resonance energy transfer; G, Gboxin; GA, Glycyrrhetinic acid; GFLG, Cathepsin B cleavable peptide; GFP, Green fluorescent protein; GLUT1, Glucose transporter 1; GNPs, Gelatin nanoparticles; GSH, Glutathione; GTP, Guanosine triphosphate; HA, Hyaluronic acid; HER-2, Epidermal growth factor receptor-2; HFn, Heavy chain ferritin; HM, Hybrid membrane; hMT1A, Antioxidant protein human metallothionein 1A; HPLC, High-performance liquid chromatography; HPSC, HER-2 peptide-PEG2000-Schiff base-cholesterol; HSA, Human serum albumin; ICP-MS, Inductively-coupled plasma mass spectrometry; IMM, Inner Mitochondrial Membrane; IMS, Intermembrane space; INH, Isoniazid; iPhos, Ionizable phospholipid; iRGD, CRGDKGPDC peptide; JC-1, 5,5′,6,6 -tetrachloro-1,1′,3,3 -tetra-ethylbenzimidazolcarbocyanine iodide; Kim-1, Kidney injury molecule-1; KLA, Proapoptotic peptide; KLAK, CGGG(KLAKLAK)2 peptide; Lap, Lapatinib; LND, Lonidamine; LPHNPs, Lipid-small molecule hybrid nanoparticles; Luc, D-Luciferin; *m/z*, Mass-to-charge ratio; MA, Mycolic acid; Mal, Maleimide; MCAO, Middle cerebral artery occlusion; Met, Metformin; Mitocur, Mitochondrially targeted curcumin; MMP, Mitochondrial membrane potential; MMP2, Matrix metalloproteinase 2; mPEG, Monomethyl polyethylene glycol; mPoP NPs, PGA and PFK nanoparticles; MPP, Mitochondria-penetrating peptide; mPTP, Mitochondrial permeability transition pore; MS, Mass spectrometry; MSI, Mass spectrometry imaging; mtDNA, Mitochondrial DNA; MTS, Mitochondria-targeting sequence; NAD^+, Nicotinamide adenine dinucleotide; NBD, Nitrobenzoxadiazole; NMR, Nuclear magnetic resonance; NO, Nitric oxide; NOC-18, Nitric oxide donor; NPs, Nanoparticles; NQC, N-quaternary ammonium-chitosan; OCR, Oxygen consumption rate; oHASS, Oligomeric hyaluronic acid-dithiodipropionic acid; OMM, Outer mitochondrial membrane; OPDEA, Poly[2-(N-oxide-N,N-diethylamino)ethyl methacrylate; OXPHOS, Oxidative phosphorylation; P1, Oligolysine; PA, Phosphatidic acid; PAGA, poly(alkylene glycol); PAMAM, Polyamidoamine; PAsp(DET), Poly{N-[N -(2-aminoethyl)-2-aminoethyl]aspartamide}; PBAEs, Poly(beta-amino esters); PBS, Phosphate buffered saline; PDAA, ROS-sensitive thioketal crosslinker; PD-L1, Programmed death-ligand 1; PDMAEMA, Poly(2-dimethylaminoethyl methacrylate); PDT, Photodynamic therapy; PE, Phosphatidylethanolamine; PEG, Poly(ethylene glycol); PEI, Polyethyleneimine; PEOGMA, Poly[oligo(ethylene glycol) methyl ether methacrylate; Pep, Metalloproteinases-responsive peptide; PFK, (Pro-(Lys-Phe)5-Lys-Pro peptide; PGA, Poly-L-glutamic acid; P-gp, ATP-dependent efflux pump; pIC, Polyinosine-polycytidylic acid; PKG, Protein kinase G; PLA, Poly(D, L-lactide); PLGA, Poly(lactide-co-glycolide); PLL, Poly-L-lysine; PLO, Polyornithine; PN, Polydrug nanoreactor; PNIPAM, Poly(N-isopropylacrylamide); POEGMA, Poly[oligo-(ethylene glycol) methyl ether methacrylate]; POSS, Octaammonium polyhedral oligomeric silsesquioxane; Pox, Poly(2-oxazoline); PPA, Polyamidoamine nanoparticles; PPa, Pyropheophorbide-a; PPCs, Polymer-peptide conjugates; PPro, Polyproline; PQC-PS, Pheophorbide A-quinolinium conjugate; pRBCs, Red blood cells; PSar, Polysarcosine; PSC, PEG2k-Schiff base bond-cholesterol; PTX, Paclitaxel; PU, Puerarin; PVP, Polyvinyl pyrrolidone; R8, Octaarginine; RES, Reticuloendothelial system; Rh, Rhodamine; ROS, Reactive oxygen species; rTPA, Porphyrin-type photosensitizer; SA, Succinic anhydride; SARS-CoV-2, Severe acute respiratory syndrome coronavirus 2; SC, L-serine-modified chitosan; SDH, Succinate dehydrogenase; SIMS, Secondary-ion mass spectrometry; siRNA, Small interfering RNA; SOSG, Singlet oxygen sensor; SRM, Super-resolution microscopy; SS, Szeto-Schiller; -SS-, Disulfide bond; STR-R8, Stearylated octaarginine; SWNTs, Single-walled carbon nanotubes; TAMs, Tumor-associated macrophages; TCA, Tricarboxylic acid; TCC, 2,3,5-Triphenyltetrazolium chloride; TEM, Transmission electron microscopy; TfR1, Transferrin receptor 1; TGF-β, Transforming growth factor beta; TIM, Translocase of the inner mitochondrial membrane; TK, Thioketal; TME, Tumor microenvironment; TMRE, Tetramethylrhodamine ethyl ester; TMRM, Tetramethylrhodamine methyl ester; TOM, Translocase of the mitochondrial outer membrane; TPP, Triphenylphosphonium; TSPO, Translocator protein; UV–Vis, Ultraviolet–visible; VDAC, Voltage-dependent anion channel; VES, Vitamin E succinate; γ-PGA, Poly-γ-glutamic acid.

clinical significance of targeting mitochondria in disease treatment, we discuss the strategies developed to target mitochondria effectively and present a comprehensive portfolio of the techniques used to evaluate mitochondrial targeting and validate efficacy (Fig. 1). We aim to highlight challenges and recent advancements in achieving precise and efficient intracellular delivery to mitochondria and the potential application of this approach in precision medicine.

2. Improving the Delivery of Nanomedicines: Moving Beyond Adequate

Recent decades have seen the clinical approval of a range of nanomedicines, from Doxil in 1995 [9] to SpikeVax in 2021 [10] - the coronavirus disease 2019 (COVID-19) vaccine developed by Moderna. Nanomedicines leverage the well-established enhanced permeability and retention (EPR) effect observed in diseased tissues in conditions such as cancer, infection, and heart failure [11–13], as well as more recently explored strategies, which include transcytosis or specific active cell targeting [14,15], to enhance selective tissue/cell accumulation [16]. Despite advances in the nanomedicine field, successful targeting of a desired pathological site remains relatively low; a recent study by Wilhelm et al. reported that only 0.7 % of the injected nanomedicines analyzed from 117 published preclinical studies effectively reached solid tumor sites [17].

Many factors impact insufficient delivery of nanomedicine; however, rational design guided by an in-depth comprehension of both normal

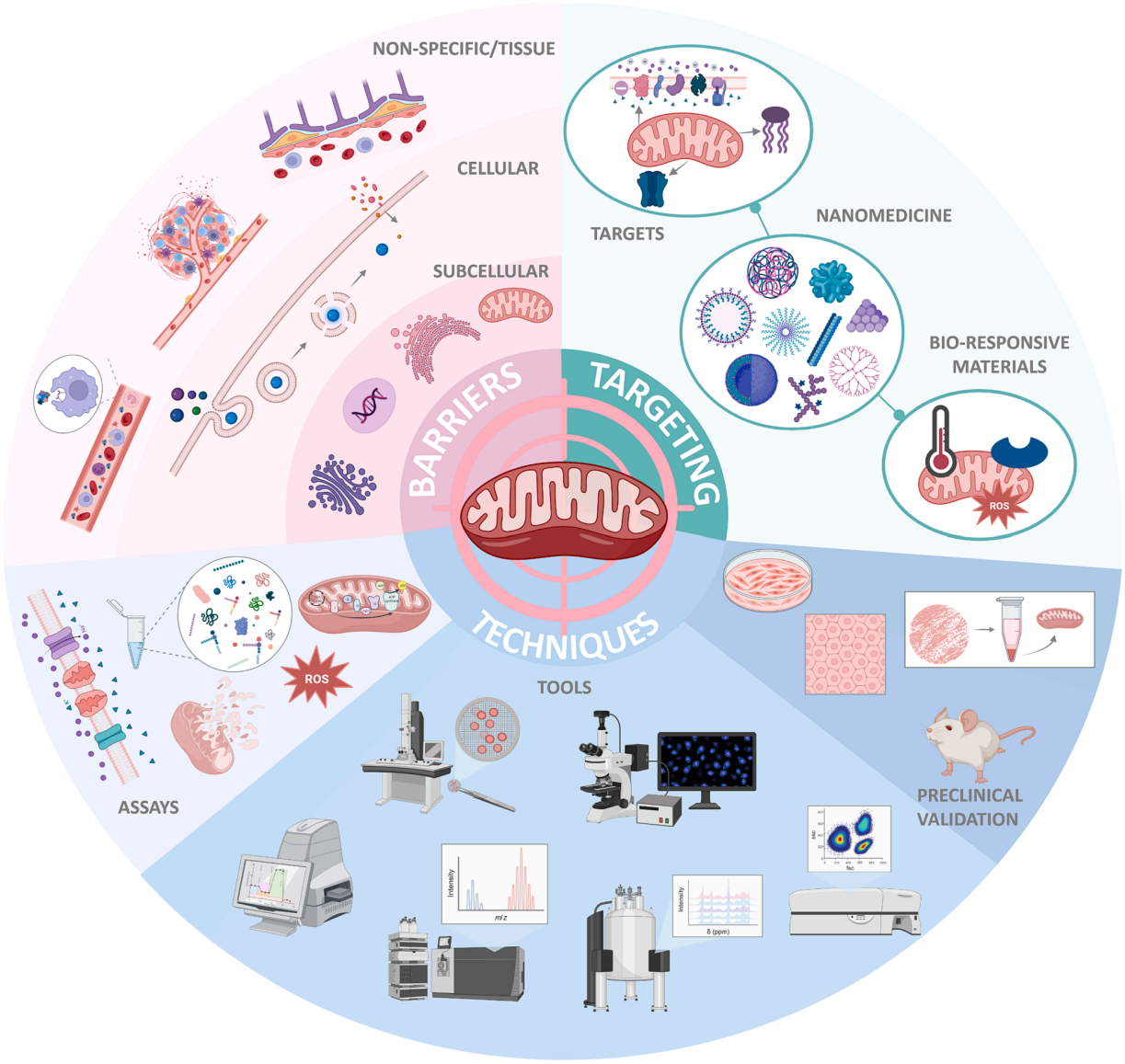


Fig. 1. Unlocking the challenges and opportunities in the design of Mitochondria-targeted Nanomedicines. i) A description of the physiological barriers - including non-specific barriers (e.g., reticuloendothelial system), tissue-specific barriers and microenvironments (e.g., tumor microenvironment (TME), blood–brain barrier), cell membrane and subcellular barriers (e.g., mitochondria) - hindering efficient intracellular delivery of nanomedicines and strategies to overcome these limitations. ii) An overview of polymer, lipid, and hybrid-based nanomedicines targeting mitochondria, focusing on specific mitochondrial features critical for targeting (e.g., negative membrane potential, cardiolipin, specific proteins), mitochondria targeting moieties, stimuli-responsive materials, and design strategies successfully translated into preclinical models of disease. iii) A comprehensive portfolio of tools (e.g., confocal laser scanning microscopy, Seahorse XF Analyzer) and assays (e.g., JC-1 for mitochondria depolarization analysis, reactive oxygen species (ROS) generation) to evaluate mitochondrial targeting efficiency and pharmacological activity of designed nanomedicines in preclinical models (in vitro 2D and 3D, *in vivo* models and isolated mitochondria), to facilitate the clinical translation of mitochondrially-targeted precision nanomedicines.

and disease-related physiological conditions can yield the required pharmacokinetic features and the ability to adjust crucial interactions with biological barriers influencing nanomedicine uptake efficiency and its fate within the intracellular/subcellular environment [18–21].

2.1. Biological barriers

Following systemic administration, biological barriers exist in a hierarchical order, including non-specific/circulatory, tissue-specific/microenvironmental, cellular, and subcellular barriers. Numerous factors increase the complexity of this general classification, such as the administration route employed, the disease targeted, and the degree of patient-to-patient variability; therefore, a one-size-fits-all approach for crossing a biological barrier does not currently exist.

2.1.1. Non-specific/circulatory barriers

The phagocytic reticuloendothelial system (RES) system is the main non-specific obstacle to nanomedicines in the bloodstream, with interactions depending on their intrinsic physicochemical characteristics [22]. The decoration of nanomedicines with poly(ethylene glycol) ("PEGylation") represents an effective stealth strategy that prolongs the half-lives of nanomedicines *in vivo* by preventing their recognition by the RES; however, the net surface charge change and the size modulation involved can reduce cellular uptake, thereby limiting efficacy [23–25]. PEGylation can also trigger hypersensitivity reactions by activating the complement system [26]; therefore, researchers have proposed alternative hydrophilic polymers with enhanced targeting abilities and lower immunogenic response, such as poly(2-oxazoline)s (Pox), polysarcosines (PSar), and zwitterionic polymers (e.g., phosphorylcholine) [27,28]. The use of biomimicry camouflage exploiting endogenous cell components (e.g., red blood cells) and the design of non-spherical nanoparticles (e.g., ellipsoidal, cylindrical, and discoidal nanoparticles) represent other strategies followed to avoid the RES [29]. Interestingly, non-spherical shapes favor the interaction of nanomedicines with vessel endothelial cells ("lateral drift" or "margination dynamics"), which holds relevance for nanomedicine-cell/receptor-ligand interactions and extravasation prior to RES recognition [30].

Using the EPR effect concept as a driver to enhance nanomedicine accumulation represents another factor that requires consideration, as recent studies have provided evidence for the heterogeneous nature of this dynamic phenomenon and strict dependence on blood flow, vascularization, fluid pressure, and vascular occlusion [31]. Recent reviews have described the contribution of two additional processes in nanomedicine accumulation at the tumor site – i) nanomedicine hitchhiking (also called "back-packing") by macrophages and other immune cells [32–34] in which circulating monocytes, due to their natural phagocytic properties, are harnessed for nanomedicine loading, and ii) active endothelial transcytosis [35], a mechanism that assists in enhancing the effectiveness of nanomedicine tumor homing thanks to the active extravasation of tumor endothelial cells without relying on the EPR effect.

2.1.2. Tissue-specific barriers/microenvironments

Specific organs contain critical blood-tissue barriers, such as the gastrointestinal and pulmonary epithelial/mucosal barrier, the blood-aqueous ocular barrier [36], or one of the most challenging, the blood–brain barrier with < 5 % brain-targeted nanomedicine entering clinical trials and none reaching yet the market [37–39].

Tissue microenvironments under physiological or pathological conditions significantly affect targeted nanomedicine delivery due to the need to overcome significant pH variations, enzymatic activities, the presence of mucosal barriers, or the gut microbiome as in the case of the gastrointestinal barrier [40–42]. In particular, the TME represents a crucial and complex milieu containing abundant stromal components such as tumor-associated macrophages (TAMs) or cancer-associated fibroblasts (CAFs), which prevent extracellular matrix (ECM) enzymatic breakdown, thereby enhancing compactness. The TME presents high interstitial fluid pressure, heterogeneous tumor vascularization, hypoxia, and acidic pH [43]. An understanding of these limitations represented the driver of nanomedicines that have reached the clinic, such as the PEGylated recombinant human hyaluronidase (PEGPH20, Halozyme Therapeutics) [44] or innovative designs such as that reported by Duan et al., who described a detachable dual-targeting anti-tumor nanomedicine based on a hyaluronic acid- DOX (HA-DOX) conjugate loaded into gelatin nanoparticles (GNPs) and metformin (Met) loaded into heavy chain ferritin (HFn) cages linked by an amide bond to form HA-DOX@GNPs-Met@HFn nanoparticles [45]. Overexpression of matrix metalloproteinase 2 (MMP2) within the TME prompted GNP degradation, leading to decomposition into smaller-sized HA-DOX and Met@HFn nanoparticles with enhanced tumor permeation abilities. Importantly, HFn undergoes depolymerization in the acidic TME and targets the transferrin receptor 1 (TfR1), which displays high expression levels on the tumor cell surface. After the internalization of detached Met@HFn within tumor cells, free Met downregulated Transforming growth factor beta (TGF-β) activity, thereby suppressing CAF activity to finally result in ECM depletion. Stromal depletion ensured deeper HA-DOX penetration into tumor tissues, improving chemotherapy efficiency *in vivo*.

While representing a significant physiological barrier, the TME also possesses differential features that we exploited to design stimuli-responsive nanomedicines that release cargo only in the presence of disease-associated stimuli, including the presence of specific proteases [46] and altered pH values/redox balance [47] (See [48–50] for more detailed reading on this topic).

2.1.3. Cellular and subcellular barriers

After reaching the pathological environment, most engineered nanomedicines have intracellular or subcellular targets [51]; therefore, the internalization pathway followed, including the various forms of endocytosis facilitated by lipid rafts and proteins [52,53] or the use of direct cell membrane penetration strategies [54], remains of critical importance to control nanomedicine fate and efficiency. Optimizing nanomedicines to target subcellular organelles or compartments holds enormous appeal, as this strategy can enhance efficacy while minimizing the required dosages and, therefore, off-target effects [51].

Despite the promising advantages of sub-cellular targeting, two main challenges require consideration: endosomal escape and basic organelle characteristics. Most nanomedicines become internalized through clathrin-mediated endocytosis (CME) due to the versatility in size and ubiquity of clathrin-coated vesicles in eukaryotic cells and then undergo trafficking through early endosomes, late endosomes, and lysosomes, where hydrolases degrade their content [55,56]. In contrast, caveolae-mediated endocytosis (CVME) relies on plasma membrane invaginations coated with caveolin ("caveolae") that typically display a size of 50–80 nm. Caveolae subsequently become transported to the cell interior, eventually maturing in caveosomes, bypassing endosomes and lysosomes [57], and reaching intracellular destinations like the Golgi apparatus and the endoplasmic reticulum. In the case of CME, strategies facilitating endosomal escape must be considered during nanomedicine design to ensure organelle-specific targeting (when not specifically targeting the endosomal/lysosomal compartment). Alternatively, CVME appears as an appealing uptake mechanism that prevents lysosomal degradation, facilitates cytosolic delivery, and targets specific subcellular compartments when considering nanomedicines. Another prominent form of endocytosis – macropinocytosis - involves the extension of the plasma membrane because of cytoskeleton rearrangements supported by actin, which enables the cell to internalize a variety of macromolecules dissolved in the extracellular fluid in large vesicular structures known as macropinosomes (0.2–5 μm) [58].

Notably, subcellular organelles, such as the nucleus, mitochondria, endoplasmatic reticulum, and Golgi apparatus, are characterized by highly specific functions, membranes, and defense mechanisms,

necessitating careful consideration in nanomedicine design [59]. These features can be exploited in the fabrication of subcellular-targeting nanomedicines; however, efficient delivery systems have been developed for only mitochondria and nuclei, as we currently lack sufficient information to support a comprehensive design strategy targeting either the Golgi apparatus or the endoplasmatic reticulum [60].

Uptake efficiency and the pathway employed result from complex interactions between nanomedicines and cells; therefore, careful planning of nanomedicine design with in-depth "know-how" regarding the cell type and subcellular target can allow the engineering of nanomedicine that preferentially uses a desired uptake mechanism.

2.2. Tailoring the subcellular targeting of nanomedicines

Using a rational design approach to customize the physico-chemical features of nanomedicines to target a specific internalization pathway can determine the final subcellular fate. This issue represents an ongoing endeavor, and understanding design features tailoring nanomedicine fate represents a critical challenge.

Size remains a critical factor for cellular uptake as this parameter influences diffusion, the contact area, and membrane deformation energy. Gimondi *et al.* demonstrated that various poly(lactide-co-glycolide)-block-poly(ethylene glycol) (PLGA-PEG) nanoparticles of different sizes (30, 50, and 70 nm) used differing internalization mechanisms [61]; overall, endothelial cells employed CVME to uptake 50 nm nanoparticles but CME to uptake 70 nm nanoparticles, even though macropinocytosis represents the preferential uptake mechanism in endothelial cells and inflammation-stimulated macrophages.

Shape represents another crucial factor modulating nanomedicine uptake; for example, Xie *et al.* demonstrated that gold nanotriangles exhibited more significant cellular uptake in murine macrophage cells, followed by gold nanorods and nanostars [62]. Even though all three shapes employed CME, nanorods also used CVME, while nanotriangle uptake strongly depended on cytoskeleton rearrangements (i.e., macropinocytosis). Nevertheless, the potential benefits of non-spherical-shaped nanomedicines in enhancing cell uptake remain under debate. Predictive mathematical modeling tools, such as quantitative structure–activity relationship approaches (to study the physicochemical properties of a variety of non-spherical compounds), continuum membrane models (to study the mechanical properties of membranes), and molecular dynamic simulations (to study the receptor-mediated membrane wrapping processes) should be used to comprehensively explore improved uptake capabilities, thus facilitating a deeper understanding of their impact [63,64].

Net surface charge (zeta potential) also influences nanomedicine uptake and may change in response to environmental conditions after administration, including the protein corona formation [65]. Arezki *et al.* conducted a systematic proteomic analysis demonstrating that the zeta potential and surface charge density of nanoparticles impact protein corona formation and the uptake and cytotoxicity of polyamine surface-passivated cationic carbon dots in macrophages [66]. Interestingly, they observed a direct correlation between carbon dots with higher surface charge density (>2 μmol/mg) and the presence of specific proteins (e.g., complement, fibulin, fetuin, alpha-glycoprotein) in enhancing cellular uptake. The electrostatic interaction between nanoparticles and the cell membrane significantly affects nanoparticle internalization. Cationic nanoparticles suffer from a more significant electrostatic attraction and cell accumulation [67] but also commonly manifest cytotoxic effects owing to the perturbation of membrane bilayer structural integrity, which increases with high charge density [68]. Using anionic carboxylated surface chemistry can also determine cell interaction and differential subcellular trafficking of a given nanomedicine [69]. Vicente-Ruiz et al. [70] recently demonstrated this phenomenon, reporting that poly-L-glutamic acid (PGA) conjugation to an anti-insulin growth factor 1 receptor antibody (AVE1642) changed internalization pathways from CME to CVME. The authors showed that conjugation did not interfere with the antibody-receptor binding domains but triggered the modification of the antibody cell uptake mechanism, changing its molecular mechanism of action upon conjugation and enhancing its anticancer activity in an orthotopic *in vivo* prostate cancer model [70].

Finally, the ***effect of nanoparticle stiffness*** (better simplified as rigidity/elasticity/deformability) remains incompletely understood; although different studies have indicated that macrophages preferentially phagocytose rigid materials compared to softer analogs (resulting in shorter blood circulation times) [71–73], the same trends have not been reported in other cell types. Sun *et al.* reported that lipid-polymer hybrid nanoparticles with higher rigidity synthesized via microfluidics provided significantly higher cellular uptake in HeLa ovarian cancer cells [74]. The authors hypothesized that the deformation of softer materials into ellipsoidal shapes required over 30 % more "wrapping energy" from the membrane than spherical rigid analogs, thereby inhibiting their cellular uptake. Gurnani *et al.* observed increased uptake of softer PEG-based core–shell nanoparticles compared to a more rigid analog in the prostate (PC3) and colon (Caco-2) adenocarcinoma cell lines through CVME, with enhanced uptake attributed to cooperative particle internalization [75]. Even given the electrostatic repulsion between multiple nanoparticles, multiple flexible or larger nanoparticles become preferentially internalized. Interestingly, the authors only observed this phenomenon for those with 100 nm size (and not for 50 nm), suggesting a degree of size dependence.

2.2.1. Endosomal escape: A tool aiding the intracellular journey of nanomedicines

After CME, the adoption of various chemical and physical strategies promotes escape from endosomal membranes and the cytosolic release of cargo while minimizing cell damage [76,77].

Lipid-based formulations mainly leverage ionizable lipids with efficient endosomal escape properties. Ionizable lipids present an electrostatic charge depending on lipid dissociation constant (pKa) values and the environmental pH, resulting in a neutral net charge at physiological pH (7.4), which ensures an enhanced biosafety profile and longer blood-circulation time and a positive net charge in endosomal compartments, due to lipid head protonation at pH 5.5–6.6. The binding of positively charged ionizable lipids and negatively charged phospholipids of endosomal vesicles, resulting in an inverted cone shape, perturbs the original endosomal membrane organization, leading to the formation of non-bilamellar, hexagonal structures, consequent membrane fusion, and endosomal disruption [78]. In recent decades, several ionizable lipids (e.g., 1,2-dioleoyl-3-dimethylammonium propane; DODAP [79], and the potent dilinoleylmethyl-4-dimethylaminobutyrate; DLin-MC3-DMA [80]) saw increasing interest from the scientific community thanks to their applications in the design of ionizable lipid nanoparticles and advanced non-viral vectors for the delivery of nucleic acids. Indeed, recent advances in lipid nanoparticle designs culminated in the FDA (Food and Drug Administration) and EMA (European Medicines Agency) approval of Onpattro® (Patisiran), an siRNA liposomal nanomedicine for the treatment of hereditary transthyretin-mediated amyloidosis, or the mRNA-based vaccines against severe acute respiratory syndrome coronavirus 2 (SARS-CoV-2) [10 81].

Despite these successful examples of lipid nanoparticles, endosomal escape still represents the most challenging step in efficient nucleic acid delivery. To overcome these limitations, tailor-made lipid nanoparticle designs represent a promising approach. For instance, Liu *et al.* recently developed an ionizable phospholipid (iPhos) multi-library consisting of differential ionizable amine derivatives (the pH-dependent zwitterion head) and three hydrophobic tails which would adopt a cone shape more easily when in contact with the endosomal membrane phospholipids, inducing a strong trend of hexagonal phase transformation [82]. Compared to cationic lipids, iPhos as a component of lipid nanoparticles ensured the enhanced cytosolic release of plasmid DNAs, small-interfering (si)RNAs, and Cas9 mRNA/single guide RNAs for CRISPR/

Cas gene editing. Functionalizing viral peptides with efficient endosomal escape properties represents another approach to enhancing cytosolic delivery. For instance, the pH-sensitive GALA peptide - a 30 amino acid synthetic peptide with a glutamic acid-alanine-leucine-alanine repeat – changes conformation under the endosomal acidic pH from random coil to α-helix to form an oligomeric complex and finally a transient circular pore within the endosomal membrane [83]. In a recent study, Elwakil et al. developed novel lipid nanoparticles incorporating the pH-sensitive lipid (YSK05) decorated with a GALA-cholesterol conjugate for siRNA delivery, which resulted in synergized endosomal escape mechanism and enhanced transfection efficiency demonstrated in a metastatic lung cancer model [84].

Most polymer-based formulations rely on the proton sponge mechanism for endosomal escape [85–87]. Indeed, polycationic polymers, such as polyethyleneimine (PEI) [88,89], polypeptides [90] such as poly-L-lysine (PLL) [91,92], polyornithine (PLO) [93,94] or poly{N-[N′-(2-aminoethyl)-2-aminoethyl]aspartamide} (PAsp(DET)) [95], polyamidoamine (PAMAM) dendrimers [96], chitosan [97], poly(beta-amino esters) (PBAEs) [98–100], or poly(2-dimethylaminoethyl methacrylate) (PDMAEMA) [101] possess buffering capacities that lead to increased osmotic pressure within the maturing endosome and prompt vesicle bursting. The BO-112 non-viral vector - a polyplex consisting of the double-stranded (ds)RNA mimic polyinosine-polycytidylic acid (pIC) and PEI – is undergoing clinical trials in combination with intravenous pembrolizumab for melanoma treatment (Phase II study NCT04570332) and relies on the proton sponge mechanism for dsRNA cytosolic delivery. Despite several successful applications, the proton sponge's precise escape mechanism remains controversial. For instance, Joubert et al. observed that p-toluylsulfonyl arginine (a 'molecular string' that stabilizes the α-helix conformation of cationic polymers) boosted the endosomal escape mechanism of functionalized PAMAM and PLL dendrimers to a greater degree than imidazole (to increase the buffering capacity) [102]. These results question the importance of the polymer's buffering capacity, thereby suggesting that other factors (e.g., the polymer conformation, geometry, and acid degradability) and mechanisms (e.g., pore formation) may be involved [103].

Due to critical issues related to the therapeutic use of toxic polycations, recent alternatives using stimuli-responsive materials have been sought to enhance nanomedicine's therapeutic output [104]. Dirisala *et al.* designed PLO-based mRNA polyplexes wrapped in charge conversion polymers that revert negative charges to positive charges in response to the acidic pH of endosomal compartments. They exploited a negatively charged PAsp(DET) derivative modified with *cis*-aconitic acid [PAsp(DET-Aco)] as a charge conversion polymer, which undergoes pH-sensitive cleavage of a *cis*-aconitylamide bond at pH 5.5 to produce cationic PAsp(DET), which employs a doubly protonated diaminoethane sidechain to promote the safer and more efficient endosomal escape of RNA [104,105].

Recently proposed alternative approaches can avoid the limitations and controversy of both lipid and polymer-based endosomal escape mechanisms. For instance, photochemical disruption - in which ROS or heat from visible light-exposed photosensitizers damage the endosomal membrane to aid cytosolic delivery. This strategy has already demonstrated the enhancement of the delivery of siRNA from amphiphilic copolymers-based micelles [106] and clinically approved Onpattro® formulation [107] when bearing porphyrin derivatives as photosensitizers in 4 T1 breast cancer and PC3 prostate cancer *in vivo* models, respectively. Another approach involves extracellular vesicles (EVs) [108] – naturally occurring nanoparticles with fusogenic properties that have recently garnered attention for delivering nucleic acid, small molecules, and proteins [109,110]. While the fusion of EVs with recipient cell membranes may induce the release of their contents, endocytosis remains the primary uptake route for EVs [111]; therefore, efficient endosomal escape must be ensured [112]. In this context, Pham et al. demonstrated that red blood cell-derived EVs released their siRNA cargo in the cytosol after endosomal escape by membrane fusion [113], resulting in significant tumor suppression in an acute myeloid leukemia murine model [114]. Despite the promising results, both approaches require further optimization and translation into preclinical models. Nevertheless, combining different endosomal escape mechanisms within the same formulation represents the best option for efficient cytosolic delivery of nanomedicine.

2.2.2. *Tailoring the direct cell membrane penetration of nanoparticles*

Direct cytoplasmic nanomedicine delivery - a non-energy-dependent cell internalization process that bypasses the need for an endosomal escape - can be broadly categorized into *membrane fusion* and *direct permeation* processes. Whereas *membrane fusion* has been mainly exploited in the design of lipid-based materials, direct permeation applies to nanomedicines with fundamental physico-chemical properties, such as compactness, small size (<10 nm), cationic character [115,116] or surface amphiphilic patterns [117–119], due to the need of a lower energy barrier for membrane insertion that facilitates translocation.

Using cell-penetrating peptides (CPPs) as nanomedicine surface modifiers represents a primary strategy for achieving direct membrane penetration [120,121]. A range of studies have reported non-amphipathic cationic CPPs (e.g., arginine/lysine-rich peptides), primary amphipathic CPPs (e.g., MPG [122] - derived from the NLS of SV40 large T antigen - and the fusion peptide domain of HIV-1 gp41 and penetratin [123] - derived from the Drosophila Antennapedia homeodomain), and secondary amphipathic CPPs with a hydrophobic block and an ionic/polar block, which acquire a secondary conformation (such as α-helix or β-sheet) when in contact with the phospholipid membranes (e.g., proline-rich peptides)[124]. Specific CPPs enter cells using direct penetration mechanisms (such as inverted micelle creation) and pore formation or according to carpet-like and membrane-thinning models [125]; however, the precise process of CPP cell entry remains partially understood and is influenced by factors such as physico-chemical properties and experimental conditions, such as CPP concentration, cargo, and cell line (particularly for cationic CPPs such as arginine-rich peptides) [126]. Concentration-dependent uptake seems not to occur for amphipathic CPPs, where the α-helix conformation prompts direct cell membrane permeation [127,128]. Due to the plethora of developed CPPs, the recently published CPPsite 2.0 database streamlined the identification of suitable peptides for a particular application, including small molecules, nucleic acid, proteins, and nanoparticles [129].

Favoring the direct cell-membrane penetration of nanomedicines by fine-tuning physico-chemical properties such as reduced size (<10 nm), surface functionalization with biodegradable CPPs, and engineering amphiphilic materials may constitute valuable strategies that facilitate *in vivo* translation. The following sections center on developing nanomedicines tailored for precise subcellular targeting after cytosolic release, particularly emphasizing mitochondrial delivery.

3. Organelle-Specific Targeting: Mitochondria in the Spotlight

Once a given nanomedicine enters the cytosol, specific trafficking to appropriate organelles via targeting strategies can enhance therapeutic output. Mitochondria play a significant role in cellular metabolism, homeostasis, and apoptosis; however, due to their critical activities, mitochondrial dysfunction represents a typical hallmark of a broad spectrum of diseases. Primary mitochondrial disorders arise due to mutations in mitochondrial DNA (mtDNA) [130], while secondary mitochondrial diseases involve mitochondrial dysfunction associated with the pathogenesis of multifactorial diseases such as neurodegeneration, obesity, diabetes, and cancer [8]. Therefore, 'mitochondrial medicine' represents a promising field of biomedical research where mitochondria-targeting nanomedicine may play a crucial role. The following sections will discuss mitochondrial dysfunction and any unique features for targeting and provide an overview of mitochondria-targeted organic nanomedicines.

3.1. Mitochondria structure and dysfunctions in disease

Mitochondria are double membrane-bound organelles composed of four compartments. The porous outer mitochondrial membrane (OMM) displays permeability to molecules smaller than 6 kDa - in particular, the protein import pores (translocase of the OMM complex [TOM complex]) and the voltage-dependent anion channel (VDAC) remain fundamental to permeation. The intermembrane space (IMS) contains several specialized proteins, such as apoptogenic proteins (e.g., cytochrome *C* [Cyt-C], while the highly lipophilic inner mitochondrial membrane (IMM) is rich in unsaturated fatty acids (e.g., the unique phospholipid cardiolipin) and presents with a maximum pore dimension of 1.3 nm (the translocase of the IMM complex [TIM complex]). The convoluted and invaginated IMM contains metabolite carrier proteins and the enzymes responsible for oxidative phosphorylation (OXPHOS), which involves cell energy production in the form of adenosine triphosphate (ATP) [131]. ATP synthesis requires the formation of an electrochemical gradient (i.e., a proton gradient) between the IMS and the mitochondrial matrix, a process that makes the IMM highly negative polarized (approximately ranging from − 108 to − 180 mV), leading to higher proton concentrations (pH 6.8–7.4) in the intermembrane space than in the mitochondrial matrix (pH 7.5–8.2). Lastly, the mitochondrial matrix contains the enzymes involved in multiple metabolic pathways, including the citric acid cycle, fatty acid oxidation, and the urea cycle [132].

Mitochondria are self-replicating dynamic organelles that can exchange material and information by fusion, a self-protective mechanism that prevents mitochondria defects due to an extremely high mutation rate of mtDNA [133]. mtDNA encodes only thirteen proteins essential to OXPHOS; however, they also contain the 12S and 16S rRNA genes and the twenty-two tRNA genes required for mitochondrial protein synthesis. Nuclear DNA encodes genes for other essential mitochondrial proteins, which are synthesized in the cytoplasm and localized to the mitochondria via post-translational modifications. Specifically, mitochondrial proteins contain an N-terminal mitochondria-targeting sequence (MTS) that contains positively charged amino acids (e.g., arginine and lysine), displays amphiphilicity (ensures the insertion into phospholipid monolayer), and forms helical secondary structure (increases import efficiency [134]). Precursor peptides become recognized and translocated into the mitochondrial matrix thanks to interactions between the MTS and TOM/TIM complexes. After reaching the matrix, the mitochondrial processing peptidase removes the MTS [135].

The pathology of primary mitochondrial disorders relates to the high mutation rate of mtDNA; however, secondary mitochondrial diseases occur in multifactorial scenarios, where the disruption of mitochondrial bioenergetics and metabolism usually represents a downstream effect [136]. The overproduction of ROS, generated as a byproduct of ATP synthesis, lies among the leading causes of mitochondria dysfunction in these diseases. Under physiological conditions, ROS play a crucial role in cytoprotection (e.g., the cellular response against infections) and cell survival (e.g., apoptotic signal transduction, cell growth, and proliferation). Various cytosolic enzymes (e.g., superoxide dismutase or catalase) or antioxidants (e.g., glutathione [GSH], vitamin E, and vitamin C) usually scavenge ROS; however, ROS levels can increase due to pathological conditions or in response to specific stimuli and lead to irreparable DNA damage, carcinogenesis, lipid peroxidation, and apoptosis through the intrinsic mitochondria-mediated pathway [137].

Other typical dysfunctions in heterogeneous mitochondria-related pathologies include calcium dysregulation, defective mitochondrial biogenesis, lack of mitochondrial dynamics and quality control, necrotic cell death induced by the mitochondrial permeability transition pore, and inefficient ATP and nicotinamide adenine dinucleotide (NAD^+) production [138]. The damaging effects of mitochondria dysregulation have been extensively reported in several conditions, such as neurodegenerative diseases (e.g., Parkinson's disease and Alzheimer's disease) [139,140], cancer [141], atherosclerosis [142], diabetes [143], pulmonary fibrosis [144], and cardiovascular diseases [145]. Overall, mitochondria contribute to the clinical progression of a wide range of diseases and disorders, even when not the primary drivers of pathology. Therefore, engineering innovative materials and nanomedicines for mitochondria targeting represents a promising therapeutic avenue.

3.2. Mitochondria: "Stand-out" features and targeting molecules

Mitochondria present unique features that differ from other organelles and, thus, can be exploited for specific targeting (Fig. 2).

The mitochondria membrane potential represents the first property that can be leveraged for targeting, as molecules exhibiting a positive charge become attracted to mitochondria due to the highly negative mitochondria membrane potential; however, the cation charge should be distributed over a large hydrophobic surface area to lower the activation energy for movement across the membrane as the IMM remains impermeable to polar molecules. *Delocalized lipophilic cations (DLCs)* represent the first developed mitochondriotropic compounds; they display a high affinity for mitochondria, move quickly through mitochondrial membranes without a specific import mechanism, and accumulate in the mitochondrial matrix. Their preferential accumulation is described by the Nernst equation, indicating that every 61.5 mV increase in mitochondrial membrane potential causes a ten-fold increase in DLC accumulation [146], which becomes enhanced in specific disease states. Increased metabolic activities induce a mitochondria membrane potential about 60 mV higher in cancer cells than in normal cells [147]. Triphenylphosphonium (TPP) - positively charged phosphorus ions linked to three phenyl groups (which confers lipophilic and cationic properties) - and its derivatives represent the most widely used DLC [148,149]. Formulations comprising TPP-drug conjugates, such as SkQ1 (plastoquinone-TPP) and mitoQ (ubiquinone-TPP) - two potent mitochondria-targeted antioxidants with immunomodulatory and anti-inflammatory properties - have been evaluated in a wide range of clinical trials, including in the reduction of fatigue in multiple sclerosis (Phase 1/2 study NCT03166800, oral mitoQ 20 and 40 mg) and dry eye syndrome (Phase III study NCT03764735, ophthalmic solution SkQ1 1.55 and 0.155 μg/mL). Other relevant DLCs include dequalinium (DQA, a dicationic amphiphilic molecule with two quinolinium rings connected by ten methylene groups) [150], the rhodamine dye rhodamine 123 [151], the rhodacyanine dye 17-dimethylaminoethylamino-17-demethoxygeldanamycin (MTK-077) [152], the cytotoxic compound (E)-4-(1H-indol-3-ylvinyl)-N-methylpyridineiodide (F16) [153], guanidine/biguanidine [154,155], and the transition metal iridium(III) [156] (See Wang et al. [157] for more detailed reading on DLCs). Interestingly, DQA can self-assemble to form positively charged vesicles-liposomes ("DQAsomes") for gene delivery and cancer therapy [158] (Section 3.3.2.1 provides detailed examples).

The concentration-dependent toxicity displayed by most DLCs can be exploited as a targeting mechanism for cancer cells. Cancer cells possess higher membrane potentials; therefore, they accumulate higher levels of DLCs than normal cells, leading to more significant mitochondrial toxicity and selective killing.

The protein import machinery (TOM/TIM complex) - used by 99 % of mitochondrial proteins for translocation from the cytosol to the IMM - represents another unique property to target. Specifically, the amphiphilic α-helix *MTS sequences* [135], which target the OMM or IMS [159], have been employed in mitochondria-targeted gene-delivery strategies [160]. Yu et al. investigated the effects of the MTS-modified adeno-associated virus (AAV) on the delivery of plasmid DNA encoding wild-type human NADH dehydrogenase subunit 4 (MT-ND4), an IMM protein defective in Leber hereditary optic neuropathy (a mitochondria-related disorder) due to the G11778A genetic mutation. Adding the MTS enhanced plasmid DNA accumulation in the mitochondria, leading to the recovery of optic atrophy in mice [161].

Unfortunately, distinct factors limit the application of MTS, such as the lack of an MTS consensus sequence (which depends on the origin and

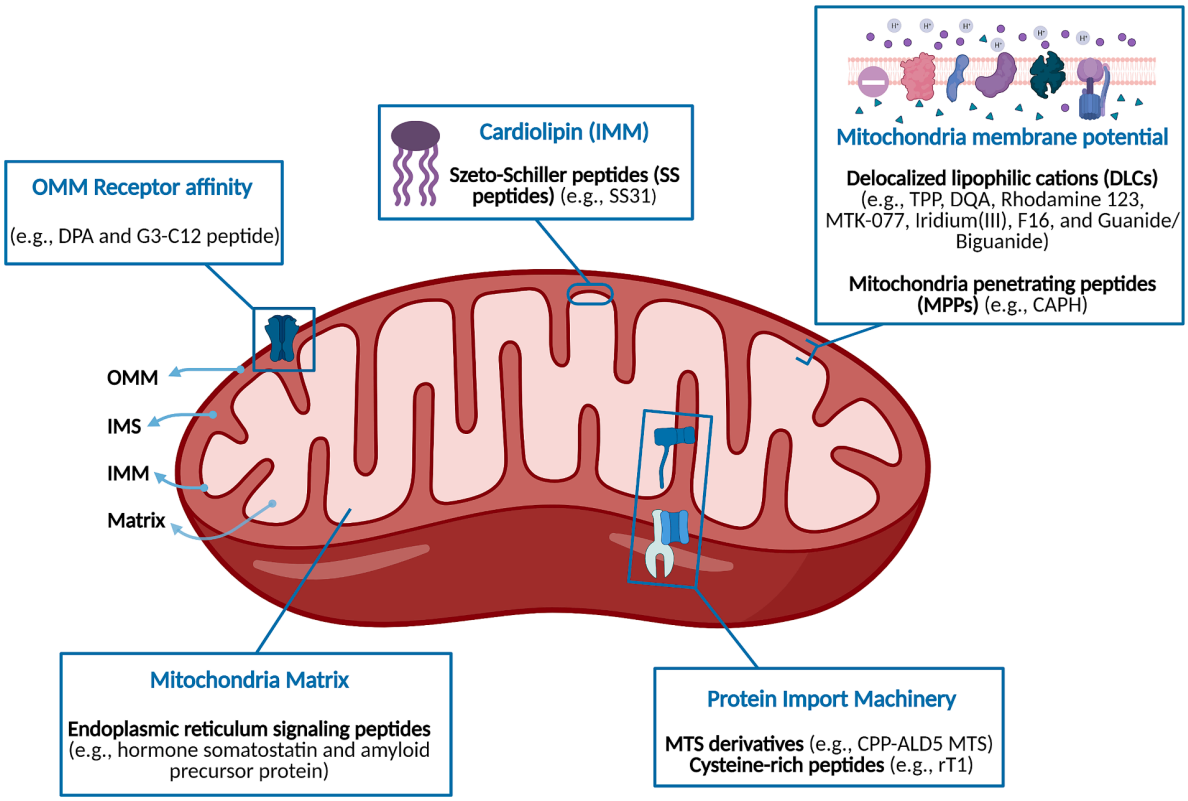


Fig. 2. Distinctive mitochondrial attributes and targeting molecules. Overview of unique mitochondria features (mitochondria membrane potential, cardiolipin, TOM/TIM complex, and OMM receptor-specific affinity) and small molecules that support mitochondrial targeting; Outer Mitochondrial Membrane (OMM), Inner Mitochondrial Membrane (IMM), Intermembrane space (IMS), Mitochondria-targeting sequence (MTS).

physico-chemical parameters for each application [162]) or the inability of the MTS sequences to cross plasma membranes [163] unless combined with a carrier molecule or CPP [164]. Klimpel *et al.* discovered that coupling the sC18 CPP to MTS sequences from various sources significantly improved the cellular uptake of MTS-CPP chimeras in different cell types; in particular, an sC18 CPP-ALD5 MTS conjugate exhibited the most robust mitochondrial localization, with specific accumulation in the mitochondrial matrix [165]. Moreover, the authors conjugated chlorambucil (a DNA alkylating drug that induces mtDNA damage) to the ALD5 MTS (directly linked to the sC18 CPP or using a cathepsin B cleavable motif; Gly-Phe-Leu-Gly). The chimera with the cathepsin B sensitive linker did not enhance cytotoxicity, suggesting that CPP and MTS remain essential for mitochondrial localization. In another study, Chuah et al. demonstrated the successful mitochondrial transfection of a phMGFP plasmid delivered by polyplexes based on lysine-histidine (KH) peptides functioning as CPPs and two different MTSs (a 12-mer peptide from cytochrome *c* oxidase and a 32-mer peptide from ornithine transaminase) [166].

Mitochondria also exhibit exclusive structural features that affinity-driven molecules can target. ***Cardiolipin*** is a unique dimeric phospholipid of mitochondrial membranes - constituting about 20 % of the total lipid composition in the IMM – comprising a glycerol molecule linking two phosphatidyl moieties and two acyl chains. Cardiolipin's structure remains essential for numerous mitochondria processes, including mitochondrial cristae morphology and stability, fission and fusion, biogenesis, protein import, and apoptosis [167]. *Szeto-Schiller (SS) (tetra)peptides* can permeate the plasma membrane and selectively accumulate in the IMM through interactions with cardiolipin [168]. The structural motif of Szeto-Schiller peptides centers on alternating aromatic residues and basic amino acids (aromatic-cationic peptides), and their cellular uptake involves an energy-independent, non-saturable approach rationalized by the electrostatic interaction between the two basic amino acids (lysine and arginine) and the phosphate head groups of cardiolipin and the alignment of the aromatic residues (or 2,6-dimethyl-L-tyrosine residues and phenylalanine) within the hydrophobic acyl chain region [169]. However, Szeto-Schiller peptides not only function as mitochondria-targeting molecules but also as bioactive compounds; for instance, the Szeto-Schiller peptide SS-31 (D-Arg-Dmt-Lys-Phe-NH_2) inhibits Cyt-C/cardiolipin complex peroxidase activity, which catalyzes cardiolipin peroxidation and results in ROS production [170,171]. Given these abilities, SS-31 is undergoing clinical trials for primary mitochondrial myopathy (Phase III study NCT03323749). The scavenging capacity of Szeto-Schiller peptides has been attributed to the 2,6-dimethyl-L-tyrosine residue (Dmt) in the second position due to its structural similarity to vitamin E [172]. An alternative Szeto-Schiller peptide that maintains Dmt but changes the lysine by an ornithine residue (D-Arg-Dmt-Orn-Phe-NH_2) demonstrated increased cellular and mitochondria uptake and ROS scavenging capacity compared to SS-31, probably due to a higher mitochondrial accumulation [173]. Additional peptides, including *cysteine-rich peptides* (e.g., roseltide rT1 with high specificity for OMM) [174] and intrinsically disordered N-terminal domains of the *endoplasmic reticulum signaling peptides* of specific proteins (e.g., hormone somatostatin and amyloid precursor protein, with high specificity for the mitochondria matrix) [175] possess proven mitochondria affinity-driven targeting abilities; however, their potential as delivery molecules remains unexplored.

Based on previous studies on CPPs, MTS sequences, and Szeto-Schiller peptides, Kelley *et al.* provided the first conceptual framework for mitochondrial localization with synthetic compounds called *mitochondria-penetrating peptides (MPPs)* [176]. First, they identified MPP positive charge and lipophilic character as the leading property regulating plasma membrane (independently from endocytosis) and

mitochondria membrane crossing. The positive charge of the mitochondrial membrane potential ensures potential-dependent localization with mitochondria, while MPP lipophilicity allows passage through the highly hydrophobic and packed IMM. Specifically, the authors discovered that MPPs must meet a minimal charge-dependent lipophilicity threshold, which strongly depends on the number of charges and the logarithm of the partition coefficient (LogP) - which represents the lipophilicity of a molecule - (n° charges/LogP) and a maximum cluster of three basic amino acids for an eight-amino acid MPP for mitochondria localization. They demonstrated that a minimum logP of −2.5 and + 4 charges ensures the mitochondria colocalization of acid and zwitterionic model cargo molecules (biotin and the vitamin E analog Trolox) [177]. MPPs also represent biodegradable and tunable alternatives to DLCs [178,179], including the delivery of small-molecule probes for cancer therapy [180–182], fluorescent dyes [183], theranostics [184], and a potent anti-Plasmodium therapeutic [185].

Interestingly, the Chmielewski research group identified a specific class of MPPs; they observed that a cationic amphiphilic polyproline (PPro) helix (CAPH) with a helix type II and alternating leucine and arginine mimics within the PPro chain, colocalized with mitochondria after direct cell membrane permeation in a potential-dependent fashion [186,187]. To ensure direct penetration and, thus, mitochondria colocalization at lower concentrations, they tuned the design via CAPH dimerization [188] or PPro scaffold elongation [189].

Most mitochondria-targeting molecules rely on short peptides and tunable properties; however, as for CPPs, their physiological instability due to proteolytic degradation, hepatic and renal clearance, and lack of selectivity between normal and unhealthy tissues has limited the *in vivo*/clinical translation of promising in vitro results [160,190]. The use of nanomedicine can shield these short peptides from enzymatic degradation during blood circulation [191], be tuned to control size and surface properties, allowing the surpass of biological barriers, actively target a specific tissue and the desired subcellular target, such as the mitochondria, while minimizing their systemic toxicity.

3.3. Mitochondria targeting strategies using nanomedicines

Crossing several levels of biological barriers requires the customization of mitochondrially-targeted nanomedicines, with each step of the *in vivo* journey considered in the design [192,193]. The following sections will consider the design strategies and physico-chemical properties applied to target the mitochondria after intravenous administration. Specific mitochondria features in cancer cells (e.g., enhanced mitochondria depolarization, high ROS and GSH levels, abnormal ATP production, increased O_2 consumption rate, and upregulation of anti-apoptotic signals [147]) and the design of drugs and mitochondria-targeting molecules (such as TPP) with inherent mitochondria toxicity have contributed to center mitochondria-targeting therapies in cancer. Therefore, this review examines the preclinical use of intravenously administered organic nanomedicines that target mitochondria, primarily focusing on applications in cancer; however, we also include novel targeting molecules and applications relevant to mitochondria-targeting research in other diseases and disorders (Table 1). Recent review articles provide a more comprehensive coverage of alternative administration routes, inorganic nanomedicine, and the use of mitochondria-targeting nanomedicine in other mitochondria-related diseases [194–198].

3.3.1. Mitochondria-targeted Polymeric-based nanomedicines

Polymeric-based materials offer a versatile platform for designing mitochondria-targeting nanomedicines. Biodegradability, multivalency (supporting combination therapies), and tunable responsiveness to specific stimuli make them exciting candidates for subcellular targeting. Most developed polymeric systems that target mitochondria employ mitochondria-targeting molecules for organelle targeting, such as DLCs or MPPs integrated in engineered responsive materials (Section 3.3.1.1), or use hierarchical targeting strategies, which involves complex multi-level drug targeting design (Section 3.3.1.2); however, these strategies still present challenges, such as the intrinsic toxicity of DLCs, the physiological instability of MPPs, or the requirement of a complex design when used to target the mitochondria. These challenges have prompted the exploration and development of polymeric carriers modified with novel mitochondria-specific targeting ligands (Section 3.3.1.3) or characterized by intrinsic mitochondrial tropism (Section 3.3.1.4).

3.3.1.1. Smart materials. Innovative materials with unique dynamic properties can change in response to specific stimuli or microenvironments and improve further mitochondria-targeted objectives. *Charge reverse materials* exhibit a negative charge after administration (offering stealth-like characteristics) but revert to a positive charge under specific microenvironmental conditions, such as the acidic pH of the lysosomes or the TME, to promote enhanced cellular internalization [219]. Self-assembled Vitamin B6-oligomeric hyaluronic acid (HA)-dithiodipropionic acid-berberine (B6-oHASS-Ber) micelles, encapsulating curcumin as pro-apoptotic drug [220] displayed charge conversion capacity due to the pKa of its pyridine group meanwhile, the DLC berberine (Ber) prompted cancer cell apoptosis associated with mitochondria targeting in HepG2-based preclinical models [199]. These micelles colocalized with the mitochondria and induced more anti-tumor activity than analogs without vitamin B6 (oHA-SS-Ber/Cur) or free curcumin *in vivo*.

Adopting a similar strategy for breast cancer treatment, Deng *et al.* prepared an α- cyclodextrin (α-CD) nanocarrier bearing i) the chemotherapeutic drug and mitochondrial-ROS inducer DOX conjugated via a pH-sensitive hydrazone linker; ii) nitric oxide (NO) conjugated as precursor S-nitrosothiol NO donors, which support GSH-triggered NO release; and iii) an acid-cleavable dimethylmaleic anhydride (DA) moiety-modified PEG conjugated to an MPP ((KLAKLAK)2CGKRK) to form α-CD-DOX-DA nanoparticles [200]. They demonstrated that the acid-cleavable DA moiety possessed sufficient charge reversal properties to ensure increased blood circulation time and tumor accumulation due to stability at pH 7.4 and induced specific mitochondrial localization after the acid-induced hydrolysis of the DA moiety in the acidic extracellular pH (6.5) of the tumor. The specific release of NO within the mitochondria significantly amplified the effect of DOX-bearing nanoparticles in 4 T1 and drug-resistant MCF-7/DOX *in vivo* breast cancer models, facilitating more robust mitochondrial membrane permeabilization and downregulated ATP levels by inhibiting mitochondria respiration when compared to control nanoparticles containing a succinic anhydride (SA) linker (α-CD-DOX-SA), which does not degrade at acidic pH. NO delivery to the mitochondria strengthened the uptake and retention of DOX by suppressing the ATP-dependent functions of efflux pump (P-gp) transporters and tumor-derived microvesicles – critical messengers controlling tumor progression and metastasis - thus helping to overcome drug resistance and cancer metastasis (Fig. 3).

Although these studies may be successful examples, the charge reverse strategy remains limited by low yield charge conversion efficiency and dependence on heterogeneous stimuli (e.g., pH fluctuations in the tumor tissue and resistance mechanisms), which can lead to off-target toxicity.

3.3.1.2. Hierarchical targeting. Hierarchical targeting is a multi-stage approach combining multiple targeting elements and responsive release mechanisms to ensure therapeutic agents reach their intended subcellular destination. Compared to charge reverse materials, hierarchical targeting ensures enhanced specificity, therapeutic efficacy, and minimized off-target effects [60].

Zhang *et al.* prepared DOX-loaded micelles obtained by the self-assembly of TPP grafted PEG-poly(D, L-lactide) (PLA) copolymers using GSH-sensitive disulfide bonds (ss) as an intermediate linker (TPP-PEG-ss-PLA) for the treatment of hepatocellular carcinoma [201]. The surface positive charges provided by TPP were hidden by coating

Table 1
Relevant examples of mitochondrially-targeted organic nanomedicines (including the targeting molecules employed and their mechanism) that have reached preclinical stages in different applications (primary focus on cancer).

Strategy	Nanomedicine	Material	Therapeutic Cargo	Targeting Moiety	Targeting Mechanism	Disease (preclinical model)	Ref.
			POLYMER-BASED SYSTEMS				
SMART MATERIALS	B6-oHASS-Ber@Cur	Vitamin B6- HA-dithiodipropionic acid-berberine micelles	Cur (encapsulated)	HA (CD44 receptor affinity) (cellular targeting) Ber (DLC) (mitochondria targeting)	Receptor-mediated endocytosis (CD44), pH-responsive trigger (vitamin B6 pyridine group protonated at acidic pH) promoting charge-reversal, mitochondria targeting by Ber	Hepatocellular carcinoma (HepG2-cells and tumor bearing-mice)	[199]
	α-CD-DOX-NO-DA nanoparticles	α-CD nanocarrier with an acid-cleavable dimethylmaleic anhydride (DA) moiety-modified PEG conjugated to an MPP (KLAKLAK)2CGKRK	DOX (hydrazone linker), NO (disulfide bond)	(KLAKLAK)2CGKRK (MPP) (mitochondria targeting)	Charge reversal (acid-cleavable DA), NO membrane permeabilization, mitochondria targeting by MPP	Breast cancer (4 T1 and MCF7 mice models)	[200]
HIERARCHICAL TARGETING	CS/TPP-PEG-ss-PLA@DOX	TPP grafted PEG-ss-PLAcopolymers coated with CS	DOX (encapsulated)	CS (CD44 receptor affinity) (cellular targeting) TPP (mitochondria targeting)	Receptor-mediated endocytosis (CD44), mitochondrial targeting via TPP exposure due to pH response, DOX released due to GSH-triggered disassembly.	Hepatocellular carcinoma (HepG2 cells and H22 bearing Balb/c mice)	[201]
	Glucose-PEG−MMP2 peptide − TPP− PAMAM − PTX conjugate	PAMAM dendrimer-based conjugate derivatized with glucose-PEG-GPLGIAGQ (MMP2-degradable peptide)	PTX (disulfide bond)	Glucose-PEG (GLUT1 receptor affinity) (cellular targeting) TPP (mitochondria targeting)	Receptor-mediated endocytosis (GLUT1), PEG layer detaching via MMP2 expression in TME, mitochondria targeting via TPP, PTX released due to GSH-disulfide linker in the cytosol.	Breast cancer (MCF7 cells and MCF7 tumor-bearing mice)	[202]
SPECIFIC MITOCHONDRIA TARGETING LOCALIZATION	PAMAM-DPA	PAMAM dendrimer with (5,7-dimethylpyrazolo[1,5-α]pyrimidin-3-ylacetamide (DPA)	DPA (triazole linkage)	DPA (TSPO = translocator protein at the OMM) (mitochondria targeting)	Cellular uptake and mitochondria targeting DPA ligand	HMC3 human macrophages /GL261 orthotopic immunocompetent glioblastoma model	[203]
	C-g-SS-31/ PDAA@PU	Chitosan-SS-31 conjugate via cross-linked ROS-sensitive thioketal (PDAA)	PU (Puerarin) (thioketal cross-linking)/SS-31	SS-31 (mitochondria targeting)	Intranasal admin. (ischemic penumbra), intracellular transport, and mitochondria targeting via SS-31 peptide	Ischemia-reperfusion injury (SH-SY5Y /middle cerebral artery occlusion rats)	[204]
	G3-C12-HPMA-KLA	HPMA conjugated to KLA (D(KLAKLAK) 2) and G3-C12 peptide (ANTPCGPYTHDCPVKR)	KLA peptide	G3-C12 peptide, galectin-3-targeting ligand (dual targeting, cellular and mitochondrial)	Cellular uptake and mitochondria targeting G3-C12 peptide ligand	PC-3 cells and tumor-bearing nude mice	[205]
	GNPs-HPMA-Dox-GA	HPMA-hydrazone-Dox attached to the surface of gelatin nanoparticles	DOX (hydrazone linker)	Glycyrrhetinic acid (GA) targeting protein kinase Cα (cellular targeting) and serine hydroxy-methyltransferase 2 (SHMT2) (mitochondria targeting) [206]	Gelatin degradation by MMP2 in TME, GA for tumor cell internalization and mitochondria targeting	Hepatocellular carcinoma (HepG2/ADR heterotopic tumor nude mice)	[207]
INHERENT TARGETING ABILITY	OPDEA	Zwitterionic poly[2-(N-oxide-N, N-diethylamino)ethyl methacrylate]	N/A	Inherent capability targeting (mitochondria targeting)	Macropinocytosis, mitochondria internalization (mechanism unknown)	Osteosarcoma (HepG2 cells in vitro and *in vivo* model)	[208]
	PEG-Fn	PEG-fluorinated micelles with fluorocarbon segments	Fluorescent dyes or vitamin E succinate as cargo (encapsulated)	Fluoroamphiphiles (mitochondria targeting)	Clathrin-dependent endocytosis followed by endosomal escape, mitochondria targeting via Fn (cardiolipin affinity)	HeLa, ovarian NCI/ADR-RES, and breast cancer cell lines/orthotopic 4 T1 mouse model	[209]
	cRGD-P(DMA-co-CSMA) @R848	NIR-absorbing Changsha Red monomer and dimethylacrylamide (DMA) to generate a DMA-co-CSMA precursor, functionalized with the cyclic Arg-Gly-Asp (cRGD)	Immunomodulator R848 (encapsulated)	cRGD for αvβ3 integrin receptor-targeting (cellular targeting) CSMA-based copolymer (mitochondria targeting)	Endocytosis mediated by cRGD/integrin receptor, native mitochondria targeting by charge affinity	Melanoma models (B16F10 cells and mice)	[210]

(*continued on next page*)

Table 1 (*continued*)

Strategy	Nanomedicine	Material	Therapeutic Cargo	Targeting Moiety	Targeting Mechanism	Disease (preclinical model)	Ref.
	mPoP nanoparticles @LND	poly-γ-glutamic acid (γ-PGA) and the β-sheet positively charged peptide PFK as a coating layer	Lonidamine (LND) encapsulation	PFK coating peptide (Pro-(Lys-Phe)5-Lys-Pro) (mitochondria targeting)	Cell uptake and mitochondria proximity targeting via PFK peptide	HMC3 human macrophages/ BV2 murine microglia /MDA-MB-231 xenograft breast cancer model	[211]
				LIPID-BASED SYSTEMS			
MITOCHONDRIA MEMBRANE FUSION	DOX-MITO-Porter	DOPE/SM/Chol/STR-R8/DSPE-PEG2000	DOX (encapsulated)	STR-R8 (cytoplasm delivery + mitochondria targeting)/ fusogenic lipids	Macropinocytosis and endosomal escape via fusogenic lipids, mitochondrial targeting via STR-R8, and DOX release into the interior of mitochondria aftermembrane fusion	Renal carcinoma OS-RC-2 cells/DOX-resistant OS-RC-2 tumor-bearing mouse model	[212]
	rTPA-MITO-Porter	DOPE/SM-R8	NIR-activated porphyrin-type photosensitizer (rTPA)	R8 (cytoplasm delivery + mitochondria targeting)/ fusogenic lipids	Macropinocytosis stimulated by R8, intracellular interaction with the mitochondrial membrane via electrostatic interactions, fusion of the fusogenic lipid of the MITO-Porter with the mitochondrial membrane	Squamous cell carcinoma cell line (SAS) and mouse model	[213]
DQAsomes	HPSC-DQAsomes @DOX	Dequalinium (DQA) chloride liposome-like vesicles	DOX (encapsulated)	HER2 peptide ligand (YCDGFYACYMD) (cellular targeting) DQA (mitochondria targeting)	Receptor-mediated endocytosis via HER-2, PEG detachment under acidic conditions, mitochondria targeting via DQAsome charge	Breast cancer (nude mice bearing MCF7/ADR tumor)	[214]
				HYBRID MATERIALS			
	DSPE-PEG/PLGA/ MTP/cRGD @ Calycosin/ Tanshinone	DSPE-PEG-COOH, injectable soya lecithin, PLGA, SS-31, cRGD-PEG-DSPE	O-methylated isoflavone Calycosin + Tanshinone (encapsulated)	cRGD for αvβ3 integrin receptor-targeting (cellular targeting) SS-31 (mitochondria targeting)	Endocytosis mediated by cRGD/integrin receptor, mitochondria targeting by SS-31	Acute myocardial infarction (human cardiac myocyte cells/acute myocardial infarction in rats)	[215]
	PLGA/CPEGT/ DSSP@PTX	Lipid shell: (C18-PEG2k-TPP, CPEGT) (DLPE-SS-mPEG4K, DSSP) Polymeric core: PLGA	PTX (encapsulated)	TPP (mitochondria targeting)	Macropinocytosis, PEG coating detaching under reductive conditions, PLGA/DSSP converted to be highly positive, mitochondria targeting upon TPP exposure	Breast cancer (MCF7 cells/ MCF7 tumor-bearing mice)	[216]
	LPHNPs@PQC-PS	EPC/DSPE/PEG	PQC pheophorbide α−quinolinium conjugate encapsulated photosensitizer, PDT	Quinolinium (DLC) (part of PQC photosensitizer) (mitochondria targeting)	Cellular uptake and mitochondria targeting via PQC	Glioblastoma (Glioma model GL261 in immune-competent mice)	[217]
	POSS-HPMA-(TPP-DOX)-(GA-DOX)	Amphiphilic conjugates of an octaammonium polyhedral oligomeric silsesquioxane (POSS-NH2) core/cage and HPMA. TPP-DOX loaded in the cage, and GA-DOX conjugated to HPMA	TPP/DOX) (encapsulated and conjugated (hydrazone))	TPP/GA (mitochondria targeting)	Endocytosis, acid pH release of GA-Dox from HPMA, which subsequently diffuses outside of the lysosome, GSH cleavage of POSS and HPMA leading to the disassembly and release of the loaded TPP-DOX, mitochondria targeting via TPP and MPTP opening via GA	Breast cancer (4 T1 orthotopic tumor mice)	[218]

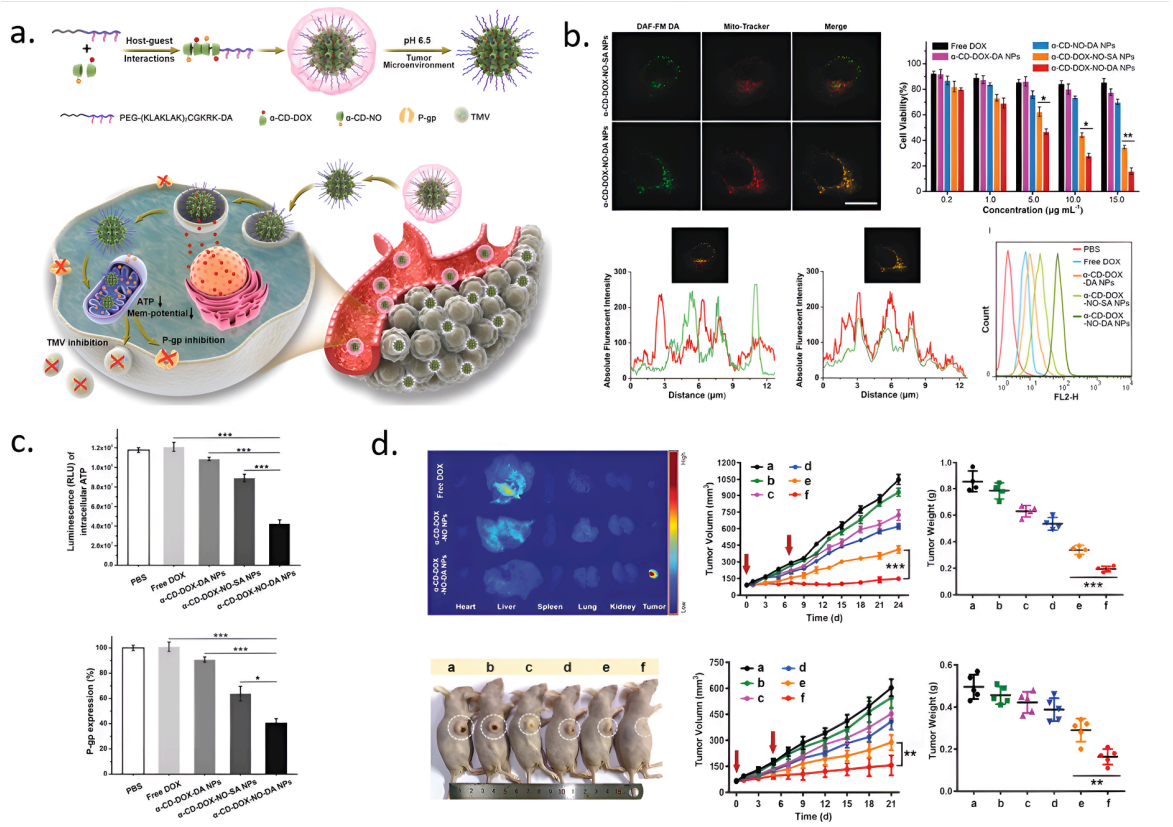


Fig. 3. A cyclodextrin-based nanomedicine targeting mitochondria through MMP and charge-reversal strategies. a) Synthetic scheme, mitochondria targeting, and delivery mechanism of α-CD-based nanoparticles bearing NO (GSH linker) and DOX (hydrazine linker) functionalized with a DA moiety-modified PEG conjugated to the MPP (KLAKLAK)2CGKRK (α-CD-DOX-DA nanoparticles) for breast cancer treatment. b) Fluorescence images (top left), cytotoxicity (incubation 48 h, top right), and colocalization analysis by fluorescence imaging using image J (bottom left) and flow cytometry (incubation 4 h, bottom right) of α-CD-DOX-DA nanoparticles and controls in drug-resistant MCF-7/DOX cells. c) In vitro effects of NO on mitochondria for drug-resistance reversal, including intracellular ATP levels (top) and P-gp expression (bottom) after treatment with α-CD-DOX-DA in drug-resistant MCF-7/DOX cells. d) In vivo tumor accumulation (after 24 h, top left) and synergistic anticancer therapy analysis by analysis of tumor growth curve, tumor weight, and imaging after 21 days of treatment [(a) Phosphate Buffered Saline (PBS), (b) free DOX, (c) α-CD-DOX-DA nanoparticles, (d) α-CD NO-DA nanoparticles, (e) α-CD-DOX-NO-SA nanoparticles, and (f) α-CD-DOX-NO-DA nanoparticles] in subcutaneous (top illustrations) or orthotopic (bottom illustrations) MCF-7/DOX tumor-bearing mice. Reprinted with permission [200].

nanoparticles with negatively-charged chondroitin sulfate (CS), thus increasing the blood circulation time and reducing toxicity. CS can also induce CD44-mediated endocytosis, with CD44 representing the most common receptor overexpressed in human cancers. CS is hydrophilic and stable at pH 7.4 but becomes hydrophobic when the pH decreases to 5.5 in lysosomes/endosomes due to the dissociation of the carboxyl group; hence, the CS layer becomes removed when shifting from a pH value of 7.4 to 5.5, thus exposing the positively charged TPP that supports cytosolic delivery. Once in the cytosol, CS/TPP-PEG-ss-PLA micelles disassemble in response to GSH levels and release TPP, which induces membrane depolarization, ROS generation, and apoptosis. TPP-induced mitochondria membrane permeabilization facilitates DOX diffusion into the mitochondria, which induces mtDNA damage. Moreover, DOX induced nuclear DNA damage, providing an additional pro-apoptotic effect. The combined activity of DOX and TPP, released after hierarchical receptor-dependent endocytosis (CS-CD44 interaction) and mitochondria targeting by TPP, synergistically enhanced the anti-tumor efficacy in mice with H22 cell-based hepatic tumors [201].

In a related study, Ma *et al.* designed an innovative breast cancer treatment based on mitochondrially-targeted paclitaxel (PTX) delivery through a TPP-PAMAM dendrimer-PTX nanoconjugate [202]. TPP was linked to PAMAM via an amide bond and PTX via a disulfide bond; the authors also conjugated glucose-PEG moieties via an MMP2-responsive GPLGIAGQ peptide as a linker to trigger active targeting via Glucose Transporter 1 (GLUT1) protein overexpressed in MCF7/ADR cells. In vivo studies demonstrated that MMP2 overexpression in the TME triggered PEG layer detachment with the subsequent exposure of TPP moieties after nanoconjugate accumulation in the tumor. This supported mitochondrial targeting by direct cell penetration and PTX release after the GSH-induced cleavage of the disulfide linker, showing a significant improvement in tumor growth inhibition compared to free PTX. Additionally, the authors observed the downregulated expression of efflux pump transporters (suppressed through ATP deprivation and MMP2-mediated degradation), thus protecting PTX from being pumped out of the cell and thereby demonstrating that hierarchical targeting could be applied to overcome multidrug resistance in cancer.

3.3.1.3. Specific Mitochondria-Targeting localization. DLCs represent the most used mitochondria-targeting molecules in nanomedicine. While their well-established proficiency in targeting mitochondria has yielded favorable preclinical outcomes for numerous nanomedicines, several critical factors deserve consideration. Firstly, their reliance on the mitochondrial membrane potential for accumulation limits their retention within mitochondria following treatment-induced mitochondrial depolarization. Furthermore, their preferential accumulation in cancer cell mitochondria, attributed to the higher mitochondrial membrane potential, does not consistently hold true due to the inherent heterogeneity of tumor cells. Additionally, the concentration-dependent toxicity exhibited by DLCs (which the design of nanomedicines targeting

mitochondria for cancer applications can strategically leverage) may impose constraints on their applicability for diseases beyond cancer [148,149]. DLCs such as TPP cations also exhibit non-specific targeting to various compartments within the mitochondria; studies have identified multiple sites where TPP accumulates, including the mitochondria matrix [221] and IMM [222], without displaying a precise accumulation mechanism.

Hence, incorporating mitochondria-targeting moieties with specific molecular targets independent of mitochondrial membrane potential can significantly enhance the specificity and efficacy of nanomedicines, mainly when the target displays notable alterations associated with specific pathological conditions. Sharma *et al.* prepared a generation 4 hydroxyl-terminated PAMAM dendrimer conjugated by copper-catalyzed azide-alkyne-cycloaddition-mediated click chemistry to an OMM translocator protein (TSPO) targeting ligand (5,7-dimethylpyrazolo[1,5-α]pyrimidin-3-ylacetamide, DPA) (overall name - D-DPA) for glioblastoma treatment [203]. The typically low levels of TSPO in healthy tissues play a crucial role in moving cholesterol into mitochondria to produce steroids; however, neuroinflammation and cancer associate with increased TSPO levels [223,224]. In glioblastoma, TSPO upregulation in anti-inflammatory immunosuppressive TAMs associates with poor prognosis [225]. In vivo studies in glioblastoma-bearing mice confirmed the ability of D-DPA to target TAMs and undergo internalization; furthermore, the authors demonstrated that D-DPA colocalized with mitochondria thanks to TSPO binding (while unmodified dendrimers did not). D-DPA also specifically stimulated enhanced anti-tumor immune signaling in TAMs (e.g., generation of proinflammatory cytokine tumor necrosis factor-α and Interleukin1β) and lower cytotoxicity in non-cancer cell lines (e.g., BV-2 murine microglia) than a classical TSPO ligand (PK11195). This novel study represents an example of intracellular targeting (mitochondria) and cell-specific targeting (tumor-associated macrophages) with promising preclinical results.

Zhang *et al.* exploited the SS-31 peptide for mitochondria targeting, which they conjugated to a chitosan main chain via a cross-linked ROS-sensitive thioketal (TK) crosslinker (PDAA) generating multifunctional nanoparticles with ROS-responsiveness and mitochondrial-targeting properties (SPNPs) for the treatment of ischemic stroke via intranasal administration [204]. Ischemic stroke involves increased oxidative stress, inflammation, and dysfunctional mitochondria [226] in the ischemic penumbra, the brain tissue surrounding the irreversibly damaged ischemic core where blood flow becomes reduced but remains sufficient to maintain cell viability [227]. SS-31 selectively targets cardiolipin in the IMM in a membrane potential-independent manner and displays anti-oxidative abilities by reducing mitochondrial ROS production and inhibiting mitochondrial permeability transition by suppressing mitochondrial permeability transition pore formation [228]. The authors employed a water-in-oil approach to fabricate the nanoparticles, which they used to encapsulate Puerarin (PU), an anti-oxidative and anti-inflammatory compound that acts in the mitochondria within the hydrophobic core. The authors placed these nanoparticles within a thermo-sensitive hydrogel that transitions from a liquid state for intranasal administration to a gel-like state at body temperature, which helps adhesion to the nasal mucosa. These multifunctional ROS-sensitive nanoparticles effectively targeted the mitochondria of SH-SY5YS neuroblastoma cells treated with H_2O_2 as an in vitro oxidative stress cell model, preserved the membrane potential, and protected against insult. In vivo experiments using a middle cerebral artery occlusion (MCAO) mouse model of stroke reported a significant reduction of the infarct area compared to treatment with free PU or hydrogel-loaded nanoparticles lacking SS-31, thus highlighting the importance of mitochondrial targeting. Moreover, treatment in the stroke mouse model reduced the production of oxidative stress and inflammation factors, renovated the mitochondrial function, and decreased neuronal apoptosis [204].These findings underscore the potential use of nanomedicines that specifically target mitochondria in a context unrelated to cancer.

3.3.1.4. Inherent mitochondria targeting polymeric carriers. The use of polymeric carriers with intrinsic mitochondria-targeting possibilities presents essential advantages compared with the strategies mentioned above with regards to cost-effectiveness and safety. Geng *et al.* demonstrated the mitochondria colocalization of zwitterionic poly[2-(N-oxide-N, N-diethylamino)ethyl methacrylate] (OPDEA) after internalization by micropinocytosis in HepG2 cells in vitro and *in vivo* models [208]. A related study by Jin *et al.* designed an amphiphilic block polymer based on OPDEA and dichloroacetate to prompt mitochondrially-induced pyroptosis in *in vivo* osteosarcoma models through the activation of mitochondrial oxidative stress [229].

While OPDEA displays significant mitochondria affinity through an unknown mechanism, other polymeric properties can be tuned to enhance cellular uptake and mitochondrial targeting. Liu *et al.* observed that the fluorination of phosphatidylethanolamine (PE)-PEG and PEG with non-toxic, low molecular weight fluorocarbon segments (Fn) induced the formation of self-assembled fluoroamphiphiles with increased cellular uptake and novel mitochondria targeting properties for potential applications in cancer treatment [209]. PEGm-Fn (Fn [n = 3,5, 7, or 9] and linear PEGm [m = 1, 2, and 5 kDa]) derivatives demonstrated more efficient cellular uptake due to their lower critical micelle concentration, size, and higher stability than PE-PEGm-Fn derivatives. Among various combinations of perfluorinated carbons used to synthesize the polymer, PEG2k-F7 displayed the highest cellular internalization levels in cancer cell lines (HeLa, ovarian NCI/ADR-RES, and breast cancer cell lines) due to an optimal hydrophilicity/hydrophobicity ratio, with 50 % depending on a direct cell membrane mechanism due to a rapid (1 h) membrane fusion mechanism demonstrated both at pH 7.4 and pH 5.0 at 4° and 50 % based on clathrin-dependent endocytosis followed by endosomal escape. PEGm-Fn (PEG2k-F7 specifically) derivatives colocalized with the mitochondria in a potential-independent manner due to the binding affinity for cardiolipin demonstrated in isolated mitochondria and mitochondria-like liposomes. The authors confirmed their in vitro findings (2D monolayers and 3D spheroids) in a 4 T1 tumor-bearing mice model, where PEG2k-F7 micelles loaded with the anti-cancer drug vitamin E succinate (VES, an IMM complex II inhibitor of the OXPHOS) boosted drug effectivity even at low doses, inducing a significant reduction in tumor size after two weeks compared to the free drug (Fig. 4).

Polymeric nanomedicine design can also integrate mitochondria targeting moieties within the polymeric structure. Zhang *et al.* copolymerized a near-infrared-absorbing Changsha Red monomer (a DLC of the rhodamine family) for photothermal therapy and dimethylacrylamide (DMA) to generate a DMA-co-CSMA precursor, which they further functionalized with the tumor-targeting cyclic Arg-Gly-Asp (cRGD) peptide (targets the αvβ3 integrin receptor overexpressed by melanoma cells) to generate cRGD-P(DMA-co-CSMA) [210]. Upon loading with the immunomodulator R848 (resiquimod), the authors obtained self-assembling nanoparticles that displayed native mitochondria-targeting properties without modification with mitochondria-targeting ligands due to the mitochondria-dependent accumulation of the Changsha Red-based copolymer. Preclinical experiments in melanoma models demonstrated that the mild photothermal effect induced by these dual-targeting nanoparticles can trigger precise in situ mitochondrial damage and promote tumor-associated antigen release; moreover, precise mild photothermal therapy in mitochondria synergized with immunotherapy with Programmed death-ligand 1 (PD-L1) to inhibit both primary and metastatic tumors.

Cohen-Erez *et al.* fabricated polypeptide-based nanoparticles via the coassembly of poly-γ-glutamic acid (γ-PGA) and the β-sheet positively-charged peptide PFK (Pro-(Lys-Phe)5-Lys-Pro) to form PoP-NP (PFK: γ-PGA 1:2 charge ratio, negatively charged nanoparticle), which could entrap lonidamine (LND, an OMM inhibitor for breast cancer treatment)

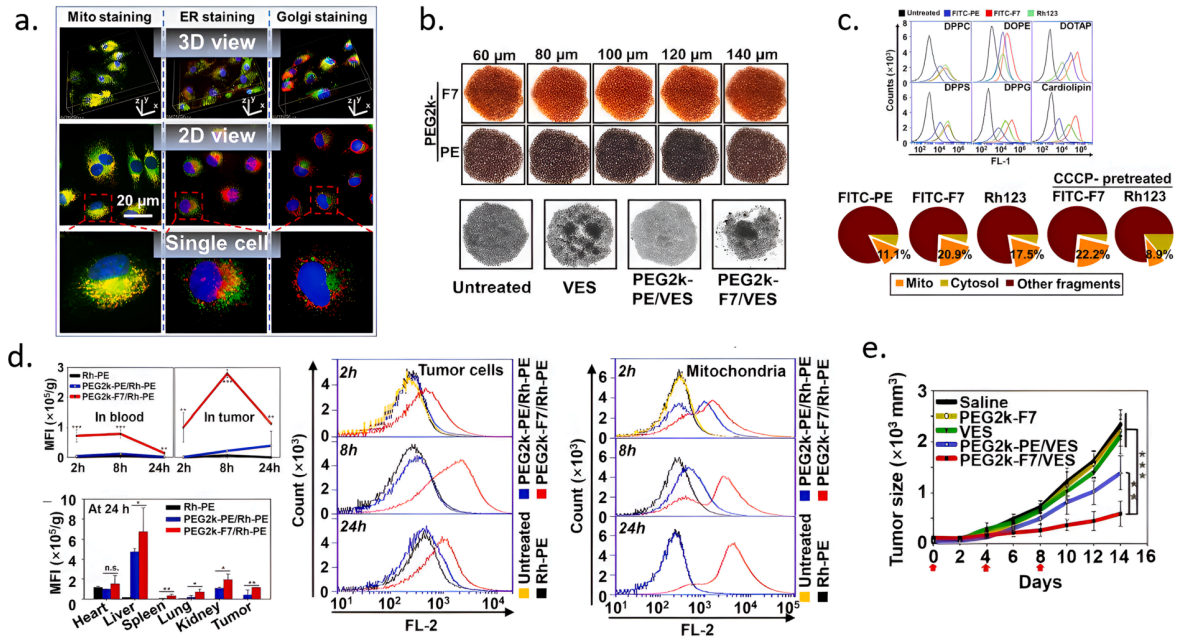


Fig. 4. Inherent mitochondria targeting abilities of a zwitterionic polymer. a) Intracellular localization study of Rh-PE-labeled PEG2k-F7 micelles with different subcellular organelle show preferential mitochondria colocalization after 1 h, example in Hela cell line (Rh-PE: rhodamine-phosphatidylethanolamine, fluorescent label). b) Spheroid penetration capability of PEG2k-F7 compared to PEG2k-PE micelles (top) and morphological changes (bottom) after 72 h of treatment with PEG2k-F7 micelles loaded with VES and controls in HeLa cell spheroids. c) Mitochondria colocalization quantification (top) by fluorescence quantitation and lipid-binding analysis by flow cytometry (bottom) of FITC-labeled polymers (PEG2k, F7, and PE) compared to the DLC rhodamine 123 in isolated mitochondria from Hela cells after a 1-h incubation and upon the carbonyl cyanide m-chlorophenyl hydrazine (CCP)-mitochondria depolarization inducer; results reveal higher mitochondrial accumulation and cardiolipin affinity for FITC-F7. d) Biodistribution of different Rh-PE-labeled micelles in the blood, tumor (top left), and major organs (bottom left) after 24 h in a 4 T1 tumor-bearing mice model; flow cytometry quantified further accumulation of Rh-PE-labeled micelles in cells (central) and mitochondria (right) isolated from tumor tissues. e) Antitumor effect of PEG2k-F7 micelles loaded with VES compared to controls (PBS, free VES, PEG2k-F7 and PEG2k-PE/VES) in 4 T1 tumor-bearing mice model after 15 days of treatment. Reprinted with permission [209].

within hydrophobic niches [211]. Previous studies conducted by the authors demonstrated that PFK coating of PoP-NP (mPoP-NP) formed slightly positively charged nanoparticles that targeted mitochondria, probably due to the electrostatic interaction with the negatively-charged mitochondria membranes [230]; however, the authors developed mPoP-NP with a higher (h) LND concentration and a lower PFK surface coating to reduce the cytotoxicity due to the positive charges, which resulted in a negatively charged formulation (h-LND-PoP-NPs). To avoid uncontrolled polypeptide aggregation, they snap-frozen, lyophilized, and redissolved h-LND-PoP-NPs in a tenth of their original volume (C) to obtain C-LND-mPoP-NPs. Interestingly, C-LND-mPoP-NPs maintained mitochondria-targeting properties despite the overall negative zeta potential; moreover, the advanced negatively charged formulation failed to induce cytotoxicity in its drug-free form. Lastly, findings in MDA-MB-231 triple-negative breast cancer xenograft model confirmed the enhanced drug efficacy and tumor growth inhibition capacity of C-LND-mPoP-NPs compared to the free drug.

3.3.2. *Lipid-based nanosystems*

Lipid-based materials possess several advantages that make them suitable for mitochondria-targeting nanomedicines, including their biocompatibility, simple formulation, and self-assembly. The following sections focus on the design of lipidic formulations exploited for their intrinsic self-assembly and fusogenic properties and their combinations with polymeric materials to form hybrid nanomedicines that have demonstrated successful *in vivo* translation in different applications.

3.3.2.1. Mitochondria membrane fusion. Membrane fusion is a rapid stepwise mitochondria-targeting approach prompted by fusogenic lipids capable of merging endosomal and mitochondria membranes. First introduced by Yamada *et al.,* the MITO-Porter liposome-based carrier comprises fusogenic lipids covered in octaarginine (R8) moieties that can introduce cargos into mitochondria via membrane fusion [231,232]. The high-density R8 coating allowed mitochondria-targeting liposomes to enter the cell by macropinocytosis, thereby avoiding CME and subsequent lysosomal enzymatic degradation [233]. Following the electrostatic interaction between the R8-liposome and the negatively charged mitochondria membranes, fusogenic lipids [such as dioleoylphosphatidylethanolamine (DOPE)] favor fusogenic processes, which induces a negative spontaneous curvature in the lipid bilayer prompting membrane fusion due to its conical shape. Significantly, sphingomyelin (a component of lipid raft microdomains) [234] and phosphatidic acid (interacts with proteins involved in membrane fusion, e.g., SNARE proteins) [235] participate in said fusogenic processes.

Second-generation Mito-Porters possess optimized cell uptake and fusogenic properties. Yamada *et al.* prepared dual-function bilayered liposomes (DF-MITO-Porter) composed of a mitochondria-fusogenic inner membrane and an endosome-fusogenic outer membrane coated with R8 [236]. The results showed that DF-MITO-Porter accumulated in mitochondria more efficiently than conventional MITO-Porters and successfully delivered the DNase I protein (as a model macromolecule) to the mitochondria matrix of HeLa cells. The authors observed that surface conjugation of differing mitochondria-targeting peptides (compared to R8) did not improve the mitochondria-targeting ability of DF-MITO-Porter [237]. Indeed, only S2 (the conjugation of two Szeto-Schiller peptides) possessed similar mitochondria targeting ability but induced a decrease in liposome cytotoxicity, thus representing a safer alternative for DF-MITO-Porter formulations.

Toxicity due to their polycationic nature represents a limitation of currently developed Mito-Porters, which has hindered their *in vivo*

translation. To overcome this limitation, the Harashima group designed a Mito-Porter modified with Stearyl-R8, which possesses CPP-like properties due to a long-chain fatty acid chain that facilitates membrane translocation and PEG2k to shield positive charges, increase blood circulation, and reduce toxicity [212]. DOX-MITO-Porter modified with 10 mol% R8 and 5 mol% PEG2k represented the optimal formulation for mitochondrial DOX delivery to OS-RC-2 renal carcinoma cells. Additionally, this formulation ensured the highest blood circulation time, tumor accumulation, and anti-tumor activity through mitochondria-dependent apoptosis in a DOX-resistant OS-RC-2 tumor-bearing mouse model. This example of Mito-Porter's application in cancer therapy encouraged the authors to explore its application in mitochondria-targeted photodynamic therapy (PDT). Interestingly, a Mito-Porter encapsulating a near-infrared-activated porphyrin-type photosensitizer (rTPA) displayed significant *in vivo* anti-tumor activity with a single PDT process and minimal systemic toxicity [213]. Moreover, the mitochondria depolarization induced by rTPA–MITO-Porter treatment after PDT suggests efficient mitochondria localization and photosensitizer delivery to the mitochondria, validating Mito-Porter as an organelle-specific drug delivery factor.

These latest findings present exciting prospects for utilizing the Mito-Porter platform as an effective nanomedicine specifically focusing on mitochondria; nevertheless, harnessing the potential of Mito-Porters in this domain will require further enhancements, including refining lipid concentrations and compositions, optimizing encapsulation efficiency, and fine-tuning surface functionalization.

3.3.2.2. Dqasome evolution. DQAsomes are liposome-like positively-charged vesicles deriving from the self-assembly of DQA [238]. Discovered in the mid-1990 s, DQAsomes were first explored as mitochondria-targeting delivery systems in gene therapy [239] and chemotherapy [240,241] due to their membrane potential-driven mitochondriotropic properties. Despite their promising features, their overall low encapsulation and transfection efficiency, short half-life in the bloodstream, and toxicity due to their cationic nature limited the *in vivo* translation of DQasomes [158]; however, recently developed strategies have helped to overcome these limitations. Shi *et al.* prepared DOX-loaded DQAsomes functionalized with a pH-sensitive PEG derivative (PSC, PEG2k-Schiff base bond-cholesterol) modified with an epidermal growth factor receptor-2 (HER-2; overexpressed in breast cancer) peptide ligand to obtain HPS-DQAsomes [214]. PSC shielding ensured prolonged circulation time and reduced toxicity *in vivo* in nude mice bearing MCF7/ADR tumors, while the pH-responsive activity of PSC and HER-2 peptide-mediated endocytosis and DOX delivery to the mitochondria after DQasome accumulation ensured mitochondrially-driven apoptosis and enhanced anti-tumor activity compared to free DOX or empty DQAsomes. In a related study, Bae *et al.* reported a DQasome system called DQA80 composed of DQA, DOTAP (1,2 dioleoyl-3-trimethylammonium-propane, a cationic lipid used for gene transfection), and DOPE (another cationic lipid) as a novel potential mitochondria-targeted gene-delivery vector for several applications, including genetic disorders of the mitochondria [242]. Specifically, they combined DQA chloride at varying molar ratios with DOTAP and DOPE, obtaining a DOTAP–DOPE–DQA molar ratio of 10:10:80 (DQA80s) as the most stable preparation. DQA80s enhanced the transfection efficiency compared to DQAsomes; however, the study also reported that DQA-based preparations result in mitochondrial depolarization, which may limit their *in vivo* application in mitochondria DNA delivery.

While many of these formulations remain stalled at the in vitro testing stage, DQasomes represent promising lipid-based delivery systems for mitochondria targeting; however, limitations such as limited transfection efficiency, aggregate formation followed by recognition from the RES system, and cytotoxicity require a careful design optimization for subsequent pre-clinical evaluation.

3.3.3. Hybrid-materials

Although DQAsomes and Mito-Porters represent promising mitochondria-targeting nanomedicines, low drug encapsulation efficiency, burst release kinetics, aggregates formation, leaky architecture, and instability upon storage combine to restrict their *in vivo* application of these liposomal formulations [244]. Lipid–polymer hybrid nanoparticles - comprising a polymeric core, a lipid monolayer, and a PEG coating - represent an attractive alternative to enhance encapsulation efficiency, establish well-defined kinetics and stability, and ensure active tissue-cell-organelle targeting [243].

Yan *et al.* prepared a lipid-polymer hybrid nanosystem based on PLGA for the polymeric core and 1,2-distearoyl-*sn*-glycero-3-phosphoethanolamine-N-[carboxy(PEG)] (DSPE-PEG-COOH) for the lipid shell to treat acute myocardial infarction [215]. The authors functionalized the surface with SS-31 for mitochondria targeting and cRGD for αvβ3 integrin receptor-specific targeting, which becomes overexpressed during myocardial infarction. The lipid-polymer hybrid nanosystem encapsulated the O-methylated isoflavone Calycosin and the abietane diterpene compound Tanshinone as a combination therapy. The targeted and loaded nanosystem displayed stability and did not aggregate, which resulted in a sustained release of the drugs over 72 h when administered to human cardiac myocyte cells in vitro. The *in vivo* results in acute myocardial infarction model rats confirmed the efficacy of dual targeting, leading to increased heart accumulation and improved infarct size reduction effect compared to a non-functionalized nanosystem.

Lipid–polymer hybrid nanoparticles targeting mitochondria can also undergo stimuli-responsive release in the intracellular environment. Zhou *et al.* fabricated a hybrid system (LPNPs) composed of PLGA as the polymeric core encapsulating PTX, a TPP-containing amphiphilic polymer (C18-PEG2k-TPP), and a GSH-responsive amphiphilic polymer (1,2-dilauroyl-*sn*-glycero-3-phosphoethanolamine (DLPE)-SS-mPEG4K) [216]. The authors proved the internalization and mitochondrial targeting of TPP-based lipid-polymer hybrid nanoparticles after disulfide linker reduction by the elevated levels of GSH observed in cancer cells. They also observed enhanced apoptosis and mitochondrial dysfunction after administration of the hybrid system, which they linked to a reduced oxygen consumption rate in MCF7 cells compared to nanoparticles not containing a disulfide linker. The *in vivo* analysis performed in MCF7 tumor-bearing mice revealed significant anti-tumor activity due to the intracellular activation of the hybrid system followed by mitochondria targeting, thus opening new possibilities for applying these formulations in stimuli-responsive mitochondria-targeting cancer therapy.

Tang et al. also demonstrated the *in vivo* translatability of lipid–polymer hybrid nanoparticles; they chose these nanosystems to overcome the limited intravenous administration of photoactivable nanofibers obtained from the self-assembly of the amphiphilic mitochondrially-targeting photosensitizer pheophorbide A−quinolinium conjugate (PQC) [217], in which pheophorbide functions as the photosensitizer for PDT and quinolinium is hydrophilic cation for mitochondria targeting [244]. The hybrid nanoparticles resulting from the co-assembly of lipids (DSPE-PEG, cholesterol, and L-phosphatidylcholine) and PQC to obtain spherical nanostructures demonstrated robust drug loading capacity (up to 55 %), encapsulation efficiency (92 %), and stability. In addition, the final formulation preserved the mitochondria targeting capacity and PQC photosensitization and ensured intravenous administration by increased formulation stability compared to pheophorbide-based liposomes. After injection, the intrinsic fluorescence imaging capability of PQC supported the visualization of drug distribution and tumor accumulation *in vivo* in an orthotopic glioma model; moreover, a single dose of lipid–polymer hybrid nanoparticles with PDT led to superior tumor growth inhibition compared to simple PA-based liposomes. This study highlights the application of hybrid systems in mitochondria-targeting PDT, with promising clinical application in cancer treatment.

Table 2
Relevant examples of mitochondrially-targeted organic nanomedicines and their specifically triggered responsiveness/drug release. The proposed examples reached preclinical stages in different applications, primarily focusing on cancer.

MITOCHONDRIA-SPECIFIC TRIGGERED RELEASE							
Strategy	**Nanomedicine**	**Material**	**Therapeutic Cargo**	**Targeting Moiety**	**Targeting Mechanism**	**Disease (preclinical model)**	**Ref.**
THIOKETAL LINKER (TK) (ROS SENSITIVE)	SC-TK-SS-31	L-serine–modified chitosan (SC) conjugated using a TK linker to SS-31	SS-31 (TK linker)	L-serine (Kim-1) ligand (cellular targeting) SS-31 (mitochondria targeting)	Endocytosis mediated by Kim-1 (L-serine as a ligand), (ROS)–sensitive thioketal linker and mitochondria targeting via SS-31	AKI (tubular renal HK-2 cells/ IR-induced AKI mice) IR-ischemia–reperfusion	[245]
	PPCs@KLAK	Poly(vinyl alcohol) -TK-KLAK/PEG-TK-KLVFF	β-sheet-forming peptide KLVFF	SS-derivative cytotoxic peptide (KLAK, sequence: CGGG(KLAKLAK)2) (mitochondria-targeting)	Conformation changes due to hydrophilic/ hydrophobic imbalance after KLAK mitochondria targeting, PEG shell removal due to ROS-sensitive linker, mitochondria targeting via KLAK	HeLa cells/HeLa tumor-bearing mouse model	[246]
	TPP/FA-DOX-CNM	TPP-PEOGMA-b-P(CNM-co-DOX) + FA-PEOGMA-b-P(CNM-co-DOX)	Cinnamaldehyde (CNM) (pH-sensitive acetal linker)/DOX (TK linker)	Folic acid (FA, folate receptor) (cellular targeting) TPP (mitochondria targeting)	Cell internalization via folate receptor-mediated endocytosis and CNM release at endosomal pH 5.0, DOX release upon ROS-sensitive linker, pH and ROS-responsive release of CNM, mitochondria targeting via TPP	Breast cancer (DOX-resistant MCD-7 ADR cells/MCF7 ADR mice tumor model)	[247]
	HA-CD@TPP-CNM/Fc	HA-CD/TPP-thioacetal-CNM-Fc	CNM & Fenton organocatalyzedferrocene (Fc) (Fc for chemodynamic therapy, CDT)	HA (CD44 receptor affinity) (cellular targeting) TPP (mitochondria targeting)	Receptor-mediated endocytosis (CD44), mitochondrial targeting via TPP	Breast cancer (4 T1 cells/mouse embryo fibroblast (NIH 3 T3)/ 4T1tumor-bearing mice)	[248]
	DT-PNs	co-assembly of cRGD-PDMA-b-PCPTSM and TPP-PDMA-b-PCPTSM (PCPTMS: Camptothecin (CPT) modified with TK)	Camptothecin (CPT) (TK linker)	cRGD for αvβ3 integrin receptor-targeting (cellular targeting) TPP (mitochondria targeting)	Dual targeting (Receptor-mediated endocytosis (αvβ3) and mitochondria targeting via TPP, CPT ROS-induced release and ROS burst upon CPT increasing release	Breast cancer (4 T1 /MCF-7 cells/4T1tumor-bearing mice)	[249]
	S1P/SS-31/Lipo-encapsulated ROS-responsive composite hydrogel	Hydrogel (poly-3-amino-4-methoxybenzoic acid with TK-NH2-modified gelatin (PAMB-G-TK) and 4-arm-PEGsuccinimidyl glutarate ester (4-arm-PEG-SG) encapsulating liposomes (S1P/SS-31)	S1P (pro-angiogenic molecule) and SS-31 (encapsulated in liposomes)	SS-31 (mitochondria targeting)	Hydrogel deformation in the ROS-rich environment of the myocardial infarction area and prompt release of encapsulated S1P/SS-31/Lipo for mitochondria targeting	myocardial infarction-induced SD rats	[250]
BORONIC ESTER (ROS SENSITIVE)	NPs@Cur	PEG-b-PAGA/ PDMAEMA-r-PAAPBA)-b-PPBAE/Cur	Cur (encapsulated)	N/A	Endocytosis and endosomal escape after protonation (PDMAEMA), Cur release after ROS-induced nanoparticle degradation (PAGA and PAAPBA form cross-linked boronic esters)	Acute Kidney Injury(AKI) (tubular renal HK-2 cells/AKI mice, yes/no cisplatin treatment)	[251]

(*continued on next page*)

Table 2 (*continued*)

MITOCHONDRIA-SPECIFIC TRIGGERED RELEASE							
Strategy	**Nanomedicine**	**Material**	**Therapeutic Cargo**	**Targeting Moiety**	**Targeting Mechanism**	**Disease (preclinical model)**	**Ref.**
	HM-NPs@G	Cell-mitochondria hybrid membrane (HM) (outer shell)/ PEG-PHB (dioxaborolane-based)/ Gboxin	Gboxin (encapsulated)	HM (1:1 protein weight ratio of mitochondria membrane (MM) to cancer membrane (CM) with different proteins for targeting and penetration embedded	Endocytosis and mitochondria targeting mediated by distinct proteins (e.g., Atlastin-1, EHD2, and Mito-fusion), Gboxin release after PEG-PHB degradation (PEG, pinacol borate and p-hydroxy-methylphenol) by intracellular ROS	Orthotopic U87MG glioblastoma-bearing mouse model	[252]
TEMPERATURE	PEG-PNIPAM-TPP-iRGD@DOX	PEG-PNIPAM-TPP-iRGD	DOX (encapsulated)	iRGD (CRGDKGPDC) /TPP for αvβ3 integrin receptor- targeting (cellular targeting) TPP (mitochondria targeting)	iRGD-mediated cellular uptake and mitochondria targeting via TPP plus tunable temperature-responsiveness	Lung cancer (H69AR cell model of DOX-resistant small-cell lung cancer cells/mice bearing H69AR tumors)	[253]
pH	CTPP-CSOSA/Cela Micelles	Glucolipid-like conjugate CSOSA modified with CTPP (TPP derivative)	Celastrol (Cela) (encapsulated)	CTPP (mitochondria targeting)	Cell uptake and mitochondrial targeting via CTPP, Cela release at mitochondria pH 8 (increased solubility)	Breast cancer (MCF-7 cells and tumor-bearing mice)	[254]
ENZYMATIC CLEAVAGE	TPP11–malonate	TPP -dicarboxylate malonate	Malonate/TPP	TPP (mitochondria targeting)	Mitochondrial targeting via TPP	C2C12 mouse myoblasts and HeLa cells/C57BL/6J mice	[255]

3.3.4. *Mitochondria-specific stimuli triggered release from nanomedicines*

Mitochondria-specific features can enhance nanomedicine accumulation and targetability and specifically release therapeutic cargos at the mitochondria level in response to specific stimuli (Table 2).

As mitochondria represent the primary source of ROS (overproduced in diseases such as cancer, cardiovascular diseases, and neurodegeneration [256]), the design of ROS-responsive nanomedicines represents the primary approach for specific release at the mitochondria level. The TK linker, a biodegradable and non-toxic thioether derivative linker cleaved to a thiol-containing group and acetone upon ROS exposure, has been widely applied to mitochondrially-targeting nanomedicines. Compared to other ROS-sensitive linkers (e.g., aminoacrylate linkers and peroxalate linkers), the TK linker offers several advantages, including stability under physiological conditions, unique ROS-responsive properties, and chemical versatility (e.g., polymer-drug conjugates) [257,258].

Liu et al. developed an L-serine–modified chitosan conjugated to SS-31 using a TK linker (SC-TK-SS-31) for the treatment of acute kidney injury (AKI) [245]; notably, SS-31 ensured mitochondria targeting and antioxidant activity, while L-serine provided enhanced ligand-mediated cellular uptake, as it targets the kidney injury molecule–1 (Kim-1) protein upregulated in AKI. The authors demonstrated the ROS-responsive release and mitochondria targeting of SS-19 (a fluorescent analog of SS-31) following the exposure of H_2O_2-stimulated proximal tubular renal HK-2 cells to SC-TK-SS19, which also resulted in an increased antioxidant and anti-apoptotic activity compared to free SS-31 and controls without L-serine or the TK linker (verified an infrared light-induced AKI mouse model).

Cheng et al. designed a polymer-peptide conjugate that underwent a ROS-triggered morphology transformation at the mitochondria level, displaying enhanced mitochondria cooperative interaction and cytotoxicity in cancer cells thanks to TK linker degradation [246]. The authors fabricated nanomedicines consisting of poly(vinyl alcohol) conjugated by a thiol − ene reaction to a Szeto-Schiller-derivative mitochondria-targeting cytotoxic peptide (KLAK, sequence: CGGG (KLAKLAK)2) and a β-sheet-forming peptide KLVFF linked to PEG via a TK linker. Interestingly, they demonstrated that the self-assembled conjugates changed conformation from spherical to nano-fibers due to a hydrophilic/hydrophobic imbalance after mitochondria targeting by KLAK and PEG shell removal by ROS-induced TK cleavage, which enhanced mitochondria accumulation and apoptosis of HeLa cells. The authors confirmed the antitumor effect in a HeLa tumor-bearing mouse model, where the responsive nanoparticles significantly reduced tumor growth compared to controls without the TK linker, PEG, and KLVFFT.

Researchers have developed different mitochondria-targeting nanomedicines with inherent ROS-boosting properties to increase the efficacy of ROS-responsive drug release. For instance, Mukerabigwi et al. fabricated amphiphilic block copolymer prodrugs by the polymerization of poly[oligo-(ethylene glycol) methyl ether methacrylate] (POEGMA), cinnamaldehyde (CNM) synthesized via a pH-sensitive acetal bond, and DOX monomers, synthesized using a ROS-responsive TK linker [247]. Folic acid (FA), a ligand of the folate receptor α overexpressed in breast cancer cells, and TPP were then conjugated to the polymeric chain (TF@CNM) to ensure enhanced ligand-mediated cellular uptake and mitochondria targeting, respectively. Lastly, the encapsulation of DOX formed polymeric micelles (TF@CNM + DOX) for the treatment of multi-drug resistance in breast cancer. The authors designed TF@CNM + DOX to release the anticancer drug CNM in the acidic pH of the endosomal environment after folic acid-mediated endocytosis, which would lead to a CNM-induced increase in mitochondria membrane permeability, in situ amplification of mitochondrial ROS production, and subsequent DOX release by TK linker cleavage. Therefore, encapsulated and released DOX could further contribute to mitochondria-related cancer therapy. In vitro results in DOX-resistant MCD-7 ADR cells revealed enhanced cytotoxicity, ROS generation, and DNA damage in the presence of TF@CNM + DOX compared to free DOX, micelles

lacking targeting moieties and, notably, those lacking CNM; overall, these findings suggest the importance of the TK linker in the formulation. Subsequent *in vivo* analyses using an MCF7 ADR mice tumor model found that TF@CNM + DOX inhibited tumor growth and significantly increased survival rates, thereby ratifying the in vitro results.

Zeng et al. exploited a similar approach and designed a self-amplified antitumor therapy based exclusively on ROS generation [248]. The authors prepared a mitochondrially-targeted chemodynamic therapy for breast cancer treatment by the self-assembly of supramolecular nanoconjugates (HTCF) via the interaction of an α-cyclodextrin decorated HA conjugate with a mitochondria-targeting ROS-activated prodrug formed by CNM linked via TK linkers, TPP and Fenton organocatalyzed ferrocene (Fc), which can convert H_2O_2 into highly cytotoxic hydroxyl radicals (•OH). After HA-CD44 mediated internalization, HTCF accumulated in mitochondria where the centralized Fenton reaction benefits from the high levels of H_2O_2; moreover, CNM release after ROS-induced TK linker degradation boosted H_2O_2 production, resulting in synergistic cytotoxicity induced by HTCF compared to free CNM and Fc and the nanoassemblies lacking targeting moieties in 4 T1 cells, thereby initiating a cell apoptosis pathway mediated by mitochondria damage. The in vitro results translated into significantly reduced tumor growth after the intravenous administration of HTCF in 4 T1 tumor-bearing mice, presenting a promising perspective for mitochondria-specialized chemodynamic therapy (Fig. 5**a-d**).

Despite the recognition of TK as the most stable and versatile ROS-sensitive linker, research has continued to highlight alternative options. Boronic acids and esters have emerged as promising alternatives, known for their safe metabolic profile following oxidation by H_2O_2. Lan et al. developed Curcumin(Cur)-loaded dual-responsive nanoparticles (NPs@Cur) using PEG-b-poly(alkylene glycol) (PEG-b-PAGA) and DMAEMA-based copolymers modified with hydroxyphenyl boronic acid pinacol ester [(PDMAEMA-r-PAAPBA)-b-PPBAE] for the treatment of cisplatin-induced AKI [251]. The design of the nanoparticles to have a negative charge at pH 7.4 supported protonation in acidic, inflammatory conditions, which facilitated cellular uptake. The nanoparticles subsequently underwent degradation in a ROS-rich disease environment, enabling mitochondrial targeting of Cur. This approach reduced ROS production and stabilized mitochondria membrane potential, improving the amelioration of renal tubule injury compared to the free drug in an AKI mouse model. While a significant number of studies support the application of ROS-responsive linkers, oxidation-sensitive polymers could also represent a valuable option in the design of mitochondrially-targeted nanomedicine [259]. For instance, the Tirelli group focuses on the design of poly(propylenesulfide) nanoparticles (responsive to H_2O_2, peroxynitrite, and hypochlorite) as ROS-scavenging anti-inflammatory therapies or in ROS-triggered drug delivery systems [260–262]. Oxalate polymers represent another example (they undergo rapid oxidization to alcohol and CO_2 by H_2O_2), which have been applied to fabricate ROS-responsive nanoparticles and gels [263,264]. Although their specific application in subcellular mitochondria therapy remains incompletely explored, these oxidation-sensitive polymers hold great potential for future biomedical applications.

Even though ROS represents the primary stimuli used to guide the design of mitochondria-targeting responsive materials, alternative approaches have also been explored. Ruan et al. developed a mitochondrial temperature-responsive drug delivery to reverse DOX resistance in lung cancer [253]. Part of the energy produced during mitochondrial respiration becomes converted to heat, which increases mitochondrial temperature (~48°) [265,266]. The authors developed a poly(N-isopropylacrylamide) (PNIPAM)-based nanocarrier functionalized with TPP for mitochondria targeting and iRGD, a 9-amino acid cyclic peptide (CRGDKGPDC) targeting αvβ3 overexpressed in lung cancer cells, for increased cellular uptake. PNIPAM possesses a lower critical solution temperature (typically around 32 °C); therefore, PNIPAM is hydrophilic

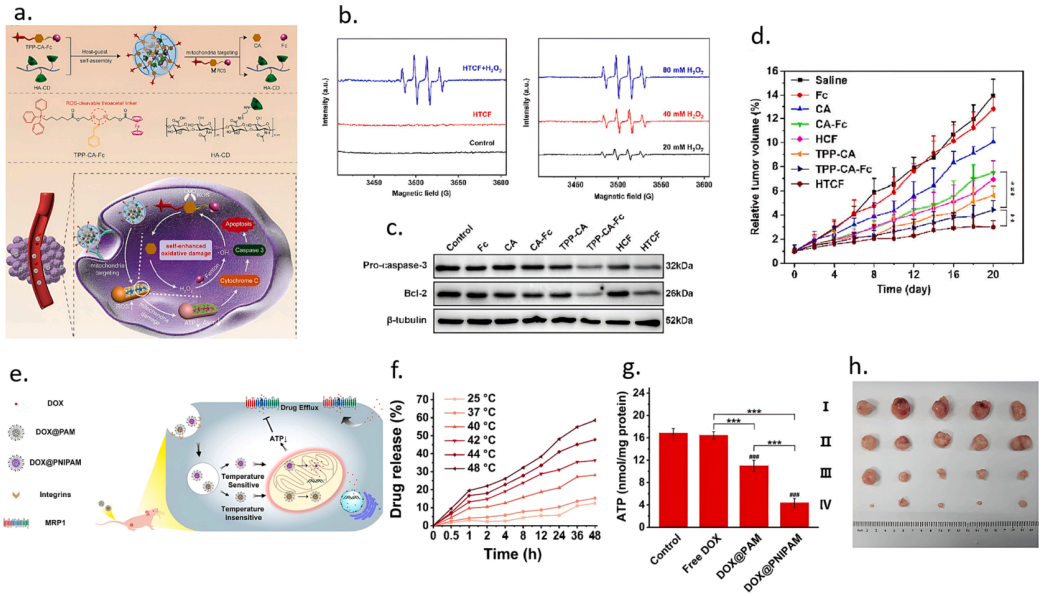


Fig. 5. Examples of Mitochondria-specific stimuli Triggered release from nanomedicines. (a-e) A ROS-sensitive thioketal linker. a) Synthetic scheme, mitochondria targeting, and self-enhance oxidative damage mechanism of self-assembled supramolecular nanoconjugates (HTCF) obtained by the interaction of α-CD decorated HA conjugate and the ROS-responsive prodrug formed by CNM linked via TK linkers TPP, and Fenton organocatalyzed ferrocene (Fc) for breast cancer treatment by chemodynamic therapy. b) H_2O_2 concentration-dependent •OH production by HTCF via electron spin resonance analysis. c) HTCF-induced mitochondria dysfunction-related apoptosis analysis by the expression level of pro-caspase-3 and B-cell lymphoma-2 (Bcl-2) in 4 T1 cells after 24 h treatments. d) Antitumor effect by tumor volume analysis after 21 days of treatments with HTCF and controls (PBS, free Fc, free CNM (CA), CA-Fc, HCF without TPP, TPP-CA, TPP-CA-Fc) in 4 T1 tumor-bearing mice. Reprinted with permission [248]. (e-h) A Temperature-responsivity. e) Schematic illustration of mitochondrial temperature-responsive DOX-bearing PNIPAM nanocarrier, functionalized with TPP and iRGD (DOX@PNIPAM) in a DOX-resistant model of small-cell lung cancer. f) DOX release from DOX@PNIPAM at different temperatures. g) Intracellular ATP levels in H69AR cells after treatment with DOX@PNIPAM and controls. h) Antitumor activity in mice bearing H69AR tumors by qualitative analysis of the tumor weight after 21 days treatments by DOX@PNIPAM and controls [(I) PBS, (II) free DOX, (III) non-temperature-responsive DOX@PAM]. Reprinted with permission [253].

and soluble in water below this temperature but forms a gel above this temperature [267]. Furthermore, PNIPAM functionalization (e.g., with PEG) can fine-tune its properties and lower critical solution temperature. The authors prepared PEG-PNIPAM to increase its lower critical solution temperature to 48° and ensure DOX release at mitochondrial temperatures. In vitro results in the H69AR cell model of DOX-resistant small-cell lung cancer confirmed mitochondrial targeting and DOX delivery, which induced mitochondria depolarization, decreased ATP production, and suppressed tumor growth in mice bearing H69AR tumors (Fig. 5**e-h**).

Compared to the IMS or other subcellular compartments, the higher pH level of the mitochondrial matrix (pH 7.5–8.2) can be used as trigger for site-specific drug release. Yamada et al. proposed an alternative to a previously developed STR-R8-based Mito-Porter via modification with STR-histidine (H) or derivatives (e.g., STRH2R4H2) to improve the delivery of antisense RNA to the mitochondria (targeting mitochondrial mRNA encoding the COX2 protein (DarmASO [COX2]) and oligo RNA not targeting COX2 (Darm Mock) [268]. Compared to Arginine (pKa ~ 12.5), which has a positive charge at all cellular pH, histidine (pKa ~ 6.0) remains positively charged in acidic and neutral environments while becoming neutralized at pH 8. Therefore, the STR-H-based Mito-Porters formed stable polyplexes via electrostatic interactions with negatively charged nucleic acids but efficiently released their cargo after collapsing in the alkaline environment of the mitochondria in HeLa cells. In another study, Tan et al. exploited the differential solubility of the weakly acid drug Celastrol (Cela) encapsulated in glucolipid-like conjugates (CSOSA) modified with 4-carboxybutyl-TPP (CTPP-CSOSA/Cela) for specific release in the mitochondrial environment [254]. The selective response of CTPP-CSOSA/Cela micelles to the alkaline pH of the mitochondria, which leads to reduced interaction between the hydrophobic core of the micelles and Cela and increased solubility at pH 8.0, resulted in increased ROS-induced apoptosis, mitochondrial depolarization, and tumor suppression (MCF-7 cells and tumor-bearing mice) when compared to free Cela and micelles without CTPP.

In another study, Prag et al. conjugated TPP to dicarboxylate malonate, which inhibits the succinate-driven production of ROS through mitochondrial complex I via an undecyl monoester linker cleavable by the mitochondria enzyme aldehyde dehydrogenase 2 [255]. The study aimed to rationally design an efficient and selective delivery of dicarboxylates to mitochondria, which can potentially treat mitochondrial dysfunction-related diseases. The specific accumulation and release of dicarboxylate malonate within the mitochondria were demonstrated both in vitro (C2C12 mouse myoblasts and HeLa cells) and *in vivo* (C57BL/6J mice), which resulted in the restoration of mitochondrial function. Even though the study did not focus on nanomedicine specifically, the linker design could become integrated into more complex designs for efficient mitochondrial drug delivery.

Despite the novel approaches in mitochondria-specific drug delivery using specific responsive linkers and materials, challenges and areas for improvement remain, such as mitochondria-release selectivity, fine-tuning release kinetics within the levels, and real-time release monitoring, which could be beneficial for their *in vivo* translation.

4. Identifying the Tools to Validate Mitochondria Targeting

The design and development of nanomedicines that target mitochondria require specialized techniques that evaluate drug uptake by this organelle to support the early prediction of mitochondrial toxicity and accelerate drug development. Most currently available tools focus on whole-cell drug uptake; however, a small number of specific tools can determine mitochondria targeting efficacy/efficiency of nanomedicines.

4.1. Transmission Electron Microscopy

Transmission electron microscopy (TEM), a powerful imaging technique that discriminates atomic-scale objects, transmits an electron beam onto samples and uses the pattern of scattered electrons to create an image. The ability of TEM to magnify images several million times has prompted its widespread use in multiple fields, including materials and biological sciences [269].

Multiple research groups have successfully applied TEM to evaluate cellular trafficking and study the interactions of nanomedicines with mitochondria. TEM can localize and track nanomedicines in the biological environment - from uptake to eventual biodegradation – to provide basic information supporting efficient administration strategies for therapeutic/diagnostic purposes and facilitating safety assessments. The resolution of TEM in the nanometer range allows the determination of the exact number of particles uptaken by cells and the detection of aggregates, which remains challenging to achieve by other methods. TEM is a particularly interesting technique for nanomedicines with electron-dense components [270]; however, TEM suffers from limitations regarding the visualization of organic compounds, which include poor contrast within biological systems. Using TEM with heavy metal staining methods to improve sample contrast allows the visualization of morphological and structural details that help to understand the nanoparticle uptake mechanism by localization in subcellular structures such as endosomes, lysosomes, secondary lysosomes, mitochondria, vacuolar structures, and residual bodies [270]. Mitochondria themselves can be recognized by their characteristic winkled form.

Despite the enormous potential of TEM in the nanomedicine field, the need for relatively thin slices and the sensitivity of biological samples to irradiation [269] have made evaluating biological samples a more challenging task. Moreover, the similarity in shape of specific nanomaterials to intracellular organelles or vesicles in biological samples can further confuse experimental interpretation; however, modifications of conventional TEM – such as immune-TEM, energy-filtered TEM-EFTEM or correlative light-electron microscopy (CLEM) [271] - can overcome such limitations.

Immuno-TEM comprises cell molecule visualization via the attachment of a gold-labeled antibody to the desired molecule [271]. Once the antibody recognizes the antigen, the labeled gold facilitates TEM visualization due to its high electron density. In the case of mitochondrial targeting nanomedicines, adding gold nanoparticles would represent a small step to make TEM visualization easier. Yu et al. demonstrated the enhanced mitochondrial localization of ND4 DNA delivered from an MTS-modified AAV to suppress optic atrophy in Leber's hereditary optic atrophy (Section 3.2) [161]. The authors applied immuno-TEM to visualize ND4 DNA in the optic nerves of a mouse model after intraocular injection of the MTS-modified AAV. Silver-enhanced immunogold labeling of the DNA plasmid allowed visualization in optic nerve mitochondria (labeled by manganese sodium dismutase). Labeling the mitochondria and cargo with electron-dense compounds in this example ensured robust contrast for their recognition and differentiation by TEM. Importantly, immune-TEM is not always possible, as this approach requires an antigen (e.g., DNA, protein) to bind the labeled antibody.

EFTEM employs an energy filter between the sample and the detector [272]; the electrons that lose energy during their passage through the sample are not considered for image generation, and only well-energy-defined electrons are used to obtain images of optimal quality. Meanwhile, ***CLEM*** represents a combination of fluorescence microscopy and TEM, which provides two types of information: the localization of molecules within biological samples using dyes and the visualization of cell ultrastructure [273]. As an example of applications related to nanomedicines, Han et al. identified, localized, and quantified self-reporting fluorescent nanodiamonds coated with a human serum albumin (HSA)-derived copolymer and linked to PEG (fNDs) in HeLa cells by EFTEM and CLEM [274].

The resolution of TEM in the nanometer range allows the visualization of subcellular structures in detail and the shape of the nanoparticles internalized at different subcellular sites. Therefore, the evaluation of mitochondrial targeting by TEM allows the quantification of internalized nanoparticles, the identification of the exact accumulation site, and

the conformational changes that may affect mitochondria and the nanosystem once they have reached the target; however, applying TEM to the visualization of non-metallic nanomedicines may represent a challenging task as, for example, polypeptide-based nanosystems present low contrast for TEM analysis [90]. Moreover, the need for sample preparation based on drying/freezing or diluting the sample and adding conducting agents can affect sample morphology [275].

4.2. Confocal Laser Scanning Microscopy

Fluorescence microscopy, an imaging technique based on optical microscopy that employs fluorophores to detect specific molecules, emits excitation light at the desired wavelength, which interacts with the sample, moves electrons to a higher energy state, and induces emission of light at different energies and wavelengths that can be detected [276]. The development of ***confocal laser scanning microscopy (CLSM)*** represented a significant advance in fluorescence microscopy, given its ability to remove background fluorescence, a crucial feature for thick samples where the traditional detectors used to capture light from out-of-focus regions and worsened image resolution [277]. Compared to TEM, CLSM requires less complex sample preparation and displays compatibility with 3D live imaging [278].

The fluorescent probes used for mitochondria visualization are based on cationic lipophilic dyes that attach to the negatively charged IMM in a charge-dependent manner [279]. Commonly used dyes include 5,5′,6,6′-tetrachloro-1,1′,3,3′-tetra-ethylbenzimidazolcarbocyanine iodide (JC-1), rhodamine 123, MitoTracker green, and red, tetramethylrhodamine methyl ester (TMRM), and tetramethylrhodamine ethyl ester (TMRE), which can be visualized by fluorescent microscopy or quantified by flow cytometry/fluorescence spectroscopy [280,281].

The ability of CLSM to obtain serial optical sections allows the accurate determination of a given nanomedicine's subcellular localization [277], thereby providing information regarding internalization mechanisms, intracellular trafficking, and compartment binding [21]. These abilities have made CLSM a standard tool in studies of mitochondrially-targeted nanomedicines, with multiple examples present in the literature. Sharma et al. demonstrated the mitochondrial localization of D-DPA (Section 3.3.1.3) in tumors from a glioblastoma mouse model by CLSM [203]. Fluorescence detection employed the intravenous injection of Cy5-D-DPA in mice and the excision, dissection, and staining with anti-apoptosis-inducing factor (AIF) after 24 h for mitochondria labeling. CLSM revealed that D-DPA colocalized with glioblastoma cell mitochondria, while minimal amounts found in the surrounding tissue indicated specific tumor targeting.

CLSM with grating optics allows the detection of spectral changes of a fluorescent dye, such as that which occurs in ***Förster resonance energy transfer (FRET)*** - a non-radiative process based on energy transfer between fluorescent molecules by dipole–dipole interactions upon excitation, which makes the process highly dependent on the distance between molecules [282]. This phenomenon allows the evaluation of various chemical and biological processes, such as conformational changes, membrane fusion, molecule interactions, and enzyme cleavage [283], making FRET a valuable tool for studying mitochondrial-targeting nanomedicines. Yamada et al. used FRET to describe the mitochondrial uptake mechanism (membrane fusion) of MITO-Porters [231,232], liposome-based nanoplatforms (Section 3.3.2.1).

As an alternative to FRET, ***bioluminescence resonance energy transfer (BRET)*** uses a bioluminescent protein to excite an acceptor through resonance energy transfer [284]. BRET represents a powerful tool for studying organelle interactions [285]. Therefore, this phenomenon could represent a valuable approach for visualizing protein-based nanomedicines and evaluating mitochondrial modifications upon nanomedicine treatment.

Overall, the ability to collect images from biological samples at high resolution and the straightforward sample preparation/outcome interpretation have made CLSM a widely used technique for evaluating mitochondrial targeting nanomedicines.

4.3. Methods to evaluate mitochondrial targeting in isolated mitochondria

The assessment of mitochondrial targeting in isolated mitochondria requires selecting a method to adequately separate and purify mitochondria from cells/tissues. Pallade first isolated mitochondria in 1946 through the homogenization and differential centrifugation of liver samples [286]; the differential sedimentation properties of distinct cell constituents allowed for the separation of mitochondria by centrifugation at various speeds (differential centrifugation). Novel methodologies developed since this time include affinity purification using antibody-coupled magnetic beads [287], commercial kits consisting of reagent-based homogenization and fractionation [288], and advanced techniques such as capillary electrophoresis, free-flow electrophoresis, field-flow fractionation, and microfluidics [289,290]. Despite the various available mitochondrial isolation approaches, homogenization of cells/tissues followed by differential centrifugation remains the most widely used method due to its cost-effectiveness, applicability to different laboratory settings, and straightforward approach.

The assessment of nanomedicines' ability to target mitochondria in isolated mitochondria samples cannot only be performed by fluorescence detection, but also by Western blotting and by inductively-coupled plasma-mass spectrometry (ICP-MS; described below), which have more specific uses in detecting encapsulated proteins and metal-based drugs, respectively. Additionally, high-performance liquid chromatography (HPLC) coupled with diverse types of detectors and mass spectrometry (MS) represent two promising analytical techniques that allow the quantification of nanomedicine components in isolated mitochondria.

4.3.1. Fluorescence detection

Fluorescence detection (either from dyes or drugs) represents the most common and cost-effective technique for quantifying nanomedicine internalization by mitochondria. Liu et al. assessed the mitochondrial uptake of PEG2k-F7 micelles labelled with Rh and compared with the parent non-fluorinated derivative in the mitochondria of tumoral cells isolated from a 4 T1 tumor-bearing mouse model 24 h after the intravenous injection (Fig. 4**D**) [209]. The authors employed a kit to isolate mitochondria from dissociated cells and quantified the fluorescence emitted by mitochondrially-associated micelles by flow cytometry. PEG2k-F7 displayed higher accumulation in tumor cell mitochondria compared to the free dye (Rh) and non-fluorinated PEG2k-PE, indicating a relevant role for fluorine in mitochondrial targeting.

4.3.2. Western Blotting

Western blotting represents the most used technique for detecting and quantifying proteins in biological samples [291]; this technique can evaluate mitochondrial targeting by detecting the peptides or proteins that can form parts of nanomedicines in mitochondrial fractions isolated from cells. As described in Section 3.2, Klimpel et al. demonstrated the mitochondrial localization of the sC18 CPP-ALD5 MTS conjugate in HeLa cells [165]. Western Blotting of isolated mitochondria further confirmed the mitochondrial colocalization observed by CLSM in cells treated with the targeting peptide after biotinylation. The authors reported the expression of the biotinylated peptide in the mitochondrial fraction (with a small amount in the cytosol), proving the effective targeting of mitochondria.

To the best of our knowledge, no study has applied Western blotting in animal model samples to determine the mitochondrial localization of nanomedicines; however, this technique could be applied following the same rational as for in vitro samples.

4.3.3. High-Performance Liquid Chromatography

HPLC separates, identifies, and quantifies compounds by running components through a column in a mobile phase to support separation

according to covalent interactions with the stationary phase [292]. Depending on the chemical nature of the components, HPLC can be coupled to ultraviolet–visible (UV/Vis), fluorescence, MS, radiochemical, or electrochemical detectors [293]. HPLC can also quantify the amount of drug internalized by mitochondria. Zhou et al. employed HPLC to evaluate whether the *in vivo* antitumor effect of PTX-loaded LNPs (composed of C18-PEG2k-TPP and (DLPE)-SS-mPEG4K; Section 3.3.3) was the consequence of a high tumor accumulation or it was mainly due to the capability of mitochondrial-targeting [216]. 24 h after the intravenous injection of PTX-loaded LPNPs into an MCF7 xenograft model, the authors quantified PTX in isolated tumor cell mitochondria; they confirmed mitochondria targeting by the HPLC-UV-mediated detection of high PTX levels compared to treatment with the parent amphiphilic polymer C18-PEG2k and free PTX.

4.3.4. Mass Spectrometry

MS represents a powerful tool for biochemical studies, which detect drugs released from mitochondrially-targeted nanomedicines in isolated mitochondria. Various ionization techniques, such as electrospray ionization (ESI) and matrix-assisted laser desorption ionization (MALDI), can be used in conjunction with MS to generate gas-phase ions that can be detected by their mass-to-charge ratio (m/z) [294]. Reddy et al. used ESI-MS to detect curcumin (Cur) released from mitocurcuminoids (Mitocur-1,2,3; mitochondrially targeted Cur conjugates with TPP linked at various positions) within mitochondria in vitro, which resulted in higher accumulation in the mitochondria than the cytosol [295].

ICP-MS – a sensitive analytical technique that detects elements with an ionization potential below argon [296] – can also detect targeted nanomedicine components from isolated mitochondria. The equipment introduces the sample as an aerosol that hits an argon plasma to ionize the sample, the ion beam then becomes directed to the ion optics that guide ions to the MS detector, where they become separated and analyzed according to their m/z ratio. Marrache et al. used ICP-MS to detect the cadmium components of quantum dots included in a polymeric system (PLGA-b-PEG-TPP) in mitochondria isolated from HeLa cells to confirm successful uptake by mitochondria [297]. The requirement for the nanomedicine internalized by mitochondria to include an ICP-MS-detectable element represents the main drawback of this technique. Quantifying the internalization of nanomedicines by mitochondria *in vivo* could also employ MS and ICP-MS techniques following mitochondrial isolation from the dissociated cells of animal tissues.

The assessment of nanomedicine delivery to mitochondria remains indispensable when studying mitochondrially-targeted nanomedicines. Mitochondrial targeting can be assessed both in cell/tissues or in isolated mitochondria from these samples; however, due to the sample manipulation and time required for sample preparation in the analysis of isolated mitochondria samples, the evaluation of mitochondrial delivery in whole cell/tissues remains the first option. CLSM represents the most widely applied technique to evaluate mitochondrial targeting due to its simplicity and applicability to all types of nanomedicine; however, TEM provides a visualization of the mitochondrial ultrastructure, allowing the more precise localization of the internalized molecule and the evaluation of structural changes. Therefore, we believe that the combination of CLSM and TEM or the application of CLEM would provide more comprehensive validation; subsequently, analysis in isolated mitochondria could help to validate the identified findings further.

4.4. Promising techniques for future application in mitochondrial targeting evaluation

Despite the elevated resolution of CLSM images and the widespread applicability, CLSM cannot visualize cellular ultrastructures below 100 nm; however, ***super-resolution microscopy (SRM) techniques*** that break the optical diffraction limit have been developed [298]. SRM has become popular in live-cell imaging thanks to its applicability in studying drug delivery and kinetics at the subcellular level, enabling the evaluation of a drug's mechanisms of action and certifying the efficacy of targets *in vivo*. A recent review has compiled the applications of SRM in mitochondrial analyses to understand the organization of subcellular compartments (including the IMM and OMM, cristae, and mitochondrial nucleoids) [299]. Zou et al. also highlighted the ability of SRM to evaluate mitochondrial dynamics and provided tools for studying diseases related to mitochondrial dynamics [300].

Live-cell imaging demands strict control of environmental conditions, such as temperature and humidity, with cells maintaining activity only during short exposures to prevent cell death. Challenges persist in achieving subcellular drug dynamic imaging with SRM; additionally, SRM relies on the expression of fluorescent molecules within cells, potentially altering cell physiology and not reflecting the molecular action of drugs [301]. The design of super-resolution fluorescence probes also remains limited regarding photobleaching and wavelength selection; nevertheless, super-resolution technology represents a significant advancement and a valuable tool for understanding how drug molecules interact within biological substances.

Mass Spectrometry Imaging (MSI) represents an emerging analytical technique that combines the potential of MS in molecule detection/identification and the visualization of their spatial distribution within a biological sample [302]. MSI has been applied for the visualization of molecules in tissue/spheroid sections; however, the advancement of MSI technology has enabled the use of MSI for single-cell analysis [303].

MSI has been applied in the nanomedicine field to evaluate the efficient delivery of drugs to the target site [304]. For example, Gu et al. used MSI to detect lapatinib (Lap) released from GFLG-DP/Lap nanoparticles (polymer-dendron conjugate that incorporated the pyropheophorbide-a (PPa) photosensitizer for ROS therapy and Lap for molecular targeted therapy linked with the cathepsin B cleavable peptide GFLG) in 4 T1 tumor cell spheroids [305]. After 12 h of treatment, the authors observed Lap accumulation within the tumor spheroid to a much greater extent than DP/Lap nanoparticles lacking an enzyme-responsive linker used as control.

Subcellular analysis by MSI remains under development, as reaching organelle-level analysis requires improved resolution. As an alternative analytical approach, ***secondary-ion mass spectrometry (SIMS)*** can carry out imaging at subcellular resolutions (300 nm and 50 nm for nanoSIMS). SIMS is based on irradiating the sample with an ion beam interacting with surface molecules to generate a secondary ion beam analyzed by the MS detector. nanoSIMS has been successfully applied to visualize metal-based drugs (platinum-based drugs and metal complexes) to study drug distribution in a biological sample [306]. The inability to recognize specific molecules and organelles represents a significant limitation of nanoSIMS, which makes the use of SIMS-compatible probes a necessary step [307].

SIMS provides improved spatial resolution compared to other MSI techniques at the expense of sensitivity; therefore, we require multimodal imaging techniques for visualization at the subcellular level and additional effort to evaluate nanomedicine uptake by cell organelles. The progress of MSI technology for subcellular visualization could make this a front-line technique for evaluating mitochondrial targeting in vitro and *in vivo* in future studies.

5. Evaluating Pharmacological Activity with Mitochondria-targeted Nanomedicines

Developing nanomedicines that target mitochondria requires the implementation of techniques that evaluate their impact on the mitochondrial state. Parameters typically evaluated include mitochondrial bioenergetics and OXPHOS, mitochondrial morphology, alterations in protein expression, and mitochondrial metabolism, with alterations to mitochondrial bioenergetics and OXPHOS the most commonly analyzed parameters to evaluate the impact of mitochondrially-targeted nanomedicines. Said alterations include mitochondrial respiration features

(e.g., analysis of oxygen generation and consumption, ROS species, and ATP synthesis) [308,309] and mitochondrial membrane potential (as a consequence of impaired mitochondrial respiration) [310]. Mitochondrial morphology [311], protein expression [312], and mitochondrial metabolism represent less-often analyzed parameters for the evaluation of mitochondrial damage; however, the evaluation of said parameters contributes to our understanding of a given nanomedicine's mechanism of action, especially mitochondrial metabolism (strongly associated with mitochondrial respiration) (Table 3).

5.1. Mitochondria bioenergetics and OXPHOS

Mitochondrial bioenergetics includes those processes that contribute to cell homeostasis. While OXPHOS represents the primary bioenergetic function, mitochondria participate in other processes, including calcium transport and the urea cycle [308]. Here, we present the techniques employed for the evaluation of mitochondrial bioenergetics via mitochondrial membrane potential and respiration after treatment with mitochondrially-targeted nanomedicines.

5.1.1. Mitochondrial respiration

Mitochondrial respiration involves OXPHOS and the electron transport chain (ETC) to generate ATP as a cell energy source. NADH and $FADH_2$ generated in the TCA cycle are used by Complex I and Complex II, respectively, to start OXPHOS with the leakage and transport of electrons in the ETC. During this process, oxygen forms ROS in the IMM by complexes I, II, and III. The superoxide anion (O_2^-) is the primary ROS in mitochondria, which can react with protons to form hydroxide peroxide (H_2O_2) or hydroxyl radicals (OH^-) [313]. Elevated levels of ROS can induce mitochondrial damage and cell death [309]; therefore, evaluating ROS levels can indicate the mitochondrial respiration state and cell health.

ROS can be detected by staining with different dyes (singlet oxygen sensor - SOSG -, 2′,7′-dichlorofluorescein diacetate - DCFH-DA -) and using various analytical techniques (CLSM, flow cytometry, fluorescence spectroscopy). Zhang et al. detected increased ROS levels in tumor cells isolated from H22 tumor-bearing nude mice after intravenous injection of CS/TPP-PEG-ss-PLA (Section 3.3.1.2) [201]. After 24 h of treatment, the authors employed CLSM to assess fluorescence emission after intravenous injection of DCFH-DA into mice. They reported significantly higher fluorescence levels from DCFH-DA in tumors treated with CS/TPP-PEG-ss-PLA compared to nanoparticles lacking TPP and TPP-PEG-ss-PLA nanoparticles lacking the CS coating, which indicated mitochondrial damage as a consequence of mitochondrial membrane permeabilization.

Assessing **ATP** levels in cells following exposure to therapeutic agents can provide information regarding energy production efficiency in mitochondria and mitochondrial activity. Zhang et al. assessed ATP production in brain homogenates from an MCAO mouse model of ischemic stroke to evaluate the mitochondrial function after SPNP treatment (Section 3.3.1.3) [204]. The authors used an ATP content detection kit and reported restored ATP production (higher than the positive control) and thus enhanced mitochondrial function after SPNP treatment. Overall, these findings indicated the recovery of normal energy metabolism in the ischemic brain.

Mitochondrial respiration can also be evaluated by measuring the **oxygen consumption rate (OCR)** in cells or isolated mitochondria (reflecting OXPHOS activity) using cell respirometers such as the Oroboros O2K (Oroboros Instruments, Austria) or the Seahorse XF Analyzer (Agilent, United States) [314]. The Oroboros O2K cell respirometer employs electrodes to measure the OCR in cell suspensions, tissues, or isolated mitochondria in a closed-chamber device [315]. The Seahorse XF Analyzer is a metabolic assay platform that measures changes in oxygen, pH, and metabolism-related analytes in real-time in the media of intact cells, depending on the analysis kit used. The Agilent Seahorse XF Cell Mito Stress Test Kit measures the oxygen consumption and extracellular acidification rates (ECAR) in live cells and tissues in a 96-well plate, providing information regarding OXPHOS and glycolytic flux [316]. Although multiple studies have employed the Oroboros O2K respirometer and the Seahorse XF Analyzer to measure mitochondrial bioenergetics, only a few have applied said analytical platforms to explore the in vitro impact of nanomedicines on mitochondria [317,318]. We believe that OCR measurements could provide robust data regarding mitochondrial bioenergetics though relatively straightforward experiments and could, therefore, find use during future *in vivo* studies of mitochondrial-targeted nanomedicines.

A good example of the utility of this technique were reported by Kang et al. designed a "cell-penetrating artificial mitochondria-targeting peptide" (CAMP) to specifically deliver the antioxidant protein human metallothionein 1A (hMT1A) to mitochondria to alleviate mitochondrial damage in Parkinson's disease models [317]. CAMP-conjugated hMT1A successfully localized to SH-SY5Y neuronal cell mitochondria and restored mitochondrial function. The authors applied the Oroboros O2K respirometer to measure the OCR in isolated mitochondria after treatment to demonstrate the non-cytotoxic effect of CAMP-conjugated hMT1A (OCR levels did not change after treatment). Encouragingly, subsequent *in vivo* experiments revealed that CAMP-hMT1A injection into the brain of Parkinson's disease model mice prompted the recovery of lost motor function.

Mitochondrial respiration can be assessed by evaluating ROS and ATP levels and oxygen consumption of cells. Preferred methods include ROS staining, ATP, and ROS quantification by commercially available kits due to their cost-effectiveness and straightforward procedures. Other available technologies, such as the Seahorse XF Analyzer and the Oroboros O2K respirometer, to measure cell oxygen consumption provide reliable information on mitochondria respiration; however, these approaches remain less commonly employed due to the requirement of specialized equipment.

5.1.2. Mitochondria membrane potential

Mitochondrial membrane potential (MMP) is the electrical potential generated within mitochondria due to electron transport and the proton gradient generated in the IMM during OXPHOS [319]. Elevated levels of ROS prompt mitochondrial depolarization; hence, the loss of mitochondrial membrane potential associates with mitochondrial damage and often precedes cell death [310]. Consequently, mitochondrial membrane potential indicates mitochondrial respiration and the global status of mitochondria; therefore, assessing mitochondrial membrane potential can also reveal the impact of mitochondrial-targeted nanomedicines. For example, Zhang et al. demonstrated mitochondrial membrane depolarization in vitro and *in vivo* after treatment with CS/TPP-PEG-ss-PLA in hepatocellular carcinoma models (Section 3.3.1.2) by measuring the MMP [201]. The authors employed the JC-1 dye to quantify the MMP by flow cytometry and CLSM in this case. A related study employed TMRM staining of tumor tissue to observe the previously described mitochondrial depolarization in the cancer cells of a DOX-resistant OS-RC-2 tumor-bearing mouse model treated with rTPA-MITO-Porter after PDT (Section 3.3.2.1) [213]. CLSM-mediated visualization revealed decreased TMRM fluorescence intensity in treated tumors, indicating mitochondrial depolarization and photosensitizer delivery to the mitochondria.

Overall, evaluating changes in the mitochondrial membrane potential of cells can use mitochondrial membrane staining dyes and fluorescent microscopes or spectrofluorometers, CLSM, and flow cytometry. The relative simplicity of the mitochondrial membrane potential evaluation assay makes this approach a common strategy when assessing mitochondrial damage after treatment with mitochondrial-targeting nanomedicines.

Table 3
Summary of the techniques employed in mitochondrially-targeted nanomedicine studies for the evaluation of targeting and alterations, including their strengths and limitations and providing relevant studies applying the techniques.

Technique	Type of analysis	Strengths	Limitations	Application in relevant studies
TEM	Mitochondrial targeting Morphological alterations	Ultrastructure visualization Detects the number and shape of nanoparticles and aggregates Improves contrast through metal staining Modified TEM methods (immune-TEM, EFTEM) overcome poor contrast	Need for electron-dense components Poor contrast for biological systems Sensitivity of biological samples to irradiation Need for thin slices Incompatibility with live sample analysis Sample preparation impacts sample integrity Incompatible with 3D imaging Destructive technique	[161,245]
CLSM	Mitochondrial targeting Morphological alterations MMP ROS levels	Simple sample preparation and analysis Compatible with 3D live imaging Detects spectral changes of a fluorescent dye (FRET and BRET phenomena) Localizes fluorescent molecules within biological samples Non-destructive technique	Poor ultrastructure definition Unable to detect the exact number of internalized nanoparticles Laborious identification of structural changes	[201,203,252]
Fluorescence spectroscopy	Mitochondrial targeting ROS levels ATP levels MMP	Cost-effective technique Straightforward and rapid analysis Highly selective and sensitive Non-destructive technique	Mitochondria isolation required to assess mitochondrial targeting Introduction of artifacts when using fluorophores Susceptibility to autofluorescence Environmental sensitivity	[204]
Western Blotting	Mitochondrial targeting Mitochondrial protein expression	Widely available method Selectivity for the desired protein	Mitochondria isolation required to assess mitochondrial targeting Mitochondrial targeting can only be assessed for protein cargo Laborious and time-consuming Destructive technique	[252]
HPLC-UV	Mitochondrial targeting	Precise and reproducible quantitative analysis Rapid and automated analysis Non-destructive technique	Expertise required Expensive equipment Mitochondria isolation required to assess mitochondrial targeting	[216]
ESI-MS	Mitochondria targeting	Soft ionization Rapid and automated analysis Multiple charging provides *m/z* accuracy No matrix interferences	Complexity of the MS spectra Expertise required Expensive equipment Mitochondria isolation required to assess mitochondrial targeting Destructive technique	[295]
ICP-MS	Mitochondria targeting	Sensitive Multi-element analysis Low sample volume needed High throughput	Detection not always possible (should have an ionization potential below argon) Mitochondria isolation required to assess mitochondrial targeting Expensive equipment Destructive technique Matrix interferences	[361]
Flow cytometry	ROS levels ATP levels MMP	Individual cell analysis Exclusion of unclear signals Non-destructive technique	Dyes required Requires initial visual evaluation Slow analysis Expertise required Expensive technique	[201]

(*continued on next page*)

Table 3 (*continued*)

Technique	Type of analysis	Strengths	Limitations	Application in relevant studies
Seahorse XF Analyzer	Mitochondrial respiration Metabolic alterations	Mitochondrial integrity Reliable intracellular context Mitochondrial respiration (OCR) and glycolysis (ECAR) information obtained simultaneously No need to isolate mitochondria (although possible) Assessment of metabolic alterations using specific kits Tissue measurements possible Non-destructive technique	Cell culture conditions and confluence influence results Requires specific and expensive materials/reagents Laborious protocol and slow measurement Normalization to cell number required	[209]
Oroboros O2K	Mitochondrial respiration ROS levels ATP levels Calcium retention	Possibility to design experimental conditions (e.g., temperature, substrate availability) No need to isolate mitochondria (although possible) Tissue measurements possible Cost-effective assays High-resolution Tandem fluorescence attachments	Labor intensive protocols Expensive equipment Careful maintenance of equipment required Low throughput	[317]

5.2. Mitochondrial morphology

Mitochondrial morphology dynamically changes due to fusion and fission processes, which strongly associate with bioenergetics and function and respond to the energetic demand and alterations in metabolic flux [311,320]. Therefore, a wide range of mitochondrial morphologies can be observed - from small spheres with short tubules to more oval shapes with long tubules - depending on the cell type and the metabolic and energetic state. For example, mitochondria present as interconnected tubular networks in endothelial cells, long filaments in fibroblasts, and uniform spheres in hepatocytes [321]. Meanwhile, mitochondrial fragmentation has been described as characteristic of proliferative cancer cells and associated with fission processes [311]; therefore, visualization of mitochondrial morphology may provide valuable information regarding mitochondrial health and may indicate mitochondrial damage caused by therapeutic activity. TEM and CLSM represent commonly used tools in the study of morphological changes in mitochondria in live cells. Due to the poor ultrastructure definition provided by CLSM imaging, visualization of mitochondria and identification of structural changes by CLSM can represent a laborious task; fortunately, Chu et al. summarized the tools available for automatic/semiautomatic analysis of CLSM images to analyze mitochondrial dynamics and morphology in cells [311], including software and algorithms such as MitoGraph [322] and Cell Profiler [323].

Mitochondrial morphology has been evaluated to assess mitochondrial-targeted nanomedicines in vitro and *in vivo*. Yang et al. evaluated the morphological changes of mitochondria by TEM in renal cortices of diabetic mice to evaluate the ability of the mitochondrial-targeted peptide SS-31 to protect diabetic mice against renal tubulointerstitial injury [324]. The authors reported the enlargement of mitochondria and swelling of cristae in renal tubular cells of untreated mice; treatment with SS-31 partially inhibited this effect, contributing to the hypothesis confirmation that SS-31 had a protective effect on diabetes-induced renal tubulointerstitial injury. In a similar study, Liu and colleagues employed TEM to demonstrate how SC-TK-SS-31 treatment in AKI model mice (Section 3.3.4) decreased the number of damaged mitochondria (swollen with loss of cristae) and increased the number of elongated mitochondria [245]. These data support that SC-TK-SS-31 treatment as a means to inhibit mitochondrial damage and alleviate AKI.

Although mitochondrial morphology constantly changes according to cell state, evaluation of structural changes in mitochondria of cells treated with mitochondrial-targeting nanomedicines by comparing TEM or CSLM images of treated cells to images of untreated cells can provide helpful information regarding the mitochondrial response to treatment. Moreover, the development of algorithms and software has facilitated the visualization and classification of distinct mitochondrial morphologies, which could aid in the evaluation of mitochondrial-targeting nanomedicines.

5.3. Alterations in mitochondrial protein expression

Mitochondrial proteins, the vast majority synthesized in the cytosol and transported to the mitochondria by protein translocases [325], play roles in respiration, metabolite transport, protein translocation, and membrane interaction [312]. Evaluating the expression of mitochondrial proteins can serve as an indicator of mitochondrial damage and help the understanding of the effect of mitochondrial-targeting treatments on mitochondria. For example, assessing enzymes involved in OXPHOS can provide crucial information regarding mitochondrial respiration deficiency [346]. In this context, Cyt-C (intimately involved in electron transport) becomes released from mitochondria and translocated to the cytosol to trigger apoptosis [326]; therefore, evaluation of Cyt-C expression in the mitochondria and the cytosol of treated cells would reveal information regarding mitochondrial damage and the cell death mechanism. Zou et al. designed a promising treatment for brain

tumors using the OXPHOS inhibitor Gboxin loaded within ROS-responsive polymeric nanoparticles and coated with a cancer-cell mitochondria hybrid membrane (HM-NPs@G) [252]. This therapeutic strategy demonstrated biocompatibility, blood–brain barrier permeability, and dual tumor and mitochondrial targeting in vitro and in glioblastoma xenografts. The authors demonstrated triggered apoptosis and, thus, the antitumor activity of HM-NPs@G by evaluating Cyt-C and apoptosis-related protein expression through ***Western blotting***. Both in vitro and *in vivo* results revealed the upregulated expression of Cyt-C and apoptosis-related proteins after HM-NPs@G treatment compared to free Gboxin and single membrane-coated nanoparticles, demonstrating how mitochondria-mediated apoptosis prompts tumor inhibition.

In addition to immunoblotting, ***MS-proteomic analysis*** may reveal changes to the mitochondrial proteome. While not yet applied for the specific study of the impact of nanomedicines on the mitochondrial proteome, proteomic analysis represents a potentially robust strategy to evaluate mitochondrial alterations. Umbrasas et al. evaluated the effect of NOC-18 (an NO donor) on the mitochondrial proteins of rat hearts with ischemia, as a previous report noted that NOC-18 reduced ischemic injury in mitochondria [327]. The authors analyzed extracted proteins by liquid chromatography (LC)-MS; the differentially expressed proteins included phosphorylated proteins involved in the NO/protein kinase G/mitochondrial permeability transition pore (NO/PKG/mPTP) pathway, which are responsible for the positive effects of NO regarding the prevention of ischemic injury in mitochondria.

The evaluation of protein alterations in mitochondria can be assessed by detecting and quantifying specific proteins described as altered in mitochondrial-related processes (e.g., apoptosis) by Western blotting or by broader proteomic analyses that can detect hundreds of proteins and their modifications. Both techniques can provide helpful information regarding the mechanism of action of the mitochondrial-targeting treatment and their triggered effects on mitochondria.

5.4. Promising tools to evaluate mitochondria metabolism

Metabolic pathways involving the mitochondria, such as the TCA cycle or OXPHOS for ATP production, remain central to maintaining cell functioning; therefore, assessing mitochondrial metabolism may provide critical information regarding the metabolic rewiring in the mitochondria of diseased cells. Analysis of mitochondrial metabolism in cells treated with mitochondrially-targeted nanomedicines could provide information on how treatments affect the metabolic routes, which could help to understand their mechanism of action. Despite the relevance of metabolism to mitochondria, we lack studies on the impact of mitochondrial-targeting nanomedicines; instead, this section describes the tools employed to evaluate the mitochondrial metabolism of treated cells or mitochondria isolated from treated cells.

5.4.1. Metabolic assays

As described in the previous section for ATP and ROS, commercial kits based on ***colorimetric/fluorometric assays*** detect specific metabolites in mitochondria. Intermediates of the TCA cycle [328] (citrate, α-ketoglutarate, succinate, fumarate, malate, and 2-hydroxyglutarate), substrates of the TCA cycle (acetyl-CoA [329], glutamine [330]/glutamate [331], methionine [332], aspartate [333], phenylalanine, and tyrosine [334]), and the dinucleotides involved in OXPHOS (NAD^+/NADH [335] or FAD [336]) can be detected and quantified in isolated mitochondria of cells treated with mitochondrial-targeting nanomedicines.

An alternative approach involves the ***Seahorse XF Analyzer***, which, other than measuring oxygen and pH, also measures metabolite levels in intact live cells. Complementary kits applied using this technology measure alterations in primary mitochondrial substrates: glucose/pyruvate (Seahorse XF Glucose/Pyruvate Oxidation Stress Test Kit), long chain fatty acids (The Agilent Seahorse XF Substrate Oxidation Stress Test Kit and Agilent Seahorse XF Palmitate Oxidation Stress Test Kit), and glutamine (Seahorse XF Glutamine Oxidation Stress Test Kit) [337]. Similarly, the Seahorse XF Mito Fuel Flex Test Kit explains how glucose, glutamine, and fatty acid oxidation fuel mitochondrial function [338]. The Seahorse XF Glycolytic Rate Assay Kit also evaluates glycolysis and provides information regarding acetyl-CoA generation for the TCA cycle [339].

Very few studies have used metabolic assays to evaluate nanomedicines [330,331], and, to the best of our knowledge, no study of metabolic changes has employed the Seahorse XF Analyzer. Alterations to mitochondrial metabolism remain relatively unexplored in studies of nanomedicines targeting mitochondria, with more straightforward evaluations of mitochondrial damage, such as mitochondrial depolarization, preferred; however, we believe that assessment of the mitochondrial metabolism can provide helpful information regarding how much damage has been caused by treatments and how mitochondria can respond and compensate for its disruption by altering metabolic flux.

5.4.2. Metabolomics

Metabolomics encompasses the study of substrates, intermediates, and end-products of metabolic routes, thereby providing an alternative means of studying mitochondrial metabolism in cells or tissues treated with mitochondrial-targeting nanomedicines. Nuclear magnetic resonance (NMR) and MS represent the two main instruments used for metabolomic studies [340], with diverse types of biological samples available for analysis, including biofluids [341], cell extracts [342], tissues [343], and isolated organelles such as mitochondria [344].

Although studies on ***mitochondria metabolomics*** have been previously reported [344], we currently lack any published research that describes the impact of mitochondrial-targeting nanomedicines. Mitochondria from treated cells or tissues must be isolated using an optimized method before metabolite extraction. The Folch extraction method, based on using a chloroform/methanol/water mixture to extract hydrophilic and hydrophobic metabolites, represents the most used technique before NMR and MS metabolomics [345]. The analysis of the resulting data will provide information regarding metabolites that undergo an increase or decrease and, therefore, what metabolic pathways become affected after treatment with mitochondria-targeting nanomedicines. Assorted studies have performed NMR-based metabolomic studies of isolated mitochondria in mouse brains [346], mouse quadriceps [347], and in HCT116 cells [348]; meanwhile, MS-based mitochondrial metabolomic studies have employed various cell [349–352] and tissue samples [353,354].

NMR and MS ***metabolomic analyses*** can be performed ***in whole cells***, as Awashra et al. reported in their review of metabolomic analysis to assess nanoparticle cytotoxicity [355]. Yaşacan et al. used MS metabolomics to assess the effect of L-carnitine-loaded liposomes (lipo-carnitine) and L-carnitine HCl–loaded PLGA nanoparticles (nano-carnitine) on the metabolism of cardiac fibroblasts [356]. In general, both formulations caused alterations in amino acid, carbohydrate, and lipid metabolism; however, nano-carnitine increased TCA cycle intermediates, which the authors did not observe in cells treated with lipo-carnitine and indicated mitochondrial deregulation. Analysis of whole-cell samples for the evaluation of mitochondrial-targeting nanomedicines should focus on those metabolites involved in mitochondria metabolism; however, the analysis of isolated mitochondria may provide more specific information regarding mitochondrial metabolism.

5.4.3. Fluxomics

Both NMR and MS offer additional options to evaluate mitochondria metabolism. ***Fluxomics*** enables the analysis of intracellular fluxes in the metabolic pathways using isotopically labeled metabolites to provide the "big picture" of metabolic dynamics [357]. In this context, studying the impact of mitochondrially-targeted nanomedicines on mitochondrial metabolism by fluxomics should focus on labeling metabolites of the mitochondrial metabolic pathways. Interestingly, recent studies have performed fluxomics in isolated mitochondria, which provided specific

information regarding mitochondrial metabolic dynamics [358,359]. Gowda et al. isolated mitochondria from mouse skeletal myoblast cells and monitored mitochondrial metabolism by adding ^{13}C-labelled pyruvate as a tracer substrate to the isolated mitochondria [359]. Incubation of the isolated mitochondria with inhibitors of mitochondrial respiration (carbonyl cyanide-p-trifluoromethoxyphenylhydrazone (FCCP) and rotenone) led to a decrease in ^{13}C-acetyl-coenzyme A levels (the primary precursor of the TCA cycle), suggesting the slowdown of pyruvate conversion, due to the decreased mitochondrial demand.

An alternative method for fluxomics in isolated mitochondria comprises selectively permeabilizing the cytosolic membrane to wash away cytosolic components, adding ^{13}C-labelled metabolites, extracting the mitochondrial metabolites, and analyzing the mitochondrial labeled metabolites by MS [360]. Nonnenmacher et al. demonstrated the effectiveness of the described method by incubating A595 cells with ^{13}C-pyruvate and ^{13}C-glutamine to evaluate all the metabolic pathways occurring in mitochondria.

Although metabolomics and fluxomics have not yet been used to study mitochondria-targeted nanomedicine in cells/tissues, we believe these techniques can become promising tools for the evaluation of the impact of nanomedicines on mitochondrial metabolism.

Evaluating the impact of mitochondrially-targeted nanomedicines remains crucial for several elements related to the treatment of various diseases and disorders, such as ensuring treatment effectiveness and understanding the mechanism of action of the designed nanomedicine. This section describes potential strategies to evaluate mitochondrial alterations by evaluating distinct mitochondrial features. We believe that complementing distinct evaluation strategies will provide a more comprehensive understanding of a given nanomedicine's mechanism of action. Moreover, we encourage researchers to take advantage of the available tools for mitochondrial metabolism evaluation, which provide reliable information on the mitochondria metabolic response to treatment.

6. Conclusion and Future Challenges

At the global forefront of personalized medicine, the subcellular targeting of nanomedicines may gain an efficient and multifaceted means of providing precision treatment. By targeting subcellular compartments where disease-related processes develop, nanomedicine can offer higher efficacy, monitoring capabilities, and an enhanced overall safety profile of a given therapeutic.

Over the past decade, the surge in published research proposing innovative mitochondria-specific materials, therapeutics, and targeting agents underscores the increasing potential of mitochondrially-targeted nanomedicines in addressing pathologies associated with these energy-producing subcellular organelles. However, despite these advancements, substantial hurdles and issues persist. First and foremost, the design of mitochondria-targeting nanomedicines must carefully consider physicochemical features such as size, shape, net surface charge, and stiffness. These factors play a crucial role in effective tissue accumulation and specific cell trafficking, ultimately leading to mitochondria accumulation. Conducting a comprehensive physicochemical characterization is essential for exploring structure–activity relationships, directly influencing the ultimate biological fate. Secondly, achieving an efficient pharmacokinetic profile after *in vivo* administration is paramount. Unfortunately, many published studies have encountered challenges in translating promising in vitro results into preclinical models, impeding the successful translation of mitochondrially-targeted nanomedicines. In this context, our efforts aim to systematically outline the biological barriers that mitochondrially-targeted nanomedicines encounter after systemic administration. Our goal is to contribute to a better understanding that facilitates the rational design of efficient mitochondria-targeted nanomedicines.

Rational design involves selecting biosafe materials that exhibit biodegradability and biocompatibility while lacking immunogenicity [90,362]. This consideration is particularly crucial for diseases that are chronic and require prolonged treatment. Recent advancements in polymeric and lipid-based systems have shown success *in vivo*, underscoring the need for a standardized evaluation criteria and established techniques to verify the biosafety of mitochondrially targeted nanomedicines. Addressing this lack of uniformity poses a significant challenge for all applied nanomaterials. Therefore, forthcoming studies must prioritize confirming *in vivo* biodegradation and biocompatibility of nanomedicines to mitigate the risk of potential toxicity[363].

While numerous surface modifications can enhance blood circulation times and facilitate efficient intracellular/subcellular delivery, it is essential to emphasize the importance of developing materials with reduced complexity. This approach aims at enabling cost-efficient manufacturing and scaling up processes, thereby facilitating the clinical translation of mitochondrially-targeted nanomedicines. To date, the majority of developed mitochondrially-targeted nanomedicines have primarily focused on cancer treatment. This emphasis is due to inherent properties, including the ability to reduce off-target effects in healthy tissues, overcome multi-drug resistance, the increased availability of mitochondrial biomarkers in cancer cells, and the application of mitochondria-targeting moieties such as DLCs with intrinsic anti-cancer activity. Among these moieties, triphenylphosphonium (TPP) stands out as one of the most explored and advanced mitochondria-targeting ligands for anticancer purposes. Numerous successful examples exist *in vivo*, showcasing TPP-drug conjugates, drug delivery systems (e.g., micelles, liposomes, polymeric nanoparticles, and dendrimers), and derivatives in clinical trials. Notably, SkQ1 (plastoquinone-TPP; Visomitin®) has received approval for the treatment of eye disease in Russia [149], demonstrating the capability of such systems to attain favorable pharmacological properties with a desired therapeutic window through rational design. It's important to note that this poses a significant challenge when applying mitochondria-targeted nanomedicines to diseases other than cancer, particularly when using mitochondrial penetrating peptides (MPPs).

Indeed, the development of mitochondrially-targeted nanomedicine in applications related to neurodegeneration, cardiovascular diseases, and mitochondria-genetic disorders faces challenges, primarily stemming from toxicological concerns associated with the cationic nature of most identified target moieties. To advance in these areas, there is a critical need to identify novel mitochondria-targeting ligands that are non-toxic, breaking away from the reliance on passive accumulation driven by the highly negative mitochondria membrane potential (an attribute particularly pronounced in cancer). Active targeting strategies should focus on unique mitochondrial molecules (e.g., cardiolipin expression) or properties (e.g., differential pH within mitochondria membranes).

Achieving effective active targeting to mitochondria will also pave the way for the further development of controllable site-specific drug release strategies within specific mitochondrial compartments, such as the outer mitochondrial membrane (OMM), inner mitochondrial membrane (IMM), or the mitochondrial matrix. This can be achieved by gaining a deeper understanding of the mitochondria environment and incorporating mitochondria-specific responsive elements into engineered nanomaterials. For instance, stimuli-driven disassembly of nanomedicines modified with mitochondrial penetrating peptides (MPPs) or cell-penetrating peptides (CPPs) can provide stability upon targeted cell arrival and mitochondrial localization. Subsequently, fine-tuning the release kinetics of the carried drug/bioactive agent at the mitochondria level through responsive systems, such as those activated by reactive oxygen species (ROS) or temperature, could significantly enhance the selectivity and effectiveness of therapeutic outcomes [121,176]. This approach represents a promising avenue for achieving precise and controlled drug delivery within mitochondria for improved therapeutic efficacy.

In addition to rational design, the validation of the mitochondria-targeting capabilities for a given nanomedicine requires the

application of multiple complementary physico-chemical techniques to evaluate the effectiveness of organelle targeting and monitor the molecular events that occur in mitochondria after treatment, ideally in a complex physiological milieu. Transmission Electron Microscopy (TEM) and Confocal Laser Scanning Microscopy (CLSM) are commonly used techniques for validating mitochondria drug delivery designs due to their ease of sample preparation and equipment availability. CLSM, particularly when co-localized with fluorescently labeled organelles, is widely used for its fluorescence visualization of nanomedicine in targeted cell locations. While alternatives to CLSM are under evaluation to overcome limitations related to visualizing one single plane at a time and the exclusive dependence on fluorescently labeled molecules, the development of super-resolution technology represents a significant advance in fluorescent imaging, offering enhanced insights into drug delivery to mitochondria [298]. TEM supports the study of electron-dense nanomedicines, providing ideal morphological features. Combining CLSM and TEM using innovative techniques such as correlative light electron microscopy (CLEM) is highly recommended, especially for nanomedicines lacking electron-dense components, as it minimizes the drawbacks of each technique. However, for organic-based nanomedicines, the complexity of TEM and the additional steps involved in mitochondria isolation make them less commonly employed techniques. In this context, NanoSIMS, a cutting-edge mass spectrometry imaging technique, has shown high spatial resolution capacity up to a subcellular organelle level (50–150 nm) [364]. NanoSIMS presents an opportunity to produce subcellular maps of metabolic turnover with extreme sensitivity, serving as a potential tool for analyzing the combination of mitochondria visualization and nanomedicine quantification [365].

After internalization by mitochondria, common pharmacological impacts include alterations in mitochondrial respiration and membrane potential. To directly assess mitochondrially-associated molecular events, advances in the field have been fostered by cell respirometers such as the Seahorse XF Analyzer. This critical tool measures oxygen, pH, and metabolite levels in real-time in the media of intact cells. However, for a comprehensive evaluation of mitochondria-targeted nanomedicines, additional tools are needed to assess events beyond respiration, such as metabolism or the activation of crucial signaling cascades. Ever-developing tools like metabolomics and proteomics can enhance our understanding of a given nanomedicine's mechanism of action. Machine-learning methods hold the potential to develop robust and accurate methods for measuring mitochondrial morphology, depolarization, or other events [366], contributing to the quantitative evaluation of nanomedicine therapeutic activity and disease evolution [367].

The current advancements in mitochondrially-targeted nanomedicines underscore their potential to revolutionize cancer treatment and address various common pathologies associated with mitochondrial damage or dysfunction. The ongoing progress in efficient mitochondrially-targeted nanomedicines is expected to drive subsequent breakthroughs, supporting the development of safe, exquisitely tailored, and personalized therapies.

7. Funding sources

The authors would like to thank BIOMOLMACS, a European project funded by the European Union's Horizon 2020 research and innovation program under the Marie Skłodowska-Curie grant agreement n° 859416, the European Research Council Grant ERC-PoC-2022–101069391 (Polybraint), La Caixa Health Foundation NanoPanTher Project (LCF/PR/HR19/52160021), and the NanoGBA Project (HR22-00602). The Spanish Ministry of Economy and competitiveness (PID2019-108806RB-I00; I.D.-O. is supported by an FPU grant (FPU19/03729)) and NextGenerationEU funds Pol@Mets (MFA/2022/065), AECC (I.C.S. is funded by AEEC Junior Grant Ref INVES211323CONE) and the European Regional Development Fund (FEDER) (PO FEDER Comunitat Valenciana 2014–2020) are acknowledged for financial support.

Declaration of competing interest

The authors declare that they have no known competing financial interests or personal relationships that could have appeared to influence the work reported in this paper.

Data availability

No data was used for the research described in the article.

Acknowledgements

The authors acknowledge Stuart P. Atkinson for critical English editing and the use of Biorender.com in the Graphical abstracts and Figs. 1 and 2.

References

[1] Z. Li, J. Zou, X. Chen, In response to precision medicine: Current subcellular targeting strategies for cancer therapy, Adv. Mater. 35 (2023) 1–31, https://doi.org/10.1002/adma.202209529.
[2] O.K. Nag, J.B. Delehanty, Active cellular and subcellular targeting of nanoparticles for drug delivery, Pharmaceutics. 11 (2019) 7–9, https://doi.org/10.3390/pharmaceutics11100543.
[3] Z. Tang, W. Tian, H. Long, S. Jiang, J. Zhao, J. Zhou, Q. He, X. Luo, Subcellular-targeted near-infrared-responsive nanomedicine with synergistic chemo-photothermal therapy against multidrug resistant cancer, Mol. Pharm. 19 (2022) 4538–4551, https://doi.org/10.1021/acs.molpharmaceut.1c00998.
[4] W. Chen, G. Luo, X. Zhang, Recent Advances in Subcellular Targeted Cancer Therapy Based on Functional Materials, Adv. Mat. 1802725 (2019) 1–39, https://doi.org/10.1002/adma.201802725.
[5] X. Shao, C. Meng, W. Song, T. Zhang, Q. Chen, Subcellular visualization: Organelle-specific targeted drug delivery and discovery, Adv. Drug Deliv. Rev. 199 (2023) 114977, https://doi.org/10.1016/j.addr.2023.114977.
[6] O.S. Thomas, W. Weber, Overcoming physiological barriers to nanoparticle delivery —, Are We There yet ? 7 (2019) https://doi.org/10.3389/fbioe.2019.00415.
[7] N. Veiga, Y. Diesendruck, D. Peer, Targeted nanomedicine: Lessons learned and future directions, J. Control. Release. 355 (2023) 446–457, https://doi.org/10.1016/j.jconrel.2023.02.010.
[8] S. Javadov, A.V. Kozlov, A.K.S. Camara, Mitochondria in Health and Diseases, Cells. 9 (2020), https://doi.org/10.3390/cells9051177.
[9] Y. Chezy Barenholz, Doxil® — The first FDA-approved nano-drug: Lessons learned, J. Control. Release. 160 (2012) 117–134, https://doi.org/10.1016/j.jconrel.2012.03.020.
[10] L.R. Baden, H.M. El Sahly, B. Essink, K. Kotloff, S. Frey, R. Novak, D. Diemert, S. A. Spector, N. Rouphael, C.B. Creech, J. McGettigan, S. Khetan, N. Segall, J. Solis, A. Brosz, C. Fierro, H. Schwartz, K. Neuzil, L. Corey, P. Gilbert, H. Janes, D. Follmann, M. Marovich, J. Mascola, L. Polakowski, J. Ledgerwood, B. S. Graham, H. Bennett, R. Pajon, C. Knightly, B. Leav, W. Deng, H. Zhou, S. Han, M. Ivarsson, J. Miller, T. Zaks, Efficacy and Safety of the mRNA-1273 SARS-CoV-2 Vaccine, N. Engl. J. Med. 384 (2021) 403–416, https://doi.org/10.1056/nejmoa2035389.
[11] M.A. Subhan, S.S.K. Yalamarty, N. Filipczak, F. Parveen, V.P. Torchilin, Recent advances in tumor targeting via epr effect for cancer treatment, J. Pers. Med. 11 (2021), https://doi.org/10.3390/jpm11060571.
[12] E.A. Azzopardi, E.L. Ferguson, D.W. Thomas, The enhanced permeability retention effect: A new paradigm for drug targeting in infection, J. Antimicrob. Chemother. 68 (2013) 257–274, https://doi.org/10.1093/jac/dks379.
[13] R.P. Prajnamitra, H.C. Chen, C.J. Lin, L.L. Chen, P.C.H. Hsieh, Nanotechnology approaches in tackling cardiovascular diseases, Molecules 24 (2019), https://doi.org/10.3390/molecules24102017.
[14] A. Nel, E. Ruoslahti, H. Meng, New insights into "permeability" as in the enhanced permeability and retention effect of cancer nanotherapeutics, ACS Nano 11 (2017) 9567–9569, https://doi.org/10.1021/acsnano.7b07214.
[15] M.B. Ashford, R.M. England, N. Akhtar, Highway to success—developing advanced polymer therapeutics, Adv. Ther. 4 (2021) 2000285, https://doi.org/10.1002/adtp.202000285.
[16] L. Kou, Y.D. Bhutia, Q. Yao, Z. He, J. Sun, V. Ganapathy, Transporter-guided delivery of nanoparticles to improve drug permeation across cellular barriers and drug exposure to selective cell types, Front. Pharmacol. 9 (2018) 1–16, https://doi.org/10.3389/fphar.2018.00027.
[17] S. Wilhelm, A.J. Tavares, Q. Dai, S. Ohta, J. Audet, H.F. Dvorak, W.C.W. Chan, Analysis of nanoparticle delivery to tumours, Nat. Rev. Mat. (2016), https://doi.org/10.1038/natrevmats.2016.14.
[18] Y.H. Choi, H.K. Han, Nanomedicines: current status and future perspectives in aspect of drug delivery and pharmacokinetics, J. Pharm. Investig. 48 (2018) 43–60, https://doi.org/10.1007/s40005-017-0370-4.

[19] M.J. Ernsting, M. Murakami, A. Roy, S.D. Li, Factors controlling the pharmacokinetics, biodistribution and intratumoral penetration of nanoparticles, J. Control. Release. 172 (2013) 782–794, https://doi.org/10.1016/j.jconrel.2013.09.013.

[20] J. Zhao, M.H. Stenzel, Entry of nanoparticles into cells: The importance of nanoparticle properties, Polym. Chem. 9 (2018) 259–272, https://doi.org/10.1039/c7py01603d.

[21] S. Behzadi, V. Serpooshan, W. Tao, M.A. Hamaly, M.Y. Alkawareek, E.C. Dreaden, D. Brown, A.M. Alkilany, O.C. Farokhzad, M. Mahmoudi, Cellular uptake of nanoparticles: Journey inside the cell, Chem. Soc. Rev. 46 (2017) 4218–4244, https://doi.org/10.1039/c6cs00636a.

[22] H.H. Gustafson, D. Holt-Casper, D.W. Grainger, H. Ghandehari, Nanoparticle uptake: The phagocyte problem, Nano Today 10 (2015) 487–510, https://doi.org/10.1016/j.nantod.2015.06.006.

[23] Y. Fang, J. Xue, S. Gao, A. Lu, D. Yang, H. Jiang, Y. He, K. Shi, Cleavable PEGylation: a strategy for overcoming the "PEG dilemma" in efficient drug delivery, Drug Deliv. 24 (2017) 22–32, https://doi.org/10.1080/10717544.2017.1388451.

[24] D.B. Chithrani, Polyethylene glycol density and length affects nanoparticle uptake by cancer cells, J. Nanomedicine Res. 1 (2014), https://doi.org/10.15406/jnmr.2014.01.00006.

[25] J.J.F. Verhoef, T.J. Anchordoquy, Questioning the use of PEGylation for drug delivery, Drug Deliv Transl. Res. 3 (2013) 499–503, https://doi.org/10.1007/s13346-013-0176-5.

[26] M. Estapé Senti, C.A. de Jongh, K. Dijkxhoorn, J.J.F. Verhoef, J. Szebeni, G. Storm, C.E. Hack, R.M. Schiffelers, M.H. Fens, P. Boross, Anti-PEG antibodies compromise the integrity of PEGylated lipid-based nanoparticles via complement, J. Control. Release. 341 (2022) 475–486, https://doi.org/10.1016/j.jconrel.2021.11.042.

[27] D. Shi, D. Beasock, A. Fessler, J. Szebeni, J.Y. Ljubimova, K.A. Afonin, M. A. Dobrovolskaia, To PEGylate or not to PEGylate: Immunological properties of nanomedicine's most popular component, polyethylene glycol and its alternatives, Adv. Drug Deliv. Rev. 180 (2022) 114079, https://doi.org/10.1016/j.addr.2021.114079.

[28] X. Yao, C. Qi, C. Sun, F. Huo, X. Jiang, Poly(ethylene glycol) alternatives in biomedical applications, Nano Today 48 (2023) 101738, https://doi.org/10.1016/j.nantod.2022.101738.

[29] J. Cao, D. Huang, N.A. Peppas, Advanced engineered nanoparticulate platforms to address key biological barriers for delivering chemotherapeutic agents to target sites, Adv. Drug Deliv. Rev. 167 (2020) 170–188, https://doi.org/10.1016/j.addr.2020.06.030.

[30] E. Blanco, H. Shen, M. Ferrari, Principles of nanoparticle design for overcoming biological barriers to drug delivery, Nat. Biotechnol. 33 (2015) 941–951, https://doi.org/10.1038/nbt.3330.

[31] J. Fang, W. Islam, H. Maeda, Exploiting the dynamics of the EPR effect and strategies to improve the therapeutic effects of nanomedicines by using EPR effect enhancers, Adv. Drug Deliv. Rev. 157 (2020) 142–160, https://doi.org/10.1016/j.addr.2020.06.005.

[32] Y. Wang, S.-K. Sun, Y. Liu, Z. Zhang, Advanced hitchhiking nanomaterials for biomedical applications, Theranostics. 13 (2023) 4781–4801, https://doi.org/10.7150/thno.88002.

[33] M.A. Miller, R. Chandra, M.F. Cuccarese, C. Pfirschke, C. Engblom, S. Stapleton, U. Adhikary, R.H. Kohler, J.F. Mohan, M.J. Pittet, R. Weissleder, Radiation therapy primes tumors for nanotherapeutic delivery via macrophage-mediated vascular bursts, Sci. Transl. Med. 9 (2017) eaal0225, https://doi.org/10.1126/scitranslmed.aal0225.

[34] A.M. Sofias, Y.C. Toner, A.E. Meerwaldt, M.M.T. van Leent, G. Soultanidis, M. Elschot, H. Gonai, K. Grendstad, Å. Flobak, U. Neckmann, C. Wolowczyk, E. L. Fisher, T. Reiner, C.de L. Davies, G. Bjørkøy, A.J.P. Teunissen, J. Ochando, C. Pérez-Medina, W.J.M. Mulder, S. Hak, Tumor targeting by αvβ3-integrin-specific lipid nanoparticles occurs via phagocyte hitchhiking, ACS Nano 14 (2020) 7832–7846, https://doi.org/10.1021/acsnano.9b08693.

[35] S. Sindhwani, A.M. Syed, J. Ngai, B.R. Kingston, L. Maiorino, J. Rothschild, P. MacMillan, Y. Zhang, N.U. Rajesh, T. Hoang, J.L.Y. Wu, S. Wilhelm, A. Zilman, S. Gadde, A. Sulaiman, B. Ouyang, Z. Lin, L. Wang, M. Egeblad, W.C.W. Chan, The entry of nanoparticles into solid tumours, Nat. Mater. 19 (2020) 566–575, https://doi.org/10.1038/s41563-019-0566-2.

[36] S. Waheed, Z. Li, F. Zhang, A. Chiarini, U. Armato, J. Wu, Engineering nano-drug biointerface to overcome biological barriers toward precision drug delivery, J. Nanobiotechnology. 20 (2022) 1–25, https://doi.org/10.1186/s12951-022-01605-4.

[37] F. Rodriguez-Otormin, A. Duro-Castano, I. Conejos-Sánchez, M.J. Vicent, Envisioning the future of polymer therapeutics for brain disorders, WIREs Nanomed. Nanobiotechnol. 11 (2019) e1532.

[38] K. Jiang, Y. Yu, W. Qiu, K. Tian, Z. Guo, J. Qian, H. Lu, C. Zhan, Protein corona on brain targeted nanocarriers: Challenges and prospects, Adv. Drug Deliv. Rev. 202 (2023) 115114, https://doi.org/10.1016/j.addr.2023.115114.

[39] M. Nowak, M.E. Helgeson, S. Mitragotri, Delivery of nanoparticles and macromolecules across the blood-brain barrier, Adv. Ther. 3 (2020) 1900073, https://doi.org/10.1002/adtp.201900073.

[40] A. Sumiyoshi, H. Fujii, Y. Okuma, Targeting microbiome, drug metabolism, and drug delivery in oncology, Adv. Drug Deliv. Rev. 199 (2023) 114902, https://doi.org/10.1016/j.addr.2023.114902.

[41] X. Li, C. Lu, Y. Yang, C. Yu, Y. Rao, Site-specific targeted drug delivery systems for the treatment of inflammatory bowel disease, Biomed. Pharmacother. 129 (2020), https://doi.org/10.1016/j.biopha.2020.110486.

[42] T.G. Chu JN, Foundations of gastrointestinal-based drug delivery and future developments., Nat Rev Gastroenterol Hepatol. 19(4):219- (2022).

[43] Y. Xiao, D. Yu, Tumor microenvironment as a therapeutic target in cancer, Pharmacol. Ther. 221 (2021) 107753, https://doi.org/10.1016/j.pharmthera.2020.107753.

[44] E. Van Cutsem, M.A. Tempero, D. Sigal, D.-Y. Oh, N. Fazio, T. Macarulla, E. Hitre, P. Hammel, A.E. Hendifar, S.E. Bates, C.-P. Li, S.R. Hingorani, C. de la Fouchardiere, A. Kasi, V. Heinemann, A. Maraveyas, N. Bahary, L. Layos, V. Sahai, L. Zheng, J. Lacy, J.O. Park, F. Portales, P. Oberstein, W. Wu, D. Chondros, A.J. Bullock, Randomized phase III trial of pegvorhyaluronidase alfa with nab-paclitaxel plus gemcitabine for patients with hyaluronan-high metastatic pancreatic adenocarcinoma, J. Clin. Oncol. 38 (2020) 3185–3194, https://doi.org/10.1200/JCO.20.00590.

[45] S. Duan, F. Sun, P. Qiao, Z. Zhu, M. Geng, X. Gong, Y. Li, H. Yao, Detachable dual-targeting nanoparticles for improving the antitumor effect by extracellular matrix depletion, ACS Biomater. Sci. Eng. 9 (2023) 1437–1449, https://doi.org/10.1021/acsbiomaterials.2c01179.

[46] M.M. Hadi, H. Nesbitt, H. Masood, F. Sciscione, S. Patel, B.S. Ramesh, M. Emberton, J.F. Callan, A. MacRobert, A.P. McHale, N. Nomikou, Investigating the performance of a novel pH and cathepsin B sensitive, stimulus-responsive nanoparticle for optimised sonodynamic therapy in prostate cancer, J. Control. Release. 329 (2021) 76–86, https://doi.org/10.1016/j.jconrel.2020.11.040.

[47] J.J. Arroyo-Crespo, A. Armiñán, D. Charbonnier, L. Balzano-Nogueira, F. Huertas-López, C. Martí, S. Tarazona, J. Forteza, A. Conesa, M.J. Vicent, Tumor microenvironment-targeted poly-L-glutamic acid-based combination conjugate for enhanced triple negative breast cancer treatment, Biomaterials 186 (2018) 8–21, https://doi.org/10.1016/j.biomaterials.2018.09.023.

[48] S. Puri, M. Mazza, G. Roy, R.M. England, L. Zhou, S. Nourian, J. Anand Subramony, Evolution of nanomedicine formulations for targeted delivery and controlled release, Adv. Drug Deliv. Rev. 200 (2023) 114962, https://doi.org/10.1016/j.addr.2023.114962.

[49] M. Tufail, Unlocking the potential of the tumor microenvironment for cancer therapy, Pathol. - Res. Pract. 251 (2023) 154846, https://doi.org/10.1016/j.prp.2023.154846.

[50] B.B. Mendes, D.P. Sousa, J. Conniot, J. Conde, Nanomedicine-based strategies to target and modulate the tumor microenvironment, Trends in Cancer. 7 (2021) 847–862, https://doi.org/10.1016/j.trecan.2021.05.001.

[51] T. Sun, C. Jiang, Stimuli-responsive drug delivery systems triggered by intracellular or subcellular microenvironments, Adv. Drug Deliv. Rev. 196 (2023) 114773, https://doi.org/10.1016/j.addr.2023.114773.

[52] K. Sapoń, R. Mańka, T. Janas, T. Janas, The role of lipid rafts in vesicle formation, J. Cell Sci. 136 (2023) jcs260887, https://doi.org/10.1242/jcs.260887.

[53] J.J. Rennick, A.P.R. Johnston, R.G. Parton, Key principles and methods for studying the endocytosis of biological and nanoparticle therapeutics, Nat. Nanotechnol. 16 (2021) 266–276, https://doi.org/10.1038/s41565-021-00858-8.

[54] N.D. Donahue, H. Acar, S. Wilhelm, Concepts of nanoparticle cellular uptake, intracellular trafficking, and kinetics in nanomedicine, Adv. Drug Deliv. Rev. 143 (2019) 68–96, https://doi.org/10.1016/j.addr.2019.04.008.

[55] M. Sousa de Almeida, E. Susnik, B. Drasler, P. Taladriz-Blanco, A. Petri-Fink, B. Rothen-Rutishauser, Understanding nanoparticle endocytosis to improve targeting strategies in nanomedicine, Chem. Soc. Rev. 50 (2021) 5397–5434, https://doi.org/10.1039/D0CS01127D.

[56] Y. Ju, H. Guo, M. Edman, S.F. Hamm-Alvarez, Application of advances in endocytosis and membrane trafficking to drug delivery, Adv. Drug Deliv. Rev. 157 (2020) 118–141, https://doi.org/10.1016/j.addr.2020.07.026.

[57] P.U. Le, I.R. Nabi, Distinct caveolae-mediated endocytic pathways target the Golgi apparatus and the endoplasmic reticulum, J. Cell Sci. 116 (2003) 1059–1071, https://doi.org/10.1242/jcs.00327.

[58] X.P. Lin, J.D. Mintern, P.A. Gleeson, Macropinocytosis in different cell types: Similarities and differences, Membranes (basel). 10 (2020), https://doi.org/10.3390/membranes10080177.

[59] J. Yang, A. Griffin, Z. Qiang, J. Ren, Organelle-targeted therapies: a comprehensive review on system design for enabling precision oncology, Signal Transduct. Target. Ther. 7 (2022) 379, https://doi.org/10.1038/s41392-022-01243-0.

[60] X. Fu, Y. Shi, T. Qi, S. Qiu, Y. Huang, X. Zhao, Q. Sun, G. Lin, Precise design strategies of nanomedicine for improving cancer therapeutic efficacy using subcellular targeting, Signal Transduct. Target. Ther. 5 (2020) 262, https://doi.org/10.1038/s41392-020-00342-0.

[61] S. Gimondi, J. Vieira, D. Castro, R.L. Reis, H. Ferreira, M. Neves, Colloids and Surfaces B : Biointerfaces On the size-dependent internalization of sub-hundred polymeric nanoparticles, 225 (2023) 113245. 10.1016/j.colsurfb.2023.113245.

[62] X. Xie, J. Liao, X. Shao, Q. Li, Y. Lin, The effect of shape on cellular uptake of gold nanoparticles in the forms of stars, rods, and triangles, Sci. Rep. 7 (2017) 1–9, https://doi.org/10.1038/s41598-017-04229-z.

[63] S. Niaz, B. Forbes, B.T. Raimi-Abraham, Exploiting endocytosis for non-spherical nanoparticle cellular uptake, Nanomanufacturing. 2 (2022) 1–16, https://doi.org/10.3390/nanomanufacturing2010001.

[64] S. Dasgupta, T. Auth, G. Gompper, Shape and orientation matter for the cellular uptake of nonspherical particles, Nano Lett. 14 (2014) 687–693, https://doi.org/10.1021/nl403949h.

[65] I. Lynch, A. Salvati, K.A. Dawson, Protein-nanoparticle interactions: What does the cell see? Nat. Nanotechnol. 4 (2009) 546–547, https://doi.org/10.1038/nnano.2009.248.

[66] Y. Arezki, F. Delalande, C. Schaeffer-Reiss, S. Cianférani, M. Rapp, L. Lebeau, F. Pons, C. Ronzani, Surface charge influences protein corona, cell uptake and biological effects of carbon dots, Nanoscale 14 (2022) 14695–14710, https://doi.org/10.1039/d2nr03611h.
[67] S. Salatin, S. Maleki Dizaj, A. Yari Khosroushahi, Effect of the surface modification, size, and shape on cellular uptake of nanoparticles, Cell Biol. Int. 39 (2015) 881–890, https://doi.org/10.1002/cbin.10459.
[68] S. Jeon, J. Clavadetscher, D.K. Lee, S.V. Chankeshwara, M. Bradley, W.S. Cho, Surface charge-dependent cellular uptake of polystyrene nanoparticles, Nanomaterials 8 (2018) 1–11, https://doi.org/10.3390/NANO8121028.
[69] S. Correa, N. Boehnke, A.E. Barberio, E. Deiss-Yehiely, A. Shi, B. Oberlton, S. G. Smith, I. Zervantonakis, E.C. Dreaden, P.T. Hammond, Tuning nanoparticle interactions with ovarian cancer through layer-by-layer modification of surface chemistry, ACS Nano 14 (2020) 2224–2237, https://doi.org/10.1021/acsnano.9b09213.
[70] S. Vicente-Ruiz, A. Armiñán, K. Maso, E. Gallon, O. Zagorodko, J. Movellan, F. Rodríguez-Otormín, M. Baues, J.-N. May, F. De Lorenzi, T. Lammers, M. J. Vicent, Poly-l-glutamic acid modification modulates the bio-nano interface of a therapeutic anti-IGF-1R antibody in prostate cancer, Biomaterials 301 (2023) 122280, https://doi.org/10.1016/j.biomaterials.2023.122280.
[71] B. Eshaghi, N. Alsharif, X. An, H. Akiyama, K.A. Brown, S. Gummuluru, B. M. Reinhard, Stiffness of HIV-1 mimicking polymer nanoparticles modulates ganglioside-mediated cellular uptake and trafficking, Adv. Sci. 7 (2020) 1–13, https://doi.org/10.1002/advs.202000649.
[72] J. Key, A.L. Palange, F. Gentile, S. Aryal, C. Stigliano, D. Di Mascolo, E. De Rosa, M. Cho, Y. Lee, J. Singh, P. Decuzzi, Soft discoidal polymeric nanoconstructs resist macrophage uptake and enhance vascular targeting in tumors, ACS Nano 9 (2015) 11628–11641, https://doi.org/10.1021/acsnano.5b04866.
[73] Y. Hui, X. Yi, D. Wibowo, G. Yang, A.P.J. Middelberg, H. Gao, C.X. Zhao, Nanoparticle elasticity regulates phagocytosis and cancer cell uptake, Sci. Adv. 6 (2020) 1–10, https://doi.org/10.1126/sciadv.aaz4316.
[74] J. Sun, L. Zhang, J. Wang, Q. Feng, D. Liu, Q. Yin, D. Xu, Y. Wei, B. Ding, X. Shi, X. Jiang, Tunable rigidity of (polymeric core)-(lipid shell) nanoparticles for regulated cellular uptake, Adv. Mater. 27 (2015) 1402–1407, https://doi.org/10.1002/adma.201404788.
[75] P. Gurnani, C. Sanchez-Cano, H. Xandri-Monje, J. Zhang, S.H. Ellacott, E.D. H. Mansfield, M. Hartlieb, R. Dallmann, S. Perrier, Probing the effect of rigidity on the cellular uptake of core-shell nanoparticles: stiffness effects are size dependent, Small 18 (2022), https://doi.org/10.1002/smll.202203070.
[76] S.A. Smith, L.I. Selby, A.P.R. Johnston, G.K. Such, The endosomal escape of nanoparticles: Toward more efficient cellular delivery, Bioconjug. Chem. 30 (2019) 263–272, https://doi.org/10.1021/acs.bioconjchem.8b00732.
[77] W. He, X. Xing, X. Wang, D. Wu, W. Wu, J. Guo, S. Mitragotri, Nanocarrier-mediated cytosolic delivery of biopharmaceuticals, Adv. Funct. Mater. 30 (2020) 1–22, https://doi.org/10.1002/adfm.201910566.
[78] X. Hou, T. Zaks, R. Langer, Y. Dong, Lipid nanoparticles for mRNA delivery, Nat. Rev. Mater. 6 (2021) 1078–1094, https://doi.org/10.1038/s41578-021-00358-0.
[79] S.C. Semple, S.K. Klimuk, T.O. Harasym, N. Dos Santos, S.M. Ansell, K.F. Wong, N. Maurer, H. Stark, P.R. Cullis, M.J. Hope, P. Scherrer, Efficient encapsulation of antisense oligonucleotides in lipid vesicles using ionizable aminolipids: formation of novel small multilamellar vesicle structures, Biochim. Biophys. Acta - Biomembr. 1510 (2001) 152–166, https://doi.org/10.1016/S0005-2736(00)00343-6.
[80] M. Jayaraman, S.M. Ansell, B.L. Mui, Y.K. Tam, J. Chen, X. Du, D. Butler, L. Eltepu, S. Matsuda, J.K. Narayanannair, K.G. Rajeev, I.M. Hafez, A. Akinc, M. A. Maier, M.A. Tracy, P.R. Cullis, T.D. Madden, M. Manoharan, M.J. Hope, Maximizing the potency of siRNA lipid nanoparticles for hepatic gene silencing In Vivo**, Angew. Chemie Int. Ed. 51 (2012) 8529–8533, https://doi.org/10.1002/anie.201203263.
[81] M. Schlich, R. Palomba, G. Costabile, S. Mizrahy, M. Pannuzzo, D. Peer, P. Decuzzi, Cytosolic delivery of nucleic acids: The case of ionizable lipid nanoparticles, Bioeng. Transl. Med. 6 (2021) e10213.
[82] S. Liu, Q. Cheng, T. Wei, X. Yu, L.T. Johnson, L. Farbiak, D.J. Siegwart, Membrane-destabilizing ionizable phospholipids for organ-selective mRNA delivery and CRISPR–Cas gene editing, Nat. Mater. 20 (2021) 701–710, https://doi.org/10.1038/s41563-020-00886-0.
[83] W. Li, F. Nicol, F.C. Szoka, GALA: a designed synthetic pH-responsive amphipathic peptide with applications in drug and gene delivery, Adv. Drug Deliv. Rev. 56 (2004) 967–985, https://doi.org/10.1016/j.addr.2003.10.041.
[84] M.M. Abd Elwakil, I.A. Khalil, Y.H.A. Elewa, K. Kusumoto, Y. Sato, N. Shobaki, Y. Kon, H. Harashima, Lung-endothelium-targeted nanoparticles based on a pH-sensitive lipid and the GALA peptide enable robust gene silencing and the regression of metastatic lung cancer, Adv. Funct. Mater. 29 (2019) 1–13, https://doi.org/10.1002/adfm.201807677.
[85] L.M.P. Vermeulen, S.C. De Smedt, K. Remaut, K. Braeckmans, The proton sponge hypothesis: Fable or fact? Eur. J. Pharm. Biopharm. 129 (2018) 184–190, https://doi.org/10.1016/j.ejpb.2018.05.034.
[86] T. Bus, A. Traeger, U.S. Schubert, The great escape: how cationic polyplexes overcome the endosomal barrier, J. Mater. Chem. b. 6 (2018) 6904–6918, https://doi.org/10.1039/C8TB00967H.
[87] L. Tortajada, C. Felip-León, M.J. Vicent, Polymer-based non-viral vectors for gene therapy in the skin, Polym. Chem. 13 (2022) 718–735, https://doi.org/10.1039/D1PY01485D.
[88] W.-W. Hu, C.-C. Yeh, C.-W. Tsai, The conjugation of indolicidin to polyethylenimine for enhanced gene delivery with reduced cytotoxicity, J. Mater. Chem. b. 6 (2018) 5781–5794, https://doi.org/10.1039/C8TB01408F.
[89] A. Zakeri, M.A.J. Kouhbanani, N. Beheshtkhoo, V. Beigi, S.M. Mousavi, S.A. R. Hashemi, A. Karimi Zade, A.M. Amani, A. Savardashtaki, E. Mirzaei, S. Jahandideh, A. Movahedpour, Polyethylenimine-based nanocarriers in co-delivery of drug and gene: a developing horizon, Nano Rev. Exp. 9 (2018) 1488497, https://doi.org/10.1080/20022727.2018.1488497.
[90] T. Melnyk, S. Đorđević, I. Conejos-Sánchez, M.J. Vicent, Therapeutic potential of polypeptide-based conjugates: Rational design and analytical tools that can boost clinical translation, Adv. Drug Deliv. Rev. 160 (2020) 136–169, https://doi.org/10.1016/j.addr.2020.10.007.
[91] H. Fang, Z. Guo, L. Lin, J. Chen, P. Sun, J. Wu, C. Xu, H. Tian, X. Chen, Molecular strings significantly improved the gene transfection efficiency of polycations, J. Am. Chem. Soc. 140 (2018) 11992–12000, https://doi.org/10.1021/jacs.8b05341.
[92] S. Stefanovic, K. McCormick, S. Fattah, R. Brannigan, S.-A. Cryan, A. Heise, Star-shaped poly(l-lysine) with polyester bis-MPA dendritic core as potential degradable nano vectors for gene delivery, Polym. Chem. 14 (2023) 3151–3159, https://doi.org/10.1039/D3PY00346A.
[93] S.E. Barrett, R.S. Burke, M.T. Abrams, C. Bason, M. Busuek, E. Carlini, B.A. Carr, L.S. Crocker, H. Fan, R.M. Garbaccio, E.N. Guidry, J.H. Heo, B.J. Howell, E. A. Kemp, R.A. Kowtoniuk, A.H. Latham, A.M. Leone, M. Lyman, R.G. Parmar, M. Patel, S.Y. Pechenov, T. Pei, N.T. Pudvah, C. Raab, S. Riley, L. Sepp-Lorenzino, S. Smith, E.D. Soli, S. Staskiewicz, M. Stern, Q. Truong, M. Vavrek, J.H. Waldman, E.S. Walsh, J.M. Williams, S. Young, S.L. Colletti, Development of a liver-targeted siRNA delivery platform with a broad therapeutic window utilizing biodegradable polypeptide-based polymer conjugates, J. Control. Release. 183 (2014) 124–137, https://doi.org/10.1016/j.jconrel.2014.03.028.
[94] I. Conejos-Sánchez, E. Gallon, A. Niño-Pariente, J.A. Smith, A.G. De la Fuente, L. Di Canio, S. Pluchino, R.J.M. Franklin, M.J. Vicent, Polyornithine-based polyplexes to boost effective gene silencing in CNS disorders, Nanoscale 12 (2020) 6285–6299, https://doi.org/10.1039/C9NR06187H.
[95] S. Abbasi, S. Uchida, K. Toh, T.A. Tockary, A. Dirisala, K. Hayashi, S. Fukushima, K. Kataoka, Co-encapsulation of Cas9 mRNA and guide RNA in polyplex micelles enables genome editing in mouse brain, J. Control. Release. 332 (2021) 260–268, https://doi.org/10.1016/j.jconrel.2021.02.026.
[96] F. Abedi-Gaballu, G. Dehghan, M. Ghaffari, R. Yekta, S. Abbaspour-Ravasjani, B. Baradaran, J. Ezzati Nazhad Dolatabadi, M.R. Hamblin, PAMAM dendrimers as efficient drug and gene delivery nanosystems for cancer therapy, Appl. Mater. Today. 12 (2018) 177–190, https://doi.org/10.1016/j.apmt.2018.05.002.
[97] N. Aibani, R. Rai, P. Patel, G. Cuddihy, E.K. Wasan, Chitosan nanoparticles at the biological interface: Implications for drug delivery, Pharmaceutics. 13 (2021), https://doi.org/10.3390/pharmaceutics13101686.
[98] F.E. Freeman, P. Dosta, L.C. Shanley, N. Ramirez Tamez, C.J. Riojas Javelly, O. R. Mahon, D.J. Kelly, N. Artzi, Localized nanoparticle-mediated delivery of miR-29b normalizes the dysregulation of bone homeostasis caused by osteosarcoma whilst simultaneously inhibiting tumor growth, Adv. Mater. 35 (2023) 2207877, https://doi.org/10.1002/adma.202207877.
[99] D. Routkevitch, D. Sudhakar, M. Conge, M. Varanasi, S.Y. Tzeng, D.R. Wilson, J. J. Green, Efficiency of cytosolic delivery with poly(β-amino ester) nanoparticles is dependent on the effective pKa of the polymer, ACS Biomater. Sci. Eng. 6 (2020) 3411–3421, https://doi.org/10.1021/acsbiomaterials.0c00271.
[100] J. Wei, L. Zhu, Q. Lu, G. Li, Y. Zhou, Y. Yang, L. Zhang, Recent progress and applications of poly(beta amino esters)-based biomaterials, J. Control. Release. 354 (2023) 337–353, https://doi.org/10.1016/j.jconrel.2023.01.002.
[101] Y. Cheng, Peptide-Modified Polycations with Acid-Triggered Lytic Activity for Efficient Gene Delivery, Gene Deliv (2021) 1–17, https://doi.org/10.1007/978-981-33-6198-0_1-1.
[102] F. Joubert, M.J. Munson, A. Sabirsh, R.M. England, M. Hemmerling, C. Alexander, M.B. Ashford, Precise and systematic end group chemistry modifications on PAMAM and poly(l-lysine) dendrimers to improve cytosolic delivery of mRNA, J. Control. Release. 356 (2023) 580–594, https://doi.org/10.1016/j.jconrel.2023.03.011.
[103] B. Winkeljann, D.C. Keul, O.M. Merkel, Engineering poly- and micelleplexes for nucleic acid delivery – A reflection on their endosomal escape, J. Control. Release. 353 (2023) 518–534, https://doi.org/10.1016/j.jconrel.2022.12.008.
[104] A. Dirisala, S. Uchida, J. Li, J.F.R. Van Guyse, K. Hayashi, S.V.C. Vummaleti, S. Kaur, Y. Mochida, S. Fukushima, K. Kataoka, Effective mRNA Protection by Poly(l-ornithine) Synergizes with Endosomal Escape Functionality of a Charge-Conversion Polymer toward Maximizing mRNA Introduction Efficiency, Macromol. Rapid Commun. 43 (2022) 1–9, https://doi.org/10.1002/marc.202100754.
[105] K. Miyata, M. Oba, M. Nakanishi, S. Fukushima, Y. Yamasaki, H. Koyama, N. Nishiyama, K. Kataoka, Polyplexes from poly(aspartamide) bearing 1,2-diaminoethane side chains induce pH-selective, endosomal membrane destabilization with amplified transfection and negligible cytotoxicity, J. Am. Chem. Soc. 130 (2008) 16287–16294, https://doi.org/10.1021/ja804561g.
[106] S. Deng, S. Wang, Z. Xiao, D. Cheng, Unprotonatable and ROS-Sensitive Nanocarrier for NIR Spatially Activated siRNA Therapy with Synergistic Drug Effect, Small 18 (2022), https://doi.org/10.1002/smll.202203823.
[107] Y. Mo, M.H.Y. Cheng, A. D'Elia, K. Doran, L. Ding, J. Chen, P.R. Cullis, G. Zheng, Light-Activated siRNA Endosomal Release (LASER) by Porphyrin Lipid Nanoparticles, ACS Nano 17 (2023) 4688–4703, https://doi.org/10.1021/acsnano.2c10936.
[108] M. Patil, A. Hussain, M.A. Altamimi, S. Ashique, N. Haider, A. Faruk, T. Khuroo, A. Sherikar, M.U.M. Siddique, A. Ansari, T.K. Barbhuiya, An insight of various vesicular systems, erythrosomes, and exosomes to control metastasis and cancer,

Adv. Cancer Biol. - Metastasis. 7 (2023) 100103, https://doi.org/10.1016/j.adcanc.2023.100103.
[109] I.K. Herrmann, M.J.A. Wood, G. Fuhrmann, Extracellular vesicles as a next-generation drug delivery platform, Nat. Nanotechnol. 16 (2021) 748–759, https://doi.org/10.1038/s41565-021-00931-2.
[110] Y. Zhang, Q. Liu, X. Zhang, H. Huang, S. Tang, Y. Chai, Z. Xu, M. Li, X. Chen, J. Liu, C. Yang, Recent advances in exosome-mediated nucleic acid delivery for cancer therapy, J. Nanobiotechnology. 20 (2022) 279, https://doi.org/10.1186/s12951-022-01472-z.
[111] S. Gurung, D. Perocheau, L. Touramanidou, J. Baruteau, The exosome journey: from biogenesis to uptake and intracellular signalling, Cell Commun, Signal. 19 (2021) 1–19, https://doi.org/10.1186/s12964-021-00730-1.
[112] L. Ribovski, B. Joshi, J. Gao, I. Zuhorn, Breaking free: endocytosis and endosomal escape of extracellular vesicles, Extracell. Vesicles Circ. Nucleic Acids. 4 (2023) 283–305, https://doi.org/10.20517/evcna.2023.26.
[113] B.S. Joshi, M.A. de Beer, B.N.G. Giepmans, I.S. Zuhorn, Endocytosis of Extracellular Vesicles and Release of Their Cargo from Endosomes, ACS Nano 14 (2020) 4444–4455, https://doi.org/10.1021/acsnano.9b10033.
[114] T.T. Pham, H. Chen, P.H.D. Nguyen, M.K. Jayasinghe, A.H. Le, M.T.N. Le, Endosomal escape of nucleic acids from extracellular vesicles mediates functional therapeutic delivery, Pharmacol. Res. 188 (2023) 106665, https://doi.org/10.1016/j.phrs.2023.106665.
[115] H.M. Ding, Y.Q. Ma, Theoretical and computational investigations of nanoparticle-biomembrane interactions in cellular delivery, Small 11 (2015) 1055–1071, https://doi.org/10.1002/smll.201401943.
[116] Y. Jiang, S. Huo, T. Mizuhara, R. Das, Y.W. Lee, S. Hou, D.F. Moyano, B. Duncan, X.J. Liang, V.M. Rotello, The Interplay of Size and Surface Functionality on the Cellular Uptake of Sub-10 nm Gold Nanoparticles, ACS Nano 9 (2015) 9986–9993, https://doi.org/10.1021/acsnano.5b03521.
[117] Y. Liu, S. Li, X. Liu, H. Sun, T. Yue, X. Zhang, B. Yan, D. Cao, Design of Small Nanoparticles Decorated with Amphiphilic Ligands: Self-Preservation Effect and Translocation into a Plasma Membrane, ACS Appl. Mater. Interfaces. 11 (2019) 23822–23831, https://doi.org/10.1021/acsami.9b03638.
[118] A. Verma, O. Uzun, Y. Hu, Y. Hu, H. Han, N. Watson, S. Chen, D.J. Irvine, F. Stellacci, Surface-structure-regulated cell-membrane penetration by monolayer-protected nanoparticles, Nat. Mat. (2008) 1–8, https://doi.org/10.1038/nmat2202.
[119] D.A. Links, Nanoscale Surface-structure-regulated penetration of nanoparticles across a cell, Nanoscale (2012) 3768–3775, https://doi.org/10.1039/c2nr30379e.
[120] I. Gessner, I. Neundorf, Nanoparticles modified with cell-penetrating peptides: Conjugation mechanisms, physicochemical properties, and application in cancer diagnosis and therapy, Int. J. Mol. Sci. 21 (2020), https://doi.org/10.3390/ijms21072536.
[121] S. Silva, A.J. Almeida, N. Vale, Combination of cell-penetrating peptides with nanoparticles for therapeutic application: A Review, Biomolecules 9 (2019), https://doi.org/10.3390/biom9010022.
[122] M.C. Morris, L. Chaloin, J. Méry, F. Heitz, G. Divita, A novel potent strategy for gene delivery using a single peptide vector as a carrier, Nucleic Acids Res. 27 (1999) 3510–3517, https://doi.org/10.1093/nar/27.17.3510.
[123] D. Derossi, A.H. Joliot, G. Chassaing, A. Prochiantz, The third helix of the Antennapedia homeodomain translocates through biological membranes, J. Biol. Chem. 269 (1994) 10444–10450, https://doi.org/10.1016/s0021-9258(17)34080-2.
[124] A. Gori, G. Lodigiani, S. Garcia Colombarolli, G. Bergamaschi, A. Vitali, Cell Penetrating Peptides: classification, mechanisms, methods of study and applications, ChemMedChem (2023), https://doi.org/10.1002/cmdc.202300236.
[125] I. Ruseska, A. Zimmer, Internalization mechanisms of cell-penetrating peptides, Beilstein J. Nanotechnol. 11 (2020) 101–123, https://doi.org/10.3762/bjnano.11.10.
[126] I. Nakase, Cellular Uptake Mechanisms of Arginine-Rich Cell-Penetrating Peptides, Cell-Penetrating Pept. (2023) 141–157, https://doi.org/10.1002/9783527835997.ch9.
[127] H. Yamashita, T. Kato, M. Oba, T. Misawa, T. Hattori, N. Ohoka, M. Tanaka, M. Naito, M. Kurihara, Y. Demizu, Development of a Cell-penetrating Peptide that Exhibits Responsive Changes in its Secondary Structure in the Cellular Environment, Sci. Rep. 6 (2016) 2–9, https://doi.org/10.1038/srep33003.
[128] D. Kalafatovic, E. Giralt, Cell-penetrating peptides: Design strategies beyond primary structure and amphipathicity, Molecules 22 (11) (2017) 1929, https://doi.org/10.3390/molecules22111929.
[129] P. Agrawal, S. Bhalla, S.S. Usmani, S. Singh, K. Chaudhary, G.P.S. Raghava, A. Gautam, CPPsite 2.0: A repository of experimentally validated cell-penetrating peptides, Nucleic Acids Res. 44 (2016) D1098–D1103, https://doi.org/10.1093/nar/gkv1266.
[130] P.F. Chinnery, Primary Mitochondrial Disorders Overview 1, Clinical Characteristics of Mitochondrial, Disorders (2023) 1–16. https://www.ncbi.nlm.nih.gov/books/NBK1224/.
[131] M. Giacomello, A. Pyakurel, C. Glytsou, L. Scorrano, The cell biology of mitochondrial membrane dynamics, Nat. Rev. Mol. Cell Biol. 21 (2020), https://doi.org/10.1038/s41580-020-0210-7.
[132] S. Krauss. Mitochondria : Structure and Role in Respiration, Encyclopedia of Life Science, 2001, pp. 1–6, https://doi.org/10.1038/npg.els.0001380.
[133] B. Westermann, Mitochondrial fusion and fission in cell life and death, Nat Rev Mol Cell Biol 11 (12) (2010) 872–884, https://doi.org/10.1038/nrm3013.
[134] S.R. Doyle, N.R.P. Kasinadhuni, C.K. Chan, W.N. Grant, Evidence of Evolutionary Constraints That Influences the Sequence Composition and Diversity of Mitochondrial Matrix Targeting Signals, PLoS One 8 (2013) e67938, https://doi.org/10.1371/journal.pone.0067938.
[135] T. Omura, Mitochondria-targeting sequence, a multi-role sorting sequence recognized at all steps of protein import into mitochondria, J. Biochem. 123 (1998) 1010–1016, https://doi.org/10.1093/oxfordjournals.jbchem.a022036.
[136] D.M. Niyazov, G. Kahler, R.E. Frye, Primary Mitochondrial Disease and Secondary Mitochondrial Dysfunction : Importance of Distinction for Diagnosis and Treatment, Mol Syndromol 7 (3) (2016) 122–137, https://doi.org/10.1159/000446586.
[137] H. Cui, Y. Kong, H. Zhang, Oxidative Stress, Mitochondrial Dysfunction, and Aging (2012 (2012).), https://doi.org/10.1155/2012/646354.
[138] M.P. Murphy , R.C. Hartley , Mitochondria as a therapeutic target for common pathologies , Nat. Publ. Gr. (n.d), doi: 10.1038/nrd.2018.174.
[139] R.H. Swerdlow, Mitochondria and Mitochondrial Cascades in Alzheimer's Disease, J. Alzheimer's Dis. 62 (2018) 1403–1416, https://doi.org/10.3233/JAD-170585.
[140] A. Grünewald, K.R. Kumar, C.M. Sue, New insights into the complex role of mitochondria in Parkinson's disease, Prog. Neurobiol. 177 (2019) 73–93, https://doi.org/10.1016/j.pneurobio.2018.09.003.
[141] N. Badrinath, S.Y. Yoo, Mitochondria in cancer: In the aspects of tumorigenesis and targeted therapy, Carcinogenesis 39 (2018) 1419–1430, https://doi.org/10.1093/carcin/bgy148.
[142] J.M. Suárez-Rivero, C.J. Pastor-Maldonado, S. Povea-Cabello, M. Álvarez-Córdoba, I. Villalón-García, M. Talaverón-Rey, A. Suárez-Carrillo, M. Munuera-Cabeza, J.A. Sánchez-Alcázar, From Mitochondria to Atherosclerosis: The Inflammation Path, Biomedicines. 9 (2021), https://doi.org/10.3390/biomedicines9030258.
[143] P. Newsholme, C. Gaudel, M. Krause, Mitochondria and diabetes. An intriguing pathogenetic role BT - advances in mitochondrial medicine, Springer, Netherlands, Dordrecht, 2012, pp. 235–247, https://doi.org/10.1007/978-94-007-2869-1_10.
[144] M. Bueno, J. Calyeca, M. Rojas, A.L. Mora, Mitochondria dysfunction and metabolic reprogramming as drivers of idiopathic pulmonary fibrosis, Redox Biol. 33 (2020) 101509, https://doi.org/10.1016/j.redox.2020.101509.
[145] A.V. Poznyak, E.A. Ivanova, I.A. Sobenin, S.-F. Yet, A.N. Orekhov, The Role of Mitochondria in Cardiovascular Diseases, Biology (basel). 9 (2020), https://doi.org/10.3390/biology9060137.
[146] R.J. Ritchie, A critical assessment of the use of lipophilic cations as membrane potential probes, Prog. Biophys. Mol. Biol. 43 (1984) 1–32, https://doi.org/10.1016/0079-6107(84)90002-6.
[147] H. Cho, Y.Y. Cho, M.S. Shim, J.Y. Lee, H.S. Lee, H.C. Kang, Mitochondria-targeted drug delivery in cancers, Biochim. Biophys. Acta - Mol. Basis Dis. 1866 (2020) 165808, https://doi.org/10.1016/j.bbadis.2020.165808.
[148] X. Cheng, D. Feng, J. Lv, X. Cui, Y. Wang, Q. Wang, L. Zhang, Application Prospects of Triphenylphosphine-Based Mitochondria-Targeted Cancer Therapy, Cancers (basel). 15 (2023), https://doi.org/10.3390/cancers15030666.
[149] J. Zielonka, J. Joseph, A. Sikora, M. Hardy, O. Ouari, J. Vasquez-Vivar, G. Cheng, M. Lopez, B. Kalyanaraman, Mitochondria-Targeted Triphenylphosphonium-Based Compounds: Syntheses, Mechanisms of Action, and Therapeutic and Diagnostic Applications, Chem. Rev. 117 (2017) 10043–10120, https://doi.org/10.1021/acs.chemrev.7b00042.
[150] V. Weissig, From Serendipity to Mitochondria-Targeted Nanocarriers, Pharm. Res. 28 (2011) 2657–2668, https://doi.org/10.1007/s11095-011-0556-9.
[151] L.D. Zorova, E.A. Demchenko, G.A. Korshunova, V.N. Tashlitsky, S.D. Zorov, N. V. Andrianova, V.A. Popkov, V.A. Babenko, I.B. Pevzner, D.N. Silachev, E. Y. Plotnikov, D.B. Zorov, Is the Mitochondrial Membrane Potential Correctly Assessed? Intracellular and Intramitochondrial Modifications of the ΔΨ Probe, Rhodamine 123, Int. J. Mol. Sci. 23 (2022), https://doi.org/10.3390/ijms23010482.
[152] R. Wadhwa, T. Sugihara, A. Yoshida, H. Nomura, R.R. Reddel, R. Simpson, H. Maruta, S.C. Kaul, Advances in Brief Selective Toxicity of MKT-077 to Cancer Cells Is Mediated by Its Binding to the hsp70 Family Protein mot-2 and Reactivation of p53 Function, Cancer Res Advances in Brief (2000) 6818–6821.
[153] A.Y. Spivak, D.A. Nedopekina, R.R. Gubaidullin, E.V. Davletshin, A. A. Tukhbatullin, V.A. D'yakonov, M.M. Yunusbaeva, L.U. Dzhemileva, U. M. Dzhemilev, Pentacyclic triterpene acid conjugated with mitochondria-targeting cation F16: Synthesis and evaluation of cytotoxic activities, Med. Chem. Res. 30 (2021) 940–951, https://doi.org/10.1007/s00044-021-02702-z.
[154] T. Sakai, Y. Matsuo, K. Okuda, K. Hirota, M. Tsuji, T. Hirayama, H. Nagasawa, Development of antitumor biguanides targeting energy metabolism and stress responses in the tumor microenvironment, Sci. Rep. 11 (2021) 4852, https://doi.org/10.1038/s41598-021-83708-w.
[155] S.A. Dyshlovoy, E.K. Kudryashova, M. Kaune, T.N. Makarieva, L.K. Shubina, T. Busenbender, V.A. Denisenko, R.S. Popov, J. Hauschild, S.N. Fedorov, C. Bokemeyer, M. Graefen, V.A. Stonik, G. von Amsberg, Urupocidin C: a new marine guanidine alkaloid which selectively kills prostate cancer cells via mitochondria targeting, Sci. Rep. 10 (2020) 9764, https://doi.org/10.1038/s41598-020-66428-5.
[156] W.-W. Qin, Z.-Y. Pan, D.-H. Cai, Y. Li, L. He, Cyclometalated iridium(iii) complexes for mitochondria-targeted combined chemo-photodynamic therapy, Dalt. Trans. 49 (2020) 3562–3569, https://doi.org/10.1039/D0DT00180E.
[157] H. Wang, B. Fang, B. Peng, L. Wang, Y. Xue, H. Bai, S. Lu, N.H. Voelcker, L. Li, L. Fu, W. Huang, Recent Advances in Chemical Biology of Mitochondria Targeting, Front. Chem. 9 (2021), 683220, doi: 10.3389/fchem.2021.683220.

[158] V. Weissig, M. Lozoya, N. Yu, G.G.M. D'Souza, DQAsomes as the Prototype of Mitochondria-Targeted Pharmaceutical Nanocarriers : An Update, Methods Mol. Biol. 2275 (2021) 13–25, https://doi.org/10.1007/978-1-0716-1262-0_2.
[159] A.N. Bayne, J. Dong, S. Amiri, S.M.K. Farhan, J.-F. Trempe, MTSviewer: A database to visualize mitochondrial targeting sequences, cleavage sites, and mutations on protein structures, PLoS One 18 (2023) e0284541, doi: 10.1371/journal.pone.0284541.
[160] N. Yoshinaga, K. Numata, Rational Designs at the Forefront of Mitochondria-Targeted Gene Delivery: Recent Progress and Future Perspectives, ACS Biomater. Sci. Eng. 8 (2022) 348–359, https://doi.org/10.1021/acsbiomaterials.1c01114.
[161] H. Yu, R.D. Koilkonda, T. Chou, V. Porciatti, S.S. Ozdemir, Chiodo, Gene delivery to mitochondria by targeting modified adenoassociated virus suppresses Leber ' s hereditary optic neuropathy in a mouse model, Proc. Nat. Am. Soc. 109 (2012), https://doi.org/10.1073/pnas.1119577109.
[162] M.-H. Avelange-Macherel, A. Candat, M. Neveu, D. Tolleter, D. Macherel, Decoding the Divergent Subcellular Location of Two Highly Similar Paralogous LEA Proteins, Int. J. Mol. Sci. 19 (2018), https://doi.org/10.3390/ijms19061620.
[163] Y.K. Pak, H. Weiner, Import of chemically synthesized signal peptides into rat liver mitochondria, J. Biol. Chem. 265 (1990) 14298–14307, https://doi.org/10.1016/s0021-9258(18)77300-6.
[164] L.F. Yousif, K.M. Stewart, S.O. Kelley, Targeting Mitochondria with Organelle-Specific Compounds: Strategies and Applications, Chembiochem 10 (2009) 1939–1950, https://doi.org/10.1002/cbic.200900185.
[165] A. Klimpel, I. Neundorf, Bifunctional peptide hybrids targeting the matrix of mitochondria, J. Control. Release. 291 (2018) 147–156, https://doi.org/10.1016/j.jconrel.2018.10.029.
[166] J.-A. Chuah, A. Matsugami, F. Hayashi, K. Numata, Self-Assembled Peptide-Based System for Mitochondrial-Targeted Gene Delivery: Functional and Structural Insights, Biomacromolecules 17 (2016) 3547–3557, https://doi.org/10.1021/acs.biomac.6b01056.
[167] G. Paradies, V. Paradies, F.M. Ruggiero, G. Petrosillo, Role of Cardiolipin in Mitochondrial Function and Dynamics in Health and Disease : Molecular and Pharmacological Aspects Cells 8 (7) (2019) 728, https://doi.org/10.3390/cells8070728.
[168] H.H. Szeto, First-in-class cardiolipin-protective compound as a therapeutic agent to restore mitochondrial bioenergetics, Br. J. Pharmacol. 171 (2014) 2029–2050, https://doi.org/10.1111/bph.12461.
[169] H.H. Szeto, A.V. Birk, Serendipity and the Discovery of Novel Compounds That Restore Mitochondrial Plasticity, Clin Pharmacol Ther 96 (6) (2014) 672–683, https://doi.org/10.1038/clpt.2014.174.
[170] A.V. Birk, W.M. Chao, C. Bracken, J.D. Warren, H.H. Szeto, Targeting mitochondrial cardiolipin and the cytochrome c/cardiolipin complex to promote electron transport and optimize mitochondrial ATP synthesis, Br. J. Pharmacol. 171 (2014) 2017–2028, https://doi.org/10.1111/bph.12468.
[171] A.V. Birk, S. Liu, Y. Soong, W. Mills, P. Singh, J.D. Warren, S.V. Seshan, J. D. Pardee, H.H. Szeto, The mitochondrial-targeted compound SS-31 re-energizes ischemic mitochondria by interacting with cardiolipin, J. Am. Soc. Nephrol. 24 (2013) 1250–1261, https://doi.org/10.1681/ASN.2012121216.
[172] K. Zhao, G.-M. Zhao, D. Wu, Y. Soong, A.V. Birk, P.W. Schiller, H.H. Szeto, Cell-permeable Peptide Antioxidants Targeted to Inner Mitochondrial Membrane inhibit Mitochondrial Swelling, Oxidative Cell Death, and Reperfusion Injury*, J. Biol. Chem. 279 (2004) 34682–34690, https://doi.org/10.1074/jbc.M402999200.
[173] C.P. Cerrato, M. Pirisinu, E.N. Vlachos, Novel cell-penetrating peptide targeting mitochondria, (2015) 1–11. 10.1096/fj.14-269225.
[174] A. Kam, S. Loo, B. Dutta, S.K. Sze, J.P. Tam, Plant-derived mitochondria-targeting cysteine-rich peptide modulates cellular bioenergetics, J. Biol. Chem. 294 (2019) 4000–4011, https://doi.org/10.1074/jbc.RA118.006693.
[175] N.V. Pfeiffer, D. Dirndorfer, S. Lang, U.K. Resenberger, L.M. Restelli, C. Hemion, M. Miesbauer, S. Frank, A. Neutzner, R. Zimmermann, K.F. Winklhofer, J. Tatzelt, Structural features within the nascent chain regulate alternative targeting of secretory proteins to mitochondria, EMBO J. 32 (2013) 1036–1051, https://doi.org/10.1038/emboj.2013.46.
[176] K.L. Horton, K.M. Stewart, S.B. Fonseca, Q. Guo, S.O. Kelley, Mitochondria-Penetrating Peptides, Chem. Biol. 15 (2008) 375–382, https://doi.org/10.1016/j.chembiol.2008.03.015.
[177] L.F. Yousif, K.M. Stewart, K.L. Horton, S.O. Kelley, Mitochondria-penetrating peptides: Sequence effects and model cargo transport, Chembiochem 10 (2009) 2081–2088, https://doi.org/10.1002/cbic.200900017.
[178] S.R. Jean, M. Ahmed, E.K. Lei, S.P. Wisnovsky, S.O. Kelley, Peptide-Mediated Delivery of Chemical Probes and Therapeutics to Mitochondria, Acc. Chem. Res. 49 (2016) 1893–1902, https://doi.org/10.1021/acs.accounts.6b00277.
[179] J. Wu, J. Li, H. Wang, C.B. Liu, Mitochondrial-targeted penetrating peptide delivery for cancer therapy, Expert Opin. Drug Deliv. 15 (2018) 951–964, https://doi.org/10.1080/17425247.2018.1517750.
[180] S.B. Fonseca, M.P. Pereira, R. Mourtada, M. Gronda, K.L. Horton, R. Hurren, M. D. Minden, A.D. Schimmer, S.O. Kelley, Rerouting chlorambucil to mitochondria combats drug deactivation and resistance in cancer cells, Chem. Biol. 18 (2011) 445–453, https://doi.org/10.1016/j.chembiol.2011.02.010.
[181] G.R. Chamberlain, D.V. Tulumello, S.O. Kelley, Targeted Delivery of Doxorubicin to Mitochondria, ACS Chem. Biol. 8 (2013) 1389–1395, https://doi.org/10.1021/cb400095v.
[182] E.K. Lei, S.O. Kelley, Delivery and Release of Small-Molecule Probes in Mitochondria Using Traceless Linkers, J. Am. Chem. Soc. 139 (2017) 9455–9458, https://doi.org/10.1021/jacs.7b04415.
[183] T. Zhao, X. Liu, S. Singh, X. Liu, Y. Zhang, J. Sawada, M. Komatsu, K.D. Belfield, Mitochondria Penetrating Peptide-Conjugated TAMRA for Live-Cell Long-Term Tracking, Bioconjug. Chem. 30 (2019) 2312–2316, https://doi.org/10.1021/acs.bioconjchem.9b00465.
[184] C.S. Burke, A. Byrne, T.E. Keyes, Highly Selective Mitochondrial Targeting by a Ruthenium(II) Peptide Conjugate: Imaging and Photoinduced Damage of Mitochondrial DNA, Angew. Chemie - Int. Ed. 57 (2018) 12420–12424, https://doi.org/10.1002/anie.201806002.
[185] S. Somsri, M. Mungthin, N. Klubthawee, P. Adisakwattana, W. Hanpithakpong, R. Aunpad, A mitochondria-penetrating peptide exerts potent anti-plasmodium activity and localizes at parasites' mitochondria, Antibiotics 10 (2021), https://doi.org/10.3390/antibiotics10121560.
[186] Y.A. Fillon, J.P. Anderson, J. Chmielewski, Cell Penetrating Agents Based on a Polyproline Helix Scaffold, J. Am. Chem. Soc. 127 (2005) 11798–11803, https://doi.org/10.1021/ja052377g.
[187] L. Li, I. Geisler, J. Chmielewski, J. Cheng, Cationic amphiphilic polyproline helix P11LRR targets intracellular mitochondria, J. Control. Release. 142 (2010) 259–266, https://doi.org/10.1016/j.jconrel.2009.10.012.
[188] I.M. Geisler, J. Chmielewski, Dimeric cationic amphiphilic polyproline helices for mitochondrial targeting, Pharm. Res. 28 (2011) 2797–2807, https://doi.org/10.1007/s11095-011-0493-7.
[189] D. Kalafut, T.N. Anderson, J. Chmielewski, Mitochondrial targeting of a cationic amphiphilic polyproline helix, Bioorganic Med, Chem. Lett. 22 (2012) 561–563, https://doi.org/10.1016/j.bmcl.2011.10.077.
[190] G.C. Kim, D.H. Cheon, Y. Lee, BBA - Proteins and Proteomics Challenge to overcome current limitations of cell-penetrating peptides, BBA - Proteins Proteomics. 1869 (2021) 140604, https://doi.org/10.1016/j.bbapap.2021.140604.
[191] I. Szabó, M. Yousef, D. Soltész, C. Bató, G. Mező, Z. Bánóczi, Redesigning of Cell-Penetrating Peptides to Improve Their Efficacy as a Drug Delivery System, Pharmaceutics. 14 (2022), https://doi.org/10.3390/pharmaceutics14050907.
[192] P. Zhang, Y. Xiao, X. Sun, X. Lin, S. Koo, A.V. Yaremenko, D. Qin, N. Kong, O. C. Farokhzad, W. Tao, Cancer nanomedicine toward clinical translation: Obstacles, opportunities, and future prospects, Med. 4 (2023) 147–167, https://doi.org/10.1016/j.medj.2022.12.001.
[193] X. Shan, X. Gong, J. Li, J. Wen, Y. Li, Z. Zhang, Current approaches of nanomedicines in the market and various stage of clinical translation, Acta Pharm. Sin. b. 12 (2022) 3028–3048, https://doi.org/10.1016/j.apsb.2022.02.025.
[194] K. Sato, H. Kawakami, Mitochondrial Dysfunction and Nanocarrier-Based Treatments in Chronic Obstructive Pulmonary Disease (COPD), Oxygen. 3 (2023) 394–406, https://doi.org/10.3390/oxygen3040026.
[195] Z. Xu, X. Chen, Z. Sun, C. Li, B. Jiang, Recent progress on mitochondrial targeted cancer therapy based on inorganic nanomaterials, Mater. Today Chem. 12 (2019) 240–260, https://doi.org/10.1016/j.mtchem.2019.02.004.
[196] Y. Liu, Y. Huang, C. Xu, P. An, Y. Luo, L. Jiao, J. Luo, Y. Li, Mitochondrial Dysfunction and Therapeutic Perspectives in Cardiovascular Diseases, Int. J. Mol. Sci. 23 (2022), https://doi.org/10.3390/ijms232416053.
[197] Y. Zhang, H. Yang, D. Wei, X. Zhang, J. Wang, X. Wu, J. Chang, Mitochondria-targeted nanoparticles in treatment of neurodegenerative diseases, Exploration. 1 (2021) 20210115, https://doi.org/10.1002/EXP.20210115.
[198] L.F. González, L.E. Bevilacqua, R. Naves, Nanotechnology-Based Drug Delivery Strategies to Repair the Mitochondrial Function in Neuroinflammatory and Neurodegenerative Diseases, Pharmaceutics. 13 (2021), https://doi.org/10.3390/pharmaceutics13122055.
[199] L. Fang, H. Fan, C. Guo, L. Cui, P. Zhang, H. Mu, H. Xu, F. Zhao, D. Chen, Novel Mitochondrial Targeting Multifunctional Surface Charge-Reversal Polymeric Nanoparticles for Cancer Treatment, J. Biomed. Nanotechnol. 15 (2019) 2151–2163, https://doi.org/10.1166/jbn.2019.2854.
[200] Y. Deng, F. Jia, X. Chen, Q. Jin, J. Ji, ATP Suppression by pH-Activated Mitochondria-Targeted Delivery of Nitric Oxide Nanoplatform for Drug Resistance Reversal and Metastasis Inhibition, Small 16 (2020), https://doi.org/10.1002/smll.202001747.
[201] X. Zhang, Y. Wang, G. Wei, J. Zhao, G. Yang, S. Zhou, Stepwise dual targeting and dual responsive polymer micelles for mitochondrion therapy, J. Control. Release. 322 (2020) 157–169, https://doi.org/10.1016/j.jconrel.2020.03.011.
[202] P. Ma, J. Chen, X. Bi, Z. Li, X. Gao, H. Li, H. Zhu, Y. Huang, J. Qi, Y. Zhang, Overcoming Multidrug Resistance through the GLUT1-Mediated and Enzyme-Triggered Mitochondrial Targeting Conjugate with Redox-Sensitive Paclitaxel Release, ACS Appl. Mater. Interfaces. 10 (2018) 12351–12363, https://doi.org/10.1021/acsami.7b18437.
[203] A. Sharma, K. Liaw, R. Sharma, A. Thomas, B. Slusher, S. Kannan, R. Kannan, Targeting Mitochondria in Tumor-Associated Macrophages using a Dendrimer Conjugated TSPO Ligand Stimulates Anti-Tumor Signaling in Glioblastoma, Biomacromolecules XXXX (2020), https://doi.org/10.1021/acs.biomac.0c01033.
[204] Y. Zhang, H. Zhang, F. Zhao, Z. Jiang, Mitochondrial-targeted and ROS-responsive nanocarrier via nose-to-brain pathway for ischemic stroke treatment, Acta Pharm. Sin. b. (2023), https://doi.org/10.1016/j.apsb.2023.06.011.
[205] W. Sun, L. Li, L. Li, Q. Yang, Z. Zhang, Y. Huang, Two birds, one stone: dual targeting of the cancer cell surface and subcellular mitochondria by the galectin-3-binding peptide G3–C12, Acta Pharmacol. Sin. 38 (2017) 806–822, https://doi.org/10.1038/aps.2016.137.
[206] X. Jin, L. Li, Q. Peng, C. Gan, L. Gao, S. He, S. Tan, W. Pu, Y. Liu, Y. Gong, Y. Yao, G. Wang, X. Liu, M. Gong, P. Lei, H. Zhang, S. Qi, H. Xu, H. Hu, B. Dong, Y. Peng, D. Su, L. Dai, Glycyrrhetinic acid restricts mitochondrial energy metabolism by

targeting SHMT2, Iscience. 25 (2022), https://doi.org/10.1016/j.isci.2022.104349.
[207] Y. Liu, Z. Zhou, X. Lin, X. Xiong, R. Zhou, M. Zhou, Y. Huang, Enhanced Reactive Oxygen Species Generation by Mitochondria Targeting of Anticancer Drug To Overcome Tumor Multidrug Resistance, Biomacromolecules 20 (2019) 3755–3766, https://doi.org/10.1021/acs.biomac.9b00800.
[208] Y. Geng, Y. Zhong, Q. Zhou, S. Chen, Y. Piao, W. Yin, H. Lu, Y. Shen, A neutral water-soluble mitochondria-targeting polymer, Chem. Commun. 55 (2019) 10015–10018, https://doi.org/10.1039/c9cc04291a.
[209] Y. Liu, J. Zhang, Y. Tu, L. Zhu, Potential-Independent Intracellular Drug Delivery and Mitochondrial Targeting, ACS Nano 16 (2022) 1409–1420, https://doi.org/10.1021/acsnano.1c09456.
[210] Y. Zhang, X. He, Y. Zhang, Y. Zhao, S. Lu, Y. Peng, L. Lu, X. Hu, M. Zhan, Native Mitochondria-Targeting polymeric nanoparticles for mild photothermal therapy rationally potentiated with immune checkpoints blockade to inhibit tumor recurrence and metastasis, 424 (2021). 10.1016/j.cej.2021.130171.
[211] I. Cohen-Erez, C. Issacson, Y. Lavi, R. Shaco-Levy, J. Milam, B. Laster, L. A. Gheber, H. Rapaport, Antitumor effect of lonidamine-polypeptide-peptide nanoparticles in breast cancer models, ACS Appl. Mater. Interfaces. 11 (2019) 32670–32678, https://doi.org/10.1021/acsami.9b09886.
[212] Y. Yamada, R. Munechika, F. Satrialdi, Y. Kubota, Y. Sato, H.H. Sakurai, Mitochondrial delivery of an anticancer drug via systemic administration using a mitochondrial delivery system that inhibits the growth of drug-resistant cancer engrafted on mice, J. Pharm. Sci. 109 (2020) 2493–2500, https://doi.org/10.1016/j.xphs.2020.04.020.
[213] Satrialdi, Y. Takano, E. Hirata, N. Ushijima, H. Harashima, Y. Yamada, An effective in vivo mitochondria-targeting nanocarrier combined with a π-extended porphyrin-type photosensitizer, Nanoscale Adv. 3 (2021) 5919–5927, https://doi.org/10.1039/D1NA00427A.
[214] M. Shi, J. Zhang, X. Li, S. Pan, J. Li, C. Yang, H. Hu, M. Qiao, D. Chen, X. Zhao, Mitochondria-targeted delivery of doxorubicin to enhance antitumor activity with HER-2 peptide-mediated multifunctional pH-sensitive DQAsomes, Int. J. Nanomedicine. 13 (2018) 4209–4226, https://doi.org/10.2147/IJN.S163858.
[215] J. Yan, J. Guo, Y. Wang, X. Xing, X. Zhang, G. Zhang, Z. Dong, Acute myocardial infarction therapy using calycosin and tanshinone co-loaded; mitochondrion-targeted tetrapeptide and cyclic arginyl-glycyl-aspartic acid peptide co-modified lipid-polymer hybrid nano-system: preparation, characterization, and anti myocard, Drug Deliv. 29 (2022) 2815–2823, https://doi.org/10.1080/10717544.2022.2118401.
[216] W. Zhou, H. Yu, L.J. Zhang, B. Wu, C.X. Wang, Q. Wang, K. Deng, R.X. Zhuo, S. W. Huang, Redox-triggered activation of nanocarriers for mitochondria-targeting cancer chemotherapy, Nanoscale 9 (2017) 17044–17053, https://doi.org/10.1039/c7nr06130g.
[217] M. Tang, K. Lin, M. Ramachandran, L. Li, H. Zou, H. Zheng, Z. Ma, Y. Li, A mitochondria-targeting lipid–small molecule hybrid nanoparticle for imaging and therapy in an orthotopic glioma model, Acta Pharm. Sin. b. 12 (2022) 2672–2682, https://doi.org/10.1016/j.apsb.2022.04.005.
[218] X. Lin, L. Li, S. Li, Q. Li, D. Xie, M. Zhou, Y. Huang, Targeting the opening of mitochondrial permeability transition pores potentiates nanoparticle drug delivery and mitigates cancer metastasis, Adv. Sci. 8 (2021) 2002834, https://doi.org/10.1002/advs.202002834.
[219] M. Zhang, X. Chen, C. Li, X. Shen, Charge-reversal nanocarriers: An emerging paradigm for smart cancer nanomedicine, J. Control. Release. 319 (2020) 46–62, https://doi.org/10.1016/j.jconrel.2019.12.024.
[220] P. Joshi, K. Verma, D. Kumar Semwal, J. Dwivedi, S. Sharma, Mechanism insights of curcumin and its analogues in cancer: An update, Phyther. Res. n/a (2023), https://doi.org/10.1002/ptr.7983.
[221] S. Uno, A.H. Harkiss, R. Chowdhury, S.T. Caldwell, T.A. Prime, A.M. James, B. Gallagher, J. Prudent, R.C. Hartley, M.P. Murphy, Incorporating a Polyethyleneglycol Linker to Enhance the Hydrophilicity of Mitochondria-Targeted Triphenylphosphonium Constructs, Chembiochem 24 (2023) e202200774, https://doi.org/10.1002/cbic.202200774.
[222] M.P. Murphy, Targeting lipophilic cations to mitochondria, Biochim. Biophys. Acta - Bioenerg. 1777 (2008) 1028–1031, https://doi.org/10.1016/j.bbabio.2008.03.029.
[223] N.H. Bhoola, Z. Mbita, R. Hull, Z. Dlamini, Translocator Protein (TSPO) as a Potential Biomarker in Human Cancers, Int. J. Mol. Sci. 19 (2018), https://doi.org/10.3390/ijms19082176.
[224] Y. Lee, Y. Park, H. Nam, J.-W. Lee, S.-W. Yu, Translocator protein (TSPO): the new story of the old protein in neuroinflammation, BMB Rep. 53 (2020) 20–27, https://doi.org/10.5483/BMBRep.2020.53.1.273.
[225] L.-M. Ammer, A. Vollmann-Zwerenz, V. Ruf, C.H. Wetzel, M.J. Riemenschneider, N.L. Albert, P. Beckhove, P. Hau, The Role of Translocator Protein TSPO in Hallmarks of Glioblastoma, Cancers (basel). 12 (2020), https://doi.org/10.3390/cancers12102973.
[226] F. Liu, J. Lu, A. Manaenko, J. Tang, Q. Hu, Mitochondria in Ischemic Stroke: New Insight and Implications, Aging Dis. 9 (2018) 924–937, https://doi.org/10.14336/ad.2017.1126.
[227] P. Ramos-Cabrer, F. Campos, T. Sobrino, J. Castillo, Targeting the ischemic penumbra, Stroke 42 (2011) S7–S11, https://doi.org/10.1161/STROKEAHA.110.596684.
[228] W. Zhao, Z. Xu, J. Cao, Q. Fu, Y. Wu, X. Zhang, Y. Long, X. Zhang, Elamipretide (SS-31) improves mitochondrial dysfunction , synaptic and memory impairment induced by lipopolysaccharide in, mice 9 (2019) 1–19, https://doi.org/10.1186/s12974-019-1627-9.
[229] J. Jin, P. Yuan, W. Yu, J. Lin, A. Xu, X. Xu, J. Lou, T. Yu, C. Qian, B. Liu, J. Song, L. Li, Y. Piao, T. Xie, Y. Shen, H. Tao, J. Tang, Mitochondria-Targeting Polymer Micelle of Dichloroacetate Induced Pyroptosis to Enhance Osteosarcoma Immunotherapy, ACS Nano 16 (2022) 10327–10340, https://doi.org/10.1021/acsnano.2c00192.
[230] I. Cohen-Erez, H. Rapaport, Coassemblies of the Anionic Polypeptide γ-PGA and Cationic β-Sheet Peptides for Drug Delivery to Mitochondria, Biomacromolecules 16 (2015) 3827–3835, https://doi.org/10.1021/acs.biomac.5b01140.
[231] Y. Yasuzaki, Y. Yamada, H. Harashima, Mitochondrial matrix delivery using MITO-Porter, a liposome-based carrier that specifies fusion with mitochondrial membranes, Biochem. Biophys. Res. Commun. 397 (2010) 181–186, https://doi.org/10.1016/j.bbrc.2010.05.070.
[232] Y. Yamada, H. Akita, H. Kamiya, K. Kogure, T. Yamamoto, Y. Shinohara, K. Yamashita, H. Kobayashi, H. Kikuchi, H. Harashima, MITO-Porter: A liposome-based carrier system for delivery of macromolecules into mitochondria via membrane fusion, Biochim. Biophys. Acta - Biomembr. 1778 (2008) 423–432, https://doi.org/10.1016/j.bbamem.2007.11.002.
[233] I.A. Khalil, K. Kogure, S. Futaki, H. Harashima, High density of octaarginine stimulates macropinocytosis leading to efficient intracellular trafficking for gene expression, J. Biol. Chem. 281 (2006) 3544–3551, https://doi.org/10.1074/jbc.M503202200.
[234] T. Rogasevskaia, J. Coorssen, Sphingomyelin-enriched microdomains define the efficiency of native Ca2+-triggered membrane fusion, J. Cell Sci. 119 (2006) 2688–2694, https://doi.org/10.1242/jcs.03007.
[235] M.A. Zhukovsky, A. Filograna, A. Luini, D. Corda, C. Valente, Phosphatidic acid in membrane rearrangements, FEBS Lett. 593 (2019) 2428–2451, https://doi.org/10.1002/1873-3468.13563.
[236] Y. Yamada, R. Furukawa, Y. Yasuzaki, H. Harashima, Dual function MITO-Porter, a nano carrier integrating both efficient cytoplasmic delivery and mitochondrial macromolecule delivery, Mol. Ther. 19 (2011) 1449–1456, https://doi.org/10.1038/mt.2011.99.
[237] E. Kawamura, Y. Yamada, H. Harashima, Mitochondrial targeting functional peptides as potential devices for the mitochondrial delivery of a DF-MITO-Porter, Mitochondrion 13 (2013) 610–614, https://doi.org/10.1016/j.mito.2013.08.010.
[238] V. Weissig, J. Lasch, G. Erdos, H.W. Meyer, T.C. Rowe, J. Hughes, DQAsomes: A Novel Potential Drug and Gene Delivery System Made from Dequalinium™, Pharm. Res. 15 (1998) 334–337, https://doi.org/10.1023/A:1011991307631.
[239] V. Weissig, G.G.M. D'Souza, V.P. Torchilin, DQAsome/DNA complexes release DNA upon contact with isolated mouse liver mitochondria, J. Control. Release. 75 (2001) 401–408, https://doi.org/10.1016/S0168-3659(01)00392-3.
[240] G.G.M. D'Souza, S.M. Cheng, S. Boddapati, R.W. Horobin, V. Weissig, Nanocarrier-assisted sub-cellular targeting to the site of mitochondria improves the pro-apoptotic activity of paclitaxel, J. Drug Target. 16 (2008) 578–585, https://doi.org/10.1080/10611860802228855.
[241] A. Drugs, S. Cheng, S. V Boddapati, G.M.D. Souza, V. Weissig, DQAsomes as Mitochondria- Targeted Nanocarriers for Anti-Cancer Drugs, (2007).
[242] Y. Bae, M.K. Jung, S.J. Song, E.S. Green, S. Lee, H.S. Park, S.H. Jeong, J. Han, J. Y. Mun, K.S. Ko, J.S. Choi, Functional nanosome for enhanced mitochondria-targeted gene delivery and expression, Mitochondrion 37 (2017) 27–40, https://doi.org/10.1016/j.mito.2017.06.005.
[243] A. Mukherjee, A.K. Waters, P. Kalyan, A.S. Achrol, S. Kesari, V.M. Yenugonda, Lipid-polymer hybrid nanoparticles as a nextgeneration drug delivery platform: State of the art, emerging technologies, and perspectives, Int. J. Nanomedicine. 14 (2019) 1937–1952, https://doi.org/10.2147/IJN.S198353.
[244] K. Lin, Z. Ma, J. Li, M. Tang, A. Lindstrom, M. Ramachandran, S. Zhu, T. Lin, L. Zhang, Y. Li, Single small molecule-assembled mitochondria targeting nanofibers for enhanced photodynamic cancer therapy in vivo, Adv. Funct. Mater. 31 (2021) 2008460, https://doi.org/10.1002/adfm.202008460.
[245] D. Liu, G. Shu, F. Jin, J. Qi, X. Xu, Y. Du, H. Yu, J. Wang, M. Sun, Y. You, M. Zhu, M. Chen, L. Zhu, Q. Shen, X. Ying, X. Lou, S. Jiang, Y. Du, ROS-responsive chitosan-SS31 prodrug for AKI therapy via rapid distribution in the kidney and long-term retention in the renal tubule, Sci. Adv. 6 (2023) eabb7422, https://doi.org/10.1126/sciadv.abb7422.
[246] D.-B. Cheng, X.-H. Zhang, Y.-J. Gao, L. Ji, D. Hou, Z. Wang, W. Xu, Z.-Y. Qiao, H. Wang, Endogenous reactive oxygen species-triggered morphology transformation for enhanced cooperative interaction with mitochondria, J. Am. Chem. Soc. 141 (2019) 7235–7239, https://doi.org/10.1021/jacs.8b07727.
[247] J.F. Mukerabigwi, R. Tang, Y. Cao, F. Mohammed, Q. Zhou, M. Zhou, Z. Ge, Mitochondria-targeting polyprodrugs to overcome the drug resistance of cancer cells by self-amplified oxidation-triggered drug release, Bioconjug. Chem. 34 (2023) 377–391, https://doi.org/10.1021/acs.bioconjchem.2c00559.
[248] Z. Zeng, Y. Luo, X. Xu, T. Shan, M. Chen, Z. Huang, Y. Huang, C. Zhao, A mitochondria-targeting ROS-activated nanoprodrug for self-augmented antitumor oxidation therapy, J. Control. Release. 359 (2023) 415–427, https://doi.org/10.1016/j.jconrel.2023.06.004.
[249] W. Zhang, X. Hu, Q. Shen, D. Xing, Mitochondria-specific drug release and reactive oxygen species burst induced by polyprodrug nanoreactors can enhance chemotherapy, Nat. Commun. 10 (2019) 1704, https://doi.org/10.1038/s41467-019-09566-3.
[250] Z. Zheng, C. Lei, H. Liu, M. Jiang, Z. Zhou, Y. Zhao, C.-Y. Yu, H. Wei, A ROS-Responsive liposomal composite hydrogel integrating improved mitochondrial function and pro-angiogenesis for efficient treatment of myocardial infarction, Adv. Healthc. Mater. 11 (2022) 2200990, https://doi.org/10.1002/adhm.202200990.
[251] T. Lan, H. Guo, X. Lu, K. Geng, L. Wu, Y. Luo, J. Zhu, X. Shen, Q. Guo, S. Wu, Dual-responsive curcumin-loaded nanoparticles for the treatment of cisplatin-

induced acute kidney injury, Biomacromolecules 23 (2022) 5253–5266, https://doi.org/10.1021/acs.biomac.2c01083.
[252] Y. Zou, Y. Sun, Y. Wang, D. Zhang, H. Yang, X. Wang, M. Zheng, B. Shi, Cancer cell-mitochondria hybrid membrane coated Gboxin loaded nanomedicines for glioblastoma treatment, Nat. Commun. 14 (2023) 4557, https://doi.org/10.1038/s41467-023-40280-3.
[253] L. Ruan, J. Chen, C. Du, H. Lu, J. Zhang, X. Cai, R. Dou, W. Lin, Z. Chai, G. Nie, Y. Hu, Mitochondrial temperature-responsive drug delivery reverses drug resistance in lung cancer, Bioact. Mater. 13 (2022) 191–199, https://doi.org/10.1016/j.bioactmat.2021.10.045.
[254] Y. Tan, Y. Zhu, Y. Zhao, L. Wen, T. Meng, X. Liu, X. Yang, S. Dai, H. Yuan, F. Hu, Mitochondrial alkaline pH-responsive drug release mediated by Celastrol loaded glycolipid-like micelles for cancer therapy, Biomaterials 154 (2018) 169–181, https://doi.org/10.1016/j.biomaterials.2017.07.036.
[255] H.A. Prag, D. Kula-Alwar, L. Pala, S.T. Caldwell, T.E. Beach, A.M. James, K. Saeb-Parsy, T. Krieg, R.C. Hartley, M.P. Murphy, selective delivery of dicarboxylates to mitochondria by conjugation to a lipophilic cation via a cleavable linker, Mol. Pharm. 17 (2020) 3526–3540, https://doi.org/10.1021/acs.molpharmaceut.0c00533.
[256] Z. Liu, Z. Ren, J. Zhang, C.-C. Chuang, E. Kandaswamy, T. Zhou, L. Zuo, Role of ROS and nutritional antioxidants in human diseases, Front. Physiol. 9 (2018) 477, https://doi.org/10.3389/fphys.2018.00477.
[257] A. Rinaldi, R. Caraffi, M.V. Grazioli, N. Oddone, L. Giardino, G. Tosi, M. A. Vandelli, L. Calzà, B. Ruozi, J.T. Duskey, Applications of the ROS-responsive thioketal linker for the production of smart nanomedicines, Polymers (basel). 14 (2022), https://doi.org/10.3390/polym14040687.
[258] J. Liang, B. Liu, ROS-responsive drug delivery systems, Bioeng. Transl. Med. 1 (2016) 239–251, https://doi.org/10.1002/btm2.10014.
[259] J. Liu, B. Jia, Z. Li, W. Li, Reactive oxygen species-responsive polymer drug delivery systems, Front. Bioeng Biotechnol. 11 (2023) 1–11, https://doi.org/10.3389/fbioe.2023.1115603.
[260] D. Jeanmaire, J. Laliturai, A. Almalik, P. Carampin, R. d'Arcy, E. Lallana, R. Evans, R.E.P. Winpenny, N. Tirelli, Chemical specificity in REDOX-responsive materials: the diverse effects of different Reactive Oxygen Species (ROS) on polysulfide nanoparticles, Polym. Chem. 5 (2014) 1393–1404, https://doi.org/10.1039/C3PY01475D.
[261] A. Siani, L. Infante-Teixeira, R. d'Arcy, I.V. Roberts, F. El Mohtadi, R. Donno, N. Tirelli, Polysulfide nanoparticles inhibit fibroblast-to-myofibroblast transition via extracellular ROS scavenging and have potential anti-fibrotic properties, Biomater. Adv. 153 (2023) 213537, https://doi.org/10.1016/j.bioadv.2023.213537.
[262] A. Rehor, H. Schmoekel, N. Tirelli, J.A. Hubbell, Functionalization of polysulfide nanoparticles and their performance as circulating carriers, Biomaterials 29 (2008) 1958–1966, https://doi.org/10.1016/j.biomaterials.2007.12.035.
[263] H.J. Lee, B. Jeong, ROS-sensitive degradable PEG–PCL–PEG micellar thermogel, Small 16 (2020) 1903045, https://doi.org/10.1002/smll.201903045.
[264] Y. Huang, Q. Chen, P. Ma, H. Song, X. Ma, Y. Ma, X. Zhou, S. Gou, Z. Xu, J. Chen, B. Xiao, Facile fabrication of oxidation-responsive polymeric nanoparticles for effective anticancer drug delivery, Mol. Pharm. 16 (2019) 49–59, https://doi.org/10.1021/acs.molpharmaceut.8b00634.
[265] D. Wang, M. Zhou, H. Huang, L. Ruan, H. Lu, J. Zhang, J. Chen, J. Gao, Z. Chai, Y. Hu, Gold nanoparticle-based probe for analyzing mitochondrial temperature in living cells, ACS Appl. Bio Mater. 2 (2019) 3178–3182, https://doi.org/10.1021/acsabm.9b00463.
[266] D. Chrétien, P. Bénit, H.-H. Ha, S. Keipert, R. El-Khoury, Y.-T. Chang, M. Jastroch, H.T. Jacobs, P. Rustin, M. Rak, Mitochondria are physiologically maintained at close to 50 °C, PLOS Biol. 16 (2018) e2003992, doi: 10.1371/journal.pbio.2003992.
[267] X. Xu, Y. Liu, W. Fu, M. Yao, Z. Ding, J. Xuan, D. Li, S. Wang, Y. Xia, M. Cao, Poly (N-isopropylacrylamide)-based thermoresponsive composite hydrogels for biomedical applications, Polymers (basel). 12 (2020), https://doi.org/10.3390/polym12030580.
[268] Y. Yamada, Y. Fukuda, D. Sasaki, M. Maruyama, H. Harashima, Development of a nanoparticle that releases nucleic acids in response to a mitochondrial environment, Mitochondrion 52 (2020) 67–74, https://doi.org/10.1016/j.mito.2020.02.009.
[269] L.E. Franken, K. Grünewald, E.J. Boekema, M.C.A. Stuart, A technical introduction to transmission electron microscopy for soft-matter: Imaging, Possibilities, Choices, and Technical Developments, Small. 16 (2020) 1906198, https://doi.org/10.1002/smll.201906198.
[270] M. Reifarth, S. Hoeppener, U.S. Schubert, Uptake and intracellular fate of engineered nanoparticles in mammalian cells: Capabilities and limitations of transmission electron microscopy—polymer-based nanoparticles, Adv. Mater. 30 (2018) 1703704, https://doi.org/10.1002/adma.201703704.
[271] M. Malatesta, Transmission electron microscopy as a powerful tool to investigate the interaction of nanoparticles with subcellular structures, Int. J. Mol. Sci. 22 (2021), https://doi.org/10.3390/ijms222312789.
[272] H. Kurata, Advantages of elemental mapping by high-voltage EFTEM, Ultramicroscopy 78 (1999) 233–240, https://doi.org/10.1016/S0304-3991(99)00023-6.
[273] P. de Boer, J.P. Hoogenboom, B.N.G. Giepmans, Correlated light and electron microscopy: ultrastructure lights up!, Nat. Methods. 12 (2015) 503–513, https://doi.org/10.1038/nmeth.3400.
[274] S. Han, M. Raabe, L. Hodgson, J. Mantell, P. Verkade, T. Lasser, K. Landfester, T. Weil, I. Lieberwirth, High-contrast imaging of nanodiamonds in cells by energy filtered and correlative light-electron microscopy: Toward a quantitative nanoparticle-cell analysis, Nano Lett. 19 (2019) 2178–2185, https://doi.org/10.1021/acs.nanolett.9b00752.
[275] J.-B. Guilbaud, A. Saiani, Using small angle scattering (SAS) to structurally characterise peptide and protein self-assembled materials, Chem. Soc. Rev. 40 (2011) 1200–1210, https://doi.org/10.1039/C0CS00105H.
[276] M.J. Sanderson, I. Smith, I. Parker, M.D. Bootman, Fluorescence microscopy, Cold Spring Harb. Protoc. 2014 (2014) 1042–1065, https://doi.org/10.1101/pdb.top071795.
[277] A.D. Elliott, Confocal microscopy: Principles and modern practices, Curr. Protoc. Cytom. 92 (2020) e68.
[278] A. Canette, R. Briandet, Microscopy: Confocal laser scanning microscopy, in: Encycl. Food Microbiol., Second Ed., 2014, pp. 676–683, 10.1016/B978-0-12-384730-0.00214-7.
[279] P.E.Z. Klier, J.G. Martin, E.W. Miller, Imaging reversible mitochondrial membrane potential dynamics with a masked rhodamine voltage reporter, J. Am. Chem. Soc. 143 (2021) 4095–4099, https://doi.org/10.1021/jacs.0c13110.
[280] S. Samanta, Y. He, A. Sharma, J. Kim, W. Pan, Z. Yang, J. Li, W. Yan, L. Liu, J. Qu, J.S. Kim, Fluorescent probes for nanoscopic imaging of mitochondria, Chem 5 (2019) 1697–1726, https://doi.org/10.1016/j.chempr.2019.03.011.
[281] L.de B. Monteiro, G.G. Davanzo, C.F. de Aguiar, P.M.M. Moraes-Vieira, Using flow cytometry for mitochondrial assays, MethodsX. 7 (2020), https://doi.org/10.1016/j.mex.2020.100938.
[282] W.R. Algar, N. Hildebrandt, S.S. Vogel, I.L. Medintz, FRET as a biomolecular research tool — understanding its potential while avoiding pitfalls, Nat. Methods. 16 (2019) 815–829, https://doi.org/10.1038/s41592-019-0530-8.
[283] A. Kaur, P. Kaur, S. Ahuja, Förster resonance energy transfer (FRET) and applications thereof, Anal. Methods. 12 (2020) 5532–5550, https://doi.org/10.1039/d0ay01961e.
[284] H. Kobayashi, L.-P. Picard, A.-M. Schönegge, M. Bouvier, Bioluminescence resonance energy transfer–based imaging of protein–protein interactions in living cells, Nat. Protoc. 14 (2019) 1084–1107, https://doi.org/10.1038/s41596-019-0129-7.
[285] V. Hertlein, H. Flores-Romero, K.K. Das, S. Fischer, M. Heunemann, M. Calleja-Felipe, S. Knafo, K. Hipp, K. Harter, J.C. Fitzgerald, A.J. García-Sáez, MERLIN: a novel BRET-based proximity biosensor for studying mitochondria–ER contact sites, Life Sci. Alliance. 3 (2020) e201900600, https://doi.org/10.26508/lsa.201900600.
[286] G.H. Hogeboom, W.C. Schneider, G.E. Pallade, Cytochemical Studies of Mammalian Tissues, J. Biol. Chem. 172 (1948) 619–635, https://doi.org/10.1016/s0021-9258(19)52749-1.
[287] W.W. Chen, E. Freinkman, D.M. Sabatini, Rapid immunopurification of mitochondria for metabolite profiling and absolute quantification of matrix metabolites, Nat. Protoc. 12 (2017), https://doi.org/10.1038/nprot.2017.104.Rapid.
[288] P. Azimzadeh, H.A. Aghdaei, P. Tarban, M.M. Akhondi, A. Shirazi, H.R. K. Khorshid, Comparison of three methods for mitochondria isolation from the human liver cell line (HepG2), Gastroenterol. Hepatol. from Bed to Bench. 9 (2016) 105–113, https://doi.org/10.22037/ghfbb.v9i2.787.
[289] A.G. Bury, A.E. Vincent, D.M. Turnbull, P. Actis, G. Hudson, Mitochondrial isolation: when size matters, Wellcome Open Res. 5 (2020) 226, https://doi.org/10.12688/wellcomeopenres.16300.2.
[290] W. Kang, R.L. McNaughtonb, H.D. Espinosaa, Micro- and nano-scale technologies for delivery into adherent cells, Trends Biotechnol 34 (2016), https://doi.org/10.1016/j.tibtech.2016.05.003.
[291] G.H. Meftahi, Z. Bahari, A. Zarei Mahmoudabadi, M. Iman, Z. Jangravi, Applications of western blot technique: From bench to bedside, Biochem. Mol. Biol. Educ. 49 (2021) 509–517, https://doi.org/10.1002/bmb.21516.
[292] R.M. Guijt, Lab on a chip - future technology for characterizing biotechnology products, Third edit, Elsevier, 2019.
[293] J.P. Shockcor, HPLC-NMR, pharmaceutical applications, 3rd ed., Elsevier Ltd., 2016.
[294] P. Gurpur Rakesh D., E. R. Williams, M. Wilm, P. L. Urban, Mass spectrometry using electrospray ionization, Nat. Rev. Methods Prim. 3 (2023). doi:10.1038/s43586-023-00203-4.
[295] C.A. Reddy, V. Somepalli, T. Golakoti, A.K.R. Kanugula, S. Karnewar, K. Rajendiran, N. Vasagiri, S. Prabhakar, P. Kuppusamy, S. Kotamraju, V. K. Kutala, Mitochondrial-targeted curcuminoids: A strategy to enhance bioavailability and anticancer efficacy of curcumin, PLoS One 9 (2014), https://doi.org/10.1371/journal.pone.0089351.
[296] S.C. Wilschefski, M.R. Baxter, Inductively coupled plasma mass spectrometry: Introduction to analytical aspects, Clin. Biochem. Rev. 40 (2019) 115–133, https://doi.org/10.33176/AACB-19-00024.
[297] S. Marrache, S. Dhar, Engineering of blended nanoparticle platform for delivery of mitochondria-acting therapeutics, Proc. Natl. Acad. Sci. U. S. A. 109 (2012) 16288–16293, https://doi.org/10.1073/pnas.1210096109.
[298] C. Zhang, Z. Tian, R. Chen, F. Rowan, K. Qiu, Y. Sun, J.-L. Guan, J. Diao, Advanced imaging techniques for tracking drug dynamics at the subcellular level, Adv. Drug Deliv. Rev. 199 (2023), https://doi.org/10.1016/j.addr.2023.114978.
[299] S. Jakobs, T. Stephan, P. Ilgen, C. Brüser, Light microscopy of mitochondria at the nanoscale, Annu. Rev. Biophys. 49 (2020) 289–308, https://doi.org/10.1146/annurev-biophys-121219-081550.
[300] W. Zou, L. Yang, H. Lu, M. Li, D. Ji, J. Slone, T. Huang, Application of super-resolution microscopy in mitochondria-dynamic diseases, Adv. Drug Deliv. Rev. 200 (2023) 115043, https://doi.org/10.1016/j.addr.2023.115043.
[301] M. Lelek, M.T. Gyparaki, G. Beliu, F. Schueder, J. Griffié, S. Manley, R. Jungmann, M. Sauer, M. Lakadamyali, C. Zimmer, Single-molecule localization

microscopy, Nat. Rev. Methods Prim. 1 (2021) 39, https://doi.org/10.1038/s43586-021-00038-x.
[302] A.R. Buchberger, K. DeLaney, J. Johnson, L. Li, Mass spectrometry imaging: A review of emerging advancements and future insights, Anal. Chem. 90 (2018) 240–265, https://doi.org/10.1021/acs.analchem.7b04733.
[303] D. Li, Z. Ouyang, X. Ma, Mass spectrometry imaging for single-cell or subcellular lipidomics: A review of recent advancements and future development, Molecules 28 (2023), https://doi.org/10.3390/molecules28062712.
[304] F.P.Y. Barre, R.M.A. Heeren, N. Ogrinc Potocnik, Mass spectrometry imaging in nanomedicine: unraveling the potential of MSI for the detection of nanoparticles in neuroscience, Curr. Pharm. Des. 23 (2017), https://doi.org/10.2174/1381612823666170111112550.
[305] L. Gu, Z. Duan, X. Li, X. Li, Y. Li, X. Li, G. Xu, P. Gao, H. Zhang, Z. Gu, J. Chen, Q. Gong, K. Luo, Enzyme-triggered deep tumor penetration of a dual-drug nanomedicine enables an enhanced cancer combination therapy, Bioact. Mater. 26 (2023) 102–115, https://doi.org/10.1016/j.bioactmat.2023.02.015.
[306] R.F.S. Lee, S. Theiner, A. Meibom, G. Koellensperger, B.K. Keppler, P.J. Dyson, Application of imaging mass spectrometry approaches to facilitate metal-based anticancer drug research, Metallomics 9 (2017) 365–381, https://doi.org/10.1039/c6mt00231e.
[307] F. Li, E.F. Fornasiero, T.M. Dankovich, V. Kluever, S.O. Rizzoli, A reliable approach for revealing molecular targets in secondary ion mass spectrometry, Int. J. Mol. Sci. 23 (2022), https://doi.org/10.3390/ijms23094615.
[308] D. Valenti, A. Atlante, Mitochondrial bioenergetics in different pathophysiological conditions 2.0, Int. J. Mol. Sci. 23 (2022), https://doi.org/10.3390/ijms23105552.
[309] H. Nakamura, K. Takada, Reactive oxygen species in cancer: Current findings and future directions, Cancer Sci. 112 (2021) 3945–3952, https://doi.org/10.1111/cas.15068.
[310] K. Vasan, M. Clutter, S. Fernandez Dunne, M.D. George, C.H. Luan, N.S. Chandel, I. Martínez-Reyes, Genes involved in maintaining mitochondrial membrane potential upon electron transport chain disruption, Front. Cell Dev. Biol. 10 (2022) 1–6, https://doi.org/10.3389/fcell.2022.781558.
[311] C.H. Chu, W.W. Tseng, C.M. Hsu, A.C. Wei, Image analysis of the mitochondrial network morphology with applications in cancer research, Front. Phys. 10 (2022) 1–16, https://doi.org/10.3389/fphy.2022.855775.
[312] N. Pfanner, B. Warscheid, N. Wiedemann, Mitochondrial proteins: from biogenesis to functional networks, Nat. Rev. Mol. Cell Biol. 20 (2019) 267–284, https://doi.org/10.1038/s41580-018-0092-0.
[313] C.M. Andrés, J.M. Pérez de la Lastra, C. Andrés Juan, F.J. Plou, E. Pérez-Lebeña, Superoxide anion chemistry—its role at the core of the innate immunity, Int. J. Mol. Sci. 24 (2023), https://doi.org/10.3390/ijms24031841.
[314] L. Zdrazilova, H. Hansikova, E. Gnaiger, Comparable respiratory activity in attached and suspended human fibroblasts, PLoS One 17 (2022) 1–13, https://doi.org/10.1371/journal.pone.0264496.
[315] B. Ebanks, N. Moisoi, L. Chakrabarti, A method to assess the mitochondrial respiratory capacity of complexes I and II from frozen tissue using the Oroboros O2k-FluoRespirometer, BioRxiv. (2022), https://doi.org/10.1101/2022.10.02.510534.
[316] G.W. Rogers, H. Trockmorton, S.E. Burroughs, Targeting energy metabolism for cancer therapeutic discovery using Agilent Seahorse XF technology, Agilent. (2019).
[317] Y.C. Kang, M. Son, S. Kang, S. Im, Y. Piao, K.S. Lim, M.Y. Song, K.S. Park, Y. H. Kim, Y.K. Pak, Cell-penetrating artificial mitochondria-targeting peptide-conjugated metallothionein 1A alleviates mitochondrial damage in Parkinson's disease models, Exp. Mol. Med. 50 (2018), https://doi.org/10.1038/s12276-018-0124-z.
[318] T. Tsujioka, D. Sasaki, A. Takeda, H. Harashima, Y. Yamada, Resveratrol-encapsulated mitochondria-targeting liposome enhances mitochondrial respiratory capacity in myocardial cells, Int. J. Mol. Sci. 23 (2022), https://doi.org/10.3390/ijms23010112.
[319] L.D. Zorova, V.A. Popkov, E.Y. Plotnikov, D.N. Silachev, I.B. Pevzner, S. S. Jankauskas, V.A. Babenko, S.D. Zorov, A.V. Balakireva, M. Juhaszova, S. J. Sollott, D.B. Zorov, Mitochondrial membrane potential, Anal. Biochem. 552 (2018) 50–59, https://doi.org/10.1016/j.ab.2017.07.009.
[320] D.E. Borchmann, T.P. Carberry, M. Weck, "Bio"-macromolecules: polymer-protein conjugates as emerging scaffolds for therapeutics, Macromol. Rapid Commun. 35 (2014) 27–43, https://doi.org/10.1002/marc.201300792.
[321] J.G. McCarron, C. Wilson, M.E. Sandison, M.L. Olson, J.M. Girkin, C. Saunter, S. Chalmers, From structure to function: Mitochondrial morphology, motion and shaping in vascular smooth muscle, J. Vasc. Res. 50 (2013) 357–371, https://doi.org/10.1159/000353883.
[322] M.C. Harwig, M.P. Viana, J.M. Egner, J.J. Harwig, M.E. Widlansky, S.M. Rafelski, R.B. Hill, Methods for imaging mammalian mitochondrial morphology: A prospective on MitoGraph, 2018. 10.1016/j.ab.2018.02.022.
[323] D.R. Stirling, M.J. Swain-Bowden, A.M. Lucas, A.E. Carpenter, B.A. Cimini, A. Goodman, Cell profiler 4: improvements in speed, utility and usability, BMC Bioinf. 22 (2021) 1–11, https://doi.org/10.1186/s12859-021-04344-9.
[324] S.K. Yang, A.M. Li, Y.C. Han, C.H. Peng, N. Song, M. Yang, M. Zhan, L.F. Zeng, P. A. Song, W. Zhang, S.Q. Tang, H. Zhang, Mitochondria-targeted peptide SS31 attenuates renal tubulointerstitial injury via inhibiting mitochondrial fission in diabetic mice, Oxid. Med. Cell. Longev. 2019 (2019), https://doi.org/10.1155/2019/2346580.
[325] C. Priesnitz, T. Becker, Pathways to balance mitochondrial translation and protein import, Genes Dev. 32 (2018) 1315–1320, https://doi.org/10.1101/GAD.317073.118.
[326] T. Eleftheriadis, G. Pissas, V. Liakopoulos, I. Stefanidis, Cytochrome c as a potentially clinical useful marker of mitochondrial and cellular damage, Front. Immunol. 7 (2016), https://doi.org/10.3389/fimmu.2016.00279.
[327] D. Umbrasas, R. Jokubka, A. Kaupinis, M. Valius, O. Arandarčikaitė, V. Borutaitė, Nitric oxide donor NOC-18-induced changes of mitochondrial phosphoproteome in rat cardiac ischemia model, Med. 55 (2019) 1–11, https://doi.org/10.3390/medicina55100631.
[328] K.H. Tsui, M.Y. Wu, L. Te Lin, Z.H. Wen, Y.H. Li, P.Y. Chu, C.J. Li, Disruption of mitochondrial homeostasis with artemisinin unravels anti-angiogenesis effects via auto-paracrine mechanisms, Theranostics. 9 (2019) 6631–6645, https://doi.org/10.7150/thno.33353.
[329] E. Cappelli, N. Bertola, S. Bruno, P. Degan, S. Regis, F. Corsolini, B. Banelli, C. Dufour, S. Ravera, A multidrug approach to modulate the mitochondrial metabolism impairment and relative oxidative stress in fanconi anemia complementation group a, Metabolites 12 (2022), https://doi.org/10.3390/metabo12010006.
[330] Y. Tang, S. Wang, Y. Li, C. Yuan, J. Zhang, Z. Xu, Y. Hu, H. Shi, S. Wang, Simultaneous glutamine metabolism and PD-L1 inhibition to enhance suppression of triple-negative breast cancer, J. Nanobiotechnology. 20 (2022) 1–10, https://doi.org/10.1186/s12951-022-01424-7.
[331] W.S. Lee, J.H. Kang, J.H. Lee, Y.S. Kim, J.J. Kim, H.S. Kim, H.W. Kim, U.S. Shin, B.E. Yoon, Improved gliotransmission by increasing intracellular Ca2+ via TRPV1 on multi-walled carbon nanotube platforms, J. Nanobiotechnology. 20 (2022) 1–16, https://doi.org/10.1186/s12951-022-01551-1.
[332] Y. Bian, W. Li, D.M. Kremer, P. Sajjakulnukit, S. Li, J. Crespo, Z.C. Nwosu, L. Zhang, A. Czerwonka, A. Pawłowska, H. Xia, J. Li, P. Liao, J. Yu, L. Vatan, W. Szeliga, S. Wei, S. Grove, J.R. Liu, K. McLean, M. Cieslik, A.M. Chinnaiyan, W. Zgodziński, G. Wallner, I. Wertel, K. Okła, I. Kryczek, C.A. Lyssiotis, W. Zou, Cancer SLC43A2 alters T cell methionine metabolism and histone methylation, Nature 585 (2020) 277–282, https://doi.org/10.1038/s41586-020-2682-1.
[333] S. Naz, A.J. Leiker, R. Choudhuri, O. Preston, A.L. Sowers, S. Gohain, J. Gamson, A. Mathias, C. Van Waes, J.A. Cook, J.B. Mitchell, Pharmacological inhibition of HSP90 radiosensitizes head and neck squamous cell carcinoma xenograft by inhibition of DNA damage repair, nucleotide metabolism, and radiation-induced tumor vasculogenesis, Int. J. Radiat. Oncol. Biol. Phys. 110 (2021) 1295–1305, https://doi.org/10.1016/j.ijrobp.2021.03.048.
[334] A. Tyagi, N. Sarodaya, K. Kaushal, A.P. Chandrasekaran, A.M. Antao, B. Suresh, B. H. Rhie, K.S. Kim, S. Ramakrishna, E3 ubiquitin ligase apc/ccdh1 regulation of phenylalanine hydroxylase stability and function, Int. J. Mol. Sci. 21 (2020) 1–19, https://doi.org/10.3390/ijms21239076.
[335] L. Zhou, J. Chen, Y. Sun, K. Chai, Z. Zhu, C. Wang, M. Chen, W. Han, X. Hu, R. Li, T. Yao, H. Li, C. Dong, S. Shi, A self-amplified nanocatalytic system for achieving "1 + 1 + 1 > 3" chemodynamic therapy on triple negative breast cancer, J. Nanobiotechnology. 19 (2021) 1–13, https://doi.org/10.1186/s12951-021-00998-y.
[336] T. Nagano, Y. Awai, S. Kuwaba, T. Osumi, K. Mio, T. Iwasaki, S. Kamada, Riboflavin transporter SLC52A1, a target of p53, suppresses cellular senescence by activating mitochondrial complex II, Mol. Biol. Cell. 32 (2021) 1–10, https://doi.org/10.1091/mbc.E21-05-0262.
[337] G.W. Rogers, L.P. Winer, A. Gao, J. Hynes, Revealing Cellular Metabolic Phenotype and Function Using Agilent XF Substrate Oxidation Stress Tests, Seahorse, Agil. (2020).
[338] K. Mamouni, J. Kim, B.L. Lokeshwar, G. Kallifatidis, Arrb1 regulates metabolic reprogramming to promote glycolysis in stem cell-like bladder cancer cells, Cancers (basel). 13 (2021), https://doi.org/10.3390/cancers13081809.
[339] Y.S. Sohn, A. Iosub-Amir, A.E. Cardenas, O. Karmi, M.D. Yahana, T. Gruman, L. Rowland, H.B. Marjault, L.J. Webb, R. Mittler, R. Elber, A. Friedler, R. Nechushtai, A peptide-derived strategy for specifically targeting the mitochondria and ER of cancer cells: a new approach in fighting cancer, Chem. Sci. 13 (2022) 6929–6941, https://doi.org/10.1039/d2sc01934e.
[340] M. Mussap, C. Loddo, C. Fanni, V. Fanos, Metabolomics in pharmacology - a delve into the novel field of pharmacometabolomics, Expert Rev. Clin. Pharmacol. 13 (2020) 115–134, https://doi.org/10.1080/17512433.2020.1713750.
[341] G.F. Giskeødegård, T.S. Madssen, L.R. Euceda, M.B. Tessem, S.A. Moestue, T. F. Bathen, NMR-based metabolomics of biofluids in cancer, NMR Biomed. 32 (2019) 1–12, https://doi.org/10.1002/nbm.3927.
[342] A. Zhang, H. Sun, H. Xu, S. Qiu, X. Wang, Cell metabolomics, Omi. A J. Integr. Biol. 17 (2013) 495–501, https://doi.org/10.1089/omi.2012.0090.
[343] M. Saoi, P. Britz-Mckibbin, New advances in tissue metabolomics: A review, Metabolites 11 (2021), https://doi.org/10.3390/metabo11100672.
[344] S. Qin, Y. Zhang, Y. Tian, F. Xu, P. Zhang, Subcellular metabolomics: Isolation, measurement, and applications, J. Pharm. Biomed. Anal. 210 (2022), https://doi.org/10.1016/j.jpba.2021.114557.
[345] J. Folch, M. Lees, G.H. Sloane Stanley, A simple method for the isolation and purification of total lipides from animal tissues, J. Biol. Chem. 226 (1957) 497–509, https://doi.org/10.1016/s0021-9258(18)64849-5.
[346] G. van der Walt, R. Louw, Novel mitochondrial and cytosolic purification pipeline for compartment-specific metabolomics in mammalian disease model tissues, Metabolomics 16 (2020) 78, https://doi.org/10.1007/s11306-020-01697-9.
[347] G. van der Walt, J.Z. Lindeque, S. Mason, R. Louw, Sub-cellular metabolomics contributes mitochondria-specific metabolic insights to a mouse model of leigh syndrome, Metabolites 11 (2021), https://doi.org/10.3390/metabo11100658.
[348] W.J. Xu, H. Wen, H.S. Kim, Y.-J. Ko, S.-M. Dong, I.-S. Park, J.I. Yook, S. Park, Observation of acetyl phosphate formation in mammalian mitochondria using real-time in-organelle NMR metabolomics, Proc. Natl. Acad. Sci. 115 (2018) 4152–4157, https://doi.org/10.1073/pnas.1720908115.

[349] L. Kappler, J. Li, H.-U. Häring, C. Weigert, R. Lehmann, G. Xu, M. Hoene, Purity matters: A workflow for the valid high-resolution lipid profiling of mitochondria from cell culture samples, Sci. Rep. 6 (2016) 21107, https://doi.org/10.1038/srep21107.
[350] T. Nomiyama, D. Setoyama, T. Yasukawa, D. Kang, Mitochondria metabolomics reveals a role of β-nicotinamide mononucleotide metabolism in mitochondrial DNA replication, J. Biochem. 171 (2022) 325–338, https://doi.org/10.1093/jb/mvab136.
[351] J.-C. Matuszczyk, A. Teleki, J. Pfizenmaier-Wu, R. Takors, Compartment-specific metabolomics for CHO reveals that ATP pools in mitochondria are much lower than in cytosol, Biotechnol. J. 10 (2015), https://doi.org/10.1002/biot.201500060.
[352] Q. Long, L. Huang, K. Huang, Q. Yang, Assessing mitochondrial bioenergetics in isolated mitochondria from mouse heart tissues using oroboros 2k-Oxygraph, Methods Mol. Biol. (2019) 237–246, https://doi.org/10.1007/978-1-4939-9195-2_19.
[353] J.R. Roede, Y. Park, S. Li, F.H. Strobel, D.P. Jones, Detailed mitochondrial phenotyping by high resolution metabolomics, PLoS One 7 (2012) e33020, https://doi.org/10.1371/journal.pone.0033020.
[354] E.C. Bayraktar, L. Baudrier, C. Özerdem, C.A. Lewis, S.H. Chan, T. Kunchok, M. Abu-Remaileh, A.L. Cangelosi, D.M. Sabatini, K. Birsoy, W.W. Chen, MITO-Tag Mice enable rapid isolation and multimodal profiling of mitochondria from specific cell types in vivo, Proc. Natl. Acad. Sci. 116 (2019) 303–312, https://doi.org/10.1073/pnas.1816656115.
[355] M. Awashra, P. Młynarz, The toxicity of nanoparticles and their interaction with cells: an in vitro metabolomic perspective, Nanoscale Adv. 5 (2023) 2674–2723, https://doi.org/10.1039/d2na00534d.
[356] M. Yaşacan, A. Erikçi, C.C. Eylem, S.Y. Çiftçi, E. Nemutlu, K. Ulubayram, İ. Eroğlu, Polymeric nanoparticle versus liposome formulations: comparative physicochemical and metabolomic studies as l-carnitine delivery systems, AAPS PharmSciTech 21 (2020) 308, https://doi.org/10.1208/s12249-020-01852-4.
[357] A.H. Emwas, K. Szczepski, I. Al-Younis, J.I. Lachowicz, M. Jaremko, Fluxomics - new metabolomics approaches to monitor metabolic pathways, Front. Pharmacol. 13 (2022) 1–13, https://doi.org/10.3389/fphar.2022.805782.
[358] W.D. Lee, D. Mukha, E. Aizenshtein, T. Shlomi, Spatial-fluxomics provides a subcellular-compartmentalized view of reductive glutamine metabolism in cancer cells, Nat. Commun. 10 (2019) 1351, https://doi.org/10.1038/s41467-019-09352-1.
[359] G.A. Nagana Gowda, V. Pascua, J.A. Lusk, N.N. Hong, L. Guo, J. Dong, I.R. Sweet, D. Raftery, Monitoring live mitochondrial metabolism in real-time using NMR spectroscopy, Magn. Reson. Chem. n/a (2023), https://doi.org/10.1002/mrc.5341.
[360] Y. Nonnenmacher, R. Palorini, A.F. d'Herouël, L. Krämer, M. Neumann-Schaal, F. Chiaradonna, A. Skupin, A. Wegner, K. Hiller, Analysis of mitochondrial metabolism in situ: Combining stable isotope labeling with selective permeabilization, Metab. Eng. 43 (2017) 147–155, https://doi.org/10.1016/j.ymben.2016.12.005.
[361] Y. Zhang, C. Zhang, J. Chen, L. Liu, M. Hu, J. Li, H. Bi, Trackable mitochondria-targeting nanomicellar loaded with doxorubicin for overcoming drug resistance, ACS Appl. Mater. Interfaces. 9 (2017) 25152–25163, https://doi.org/10.1021/acsami.7b07219.
[362] D. Gao, Q. Zhu, J. Ruan, T. Sun, L. Han, Polyplexes by polymerized dequalinium and bifunctional aptamer for mitochondrial targeting drug release to overcome drug resistance, ACS Appl. Bio Mater. 3 (2020) 5182–5192, https://doi.org/10.1021/acsabm.0c00610.
[363] S. Đorđević, M.M. Gonzalez, I. Conejos-Sánchez, B. Carreira, S. Pozzi, R. C. Acúrcio, R. Satchi-Fainaro, H.F. Florindo, M.J. Vicent, Current hurdles to the translation of nanomedicines from bench to the clinic, Drug Deliv. Transl. Res. 12 (2022), https://doi.org/10.1007/s13346-021-01024-2.
[364] A. Thomen, N. Najafinobar, F. Penen, E. Kay, P.P. Upadhyay, X. Li, N.T.N. Phan, P. Malmberg, M. Klarqvist, S. Andersson, M.E. Kurczy, A.G. Ewing, Subcellular mass spectrometry imaging and absolute quantitative analysis across organelles, ACS Nano 14 (2020) 4316–4325, https://doi.org/10.1021/acsnano.9b09804.
[365] S. Spataro, B. Maco, S. Escrig, L. Jensen, L. Polerecky, G. Knott, A. Meibom, B. L. Schneider, Stable isotope labeling and ultra-high-resolution NanoSIMS imaging reveal alpha-synuclein-induced changes in neuronal metabolism in vivo, Acta Neuropathol. Commun. 11 (2023) 157, https://doi.org/10.1186/s40478-023-01608-8.
[366] G. Fogo, A. Anzell, K. Maheras, S. Raghunayakula, J. Wider, K. Emaus, T. Bryson, M. Bukowski, R. Neumar, T. Sanderson, Machine learning-based classification of mitochondrial morphology in primary neurons and brain, Sci. Rep. 11 (2021), https://doi.org/10.1038/s41598-021-84528-8.
[367] J.J. Collier, R.W. Taylor, Machine learning algorithms reveal the secrets of mitochondrial dynamics, EMBO Mol. Med. 13 (2021) e14316, https://doi.org/10.15252/emmm.202114316.

2 OBJECTIVES

The design and evaluation of polypeptide-based nanomedicines capable of targeting mitochondria, either through inherent tropism or the integration of well-characterized targeting moieties, and the assessment of their effectiveness in a triple negative breast cancer cell (TNBC) model represent the main objectives of this Ph.D. thesis.

We divided this main objective into the following sub-objectives:

1) **Design, Synthesis, Characterization, and Biological Evaluation of Diblock Copolymers as Mitochondria-Targeting Cell-Penetrating Oligomers (mt-CPOs) (Article II)**
   - Comprehensive physicochemical characterization of a library of poly-L-ornithine–poly-L-proline (PLO_n-PLP_m) diblock copolymers, focusing on secondary structure, diblock ratios, and CL binding affinity using CL-rich membrane model systems
   - Investigation of cellular uptake, mitochondrial targeting, and biological activity of selected PLO_n-PLP_m copolymers in MDA-MB-231 TNBC cells, with a comparative analysis of different block nature, n:m ratios, and cell lines
   - Synthesis, physicochemical characterization, and biological evaluation of PGA-based nanoconjugates functionalized with PLO_6-PLP_{22} for preclinical translation and alternative future application
2) **Application of PGA-Based Nanoconjugates Functionalized with PLO_6-PLP_{22} in Molecular Motors (Article III)**
   - Development of a novel polypeptide-conjugated molecular motor (P-MM) using copper-catalyzed azide-alkyne cycloaddition (click chemistry) and analysis of light-driven rotational properties and supramolecular conformational changes
   - Study of the light-induced activity of P-MM and its effect on cellular uptake and subcellular localization in MDA-MB-231 TNBC cells
3) **Development of TPP-Functionalized Polypeptide-Based Nanoconjugates for Mitochondrial Targeting and Non-Viral Gene Therapy Applications (Article IV)**

- Synthesis, physicochemical, and biological characterization of a PLO-based, polyethylene glycol (PEG)-modified carrier functionalized with a custom-designed trivalent compound (TRV3) via a disulfide linker (C-TRV3-A)
- Formulation of polyplexes by combining the cationic nanoconjugate C-TRV3-A with the anionic polypeptide VLC-3 and plasmid DNA coding luciferase (pDNA-Luc) and stability assessments
- Investigation of the transfection efficiency and cytotoxicity of polyplexes in 2D monolayer and 3D spheroid culture models of MDA-MB-231 TNBC cells

4) Synthesis and Characterization of Mitochondria-targeted Polypeptide-Drug Nanoconjugates for TNBC Treatment (General Discussion)

- Synthesis and characterization of polypeptide-drug conjugates based on PLO_6-PLP_{22} and carrying lonidamine (Loni) (conj-Loni) and α-tocopherol succinate (α-TOS) (conj-α-TOS) for mitochondrial-dependent TNBC treatment
- Cell viability and biological activity of conj-Loni and conj-α-TOS in MDA-MB-231 TNBC cells

3 PUBLICATIONS

This PhD thesis has been compiled as a compendium of scientific articles. To facilitate readability and provide context, we include an introduction for each article within the thesis, summarizing key concepts and contributions. The final chapter presents a comprehensive discussion integrating the findings from all articles. The Supporting Information provided in the annexes (as outlined in Chapter 6) provides additional details related to each article.

Reference scientific article I[344]: Pegoraro, C., Karpova, E., Qutbuddin, Y., Masía Sanchis, E., Dimitrijevs, P., Huck-Iriart, C., Gavrilović, S., Arsenyan, P., Schwille, P., Felip-León, C., Duro-Castano, A., Conejos-Sanchez, I., & Vicent, M. J. (2025). Polyproline-Polyornithine Diblock Copolymers with Inherent Mitochondria Tropism. Advanced Materials, 37(1), 2411595. DOI: 10.1002/adma.202411595.

Reference scientific article II[345]: Pegoraro, C.; Guinart, A.; Masiá Sanchis, E.; Doellerer, D.; Stuart, M. C. A.; Conejos-Sánchez, I.; Feringa, B. L.; Vicent, M. J. A Light-Driven Molecular Motor-Polypeptide Conjugate Supports Controlled Cell Uptake. *J. Mater. Chem. B* **2025**. DOI: 10.1039/D4TB02434F.

Reference scientific article III[346]: Pegoraro, C.; Masiá Sanchis, E.; Đorđević, S.; Dolz-Pérez, I.; Huck-Iriart, C.; Herrera, L.; Esteban-Pérez, S.; Conejos-Sanchez, I.; Vicent, M. J. Multifunctional Polypeptide-Based Nanoconjugates for Targeted Mitochondrial Delivery and Nonviral Gene Therapy. *Chem. Mater.* **2025**. DOI: 10.1021/acs.chemmater.4c02742.

3.1 Manuscript II

3.1.1 Scientific Article I: Introduction and Background

This study introduces a novel class of poly-L-ornithine–poly-L-proline (PLO_n-PLP_m) diblock copolymers designed for mitochondrial-specific targeting through a cardiolipin (CL)-mediated mechanism[344]. These diblock copolymers overcome limitations associated with traditional mitochondrial-targeting strategies, such as reliance on mitochondrial membrane potential or complex synthetic pathways, by leveraging a scalable and modular synthesis via N-carboxyanhydride ring-opening polymerization. The selected diblock ratio (n:m = 1:3) ensures an optimal balance of cellular uptake efficiency, mitochondrial targeting, and CL specificity, functioning as efficient mitochondrial-targeting cell-penetrating oligomers (mt-CPOs).

Key advancements include:

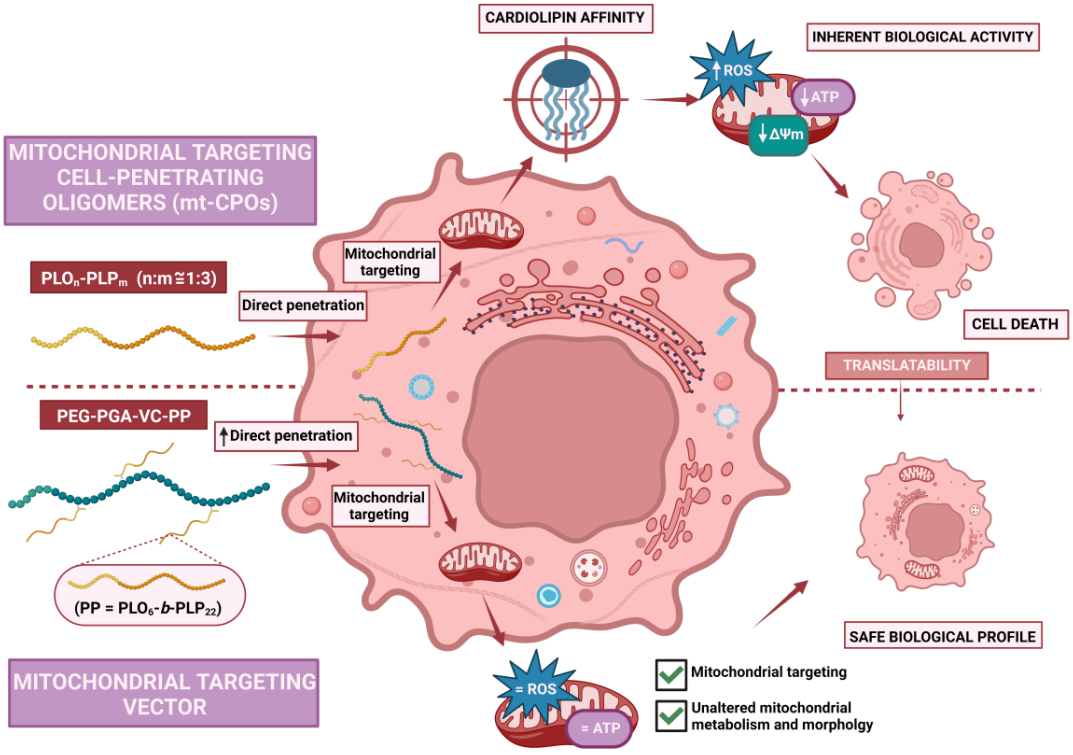
- **Energy-Independent Cellular Uptake**: The diblock copolymers employ an energy-independent uptake mechanism that bypasses endosomal pathways to support accumulation in the mitochondria even under conditions of membrane depolarization
- **Validation in Physical Membrane Models**: Studies of interaction with CL-rich membranes using various model systems (including small unilamellar vesicles and mitoplasts) revealed the critical nature of localized membrane remodeling and patch formation for PLO_n-PLP_m (n:m = 1:3) mitochondrial targeting
- **Biological Functionality in Triple Negative Breast Cancer Models**: PLO_n-PLP_m (n:m = 1:3) exhibited inherent, concentration-dependent anti-tumorigenic activity at the mitochondrial level in the MDA-MB-231 triple negative breast cancer (TNBC) cell line at sub-IC_{50} concentrations (>IC_{15})
- **Translational Potential through Polyglutamic Acid Conjugation**: Functionalization of the PGA nanocarrier with diblock copolymer PLO_6-PLP_{22} at sub-IC_{15} concentrations demonstrated versatility and potential for preclinical translation within larger drug delivery systems for mitochondrial targeting

By integrating rational design and rigorous mechanistic studies and highlighting translational adaptability, this work advances the field of mitochondrial-targeted therapeutics. These findings

contribute to the broader objectives of this thesis by demonstrating a novel and effective strategy for precision nanomedicine, with potential applications in treating aggressive cancers such as TNBC.

In this work, I led the synthesis of the PGA-based nanoconjugate and the physicochemical characterization of the diblock copolymers, including Circular Dichroism, Zeta potential, and NMR-DOSY analyses. I also performed cell viability assays and biological studies and contributed to the physical studies in membrane model systems during my short stay at the Max Planck Institute of Biochemistry in Petra Schwille's group. Additionally, I was responsible for data curation, formal analysis, investigation, methodology development, and the writing of the original draft. Contributions by co-authors are detailed in the manuscript.

Table of Content



Novel diblock copolymers support efficient mitochondrial targeting. *Above the dotted line* depicts diblock copolymers (PLO_n-PLP_m, n:m ratio 1:3; **6b, h, i**) as cell-penetrating oligomers (CPOs) with cardiolipin-specific mitochondrial targeting (mt-CPOs). At sub-IC_{50} concentrations (>IC_{15}), they induce ROS production, ATP depletion, mitochondrial depolarization, and morphological changes, leading to mitochondria-induced cell death in triple-negative breast cancer cells (MDA-MB-231). *Below the dotted line* illustrates conjugation of a selected diblock copolymer (PLO_6-PLP_{22}, **6b**) to a PEG-PGA carrier via a valine-citrulline (VC) linker. This conjugate (**16**) retains mitochondrial targeting, metabolism and morphology and enables delivery of macromolecules (e.g., drugs, dyes) to mitochondria, with potential for preclinical translation in mitochondria-related diseases. *Figure created with Biorender.*

Check for updates

RESEARCH ARTICLE

ADVANCED MATERIALS
www.advmat.de

Polyproline-Polyornithine Diblock Copolymers with Inherent Mitochondria Tropism

Camilla Pegoraro, Ekaterina Karpova, Yusuf Qutbuddin, Esther Masiá Sanchis, Pavels Dimitrijevs, Cristián Huck-Iriart, Svetozar Gavrilović, Pavel Arsenyan, Petra Schwille, Carles Felip-León, Aroa Duro-Castano, Inmaculada Conejos-Sanchez, and María J. Vicent**

Mitochondria play critical roles in regulating cell fate, with dysfunction correlating with the development of multiple diseases, emphasizing the need for engineered nanomedicines that cross biological barriers. Said nanomedicines often target fluctuating mitochondrial properties and/or present inefficient/insufficient cytosolic delivery (resulting in poor overall activity), while many require complex synthetic procedures involving targeting residues (hindering clinical translation). The synthesis/characterization of polypeptide-based cell penetrating diblock copolymers of poly-L-ornithine (PLO) and polyproline (PLP) (PLO_n-PLP_m, n:m ratio 1:3) are described as mitochondria-targeting nanocarriers. Synthesis involves a simple two-step methodology based on N-carboxyanhydride ring-opening polymerization, with the scale-up optimization using a "design of experiments" approach. The molecular mechanisms behind targetability and therapeutic activity are investigated through physical/biological processes for diblock copolymers themselves or as targeting moieties in a poly-L-glutamic (PGA)-based conjugate. Diblock copolymers prompt rapid cell entry via energy-independent mechanisms and recognize mitochondria through the mitochondria-specific phospholipid cardiolipin (CL). Stimuli-driven conditions and mitochondria polarization dynamics, which decrease efficacy depending on disease type/stage, do not compromise diblock copolymer uptake/targetability. Diblock copolymers exhibit inherent concentration-dependent anti-tumorigenic activity at the mitochondrial level. The diblock copolymer conjugate possesses improved safety, significant cell penetration, and mitochondrial accumulation via cardiolipin recognition. These findings may support the development of efficient and safe mitochondrial-targeting nanomedicines.

1. Introduction

Subcellular targeting has emerged as a promising strategy in precision medicine, offering advantages such as enhanced specificity and efficacy, minimized resistance issues, and reduced off-target toxicities. Reports of multivalent approaches and studies tracking specific subcellular biomarkers or metabolites have paved the way forward;[1] however, only a few drug delivery platforms have successfully crossed biological barriers and arrived at a target subcellular location. Mitochondria represent the principal target of subcellular targeting efforts due to their critical role in energy generation and cell survival.[2] Multiple studies have reported the design of mitochondrially-targeted nanomedicines that navigate the complex routes required to influence function; nonetheless, significant hurdles remain before they become suitable for clinical use.[3]

Drawbacks associated with mitochondrially-targeted nanomedicines have hampered their clinical progress. For example, mitochondria-targeting moieties such as triphenylphosphonium (TPP) require molecular functionalization,[4] and mitochondrial targeting relies exclusively

C. Pegoraro, E. M. Sanchis, I. Conejos-Sanchez, M. J. Vicent
Príncipe Felipe Research Center
Polymer Therapeutics Lab.
Valencia 46012, Spain
E-mail: iconejos@cipf.es; mjvicent@cipf.es

The ORCID identification number(s) for the author(s) of this article can be found under https://doi.org/10.1002/adma.202411595

© 2025 The Author(s). Advanced Materials published by Wiley-VCH GmbH. This is an open access article under the terms of the Creative Commons Attribution-NonCommercial-NoDerivs License, which permits use and distribution in any medium, provided the original work is properly cited, the use is non-commercial and no modifications or adaptations are made.

DOI: 10.1002/adma.202411595

E. Karpova, C. Felip-León, A. Duro-Castano
Curapath
Av. Benjamín Franklin, 19, Paterna, Valencia 46980, Spain

Y. Qutbuddin, S. Gavrilović, P. Schwille
Max Planck Institute of Biochemistry
Am Klopferspitz 18, 82152 Martinsried, Germany

E. M. Sanchis, I. Conejos-Sanchez, M. J. Vicent
Centro de Investigación Biomédica en Red en Cáncer (CIBERONC)
Instituto de Salud Carlos III
Madrid 28029, Spain

E. M. Sanchis, M. J. Vicent
Príncipe Felipe Research Center
Screening Platform, Valencia 46012, Spain

15214095, 0, Downloaded from https://advanced.onlinelibrary.wiley.com/doi/10.1002/adma.202411595 by Camilla Pegoraro - Readcube (Labtiva Inc.) , Wiley Online Library on [26/01/2025]. See the Terms and Conditions (https://onlinelibrary.wiley.com/terms-and-conditions) on Wiley Online Library for rules of use; OA articles are governed by the applicable Creative Commons License

on mitochondrial membrane potential (promoting charge-based accumulation) that fluctuates as a mode of, e.g., cell cycle status after pharmacological intervention or disease stage.[5] Furthermore, mitochondrially-targeted nanomedicine internalization via endocytic uptake requires endosomal escape (often limiting efficiency,[6]) while the complex synthetic procedures for mitochondrially-targeted nanomedicines remain untranslatable to industrial processes. Overall, we require the definition of alternative designs that solve these issues and must consider rational design approaches to support precise subcellular therapeutic targeting/delivery.

We here report the design of novel diblock copolymers based on the PLO and PLP polypeptides that target mitochondria without functionalization and that can be easily manufactured to support clinical translation. We based the selection of PLP on the results of Chmielewski et al., which highlighted N-functionalized PLP with hydrophobic and/or cationic residues as a concentration- and potential-dependent cell-penetrating mitochondria-targeting peptide.[7–10] We selected PLO given its polycationic nature, which we leveraged to enhance cell uptake and favor cell internalization (by impairing amphiphilicity).[11,12] As opposed to previous related studies, we developed a universal, rapid (two-step), and scalable N-carboxyanhydride ring-opening polymerization (NCA-ROP) methodology for the synthesis of novel biodegradable diblock copolymers that target mitochondria – **PLO_n-PLP_m**. Selected diblocks (at a 1:3 n:m ratio) targeted mitochondria through a CL-specific potential-independent mechanism following direct cell membrane permeation. Notably, these diblock copolymers exhibited inherent concentration-dependent anti-tumorigenic activity at the mitochondrial level, highlighting their potential as standalone anti-cancer agents or as components of larger drug delivery systems that could provide adequate safety and pharmacokinetic profiles toward clinical translation. To achieve proof of concept in this latter concept, we designed and synthesized a non-toxic polypeptide-based conjugate derivative of **PLO_6-PLP_{22}** that displayed an improved safety profile, significant direct cell penetration, and subsequent mitochondria tropism. Overall, our results emphasize the versatility of these novel diblock copolymers, establishing a mitochondrial targeting platform that can be translated to an industrial-scale clinical translation.

2. Results and Discussion

2.1. Synthesis and Characterization of Novel Polyproline-based Diblock Polymers

PLO and PLP possess characteristics that aid cellular internalization via direct membrane penetration;[7–12] therefore, we evaluated the suitability of diblock copolymers of PLO and PLP (PLO_n-PLP_m) as mitochondrially-targeted cell-penetrating oligomers (**mt-CPOs**). To screen candidate mt-CPOs, we first synthesized a family of well-defined PLO_n-PLP_m diblock copolymers with different block (n:m) ratios and lengths (**Table 1**, diblock copolymers **6a–i**). We also explored replacing the PLO block with polylysine (PLL), polyhistidine (PHis), or polyarginine (PArg) to evaluate the impact of different polycationic blocks on mitochondrial targeting (Table 1; diblock copolymers 7, 11, and 14). These diblock copolymers were synthesized with the same block ratios and lengths as **6b**, providing analogs to **6b** for comparison. We next performed extensive physicochemical characterization of the above-described diblock copolymers. Table 1 summarizes the critical features, including molecular weight (Mw), polydispersity index (PDI), identity confirmation via gel permeation chromatography (GPC) and nuclear magnetic resonance (NMR), secondary structure analysis using circular dichroism (CD), Zeta potential through dynamic light scattering (DLS), particle size distribution, and aggregation profile determined by small angle x-ray scattering (SAXS). For the sake of brevity, **Figure 1** presents the physicochemical profiles of diblock copolymers **6b**, **h**, and **i** (n:m ratio 1:3), identified as effective mt-CPOs among all evaluated diblock copolymers (detailed in the following sections). The Supporting Information contains comprehensive characterization data for all remaining diblock copolymers. Due to its safer biological profile compared to **6 h** and **i** (detailed in the following sections), we selected diblock copolymer **6b** as our primary mt-CPO candidate.

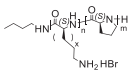
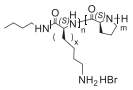
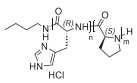
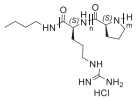
Scheme 1 (and Schemes S1 and S2, Supporting Information) illustrates the synthesis of diblock copolymers (summarized in Table 1). In brief, we performed the ROP of the protected NCA corresponding to the polycationic component as a first block, adjusting the theoretical degree of polymerization (DP) using n-butylamine ($nBuNH_2$) as the initiator and anhydrous dimethylformamide (DMF) as the solvent. After converting ornithine (Orn) benzyloxycarbonyl (Z), lysine (Lys) benzyloxycarbonyl (Z), and histidine (His) dinitrophenyl (DNP) monomers (in the form of N-carboxyanhydride (NCA) derivatives, Orn(Z)-NCA, Lys(Z)-NCA, and His(DNP)-NCA) into their corresponding polycationic polypeptides PLO(Z), PLL(Z), or PHis(DNP), we added them to a suspension of proline (Pro)-NCA in acetonitrile. The reactions reached completion within 1 h, resulting in good yields (>80%) of the protected diblock copolymers $PLO(Z)_n$-PLP_m, $PLL(Z)_n$-PLP_m, $PHis(DNP)_n$-PLP_m (described in the Supporting Information as intermediate diblock copolymers **4a-i**, **5** and **10** respectively), with corresponding DP values closely correlating with theoretical values. Given that PLP displays low solubility in the organic solvents typically employed for GPC, we exclusively analyzed the intermediate-protected diblock copolymers via NMR (Figures S1–S4, Supporting Information).

Next, protected diblock copolymers **4a-i** and **5** underwent deprotection with HBr in acetic acid, yielding fully water-soluble diblock copolymers PLO_n-PLP_m (diblock copolymers **6a-i**; Figure 1A) (Figures 1B and S5 (Supporting Information) depict examples of NMR spectra for diblock copolymer **6b**) and PLL_n-PLP_m (diblock copolymer **7**; NMR spectra in Figure S6, Supporting Information), which displayed a monomodal distribution (Figures 1C and S7 and S8, Supporting Information) and low PDI values (Table 1). In the case of the diblock copolymer **10**, we conducted deprotection using 2-mercaptoethanol in DMF, followed by the acidification of the histidine group to obtain $PHis_n$-PLP_m (diblock copolymer **11**, NMR spectra in Figure S9, Supporting

P. Dimitrijevs, P. Arsenyan
Latvian Institute of Organic Synthesis
Aizkraukles Street 21, Riga LV-1006, Latvia
C. Huck-Iriart
Experiments Division
ALBA Synchrotron Light Source
Cerdanyola del Vallès 08209, Spain

© 2025 The Author(s). Advanced Materials published by Wiley-VCH GmbH

Table 1. Physicochemical properties of polyproline-based diblock copolymers synthesized.

Code	Structure	DP[a] (n) for Polycation	DP[a] (m) for PLP	n:m Ratio	MW by SEC -RALS (kDa)[b]	PDI	Mean Rg_{corr} (nm)[c]	q^{-s}	Zeta Potential (mV)[d]	Secondary Structure[e]
6b		6	22	1:3	3.8	1.090	4.3 ± 0.4	0.2	2.9 ± 0.5	PPII
6h		18	54	1:3	9.5	1.180	3.5 ± ± 0.4	1.66	2.0 ± 0.2	PPII
6i	**PLO_n-PLP_m**	22	64	1:3	11.5	1.190	3.9 ± 0.5	0.36	1.6 ± 0.4	PPII
6a		14	5	3:1	3.0	1.095	1.55 ± 0.1	0.29	6.3 ± 0.2	Random coil
6c		16	30	1:2	13.1	1.289	–	–	7.5 ± 0.2	PPII
6d		35	6	6:1	10.4	1.102	3.8 ± 0.5	1.74	–	Random coil
6e		35	15	2:1	10.2	1.129	1.7 ± 0.2	0.72	13.3 ± 0.6	Random coil
6f		6	12	1:2	3.1	1.052	1.8 ± 0.3	1.31	8.2 ± 0.6	PPII
6g		6	7	1.1	2.5	1.089	1.3 ± 0.5	1.2	10.7 ± 0.3	Random coil
7		6	19	1:3	3.3	1.090	4.1 ± 0.5	0.0	3.3 ± 0.5	PPII
	PLL_n-PLP_m									
11		6	25	1:3	–	–	4.7 ± 0.3	0.2	4.4 ± 0.8	PPII
	$PHis_n$-PLP_m									
14		7	23	1:3	4.7	1.039	4.5 ± 0.5	0.0	2.0 ± 1	PPII
	$PArg_n$-PLP_m									

[a] Estimated by nuclear magnetic resonance (NMR); DP – Degree of Polymerization; PLP – Polyproline; [b] Determined by gel permeation chromatography (GPC) wherein the cited numbers are subject to a reasonable uncertainty within the range ±20%; Mw -Molecular Weight; SEC-RALS – Size Exclusion Chromatography-Right Angle Light Scattering; PDI – Polydispersity index; [c] Determined by small angle x-ray scattering (SAXS); q-s represents the power law dependence at low angles in the Guinier region, which correlates with particle aggregation; Rg_{corr} – Correlative Radius of Gyration; [d] Determined by dynamic light scattering (DLS). mV – millivolt; [e] Determined by circular dichroism (CD); PPII corresponds to type II helical conformation.

Information). Finally, we synthesized $PArg_n$-PLP_m (diblock copolymer **14**) by functionalizing the amine groups of diblock copolymer **6b** with 1-guanyl-1,2,4-triazole (Scheme S2, Supporting Information). As the reaction did not introduce new hydrogens discernible in proton NMR, we validated conversion indirectly via NMR by observing proton shifts in adjacent groups (Figure S10, Supporting Information) and through GPC (Figure S11, Supporting Information). We also synthesized homopolymers of PLP (**15a** and **b**) to validate the influence of the polycationic block in further biological studies (SchemeS3 and Table S1, Supporting Information).

We evaluated the secondary structure of all resultant diblock copolymers by CD in water to elucidate structure-activity correlations. PLP homopolymers adopt a type II helical conformation (PPII) in polar solvents, with a pronounced negative band at 206 nm and a weak positive band at 228 nm in CD[13] (example of **15a** and **b** in Figure S12, Supporting Information). Diblock copolymers **6b**, **h**, and **i** exhibited a PPII spectrum (Figure 1D), demonstrating that an n:m ratio 1:3 of PLO and PLP blocks did not alter the typical CD spectra of PLP; however, the intensity of the typical PPII bands increased with PLP block length. Diblock copolymers **6c** and **f** (n:m ratio 1:2) also maintained their PPII features (Figure S13, Supporting Information). Despite the reported increase in stability of the PPII structure due to cationic residues at the C-terminus of the proline block,[14] the higher relative content of PLO (which possesses a random coil structure)[12] masked the contribution of PLP in diblock copolymers **6a**, **d**, **e**, and **g** (Figure S13, Supporting Information). These results highlight the relevance of the PLO: PLP ratio in diblock copolymer conformation. Furthermore, the polycationic block nature did not affect the PPII of diblock copolymers **6b** or analog diblock copolymers **7**, **11**, and **14**, with Lys, His, and Arg as positively charged residues (Figure S14, Supporting Information). We also assessed the stability of the conformation of diblock copolymer **6b**, finding a stable PPII even after multiple freezing and thawing cycles

© 2025 The Author(s). Advanced Materials published by Wiley-VCH GmbH

15214095, 0, Downloaded from https://advanced.onlinelibrary.wiley.com/doi/10.1002/adma.202411595 by Camilla Pegoraro - Readcube (Labtiva Inc.) , Wiley Online Library on [26/01/2025]. See the Terms and Conditions (https://onlinelibrary.wiley.com/terms-and-conditions) on Wiley Online Library for rules of use; OA articles are governed by the applicable Creative Commons License

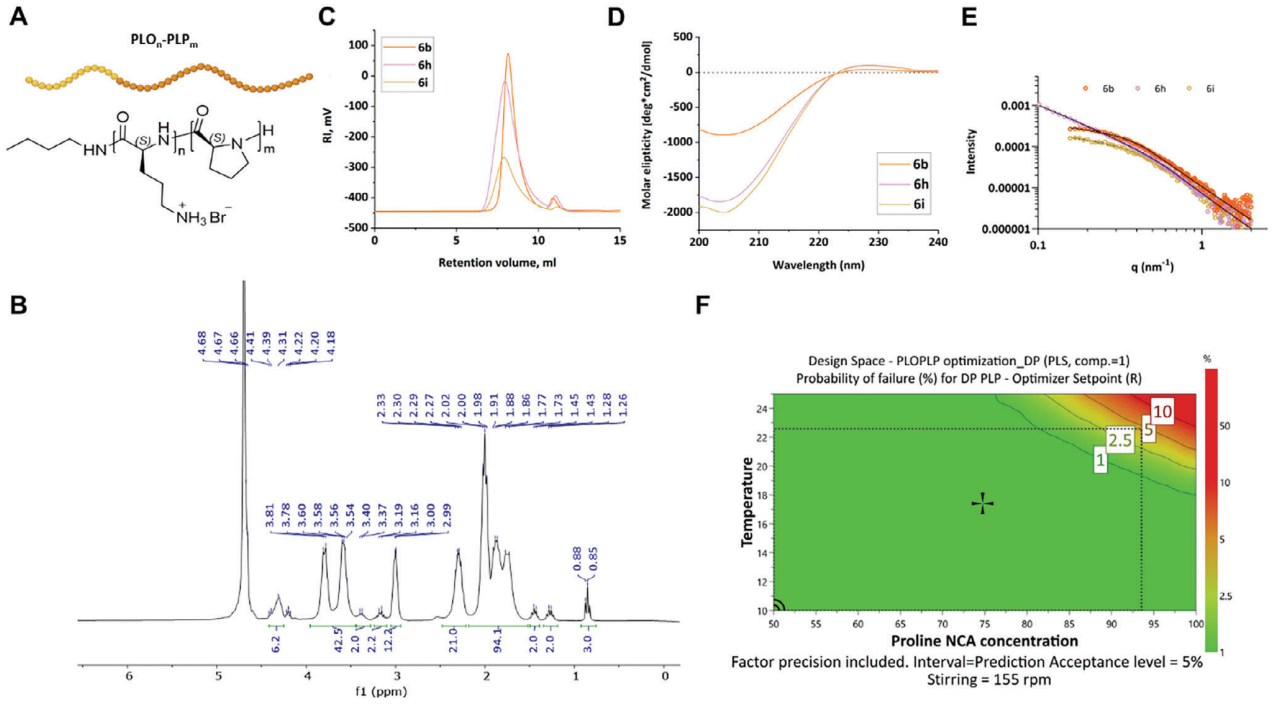


Figure 1. Physicochemical characterization of novel polyproline-based diblock copolymers. A) Schematic representation of the PLO$_n$-PLP$_m$ family of diblock copolymers. B) Nuclear magnetic resonance (NMR) spectra of diblock copolymers **6b** in deuterated water with the characteristic peaks of PLO$_n$-PLP$_m$ diblock copolymers highlighted. C) Gel permeation chromatography (GPC) elugrams of diblock copolymers **6b**, **h**, and **i** in $NaNO_3$ containing 0.005% NaN_3. D) Circular dichroism (CD) spectra of diblock copolymers **6b**, **h,** and **i** in Milli-Q water. E) Small-angle X-ray Scattering (SAXS) data for diblock copolymers **6b**, **h** and **i**. Intensity expressed as a function of the scattering momentum transfer, q ($q = 4\pi\sin(\theta)/\lambda$. F) Proven acceptable range (PAR) defined by the design space for the scale-up optimization of diblock copolymer **6b**.

(Figure S15, Supporting Information) and at physiological temperatures that mimic diblock copolymer storage and biological conditions (Figure S16, Supporting Information). We also discovered that Cy5 labeling (Scheme S4, Supporting Information) did not affect the CD spectra of all diblock copolymers (Figures S17–S19, Supporting Information), indicating that conjugation of a dye (Figure S20, Supporting Information) used for tracking diblock copolymers in vitro and in vivo did not alter diblock copolymer conformation or, potentially, any biological effects.

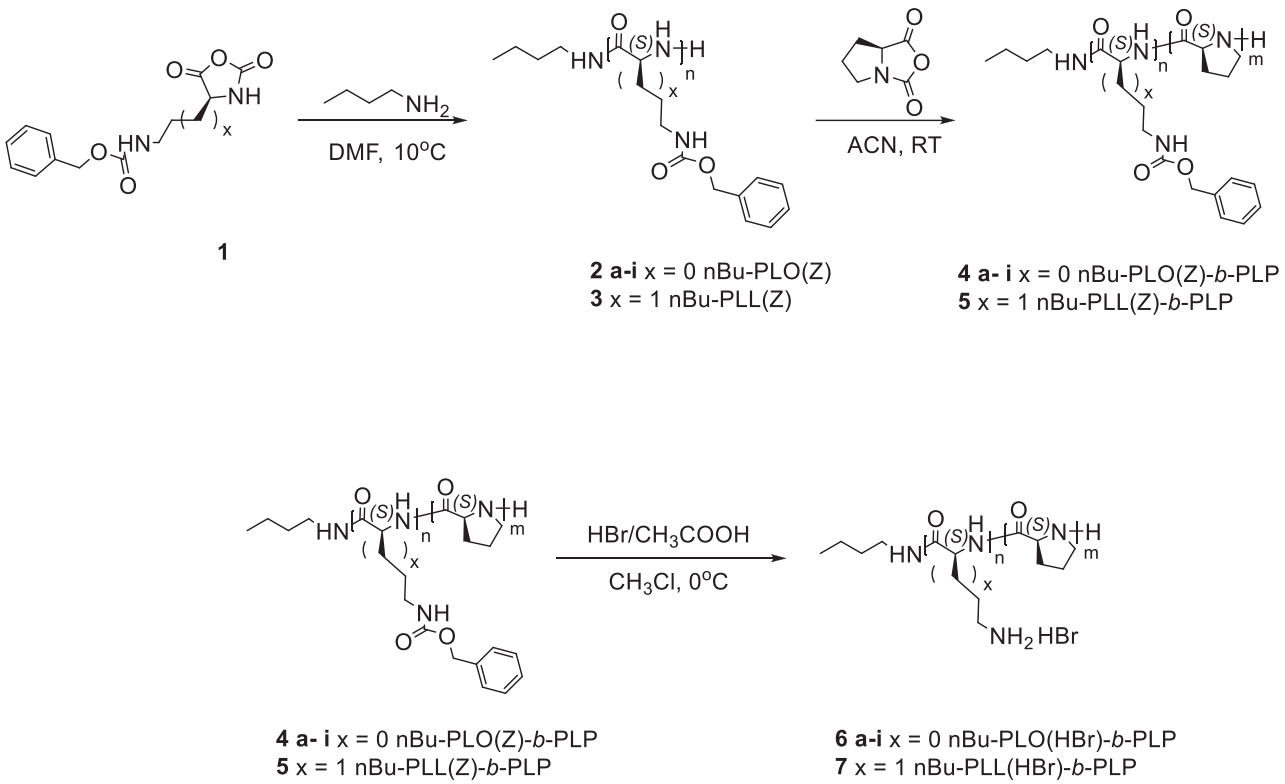
Diblock copolymers families **6**, **7**, **11**, and **14** exhibited similar radius of gyration (Rg) values, and their Porod exponent "d" of ca. 3 corresponded to the branched polymers of a dense core,[15] as determined by SAXS (Table 1, Figures 1E and S21 and S22, Supporting Information). We applied the Guinier-Porod semiempirical model to identify differences due to variations in DP and monomer composition;[16] the results revealed concentration-independent behavior in PBS – a power law dependence at low angles (q^{-s}) indicated the tendency to form aggregated structures (estimated aggregated particle of Rg maximum < 2.5 nm) for diblock copolymers such as **6 h**, **d**, and **f** (s > 0). Interestingly, diblock copolymer **6b** and analogs **7**, **11**, and **14** did not form aggregates in solution. While diblock copolymers **6b**, **h**, and **i** presented different power "s" values (Table 1), the variation in emission polarity index and the inability to determine a critical aggregation concentration (CAC) by pyrene experiment (Figure S23, Supporting Information) revealed the dynamic nature of compact domain aggregation, which had no impact on their biological effect as demonstrated in section 2.2. The evaluation of Rg values considers a correlative radius of gyration ($R_{g,corr}$) to mitigate the high correlation effects (possibly due to aggregation) in the fitting process.[17] Considering the influence of polymer branching, we considered an expected d-value of 3 for this computation (see the Supporting Information for detailed information).

Even though SAXS experiments revealed similar sizes for all evaluated diblock copolymers, the increased zeta potential for PLO$_n$-PLP$_m$ with differing n:m ratio compared to diblock copolymers **6b**, **h**, and **i** or alternative diblock copolymers (**7**, **11** and **14**) with the same n:m ratio might indicate differences in their solution conformation, which could influence uptake and mitochondrial targeting.

To prepare our synthetic approach for robust scaled-up manufacturing, we employed (for the first time to the best of our knowledge) a design of experiments (DoE)-based approach to optimize the scaled-up synthesis of diblock copolymer precursor of **6b** via one-pot cascade ROP. Given the interdependence of the polymerization processes in steps 1 and 2 (Scheme 1), we proposed sequential process development, starting with improving PLO(Z) screening by focusing on a limited number of factors. We applied critical parameters identified from this optimization to then synthesize the PLO(Z)$_n$-PLP$_m$ diblock copolymer. An initial DoE study on PLO(Z) synthesis evaluated Orn(Z)-NCA and $nBuNH_2$ concentrations and reaction temperature (T) (Table S2, Figures S24 and S25, Supporting Information). We used NMR and GPC to monitor diblock copolymer DP, confirming the attainment of

© 2025 The Author(s). Advanced Materials published by Wiley-VCH GmbH

15214095, 0, Downloaded from https://advanced.onlinelibrary.wiley.com/doi/10.1002/adma.202411595 by Camilla Pegoraro - Readcube (Labtiva Inc.) , Wiley Online Library on [26/01/2025]. See the Terms and Conditions (https://onlinelibrary.wiley.com/terms-and-conditions) on Wiley Online Library for rules of use; OA articles are governed by the applicable Creative Commons License



Scheme 1. General synthesis of PLO-*b*-PLP and PLL-*b*-PLP diblock copolymers.

desired Mw values at 4 °C. MODDE simulations predicted optimal concentrations of Orn(Z)-NCA (200-2-36 mg mL^{-1}) and $nBuNH_2$ (23–29 mg mL^{-1}), which combined to give an overall Orn(Z)-NCA concentration range of 140–170 mg mL^{-1}. We applied these values in $PLO(Z)_n$-PLP_m screening, which also considered Pro-NCA and PLO(Z) concentrations, temperature, and stirring rate (Table S3, Supporting Information). We fixed the initiator temperature at room temperature for simplicity despite PLO(Z) synthesis occurring at 4 °C. Monte Carlo simulations identified the optimal Mw and DP (Figure S26, Supporting Information). We employed NMR due to PLP's low solubility in standard GPC mobile phases (DMF and hexafluoroisopropanol); the coefficient plot (Figure S27, Supporting Information) indicated that Pro-NCA concentration, stirring, and temperature affected DP. We set Orn(Z)-NCA at 155 mg mL^{-1} and reduced stirring to 200–350 rpm for future reactor-based scale-up. The new ranges were 50–100 mg mL^{-1} for Pro-NCA, 10–20 °C, and stirring at 270–350 rpm (Figure S28, Supporting Information). Using the circumscribed central composite (CCC) design model, we optimized diblock copolymer precursor **6b** synthesis, focusing on temperature, stirring, and Pro-NCA concentration. The proven acceptable ranges (PAR) were 50–93.5 mg mL^{-1} for Pro-NCA and 10–22.6 °C, ensuring less than 1% failure risk and suitability for reactor transfer with a fixed stirring rate of 155 rpm (Figure 1F). Table S4 and Figure S29 (Supporting Information) detail the experimental matrix and model terms.

The scaled-up synthesis of the candidate diblock copolymer precursor of **6b** (7-fold scale-up concentration) using the estimated parameters obtained in the sequential DoE yielded the corresponding protected polymer with an 80% overall yield and a $PLO(Z)_6$-PLP_{20} ratio (n:m ratio 1:3). Figure S30 (Supporting Information) reports the NMR spectra of this batch. We deprotected the diblock copolymer in dry chloroform using standard conditions with HBr/CH_3COOH yielding **6b**. Figures S31–S33 (Supporting Information) present the NMR spectra, GPC, and MALDI mass spectra of **6b**.

In summary, we successfully synthesized novel PLP-based diblock copolymers using a two-step NCA-ROP method optimized for industrial scalability. The synthesized diblock copolymers exhibited small sizes (<5 nm) and a PPII secondary structure dependent on the n:m ratio and independent of the polycationic block nature. Additionally, variations in zeta potential and dynamic aggregation behavior demonstrated by SAXS suggest that different diblock copolymers may adopt distinct solution conformations. These features may help to define structure-properties relationships that define the cell uptake and mitochondrial-targeting capabilities of diblock copolymers (Table 1).

2.2. PLP-based Diblock Copolymer 6b Exhibits Enhanced Cell Viability, Uptake, and Mitochondrial Colocalization in TNBC Cells

To comprehensively evaluate the potential of PLP-based diblock copolymers as efficient **mt-CPOs**, we extensively screened the

© 2025 The Author(s). Advanced Materials published by Wiley-VCH GmbH

15214095, 0, Downloaded from https://advanced.onlinelibrary.wiley.com/doi/10.1002/adma.202411595 by Camilla Pegoraro - Readcube (Labtiva Inc.) , Wiley Online Library on [26/01/2025]. See the Terms and Conditions (https://onlinelibrary.wiley.com/terms-and-conditions) on Wiley Online Library for rules of use; OA articles are governed by the applicable Creative Commons License

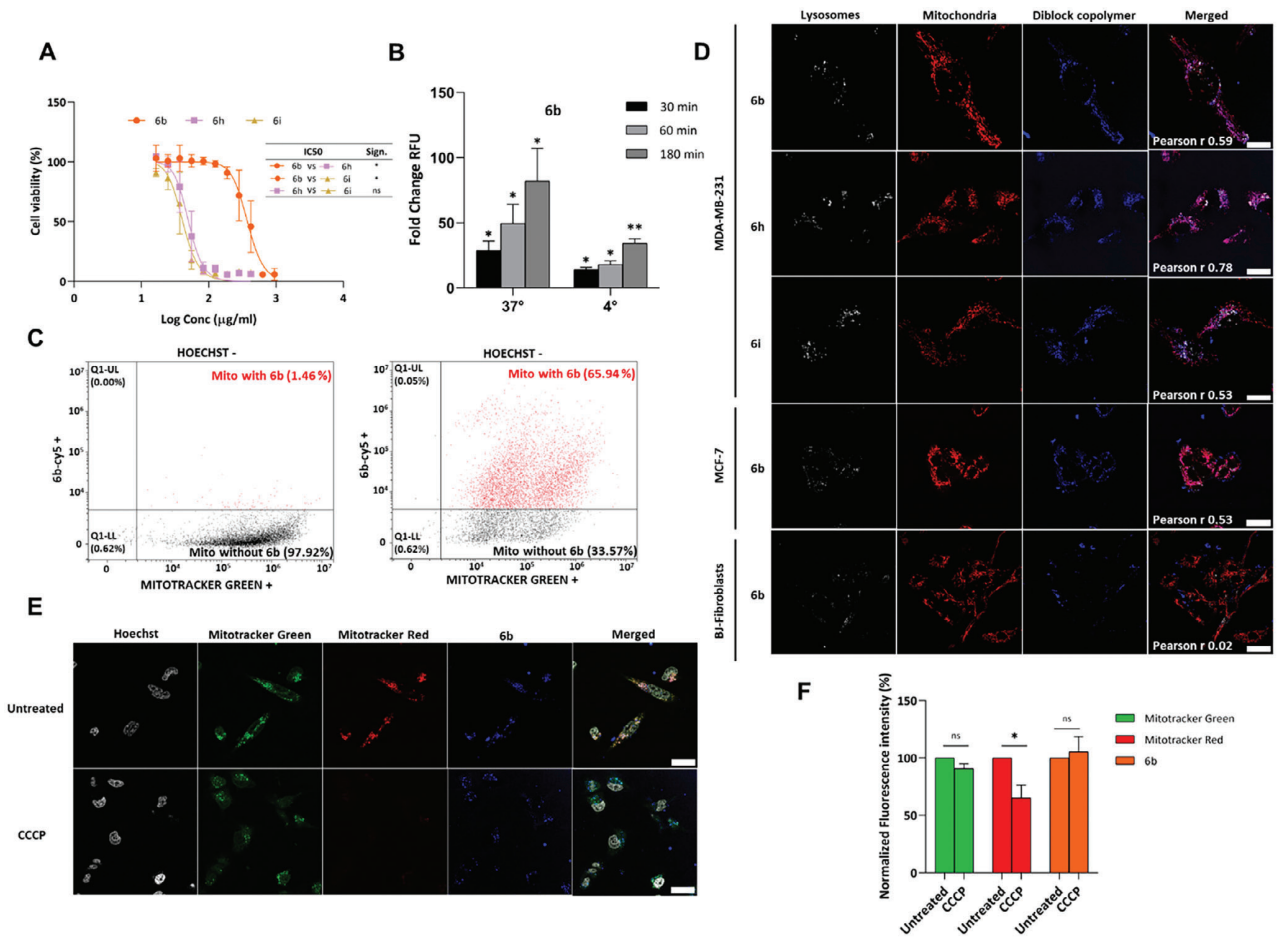


Figure 2. Uptake mechanism and mitochondrial targeting of polyproline-based Diblock Polymers. A) MDA-MB-231 cell viability by MTS assay in response to exposure to diblock copolymers **6b** (IC_{50} = 0.40 mg mL^{-1}), **6 h** (IC_{50} = 0.05 mg mL^{-1}), **6i** (IC_{50} = 0.04 mg mL^{-1}) (72 h, n = 3, mean ± SEM). Sign – Significance **B)** Internalization of diblock copolymer **6b** at 30, 60, and 180 min at 37° (endocytic-dependent pathway) and 4° (endocytic-independent pathway) by flow cytometry (n = 3, mean ± SEM). Data expressed as fold change in relative fluorescence units (RFU) to t = 0; t-test comparing to the control set as 100% (n = 3, mean ± SEM). Significance reported as $*p \leq 0.05$, $**p \leq 0.01$. **C)** Quantification of diblock copolymer **6b** in isolated mitochondria; Cy5 for **6b** and MitoTracker Green FM for isolated mitochondria (black dots: isolated mitochondria positive to MitoTracker Green FM; red dots: isolated mitochondria positive to MitoTracker Green FM and **6b**-Cy5). Upper X-axis: Hoechst-negative population (isolated mitochondria); Y-axis: **6b-Cy5** positive events; Lower X-axis: MitoTracker Green FM positive events. **D)** Confocal images of diblock copolymers **6b**, **h**, and **i** uptake at 2 h post-treatment in MDA-MB 231 cells and **6b** uptake at 2 h post-treatment in MCF-7 cells and BJ fibroblasts following a pulse-chase experiment (see Table S5, Supporting Information) (White – LysoTracker Blue for lysosomes; Red – MitoTracker Red CM-H2Xros for mitochondria; Blue – Cy5-labeled diblock copolymers **6b**, **h**, and **i**. Colocalization with Mitotracker Red was observed (purple) for MDA-MB-231 and MCF-7 cells, and the Pearson r (2 h) value was calculated using the ImageJ JACoP plugin. Scale bar: 10 µm. **E)** Confocal images of diblock copolymer **6b** at 3 h post-treatment in MDA-MB-231 cells in polarized (untreated) and depolarized mitochondria. CCCP-induced depolarization was qualitatively observed by the reduced accumulation of the potential-dependent MitoTracker Red CM-H2Xros, while the potential-independent MitoTracker Green FM maintained its mitochondrial colocalization upon CCCP treatment. Hoechst-stained nuclei in live cells. Scale bar: 10 µm. **F)** Fluorescence intensity quantification of Cy5-labeled diblock copolymer **6b** in polarized and depolarized mitochondria by InCell Analyzer 2200. Cells with polarized mitochondria set as control (100%) (n = 3, mean ± SEM). Significance reported as $*p \leq 0.05$ (ns – not significant).

compounds listed in Table 1, assessing their cell viability, cellular uptake, and subcellular localization.

Cell viability assays using the triple-negative breast cancer (TNBC) human MDA-MB-231 cells as a model revealed the safer profile of the diblock copolymer **6b** compared to **6 h** and **6i** after 72 h of exposure (**Figures** 2A and S34 (Supporting Information) depicts cell viability at 24 h) and other PLO_n-PLP_m diblocks with differing n:m ratios (Figure S35, Supporting Information). The longer length of the cationic block results in higher zeta potential (Table 1), translating into higher toxicity. In contrast, diblock copolymers with Lys, Arg, and His as positively charged residues (**7**, **14**, and **11**) exhibited a safer cytotoxicity profile than the **6b** PLO analog (Figure S36, Supporting Information) despite sharing the same block length and comparable zeta potential. Differences in toxicity profiles may suggest distinct interactions with cell membranes; for instance, PArg interacts more strongly and cooperatively with phospholipid bilayers than PLL, leading to a higher degree of membrane disruption and cytotoxicity.[18–22]

© 2025 The Author(s). Advanced Materials published by Wiley-VCH GmbH

15214095, 0, Downloaded from https://advanced.onlinelibrary.wiley.com/doi/10.1002/adma.202411595 by Camilla Pegoraro - Readcube (Labtiva Inc.) , Wiley Online Library on [26/01/2025]. See the Terms and Conditions (https://onlinelibrary.wiley.com/terms-and-conditions) on Wiley Online Library for rules of use; OA articles are governed by the applicable Creative Commons License

15214095, 0, Downloaded from https://advanced.onlinelibrary.wiley.com/doi/10.1002/adma.202411595 by Camilla Pegoraro - Readcube (Labtiva Inc.) , Wiley Online Library on [26/01/2025]. See the Terms and Conditions (https://onlinelibrary.wiley.com/terms-and-conditions) on Wiley Online Library for rules of use; OA articles are governed by the applicable Creative Commons License

Flow cytometry-based studies of Cy5-labeled diblock copolymer **6b** revealed significant internalization at 4 °C that increased steadily over time, suggesting that energy-independent mechanisms contribute to its significant cellular internalization at 37 °C, with the coexistence of different uptake pathways (Figure 2B). Further quantitation of Cy5-labeled diblock copolymer **6b** accumulation in isolated mitochondria by flow cytometry resulted in a 66% accumulation after 3-hour incubation prior to mitochondria isolation (Figure 2C). The analog diblock copolymer **7** entered MDA-MB-231 cells via energy-dependent pathways at 37 °C, with no significant uptake observed 4 °C at the different time points analyzed (Figure S37, Supporting Information). These results suggest differential uptake mechanisms between **6b** and **7**, which could impact their mitochondrial targeting abilities.

After establishing a range of non-toxic concentrations for diblock copolymer families **6** and **7**, we studied cell internalization and sub-organelle localization using Cy5-labeled derivatives for live-cell confocal fluorescence microscopy monitoring in MDA-MB-231 cells performed at different times (pulse-chase study – 1, 2, 4, 6, 24 h). We could not functionalize diblock copolymer families **11** and **14** with Cy5 (or other biologically relevant molecules such as drugs or biomacromolecules) due to the absence of secondary amines; therefore, we discarded them from further investigation. Image processing using Pearson's correlation coefficient (Pearson r) revealed significant (Pearson $r > 0.5$) mitochondrial colocalization for PLO_n-PLP_m with a 1:3 n:m ratio (Figure 2D). Interestingly, no other PLO_n-PLP_m diblock copolymer colocalized with the mitochondria (Table S5, Supporting Information), with very low Pearson r values observed at all incubation times evaluated. We observed diblock copolymer **6b** in the mitochondria after 2 h of incubation but decreased at 6 h, as observed in the pulse-chase study (Table S5, Supporting Information). The behavior of diblock copolymer **6i** remained similar to **6b**, although mitochondrial colocalization occurred earlier, while we observed the mitochondrial colocalization of **6 h** at 1 h, which remained stable even after 24 h. The lack of mitochondrial targeting observed in diblock copolymers with different n:m ratios and block lengths, compared to **6b**, **h**, and **i**, suggests that Cy5 functionalization does not affect their subcellular localization. Unlike previous studies, where anionic polymers were functionalized with high Cy5 concentration (above μ1 M, > 1 eq.) to favor passive cellular diffusion and mitochondrial targeting,[23–25] in our study, we used a lower concentration (0.015 eq. Cy5 per polymeric chain) and copolymers with a polycationic block. To evaluate the selectivity of **6b**'s mitochondrial targeting activity, we included non-cancer cell lines (BJ fibroblasts and BV-2 microglial cells), an additional cancer line (estrogen-responsive MCF-7 breast cancer cells), and HepG2 cells, a liver-derived cell line employed in toxicology. After establishing non-toxic concentration ranges in 24- and 72-h cell viability studies (Figure S38, Supporting Information), we performed a pulse-chase study for 6b-Cy5 as previously described for MDA-MB-231 cells to assess differential cell internalization and sub-organelle localization. We observed mitochondrial colocalization in MCF-7 cells at 2 h (Figure 2D), which remained stable after 24 h (Table S6, Supporting Information). In contrast, we failed to detect mitochondrial colocalization in BJ fibroblast (Figure 2D), BV-2, or HepG2 cells (Table S6, Supporting Information). These results indicate the differential targeting behavior of 6b in cancer and non-cancer cell lines, suggesting tumor mitochondria specificity. For subsequent investigations, we focused on MDA-MB-231 cells due to their metabolic profile and metastatic potential, providing an ideal model for evaluating the efficacy of our mitochondria-targeted approach in aggressive breast cancer subtypes.

We synthesized and evaluated diblock copolymer **7** as a potential alternative to **6b** given the relevance of PLL as cell-penetrating peptides and their feasible chemical functionalization; however, colocalization analysis revealed lower levels of mitochondria colocalization over time, reaching a maximum Pearson r value of 0.4 at 2 h (Table S5, Supporting Information). Interestingly, we failed to find any diblock copolymer in lysosomes before mitochondrial colocalization, suggesting their significant direct translocation through the cell membrane, as demonstrated by the uptake studies and, thereby, their suitability as efficient mt-CPOs. Moreover, the lack of lysosomal colocalization implies that, in addition to direct cell membrane permeation, the uptake of compound **6b** could be clathrin-independent. These findings would align with previous observations by Kabanov and collaborators, where amphiphilic block copolymers (Pluronics) entered the cell through a concentration-dependent caveolae-mediated endocytosis pathway and subsequently targeted mitochondria.[26–28] To address potential safety concerns related to non-specific membrane disruption that may occur through a direct translocation mechanism, we evaluated the lytic properties of diblock copolymers **6b**, **6 h**, and **6i** using erythrocytes as a model system. Our findings revealed that diblock copolymers **6b**, **6 h**, and **6i** exhibited a robust non-hemolytic profile, with less than 10% hemolysis observed under physiological extracellular conditions (pH 7.4) across all tested concentrations, even displaying lower hemolytic activity than the negative control dextran (Figure S39, Supporting Information). Additionally, the lack of hemolytic activity at a more acidic pH (pH 5.5) (Figure S39, Supporting Information), representative of the lysosomal environment, indicated that diblock copolymers **6b**, **6 h**, and **6i** did not compromise the integrity of intracellular vesicle membranes and supported clathrin-independent uptake mechanisms.

Although colocalization analysis indicated that diblock copolymers **6b**, **h**, and **i** exhibited stronger mitochondrial tropism than diblock copolymer **7**, the Pearson r values suggest that the interaction between diblock copolymer **7** and mitochondria remains non-efficient and non-specific, implying weak and non-specific binding rather than an absence of any interaction. Overall, we found significantly lower direct cellular internalization efficiency of diblock copolymer **7** compared to our candidate mt-CPO **6b**, resulting in lower levels of mitochondrial targeting.

We next explored potential conformational variances between diblock copolymers **7** and **6b** to further decipher the physicochemical reasons behind differential cell uptake patterns. CD analysis of the secondary structure revealed the prevalence of the PLP chain in both diblock copolymers in a similar PPII structure (Figure S14, Supporting Information). Given this lack of insight into the conformational distinctions, we turned to diffusion-ordered NMR spectroscopy (NMR-DOSY), which leverages variations in diffusion coefficients to differentiate between species based on their hydrodynamic radii.[29] While diblock copolymer **6b** displayed a monomodal distribution in agreement with CD, providing evidence of a PPII conformation, diblock

© 2025 The Author(s). Advanced Materials published by Wiley-VCH GmbH

15214095, 0, Downloaded from https://advanced.onlinelibrary.wiley.com/doi/10.1002/adma.202411595 by Camilla Pegoraro - Readcube (Labtiva Inc.) , Wiley Online Library on [26/01/2025]. See the Terms and Conditions (https://onlinelibrary.wiley.com/terms-and-conditions) on Wiley Online Library for rules of use; OA articles are governed by the applicable Creative Commons License

copolymer **7** displayed a temperature-independent bimodal profile, indicating the coexistence of different conformations in solution attributed to the presence of PLL (PPII from PLP contribution and most probably alpha-helix conformation from PLL block) (Figure S40, Supporting Information). These findings agree with the study of Huesmann et al., which demonstrated a similar bimodal distribution in short-protected homopolylysines using GPC, CD, and NMR-DOSY.[30] While they observed the disappearance of the bimodal profile after deprotection, we attributed the persistent bimodal profile in our deprotected diblock copolymer **7** to the charge density λ, defined as the ratio between the net charge on amino acid residues and the total number of amino acids. Notably, at a medium charge density λ ($\approx$0.3, as calculated for diblock copolymer **7**), diblock polypeptides composed of Lys and Leu exhibit a transition region where helical and random coil conformations may coexist rather than solely falling within the random coil region.[31] This transition is characterized by a gradual decrease in helicity, leading to varying solvation environments and water shell interactions that result in distinct hydration radii, as evidenced by our NMR-DOSY results. Due to the presence of PLL, the bimodal conformation in solution of diblock copolymer **7** compared to **6b** (as shown by NMR-DOSY) may justify differential interactions with biological membranes, which could result in less pronounced cellular internalization by direct penetration and reduced mitochondrial targeting of diblock copolymer **7** compared to **6b**, as demonstrated by the biological studies.

Among all evaluated PLO_n-PLP_m diblock copolymers, we identified **6b**, **h**, and **i** as mt-CPOs. Our data indicate that a 1:3 n:m ratio, which ensures PPII formation and low zeta potential (<3 mV), as potentially crucial for mitochondrial targeting. Of note, the nature of the polycationic block also plays a significant role in mitochondrial targeting.

2.3. Understanding the Mitochondrial Targeting of Polyproline-based Diblock Polymers: Binding to Cardiolipin

To investigate the mechanism driving mitochondrial targeting and rationalize the preferential accumulation of PLO_n-PLP_m diblock copolymers with an n:m ratio 1:3, we performed studies involving mitochondria depolarization, interaction with CL, and membrane transformation properties (physical changes, fluidity, and tension).

Mimicking reported mitochondria depolarization studies using flow cytometry,[32] we first explored whether mitochondrial targeting of diblock copolymer **6b** relies on charge affinity due to the highly negative mitochondrial membrane potential. We qualitatively assessed mitochondrial depolarization in MDA-MB-231 cells following a 4-h incubation with 30 µM carbonyl cyanide chlorophenyl hydrazine (CCCP), a mitochondrial uncoupler. We observed a decrease in the fluorescence intensity of the potential-dependent MitoTracker Red CM-H2Xros compared to the potential-independent MitoTracker Green FM in control cells, indicating mitochondrial depolarization (Figure 2E). We then exposed the CCCP-treated MDA-MB-231 cells to Cy5-labeled diblock copolymer **6b** for 3 h (1 h after CCCP incubation) and confirmed the mitochondrial accumulation of diblock copolymer **6b** even under depolarization conditions, as evident from the confocal fluorescence microscopy images (Figure 2E).

We further quantified the fluorescence intensity of Cy5-labeled diblock copolymer **6b** in polarized and depolarized mitochondria, labeled both by MitoTracker Red CM-H2Xros (potential-dependent) and MitoTracker Green FM (potential-independent). In depolarized mitochondria (CCCP versus untreated), we detected a significant reduction in the labeling by the potential-dependent MitoTracker Red CM-H2Xros compared to the polarized mitochondria (red bars; Figure 2F), while labeling by the potential-independent MitoTracker Green FM remained consistent (green bars; Figure 2F). Moreover, we observed no statistically significant variation in Cy5-labeled diblock copolymer **6b** fluorescence between polarized and depolarized mitochondria (orange bars; Figure 2F). These findings suggest that diblock copolymer **6b** targets mitochondria in a potential-independent manner. In contrast to conventional cationic targeting ligands like TPP, which rely solely on the mitochondria potential for their binding affinity, our candidate mt-CPO may be applied when potentials fluctuate, such as during specific cell cycles, after pharmacological interventions, or in distinct disease states.

The mitochondrial membrane differs from all other membranes due to the presence of the unique double-negative charged phospholipid CL, which plays a vital role in mitochondrial bioenergetics, dynamics, mitophagy, and apoptosis and may influence cancer progression and aggressiveness.[33] We studied multiple CL-rich membrane model systems using various approaches to investigate diblock copolymer interactions with CL. We employed a competitive binding assay to study the affinities of our diblock copolymers for CL employing a CL-specific fluorescent probe (MitoCLue)[34] and an artificial membrane model (small unilamellar vesicles (SUVs) composed of 1,2-dioleoyl-sn-glycero-3-phosphocholine (DOPC) and CL (3:1 molar ratio)) or a more complex and biologically relevant model (mitoplasts isolated from rat heart and liver) (Figures S41 and S42, Supporting Information). The results revealed the essential nature of the polycationic component of all tested diblock copolymers for interactions with CL (Table S7, Supporting Information). Diblock copolymers containing PLO (**6b**, **f**, and **g**), PLL (**7**), and PArg (**14**) blocks exhibited comparably high ($EC_{50} \approx$ 1–1.7 µM) affinity for CL in SUVs (very close to the affinity of the natural CL ligand – cytochrome c; EC_{50} = 0.323 $\pm$ 0.017 µM) while PHis: PLP diblock copolymer **11** and homopolymers of PLP (**15a and b**) did not bind to CL-rich SUVs even at a 1 mM (Table S7, Supporting Information). We observed the same trend using the mitoplast membrane model (Figures S41 and S42, Table S7, Supporting Information), although diblock copolymer **6b** had slightly higher affinity compared to other diblock copolymers regardless of mitoplast source (heart or liver tissue, EC_{50} = 3.456 $\pm$ 0.065 µM and 3.845 $\pm$ 0.314 µM, respectively).

We next confirmed the intercalation of diblock copolymers in the bilayer of CL-containing SUVs using an alternative fluorescent probe – 1,6-diphenyl-1,3,5-hexatriene (DPH) (Figure S43, Supporting Information). DPH fluorescence quenches when displaced from the bilayer hydrophobic region. We again found the superior nature of diblock copolymer **6b** compared to **f** and **g**, which quenched the fluorescence of DPH more effectively at a lower concentration when incubated with CL-containing SUVs (Figure S43, Supporting Information). In contrast, we observed

© 2025 The Author(s). Advanced Materials published by Wiley-VCH GmbH

15214095, 0, Downloaded from https://advanced.onlinelibrary.wiley.com/doi/10.1002/adma.202411595 by Camilla Pegoraro - Readcube (Labtiva Inc.) , Wiley Online Library on [26/01/2025]. See the Terms and Conditions (https://onlinelibrary.wiley.com/terms-and-conditions) on Wiley Online Library for rules of use; OA articles are governed by the applicable Creative Commons License

no interaction between the hydrophobic region of DOPC SUVs (CL-free SUVs) and diblock copolymers **6b**, **f**, and **g**, highlighting the crucial role of CL in facilitating the interaction with the polycationic block of the tested diblock copolymers (Figure S43, Supporting Information). These studies emphasize the significance of polycationic blocks to the mitochondria-targeting properties of our diblock copolymers; however, the high affinity for CL of diblock copolymers **6f** and **g** does not fully account for the lack of their mitochondria targeting in live cells, as seen in Table S5 (Supporting Information). Moreover, our in vitro results revealed mitochondria potential-independent accumulation of diblock copolymers (Figure 2E,F), suggesting that although the electrostatic interaction between the polycationic component and the negatively charged CL strengthens mutual binding, we hypothesized that this interaction does not represent the sole binding force.

To explore our hypothesis, we employed additional model-membrane systems. Supported lipid bilayers (SLBs) serve as valuable model membranes to investigate interactions between polymeric carriers, including diblock copolymers and lipid membranes. SLBs offer numerous advantages, including their ability to replicate the fluidity and composition of biological membranes, thereby creating a physiologically relevant environment for studying membrane interactions.[35] We assembled SLBs with a lipid composition of 2:1 POPC (1-palmitoyl-2-oleoyl-sn-glycero-3-phosphocholine) to CL and a lipid-conjugated dye Atto655-DOPE. We employed Atto488-labeled diblock copolymers to qualitatively image their presence on the membrane. We examined the interaction of diblock copolymers with the membrane after adding 5 µM diblock copolymers to SLBs in buffer B (150 mM KCl, 25 mM Tris, pH 7.2). Simpler model membranes based on SUVs for CL-competitive binding assays and Z-potential measurements (Figure S44, Supporting Information) revealed that diblock copolymers interacted with lipid membranes primarily through ionic interactions, owing to the high negative charge of CL. To discern interactions specific to CL from overall charged interactions, we employed a control membrane composed of equimolar POPC and POPG (1-palmitoyl-2-oleoyl-sn-glycero-3-phosphoglycerol). Notably, diblock copolymers **6b** and **h** formed membrane patches atop CL-rich SLBs that persisted after subsequent washing steps (**Figures 3A** and S45 (Supporting Information) for **6b** titration in CL-rich SLBs). Previous studies employing coarse-grained molecular dynamics (MD) simulations revealed intriguing physicochemical properties of CL-rich membranes; the presence of CL is associated with a reduction in the required lateral pressure for bilayer buckling, rendering membranes more responsive to curvature-inducing agents.[36,37] Additionally, CL tends to accumulate in regions of negative curvature, resulting in localized negative charges. Our observations revealed that diblock copolymers **6b** and **h** form membrane patches, indicating their involvement in curvature-inducing interactions with CL-containing membranes (Figure 3A). Moreover, cationic polymers can bridge these patches, as negatively curved regions display enrichment in negatively charged CL. Overall, our data suggest that polycationic diblock copolymers induce membrane remodeling by facilitating buckling and patch formation, particularly in CL-rich environments, as opposed to the membrane with the same charge distribution as POPG (Figure S46, Supporting Information).

We next employed atomic force microscopy (AFM) to determine the height of the diblock copolymer patches, revealing a doubling in height (≈6 nm) compared to a single lipid bilayer (Figure 3B), consistent with the previous reports on Langmuir monolayers that suggest CL-rich bilayers undergo folding upon increasing lateral pressure.[38] We propose that such CL-rich membranes can generate patches of membrane facilitated by ionic bridging through polycationic diblock copolymers (model shown in Figure 3C). These observations underscore the preference of diblock copolymers **6b** and **6h** to bind CL-rich membranes and induce physical changes in membrane behavior. The alternative diblock copolymer **7** did not reproduce this patch-formation effect in CL-rich membranes (Figure S47, Supporting Information), which may be attributed to its distinct conformation in solution (as previously described). Moreover, for diblock copolymer ratios such as **6a** (n:m ratio 3:1) and **6c** (n:m ratio 1:2), the initial patch formations observed in CL-rich SLBs disappeared rapidly after washing for **6a** and dramatically reduced for **6c** (Figure S48, Supporting Information). As previously discussed, membrane patch formation requires preceding membrane remodeling processes induced by the interaction of diblock copolymers such as **6b** with the CL-rich lipid bilayer. The orientation of the diblock copolymer within the membrane may vary depending on the relative mismatch between PLP length and bilayer thickness;[39] the distinction in proline unit content may prompt a weaker binding affinity to the membrane for diblock copolymer **6a** compared to **6b**, **h**, and **c**, thus resulting in the cessation of induced buckling upon washing. Overall, our data suggest that PLP content and n:m ratio may represent crucial factors controlling CL interactions. Of note, we also established a correlation between patch formation and mitochondrial colocalization in vitro for mt-CPO candidates **6b** and **h** (n:m 1:3 ratio).

Next, we explored membrane transformation upon interaction with diblock copolymers more deeply and investigated membrane fluidity responses. Membrane fluidity – reflecting the interaction of membrane-active agents – of a lipid bilayer is influenced by temperature, lipid composition, substrate (in the case of SLBs), and cholesterol content. CL presence in model membranes significantly impacts bilayer fluidity; consequently, the changing fluidity of model CL membranes after exposure to polymers indicates the degree of membrane interactions. We employed z-scan fluorescence correlation spectroscopy (z-scan FCS) to measure the diffusion of the lipid-conjugated dye Atto655-DOPE and Atto488-labeled diblock copolymers in the lipid bilayer.[40] After adding 5 µM of diblock copolymers and subsequent washing, diblock copolymers **6b** and **h** significantly decreased membrane fluidity (Figure 3D, $D_{6b} = 4.13 \pm 0.25\ \mu m^2 s^{-1}$ and $D_{6\ h} = 5.12 \pm 0.94\ \mu m^2 s^{-1}$) compared to the blank (PBS). We observed consistent membrane fluidity across different membrane regions, with no significant difference between the diffusion coefficients in membrane patches ($\mathbf{6b}_{patch}$ and $\mathbf{6h}_{patch}$ in Figure 3D) and regions without patches (**6b** and **6 h** in Figure 3D). These findings suggest that incorporating diblock copolymers **6b** and **6 h** into the membrane uniformly decreased membrane fluidity without localized effects, suggesting that these diblock copolymers induced membrane ordering to initiate buckling. Furthermore, the correlation amplitude from FCS measurements provided insight into the average number of particles in the focal area. A comparison of the average number of

© 2025 The Author(s). Advanced Materials published by Wiley-VCH GmbH

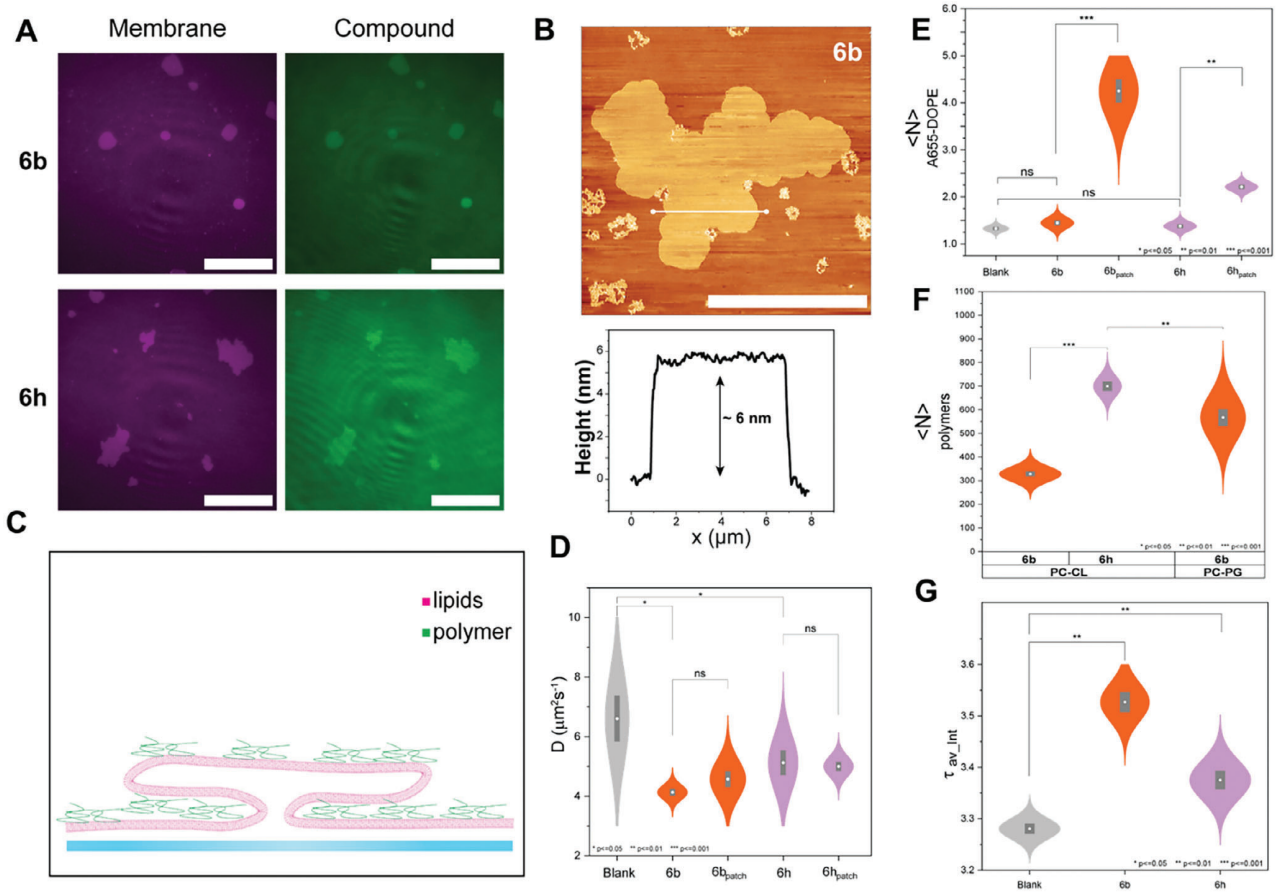


Figure 3. Physical studies of polyproline-based diblock copolymers in cardiolipin-rich membrane models. A) Total internal reflection microscopy images of POPC:CL 2:1 membrane model labeled with Atto655-DOPE (magenta) and diblock copolymers labeled with Atto488 (green). Images depict the formation of patches for diblock copolymers **6b** and **h**. Scale bar: 20 μm. B) Atomic force spectroscopy (AFM) image of a membrane patch. The top Image depicts a POPC:CL 2:1 membrane incubated with 5 μM diblock copolymer **6b** after washing. Scale bar: 10 μm. The bottom graph indicates the membrane patch height (nm) along the selected region (denoted by the white line) in the AFM top figure (x-axis – width in μm). C) Schematic of the proposed membrane buckling and folding procedure that forms patches. D) Diffusion coefficient (D, $\mu m^2 s^{-1}$) of the membrane at 28 °C for Atto655-DOPE for cardiolipin-rich membranes incubated with diblock copolymers at patch-containing (**6b**$_{patch}$ and **6h**$_{patch}$) and patch-lacking (**6b** and **6 h**) regions. E) Average number of A655-DOPE particles (<N> A655-DOPE, number of membrane particles) for cardiolipin-rich membranes incubated with diblock copolymers at patch-containing (**6b** and **6 h**) and patch-lacking (**6b**$_{patch}$ and **6h**$_{patch}$) regions acquired through fluorescence correlation spectroscopy. F) Average number of diblock copolymer particles (<N> polymer) bound to cardiolipin-rich membranes acquired through fluorescence correlation spectroscopy of labeled diblock copolymers **6b** and **6h**. G) Intensity-averaged fluorescence lifetime of Flipper-TR-stained small unilamellar vesicles (τ_{av_Int}) incubated with diblock copolymers **6b** and **6h**. Figure C, D, E, and G data were analyzed using two-way ANOVA. Significance reported as $*p \leq 0.05$, $**p \leq 0.01$, $***p \leq 0.001$ (ns = not significant).

Atto655-DOPE membrane particles revealed an $\frac{\langle N_{patch} \rangle}{\langle N_{no\ patch} \rangle}$ value for diblock copolymer **6b** of 2.94 and **6 h** of 1.60 (Figure 3E), indicating a 2-fold higher concentration of lipid particles in the focal area for **6b** compared to **6h**. We performed similar measurements for Atto488-labeled diblock copolymers, wherein diffusion in the lipid membrane reflects interaction strength (Figure S49, Supporting Information); overall, diblock copolymer **6 h** demonstrated a significantly lower diffusion coefficient than **6b**, suggesting stronger membrane interactions. Overall, diblock copolymer **6 h** displayed a significantly higher binding affinity to the CL membrane than **6b** (from the correlation amplitude), while we observed no significant differences upon incubation of **6b** with equimolar POPC-POPG control membranes (Figure 3F).

Agents inducing membrane curvature also modulate local membrane tension.[41] The fluorescent membrane tension probe, Flipper-TR (termed Flipper hereafter), displays alterations in fluorescence lifetime in response to changing membrane tension/order[42] and can probe the response of different polymers incubated with CL-containing SUVs.[43] After adding 1 μM Flipper, we incubated SUVs with 5 μM diblock copolymers; subsequently, we diluted the SUVs 10-fold before measuring Flipper fluorescence lifetime at 25 °C (Figure S50, Supporting Information). The intensity-averaged fluorescence lifetime of Flipper increased for diblock copolymers **6b** and **6 h** compared to a blank sample with CL-containing SUVs ($\tau^{blank} = 3.28 \pm 0.02$ ns), while diblock copolymer **6b** exhibited a significantly higher response compared to **6 h** ($\Delta\tau^{6b} = 0.18$ ns and $\Delta\tau^{6h} = 0.09$ ns) (Figure 3G).

© 2025 The Author(s). Advanced Materials published by Wiley-VCH GmbH

15214095, 0, Downloaded from https://advanced.onlinelibrary.wiley.com/doi/10.1002/adma.202411595 by Camilla Pegoraro - Readcube (Labtiva Inc.) , Wiley Online Library on [26/01/2025]. See the Terms and Conditions (https://onlinelibrary.wiley.com/terms-and-conditions) on Wiley Online Library for rules of use; OA articles are governed by the applicable Creative Commons License

15214095, 0, Downloaded from https://advanced.onlinelibrary.wiley.com/doi/10.1002/adma.202411595 by Camilla Pegoraro - Readcube (Labtiva Inc.) , Wiley Online Library on [26/01/2025]. See the Terms and Conditions (https://onlinelibrary.wiley.com/terms-and-conditions) on Wiley Online Library for rules of use; OA articles are governed by the applicable Creative Commons License

An increase in fluorescence lifetime indicates elevated CL membrane tension, corroborating the previously observed reduced fluidity and demonstrating the ability of diblock copolymers **6b** and **6 h** with a n:m ratio 1:3 to alter CL-containing membrane order.

Overall, the CL-specific interaction of diblock copolymers suggests their unique affinity for mitochondria, which holds relevance for developing mt-CPOs and their potential use as antitumorigenic therapeutics.

2.4. Unveiling the Inherent Biological Activity of Novel Mitochondrial Targeting Polyproline-Based Diblock Polymers at the Mitochondrial Level

Common mitochondrial abnormalities in cancer cells, such as hyperpolarized mitochondrial membrane potential (−220 vs −140 mV in normal cells), elevated pH, and increased reactive oxygen species (ROS) production, highlight the significance of targeting mitochondria in cancer therapy.[4,44] One example is the Warburg effect – using glycolysis for energy production even in the presence of oxygen – representing the primary type of metabolic reprogramming in cancer cells (including MDA-MB-231). However, flexible mitochondrial metabolism also supports cells' ability to adapt to metabolic stress and maintain their metastatic potential, which plays a crucial role in cancer cell survival.[45] For these reasons, we next performed activity studies to explore the impact of our diblock copolymers (evaluated at sub-IC_{50} concentrations (>IC_{15})) on mitochondrial metabolism and cell morphology in MDA-MB-231 cells.

Given the pivotal role of mitochondrial membrane potential in regulating membrane permeability, cell apoptosis, and the selection of non-functional mitochondria, a treatment strategy that induces mitochondrial depolarization may hold promise as an antitumorigenic therapy. First, we sought to demonstrate that diblock copolymers **6b**, **h**, and **i** induced rapid mitochondrial depolarization in cells using the fluorescent probe 5,5′,6,6′-tetrachloro-1,1′,3,3′-tetraethylbenzimidazolcarbocyanine iodide (JC-1). After accumulating in polarized mitochondria, JC-1 emits red fluorescence due to the formation of aggregates; meanwhile, JC-1 emits green fluorescence from J-monomers released into the cytosol when in depolarized mitochondria.[46] We quantified changes in membrane potential by measuring the red/green fluorescence intensity ratio; overall, we observed a significant loss of mitochondrial membrane potential after a 6-h incubation with diblock copolymers **6b** and **6 h** compared to non-treated control cells (set at 100%) that displayed partial restoration by 24 h (**Figure** 4A). Diblock copolymer **6i** initially induced significant mitochondrial depolarization, which recovered after 6 h but became re-established after 24 h (Figure 4A). Despite cell adaptation to membrane potential perturbation, induced mitochondrial depolarization may represent a crucial initial mechanism that alters the mitochondria, particularly in cancer cells. Indeed, mitochondrial depolarization may serve as a critical early event that triggers various downstream effects, including increased ROS production, disrupted ATP synthesis, and activation of apoptotic pathways.[47,48]

We next demonstrated that diblock copolymers **6b**, **h**, and **i** induced significant increases in ROS production (**6b<6h<6i**) after 24 h of treatment compared to non-treated control cells (set as 100%) (Figure 4B). Although cancer cells exhibit higher ROS levels due to increased hypoxia and levels of electrons leaking from the electron transport chain (ETC), the upregulation of antioxidant enzymes (e.g., superoxide dismutase) maintains redox homeostasis.[49,50] However, additional ROS production in cancer cells beyond basal levels can disrupt redox homeostasis and trigger oxidative stress, which leads to cell death.

Given the pivotal role of mitochondria in cellular energy production via oxidative phosphorylation (OXPHOS), we analyzed metabolic alterations following diblock copolymer **6b**, **h**, and **i** treatment at sub-IC_{50} final concentrations (>IC_{40} (C1)) and a diluted concentration (>IC_{15} (C2, dilution factor C1/C2 = 1.5)) to study concentration-dependent effects. Seahorse XF Analyzer studies revealed a compromised oxygen consumption rate (OCR; related to different mitochondrial functions) after a 24-h exposure to certain diblock copolymers (Figure 4C). Diblock copolymers **6 h** and **i** induced a significant concentration-independent reduction of OCR related to the spare respiration capacity (SRC) (Figure 4C, left), a functional parameter that measures how cells respond to increased energy demands by enhancing mitochondrial activity. Even though cancer cells compensate for ATP demand through aerobic glycolysis (the Warburg effect), which positively correlates with the aggressive nature of tumor cell lines such as MDA-MB-231,[51] the decreased SRC induced by diblock copolymers **6 h** and **i** holds relevance considering that conventional chemotherapy increases SRC as a drug resistance mechanism.[52] Diblock copolymers **6b**, **6 h** (both concentration-independent), and **6i** (concentration-dependent) significantly reduced the OCR related to ATP production, indicating decreased basal respiration to produce ATP coupled to the ETC during OXPHOS in mitochondria (Figure 4C, right), particularly by diblock copolymer **6b**.

To confirm Seahorse results and investigate the mechanisms of action of diblock copolymer with the most significant therapeutic potential, we analyzed OCR after acute treatment with diblock copolymer **6b** using a substrate-uncoupler-inhibitor titration (SUIT) protocol in the Oroboros Oxygraph O2k system (Figure 4D). We treated MDA-MB-231 cells at sub-IC_{50} final concentrations (>IC40 (C1)) and diluted concentrations (>IC_{15} (C2 and C3, dilution factor C1/C2 = 2; C2/C3 = 5)) to study potential concentration-dependent effects. Diblock copolymer **6b** induced a significant concentration-dependent reduction in OCR in LEAK and OXPHOS states in the presence of complex I (CI) substrates pyruvate and malate (Figure S51, Supporting Information). The LEAK state, characterized by a non-phosphorylating resting state, is a reference point for measuring ATP production efficiency in the OXPHOS state. Adding glutamate as another NADH-dependent CI substrate did not compensate for the **6b**-induced decreased OCR observed in the presence of pyruvate and malate (Figure 4D). These results suggest either direct CI inhibition of or CI-CL complex disruption that significantly reduces CI activity.[53] The strong dependence of CI function on CL may be compromised by **6b**-induced membrane structural rearrangements (patch formation), leading to decreased enzymatic activity. The addition of the complex II (CII) substrate succinate induced maximal electron transfer capacity (Figure 4D), as evidenced by the absence of any effect after standard uncoupler CCCP treatment (Figure S51, Supporting Information). This data indicates that diblock copolymer **6b** significantly reduces the ETC coupling

© 2025 The Author(s). Advanced Materials published by Wiley-VCH GmbH

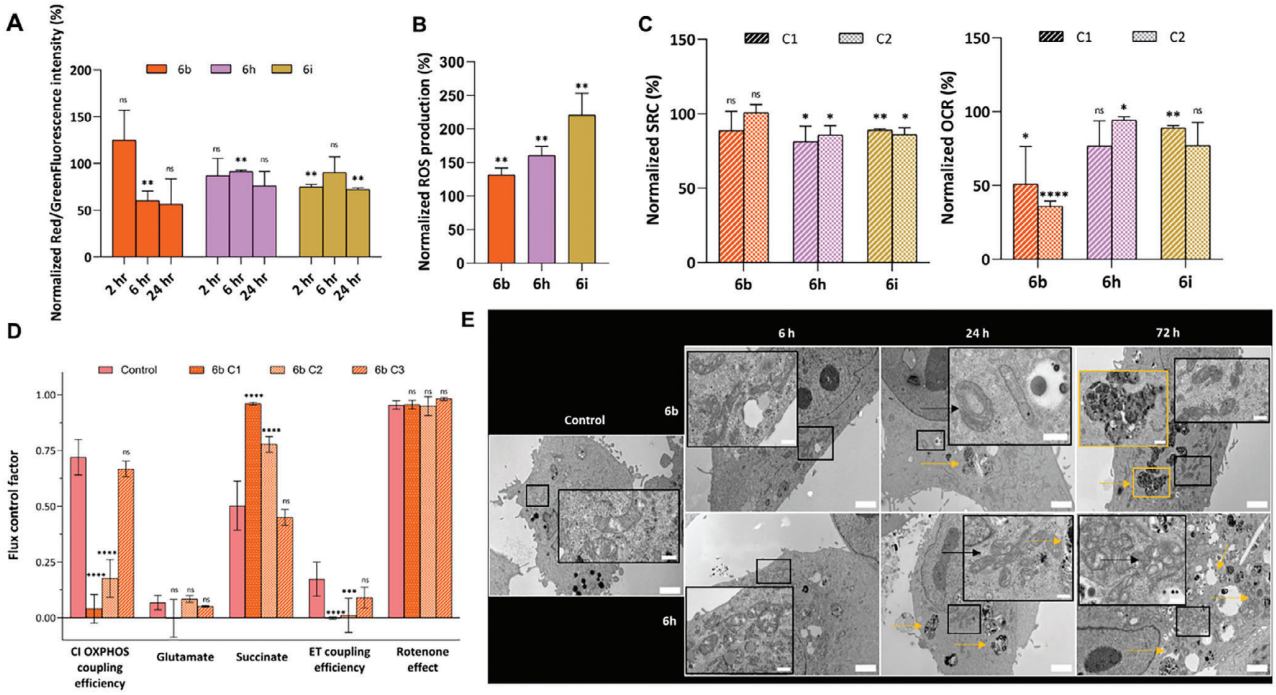


Figure 4. Mitochondria-dependent biological activity of polyproline-based diblock copolymers. **A)** Mitochondrial membrane potential measured after treatment with diblock copolymers **6b**, **h,** and **i** over time (Concentration (C): C < IC_{50}; t-test comparing to control set as 100%; $n = 3$, mean ± SEM). **B)** Reactive oxygen species (ROS) production analysis after a 24-h treatment with diblock copolymers **6b**, **h,** and **i** (Concentration (C): C < IC_{50}; t-test comparing to control set as 100%; $n = 3$, mean ± SEM) **C)** Spare respiration capacity (SRC, left) and oxygen consumption rate (OCR) (right) analysis by Seahorse XF after a 24-h treatment with diblock copolymers **6b**, **h,** and **i** (Concentration (C): C1 < IC_{50}, diluted concentration C2 (C1/C2 = 1.5); OCR measured in pmol/min/2 × 10^4 cells; t-test comparing to the control set as 100%; $n = 3$, mean ± SEM. **D)** Flux control factor analysis (see **SI** for details) after treatment with diblock copolymers **6b** (Concentration (C): C1 < IC_{50}, diluted concentration C2 and C3, dilution factor C1/C2 = 2; C2/C3 = 2); OCR measured in pmol/(s*1 × 10^6 cells), two-way-ANOVA test comparing to control, $n = 3$, mean ± SEM). **E)** Mitochondria morphological analysis by transmission electron microscopy after treatment with diblock copolymers **6b** and **h** (Concentration (C): C < IC_{50}) over time. Lysosomal degradation is highlighted by the yellow arrows. Scale bar main images: 20 µm; scale bar inset images: 500 nm. Significance reported as *$p \leq 0.05$, **$p \leq 0.01$, ***$p \leq 0.001$, ****$p \leq 0.0001$ (ns = not significant).

efficiency to OXPHOS, enabling the ETC to operate maximally independent of ATP synthesis via OXPHOS. These findings, supported by reduced CI OXPHOS and ETC coupling efficiency, provide evidence that diblock copolymer **6b** affects mitochondrial metabolism.

We morphologically analyzed MDA-MB-231 cells after treatment with diblock copolymers **6b** and **h** at various time points to investigate the relationship between metabolic alterations and mitochondrial morphology. Transmission electron microscopy (TEM) analysis revealed several changes in mitochondrial morphology in treated cells compared to control cells (Figure 4E). The qualitative analysis by TEM revealed a time-dependent increase in the number of lysosomes engulfing mitochondrial material (yellow arrows in Figure 4E), suggesting lysosomal-dependent mitophagy, a selective degradation process for damaged/dysfunctional mitochondria. Mitophagy impairments (usually preceded by lost mitochondrial homeostasis[54]) that include mitochondrial depolarization and increased ROS production have been linked to cancer progression and drug resistance;[55] however, studies have reported the efficacy of therapies targeting mitochondrial dysfunction in TNBC models via apoptotic and mitophagy-dependent mechanisms.[54] The increased presence of rounded mitochondria may indicate swelling of the mitochondrial matrix in treated cells, suggesting mitochondrial damage or stress (black arrows and squares in Figure 4E); of note, diblock copolymer **6 h** treatment induced particularly evident effects (Figure 4E). Exposure to diblock copolymer **7** did not affect mitochondrial function/morphology in MDA-MB-231 cells, as demonstrated by the unaltered OCR profile (Figure S52, Supporting Information) and morphology (FigureS53, Supporting Information). Overall, these findings underline the mitochondria-dependent biological activity of diblock copolymers **6b**, **h,** and **i**.

In summary, candidate mtCPOs **6b**, **6**, and **i** exhibited antitumorigenic properties via a concentration-dependent mitochondrial pathway. These diblock copolymers induced mitochondrial depolarization, increased ROS production, and reduced CI OXPHOS and ETC coupling efficiency, leading to altered mitochondrial metabolism. Our findings suggest that diblock copolymers may trigger lysosomal-dependent mitophagy, highlighting their potential as novel therapeutic agents for cancer treatment.

© 2025 The Author(s). Advanced Materials published by Wiley-VCH GmbH

15214095, 0, Downloaded from https://advanced.onlinelibrary.wiley.com/doi/10.1002/adma.202411595 by Camilla Pegoraro - Readcube (Labtiva Inc.) , Wiley Online Library on [26/01/2025]. See the Terms and Conditions (https://onlinelibrary.wiley.com/terms-and-conditions) on Wiley Online Library for rules of use; OA articles are governed by the applicable Creative Commons License

15214095, 0, Downloaded from https://advanced.onlinelibrary.wiley.com/doi/10.1002/adma.202411595 by Camilla Pegoraro - Readcube (Labtiva Inc.) , Wiley Online Library on [26/01/2025]. See the Terms and Conditions (https://onlinelibrary.wiley.com/terms-and-conditions) on Wiley Online Library for rules of use; OA articles are governed by the applicable Creative Commons License

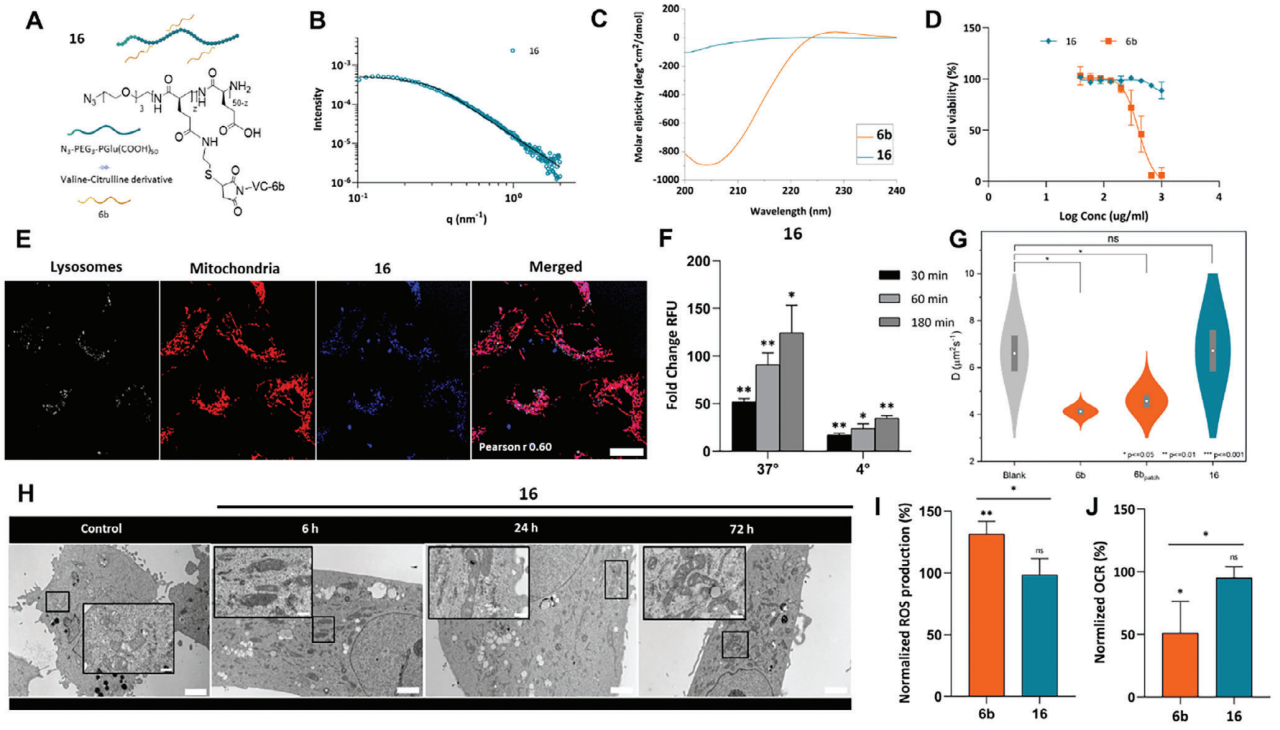


Figure 5. PGA- diblock copolymer 6b conjugate functions as a non-toxic mitochondrially-targeted cell penetrating platform. **A)** Schematic representation of nanoconjugate **16** (See **SI** for complete synthesis and characterization). **B)** Small-angle x-ray scattering (SAXS) data for nanoconjugate **16** where intensity is expressed as a function of the scattering momentum transfer, q ($q = 4\pi\sin(\theta)/\lambda$). **C)** Circular dichroism (CD) spectra of nanoconjugate **16** compared to diblock copolymer **6b**. **D)** MDA-MB 231 cell viability by MTS assay after treatment with nanoconjugate **16** or diblock copolymer **6b** (IC_{50} > 1 mg/ml) (72 h, $n = 3$, mean ± SEM). **E)** Confocal images of **16** uptake at 2 h post-treatment in MDA-MB-231 cells following a pulse-chase experiment (Table S8, Supporting Information) (White – LysoTracker Blue for lysosomes; Red – MitoTracker Red CM-H2Xros for mitochondria; Blue – Cy5 for **16**). The colocalization of nanoconjugate **16** with Mitotracker Red is shown in the merged image (in purple). The Pearson r (2 h) value was calculated using the ImageJ – JACoP plugin. Scale bar: 10 µm. **F)** Internalization of **16** measured over time at 37° (endocytic-dependent pathway) and 4° (endocytic-independent pathway) by flow cytometry ($n = 3$, mean ± SEM). Data expressed as fold change in relative fluorescence units (RFU) to $t = 0$; t-test comparing to the control set as 100% ($n = 3$, mean ± SEM). **G)** Diffusion coefficient (D, $\mu m^2 s^{-1}$) of the membrane at 28 °C for Atto655-DOPE for CL-rich membranes incubated with diblock copolymers at patch-containing (**6b**$_{patch}$) and patch-lacking (**6b** and **16**) regions. **H)** Mitochondria morphological studies by TEM after treatment with **16** (at an equivalent concentration of diblock copolymer **6b**) at 6, 24, and 48 h. Scale bar main images: 20 µm; scale bar insert images: 500 nm **I)** ROS production analysis after a 24-h treatment with nanoconjugate **16** (at an equivalent concentration of diblock copolymer **6b**) (t-test comparing to control set as 100% and treatments **6b** and **16**; $n = 3$, mean ± SEM). **J)** Oxygen consumption rate (OCR) related to ATP-production coupled respiration analysis by Seahorse XF after a 24-h treatment with **16** (at an equivalent concentration of diblock copolymer **6b**) (OCR measured in pmol/min/2^10^4 cells, t-test comparing to control set as 100% and diblock copolymer **6b** as 16%; $n = 3$, mean ± SEM). Significance reported as $*p \leq 0.05$, $**p \leq 0.01$ (ns = not significant).

2.5. Envisioning the Translatability of a Selected Mitochondrial Targeting Candidate: Targeting Mitochondria for Future Applications

Our findings have reported the biological activity of diblock copolymers **6b**, **h**, and **i**, thereby demonstrating the potential of these mtCPOs as a mitochondria-dependent anti-tumorigenic approach at sub-IC_{50} concentrations (>IC_{15}). To leverage the potential use of the selected candidate diblock copolymer **6b** as a mitochondria-targeting ligand, we selected a linear PGA modified with a short PEG chain (PEG_3-PGA_{50}, diblock copolymer **17**) as a non-toxic nanocarrier for functionalization with **6b** through a valine-citrulline (VC) linker (**Figure** 5A). The VC linker self-immolates in cathepsin B-rich lysosomal environments,[56] thus ensuring complete intracellular nanocarrier degradation and efficient diblock copolymer release. We obtained the final functionalized nanocarrier N_3-PEG_3-PGA_{50}-VC-6b (diblock copolymer conjugate **16**) through a convergent synthetic scheme (Scheme S5 (Supporting Information), detailed synthesis described in the SI) involving a VC-functionalized diblock copolymer **6b** (**6b-VC**, Scheme S6, Figures S54 and S55, Supporting Information) and N_3-PEG_3-PGA_{50} functionalized with S-(2-pyridylthio)cysteamine hydrochloride (**17-PD**, Scheme S7, Figures S56 and S58, Supporting Information). We achieved a 3.3% wt. Functionalization of **17-PD** with **6b-VC** (Figures S59 and S60, Supporting Information), ensuring that the concentration of diblock copolymer **6b** incorporated into the final nanocarrier remained below the IC_{15} threshold, the lowest concentration that we observed mitochondrial anti-tumorigenic activity.

Physicochemical characterization of nanoconjugate **16** revealed a comparable branched structure, compact core (with no aggregated structures in solution (q–s = 0)), and a Rg_{corr}

© 2025 The Author(s). Advanced Materials published by Wiley-VCH GmbH

15214095, 0, Downloaded from https://advanced.onlinelibrary.wiley.com/doi/10.1002/adma.202411595 by Camilla Pegoraro - Readcube (Labtiva Inc.) , Wiley Online Library on [26/01/2025]. See the Terms and Conditions (https://onlinelibrary.wiley.com/terms-and-conditions) on Wiley Online Library for rules of use; OA articles are governed by the applicable Creative Commons License

close to that of parental **6b** (Figure 5B). Zeta potential assessment confirmed the expected negatively-charged nature of PGA (-15.7 ± 0.2 mV), while CD analysis indicated a random coil conformation due to PGA content (Figure 5C). As expected, final functionalized nanoconjugate **16** presented a safer biological profile, demonstrating over 80% cell viability at all concentrations evaluated in MDA-MB-231 cells (Figure 5D) and BJ fibroblasts (Figure S61, Supporting Information) after 24 and 72 h. A Cy5-labeled derivative of final functionalized nanoconjugate 16 (Scheme S8, Figure S62, Supporting Information) revealed the maintenance of the mitochondria colocalization capability observed for diblock copolymer **6b**, but this time, a high Pearson r value (>0.6) was obtained after only 30 min after incubation in MDA-MB-231 cells (Figure 5E; Table S8, Supporting Information). Interestingly, we failed to find nanoconjugate **16** in lysosomes before mitochondrial colocalization, as we observed for parental **6b**, suggesting its direct translocation through the cell membrane; however, additional studies (outside the scope of the current manuscript) would be required to fully understand the whole cell internalization mechanism. These results indicate that nanocarrier charge and secondary structure play a role in mitochondrial targeting, but they do not represent the primary driving force. Furthermore, although zeta potential analysis in SUVs demonstrated no significant increase after incubation compared to the blank (SUVs treated with PBS) (Figure S63, Supporting Information), nanoconjugate **16** formed selective membrane patches in CL-rich SLBs that remained even after washing (Figure S64, Supporting Information). Reduced ionic interaction, possibly due to the small %wt of **6b** conjugated in **16**, may explain the decreased number and size of patches compared to the parent **6b**; however, we demonstrated that the nanoconjugate **16** binds to CL-rich membranes to induce folding and, as such, reproduces the behavior observed of the original diblock copolymer **6b** (Figure S64, Supporting Information).

Our flow cytometry findings revealed that the PGA nanoconjugate **16** supported significant cell internalization at 4 °C via an unconventional energy-independent uptake that increased steadily over time (as previously observed for **6b**) (Figure 5F). Indeed, although previously reported cell-penetrating peptides boost the internalization efficiency of anionic nanoparticles via an energy-dependent mechanism,[57–59] we observed significant direct cell membrane penetration for nanoconjugate **16** (Figure 5F). The small size (Rg 5.0 ± 0.3 nm by SAXS), and the suggested flexibility/deformability of **16** attributed to the VC spacer and the linear architecture of PGA, might represent primary factors contributing to preferential uptake through direct penetration. Indeed, small particle sizes (<10 nm) and surface functionalization with CPOs represent valuable strategies to tune material to use direct cell membrane permeation as an uptake mechanism.[60] Van Lehn et al. reported that the ligand flexibility, such as for diblock copolymer **6b** in our case, favors the non-disruptive interaction of anionic nanoparticles within the cell membrane.[61,62] Analysis of CL-rich SLBs, where **16** revealed a lack of significant differences in membrane fluidity ($D_{16} = 6.71 \pm 1.98\ \mu m^2 s^{-1}$) (Figure 5G) or the number of Atto655-DOPE particles (Figure S65, Supporting Information) compared to the blank (treated with PBS), suggesting a non-significant buckling phenomenon. The lower number of nanoconjugate **16** particles in the confocal volume (Figure S66, Supporting Information), which indicates lower binding strength than **6b**, may support the maintenance of the membrane's physical properties. However, we confirmed the interaction of **16** with CL-rich membranes by the intensity-averaged fluorescence lifetime of Flipper, which increased ($\Delta\ \tau^{16} = 0.1\ ns$) compared to the lifetime for a blank sample (treated with PBS) (Figure S67, Supporting Information), indicating an altered membrane order when interacting with **16** (Figure S68, Supporting Information). The comparable diffusion coefficient of Atto488-labeled **16** to **6b** through CL-rich membranes supports the affinity of the polymer derivative for the CL membrane (Figure S69, Supporting Information).

Activity studies at the mitochondria level confirmed the safer biological profile of nanoconjugate **16** compared to **6b**; specifically, we failed to observe altered mitochondrial morphology at all incubation times (Figure 5H), increased ROS production (Figure 5I) or significantly altered OCR related to ATP production (Figure 5J) compared to **6b** and control cells (set as 100%) in agreement with greater cell viability due to the absence of membrane disruption.

In conclusion, we successfully designed a nanoconjugate derivative of diblock copolymer **6b**, which retained its mitochondrial targeting ability and CL-specific interaction while exhibiting a safer biological profile and minimal activity at the mitochondrial level. Furthermore, our findings confirm the concentration-dependent behavior of diblock copolymer **6b**, functioning as a mitochondrial targeting anti-tumorigenic polymer at sub-IC_{50} concentrations (>IC_{15}) or as an efficient mitochondrial targeting moiety to functionalize different materials at low concentrations (<IC_{15}). Our proof-of-concept with diblock copolymer conjugate **16** exemplifies this concept, demonstrating the versatility and potential of diblock copolymer **6b** as a mitochondrial targeting agent for various applications.

3. Conclusion

Targeting drug delivery to subcellular compartments represents an expanding area in drug development/precision therapy due to the advantages of promoting therapeutic agent accumulation in organelles, such as reducing threshold dosages and minimizing drug-related side effects. Mitochondria represent prime targets given their role in cell metabolism $^{-1}$survival; as such, targeting these organelles may prevent/ameliorate conditions such as cancer, neurodegeneration, or diabetes, reverse multidrug resistance mechanisms, and leverage synergistic effects by applying more than one anti-cancer drug/therapeutic strategy via nanomedicine strategies. As mitochondrially-targeted nanomedicines have not achieved clinical translation, we require a deeper understanding of mitochondrial targeting and the development of novel approaches/simple synthetic procedures to facilitate industrial translation.

Our mtCPO platform – PLO_n-PLP_m – can be easily scaled up and translated to industrial development via a simple two-step methodology based on robust NCA-ROP, a rapid, cost-effective, and well-described methodology. DoE revealed the critical influence of initiator and monomer concentrations and reaction temperature, which permitted the scale-up of an optimal diblock copolymer candidate (**6b**) (7.3 g; 80% overall yield).

We introduced variations in the PLO_n-PLP_m platform by altering polycationic blocks (PLL, PHis, or PArg instead of PLO) and

© 2025 The Author(s). Advanced Materials published by Wiley-VCH GmbH

15214095, 0, Downloaded from https://advanced.onlinelibrary.wiley.com/doi/10.1002/adma.202411595 by Camilla Pegoraro - Readcube (Labtiva Inc.) , Wiley Online Library on [26/01/2025]. See the Terms and Conditions (https://onlinelibrary.wiley.com/terms-and-conditions) on Wiley Online Library for rules of use; OA articles are governed by the applicable Creative Commons License

diblock lengths (n:m ratio) to decipher each component's contribution to mitochondrial targeting. Diblock copolymers **6b**, **h**, and **i** (n:m ratio of 1:3) and nanoconjugate **16** promoted rapid energy-independent cell entry and efficient mitochondrial targeting (as such, serving as mt-CPOs), thereby overcoming problems associated with entrapment in endo/lysosomal compartments after cell entry by endocytosis, which rely on inefficient endo/lysosomal disrupting mechanisms for cytosolic delivery. PLO – the most efficient polycationic block – prompted more rapid cell internalization and significant mitochondrial accumulation than PLL, a well-known cell-penetrating peptide. Diblock copolymers **6b** and **7** – same n:m ratio and lengths but different polycationic blocks (PLO and PLL) – presented comparable size, charge, and type II helix structure. The PLO-PLP diblock displayed a monomodal distribution in solution, while the PLL-PLP diblock displayed a bimodal profile due to its favored random coil-to-helix conformational transition, which reduces helicity (affecting solvation environments and water shell interactions) and results in distinct hydration radii and lower cellular internalization by direct penetration of diblock copolymer **7**.

When evaluating targeting mechanisms, we discovered that mitochondrial depolarization did not influence diblock copolymer accumulation, suggesting that charge affinity between positively charged nanocarriers and negatively charged mitochondrial membranes does not account for targeting. This concept enhances the applicability of our diblock copolymers due to their mitochondrial targeting ability in distinct stages of disease, regardless of depolarization processes.

We studied diblock copolymer interactions with CL using artificial and biological CL-rich membrane models. Our results revealed the essential presence of the polycationic component to CL affinity (PLP homopolymers did not bind); however, this electronic interaction does not represent the only binding force involved, as n:m ratios of 1:1 and 1:2 demonstrated CL affinity but did not result in efficient mitochondrial accumulation. Instead, PLP content proved crucial to patch formation (observed here for the first time); only an n:m ratio of 1:3 supported membrane patch formation in CL-rich regions with negative curvature. These findings suggest the induction of physical changes, such as membrane remodeling, by facilitating buckling and patch formation in CL-rich environments but not in membranes with an equivalent charge distribution lacking CL. Thus, lower proline content may prompt weaker membrane-binding affinities, thereby inhibiting buckling; moreover, the lack of patch formation for diblock copolymer **7** suggests the essential nature of the polycationic block for efficient binding to CL-rich membranes. Overall, our data suggest that PLP content, n:m ratio, and polycationic block nature represent crucial factors controlling CL interactions. Further studies of membrane transforming properties corroborated the ability of PLO_n-PLP_m diblock copolymer with an n:m ratio of 1:3 to decrease membrane fluidity and increase membrane tension in CL-rich membrane regions, which can induce membrane ordering and initiate buckling phenomena.

In addition to their mitochondria-targeting capacity, diblock copolymers **6b**, **h**, and **i** displayed inherent biological activity, functioning as concentration-dependent anti-tumorigenic agents that prompted altered mitochondria metabolism, morphology, and respiration. These diblock copolymers induced mitochondrial depolarization and increased ROS production, contributing to downstream effects that induce cell death; furthermore, morphological alterations and an increased proportion of lysosomes engulfing affected mitochondria indicated impairment. We observed metabolic alterations after treatment with diblock copolymers **6b**, **h**, and **I** – OCR, which became compromised in a concentration-dependent manner, with reduced CI OXPHOS and ETC coupling efficiency.

To leverage the mitochondrial-targeting effect of our diblock copolymers, we also designed a polypeptide-based diblock copolymer nanoconjugate. Our strategy incorporated PGA to maintain biodegradability/biocompatibility and a cathepsin B-sensitive self-immolation linker to ensure stability in circulation while supporting biodegradation. PGA conjugation of diblock copolymer **6b** to yield nanoconjugate **16** enhanced cell viability and mitochondrial targeting without damaging mitochondria but maintained original physicochemical characteristics (comparable size and compact core structure compared to diblock copolymer **6b**). Despite differing from the parent diblock copolymer regarding secondary structure (random coil) and charge (negative), nanoconjugate **16** displayed enhanced energy-independent cell uptake and mitochondrial targeting via CL-affinity mechanisms. These findings suggest that the nanocarrier's small size, polyanionic nature, and the "availability" of diblock copolymer **6b**, facilitated by ligand flexibility provided by the linker, contributed to therapeutically relevant outcomes. Activity studies at the mitochondria level confirmed the safer profile of nanoconjugate **16**, which failed to alter mitochondrial morphology, increase ROS production, or significantly alter OCR, in agreement with greater cell viability due to the absence of membrane disruption.

In summary, PLO_n-PLP_m diblock copolymers with an n:m ratio of 1:3 function as efficient cell-penetrating oligomers and support cardiolipin-specific mitochondrial targeting (mt-CPOs). Mt-CPOs demonstrated inherent anti-tumorigenic properties via a mitochondrial-dependent pathway in a human TNBC cell model at sub-IC_{50} concentrations. These findings pave the way for the construction of novel mitochondrially-targeted treatments for various diseases. Our efforts focused on physicochemical characterization and providing proof-of-concept for a novel mitochondrially-targeted therapeutically relevant platform. Our materials also fulfill biodegradable and biocompatible standards, contributing to safety. Our results suggest the potential of PLO_n-PLP_m diblock copolymers as safe, mitochondria-specific nanocarriers; this supported the development of a mitochondrially-targeted polypeptide-based nanoconjugate that could provide a paradigm shift in addressing precise treatments through subcellular organelle-targeting strategies.

4. Experimental Section

Materials, selected methods, and the synthesis of compounds listed in Table 1 and nanoconjugate **16** are documented in detail in the Supporting Information. Here, a summarized selection of the materials and methods used as representative of the variety of techniques implemented in this work was presented.

Materials: All chemicals used were of analytical grade. N-carboxyanhydride (NCA) monomers, including L-Pro-NCA and L-Orn(Z)-NCA, were obtained from PMC-ISOCHEM. Solvents such as DMF, trifluoroacetic acid (TFA), and chloroform were sourced from Sigma-Aldrich and Fisher Scientific. Lipids for vesicle studies, such as

© 2025 The Author(s). Advanced Materials published by Wiley-VCH GmbH

15214095, 0, Downloaded from https://advanced.onlinelibrary.wiley.com/doi/10.1002/adma.202411595 by Camilla Pegoraro - Readcube (Labtiva Inc.) , Wiley Online Library on [26/01/2025]. See the Terms and Conditions (https://onlinelibrary.wiley.com/terms-and-conditions) on Wiley Online Library for rules of use; OA articles are governed by the applicable Creative Commons License

DOPC and CL, were purchased from Avanti Polar Lipids. Fluorescent dyes, including JC-1 and 2,7-dichlorodihydrofluorescein (DCFH), were obtained from MedChemExpress. Cell culture reagents, including DMEM/F-12 media, fetal bovine serum (FBS), and antibiotics, were purchased from Gibco Life Technologies. Ultrapure Milli-Q water (18 MΩ cm^{-1} resistivity) was used for all aqueous solutions.

Ethical Statements: Animal experiments for erythrocyte isolation were conducted in accordance with European Communities Council Directive 86/609/ECC and Spanish Royal Decree 1201/2005, with approval from the Institutional Animal Care and Use Committee. Eight-week-old female Balb/c mice were housed under specific-pathogen-free conditions with controlled temperature, humidity, a 12-hour light-dark cycle, and ad libitum food and water access. Mice were euthanized using CO_2 inhalation following ethical protocols.

Organs for mitoplast isolation were collected post-mortem from healthy animals assigned to control groups in unrelated experiments, adhering to the 3R principles (Replace, Reduce, Refine). All experimental procedures complied with EU Directive 2010/63/EU and relevant local regulations. Ethical approval for experiments involving animals used for organelle isolation was obtained from the Latvian Animal Protection Ethical Committee of the Food and Veterinary Service in Riga, Latvia (Nr.132/2022).

Physicochemical Methods: *Gel Permeation Chromatography (GPC)*: GPC measurements were conducted using a Malvern Instruments system with a TSKGel PWXL G5000 column. The mobile phase comprised 0.1 M sodium nitrate with 0.005% sodium azide, and the flow rate was set to 0.7 mL mi^{-1}n. The system was calibrated with polyethylene oxide (PEO) (molecular weight (Mw) = 24 kDa; PDI = 1.01). For Mw determination, an integrated triple detection system was used (refractive index, light scattering (2 angles: 7 and 90°), and ultraviolet-visible detectors).

Nuclear Magnetic Resonance (NMR): NMR spectra were recorded at 500 MHz on a Bruker spectrometer. Samples were dissolved in d-TFA or D_2O at a concentration of 10 mg m^{-1}. Diffusion-ordered spectroscopy (DOSY) was performed using bipolar pulse pair stimulated echo sequences with 64 gradient increments ranging from 5% to 95% of the maximum field strength. MestReNova software was used for data processing.

Circular Dichroism (CD): CD spectroscopy was conducted using a J-815 CD Spectrometer equipped with a Peltier thermostated cell holder and a recirculating cooler. A nitrogen flow of 1.5 L mi^{-1}n, regulated by a nitrogen flow monitor, was maintained throughout the experiments. Samples (0.03–0.25 mg mL^{-1}) were prepared in Milli-Q water or PBS and analyzed in a 1 mm quartz cuvette. Measurements were performed at varying temperatures, with each sample analyzed in triplicate ($n = 3$).

Small-Angle X-Ray Scattering (SAXS): SAXS experiments were conducted at the ALBA Synchrotron on the NCD-SWEET beamline. Samples were prepared in quartz capillaries (1 mm diameter) and exposed to monochromatic X-rays at 12.4 keV. Scattering intensities were collected using a Pilatus 1 M detector. Background subtraction and data reduction were performed using pyFAI, and radius of gyration (Rg) values were calculated using a Guinier-Porod model.

Fluorescence Correlation Spectroscopy (FCS): Z-scan fluorescence correlation spectroscopy (FCS) was performed on a Zeiss LSM980 confocal microscope. Measurements were collected over a 2 µm z-range in 0.2 µm steps, and autocorrelation curves were analyzed to determine diffusion times (τ_D) and particle numbers (N_0) using positional fitting and custom scripts. The temperature was maintained at 28 °C.

Atomic Force Microscopy (AFM): AFM was performed on a JPK Nanowizard 3 microscope combined with a Zeiss LSM800 confocal microscope using a C-Apochromat 20xA objective. Diblock copolymers (Atto488) and membranes (Atto655-DOPE) were excited with 488 nm and 633 nm lasers, respectively. Confocal microscopy localized areas of interest, followed by AFM imaging in quantitative mode using BioLever Mini cantilevers. Imaging parameters included a nominal force of 0.3 nN, an acquisition speed of 61.1 µm $^{-1}$s, and a Z-range of 110 nm. Images were processed in Gwyddion (v2.58) with leveling, alignment, scar correction, outlier removal, and denoising.

Membrane Model Systems: *Small Unilamellar Vesicles (SUVs)*: CL-containing SUVs were prepared using the thin-film method. Stock solutions of DOPC and CL were mixed and evaporated under reduced pressure to form a lipid film. The film was resuspended in 20 mM HEPES buffer (pH 6.8). The vesicles were sonicated at room temperature for 30 min and extruded through a 100 nm polycarbonate filter. SUV quality was confirmed by dynamic light scattering (DLS), and samples were freshly prepared for each experiment.

Mitoplasts: Mitoplasts were isolated via differential centrifugation. Heart and liver tissues from a healthy Sprague Dawley rat were homogenized in ice-cold buffer (180 mM KCl, 10 mM Tris/HCl, 1 mM EGTA, pH 7.7). The homogenate was centrifuged at 750 g to remove debris, and the supernatant was centrifuged at 6800 g to pellet mitochondria. The mitochondrial pellet was washed, resuspended in a hypotonic solution (5 mM sucrose, 5 mM HEPES, 1 mM EGTA, pH 7.2), and incubated on ice for 20 min to remove the outer membrane. To eliminate cytochrome *c*, the sample was treated with 300 mM KCl and centrifuged at 14 500 g. The pellet was washed, centrifuged, and resuspended in 20 mM HEPES buffer (pH 6.8). Mitoplasts were stored at −20 °C until use.

Biological Studies: Biological experiments were performed on MDA-MB-231, MCF-7, Hep G2, BJ fibroblasts, and BV-2 cells.

Cell Viability Assay: Cells were seeded in 96-well plates and incubated for 24 h at 37 °C with 5% CO_2. Diblock copolymer stock solutions were prepared in PBS, diluted in DMEM/F-12 medium with 10% FBS and 1% P/S, sterilized through a 0.2 µm filter, and added to wells at final concentrations of 0–1 mg mL^{-1}. After 24 or 72 h of treatment, MTS/PMS reagent was added, and cells were incubated for 4 h. Absorbance at 490 nm was measured using a plate reader, and cell viability was calculated as a percentage relative to untreated controls. Data were expressed as Mean ± SD ($n = 3$).

Cellular Uptake Studies: The uptake of Cy5-labeled diblock copolymers was analyzed using confocal microscopy and flow cytometry. For live-cell imaging, pulse-chase and time-lapse studies were performed on a Leica TCS SP8 confocal microscope equipped with a 63× oil immersion objective. MitoTracker Red and LysoTracker Blue were used to track mitochondrial and lysosomal localization. For pulse-chase studies, cells were treated with polymers for 1, 2, 4, 6, and 24 h, while the fluorescent markers were added 1 h before imaging. Time-lapse imaging captured uptake dynamics over a 20-second interval. Images were analyzed using LAS X and ImageJ for colocalization and Pearson correlation calculations. For flow cytometry, cells were incubated with polymers at 37 or 4 °C for 0, 30, 60, and 180 min. After incubation, cells were washed, harvested, and stained with propidium iodide (PI) to assess viability. Cell-associated fluorescence was measured using a CytoFLEX S flow cytometer, collecting 10 000 events per sample. Background fluorescence was subtracted, and data were expressed as fold changes relative to t = 0 using CytExpert software.

Hemocompatibility Assay: Polymer solutions were prepared in PBS (pH 7.4) and citrate buffer (pH 5.5) and added to wells in triplicate at sub-IC50 concentrations (C1 and C2, with C1/C2 = 1.5). Controls included buffer for background, Triton X-100 (1%) for positive control, and dextran (2 mg mL^{-1}) for negative control. After 1 h of incubation at 37 °C, plates were centrifuged at 3000 rpm for 10 min, and supernatants were collected for hemoglobin release assessment. Absorbance at 570 nm was measured, and hemolysis percentages were calculated relative to the 100% hemolysis control (Triton X-100).

Mitochondrial Membrane Potential: Cells were seeded in 96-well plates, treated with sub-IC50 diblock copolymer solutions (>IC40) for 2, 6, and 24 h, and stained with 2 µM JC-1 for 30 min. CCCP (50 µM) was used as a positive control. Fluorescence was measured at 550/605 nm (red) and 484/528 nm (green), and the red/green ratio was normalized to untreated controls (set as 100%). Data were presented as Mean ± SD ($n = 3$).

Oxygen Consumption Rate (OCR): OCR was measured using the Oroboros O2k and Seahorse XF systems. For Oroboros, permeabilized cells treated with diblock copolymers at sub-IC50 concentrations were sequentially exposed to pyruvate and malate for LEAK respiration, ADP for OXPHOS, and glutamate and succinate for CI-II-linked respiration. CCCP was titrated to determine maximal respiration, while rotenone and antimycin A were used to evaluate residual oxygen consumption. Flux control factors were calculated based on substrate-dependent respiration changes. For Seahorse XF analysis, intact cells treated with diblock

© 2025 The Author(s). Advanced Materials published by Wiley-VCH GmbH

15214095, 0, Downloaded from https://advanced.onlinelibrary.wiley.com/doi/10.1002/adma.202411595 by Camilla Pegoraro - Readcube (Labtiva Inc.) , Wiley Online Library on [26/01/2025]. See the Terms and Conditions (https://onlinelibrary.wiley.com/terms-and-conditions) on Wiley Online Library for rules of use; OA articles are governed by the applicable Creative Commons License

copolymers were incubated in an XF medium with pyruvate, glutamine, and glucose. Inhibitors (1.5 µM oligomycin, 1 µM FCCP, and 0.5 µM rotenone/antimycin A) were sequentially injected to assess spare and ATP-linked respiration. Results were normalized using Hoechst staining for viability and expressed relative to untreated controls as Mean ± SD ($n = 3$).

Reactive Oxygen Species (ROS): Cells were seeded in 6-well plates and treated with sub-IC50 concentrations of sterilized diblock copolymer solutions (>IC40) for 24 h. After treatment, cells were washed, trypsinized, and resuspended in a fresh medium. Cells were then incubated with 5 µg mL^{-1} DCFH for 30 min, followed by propidium iodide (2 µg mL^{-1}) for viability assessment. Samples were analyzed using a CytoFLEX S flow cytometer, collecting 10 000 events per sample. Data were normalized to untreated controls (100%) and expressed as Mean ± SD ($n = 3$).

Mitochondrial Morphology Analysis: Cells were seeded in 8-well chambers and treated with sub-IC50 concentrations (>IC40) of selected compounds for 6, 24, and 48 h. After treatment, cells were pre-fixed with 3% glutaraldehyde, post-fixed with 2% OsO_4, and stained with 2% uranyl acetate. Samples were dehydrated in ethanol, embedded in Durcupan resin, and sectioned into 0.08 µm slices. Sections were stained with lead citrate and imaged using a transmission electron microscope. Twenty images per sample were captured at 1900× and 11 000× magnifications.

Supporting Information

Supporting Information is available from the Wiley Online Library or from the author.

Acknowledgements

This project was supported by Horizon Europe H2020-MSCA-ITN-2019 BIOMOLMACS (proposal no. 859416). The authors acknowledge the Asociación Española contra el Cáncer (ICS INVES211323CONE Junior AECC grant), Ministerio de Ciencia e innovacion (PID2019-108806RB-I00, PID2023-152459OB-I00), NextGeneration EU i+d+I funding through GVA Conselleria Innovació- Pol@Mets. Ref. MFA/2022/065 and European Regional Development Fund (PO FEDER Comunitat Valenciana 2014–2020) Generalitat Valenciana for financial support. SAXS measurements were acquired at the NCD-SWEET beamline at the ALBA Synchrotron Light source in Barcelona, Spain, through Project ID 2022097124. The mass spectrometry analysis was performed in the proteomics facility of SCSIE University of Valencia. Support from the project "BioMedPharm" (VPP-EM-BIOMEDICINA-2022/1-0001) and Horizon Europe EU-OPENSCREEN IMPULSE (Grant Agreement No. 101132028) is gratefully acknowledged. Y.Q. and S.G. acknowledged support from the International Max Planck Research School for Molecules of Life (IMPRS-ML). S.G. was part of the ONE MUNICH Project supported by the Federal Ministry of Education and Research (BMBF) and the Free State of Bavaria under the Excellence Strategy of the Federal Government and the Länder. The authors thank Dr. Stuart P. Atkinson for his help in manuscript development and English editing, Alberto Hernandez for confocal imaging support, Alicia Martinez Romero for flow cytometry analysis, and Mario Soriano for TEM support. The authors thank Agustín Lahoz Rodríguez from the Instituto de Investigación Sanitaria Hospital La Fe for providing access to and help with the Seahorse XF Analyzer. The authors would also thank Prof. Beatriu Escuder from UJI and Prof. Ignacio Alonso from IQAC who facilitated the MALDI analysis. The authors would like to acknowledge Isabel Montoya for the support with the BV2 cells study and Jan-Hagen Krohn for the help with the z-scan FCS setup.

Conflict of Interest

The authors declare a filed patent. – MJ Vicent; I Conejos-Sanchez; C Pegoraro; E Karpova; G Sogorb; C Felip; VJ Nebot; P Schwille; Y Qutbuddin. PCT/EP2024/06 8352 (Priority claimed: European Patent Application no. EP23382668.4). Polyproline-based Block-copolymers 28/06/2024. CIPF, PTS SL, and Max Planck Society.

Author Contributions

C.P. led the synthesis of the conjugate, conformational studies, data curation, formal analysis, investigation, methodology, and writing of the original draft. Cell viability assays and biological studies were carried out by C.P. with support from E.M.S. E.K., C.F.-L., and A.D.-C. led to the synthesis of the diblocks and the scale-up demonstration including DoE. Y.Q. and P.S. led the synthetic membrane studies and FCS analysis. P.D. and P.A. led the cardiolipin interaction studies and the Oroboros, C.H.-I. led the SAXS analysis, I.C-S and M.J.V. cosupervise the whole study and contributed to the data curation and formal analysis, as well as in the writing process. Conceptualization, funding acquisition, and project administration were led by M.J.V. with support from I.C.S. The manuscript was revised by C.P., I.C.-S., and M.J.V., with reviewing and editing contributions from all authors. All authors have read and approved the final version of the manuscript.

Data Availability Statement

The data supporting this study's findings are available from the corresponding author upon reasonable request.

Keywords

cardiolipin-specific mitochondrial targeting, design of experiments (doe), membrane remodeling, mitochondrial tropism, polypeptide-based nanoconjugates, polyproline, subcellular organelle targeting

Received: August 6, 2024
Revised: November 25, 2024
Published online:

[1] X. Fu, Y. Shi, T. Qi, S. Qiu, Y. Huang, X. Zhao, Q. Sun, G. Lin, *Signal Transduct. Target. Ther.* **2020**, *5*, 262.
[2] S. S. Liew, X. Qin, J. Zhou, L. Li, W. Huang, S. Q. Yao, *Angew. Chem., Int. Ed.* **2021**, *60*, 2232.
[3] C. Pegoraro, I. Domingo-Ortí, I. Conejos-Sánchez, M. J. Vicent, *Adv. Drug Delivery Rev.* **2024**, *207*, 115195.
[4] H. Cho, Y. Y. Cho, M. S. Shim, J. Y. Lee, H. S. Lee, H. C. Kang, *Biochim. Biophys. Acta – Mol. Basis Dis.* **2020**, *1866*, 165808.
[5] L. D. Zorova, V. A. Popkov, E. Y. Plotnikov, D. N. Silachev, I. B. Pevzner, S. S. Jankauskas, V. A. Babenko, S. D. Zorov, A. V. Balakireva, M. Juhaszova, S. J. Sollott, D. B. Zorov, *Anal. Biochem.* **2018**, *552*, 50.
[6] S. A. Smith, L. I. Selby, A. P. R. Johnston, G. K. Such, *Bioconjug. Chem.* **2019**, *30*, 263.
[7] D. Kalafut, T. N. Anderson, J. Chmielewski, *Bioorg. Med. Chem. Lett.* **2012**, *22*, 561.
[8] Y. A. Fillon, J. P. Anderson, J. Chmielewski, *J. Am. Chem. Soc.* **2005**, *127*, 11798.
[9] I. M. Geisler, J. Chmielewski, *Pharm. Res.* **2011**, *28*, 2797.
[10] L. Li, I. Geisler, J. Chmielewski, J.-X. Cheng, *J. Control. Rel.* **2010**, *142*, 259.
[11] A. Dirisala, S. Uchida, J. Li, J. F. R. Van Guyse, K. Hayashi, S. V. C. Vummaleti, S. Kaur, Y. Mochida, S. Fukushima, K. Kataoka, *Macromol. Rapid Commun.* **2022**, *43*, 1.
[12] I. Conejos-Sánchez, E. Gallon, A. Niño-Pariente, J. A. Smith, A. G. De la Fuente, L. Di Canio, S. Pluchino, R. J. M. Franklin, M. J. Vicent, *Nanoscale* **2020**, *12*, 6285.
[13] J. L. S. Lopes, A. J. Miles, L. Whitmore, B. A. Wallace, *Protein Sci.* **2014**, *23*, 1765.
[14] K.-Y. Huang, J.-C. Horng, *J. Phys. Chem. B* **2019**, *123*, 138.
[15] B. Hammouda, *Macromol. Theory Simulations* **2012**, *21*, 372.

© 2025 The Author(s). Advanced Materials published by Wiley-VCH GmbH

[16] B. Hammouda, *J. Appl. Crystallogr.* **2010**, *43*, 716.
[17] G. Quintero-Marquina, G. Segovia, V. Oestreicher, D. Lamas, C. Huck-Iriart, *ChemRxiv* **2024**. https://doi.org/10.26434/chemrxiv-2024-8jqp7.
[18] B. Ghaemi, S. Tanwar, A. Singh, D. R. Arifin, M. T. McMahon, I. Barman, J. W. M. Bulte, *ACS Appl. Mater. Interfaces* **2024**, *16*, 11159.
[19] M. T. H. Nguyen, D. Biriukov, C. Tempra, K. Baxova, H. Martinez-Seara, H. Evci, V. Singh, R. Šachl, M. Hof, P. Jungwirth, M. Javanainen, M. Vazdar, *Langmuir* **2022**, *38*, 11284.
[20] A. D. Robison, S. Sun, M. F. Poyton, G. A. Johnson, J.-P. Pellois, P. Jungwirth, M. Vazdar, P. S. Cremer, *J. Phys. Chem. B* **2016**, *120*, 9287.
[21] C. Tempra, Z. Brkljača, M. Vazdar, *Phys. Chem. Chem. Phys.* **2023**, *25*, 27204.
[22] B. D. Monnery, M. Wright, R. Cavill, R. Hoogenboom, S. Shaunak, J. H. G. Steinke, M. Thanou, *Int. J. Pharm.* **2017**, *521*, 249.
[23] Z. Jiang, H. Liu, H. He, N. Yadava, J. J. Chambers, S. Thayumanavan, *Bioconjug. Chem.* **2020**, *31*, 1344.
[24] A. M. Mahmoud, J. P. Morrow, D. Pizzi, A. M. Azizah, T. P. Davis, R. F. Tabor, K. Kempe, *Biomacromolecules* **2020**, *21*, 3007.
[25] A. M. Mahmoud, P. A. J. M. de Jongh, S. Briere, M. Chen, C. J. Nowell, A. P. R. Johnston, T. P. Davis, D. M. Haddleton, K. Kempe, *ACS Appl. Mater. Interfaces* **2019**, *11*, 31302.
[26] G. Sahay, E. V. Batrakova, A. V. Kabanov, *Bioconjug. Chem.* **2008**, *19*, 2023.
[27] D. Y. Alakhova, N. Y. Rapoport, E. V. Batrakova, A. A. Timoshin, S. Li, D. Nicholls, V. Y. Alakhov, A. V. Kabanov, *J. Control. Rel.* **2010**, *142*, 89.
[28] G. Sahay, V. Gautam, R. Luxenhofer, A. V. Kabanov, *Biomaterials* **2010**, *31*, 1757.
[29] G. A. Morris, Diffusion-Ordered Spectroscopy (DOSY), In: R.K. Harris, R.L. Wasylishen, eds. EMagRes **2009**.
[30] D. Huesmann, A. Birke, K. Klinker, S. Türk, H. J. Räder, M. Barz, *Macromolecules* **2014**, *47*, 928.
[31] N. K. Singh, M. Agarwal, M. Radhakrishna, *Proteins Struct. Funct. Bioinforma.* **2023**, *91*, 268.
[32] Y. Liu, J. Zhang, Y. Tu, L. Zhu, *ACS Nano* **2022**, *16*, 1409.
[33] S. T. Ahmadpour, K. Mahéo, S. Servais, L. Brisson, J.-F. Dumas, *Int. J. Mol. Sci.* **2020**, *21*.
[34] P. Dimitrijevs, P. Arsenyan, *Sensors Actuators B Chem* **2021**, *346*, 130537.
[35] J. Sarkis, V. Vié, *Front. Bioeng. Biotechnol.* **2020**, *8*.
[36] K. J. Boyd, N. N. Alder, E. R. May, *Biophys. J.* **2018**, *114*, 2116.
[37] K. J. Boyd, N. N. Alder, E. R. May, *Langmuir* **2017**, *33*, 6937.
[38] M. D. Phan, K. Shin, *Biophys. J.* **2015**, *108*, 1977.
[39] V. Kubyshkin, S. L. Grage, A. S. Ulrich, N. Budisa, *Phys. Chem. Chem. Phys.* **2019**, *21*, 22396.
[40] A. J. García-Sáez, D. C. Carrer, P. Schwille, Fluorescence Correlation Spectroscopy for the study of membrane dynamics and organization in giant unilamellar vesicles In: (Eds: V. Weissig), Lipid-Proteins Interactions, vol 2: Biological membrane models, Humana Press, Totowa, NJ **2010**, pp. 493–508.
[41] P. Rangamani, K. K. Mandadap, G. Oster, *Biophys. J.* **2014**, *107*, 751.
[42] A. Colom, E. Derivery, S. Soleimanpour, C. Tomba, M. D. Molin, N. Sakai, M. González-Gaitán, S. Matile, A. Roux, *Nat. Chem.* **2018**, *10*, 1118.
[43] F. Ragaller, E. Sjule, Y. B. Urem, J. Schlegel, R. El, D. Urbancic, I. Urbancic, H. Blom, E. Sezgin, *J. Phys. Chem. B* **2024**, *128*, 2154.
[44] N. Badrinath, S. Y. Yoo, *Carcinogenesis* **2018**, *39*, 1419.
[45] A. Reda, A. Refaat, A. A. Abd-Rabou, A. M. Mahmoud, M. Adel, S. Sabet, S. S. Ali, *Sci. Rep.* **2019**, *9*, 13748.
[46] F. Sivandzade, A. Bhalerao, L. Cucullo, *Bio-protocol* **2019**, *9*, 1.
[47] C. Nguyen, S. Pandey, *Cancers* **2019**, *11*.
[48] H. M. Begum, K. Shen, *WIREs Mech. Dis.* **2023**, *15*, e1595.
[49] L. B. Sullivan, N. S. Chandel, *Cancer Metab.* **2014**, *2*, 17.
[50] C.-L. Kuo, A. Ponneri Babuharisankar, Y.-C. Lin, H.-W. Lien, Y. K. Lo, H.-Y. Chou, V. Tangeda, L.-C. Cheng, A. N. Cheng, A. Y.-L. Lee, *J. Biomed. Sci.* **2022**, *29*, 74.
[51] M. E. Zare, A. N. Kansestani, S. Hemmati, K. Mansouri, A. Vaisi-Raygani, *J. Diabetes Metab. Disord.* **2021**, *20*, 523.
[52] P. Marchetti, Q. Fovez, N. Germain, R. Khamari, J. Kluza, *FASEB J.* **2020**, *34*, 13106.
[53] A. Jussupow, A. Di Luca, V. R. I. Kaila, *Sci. Adv.* **2024**, *5*, eaav1850.
[54] T. G. Biel, V. A. Rao, *Oncotarget* **2017**, *9*, 1.
[55] C. Song, S. Pan, J. Zhang, N. Li, Q. Geng, *Cell Prolif* **2022**, *55*, e13327.
[56] J. D. Bargh, A. Isidro-Llobet, J. S. Parker, D. R. Spring, *Chem. Soc. Rev.* **2019**, *48*, 4361.
[57] J. M. Steinbach, Y.-E. Seo, W. M. Saltzman, *Acta Biomater.* **2016**, *30*, 49.
[58] Y. Shamay, L. Shpirt, G. Ashkenasy, A. David, *Pharm. Res.* **2014**, *31*, 768.
[59] Z. Niu, E. Samaridou, E. Jaumain, J. Coëne, G. Ullio, N. Shrestha, J. Garcia, M. Durán-Lobato, S. Tovar, M. J. Santander-Ortega, M. V. Lozano, M. M. Arroyo-Jimenez, R. Ramos-Membrive, I. Peñuelas, A. Mabondzo, V. Préat, M. Teixidó, E. Giralt, M. J. Alonso, *J. Control. Rel.* **2018**, *276*, 125.
[60] J. Dolai, K. Mandal, N. R. Jana, *ACS Appl. Nano Mater.* **2021**, *4*, 6471.
[61] R. C. Van Lehn, P. U. Atukorale, R. P. Carney, Y.-S. Yang, F. Stellacci, D. J. Irvine, A. Alexander-Katz, *Nano Lett.* **2013**, *13*, 4060.
[62] R. C. Van Lehn, A. Alexander-Katz, *Soft Matter* **2014**, *10*, 648.

© 2025 The Author(s). Advanced Materials published by Wiley-VCH GmbH

15214095, 0, Downloaded from https://advanced.onlinelibrary.wiley.com/doi/10.1002/adma.202411595 by Camilla Pegoraro - Readcube (Labtiva Inc.) , Wiley Online Library on [26/01/2025]. See the Terms and Conditions (https://onlinelibrary.wiley.com/terms-and-conditions) on Wiley Online Library for rules of use; OA articles are governed by the applicable Creative Commons License

3.2 Manuscript III

3.2.1 Scientific Article II: Introduction and Background

Light-driven molecular motors (MMs) represent a groundbreaking advancement in nanotechnology, offering precise control over molecular motion and dynamic responses to external stimuli. Their ability to perform repetitive, unidirectional rotations upon light activation positions them as valuable tools for manipulating biological systems; however, limitations such as poor biocompatibility, restricted solubility, and inefficient cellular delivery have hindered their broader application in therapeutic and diagnostic settings.

This study addresses these challenges by introducing a novel polypeptide-MM (P-MM) conjugate[345]. Synthesized via copper-catalyzed azide-alkyne cycloaddition (click chemistry), P-MM combines a propargyl-derivatized MM with a PGA-based carrier functionalized with PLO_6-PLP_{22} sidechains (P). These sidechains confer energy-independent cellular uptake and mitochondria-specific targeting, integrating the dynamic functionality of MMs with the biocompatibility and targeting capabilities of polypeptide carriers.

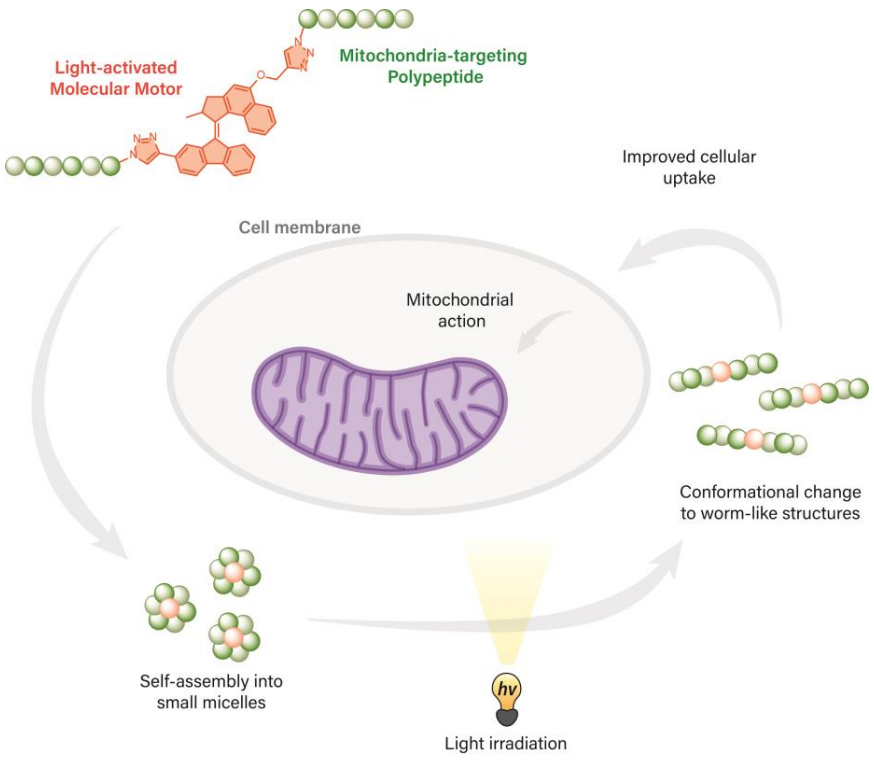
Key contributions of this work include:

- **Preservation of Dynamic Functionality**: The conjugation process retains MM's rotational cycle and unidirectional motion upon irradiation at 405 nm, ensuring light-responsive properties remain intact
- **Light-Responsive Supramolecular Behavior**: Upon irradiation, P-MM undergoes supramolecular reorganization from micellar structures to elongated worm-like assemblies, which correlates with enhanced cellular uptake, establishing a direct link between light-induced conformational changes and improved biological performance
- **Biocompatibility and Enhanced Cellular Uptake in TNBC Models**: Irradiated P-MM demonstrates biocompatibility and significantly higher uptake than a non-irradiated counterpart in MDA-MB-231 TNBC cells, which was attributed to mechanical and conformational effects rather than oxidative stress, as evidenced by the negligible production of reactive oxygen species

By combining the dynamic, light-responsive properties of MMs with the biocompatibility and targeting specificity of a PGA carrier, this study establishes P-MM as a versatile platform for light-controlled intracellular delivery. These findings contribute to the broader goals of this thesis by demonstrating the potential of integrating advanced nanotechnology with biological systems for therapeutic and diagnostic applications in aggressive cancers such as TNBC.

In this work, I led the synthesis of the PGA-based nanoconjugate and the synthesis and physicochemical characterization of the P-MM conjugate during my short stay at the University of Groningen in Ben Feringa's group in collaboration with Ainoa Guinart (A.G). I was also responsible for the cell viability assays and biological studies. The data curation, formal analysis, investigation, methodology development, and writing of the original draft were equally contributed by myself and A.G. Contributions by co-authors are detailed in the manuscript.

Table of Content



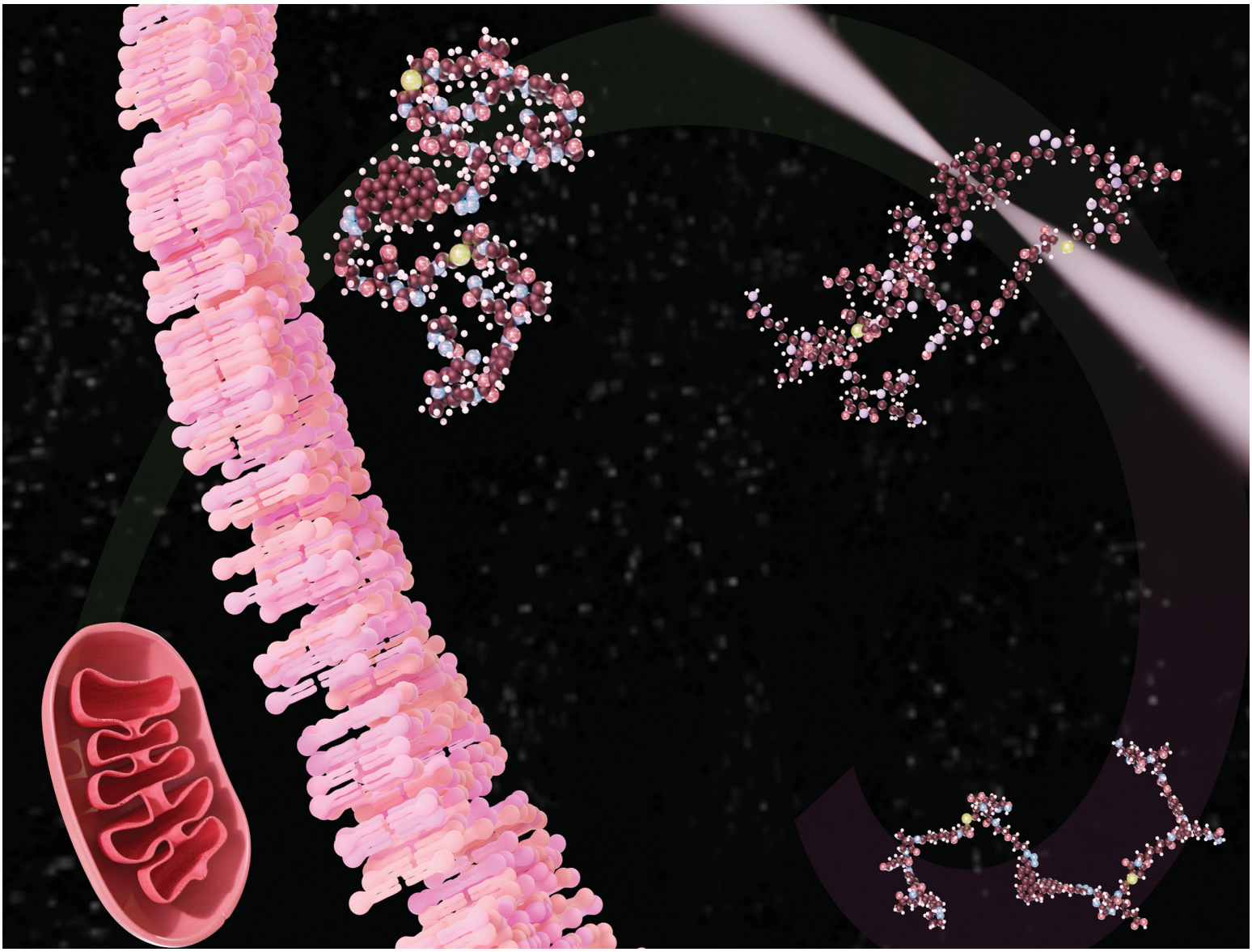
A light-driven molecular motor-polypeptide conjugate. Schematic representation of a novel light-responsive molecular motor-polypeptide conjugate synthesized via copper-catalyzed azide-alkyne cycloaddition, linking a propargyl-derivatized molecular motor to a mitochondria-targeting poly-L-glutamic acid-based carrier. Upon 405 nm irradiation, the conjugate undergoes a controlled supramolecular transition from spherical micelles (~2-3 nm) to anisotropic worm-like structures (~1 x 10 nm). This light-induced conformational change enhances cellular uptake while preserving the mitochondria-specific tropism and favorable biocompatibility of the polypeptide carrier. These results highlight the potential of this light-driven molecular motor-polypeptide conjugate as a versatile platform for light-controlled intracellular delivery and targeted therapeutic interventions.

Volume 13
Number 8
28 February 2025
Pages 2563–2880

Journal of Materials Chemistry B

Materials for biology and medicine

rsc.li/materials-b



ISSN 2050-750X

ROYAL SOCIETY OF CHEMISTRY

COMMUNICATION

B. Feringa and M.J. Vicent Labs *et al.*
A light-driven molecular motor-polypeptide conjugate supports controlled cell uptake

Journal of Materials Chemistry B

ROYAL SOCIETY OF CHEMISTRY

COMMUNICATION

View Article Online
View Journal

Check for updates

Cite this: DOI: 10.1039/d4tb02434f

Received 30th October 2024,
Accepted 9th December 2024

DOI: 10.1039/d4tb02434f

rsc.li/materials-b

A light-driven molecular motor-polypeptide conjugate supports controlled cell uptake†

Camilla Pegoraro, ‡[a] Ainoa Guinart,‡[b] Esther Masiá Sanchis, [acd] Daniel Doellerer, [b] Marc C. A. Stuart, [b] Inmaculada Conejos-Sánchez, *[ac] Ben L. Feringa *[b] and María J. Vicent *[acd]

While light-driven molecular motors (MMs) hold immense potential to control cell function, low biocompatibility and solubility have hampered their implementation. We developed a novel polypeptide-conjugated MM by linking a propargyl-derivatized light-driven MM to a poly-L-glutamic acid-based carrier (P) with inherent mitochondria tropism through click chemistry, denoted P-MM. P-MM effectively maintained the parental stability and unidirectional rotational capabilities of MM upon irradiation at 405 nm. Light-induced supramolecular conformational changes significantly increased cell uptake compared to non-irradiated controls while retaining the subcellular targeting capacity of P. P-MM exhibited minimal cytotoxicity and reactive oxygen species production, suggesting a non-disruptive interaction with cell membranes. Overall, we establish a connection between irradiation and enhanced biological responses, demonstrating the potential of integrating MMs with targeted polymeric nanocarriers for controlled, light-responsive behavior in biological systems and innovative applications in advanced therapeutic/diagnostic strategies.

Open Access Article. Published on 11 February 2025. Downloaded on 2/12/2025 5:06:18 PM.
This article is licensed under a Creative Commons Attribution-NonCommercial 3.0 Unported Licence.

Introduction

Light-based control of cell behavior offers advantages for manipulating biological systems, including rapid responses, high spatiotemporal resolution, non-invasiveness, and reversibility.[1] Incorporating photoswitches – molecules displaying reversible interconversions between conformational states upon light exposure – also supports control over cell function.[2,3] The emergence of rotary molecular motors (**MMs**) – derived from chiroptical molecular switches and based on overcrowded alkenes that support controlled molecular motion[4] – represented a significant advance due to their ability to perform repetitive, light-driven, and unidirectional rotations around a carbon–carbon double bond.[5] **MMs** meet the three fundamental criteria of a motorized machine: complete 360° unidirectional rotations, repetitive motions, and energy input from light;[6] however, low biocompatibility and solubility have limited their biological application.[7–9]

The development of **MMs** with chemical functionalities that allow further derivatization without altering motion may address these issues. Polypeptides offer biocompatibility, biodegradability, multivalency, and tunable design[10] and may enhance the biological/therapeutic applicability of **MM**. Polypeptides degrade into non-toxic metabolites, making them ideal for repeated administration without safety concerns.[11] Innovations in synthetic chemistry and polymerization techniques have significantly enhanced the precision and adaptability of polypeptide conjugation.[12] These advancements enable the integration of stimuli-responsive elements and the engineering of semitelechelic properties required for site-specific conjugation.[13] The precise control over the polypeptide structure ensures more efficient and targeted cargo delivery.

In this line, we attached an azide-derivatized poly-L-glutamic acid (PGA)-based carrier (**P**)[14,15] to a propargyl-derivatized light-driven **MM** to allow site-specific conjugation through click chemistry (**P-MM**). Apart from the semitelechelic properties in the polypeptide mainchain, **P** includes diblock oligomers of poly-L-ornithine (PLO) and polyproline (PLP) (PLO_n–PLP_m, $n:m$ ratio 1:3, referred to here as PP) as sidechains, conferring cytosolic delivery and mitochondrial targeting. We recently demonstrated the mitochondria tropism of **P** using a cardiolipin-specific interaction.[14,15] Conjugating PP to PGA preserved mitochondrial targeting abilities while enhancing safety by retaining cell uptake without compromising mitochondrial function or viability.[14,15]

Here, **P-MM** displayed stability and rotational cycling while undergoing conformational changes after irradiation at 405 nm,

[a] Príncipe Felipe Research Center, Polymer Therapeutics Lab., 46012 Valencia, Spain. E-mail: iconejos@cipf.es, mjvicent@cipf.es
[b] Stratingh Institute for Chemistry, University of Groningen, Groningen 9747 AG, The Netherlands. E-mail: b.l.feringa@rug.nl
[c] Centro de Investigación Biomédica en Red en Cáncer (CIBERONC), Instituto de Salud Carlos III, Spain
[d] Príncipe Felipe Research Center, Screening Platform, 46012 Valencia, Spain

† Electronic supplementary information (ESI) available. See DOI: https://doi.org/10.1039/d4tb02434f

‡ Authors with equal contributions.

Open Access Article. Published on 11 February 2025. Downloaded on 2/12/2025 5:06:18 PM.
This article is licensed under a Creative Commons Attribution-NonCommercial 3.0 Unported Licence.

which supported increased cell uptake compared to non-irradiated **P-MM** while maintaining mitochondrial tropism. Our findings demonstrate a correlation between light-induced conformational changes and biological outcomes, paving the way for novel applications of **P-MMs** in biological systems.

Experimental

The ESI† provides more details regarding **P**, **MM**, and **P-MM** synthesis, characterization and the materials employed.

Synthesis of the polypeptide-molecular motor conjugate (P-MM conjugate)

An oven-dried vial was charged with **MM** (1.2 mg, 2.8 μmol, 0.5 eq.) and **P** (40 mg, 5.6 μmol, 1.0 eq.) in a mixture of DMSO : H_2O (1 : 1). Sodium ascorbate (40 mg, 5.5 μmol, 5.0 eq.), copper sulfate pentahydrate (1.4 mg, 5.6 μmol, 1.0 eq., and ligand (R)-MonoPhos(R) (0.04 mg, 0.112 μmol, 0.02 eq.) were added to the mixture. The reaction mixture was stirred for three days at room temperature. After DMSO elimination using a rotavapor and freeze-drying, the product was purified by PD-10 desalting columns packed with Sephadex G-25 resin.

UV-vis spectroscopy

UV-vis spectroscopy was used to evaluate **MM** and **P-MM** isomerization and for thermodynamic studies using an Agilent 8453 UV-vis diode array system equipped with a quantum northwest peltier controller. Unless specified, irradiations were conducted using a built-in setup coupled to a light emitting diode (LED). Solutions were prepared and measured using a 10 mm quartz cuvette. The same procedure was used for UV-Vis controls on **P**.

^{1}H-NMR *in situ* irradiation studies

A 1 mM solution of **MM** in its stable form ($\mathbf{MM_{Stable}}$) was prepared in $CDCl_3$ and transferred into an NMR tube fitted with a glass optic fiber for *in situ* irradiation studies. The sample was placed in a varian unity plus 500 MHz NMR and cooled to −15 °C. ^{1}H NMR spectra were recorded before irradiation, while irradiating at 405 nm until the PSS was reached, and during the THI step until completion. See the ESI† for further details.

Fluorescence spectroscopy

Fluorescence spectroscopy was used to evaluate the CAC of **P-MM** with and without light irradiation (at 405 nm) using the Nile red assay following previously established procedures (see ESI† for details). Sample solutions were excited at 550 nm and emission was recorded from 590 to 750 nm using a JASCO FP6200 fluorometer.

Cryo-transmission electron microscopy

P-MM samples (2 mM) were placed on a glow-discharged holy carbon-coated grid (quantifoil 3.5/1, QUANTIFOIL Micro Tools GmbH). After blotting, the corresponding grid was rapidly frozen in liquid ethane (Vitrobot, FEI) and kept in liquid nitrogen until measurement. The grids were observed with a Gatan model 626 cryostage in a Tecnai T20 Field Electron and Ion Company (FEI) cryo-electron microscope operating at 200 keV. Cryo-TEM images were recorded on a slow-scan charge-coupled device (CCD) camera under low-dose conditions. All processes were performed in the dark. For irradiated samples (405 nm), the same procedure was carried out in a quartz cuvette immediately before freezing.

Circular dichroism

CD spectroscopy was performed using a J-815 CD Spectrometer (JASCO Corporation), incorporating a Peltier thermostated cell holder (PTC-423, JASCO Corporation) equipped with a recirculating cooler (JULABO F250, JASCO Corporation). A nitrogen flow of approximately 1.5 L min^{-1} was directed through the spectrometer and regulated using a nitrogen flow monitor (Afriso Euro-Index). Samples were prepared in PBS buffer and irradiated at 405 nm for 5 minutes. PP was used as a reference for a PPII profile. Each sample was analyzed three times (n = 3) in a quartz cuvette with a 1 mm diameter.

Cell viability assays

MDA-MB-231 cells were seeded in 96-well plates (5000 cells per well) and incubated for 24 h at 37 °C with 5% CO_2. **P** and **P-MM** were prepared as stock solutions in PBS buffer diluted in DMEM/F-12 medium (with 10% fetal bovine serum (FBS) and 1% penicillin/streptomycin (P/S)), sterilized, and added to cells at final concentrations of 0–1 mg ml^{-1}. Cell viability was assessed using the CellTiter-Glo® 2.0 assay after 24 or 72 h of incubation, with ATP luminescence measured using a CLARIOstar plate reader. For irradiation studies, cells were exposed to 405 nm UV light using a Lumidox® II LED system for 30 s, determined as the optimal non-toxic exposure time (see the ESI† for details) before or after **P-MM** treatment. Luminescence values were expressed as a percentage of cell viability relative to untreated controls, with results reported as mean ± SD (n = 3).

Internalization studies by high-throughput imaging in cell analyzer

Cellular uptake of **P** and **P-MM** (with and without 405 nm irradiation for 30 s) was analyzed using the high-throughput imaging HCS system IN cell analyzer 2200 with specific fluorescent markers (Invitrogen™ CellTracker™ Red CMTPX Dye (cytosol), Helix NP™ Green (nuclei), and Cy5 (**P-MM** and **P**)). MDA-MB-231 cells were seeded in 96-well plates and incubated for 24 h, followed by treatment with fluorescent markers and Cy5-labeled **P** or **P-MM**. After irradiation, fluorescence was measured every 20 min for 6 h. Data analysis involved normalizing fluorescence intensity to Cy5, accounting for quenching effects due to irradiation. Quenching conversion factors were determined (see the ESI† for details), and statistical significance was assessed using a t-test, with p-values indicating $p^{****} < 0.0001$; $p^{***} < 0.001$; $p^{**} < 0.01$; $p^{*} < 0.05$; ns: non-significant.

 This journal is © The Royal Society of Chemistry 2024

Open Access Article. Published on 11 February 2025. Downloaded on 2/12/2025 5:06:18 PM.
This article is licensed under a Creative Commons Attribution-NonCommercial 3.0 Unported Licence.

Internalization studies by confocal fluorescence microscopy

Cellular uptake of **P-MM** (with and without 405 nm irradiation) was qualitatively analyzed using confocal fluorescence microscopy with a Leica TCS SP8 confocal microscope. MDA-MB-231 cells were seeded in 384-well plates and incubated for 24 h. Pulse-chase studies were performed using MitoTracker™ Red (mitochondria), LysoTracker™ Green (lysosomes), and Cy5-labeled **P-MM** added at various time points (20, 40, 80, 120, 160, 200 min) and irradiated for 30 s when applicable. Control cells were used to establish autofluorescence levels. Image processing was carried out using Leica Application Suite X and Image J-JACoP for Pearson's correlation coefficient (Pearson *r*) calculation.

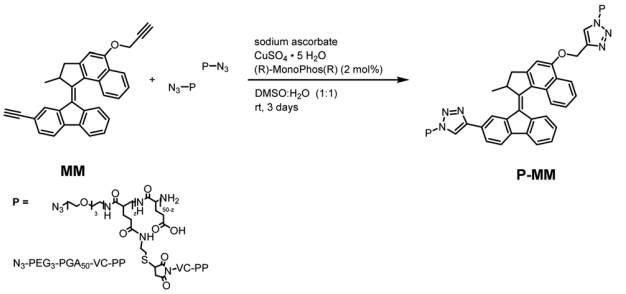
Reactive oxygen species production

MDA-MB-231 cells were seeded in 6-well plates and incubated for 24 h. Cy5-labeled **P** and **P-MM** were added and irradiated for 30 s at 405 nm. After 3 and 24 h, cells were washed, trypsinized, and resuspended in fresh medium. Cells were incubated with 2,7-dichlorodihydrofluorescein (DCFH) and propidium iodide (for viability assessment) and analyzed using flow cytometry. Data were collected with 10 000 counts per sample, analyzed using CytExpert software, and normalized to control levels. Control cells were used to determine autofluorescence. Statistical analysis was performed using a *t*-test, with significance levels set at $p^{***} < 0.0001$; $p^{***} < 0.001$; $p^{**} < 0.01$; $p^{*} < 0.05$; ns: non-significant. Values represent mean ± SD ($n = 3$).

Results and discussion

P-MM synthesis

The ESI† provides detailed reaction conditions and schemes for synthesizing **MM** functionalized with two click-chemistry handles for **P** attachment. We synthesized ketone **S1** from 1-methoxynaphthalene using a one-pot Friedel–Crafts acylation reaction followed by a Nazarov cyclization reaction.[16,17] We then deprotected **S1** with pyridine hydrochloride at elevated temperatures to yield phenol **S2**.[18] We reacted propargyl bromide protected with triisopropylsilyl chloride (**S3**)[18] with phenol **S2** in a Williamson-ether synthesis reaction to generate **S4**. We next converted the ketone moiety to a thioketone (generating **S5**) using Lawesson's reagent, completing the upper half of **MM**. We obtained the bottom half of **MM** (**S7**) by reacting the corresponding aryl halide (**S6**) with trimethylsilylacetylene using Sonogashira cross-coupling followed by transformation of **S7** into hydrazine, followed by manganese dioxide oxidation to form the respective diazo compound **S8**. We introduced the sterically overcrowded olefinic bond between both halves using Barton–Kellogg coupling between **S5** and **S8**, yielding **S9** at a 20% yield, which we further deprotected using tetra-*n*-butylammonium fluoride (TBAF) to obtain the final **MM**. Compound **MM** was isolated as a mixture of two isomers; attempts to separate the isomers by high-performance liquid chromatography (HPLC) failed due to low polarity.



Scheme 1 Synthetic procedure for **P-MM**. rt: room temperature.

As previously detailed,[14,15] the preparation of **P** followed a convergent synthetic procedure (ESI,† Scheme S1). In brief, we functionalized (3.3 wt%) a linear semitelechelic PGA bearing a short azide-polyethylene glycol (PEG) chain (N_3-PEG_3-PGA_{50}) at the N-terminus through a valine–citrulline (VC) linker with a diblock copolymer (PLO_6–PLP_{22}, **PP**) by post-polymerization modification. The final negatively charged (−15.7 ± 0.2 mV) **P** displayed an average size of 5 nm (by SAXS), lacked toxicity at tested concentrations, but displayed energy-independent cell uptake and mitochondrial targeting.[14,15]

We obtained **P-MM** by reacting **MM** and **P** (1 : 2) in a mixture of DMSO : H_2O (1 : 1) *via* a copper-catalyzed click reaction with sodium ascorbate left to stir for three days at room temperature (Scheme 1 and Scheme S2, ESI†). Purification of **P-MM** using PD-10 desalting columns packed with Sephadex G-25 resin resulted in a yield of 90%. We evaluated **P-MM** synthesis by Raman spectroscopy *via* the disappearance of the alkyne peaks of **MM** (Fig. S1, ESI†) and by InfraRed spectroscopy *via* the disappearance of P's azide peaks (Fig. S2, ESI†) due to the masking effect of **P** on **MM** signals in the **P-MM** ^{1}H-NMR spectra (see ESI† for details). Together, these results confirm the successful synthesis and characterization of a novel polypeptide-conjugated molecular motor, which represents a significant advancement in the design of multifunctional biomolecular systems.

Analysis of the rotation cycle of P-MM

We investigated the photochemical/thermodynamic behavior of **P-MM** using steady-state spectroscopy and low-temperature ^{1}H-NMR. We confirmed the rotation cycle of **MM** using direct *in situ* irradiation of the NMR probe with a glass fiber optic cable connected to a 405 nm light-emitting diode at −15 °C in $CDCl_3$. Constant irradiation of the stable isomer decreased the peak intensity of corresponding protons (Fig. 1A-i), while new peaks emerged due to the **MM** metastable isomer (Fig. 1A-ii). The photostationary state (PSS) was reached when no changes in the proton spectra occurred under constant irradiation, with a stable-to-metastable isomer ratio of 40 : 60 (Fig. 1A-ii and Fig. S3A, ESI†). Removal of irradiation led to the complete recovery of the stable isomer (Fig. 1A-iii, -iv and Fig. S3B, ESI†).

We investigated the photochemical properties of **MM** and **P-MM** using UV-Vis absorption spectroscopy in toluene (**MM**) and phosphate buffer saline (PBS) (**P-MM** and **P**). All **MM**

Open Access Article. Published on 11 February 2025. Downloaded on 2/12/2025 5:06:18 PM.
This article is licensed under a Creative Commons Attribution-NonCommercial 3.0 Unported Licence.

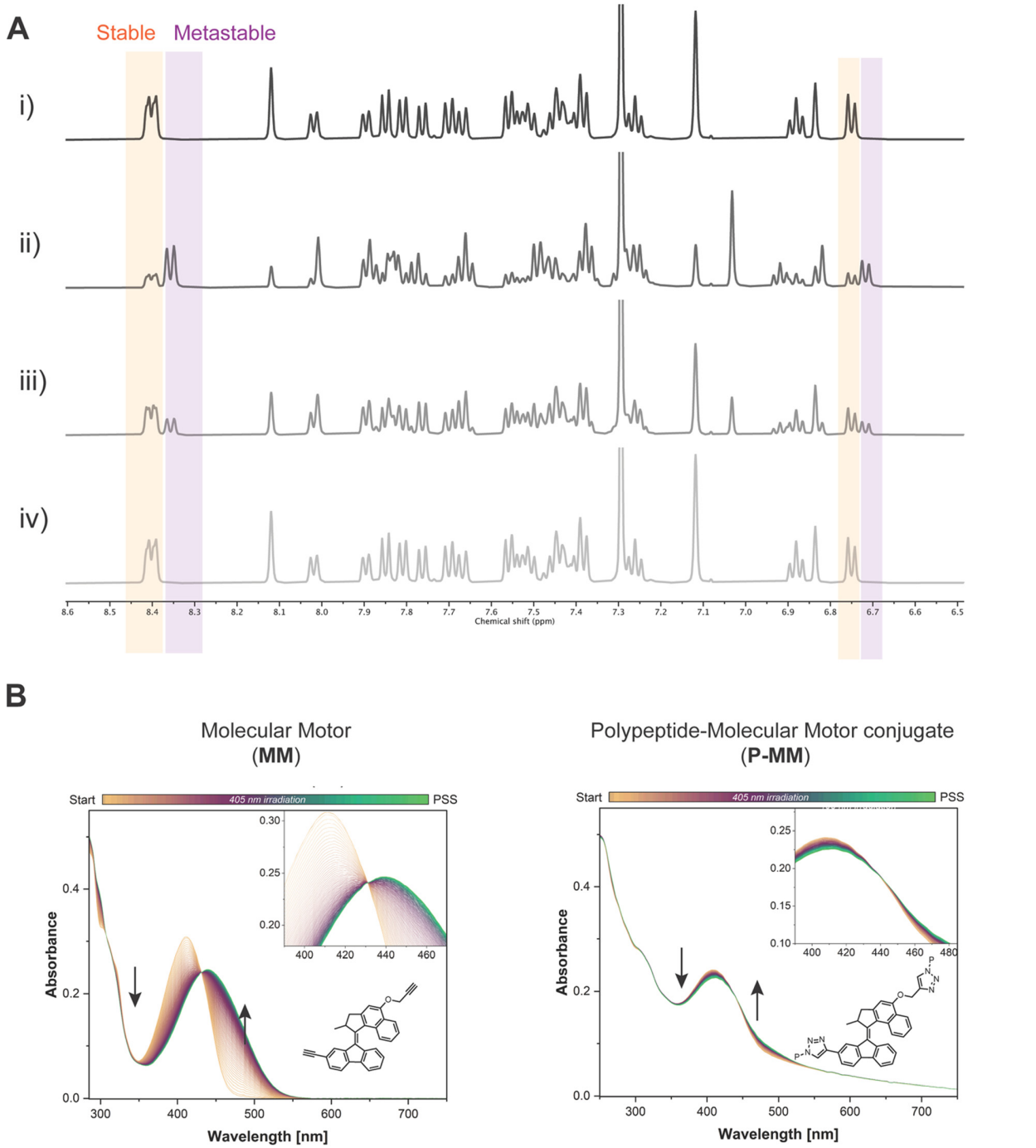


Fig. 1 Photochemical behavior of **MM** and **P-MM**. (A) ^{1}H-NMR aromatic peaks change **MM**. Starting from the stable isomer under dark conditions (i), irradiation at 405 nm until PSS (ii), turning off the irradiation, in the dark, partial thermohelix inversion (THI) (iii), in the dark, completed THI (iv). In $CDCl_3$, at −15 °C. (B) Changes to chemical structure and absorption spectra after 405 nm irradiation of **MM** (in toluene, 37 °C) and **P-MM** (in PBS, 37 °C). The inset shows the isosbestic point, with absorption changes indicated by the orange to green lines.

spectra displayed broad absorption bands with maxima centered ~410 nm, tailing further into the visible region (up to 555 nm) (Fig. 1B, orange line). The **MM** absorption exhibited a slight redshift compared to previous analogs,[19] likely due to the electron-donating effect of the oxygen atom in the upper half of **MM**, which is conjugated with the central double bond and the presence of alkyl groups. Irradiation of **MM** and **P-MM** at 405 nm at 37 °C changed the absorption spectra with a clear isosbestic point (Fig. 1B, insets).

The resulting steady-state spectra corresponded to the partial formation of metastable isomers at the PSS. We observed no change in the absorbance spectra of **P** when irradiated under the

 This journal is © The Royal Society of Chemistry 2024

Open Access Article. Published on 11 February 2025. Downloaded on 2/12/2025 5:06:18 PM.
This article is licensed under a Creative Commons Attribution-NonCommercial 3.0 Unported Licence.

same conditions (Fig. S4, ESI†). We next analyzed the thermodynamic parameters to determine the activation barriers of the thermal isomerization step (rotation cycle rate-determining process), which is the parameter defining rotational speed.[6] Eyring analysis was performed for **MM** and **P-MM** following the exponential decay at 450 nm of the absorbance in the absence of irradiation after reaching the PSS at various temperatures. Rate constants were obtained of the exponential decay function for each temperature and fitted using the linearized Eyring equation (Fig. S5, ESI†) to calculate the activation parameters of the thermal barrier. The calculated energy barriers for the metastable-to-stable transitions at 18.95 and 22.14 kcal mol for **MM** and **P-MM**, respectively (Table S1, ESI†). These values correspond to a half-life for rotation of 2 s for **MM** and 425 s for **P-MM** at 37 °C, with the significant increase attributed to a higher degree of strain in the system in accordance with observations by Foy *et al.* also showing a decreased rotational frequency for an **MM** linked to a polymer network.[20]

The investigation of the photochemical and thermodynamic behavior of **P-MM** revealed the successful rotation and stability of the molecular motor cycle and notable changes in the activation energy (rotation speed) of **P-MM** compared to parental **MM**. These findings suggest that polypeptide attachment introduces additional strain, significantly slowing the rotational cycle of the motor. These results highlight the impact of conjugation on the dynamic behavior of molecular motors, offering valuable insights for the design of hybrid systems with tunable photomechanical properties.

Supramolecular behavior of P-MM

Circular dichroism (CD) spectroscopy was employed to assess changes in the secondary structure of **P** (adopts a random coil structure in contrast to the polyproline II [PPII] helix conformation of PP) compared to **P-MM** before/after irradiation (405 nm, 5 min). CD spectra for **MM** and **P-MM** suggested random coil conformations (Fig. S6, ESI†), indicating that **MM** conjugation did not alter the secondary structure of **P**; however, we observed conformational alterations for **P-MM** in solution. We studied the self-assembly of **P-MM** in PBS by determining its critical aggregation concentration (CAC) using the Nile red fluorescence assay[21] (ESI†). We observed values of 59.4 and 25.9 μM for non-irradiated and irradiated **P-MM** (Fig. S7 and Table S2, ESI†), with differences in values indicative of light-induced changes in the supramolecular conformation of **P-MM**.

Next, we used cryo-transmission electron microscopy (cryo-TEM) before/after irradiation to characterize the nanoscopic arrangement of **P-MM** (Fig. S8 and S9, ESI†). Non-irradiated **P-MM** formed micelles (~2–3 nm in diameter) of smaller size than parental **P**, likely due to the conformational compactness afforded by the hydrophobic conjugated **MM**. Upon irradiation, the same **P-MM** solution exhibited long worm-like structures (~1 × 10 nm in length). These observations suggest that light irradiation of the conjugate induces a structural reorganization in **P-MM**, transitioning from a compact micellar form to an extended supramolecular architecture. This conformational shift reflects changes in the supramolecular interactions within the system, driven by the conformational change of **MM** under light exposure. The irradiation-induced conformational transition of **P-MM** may enhance cell uptake, consistent with studies demonstrating nanoparticle shape's influence on internalization.[22–24]

In short, light irradiation did not alter the secondary structure of the polypeptide; however, the substantial decrease in CAC following 405 nm irradiation in combination with the transformation observed in cryo-TEM images indicates a significant light-induced change in the supramolecular organization of **P-MM**. These findings suggest that integrating light-responsive polypeptide systems can support the manipulation of cellular functions in a highly controlled manner.

Exploring the feasibility of P-MM for biological applications

We evaluated potential biological applications of **P-MM** by focusing on cell uptake studies in a triple-negative breast cancer (TNBC) cell line (MDA-MB-231). Cell viability studies assessed by measuring ATP-dependent luminescence over 24/72 h confirmed that **P** and **P-MM** displayed no significant cytotoxicity (Fig. S10, ESI†), demonstrating the biocompatibility of **MM** when conjugated to **P**. We determined optimal non-toxic irradiation times by exposing cells to 405 nm irradiation for 30, 60, and 120 s without **P**/**P-MM** treatment; overall, 30 s of irradiation (65 mW per well) did not significantly affect cell viability (Table S3 and Fig. S11, ESI†). This optimization step established a reliable foundation for exploring the **P-MM** conjugate in biological applications. Cells incubated with **P-MM** and immediately irradiated for 30 s at 405 nm failed to show signs of induced cytotoxicity after 3/24 h, further validating the safety of **P-MM** (Fig. 2A).

After confirming safety, we assessed the ability of **P-MM** to enhance cellular uptake relative to non-irradiated **P-MM** and the parent polypeptide **P**. We evaluated the cell uptake of **P-MM** after irradiation using Cy5-labeled derivatives (Scheme S3 and Fig. S12, ESI†) and high-throughput imaging. We incubated cells with Cy5-labeled **P** and **P-MM**, exposed them to 30 s of 405 nm irradiation (comparing to non-irradiated controls; ESI†), and quantified fluorescence intensity after cell segmentation every 20 min for 6 h (Fig. S13, ESI†). The data analysis accounted for varying Cy5 labeling percentages in each treatment and the quenching effect caused by 405 nm irradiation (as detailed in the ESI†). Our results demonstrated a significantly higher average fluorescence intensity for irradiated compared to non-irradiated **P-MM** and both forms of **P**, indicating enhanced uptake of irradiated **P-MM** (Fig. 2B). These studies support a correlation between conformational changes and biological outcomes. Moreover, we observed a higher fluorescence intensity decay over time for **P-MM** compared to **P** using equivalent dye conditions (Fig. S14, ESI†), which we attributed to **MM**.[25] Photoisomerizing molecules function as effective Förster resonance energy transfer acceptors when close to molecular dyes, decreasing their radiative activity.[26] Quenching produced the highest fluorescence intensity at the initial timepoint (20 min), followed by a slight reduction (Fig. S14, ESI†). To confirm cell internalization and the unaltered

Open Access Article. Published on 11 February 2025. Downloaded on 2/12/2025 5:06:18 PM.
This article is licensed under a Creative Commons Attribution-NonCommercial 3.0 Unported Licence.

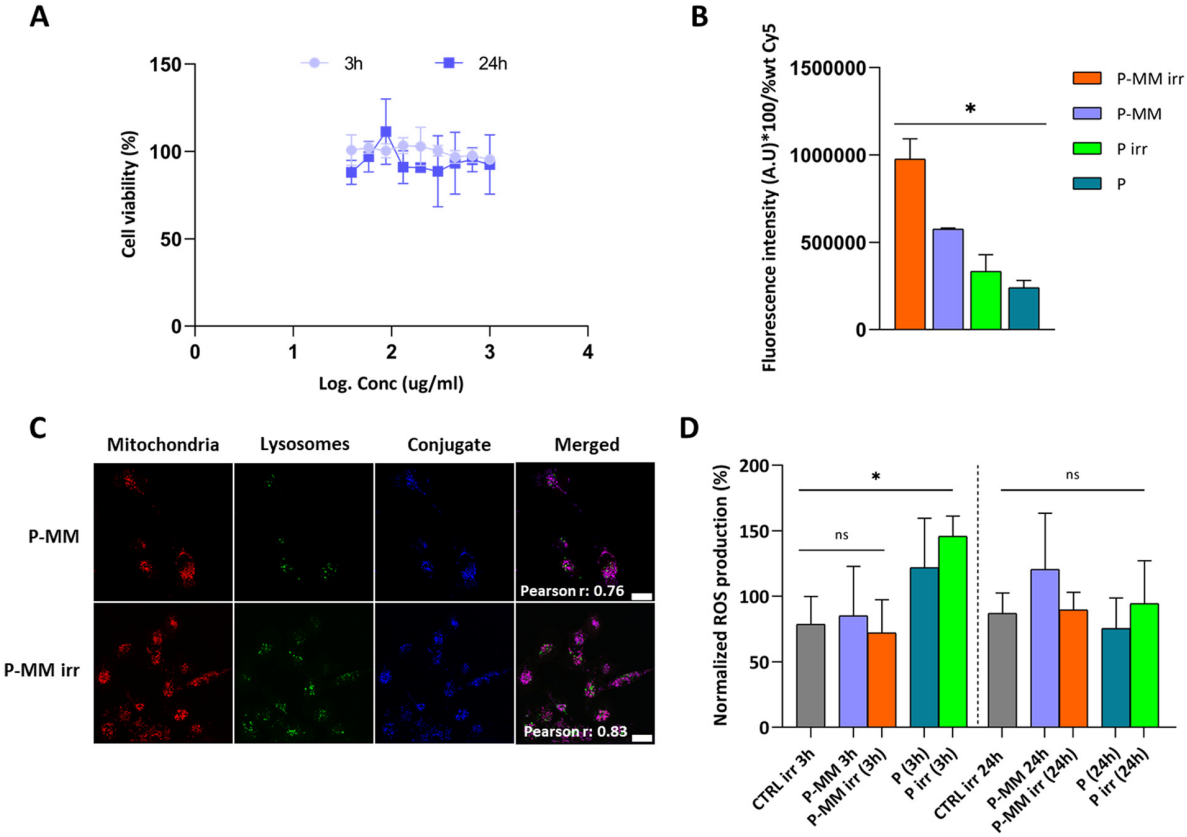


Fig. 2 Biological characterization of **P-MM**. (A) Cell viability after a 3-/24-h treatment and irradiation (405 nm, 30 s) with **P-MM** (n = 3, mean ± SEM). (B) Internalization of Cy5-labeled **P-MM** and **P** in irradiated (405 nm, 30 s) and non-irradiated conditions represented as the average fluorescence intensity measured after cell segmentation (CellTracker™ Red CMTPX Dye) in live cells (labeled with Helix NP™ Green) every 20 min over 6 h. Data normalized to wt% Cy5 (ESI†). t-Test comparing irradiated (irr) **P-MM** to **P**; n = 3, mean ± SEM; significance reported as $*p \leq 0.05$, ns = not significant. (C) Confocal images of **P-MM** uptake at 20 min post-treatment and irradiation (405 nm, 30 s) in cells following a pulse-chase experiment (Fig. S14, ESI†) (Red – MitoTracker™ Red CM-H2Xros for mitochondria; Green – LysoTracker® Green for lysosomes; Blue – Cy5 for **P-MM** and irradiated (irr) **P-MM**). Colocalization of **P-MM** and irradiated (irr) **P-MM** with Mitotracker red shown in the merge (purple). Pearson r (20 min) value calculated using the ImageJ – JACoP plugin. Scale bar: 10 μm. (D) Reactive oxygen species (ROS) levels after 3-/24-h treatment and irradiation (405 nm, 30 s) with **P** and **P-MM**. t-Test comparing to control set as 100% and treatments irradiated (irr) **P-MM**, **P-MM**, irradiated (irr) **P**, and **P** labeled with Cy5; n = 3, mean ± SEM. Significance reported as $*p \leq 0.05$, ns = not significant.

sub-organelle localization of **P** at the mitochondrial level[14,15] (even when conjugated to a molecular motor), we studied Cy5-labeled **P-MM** using live-cell confocal fluorescence microscopy before/after 30 s of 405 nm irradiation (pulse-chase study); we observed significant mitochondrial colocalization for **P-MM** after irradiation starting at 20 min (Pearson $r > 0.5$) (Fig. 2C) and remaining invariant over time (Fig. S15, ESI†). The stability of Pearson r values supports the hypothesis that light irradiation does not disrupt **P-MM**'s mitochondrial localization but rather facilitates consistent interaction with mitochondria.

To determine whether the mechanical rotation and conformational change associated with **P-MM** enhanced cell uptake, we assessed ROS generation after 3-/24-h treatment with Cy5-labeled **P-MM** and **P** with/without irradiation (30 s; 405 nm) to distinguish mechanical effects from oxidative stress induced by photosensitive systems.[27] Flow cytometry analyses revealed no significant increase in ROS levels for irradiated **P-MM** compared to control samples (Fig. 2D) at both time points; in contrast, treatment with **P** increased ROS levels at 3 h, suggesting a temporary oxidative stress response (followed by restoration of levels at 24 h).

Our results demonstrate that **P-MM** maintains a safe biological profile while significantly enhancing cellular uptake in MDA-MB-231 cells. The results suggest that increased uptake primarily derives from conformational changes induced by the mechanical rotation of **P-MM** rather than oxidative stress. These insights highlight the potential of **P-MM** for targeted delivery applications that require improved cell uptake and precise sub-organelle localization.

Conclusions

In conclusion, we report the synthesis and characterization of a light-driven rotary molecular machine bearing a polypeptide-conjugate with mitochondria tropism, which represents an

 This journal is © The Royal Society of Chemistry 2024

Open Access Article. Published on 11 February 2025. Downloaded on 2/12/2025 5:06:18 PM.
This article is licensed under a Creative Commons Attribution-NonCommercial 3.0 Unported Licence.

advance in designing multifunctional systems for biological applications. We determined that our synthetic molecular machine was suitable for click chemistry, offering numerous possibilities for biomolecular designs. **MM** conjugation did not alter P's inherent secondary structure and, therefore, mitochondrial tropism. We retained the rotation cycle of **MM**, with additional strain inducing a significant decrease in rotational speed. While the secondary structure of **P** remained unchanged, we observed significant irradiation-induced modifications in the supramolecular organization of **P-MM** – a transition from small micelles to elongated worm-like structures after irradiation. This conformational shift enhanced cell uptake compared to non-irradiated **P-MM** without a significant oxidative stress response. These findings suggest the potential of **P-MM** in acute intracellular applications, such as in targeted delivery systems and therapeutic strategies requiring improved cell uptake and precise sub-organelle localization. Future applications may include *ex vivo* lab-on-chip systems (benefit from precise control *via* an external trigger) and the acute systemic administration of biologically active agents (benefit from cytosolic transport).

Author contributions

C. P. and A. G. led the synthesis, data curation, formal analysis, investigation, methodology, and writing of the original draft. E. M. S., D. D., and M. C. A. S. contributed to the data curation, formal analysis, investigation, and methodology in supporting roles. Software development was equally contributed by C. P. and A. G. Cell viability assays and biological studies were carried out by C. P. with support from E. M. S. Supervision and project administration were equally managed by M. J. V. and B. L. F., supported by I. C.-S., C. P., A. G., I. C.-S., B. L. F. and M. J. V. contributed to the conceptualization and validation of the study. Funding acquisition was led by M. J. V. and B. L. F., with support from I. C. S. The manuscript was revised by C. P., A. G., I. C.-S., B. L. F. and M. J. V., with reviewing and editing contributions from all authors. All authors have read and approved the final version of the manuscript.

Data availability

The data supporting this article have been included as part of the ESI.† Further information if needed can be provided by the corresponding authors upon request.

Conflicts of interest

The authors declare a filed patent. M. J. Vicent; I. Conejos-Sánchez; C. Pegoraro; E. Karpova; G. Sogorb; C. Felip; V. J. Nebot; P. Schwille; Y. Qutbuddin. PCT/EP2024/068352 (Priority claimed: European Patent Application no. EP23382668.4). Polyproline-based Block-copolymers 28/06/2024. CIPF, PTS SL, and Max Planck Society.

Acknowledgements

This project was supported by the H2020-MSCA-ITN-2019 BIO-MOLMACS (proposal no. 859416). The authors acknowledge the Asociación Española contra el Cáncer (ICS INVES211323CONE Junior AECC grant), Spanish Ministry of Economy (PID2019-108806RB-I00), NextGeneration EU i + d + I funding through GVA Conselleria Innovació-Pol@Mets. Ref. MFA/2022/065 and European Regional Development Fund (PO FEDER Comunitat Valenciana 2014-2020) Generalitat Valenciana for financial support. Support from the project EU-OPENSCREEN IMPULSE (Grant Agreement No. 101132028), and the Netherlands Ministry of Education, Culture and Science (Gravitation Program no. 024.001.035) is gratefully acknowledged. We thank Dr Stuart P. Atkinson for his help in manuscript development and English editing, Alberto Hernandez for confocal imaging support, Alicia Martinez Romero for flow cytometry analysis, and Prof. Wesley Browne for Raman Spectroscopy.

Notes and references

1 C. Brieke, F. Rohrbach, A. Gottschalk, G. Mayer and A. Heckel, *Angew. Chem., Int. Ed.*, 2012, **51**, 8446–8476.
2 N. Vogt, *Nat. Methods*, 2020, **17**, 364.
3 W. A. Velema, W. Szymanski and B. L. Feringa, *J. Am. Chem. Soc.*, 2014, **136**, 2178–2191.
4 N. Koumura, R. W. J. Zijlstra, R. A. van Delden, N. Harada and B. L. Feringa, *Nature*, 1999, **401**, 152–155.
5 J. C. M. Kistemaker, A. S. Lubbe and B. L. Feringa, *Mater. Chem. Front.*, 2021, **5**, 2900–2906.
6 D. R. S. Pooler, A. S. Lubbe, S. Crespi and B. L. Feringa, *Chem. Sci.*, 2021, **12**, 14964–14986.
7 D. Liu, V. García-López, R. S. Gunasekera, L. Greer Nilewski, L. B. Alemany, A. Aliyan, T. Jin, G. Wang, J. M. Tour and R. Pal, *ACS Nano*, 2019, **13**, 6813–6823.
8 Q. Zhou, J. Chen, Y. Luan, P. A. Vainikka, S. Thallmair, S. J. Marrink, B. L. Feringa and P. van Rijn, *Sci. Adv.*, 2024, **6**, eaay2756.
9 A. Guinart, M. Korpidou, D. Doellerer, G. Pacella, M. C. A. Stuart, I. A. Dinu, G. Portale, C. Palivan and B. L. Feringa, *Proc. Natl. Acad. Sci. U. S. A.*, 2023, **120**, e2301279120.
10 T. Melnyk, S. Đorđević, I. Conejos-Sánchez and M. J. Vicent, *Adv. Drug Delivery Rev.*, 2020, **160**, 136–169.
11 A. Duro-Castano, I. Conejos-Sánchez and M. J. Vicent, *Polymers*, 2014, **6**, 515–551.
12 T. A. Bauer, L. Simić, J. F. R. Van Guyse, A. Duro-Castaño, V. J. Nebot and M. Barz, *Prog. Polym. Sci.*, 2024, **158**, 101889.
13 O. Zagorodko, J. J. Arroyo-Crespo, V. J. Nebot and M. J. Vicent, *Macromol. Biosci.*, 2017, **17**, 1–22.
14 C. Pegoraro, E. Karpova, Y. Qutbuddin, E. Masiá Sanchis, P. Dimitrijevs, C. Huck-Iriart, S. Gavrilović, P. Arsenyan, P. Schwille, C. Felip-León, A. Duro-Castaño, I. Conejos-Sánchez and M. J. Vicent, *Adv. Mater.*, 2024, DOI: **10.1002/adma.202411595**.
15 PCT/EP2024/068352, CIPF; PTS SL; and Max Planck Society, 2024.

Open Access Article. Published on 11 February 2025. Downloaded on 2/12/2025 5:06:18 PM.
This article is licensed under a Creative Commons Attribution-NonCommercial 3.0 Unported Licence.

16 F. K.-C. Leung, T. van den Enk, T. Kajitani, J. Chen, M. C. A. Stuart, J. Kuipers, T. Fukushima and B. L. Feringa, *J. Am. Chem. Soc.*, 2018, **140**, 17724–17733.
17 L. Pfeifer, M. Scherübl, M. Fellert, W. Danowski, J. Cheng, J. Pol and B. L. Feringa, *Chem. Sci.*, 2019, **10**, 8768–8773.
18 L. Pfeifer, N. V. Hoang, M. Scherübl, M. S. Pshenichnikov and B. L. Feringa, *Sci. Adv.*, 2024, **6**, eabb6165.
19 J. Vicario, A. Meetsma and B. L. Feringa, *Chem. Commun.*, 2005, 5910–5912.
20 J. T. Foy, Q. Li, A. Goujon, J.-R. Colard-Itté, G. Fuks, E. Moulin, O. Schiffmann, D. Dattler, D. P. Funeriu and N. Giuseppone, *Nat. Nanotechnol.*, 2017, **12**, 540–545.
21 M. C. A. Stuart, J. C. van de Pas and J. B. F. N. Engberts, *J. Phys. Org. Chem.*, 2005, **18**, 929–934.
22 B. Karagoz, L. Esser, H. T. Duong, J. S. Basuki, C. Boyer and T. P. Davis, *Polym. Chem.*, 2014, **5**, 350–355.
23 J. Zhao, H. Lu, S. Wong, M. Lu, P. Xiao and M. H. Stenzel, *Polym. Chem.*, 2017, **8**, 3317–3326.
24 S. Barua, J.-W. Yoo, P. Kolhar, A. Wakankar, Y. R. Gokarn and S. Mitragotri, *Proc. Natl. Acad. Sci. U. S. A.*, 2013, **110**, 3270–3275.
25 S. D. Pritzl, J. Morstein, S. Kahler, D. B. Konrad, D. Trauner and T. Lohmüller, *Langmuir*, 2022, **38**, 11941–11949.
26 A. Chevalier, P.-Y. Renard and A. Romieu, *Chem. – Asian J.*, 2017, **12**, 2008–2028.
27 J. L. Beckham, T. S. Bradford, C. Ayala-Orozco, A. L. Santos, D. Arnold, A. R. van Venrooy, V. García-López, R. Pal and J. M. Tour, *Adv. Mater.*, 2024, **36**, 2306669.

 This journal is © The Royal Society of Chemistry 2024

3.3 Manuscript IV

3.3.1 Scientific Article III: Introduction and Background

Efficient mitochondrial targeting and non-viral gene delivery remain two of the most significant challenges in nanomedicine, particularly for complex diseases such as cancer. Addressing these hurdles requires the development of multifunctional delivery platforms capable of precise subcellular localization and robust intracellular trafficking. This study introduces C-TRV3-A, a polypeptide-based nanoconjugate engineered to integrate mitochondrial targeting with non-viral gene therapy, offering a versatile solution to these challenges[346].

The design of C-TRV3-A centers on a PLO backbone functionalized with PEG and a redox-sensitive disulfide linker to conjugate a trivalent compound (TRV3). The modular architecture incorporates TPP for mitochondrial targeting, the Cyanine5 (Cy5) dye as a model drug, and the Atto488 fluorescent label for imaging and tracking. This multifunctionality ensures efficient delivery to mitochondria following endosomal escape, overcoming critical barriers to intracellular targeting.

Key advancements of this work include:

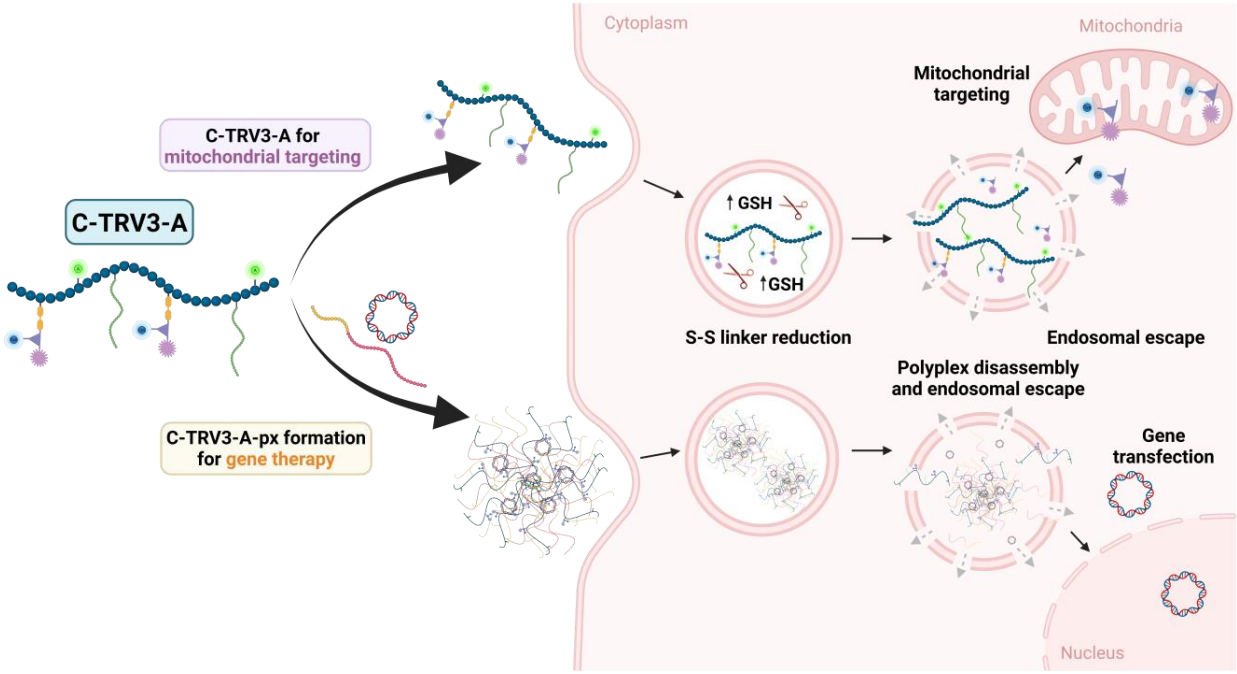
- **Precise Mitochondrial Targeting**: The integration of TPP enables selective mitochondrial localization following endosomal escape, a crucial step for achieving subcellular specificity. A redox-sensitive disulfide linker ensures the selective release of TRV3 in highly reducing environments, optimizing intracellular trafficking within cancer cells.
- **Non-Viral Gene Delivery Efficacy**: In combination with plasmid DNA coding luciferase and an anionic shielding polymer (VLC-3), C-TRV3-A forms polyplexes that demonstrate high transfection efficiency and stability in complex biological media, including human plasma. This platform achieves safe and effective gene delivery in both 2D monolayer and 3D spheroid cell culture models of TNBC.

This study represents a significant advancement in polypeptide-based nanomedicines by combining mitochondrial targeting, efficient cytosolic delivery, and gene therapy into a single platform. C-TRV3-A offers a versatile approach to overcoming key barriers in cancer treatment. The findings contribute to the broader objectives of this thesis by providing innovative strategies for

precise therapeutic delivery, paving the way for advancements in nanomedicine for aggressive cancers such as TNBC.

In this work, I carried out the synthesis, physicochemical characterization, and biological evaluation of C-TRV3-A. Additionally, I performed the polyplexes formulation, as well as the stability and transfection assays. Contributions by co-authors are detailed in the manuscript.

Table of Content



C-TRV3-A as a mitochondrial targeting nanoconjugate and a non-viral gene delivery vector. Schematic representation of C-TRV3-A, a multifunctional polypeptide-based nanoconjugate as a non-viral gene delivery vector designed for mitochondrial targeting. The engineered C-TRV3-A comprises a poly-L-ornithine (PLO) backbone modified with polyethylene glycol (PEG) and conjugated to the trivalent compound TRV3 via a redox-sensitive disulfide linker (S-S) (C-TRV3). TRV3 incorporates a Lysine (Lys) derivative functionalized with a triphenylphosphonium (TPP) derivative for mitochondrial targeting and a Cy5 fluorophore as a model drug. The resulting nanoconjugate C-TRV3 is labeled with Atto488 (C-TRV3-A). Reduction of the S-S linker (high glutathione [GSH] levels) and endosomal escape induces TRV3 release, enabling mitochondrial targeting via the TPP moiety. C-TRV3-A also serves as a polycationic carrier for polyplex formation (C-TRV3-A-px), with enhanced safety and transfection efficacy when combined with the anionic polypeptide VLC-3 for pDNA-Luc (Luciferase) transfection. *Figure created with Biorender.*

CHEMISTRY OF MATERIALS

pubs.acs.org/cm

Article

Open Access

This article is licensed under CC-BY-NC-ND 4.0

Multifunctional Polypeptide-Based Nanoconjugates for Targeted Mitochondrial Delivery and Nonviral Gene Therapy

Published as part of Chemistry of Materials special issue "Polymer-Drug Conjugate Materials".

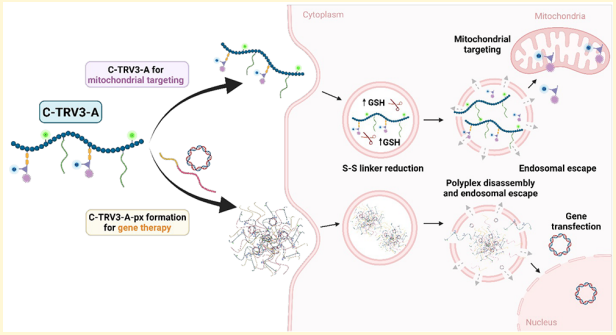
Camilla Pegoraro, Esther Masiá Sanchis, Snežana Đorđević, Irene Dolz-Pérez, Cristián Huck-Iriart, Lidia Herrera, Sergio Esteban-Pérez, Inmaculada Conejos-Sanchez,* and María J. Vicent*

Cite This: https://doi.org/10.1021/acs.chemmater.4c02742

Read Online

ACCESS | Metrics & More | Article Recommendations | Supporting Information

ABSTRACT: Despite recent advances in nanomedicine, developing multifunctional nanocarriers capable of targeted subcellular delivery and efficient gene therapy remains a significant challenge. This study reports the design, synthesis, and evaluation of a novel multifunctional polypeptide-based nanoconjugate that addresses this gap using sequential delivery, combining mitochondrial targeting and nonviral gene therapy. We engineered a poly-L-ornithine-based, polyethylene glycol-modified carrier and introduced a novel custom-designed trivalent compound (TRV3) into the structure. TRV3, conjugated to the polypeptide carrier via a redox-sensitive disulfide linker, incorporates the well-described triphenylphosphonium moiety (TPP) for mitochondrial targeting and a Cy5 fluorophore as a model drug. The resulting nanoconjugate (C-TRV3-A) demonstrated efficient endosomal escape and mitochondrial localization. Leveraging the endosomolytic properties of C-TRV3-A, we explored its potential as a nonviral vector for gene therapy. After optimizing formulation stability using a VLC-3 anionic polypeptide coating, we developed plasmid DNA polyplexes that exhibited enhanced stability and transfection efficiency in basic and advanced triple-negative breast cancer cell culture models. This multifunctional polypeptide-based nanoconjugate represents a significant advance in the field, offering a chemically versatile platform for simultaneous subcellular targeting and gene delivery that may be used in targeted cancer treatments, among other pathologies.



Downloaded via 79.21.184.36 on February 10, 2025 at 08:45:54 (UTC).
See https://pubs.acs.org/sharingguidelines for options on how to legitimately share published articles.

1. INTRODUCTION

Nanomedicine engineering presents a promising approach to enhance therapeutic outcomes in complex, multifactorial disorders such as cancer.[1] The rational design of multifunctional polymeric carriers and nanoconjugates with tailored properties enables the implementation of versatile/combination therapies, potentially improving efficacy and safety.[2,3] Biodegradable polypeptides lacking immunogenicity offer advantages when used as polymeric carriers, including tunable properties (via controlled synthesis, architecture, and post-polymerization modification) and the multivalency required for the conjugation of distinct payloads via bioresponsive linkers.[4,5] Integrating the described features will support the creation of polypeptide-based nanoconjugates with diverse functionalities.[6]

Numerous applications, including clinically tested,[7] have demonstrated polypeptide versatility,[8,9] while their potential for targeting specific subcellular compartments/delivering genetic payloads has been independently studied.[10−13] However, combining these two functionalities within a single polypeptide-based system remains mostly unexplored. Of note, mitochondria have emerged as a primary focus of subcellular targeting efforts due to their critical role in energy generation and cancer cell survival.[14]

Here, we designed a versatile multifunctional polypeptide-based nanoconjugate for mitochondrial targeting following a rational hierarchical delivery approach. We selected poly-L-ornithine (PLO) as the polymeric carrier due to its endosomal escape properties.[10,15] To enhance functionality, we modified PLO with a polyethylene glycol chain (PLO−PEG), which improves steric stability and minimizes nonspecific interactions.[16] Our group's prior research underscored the critical role of PEG modification and the significance of molecular weight (Mw).[17] Among various derivatives evaluated, PLO−PEG_{3000} - used as the starting carrier in this study -

Received: October 1, 2024
Revised: January 9, 2025
Accepted: January 10, 2025

ACS Publications

© XXXX The Authors. Published by American Chemical Society

demonstrated optimal transfection efficiency compared to alternatives such as PLO−PEG_{2000}. We conjugated a trivalent compound (TRV3), incorporating a triphenylphosphonium (TPP) derivative for mitochondrial targeting[18,19] and Cy5 as a model drug, to PLO−PEG via a redox-sensitive disulfide (S−S) linker[20] (C-TRV3). Finally, we labeled the nanoconjugate with Atto488 at ornithine pendant groups for tracking purposes (C-TRV3-A). Overall, we observed effective TRV3 release following S−S linker reduction and endosomal escape, enabling mitochondrial targeting. The endosomolytic properties of C-TRV3-A supported subcellular targeting and applications in gene therapy as a nonviral vector. While polycationic polymers such as PLO support DNA condensation and cellular uptake,[17,21−24] their toxicity can limit gene therapy applications.[25−27] We employed a polyanionic polypeptide (VLC-3)[28] as an anionic coating to improve polyplex stability and safety to address this limitation. We formulated plasmid (p)DNA polyplexes using C-TRV3-A and VLC-3, optimizing them for high stability and transfection efficiency in the triple-negative breast cancer (TNBC) MDA-MB-231 cell model.

This study explores the innovative use of polypeptide-based nanoconjugates for targeted mitochondrial delivery, paving the way for enhanced therapeutic strategies in cancer treatment and improved safety profiles in nonviral gene therapy applications.

2. EXPERIMENTAL SECTION

Details regarding materials, protocols, and conditions for the synthesis and biological evaluation of C-TRV3-A and polyplexes are extensively described in the ESI and summarized in the following sections.

2.1. Materials. PLO (5700 g mol^{-1}, n = 50) was provided by Curapath (Valencia, Spain). The heterobifunctional PEG-derivative MeO-PEG_{3000}-NHS (3023 g/mol; NHS = *N*-hydroxysuccinimide and MeO = methoxy) was purchased from Biopharma PEG (USA). N*β*-Fmoc-N*ω*-Boc-L-*β*-homolysine and 3,3′-dithiopropionic acid di(N-succinimidyl ester (S−S linker derivative) were purchased from ABCR GmbH (Germany). (3-carboxypropyl)triphenylphosphonium bromide (TPP derivative, CTPB) was purchased from Sigma-Aldrich (USA). The fluorophores $Atto_{488}$-NHS and Cyanine5-amine (Cy5-NH_2) were purchased from ATTO-TEC GmbH and Lumiprobe GmbH (Germany). Plasmid pCMV-Luc (pDNA-Luc, Luc = luciferase) was purchased from Plasmid Factory (Germany).

2.2. Methods. *2.2.1. Synthesis and Characterization of C-TRV3-A. 2.2.1.1. Synthesis of C-TRV-3-A.* Briefly, N*β*-Fmoc-N*ω*-Boc-L-*β*-homolysine (S1, 35.4 mg, 1.20 eq., 5 mg/mL) was dissolved in anhydrous dimethylformamide (DMF) in a two-neck flask in an N_2 atmosphere. 4-(4,6-dimethoxy-1,3,5-triazin-2-yl)-4-methylmorpholinium tetrafluoroborate (DMTMM BF4) (48.2 mg, 2.40 equiv) in 0.5 mL anhydrous DMF was added to activate the carboxylic groups (20 min, room temperature). Cy5-NH_2 (40 mg, 1 eq., 10 mg/mL) in anhydrous DMF was added, and the pH was adjusted to 8 with N, N-diisopropylethylamine. The reaction proceeded for 24 h at room temperature, protected from light. After solvent removal, the product (S2, theoretical yield: 68.4 mg) underwent Boc-deprotection using dichloromethane (DCM)/trifluoroacetic acid (TFA) (2:1 v/v) for 2 h at room temperature. The final product (S3) was precipitated in cold diethyl ether, centrifuged, and lyophilized (Yield: 85%, 58.1 mg).

CTPB (31.6 mg, 1.20 eq., 4 mg/mL) in DMF was activated with DMTMM BF4 (48.3 mg, 2.4 equiv) for 20 min and then added to a solution of S3 (58.1 mg, 1 eq., 7 mg/mL) in anhydrous DMF. The pH was adjusted to 8 and reacted for 24 h at room temperature. The product (S4, theoretical yield: 83.4 mg) was precipitated, centrifuged, and lyophilized. S4 underwent Fmoc-deprotection in DMF/piperidine (4:1 v/v) for 4.5 h, and the final product (S5) was isolated by precipitation (Yield: 78%, 65 mg).

A solution of S5 (65 mg, 1.00 eq, 7 mg/mL) in anhydrous DMF was reacted with the S−S linker derivative (50.1 mg, 2 eq., 5 mg/mL) and a catalytic amount of 4-dimethylaminopyridine (DMAP) at pH 8 for 24 h. The product (TRV3) was purified by solid-phase extraction using silica cartridges with a DCM/methanol gradient (Yield: 70%, 57.9 mg).

PLO (S6, 200 mg, 1 eq., 20 mg/mL) in anhydrous dimethyl sulfoxide (DMSO) was reacted with MeO-PEG_{3000}-NHS (i.e., 123 mg, 0.04 eq. for a 4% mol PEG modification) and a catalytic amount of DMAP at pH 8 for 72 h. The product (S7) was purified by size exclusion chromatography (PD-10 columns) (PEG functionalization: 3.6% mol).

TRV3 (i.e., 53.7 mg, 0.10 eq for 10% mol PEG modification) was conjugated to S7 (100 mg, 1 eq., 4 mg/mL), forming C-TRV3 and purified by size exclusion chromatography (PD-10 columns) and ultrafiltration (Vivaspin, 2000 MWCO) (C-TRV3 functionalization: 4% mol; Cy5 loading: < 1 wt %; conjugation efficiency: 40%).

C-TRV3 (1 eq., 10 mg/mL) was labeled in water with Atto488-NHS (0.010 eq., 1.0% mol) in DMSO at pH 8 overnight. The product (C-TRV3-A) was purified by size exclusion chromatography (PD-10 columns) (conjugation efficiency: 90−100%).

Reported yields calculated based on the limiting reagent in each reaction. The functionalization/conjugation efficiencies of S7, C-TRV3, and C-TRV3-A were calculated by ^1H NMR or fluorescence spectroscopy.

2.2.1.2. C-TRV3-A Physicochemical Characterization. Structural characterization was performed using ^1H NMR spectroscopy (300 MHz Bruker spectrometer in $CDCl_3$ or D_2O). Mass spectrometry (MS) analysis employed direct injection Q1 scans (20 *μ*L, 50% acetonitrile/50% H_2O with 0.1% formic acid). The mass spectra presented in the ESI are centroid *m*/*z* values and background-subtracted spectra. To note, the mass of product S4 was identified as 1273.4 *m*/*z* and attributed to the decomposition of triphenylphosphine under electron impact, which results in the loss of one phenyl group and the formation of a two-charged ion (637.2 *m*/*z*). This behavior was limited in subsequent steps by reducing the ionization temperature from 750 to 250 °C and the declustering potential to 40 V. Moreover, Dynamic light scattering (DLS) measurements were conducted using a Malvern Zetasizer NanoZS instrument in phosphate-buffered saline (PBS) at 25 °C. Transmission electron microscopy (TEM) imaging was conducted on an FEI Tecnai Spirit BioTwin microscope with samples negatively stained using 2% uranyl acetate. Small-angle X-ray scattering (SAXS) experiments were performed at the NCD-SWEET beamline (ALBA Synchrotron, Barcelona, Spain) using X-ray energies of 12.4 and 15 keV, with data analyzed using a fractal coil model.

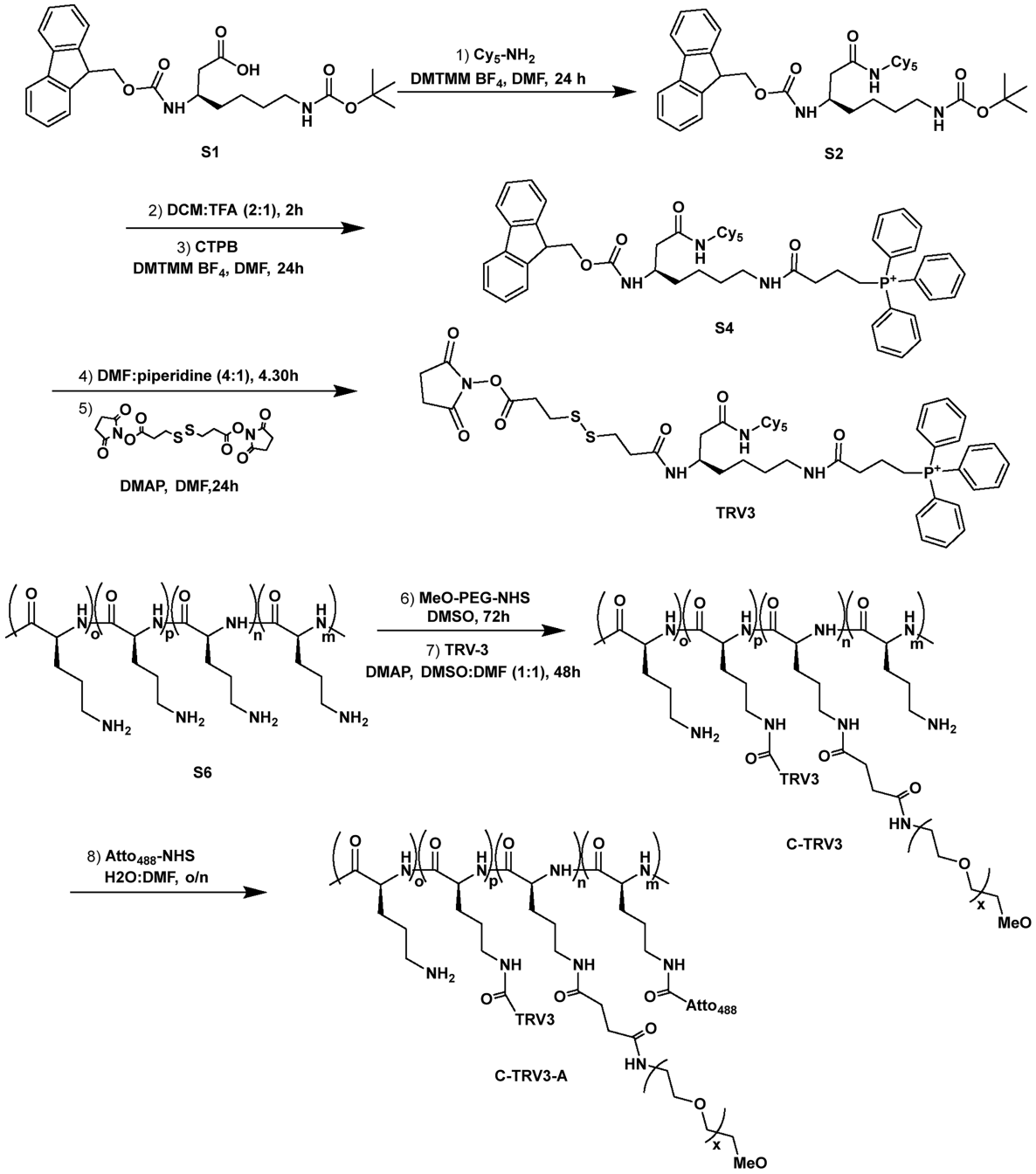
2.3. Synthesis of the Noncovalent Shielding Polyanion PSar-*b*-PGA Block Copolymer (VLC-3). The synthesis and full characterization of the block copolymer $PSar_{100}$-*b*-PGA_{15}OtBu (VLC-3) was conducted as described in the patent application ref. WO2023002014A1[28] and can be found in the ESI. Briefly, Sarcosine N-carboxyanhydride (Sar NCA) was polymerized in an anhydrous DMF solution under an inert atmosphere with *n*-butylamine as the initiator. The reaction proceeded at 10 °C overnight. Upon completion, the reaction mixture became clear and full conversion of the monomer could be detected by IR. Subsequently, Glutamic acid t-*tert*-butyl ester NCA, dissolved in anhydrous DMF, was introduced into the reaction mixture and stirred under the same conditions overnight. The resulting product was precipitated in diethyl ether, isolated by centrifugation, and dried under vacuum to yield the block copolymer as a white solid. Yield: 70−90%.

Next, the block copolymer of $PSar_{100}$-*b*-PGA_{15}OtBu was dissolved in trifluoroacetic acid at 0 °C, and the mixture was stirred at 5 °C for 1 h. The reaction mixture was then precipitated in diethyl ether, and the product was collected by centrifugation and dried under vacuum. The deprotected block copolymer was isolated as a white solid. Yield: 95%. The product was characterized by size exclusion chromatography Mw 9.2 kDa (Mw Salt), PDI: 1.09

2.4. C-TRV3-A Biological Characterization. *2.4.1. Cell Viability Assay.* MDA-MB-231 cells were seeded in 96-well plates (5,000 cells/

https://doi.org/10.1021/acs.chemmater.4c02742
Chem. Mater. XXXX, XXX, XXX−XXX

Scheme 1. Complete Synthetic Procedure for C-TRV3-A Preparation[a]



[a]S1: Nβ-Fmoc-Nω-Boc-L-β-homolysine; S2: Lys-Cy5; S4: Lys-Cy5-TPP; TRV3: Lys-Cy5-TPP−S-S; S6: PLO; C-TRV3: PLO−PEG conjugated to C-TRV3; C-TRV3-A: C-TRV3 conjugated to Atto488.

well) and incubated for 24 h at 37° and 5% CO_2. C-TRV3-A was added at a 0−1 mg/mL concentration range. Cell viability was assessed using the MTS/PMS assay after 72 h of incubation, with absorbance measured at 490 nm.

2.4.2. Cellular Uptake Studies. Confocal microscopy (Leica TCS SP8) was used to study the cellular uptake of C-TRV3-A in MDA-MB-231 cells. Cells were seeded in 384-well plates and incubated with nontoxic concentrations of C-TRV3-A. MitoTracker and LysoTracker were used to label mitochondria and lysosomes. Pulse-chase and time-lapse studies were conducted over various time points (1, 2, 4, 6 h for pulse-chase and every 20 s over 10 h for time-lapse studies). Images were processed using LAS X software and the ImageJ-JACoP plugin for colocalization analysis.

2.5. pDNAluc Polyplex Preparation and Characterization.

2.5.1. Polyplex Formation. Polyplexes were prepared using pDNA-Luc (P, 200 ng), C-TRV3-A (N, cationic polymer), and VLC-3 (O, anionic shielding polymer $PSar_{100}$-*b*-PGA_{15}) at specified amine to phosphate (N/P) and oxygen to amine (O/N) ratios. Each component was diluted in separate tubes with Milli-Q water. N/P calculations considered only protonable nitrogens, excluding amide nitrogens, and accounted for PLO functionalization with PEG (3.6 mol %), TRV3 (4 mol %), and Atto488 (1 wt %). Complexation was

https://doi.org/10.1021/acs.chemmater.4c02742
Chem. Mater. XXXX, XXX, XXX−XXX

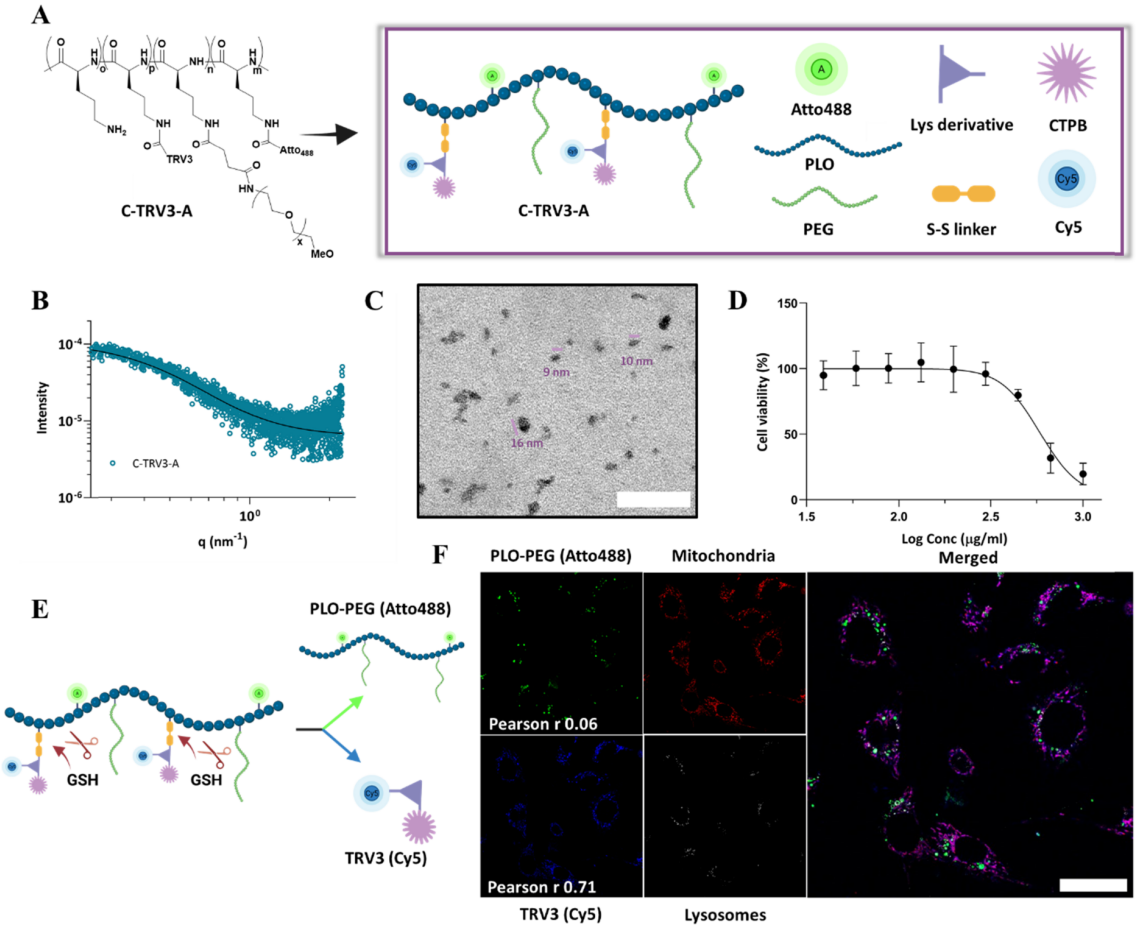


Figure 1. Physicochemical and biological characterization of C-TRV3-A. A) Chemical structure and schematic representation of C-TRV3-A. **B**) Small-angle X-ray scattering (SAXS) data for C-TRV3-A. Intensity expressed as a function of the scattering momentum transfer, q (q = $4\pi\sin(\theta)/\lambda$). **C**) Transmission electron microscopy (TEM) image of C-TRV3-A, showing a size of 10−20 nm (diameter). Scale bar = 50 nm. **D**) MDA-MB-231 cell viability by MTS/PMS in response to C-TRV3-A exposure (IC_{50} = 0.5 mg/mL, 72 h, n = 3, mean ± SEM). **E**) TRV3 (bearing Cy5) release mechanism from C-TRV3-A in MDA-MB-231 cells. Schematic illustration showing TRV3 release from PLO−PEG (labeled with Atto488) after cytosolic delivery and S−S linker cleavage in a reductive environment. **F**) Confocal images of MDA-MB-231 cells 4 h post-treatment. Lysosomes (white, LysoTracker Blue), mitochondria (red, MitoTracker Red CM-H2Xros), TRV3 (blue, Cy5), and PLO−PEG (green, Atto488) shown. Purple regions indicate TRV3-mitochondria colocalization. Pearson r values calculated using the ImageJ JACoP plugin. Scale bar: 10 μm.

achieved by mixing pDNA-Luc with VLC-3 followed by C-TRV3-A addition with vigorous pipetting and a 20 min incubation at room temperature. Size distribution was determined by DLS, and electrophoresis assays were conducted to ensure polyplex formation.

2.5.2. Polyplex Interaction and Stability Assays. Interactions between pDNAluc, VLC-3, and C-TRV3-A and polyplex stability were evaluated using complementary assays. Heparin displacement assays were conducted by incubating polyplexes with 0.75 and 50 UI/ml heparin and analyzing nucleic acid release via gel electrophoresis and ultraviolet illumination. Plasma stability was assessed by incubating polyplexes in 20% mouse or human serum at 37 °C for 1 h, followed by gel electrophoresis. Stability in cell culture media was examined by incubating polyplexes in 80% DMEM/F-12 medium (10% fetal bovine serum (FBS)/1% penicillin-streptomycin (P/S)) at 37 °C for 1 h before gel electrophoresis analysis.

2.5.3. Polyplex Hemocompatibility Assay. Mouse red blood cells were isolated from fresh blood collected via cardiac puncture. Blood was diluted with phosphate-buffered saline (PBS; pH 7.4) and then centrifuged at 3000 rpm for 10 min at 4 °C three times. The final red blood cell pellet was resuspended to 2% (v/v) in sterile PBS. C-TRV3-A and polyplex solutions were prepared in PBS (pH 7.4). Samples were evaluated in triplicate at concentrations of 0.08, 0.04, and 0.01 mg/mL; PBS and 1% (w/v) Triton X-100 served as negative control. After a 1-h incubation at 37 °C, plates were centrifuged (3000 rpm, 10 min, room temperature). Supernatants were analyzed for hemoglobin release by measuring absorbance at 570 nm. The hemolysis percentage was calculated relative to Triton X-100-induced complete lysis.

2.5.4. Polyplex Biological Characterization. 2.5.4.1. Cell Viability in 2D and 3D In Vitro Cell Models. MDA-MB-231 cells were used for 2D and 3D culture viability assays. For 2D cultures, cells were seeded in 96-well plates (5,000 cells/well) in DMEM (high glucose/no phenol red with 10% FBS/1% P/S) and incubated for 24 h. Polyplexes were prepared in PBS and added to wells after a 20 min incubation. Cell confluency was assessed at 24, 48, and 72 h using Hoechst 33342 staining, with fluorescence measured at 450 nm. For 3D cultures, cells were seeded in 96-well ultralow attachment plates (10,000 cells/well) using DMEM (high glucose/no phenol red) supplemented as described in the **ESI**. Polyplexes were added as in the 2D culture setup. After a 24-h incubation, cell viability was evaluated using an MTS/PMS assay, with absorbance measured at 490 nm. Polyethylenimine (JetPEI, referred to as PEI) (N/P = 1) and nonformulated pDNA-Luc served as positive and negative controls. Cell viability was expressed as a percentage relative to untreated controls, with values representing the mean ± SEM (n > 3).

https://doi.org/10.1021/acs.chemmater.4c02742
Chem. Mater. XXXX, XXX, XXX−XXX

2.5.4.2. Transfection in 2D and 3D In Vitro Cell Models. MDA-MB-231 cells were used for both 2D and 3D luciferase expression assays. For 2D cultures, cells were seeded for 24 h in 96-well plates (5,000 cells/well) in DMEM (high glucose, no phenol red, 10% FBS, 1% P/S). For 3D cultures, cells were seeded for 24 h in ultralow attachment plates (10,000 cells/well) in DMEM supplemented as described in the **ESI**. Polyplexes were prepared in PBS and added to wells after a 20 min incubation. PEI-based polyplexes were prepared according to the manufacturer's guidelines. Luciferase activity was measured using Bright-Glo reagent by EnSight Multimode Plate Reader (535 nm) after 24 h (3D) or 24, 48, and 72 h (2D) of incubation. Luminescence values were normalized to cell viability and background subtracted. PEI (N/P = 1) and nonformulated pDNA-Luc served as positive and negative controls. Results are expressed as the mean ± SEM (n > 3).

3. RESULTS AND DISCUSSION

3.1. C-TRV3-A Synthesis and Characterization. We synthesized nanoconjugate C-TRV3-A using a controlled eight-step procedure (Scheme 1), which involved trivalent compound TRV3 synthesis and conjugation to the polymeric carrier (**ESI**), with each intermediate characterized via ^{1}H NMR and MS.

The initial coupling of Nβ-Fmoc-Nω-Boc-L-β-homolysine (Lys derivative, S1) with Cy5-NH_2 in anhydrous DMF yielded Lys-Cy5 (S2) (Scheme S1), which we confirmed by characteristic ^{1}H NMR signals (Figure S1) and MS fragmentation patterns (Figure S2). Subsequent Boc deprotection of S2 using a DCM/TFA mixture produced S3 (85% yield) (Scheme S2; Figures S3 and S4). We then efficiently conjugated CTPB (TPP derivative) to S3, forming Lys-Cy5-TPP (S4) (Scheme S3; Figures S5 and S6). Fmoc deprotection of S4 used a 4:1 mixture of DMF and piperidine (78% yield) (Scheme S4; Figures S7 and 8). A critical step involved introducing the S−S linker to S5 using 3,3′-dithiopropionic acid di(N-succinimidyl ester) to form TRV3 (Scheme S5; Figures S9 and S10). In parallel, we conjugated MeO-PEG_{3000}-NHS to PLO (Scheme S6), with PEG functionalization quantified at 3.6 mol % (Figure S11).

The synthesis proceeded with TRV3 conjugation to PLO−PEG (S7) (Scheme S7), yielding C-TRV3 (C = nano-Conjugate) with 4 mol % TRV3 functionalization (Figure S12). We observed Cy5 loading, determined by fluorescence spectroscopy, at less than 1 mol % (Figure S13). Finally, we labeled C-TRV3 with Atto488-NHS (A) to form C-TRV3-A (Scheme S8) at 90−100% conjugation efficiency and % wt modification (Figure S14). The careful control of reaction conditions and thorough purification methods throughout synthesis ensured product quality.

The comprehensive characterization of all intermediates and the final nanoconjugate by ^{1}H NMR, MS, and fluorescence spectroscopy ensured the integrity and functionality of the final nanoconjugate C-TRV3-A (Figure 1A). Zeta potential measurements revealed a positively charged compound (7.68 ± 0.03 mV), suggesting that TRV3, Atto488, and PEG functionalization did not fully mask the cationic nature of PLO and that C-TRV3-A retains potential for electrostatic interactions with negatively charged compounds[29] or cellular membranes.[30] The SAXS pattern for C-TRV3-A exhibited a slope of approximately −3 in the Porod region (in log−log scale)[31] (Figure 1B), indicating a structure with a dense core. Although initially developed for linear polymer systems, we utilized the fractal coil model as a general framework for estimating polymer size; the lack of significant changes in polymer structural features upon labeling with Atto488 justified this approach. We found a radius of gyration (Rg) of C-TRV3-A, calculated using the fractal coil model, of 3.60 ± 0.05 nm. Transmission electron microscopy (TEM) imaging corroborated SAXS results, revealing an average nanoconjugate diameter of 5−15 nm (Figure 1C). The slight variation between SAXS and TEM measurements can be attributed to the irregular shapes and polydispersity observed in TEM images, in contrast to the mathematical model applied to the entire SAXS data set, which assumes a more uniform particle distribution.[32] Even though there is no discrepancy between the measurements, and they fall within the same range, these methodological differences account for the minor variations observed.

The multistep synthesis and thorough characterization of C-TRV3-A provided a comprehensive understanding of its structural and physicochemical properties, establishing a robust basis for subsequent biological evaluations and potential therapeutic applications.

3.2. TRV3 Release from C-TRV3-A Supports Mitochondrial Targeting. Cell viability assays using MDA-MB-231 cells as a model demonstrated the moderate cytotoxic profile of C-TRV3-A after a 72-h exposure (IC_{50} = 0.5 mg/mL) (Figure 1D), which is likely attributable to C-TRV3-A's polycationic nature. After establishing a range of nontoxic concentrations, we investigated C-TRV3-A cell internalization and subcellular localization using live-cell confocal fluorescence microscopy in MDA-MB-231 cells at various time points (1, 2, 4, and 6 h; Figure S15 - pulse-chase study). C-TRV3-A comprises PLO, a biodegradable polycationic peptide with endosomal escape properties;[15] an S−S linker, reducible in endocytic compartments rich in glutathione (GSH) and the gamma-interferon-inducible lysosomal thiol reductase GILT[33] (especially in breast cancer[34]); and CTPB, a widely exploited mitochondrial targeting moiety[18,19] (Schematic illustration, Figure 1E). The dual-monitoring probe labeling strategy of C-TRV3-A (Cy5 conjugated to TRV3 and Atto488 conjugated to PLO−PEG) enabled the observation of TRV3 release via S−S linker cleavage in the reductive endosomal compartment, followed by endosomal escape and mitochondrial targeting. Quantitative image analysis using Pearson's correlation coefficient (Pearson r) revealed distinct intracellular localization patterns for TRV3 and PLO−PEG after a 4-h incubation (Figure 1F). TRV3 demonstrated significant colocalization with mitochondria (MitoTracker Red), as indicated by a Pearson r of 0.71, visualized as purple regions in Figure 1F. Meanwhile, PLO−PEG exhibited minimal mitochondrial colocalization (Pearson r = 0.06) and non-significant interactions with lysosomes (LysoTracker Blue), reflected by a Pearson r of 0.22, suggesting endosomal escape prior to lysosomal accumulation. These results suggest that PLO facilitated successful endosomal escape following endocytosis, while S−S linker reduction ensured TRV3 release, which CTPB subsequently targeted to the mitochondria. The successful visualization of the C-TRV3-A internalization pathway and subcellular targeting corroborated the rational design of the nanoconjugate.

Our results demonstrate the successful design and functionality of C-TRV3-A, confirming an ability to undergo cellular internalization, endosomal escape, and targeted mitochondrial delivery, thus validating its potential as a versatile nanocarrier for intracellular drug delivery.

https://doi.org/10.1021/acs.chemmater.4c02742
Chem. Mater. XXXX, XXX, XXX−XXX

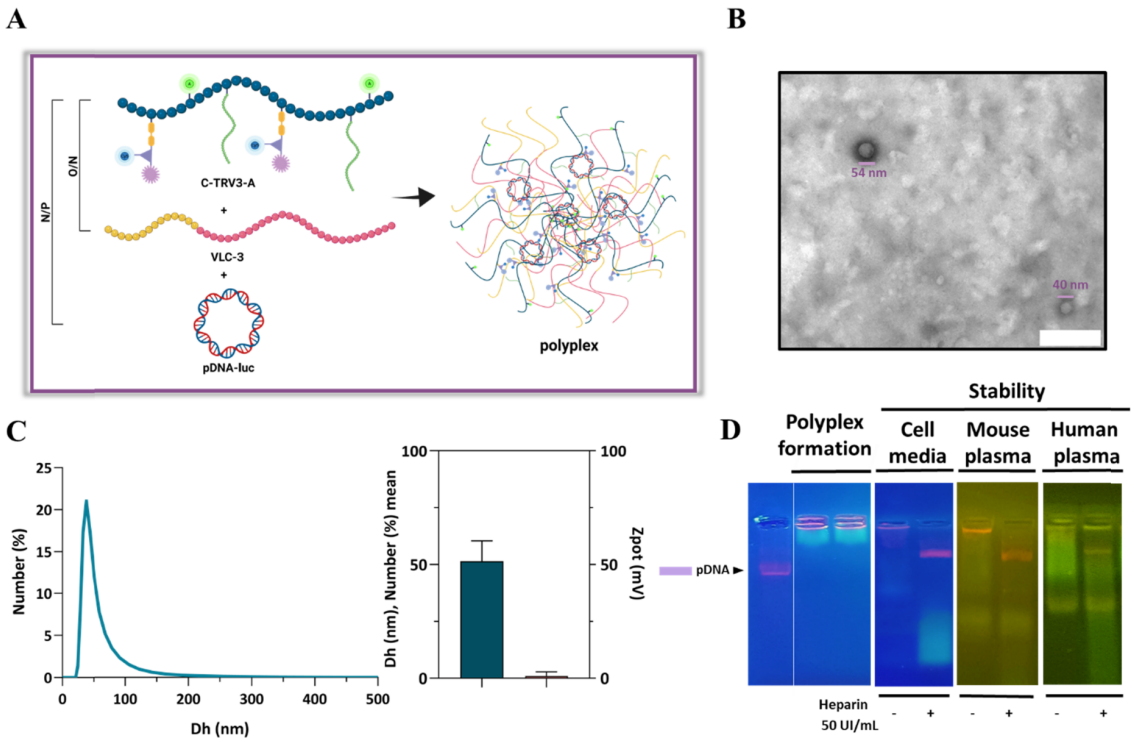


Figure 2. C-TRV3-A-based polyplex formation, physicochemical characterization, and stability. **A**) Schematic representation of C-TRV3-A-px formation using pDNA-Luc (P, 200 ng/mL), C-TRV3-A (N, cationic polymer), and VLC-3 (O, anionic shielding polymer) at specified amine to phosphate (N/P) and oxygen to amine (O/N) ratios. **B**) Transmission electron microscopy (TEM) image of Px02501 (O/*N* = 0.25, N/*P* = 1, in PBS at C-TRV3-A = 0.02 mg/mL) revealed a size of 40−70 nm (diameter). Scale bar = 100 nm. **C**) Left: Size distribution graph of Px02501 expressed as number of molecules (%) per hydrodynamic diameter (Dh) obtained by dynamic light scattering (DLS) in PBS at C-TRV3-A = 0.02 mg/mL. Right: Hydrodynamic diameter (Dh = 51 ± 9 nm) and zeta-potential (Zpot = 0.93 ± 1.8 mV) analysis of Px02501 determined by DLS. **D**) Shift-gel assays of Px02501 prepared using pDNA-Luc (P, 200 ng), C-TRV3-A (N, cationic polymer), and VLC-3 (O, anionic shielding polymer) in PBS and their stability in cell media (DMEM (high glucose/no phenol red with 10% FBS/1% P/S), mouse plasma, and human plasma. Polyplexes were incubated for 1 h at 37 °C before heparin addition. pDNA in purple, C-TRV3-A in green, and VLC-3 not visible under an ultraviolet lamp; therefore, an ultraviolet filter was applied to enhance gel visualization for mouse and human plasma.

3.3. Formulation and Characterization of C-TRV3-A-Based Polyplexes for Nonviral Gene Delivery. To harness the endosomolytic properties for nonviral gene delivery, we incorporated C-TRV3-A into polyplexes. Polycationic polymers have been widely explored for the formation of polyplexes based on electrostatic interactions between the polymer and negatively charged genetic payloads.[35] Specifically, PLO has been evaluated due to its biodegradability and ability to condense DNA and facilitate cellular uptake;[17,21−24] however, the relative toxicity of C-TRV3-A, as observed with many cationic polymers,[25−27] could limit applications in gene therapy. Approaches to mask PLO positive charges and reduce toxicity include polyplex functionalization with charge-conversion polymers[36] (anionic in the extracellular environment and cationic in the endolysosomal compartment), the guanidation of hyperbranched PLO-based polymers,[37] or the formulation of lipoplexes.[38]

We employed $PSar_{100}$-*b*-PGA_{15} diblock copolymer, a polyanionic polypeptide VLC-3,[28] as a polymeric coating to improve polyplex stability and safety (see **ESI**, Scheme S9, Figure S16). Previous examples exploiting the anionic mucopolysaccharide hyaluronic acid supported the application of this strategy,[39−41] increasing DNA/PEI polyplex safety while reducing nonspecific protein interaction and enhancing transcriptional activity. We formulated polyplexes (C-TRV3-A-px) using pDNA-Luc (P), C-TRV3-A (N, cationic polymer), and VLC-3 (O, anionic shielding polymer) at various O/N and N/P ratios (Figure 2A) in PBS and verified complexation by shift-gel assay (Figure S17). The Atto488 labeling included in the C-TRV3-A structure supported the enhanced visualization of C-TRV3-A-px components in gels and improved the interpretation of results. We identified an N/P ratio of 1 as optimal for the interaction between genetic material and polycationic polymer. Higher N/P ratios (1.25, 1.5, 5, 10, and 15) resulted in excess free C-TRV3-A, as evidenced by diffusion and smearing in the gel (Figure S17A), which could induce cytotoxicity. We evaluated the O/P at 0.25, 0.5, 1, and 2, with effective C-TRV3-A-px formation observed across all tested ratios (Figure S17B). Further characterization focused on C-TRV3-A-px with an O/P ratio of 0.25 (Px02501, N/P fixed at 1), demonstrating significantly higher in vitro transfection efficiency (detailed below). TEM and dynamic DLS analysis confirmed Px02501 formation, with TEM imaging revealing a diameter ranging from 40 to 70 nm (Figure 2B), consistent with DLS measurements that indicated an average diameter of 51 ± 9 nm (Figure 2C). Zeta potential analysis further corroborated Px02501 formation, yielding a value of 0.93 ± 1.8 mV (Figure 2C), which differed significantly from the 7.68 ± 0.03 mV previously measured for C-TRV3-A.

The successful formulation of C-TRV3-A-px with optimized N/P and O/P ratios and their physicochemical character-

https://doi.org/10.1021/acs.chemmater.4c02742
Chem. Mater. XXXX, XXX, XXX−XXX

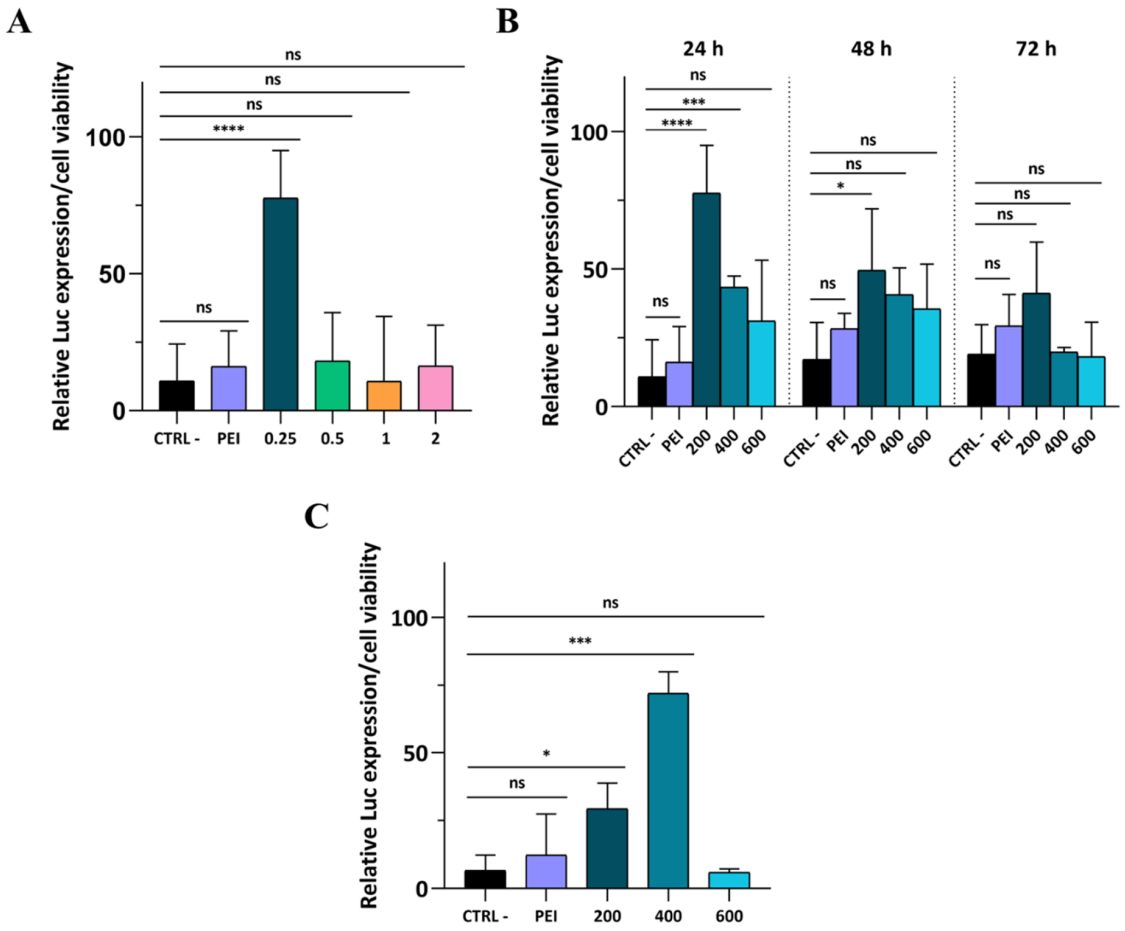


Figure 3. In vitro transfection of C-TRV3-A-px in 2D and 3D breast cancer cell culture models. A) In vitro transfection in 2D MDA-MB-231 cell cultures after a 24-h polyplex exposure (O/N ratio = 0.25, 0.5, 1, 2; N/*P* = 1). **B**) In vitro transfection in 2D MDA-MB-231 cell culture after a 24-, 48-, or 72-h Px02501 exposure at different pDNA-Luc concentrations (200, 400, 600 ng/mL). **C**) In vitro transfection in 3D MDA-MB-231 cell culture after a 24-h Px02501 exposure at different pDNA-Luc concentrations (200, 400, 600 ng/mL). Luciferase (Luc) activity quantified by measuring luminescence at 535 nm. Values normalized to cell viability and background subtracted. PEI (N/*P* = 1) used as a positive control and nonformulated pDNA-Luc used as a negative control (CTRL -). Values represent mean ± SEM ($n > 3$). Significance reported as p****<0.0001; p***<0.001; p**<0.01; p*<0.05; ns: not significant.

ization provides a promising platform for efficient and safe nonviral gene delivery, addressing the challenges of toxicity and stability associated with conventional polycationic systems.

3.4. Assessment of C-TRV3-A-Based Polyplex Stability and Hemocompatibility. Next, we conducted stability studies mimicking in vitro and in vivo conditions to assess the ability of C-TRV3-A-px to retain and release pDNA-Luc. We employed heparin displacement assays to assess C-TRV3-A-px stability and disassembly potential, leveraging the competing polyanion's ability to disrupt electrostatic interactions.[17,42]

Initially, we evaluated C-TRV3-A-px stability in DMEM + 10% FBS using shift-gel assays, as FBS contains abundant polyanionic molecules (including proteoglycans and glycosaminoglycans[43]) that may compete with polyplex components and facilitate oligonucleotide release. C-TRV3-A-px (O/P ratios = 0.25, 0.5, 1, and 2) demonstrated stability after 1-h incubation at 37 °C, while disassembly occurred upon the addition of excess heparin (50 IU/ml) (Figure 2D and S18).

To assess the potential for in vivo translation and intravenous administration, we determined the stability of Px02501 (O/P = 0.25, N/P = 1) in mouse and human plasma. Px02501 formulation remained stable after 1-h incubation at 37 °C in mouse plasma (Figure 2D and S19). Notably, Px02501 demonstrated stability in the presence of up to 0.75 IU/ml heparin, a value significantly higher than average heparin levels in human plasma (0.15 IU/ml)[44] (Figure S19). As expected, Px02501 disassembled in the presence of excess heparin (50 IU/ml) (Figure 2D and S19).

To validate the mouse model results, we also confirmed Px02501 stability in human plasma isolated from three healthy patients (Figure 2D and S20). Importantly, Px02501 disassembled in the presence of excess heparin (50 IU/ml) in human plasma (Figure 2D and S20). These results are particularly relevant considering that patient blood samples represented diverse physiological conditions. Variability in plasma components, such as proteins, lipoproteins, and coagulation factors, can influence protein corona formation, affecting polyplex stability.[45,46] The consistent stability of Px02501 in these samples suggests robustness in varying human plasma compositions, highlighting the potential of C-TRV3-A-px for clinical applications.

To evaluate hemocompatibility, we assessed the potential of Px02501 to induce the lysis of red blood cells. We conducted experiments at pH 7.4 to simulate conditions encountered in

https://doi.org/10.1021/acs.chemmater.4c02742
Chem. Mater. XXXX, XXX, XXX−XXX

the bloodstream, extracellular space, and cytosol. We examined the hemolytic activity of Px02501 across a concentration range of 0.01−0.08 mg/mL (based on C-TRV3-A content). Results demonstrated a concentration-dependent hemolytic effect, with a maximum nonsignificant 20% of hemolysis (Figure S21). The observed low hemolytic activity suggests that Px02501 possesses favorable hemocompatibility characteristics, supporting its potential for future in vivo studies upon intravenous administration. Based on these findings, we established a maximum C-TRV3-A concentration of 0.08 mg/mL for subsequent activity experiments to ensure maintenance within safe hemolytic levels.

Our comprehensive stability and hemocompatibility studies demonstrate that C-TRV3-A-px exhibit robust stability under physiological conditions, controlled disassembly in the presence of competing polyanions, and favorable hemocompatibility, collectively supporting their potential for future in vivo gene delivery applications.

3.5. In Vitro Transfection of C-TRV3-A-Based Polyplexes in 2D and 3D Cell Models. After demonstrating the formation, stability, and hemocompatibility of C-TRV3-A-px, we aimed to verify their functionality as gene delivery vectors. To ensure the safety profile of C-TRV3-A-px under varying conditions (i.e., increased O/P ratio, extended incubation times, and higher doses), we evaluated cell viability for all experimental parameters, confirming their nontoxic nature throughout the study (Figures S22−24).

Initially, we tested the transfection efficiency of C-TRV3-A-px with different O/P ratios (0.25, 0.5, 1, and 2) in 2D MDA-MB-231 cell monolayers after 24 h, comparing them to nonformulated pDNA-Luc (negative control) and PEI at the same N/P ratio (=1). Our results demonstrated that Px02501 (O/P = 0.25, N/P = 1) exhibited the highest transfection efficiency, significantly outperforming other polyplexes and the positive control (Figure 3A). The significant performance compared to the gold standard PEI (typically evaluated at N/P ratio >4 in MDA-MB-231 cells[47]) at the same N/P ratio highlights the safer profile of C-TRV3-A-px due to the lower polycationic component concentration.

Next, we evaluated the transfection effectiveness of Px02501 as a function of the transfection time and plasmid dose. We observed the highest transfection efficiency for Px02501 at an incubation time of 24 h (Figure 3B). Transfection time inherently depends on the cell type to be transfected.[48] Interestingly, we observed a dose-independent transfection efficiency, with the highest Luc expression at the lowest plasmid concentration (200 ng/mL) compared to higher doses (400 and 600 ng/mL). Lower concentrations may provide an optimal balance between Px02501 formation and cellular uptake,[49] potentially avoiding aggregation[50,51] or saturation of internalization pathways at higher doses.[52]

Given the more realistic scenario offered by three-dimensional (3D) cell cultures such as spheroids in terms of cell−cell interactions and biochemical features[53−56] that may influence the in vitro efficiency of Px02501, we evaluated Luc transfection in MDA-MB-231 cell spheroids after 24 h. Our results demonstrate maintained transfection in 3D cell spheroids, with significant dose-dependent transfection (400 > 200 ng/mL) compared to 2D monolayer cell cultures, which decreased at the highest tested dose (Figure 3C). The differential behavior between 2D and 3D cell culture models underscores the importance of evaluating gene delivery systems in more physiologically relevant models.

These results demonstrate the efficacy of Px02501 as a gene delivery vector in both 2D and 3D cell culture models, highlighting their potential as safer and more efficient alternatives to conventional transfection agents.

4. CONCLUSIONS

We report the design, synthesis, and evaluation of a novel, versatile, and multifunctional polypeptide-based nanoconjugate (C-TRV3-A) for combined mitochondrial targeting and nonviral gene therapy. The rational chemical design, incorporating a PLO backbone, PEG modification, and a custom-designed trivalent compound (TRV3), enabled the creation of a versatile nanocarrier with controlled multifunctionality. The strategic inclusion of a redox-sensitive S−S linker and a TPP moiety facilitated TRV3 release and specific mitochondrial targeting of a model drug (Cy5). The modular synthetic approach allowed for precise control over the product's chemical identity and degree of functionalization through exhaustive physicochemical characterization steps, achieving a 3.6% mol PEG modification, 4% mol TRV3 conjugation, and less than 1 wt % fluorophore functionalization. The resulting nanoconjugate exhibited endosomal escape properties while retaining mitochondrial targeting capabilities. By incorporating an anionic polypeptide (VLC-3, $Psar_{100}$-*b*-PGA_{15}) shielding into the polyplex formation procedure, we further enhanced stability and transfection efficiency while mitigating toxicity concerns associated with polycationic polymers. In vitro evaluations in 2D and 3D cancer cell models revealed the superior performance of C-TRV3-A-px compared to conventional transfection agents. The observed structure−function relationships, particularly the impact of O/P and N/P ratios on polyplex stability and transfection efficiency, provide valuable insight for the rational design of future polypeptide-based delivery systems. This versatile platform opens new possibilities for tailored therapeutic approaches; future investigations should focus on in vivo validation, exploration of alternative payloads for mitochondrial-specific therapy, and the delivery of specific nucleic acid species (e.g., small interfering RNA) for cancer treatment.

■ ASSOCIATED CONTENT

Supporting Information

The Supporting Information is available free of charge at https://pubs.acs.org/doi/10.1021/acs.chemmater.4c02742.

Additional experimental details, including materials and general procedures, synthetic protocols, and characterization data for polypeptide-based nanoconjugates; analytical techniques such as NMR spectroscopy, mass spectrometry, dynamic light scattering, and transmission electron microscopy; small-angle X-ray scattering data and polyplex formation and characterization; biological studies, including cytotoxicity assays, cellular uptake studies, hemocompatibility tests, and transfection efficiency in 2D and 3D in vitro breast cancer models; statistical analysis; and references (PDF)

Video_S1_C-TRV3-A (MOV)

■ AUTHOR INFORMATION

Corresponding Authors

Inmaculada Conejos-Sanchez − *Príncipe Felipe Research Center, Polymer Therapeutics Lab., Valencia 46012, Spain; Centro de Investigación Biomédica en Red en Cáncer*

https://doi.org/10.1021/acs.chemmater.4c02742
Chem. Mater. XXXX, XXX, XXX−XXX

(CIBERONC), Instituto de Salud Carlos III, Madrid 28029, Spain; orcid.org/0000-0002-4196-0855; Email: iconejos@cipf.es

María J. Vicent − *Príncipe Felipe Research Center, Screening Platform., Valencia 46012, Spain; Príncipe Felipe Research Center, Polymer Therapeutics Lab., Valencia 46012, Spain; Centro de Investigación Biomédica en Red en Cáncer (CIBERONC), Instituto de Salud Carlos III, Madrid 28029, Spain;* orcid.org/0000-0001-7771-3373; Email: mjvicent@cipf.es

Authors

Camilla Pegoraro − *Príncipe Felipe Research Center, Polymer Therapeutics Lab., Valencia 46012, Spain*

Esther Masiá Sanchis − *Príncipe Felipe Research Center, Polymer Therapeutics Lab., Valencia 46012, Spain; Centro de Investigación Biomédica en Red en Cáncer (CIBERONC), Instituto de Salud Carlos III, Madrid 28029, Spain; Príncipe Felipe Research Center, Screening Platform., Valencia 46012, Spain*

Snežana Đorđević − *Príncipe Felipe Research Center, Polymer Therapeutics Lab., Valencia 46012, Spain; Centro de Investigación Biomédica en Red en Cáncer (CIBERONC), Instituto de Salud Carlos III, Madrid 28029, Spain;* Present Address: S.D.: Tosoh Bioscience, Im Leuschnerpark 4, 64347 Griesheim, Germany; orcid.org/0000-0001-8429-7486

Irene Dolz-Pérez − *Curapath, Paterna, Valencia 46980, Spain;* orcid.org/0000-0002-0447-0718

Cristián Huck-Iriart − *Experiments Division, ALBA Synchrotron Light Source, Cerdanyola del Vallès 08209, Spain;* orcid.org/0000-0001-5734-2499

Lidia Herrera − *Curapath, Paterna, Valencia 46980, Spain*

Sergio Esteban-Pérez − *Curapath, Paterna, Valencia 46980, Spain*

Complete contact information is available at: https://pubs.acs.org/10.1021/acs.chemmater.4c02742

Author Contributions

C.P., I.C.-S., and M.J.V. developed the concept and design of the project. Synthesis and physicochemical characterization of the nanoconjugates were performed by C.P. and SD. Synthesis of VLC-3 L.H. Polyplex formation and stability studies were carried out by C.P. and I.C.-S, with protocols optimized by I.D.-P. and S.E.-P. for VLC-3 use. SAXS analysis was carried out by C.H.-I. In vitro setup studies were performed by C.P. and E.M. Gene transfection studies were performed by C.P. Analysis and interpretation of the data included the contribution of all authors. M.J.V. was responsible for funding acquisition and supervision together with I.C.-S. The manuscript was written and edited by C.P., I.C.-S., and M.J.V. and was revised by the rest of the authors. All authors have read and approved the final version of the manuscript.

Funding

This project was supported by the H2020-MSCA-ITN-2019 BIOMOLMACS (Grant Agreement No. 859416). The authors gratefully acknowledge financial support from the Asociación Española contra el Cáncer (ICS INVES211323CONE, Junior AECC grant), the Ministerio de Ciencia, Tecnología e Innovación (Grants PID2019−108806RB-100 and PID2023−152459OB-I00), and NextGeneration EU i+D+I funding through the GVA Conselleria de Innovación − Pol@ Mets (ref. MFA/2022/065). Additionally, support from the European Regional Development Fund (PO FEDER Comunitat Valenciana 2014−2020), Generalitat Valenciana, is acknowledged. Small-angle X-ray scattering (SAXS) measurements were conducted at the NCD-SWEET beamline of the ALBA Synchrotron Light Source (Barcelona, Spain) under Project ID 2022097124. Furthermore, we acknowledge support from the Horizon Europe EU-OPENSCREEN IMPULSE project (Grant Agreement No. 101132028).

Notes

The authors declare the following competing financial interest(s): Sergio Esteban-Perez and Lidia Herrero from Curapath are co-inventors of the patent covering the rights of VLC3.

■ ACKNOWLEDGMENTS

We thank Dr. Stuart P. Atkinson for his help in manuscript development and English editing, Alberto Hernández for confocal imaging support, and Mario Soriano for TEM support. We thank the student Kato D'Huawe from Ghent University for her help in the experimental work.

■ REFERENCES

(1) Shi, J.; Kantoff, P. W.; Wooster, R.; Farokhzad, O. C. Cancer Nanomedicine: Progress, Challenges and Opportunities. *Nat. Rev. Cancer* **2017**, *17* (1), 20−37.

(2) Gao, Y.; Wang, K.; Zhang, J.; Duan, X.; Sun, Q.; Men, K. *Multifunctional Nanoparticle for Cancer Therapy. MedComm* **2023**, *4* (1), No. e187.

(3) Chen, W.-H.; Luo, G.-F.; Zhang, X.-Z. Recent Advances in Subcellular Targeted Cancer Therapy Based on Functional Materials. *Adv. Mater.* **2019**, *31* (3), 1802725.

(4) Zagorodko, O.; Arroyo-Crespo, J. J.; Nebot, V. J.; Vicent, M. J. Polypeptide-Based Conjugates as Therapeutics: Opportunities and Challenges. *Macromol. Biosci.* **2017**, *17* (1), 1600316.

(5) Duro-Castano, A.; Conejos-Sánchez, I.; Vicent, M. J. Peptide-Based Polymer Therapeutics. *Polymers.* **2014**, *6*, 515−551.

(6) Melnyk, T.; Đorđević, S.; Conejos-Sánchez, I.; Vicent, M. J. Therapeutic Potential of Polypeptide-Based Conjugates: Rational Design and Analytical Tools That Can Boost Clinical Translation. *Adv. Drug Delivery Rev.* **2020**, *160*, 136−169.

(7) Galic, V. L.; Wright, J. D.; Lewin, S. N.; Herzog, T. J. Paclitaxel Poliglumex for Ovarian Cancer. *Expert Opin. Investig. Drugs* **2011**, *20* (6), 813−821.

(8) Wang, X.; Song, Z.; Wei, S.; Ji, G.; Zheng, X.; Fu, Z.; Cheng, J. Polypeptide-Based Drug Delivery Systems for Programmed Release. *Biomaterials* **2021**, *275*, No. 120913.

(9) Li, X.; Liu, J.; Chen, H.; Chen, Y.; Wang, Y.; Zhang, C. Y.; Xing, X.-H. Multi-Functional Engineered Polypeptide-Based Drug Delivery Systems for Improved Cancer Therapy. *Green Chem. Eng.* **2023**, *4* (2), 173−188.

(10) Liu, Y.; Yin, L. α-Amino Acid N-Carboxyanhydride (NCA)-Derived Synthetic Polypeptides for Nucleic Acids Delivery. *Adv. Drug Delivery Rev.* **2021**, *171*, 139−163.

(11) Zhao, B.; Zhang, X.; Bickle, M. S.; Fu, S.; Li, Q.; Zhang, F. Development of Polypeptide-Based Materials toward Messenger RNA Delivery. *Nanoscale* **2024**, *16* (5), 2250−2264.

(12) Pegoraro, C.; Karpova, E.; Qutbuddin, Y.; Sanchis, E. M.; Dimitrijevs, P.; Huck-Iriart, C.; Gavrilović, S.; Arsenyan, P.; Schwille, P.; Felip-León, C.; Duro-Castano, A.; Conejos-Sanchez, I.; Vicent, M. J. Polyproline-polyornithine diblock copolymers with inherent mitochondria tropism. *Adv. Mater.* **2025**, 2411595.

(13) Cohen-Erez, I.; Rapaport, H. Coassemblies of the Anionic Polypeptide γ-PGA and Cationic β-Sheet Peptides for Drug Delivery to Mitochondria. *Biomacromolecules* **2015**, *16* (12), 3827−3835.

(14) Porporato, P. E.; Filigheddu, N.; Pedro, J. M. B.-S.; Kroemer, G.; Galluzzi, L. Mitochondrial Metabolism and Cancer. *Cell Res.* **2018**, *28* (3), 265−280.
(15) Pegoraro, C.; Domingo-Ortí, I.; Conejos-Sánchez, I.; Vicent, M. J. Unlocking the Mitochondria for Nanomedicine-Based Treatments: Overcoming Biological Barriers, Improving Designs, and Selecting Verification Techniques. *Adv. Drug Delivery Rev.* **2024**, *207*, No. 115195.
(16) Suk, J. S.; Xu, Q.; Kim, N.; Hanes, J.; Ensign, L. M. PEGylation as a Strategy for Improving Nanoparticle-Based Drug and Gene Delivery. *Adv. Drug Delivery Rev.* **2016**, *99*, 28−51.
(17) Conejos-Sánchez, I.; Gallon, E.; Niño-Pariente, A.; Smith, J. A.; De la Fuente, A. G.; Di Canio, L.; Pluchino, S.; Franklin, R. J. M.; Vicent, M. J. Polyornithine-Based Polyplexes to Boost Effective Gene Silencing in CNS Disorders. *Nanoscale* **2020**, *12* (11), 6285−6299.
(18) Cheng, X.; Feng, D.; Lv, J.; Cui, X.; Wang, Y.; Wang, Q.; Zhang, L. Application Prospects of Triphenylphosphine-Based Mitochondria-Targeted Cancer Therapy. *Cancers.* **2023**, *15*, 666.
(19) Zielonka, J.; Joseph, J.; Sikora, A.; Hardy, M.; Ouari, O.; Vasquez-Vivar, J.; Cheng, G.; Lopez, M.; Kalyanaraman, B. Mitochondria-Targeted Triphenylphosphonium-Based Compounds: Syntheses, Mechanisms of Action, and Therapeutic and Diagnostic Applications. *Chem. Rev.* **2017**, *117* (15), 10043−10120.
(20) Fu, S.; Rempson, C. M.; Puche, V.; Zhao, B.; Zhang, F. Construction of Disulfide Containing Redox-Responsive Polymeric Nanomedicine. *Methods* **2022**, *199*, 67−79.
(21) Saviano, F.; Lovato, T.; Russo, A.; Russo, G.; Bouton, C. R.; Shattock, R. J.; Alexander, C.; Quaglia, F.; Blakney, A. K.; Gurnani, P.; Conte, C. Ornithine-Derived Oligomers and Dendrimers for in Vitro Delivery of DNA and Ex Vivo Transfection of Skin Cells via SaRNA. *J. Mater. Chem. B* **2020**, *8* (22), 4940−4949.
(22) Ramsay, E.; Gumbleton, M. Polylysine and Polyornithine Gene Transfer Complexes: A Study of Complex Stability and Cellular Uptake as a Basis for Their Differential in-Vitro Transfection Efficiency. *J. Drug Target.* **2002**, *10* (1), 1−9.
(23) Ramsay, E.; Hadgraft, J.; Birchall, J.; Gumbleton, M. Examination of the Biophysical Interaction between Plasmid DNA and the Polycations, Polylysine and Polyornithine, as a Basis for Their Differential Gene Transfection in-Vitro. *Int. J. Pharm.* **2000**, *210* (1), 97−107.
(24) Barrett, S. E.; Burke, R. S.; Abrams, M. T.; Bason, C.; Busuek, M.; Carlini, E.; Carr, B. A.; Crocker, L. S.; Fan, H.; Garbaccio, R. M.; Guidry, E. N.; Heo, J. H.; Howell, B. J.; Kemp, E. A.; Kowtoniuk, R. A.; Latham, A. H.; Leone, A. M.; Lyman, M.; Parmar, R. G.; Patel, M.; Pechenov, S. Y.; Pei, T.; Pudvah, N. T.; Raab, C.; Riley, S.; Sepp-Lorenzino, L.; Smith, S.; Soli, E. D.; Staskiewicz, S.; Stern, M.; Truong, Q.; Vavrek, M.; Waldman, J. H.; Walsh, E. S.; Williams, J. M.; Young, S.; Colletti, S. L. Development of a Liver-Targeted SiRNA Delivery Platform with a Broad Therapeutic Window Utilizing Biodegradable Polypeptide-Based Polymer Conjugates. *J. Controlled Release* **2014**, *183*, 124−137.
(25) Lv, H.; Zhang, S.; Wang, B.; Cui, S.; Yan, J. Toxicity of Cationic Lipids and Cationic Polymers in Gene Delivery. *J. Controlled Release* **2006**, *114* (1), 100−109.
(26) Zhao, X.; Li, X.; Zhao, Y.; Cheng, Y.; Yang, Y.; Fang, Z.; Xie, Y.; Liu, Y.; Chen, Y.; Ouyang, Y.; Yuan, W. Immune Activities of Polycationic Vectors for Gene Delivery. *Front. Pharmacol.* **2017**, *8*, 510−517.
(27) Wang, Y.; Ye, M.; Xie, R.; Gong, S. Enhancing the In Vitro and In Vivo Stabilities of Polymeric Nucleic Acid Delivery Nanosystems. *Bioconjugate Chem.* **2019**, *30* (2), 325−337.
(28) Felip, C.; Dolz, I.; Esteban-Pérez, S.; Herrera-Muñoz, L. N.-C. V.Non-Covalent Shielding Polymers. WO2023002014A1. WO EP CN JP CA. Prior. *2021−07−22, Filed 2022−07−22, Publ. 2023−01−26*.
(29) Sing, C. E. Development of the Modern Theory of Polymeric Complex Coacervation. *Adv. Colloid Interface Sci.* **2017**, *239*, 2−16.
(30) Behzadi, S.; Serpooshan, V.; Tao, W.; Hamaly, M. A.; Alkawareek, M. Y.; Dreaden, E. C.; Brown, D.; Alkilany, A. M.; Farokhzad, O. C.; Mahmoudi, M. Cellular Uptake of Nanoparticles: Journey inside the Cell. *Chem. Soc. Rev.* **2017**, *46* (14), 4218−4244.
(31) Hammouda, B. Small-Angle Scattering From Branched Polymers. *Macromol. Theory Simulations* **2012**, *21* (6), 372−381.
(32) Borchert, H.; Shevchenko, E. V.; Robert, A.; Mekis, I.; Kornowski, A.; Grübel, G.; Weller, H. Determination of Nanocrystal Sizes: A Comparison of TEM, SAXS, and XRD Studies of Highly Monodisperse CoPt3 Particles. *Langmuir* **2005**, *21* (5), 1931−1936.
(33) Brülisauer, L.; Gauthier, M. A.; Leroux, J.-C. Disulfide-Containing Parenteral Delivery Systems and Their Redox-Biological Fate. *J. Controlled Release* **2014**, *195*, 147−154.
(34) Kennedy, L.; Sandhu, J. K.; Harper, M.-E.; Cuperlovic-Culf, M. Role of Glutathione in Cancer: From Mechanisms to Therapies. *Biomolecules.* **2020**, *10*, 1429.
(35) Tros de Ilarduya, C.; Sun, Y.; Düzgüneş, N. Gene Delivery by Lipoplexes and Polyplexes. *Eur. J. Pharm. Sci.* **2010**, *40* (3), 159−170.
(36) Dirisala, A.; Uchida, S.; Li, J.; Van Guyse, J. F. R.; Hayashi, K.; Vummaleti, S. V. C.; Kaur, S.; Mochida, Y.; Fukushima, S.; Kataoka, K. Effective MRNA Protection by Poly(l-Ornithine) Synergizes with Endosomal Escape Functionality of a Charge-Conversion Polymer toward Maximizing MRNA Introduction Efficiency. *Macromol. Rapid Commun.* **2022**, *43* (12), 2100754.
(37) Cai, M.; Zhang, Z.; Su, X.; Dong, H.; Zhong, Z.; Zhuo, R. Guanidinated Multi-Arm Star Polyornithines with a Polyethylenimine Core for Gene Delivery. *Polymer (Guildf).* **2014**, *55* (18), 4634−4640.
(38) Koloskova, O. O.; Nikonova, A. A.; Budanova, U. A.; Shilovskiy, I. P.; Kofiadi, I. A.; Ivanov, A. V.; Smirnova, O. A.; Zverev, V. V.; Sebaykin, Y. L.; Andreev, S. M.; Khaitov, M. R. Synthesis and Evaluation of Novel Lipopeptide as a Vehicle for Efficient Gene Delivery and Gene Silencing. *Eur. J. Pharm. Biopharm.* **2016**, *102*, 159−167.
(39) Ito, T.; Iida-Tanaka, N.; Niidome, T.; Kawano, T.; Kubo, K.; Yoshikawa, K.; Sato, T.; Yang, Z.; Koyama, Y. Hyaluronic Acid and Its Derivative as a Multi-Functional Gene Expression Enhancer: Protection from Non-Specific Interactions, Adhesion to Targeted Cells, and Transcriptional Activation. *J. Controlled Release* **2006**, *112* (3), 382−388.
(40) Tian, H.; Lin, L.; Chen, J.; Chen, X.; Park, T. G.; Maruyama, A. RGD Targeting Hyaluronic Acid Coating System for PEI-PBLG Polycation Gene Carriers. *J. Controlled Release* **2011**, *155* (1), 47−53.
(41) He, Y.; Cheng, G.; Xie, L.; Nie, Y.; He, B.; Gu, Z. Polyethyleneimine/DNA Polyplexes with Reduction-Sensitive Hyaluronic Acid Derivatives Shielding for Targeted Gene Delivery. *Biomaterials* **2013**, *34* (4), 1235−1245.
(42) Zhang, H.; Gao, X.; Sun, Q.; Dong, X.; Zhu, Z.; Yang, C. Incorporation of Poly(γ-Glutamic Acid) in Lipid Nanoparticles for Enhanced MRNA Delivery Efficiency in Vitro and in Vivo. *Acta Biomater.* **2024**, *177*, 361−376.
(43) Pérez-Rubio, P.; Vendrell-Flotats, M.; Romero, E. L.; Enemark-Rasmussen, K.; Cervera, L.; Gòdia, F.; Lavado-García, J. Internalization of PEI-Based Complexes in Transient Transfection of HEK293 Cells Is Triggered by Coalescence of Membrane Heparan Sulfate Proteoglycans like Glypican-4. *Biomed. Pharmacother.* **2024**, *176*, No. 116893.
(44) ENGELBERG, H. Plasma Heparin Levels. Correlation with Serum Cholesterol and Low-Density Lipoproteins. *Circulation* **1961**, *23* (April), 573−577.
(45) Hartl, N.; Jürgens, D. C.; Carneiro, S.; König, A.-C.; Xiao, X.; Liu, R.; Hauck, S. M.; Merkel, O. M. Protein Corona Investigations of Polyplexes with Varying Hydrophobicity − From Method Development to in Vitro Studies. *Int. J. Pharm.* **2023**, *643*, No. 123257.
(46) Zhu, D.; Yan, H.; Zhou, Z.; Tang, J.; Liu, X.; Hartmann, R.; Parak, W. J.; Shen, Y.; Feliu, N. Influence of the Modulation of the Protein Corona on Gene Expression Using Polyethylenimine (PEI) Polyplexes as Delivery Vehicle. *Adv. Healthc. Mater.* **2021**, *10* (13), 2100125.
(47) Zhang, H.; Chen, Z.; Du, M.; Li, Y.; Chen, Y. Enhanced Gene Transfection Efficiency by Low-Dose 25 KDa Polyethylenimine by

https://doi.org/10.1021/acs.chemmater.4c02742
Chem. Mater. XXXX, XXX, XXX−XXX

the Assistance of 1.8 KDa Polyethylenimine. *Drug Delivery* **2018**, *25* (1), 1740−1745.
(48) Malloggi, C.; Pezzoli, D.; Magagnin, L.; De Nardo, L.; Mantovani, D.; Tallarita, E.; Candiani, G. Comparative Evaluation and Optimization of Off-the-Shelf Cationic Polymers for Gene Delivery Purposes. *Polym. Chem.* **2015**, *6* (35), 6325−6339.
(49) Zhang, Z.; Qiu, N.; Wu, S.; Liu, X.; Zhou, Z.; Tang, J.; Liu, Y.; Zhou, R.; Shen, Y. Dose-Independent Transfection of Hydrophobized Polyplexes. *Adv. Mater.* **2021**, *33* (25), 2102219.
(50) Pezzoli, D.; Giupponi, E.; Mantovani, D.; Candiani, G. Size Matters for in Vitro Gene Delivery: Investigating the Relationships among Complexation Protocol, Transfection Medium, Size and Sedimentation. *Sci. Rep.* **2017**, *7* (1), 44134.
(51) D'Andrea, C.; Pezzoli, D.; Malloggi, C.; Candeo, A.; Capelli, G.; Bassi, A.; Volonterio, A.; Taroni, P.; Candiani, G. The Study of Polyplex Formation and Stability by Time-Resolved Fluorescence Spectroscopy of SYBR Green I-Stained DNA. *Photochem. Photobiol. Sci.* **2014**, *13* (12), 1680−1689.
(52) Monnery, B. D. Polycation-Mediated Transfection: Mechanisms of Internalization and Intracellular Trafficking. *Biomacromolecules* **2021**, *22* (10), 4060−4083.
(53) Boix-Montesinos, P.; Soriano-Teruel, P. M.; Armiñán, A.; Orzáez, M.; Vicent, M. J. The Past, Present, and Future of Breast Cancer Models for Nanomedicine Development. *Adv. Drug Delivery Rev.* **2021**, *173*, 306−330.
(54) Satchi-Fainaro, R.; Florindo, H. F.; Vicent, M. J. Clinically-Relevant and Predictive Cancer Models for Nanomedicine Evaluation. *Adv. Drug Delivery Rev.* **2022**, *183*, No. 114140.
(55) Monfared, Y. K.; Mahmoudian, M.; Cecone, C.; Caldera, F.; Haiaty, S.; Heidari, H. R.; Rahbarghazi, R.; Matencio, A.; Zakeri-Milani, P.; Trotta, F. Hyper-Branched Cationic Cyclodextrin Polymers for Improving Plasmid Transfection in 2D and 3D Spheroid Cells. *Pharmaceutics.* **2022**, *14*, 2690.
(56) Pinto, B.; Henriques, A. C.; Silva, P. M. A.; Bousbaa, H. Three-Dimensional Spheroids as In Vitro Preclinical Models for Cancer Research. *Pharmaceutics.* **2020**, *12*, 1186.

https://doi.org/10.1021/acs.chemmater.4c02742
Chem. Mater. XXXX, XXX, XXX−XXX

4 FINAL DISCUSSION AND REMARKS

Nanomedicines have garnered increasing attention, particularly following the recent COVID-19 pandemic, which catalyzed advancements in the field[347]. The advantages of nanomedicine are manifold, encompassing improved pharmacokinetic and pharmacodynamic profiles, enhanced solubility of poorly soluble drugs, controlled release mechanisms, and reduced off-target effects[348]. These features collectively expand the therapeutic window, particularly for polymer-based therapeutics, which offer customizable properties and versatile functionalization strategies to address the limitations of traditional drug formulations[349].

Despite these promising attributes, the clinical translation and successful delivery of nanomedicines to their intended sites of action remain significant challenges. A major hurdle lies in navigating the complex biological barriers encountered during the delivery "journey"[350]. Systemically administered nanomedicines face circulatory barriers (e.g., the reticuloendothelial system), tissue and microenvironmental barriers (e.g., the tumor microenvironment), and cellular/subcellular barriers. Furthermore, many current nanomedicines lack specificity for intracellular targets, which remains critical for addressing diseases requiring precise subcellular interventions[351].

Subcellular targeting has thus emerged as a pivotal frontier in nanomedicine, offering a means to overcome these barriers and enable precision medicine[352]. Directing therapeutic agents to specific intracellular compartments promises to improve therapeutic efficacy, minimize systemic toxicity, and pave the way for personalized treatment strategies[353]. In this context, mitochondria represent a compelling subcellular target; their pivotal roles in cellular homeostasis and energy production make them critical in maintaining normal physiology and promoting disease development[354]. Dysfunction directly causes disease pathology in primary mitochondrial disorders, while mitochondrial dysregulation functions as a key contributor or consequence of disease progression in secondary mitochondrial diseases, such as cancer.

Mitochondria have represented the focus of extensive efforts to develop targeted therapeutic approaches owing to their unique structure and functions[308]. Several small molecules designed over the years - including delocalized lipophilic cations and mitochondria-penetrating peptides - exploit the mitochondrial membrane potential to achieve selective accumulation. Other approaches involve mitochondria-targeting sequences, which utilize the translocase of the outer

(TOM) and inner (TIM) mitochondria membranes for mitochondrial entry, or specific targeting molecules such as Szeto-Schiller peptides designed to bind cardiolipin (CL), a mitochondrial-specific lipid, and receptor-binding molecules for enhanced specificity.

The conjugation of small targeting molecules to therapeutic agents faces critical limitations, including reduced systemic stability, limited bioavailability, and a constrained therapeutic window; moreover, achieving selectivity between healthy and diseased tissues remains a significant challenge, posing an additional barrier to effective clinical translation. However, nanomedicines can provide innovative solutions by addressing these shortcomings through advanced design strategies.

Recent advances in mitochondrial targeting with polymer therapeutics have introduced promising approaches, including the development of smart materials with dynamic physicochemical properties that respond to specific stimuli or environmental cues, enabling controlled drug release. Hierarchical targeting has emerged as a sophisticated multi-stage strategy, integrating targeting elements and responsive release mechanisms to enhance precision in delivering therapeutic agents to their subcellular destinations. Functionalization of polymeric materials with novel mitochondrial targeting ligands, which do not rely solely on mitochondrial membrane potential for accumulation, and the engineering of polymeric systems with inherent mitochondrial tropism represent further innovations in the field[1,355].

Despite these advances, critical gaps hinder the full potential of polymer therapeutics in the field of mitochondrial targeting. A significant challenge lies in the inherently complex design of many polymeric systems, which, while enabling advanced functionalities such as precise targeting and controlled release, often require labor-intensive synthesis and intricate functionalization steps. This complexity limits scalability and reproducibility for industrial production and increases the cost and time required for development. The need for high-efficiency cellular uptake and mitochondrial localization further complicates the process, as many systems struggle to navigate biological barriers, achieve endosomal escape, and accumulate selectively within mitochondria. Additionally, the reliance on mitochondrial membrane potential for targeting, which varies across healthy and diseased states, reduces specificity and therapeutic effectiveness. Furthermore, the under-exploration of multivalent capacities - systems capable of simultaneously targeting multiple sites or functions – has limited the current versatility of reported approaches. Finally, inconsistent and poorly standardized validation methods for mitochondrial targeting and therapeutic outcomes also represent significant barriers to clinical translation. These challenges highlight the urgent need for

innovative solutions that simplify design while enhancing functionality, scalability, and targeting precision.

This thesis aimed to address critical challenges in mitochondrial targeting by leveraging the unique advantages of polypeptide-based polymer therapeutics. Polypeptides, with intrinsic biocompatibility, biodegradability, and capacity for precise functionalization, offer a versatile platform for developing advanced mitochondrially targeted polymer therapeutics. We employed rational design to overcome critical limitations - achieving selective mitochondrial accumulation, enhanced cellular uptake efficiency, and scalability - while maintaining therapeutic precision and versatility in advanced drug delivery systems. Validation stages employed a triple-negative breast cancer (TNBC) in vitro model, selected due to the central role of mitochondrial dysfunction in pathophysiology and associated metabolic vulnerabilities.

Design of Polypeptide-Based Diblock Copolymers with Inherent Mitochondrial Tropism

Our first article systematically explored the design and application of polypeptide-based diblock copolymers to address critical challenges in mitochondrial targeting. These copolymers comprised poly-L-ornithine (PLO), selected for its polycationic nature to promote cellular uptake[254,356], and poly-L-proline (PLP), chosen for its previously reported N-functionalization with hydrophobic and/or cationic residues that enable concentration- and potential-dependent mitochondrial targeting[322–325]. Using N-carboxyanhydride ring-opening polymerization, we synthesized a library of PLO_n-PLP_m copolymers with varying n:m block ratios, chain lengths, and substitutions of PLO with alternative polycationic blocks, such as polylysine (PLL), poly-L-arginine (PArg), and poly-L-histidine (PHis). This systematic approach allowed us to evaluate how structural variations influenced mitochondrial targeting efficiency, cellular uptake mechanisms, and biological outcomes. Among the physicochemical properties analyzed - size, aggregation propensity, zeta potential, block composition, conformation, and secondary structure - the composition of the polycationic block emerged as a significant determinant of functionality. Specifically, PLO_n-PLP_m copolymers with an n:m block ratio of 1:3 (n:m = 6:22 for **6b**, 18:54 for **6h**, and 23:65 for **6i**) consistently demonstrated energy-independent cellular uptake and efficient mitochondrial targeting, establishing themselves as mitochondrial-targeting cell-penetrating oligomers (mt-CPOs)[357].

When we replaced PLO with PLL (e.g., diblock copolymer **7**), the resulting copolymers exhibited comparable size, charge, and secondary structure; however, NMR-DOSY revealed a

bimodal conformational distribution in solution, which correlated with inefficient cellular uptake at 4°C and poor mitochondrial targeting. While secondary structure and zeta potential exhibited context-dependent correlations with mitochondrial targeting, their importance appeared inconsistent across systems. For example, PLO_n-PLP_m copolymers with alternative n:m ratios displayed higher zeta potential than the targeting-efficient 1:3 ratio, yet they adopted a random coil conformation and lacked mitochondrial targeting. Similarly, despite presenting a polyproline II conformation, PLO_n-PLP_m copolymers with an n:m ratio of 1:2 failed to achieve mitochondrial targeting. This finding suggests that zeta potential and secondary structure alone cannot drive effective mitochondrial localization. Supporting this finding, the functionalization PGA derivative with mt-CPO **6b** yielded a nanoconjugate with a random coil conformation, a negative zeta potential, and efficient mitochondrial targeting. These findings indicate that functionalization can outweigh specific physicochemical properties in determining mitochondrial targeting efficiency. Collectively, these results emphasize that while physicochemical properties such as zeta potential and secondary structure may contribute to functionality, they are not as critical as polycationic block composition and functionalization in ensuring effective mitochondrial targeting.

Mechanistic studies revealed that mitochondrial depolarization did not impair the targeting ability of mt-CPOs. We demonstrated that mt-CPO **6b** accumulated in mitochondria regardless of depolarization through confocal imaging and flow cytometry, unlike conventional cationic ligands such as triphenylphosphonium, which rely on mitochondrial membrane potential. This potential-independent mechanism broadens mt-CPOs' applicability to conditions involving mitochondrial depolarization, such as during fluctuations in disease progression or pharmacological interventions. Furthermore, targeting remained highly tumor-specific, with significant mitochondrial accumulation observed in MDA-MB-231 and MCF-7 breast cancer cells but not in non-cancerous BJ fibroblasts, BV-2 microglial cells, or HepG2 cells. Notably, mt-CPO **6b** exhibited minimal toxicity in non-cancerous cells, highlighting its selectivity and safety profile.

To further elucidate the targeting mechanism, we investigated the interactions of PLO_n-PLP_m copolymers with cardiolipin (CL)-rich artificial and biological membrane models. Our findings revealed the polycationic block as essential for CL binding, as PLP homopolymers exhibited no measurable affinity. While copolymers with n:m ratios of 1:1 and 1:2 demonstrated CL binding, only the 1:3 ratio induced patch formation and membrane remodeling in CL-rich regions with negative curvature. These effects displayed specificity for CL-containing membranes but were absent in membranes lacking CL, underscoring the specificity of these interactions. Additionally, we observed

that 1:3 PLO_n-PLP_m copolymers reduced membrane fluidity, increased tension, and promoted membrane ordering and curvature induction. The inability of copolymer **7** to induce patch formation further emphasized the critical role of the PLO as the polycationic block in stabilizing these interactions. The robust physical mechanisms of interaction highlight the specificity of our materials and differentiate them from other reported mitochondria-penetrating peptides, proving their feasibility for effective and selective mitochondrial targeting.

Functionally, mt-CPOs exhibited potent, concentration-dependent anti-tumorigenic activity in TNBC cells, disrupting mitochondrial functions at sub-IC_{50} concentrations (including increased reactive oxygen species (ROS) production, mitochondrial depolarization, inhibition of oxidative phosphorylation, which specifically reduced complex I activity and electron transport chain coupling efficiency and induced lysosomal-dependent mitophagy. Mt-CPOs' potential as dual targeting and therapeutic agents significantly advances mitochondrial-targeted therapies.

The scalability of our synthesis process supported the translational potential of this platform. Using a robust and cost-effective NCA-ROP methodology, we scaled up the production (optimized via a design-of-experiments approach) of mt-CPO **6b** to a high yield (7.3 g, 80%) with consistent quality. Additionally, we developed a nanoconjugate (named "**16**") by functionalizing a linear PGA backbone modified with a short azide-PEG chain (N_3-PEG_3-PGA_{50}) with mt-CPO **6b** (3.3% wt) via a valine-citrulline (VC) linker, showcasing the adaptability of our platform. This nanoconjugate retained efficient mitochondrial targeting, emphasizing the importance of ligand flexibility and functionalization strategies. Notably, this derivative enhanced cell viability while preventing mitochondrial damage, further underscoring the versatility of mt-CPOs in advancing mitochondrial-targeted therapies.

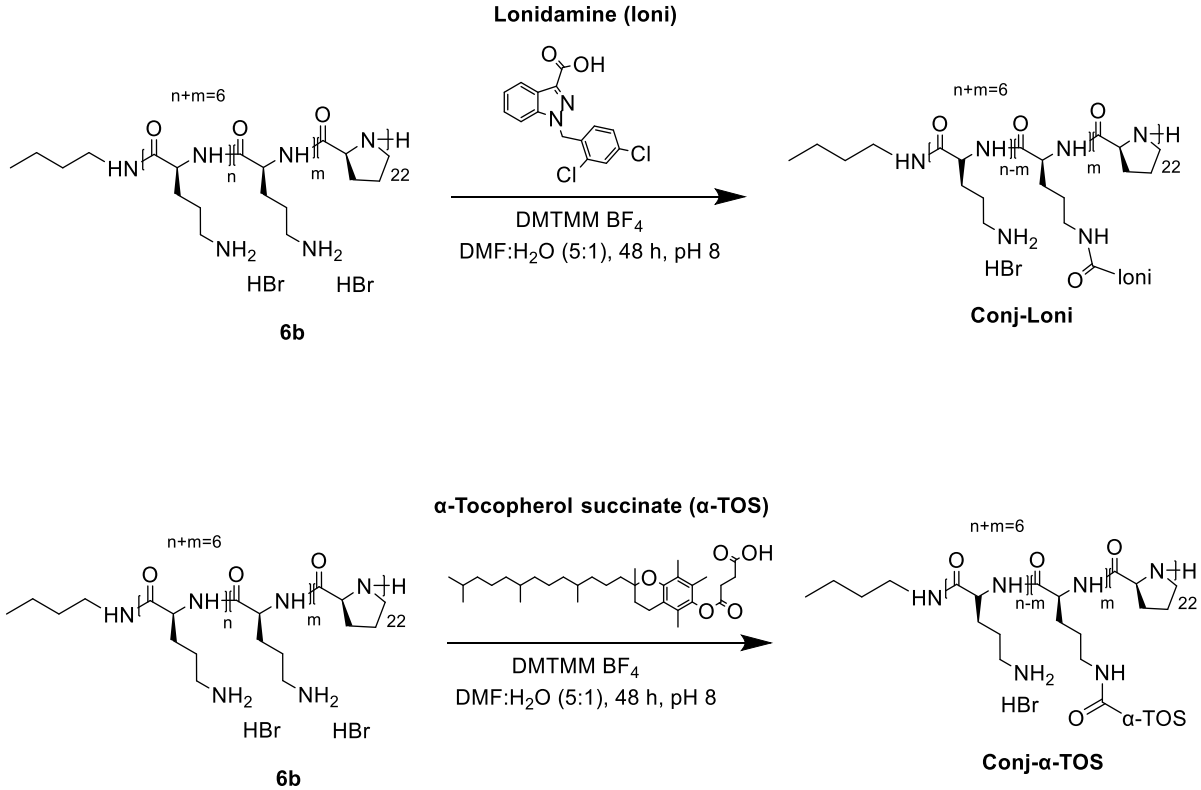
Polypeptide-Drug Conjugates for Specific Mitochondrial Activity in Triple-Negative Breast Cancer

As an extension of the work published in the first article, we synthesized polypeptide-drug conjugates by the direct conjugation of mt-CPO **6b** (PLO_6-PLP_{22}) to lonidamine (Loni) and α-tocopherol succinate (α-TOS), selected for their mitochondria-dependent mechanisms of action and reported efficacy in MDA-MB-231 TNBC cells. The promising preliminary findings from this approach are detailed below.

Loni inhibits mitochondrial-bound hexokinase II, a key enzyme in glycolysis, thereby reducing ATP production and inducing mitochondrial dysfunction, which sensitizes cancer cells to apoptosis. Additionally, Loni causes mitochondrial membrane potential depolarization, promoting the release

of pro-apoptotic factors[358,359]. While Loni has been evaluated in clinical trials for benign prostatic hyperplasia and preclinical studies for breast, ovarian, and lung cancers, its further development has faced setbacks due to hepatotoxicity and poor biodistribution[360–362]. Furthermore, Loni does not display high potency as a standalone drug, which has limited its clinical application outside of combination therapies[363]. α-TOS, a pro-apoptotic derivative of vitamin E, disrupts the mitochondrial electron transport chain at complex II, leading to ROS generation and apoptotic pathway activation through mitochondrial membrane permeabilization and cytochrome c release[364,365]. Despite promising pro-apoptotic properties, α-TOS has been predominantly investigated in combination therapies, where it complements other treatments to enhance anticancer effects[366,367].

By leveraging mt-CPO **6b** as a delivery system, we aimed to overcome the limitations of Loni and α-TOS by ensuring mitochondria-specific localization, thereby enhancing their therapeutic efficacy while minimizing off-target effects. Following the procedure outlined in **Scheme 4.1**, we synthesized mt-CPO **6b**-based conjugates - conj-Loni and conj-α-TOS. In this approach, we directly conjugated the carboxylic groups of Loni and α-TOS to the amino groups of the PLO block by forming stable amide bonds.



Scheme 4.1. Procedures followed for conj-Loni and conj-α-TOS synthesis.

We prepared several batches of conj-Loni and conj-α-TOS to achieve varying percentages of drug conjugated to mt-CPO 6b for further biological investigations. The Total Drug Loading (TDL) % was quantified using nuclear magnetic resonance (NMR) to determine the molar percentage (% mol) and ratified by UV-visible (UV-Vis) spectroscopy to calculate the weight percentage (% wt) (**Table 4.1**). For conj-α-TOS, % mol was back-calculated from % wt data obtained via UV-Vis due to significant signal overlap in the NMR spectrum between the parent polymer **6b** and the final conjugate (**Figure 4.1A**). In contrast, for conj-Loni, the % mol was directly estimated using NMR by exploiting the aromatic peaks of the drug (b, c, d; **Figure 4.1B**), while %wt was determined independently by UV-Vis. For conj-Loni, a discrepancy in the expected trend between % mol and % wt was observed across different batches. This inconsistency may be attributed to matrix effects caused by variations in the DMF:H_2O ratio used during measurements, which could influence conjugate-solvent interactions and potentially alter the extinction coefficient, particularly at higher drug loadings where conformational changes or aggregation may occur. However, it is important to emphasize that the DMF:H_2O ratio used for the measurements of the conjugates was identical to that used for preparing the free drug calibration curve for each batch, ensuring the reliability and consistency of the data.

Table 4.1. Summary of the % total drug loading for synthesized batches of conj-Loni and conj-α-TOS

% Total Drug Loading (TDL)							
conj-Loni							
Batch	1	2	3	4	5	6	
% mol[a)]	5.0	3.0	4.5	7.0	8.0	11.0	
% wt[b)]	4.4	5.8	7.0	11.0	14.0	11.9	
conj-α-TOS							
Batch	1	2	3	4	5	6	7
% mol[c)]	7.4	8.5	16.0	10.6	6.2	5.5	7
% wt[b)]	7.0	8.0	15.0	10.0	5.8	5.2	6.7

a) Estimated by nuclear magnetic resonance; b) Determined by UV-vis c) Back-calculated (theoretical) from % wt due to signal overlap in the NMR spectrum.

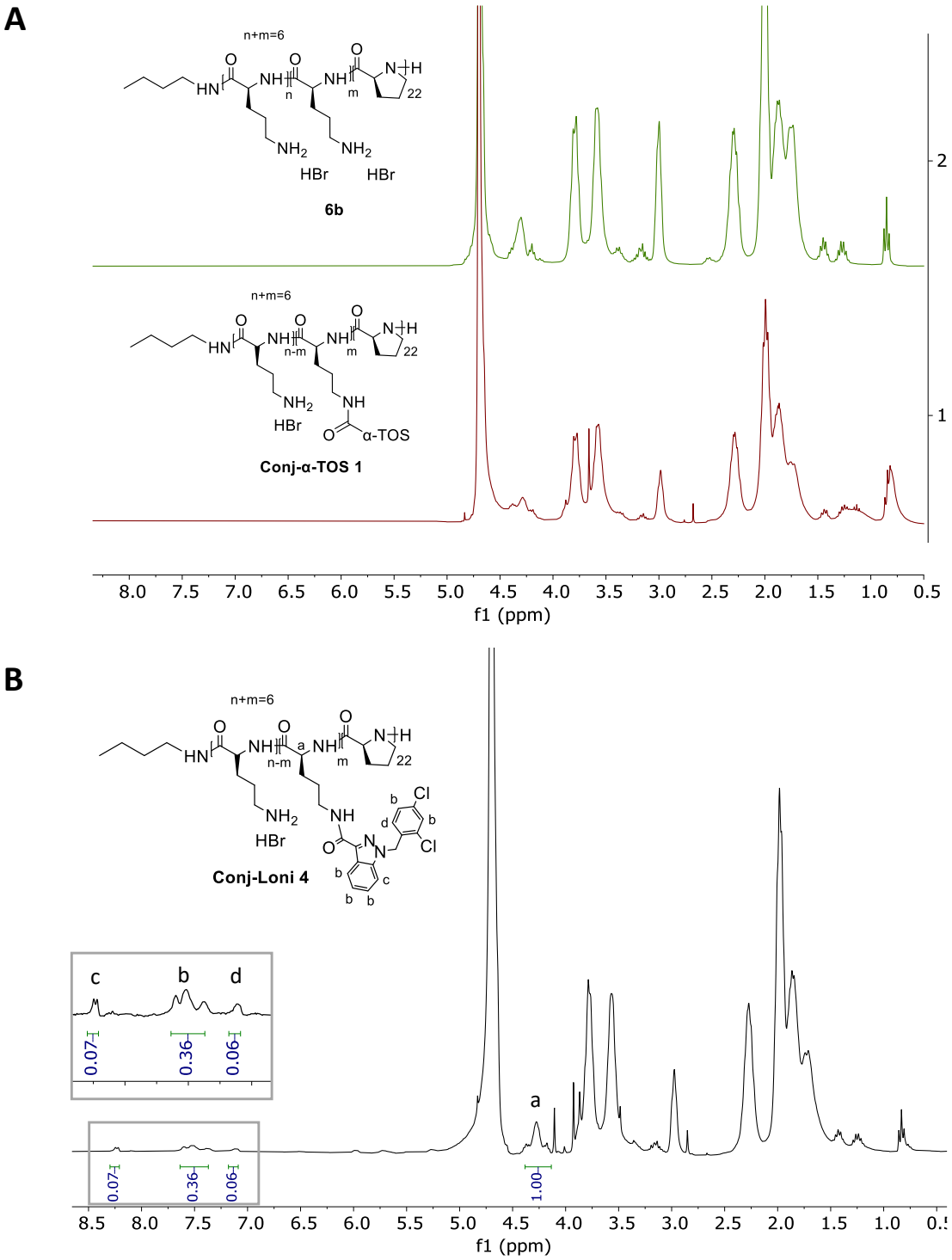


Figure 4.1. Representative NMR spectra of conj-Loni 4 and conj-α-TOS 1. A) Stacked NMR spectra of 6b and conj-α-TOS 1, illustrating overlapping peaks that hinder accurate %mol estimation. B) NMR spectrum of conj-Loni 4 in D_2O (10 mg/mL), used to determine the %mol of Loni (calculated %mol = 7).

The drugs conjugation to 6b resulted in subtle changes to the polymer's size and zeta potential. Data are presented for the conjugates (**conj-α-TOS** 1 and **conj-Loni 4**) used in the activity studies discussed below. Fluorescence correlation spectroscopy (FCS), with Atto488 as a fluorescent

probe (0.015 eq. Atto488 conjugated per polymeric chain), revealed an increase in hydrodynamic diameter from 2 nm (6b) to 5 nm for **conj-α-TOS 1** and 2.8 nm for **conj-Loni 4**, calculated using the Einstein-Stokes equation[368] (**Table 4.2**). The larger size of **conj-α-TOS 1** is attributed to possible micelle formation, driven by the amphiphilic nature of TOS, where hydrophobic alpha-tocopherol moieties might assemble within the micelle core. In contrast, **conj-Loni 4** likely remains as individual conjugates due to the less amphiphilic structure of Loni. Zeta potential measurements showed an increase from 2.9 mV (6b) to 5.22 ± 0.4 mV for **conj-Loni 4** and 5.83 ± 0.5 mV for **conj-α-TOS 1**, possibly due to polymer reorganization and the enhanced exposure of positively charged amino groups after drug conjugation.

Table 4.2. Physico-chemical characterization of **conj-α-TOS 1** and **conj-Loni 4** compared to the parent polymer **6b**

Compound	Concentration	K_d (m^2s^{-1})	Size (d.nm) [a)]	Zeta potential (mV) [b)]
Conj-Loni 4	1.5 mg/ml	1.508E-10	2.8	5.22±0.4
Conj-α-TOS 1	1.5 mg/ml	8.392E-11	5	5.83±0.5
6b	1.5 mg/ml	2.195E-10	2	2.9±0.5

a) Calculated using the Einstein-Stokes equation after the Kd determination by fluorescence correlation spectroscopy. d.nm – diameter in nm b) Determined by dynamic light scattering (DLS). mV – millivolt

Cell viability assays using MDA-MB-231 TNBC cells and the MTS/PMS assay after 24 h (Figure 4.1A left) and 72 h (**Figure 4.2A right**) of treatment revealed distinct trends for conj-Loni and conj-α-TOS. Conj-Loni induced a near-linear decrease in cell viability with increasing percentages of conjugated drugs. In contrast, conj-α-TOS exhibited a non-linear relationship between drug loading and cytotoxicity; for instance, **conj-α-TOS 4**, with a high α-TOS conjugation percentage (% wt 10), demonstrated minimal cytotoxicity (IC_{50} > 1 mg/mL) while **conj-α-TOS 5**, with approximately half the α-TOS loading (% wt 5.8), displayed more significant cytotoxicity, with an IC_{50} of 0.68 mg/mL after 24 h of treatment. We investigated this counterintuitive trend using pyrene fluorescence as a probe to determine the critical aggregation concentration values (**Figure 4.2B**). The lower critical aggregation concentration for **conj-α-TOS 4** (0.03 mg/mL) compared to **conj-α-TOS 5** (0.14 mg/mL) suggests that the drug becomes sequestered within micellar or aggregate structures at higher α-TOS loadings, thereby limiting bioavailability and biological activity; conversely, the lower drug loading in conj-α-TOS 5 may reduce micelle formation, thereby supporting α-TOS activity. After establishing a range of non-toxic concentrations for conj-Loni and conj-α-TOS families, we studied cell internalization and sub-organelle localization using Cy5-labeled derivatives for live-cell confocal fluorescence microscopy monitoring in MDA-MB-231 cells performed at different times (pulse-chase study – 1, 2, 4, 6, 24 h). Image processing using Pearson's correlation coefficient revealed

significant mitochondrial colocalization for both polypeptide-drug conjugates 2 h post-treatment, suggesting the retention of mitochondrial targeting capacity of mt-CPO **6b** after drug conjugation (**Figure 4.2C**).

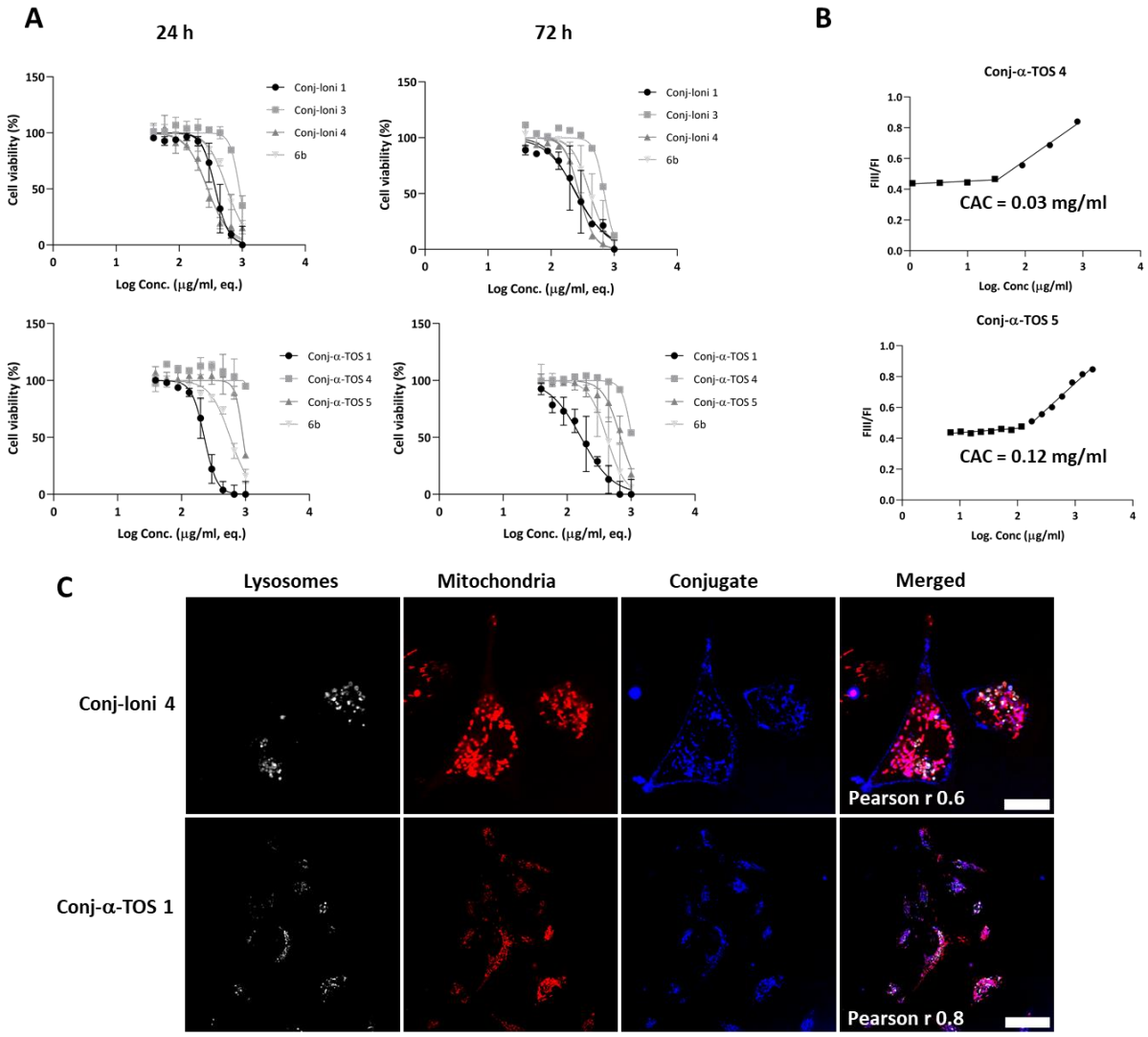


Figure 4.2. Uptake mechanism and mitochondrial targeting of 6b-based conjugates. A) MDA-MB-231 cell viability by MTS assay in response to exposure to conj-Loni and conj-α-TOS of different % drug conjugation and the parent polymer 6b at 24 and 72 h. 24 h: conj-Loni 1 (IC_{50} = 0.37 mg/ml), **conj-Loni 3** (IC_{50} = 0.90 mg/ml), **conj-Loni 4** (IC_{50} = 0.28 mg/ml); **conj-α-TOS 1** (IC_{50} = 0.23 mg/ml), **conj-α-TOS 4** (IC_{50} > 1 mg/ml), **conj-α-TOS 5** (IC_{50} = 0.90 mg/ml); **6b** (IC_{50} = 0.55 mg/ml), (24 h, n = 3, mean ± SEM). 72 h: **conj-Loni 1** (IC_{50} = 0.25 mg/ml), **conj-Loni 3** (IC_{50} = 0.70 mg/ml), **conj-Loni 4** (IC_{50} = 0.28 mg/ml); **conj-α-TOS 1** (IC_{50} = 0.17 mg/ml), **conj-α-TOS 4** (IC_{50} > 1 mg/ml), **conj-α-TOS 5** (IC_{50} = 0.68 mg/ml); **6b** (IC_{50} = 0.40 mg/ml), (72 h, n = 3, mean ± SEM). **B)** Critical aggregation concentration (CAC) determination for **conj-α-TOS 4** and **5** using pyrene fluorescence. The emission polarity index (IFIII/IFI) variation with concentration reveals lower CAC for **conj-α-TOS 4** (0.03 mg/ml) compared to **conj-α-TOS 5** (0.14 mg/ml), potentially explaining their differential viability profiles. **C)** Confocal images of diblock copolymers **conj-Loni 4** and **conj-α-TOS 1** uptake at 2 h post-treatment in MDA-MB 231 cells following a pulse-chase experiment (White – LysoTracker® Blue for lysosomes; Red – MitoTracker™ Red CM-H2Xros for mitochondria; Blue – Cy5-labeled conjugates). Colocalization with Mitotracker Red observed (purple), and the Pearson r (2 h) value calculated using the ImageJ JACoP plugin. Scale bar: 10 μm.

Furthermore, we employed a competitive binding assay to evaluate the affinity of these polypeptide-drug conjugates for CL using the CL-specific fluorescent probe MitoCLue. We performed this analysis using two models: an artificial membrane system comprising small unilamellar vesicles made of 1,2-dioleoyl-sn-glycero-3-phosphocholine and CL (3:1 molar ratio), and a biologically relevant model based on mitoplasts isolated from rat heart and liver. The results revealed that, although EC50 values remained slightly higher for conjugates compared to the parental mt-CPO 6b, the CL affinity was preserved after drug conjugation (**Table 4.3**), confirming their mitochondrial targeting specificity.

Table 4.3. Relative binding affinity of evaluated polymers (6b and conjugates) by the half maximal effective concentration (EC50) values obtained from fluorescent-based competitive binding assays conducted in various Cardiolipin (CL)-containing membranes.

Polymer	CL/DOPC liposomes, pH 6.8		Mitoplasts from rat heart		Mitoplasts from rat liver	
	EC50 average, μM	±SD	EC50 average, μM	±SD	EC50 average, μM	±SD
Conj-Loni 4	5.097	0.147	10.797	1.028	6.913	0.487
Conj-α-TOS 1	4.777	0.418	7.996	1.502	7.047	0.713
6b	1.642	0.051	3.456	0.065	3.845	0.314

Cytochrome C used as a positive control (liposomes EC50 average (N=3) for four experiments = 0.365±0.018; mitoplast from rat heart EC50 average (N=3) for three experiments = 0.857±0.016; mitoplast from rat liver EC50 average (N=3) for three experiments = 0.618 ± 0.121; CL/DOPC - Small unilamellar vesicles or SUVs, composed of 1,2-dioleoyl-sn-glycero-3-phosphocholine (DOPC) and CL (3:1 molar ratio).

Given the reported applications of Loni and α-TOS in TNBC treatment and the concentration-dependent anti-tumorigenic activity of mt-CPO **6b**, we performed mitochondrial activity studies to evaluate the impact of the two most cytotoxic conjugates, **conj-Loni 4** and **conj-α-TOS 1**. Importantly, the selected conjugates exhibited a significantly enhanced cytotoxic profile compared to the free drugs. While the IC_{50} values for the free drugs Loni and α-TOS after 24 h were 446 μM and 86 μM, respectively, the conjugated forms exhibited significantly enhanced cytotoxic profiles. Specifically, conj-Loni 4 demonstrated an IC_{50} value of 0.28 mg/mL, which corresponds to 96 μM of its conjugated Loni equivalent. Similarly, **conj-α-TOS 1** showed an IC_{50} value of 0.25 mg/mL, equivalent to 30 μM of conjugated α-TOS. These results highlight the superior potency of the conjugated drugs compared to their free forms. We conducted activity studies at sub-IC_{50} concentrations (>IC_{15}) to investigate effects on mitochondrial depolarization, ROS production, and oxygen consumption rate (OCR) in MDA-MB-231 cells, with direct comparisons to parental mt-CPO **6b** at sub-IC_{50} concentrations, as reported in our first article. Using the fluorescent probe JC-1, which

shifts from red fluorescence in polarized mitochondria to green fluorescence in depolarized states, we quantified mitochondrial membrane potential by calculating the red/green fluorescence intensity ratio. **Conj-Loni 4** and **conj-α-TOS 1** both caused a significant loss of mitochondrial membrane potential after 2 h of incubation compared to untreated control cells (set at 100%), displaying a more acute effect than parental mt-CPO 6b and maintaining depolarization over time (**Figure 4.3A**). Additionally, **conj-Loni 4** and **conj-α-TOS 1** significantly increased ROS production compared to untreated controls after 24 h of treatment, although any increase did not differ significantly from that induced by parental mt-CPO **6b** (**Figure 4.3B**).

We next examined the impact of **conj-Loni 4** and **conj-α-TOS 1** on mitochondrial respiration through Seahorse XF Analyzer studies, focusing on OCR after 24 h of treatment. **Conj-α-TOS 1** induced a significant, concentration-dependent reduction in spare respiratory capacity (SRC) (**Figure 4.3C, left**), a critical parameter reflecting the ability of mitochondria to adapt to increased energy demands. This reduction in SRC has particular relevance, as cancer cells often rely on enhanced SRC as a resistance mechanism against conventional chemotherapy. Furthermore, conj-Loni 4 and conj-α-TOS 1 induced significant decreases in OCR associated with ATP production, indicating impaired basal respiration and decreased oxidative phosphorylation efficiency (**Figure 4.3C, right**). These findings suggest that **conj-Loni 4** and **conj-α-TOS 1** disrupt mitochondrial energy metabolism, impairing the capacity of cancer cells to maintain their bioenergetic demands.

We achieved these activity results at the mitochondrial level at sub-IC_{50} concentrations of the conjugates, whereas equivalent concentrations of mt-CPO **6b** alone ($<IC_{15}$, as demonstrated in the first article) failed to induce significant mitochondrial effects, and the free drugs remained below their effective thresholds. These findings suggest a synergistic interaction between mt-CPO **6b** and drugs when conjugated, likely due to increased mitochondrial localization of the drugs or the additive contribution of mt-CPO **6b**'s anti-tumorigenic effects, even at low concentrations. This observed synergy highlights the potential of combining mt-CPO **6b** with mitochondria-active drugs to enhance therapeutic efficacy in TNBC cells. The increased mitochondrial localization and retention of drug activity within mitochondria likely contribute to this enhanced efficacy.

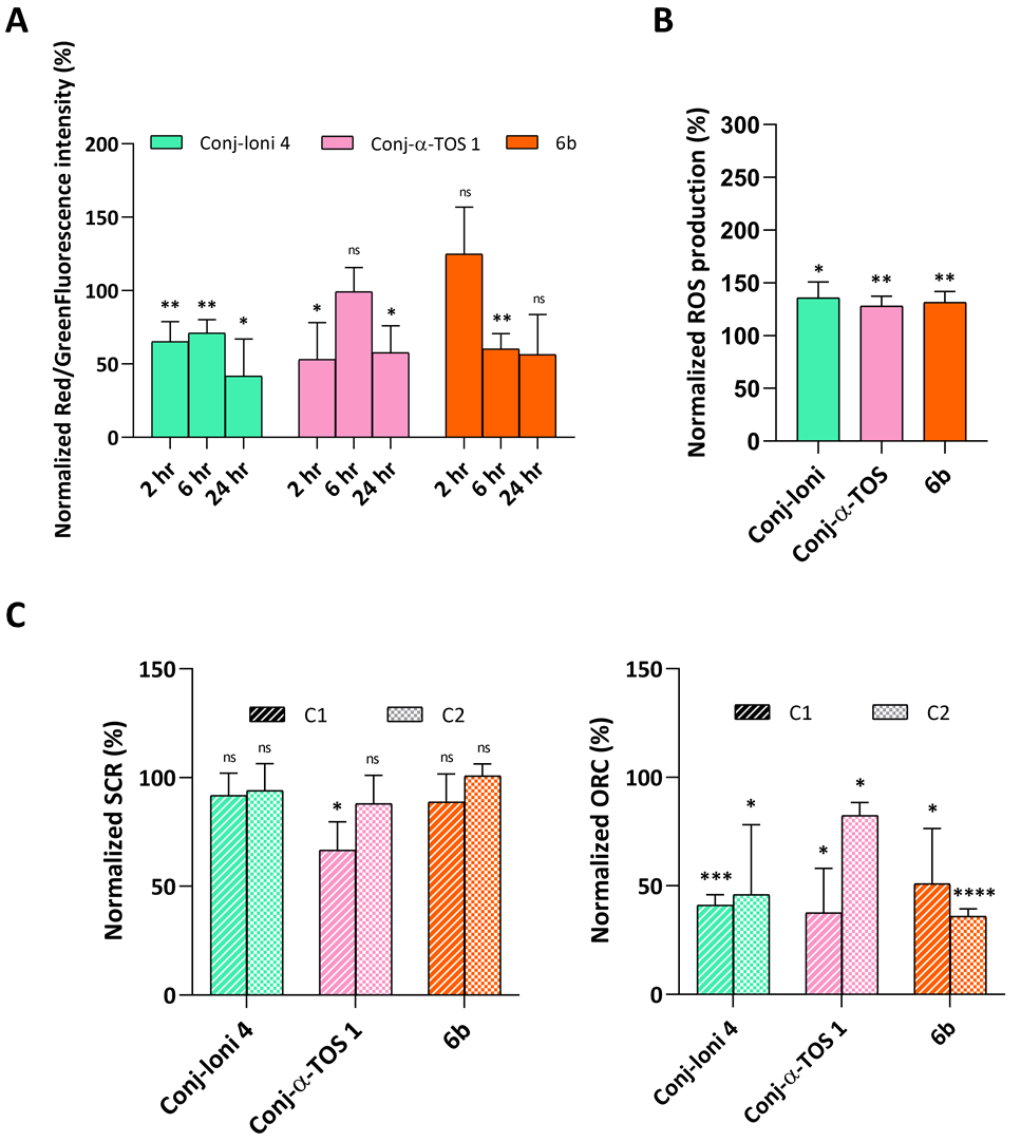


Figure 4.3. Mitochondria-dependent biological activity of 6b-based conjugates. A) Mitochondrial membrane potential measured after treatment with **conj-Loni 4**, **conj-α-TOS 1**, and **6b** over time (Concentration (C): C < IC_{50}; t-test comparing to control set as 100%; n = 3, mean ± SEM). **B)** Reactive oxygen species (ROS) production analysis after a 24-h treatment with **conj-Loni 4**, **conj-α-TOS 1**, and 6b (Concentration (C): C < IC_{50}; t-test comparing to control set as 100%; n = 3, mean ± SEM) **C)** Spare respiration capacity (SRC, left) and oxygen consumption rate (OCR) (right) analysis by Seahorse XF after a 24-h treatment with **conj-Loni 4**, **conj-α-TOS 1**, and **6b** (Concentration (C): C1 < IC_{50}, diluted concentration C2 (C1/C2 =1.5); OCR measured in pmol/min/2x10^4 cells; t-test comparing to the control set as 100%; n = 3, mean ± SEM.

These results provide compelling preliminary evidence of the benefits of targeting mitochondrial vulnerabilities in cancer cells through polypeptide-drug conjugates and underscore the need for further studies to elucidate the underlying mechanisms driving this synergistic effect. Moreover, as a complementary non-therapeutic application of the polypeptide-drug conjugate bearing α-TOS, a collaboration with Curapath demonstrated its potential in mRNA delivery. Specifically, LNPs formulated with conj-TOS (at non-toxic concentrations) were evaluated as an additional component in LNPs containing 1,2-dioleyloxy-3-dimethylaminopropane (DODMA) as the

ionizable lipid, 1,2-Dimyristoyl-rac-glycero-3-methoxypolyethylene glycol-$_{2000}$ (DMG-PEG$_{2000}$) as the shielding lipid, and dioleoylphosphatidylethanolamine (DOPE) and cholesterol as structural lipids, with a molar ratio of 10:40:10:38.5:1.5. These modified LNPs exhibited a significantly higher transfection efficiency (140 ± 20%) compared to the standard DODMA/DOPE/cholesterol/DMG-PEG formulation (50/10/38.5/1.5), which was set at 100%, in human embryonic kidney (HEK293) cells. Importantly, the modified LNPs maintained a non-toxic profile at the tested concentrations. Further details on these findings can be found in the patent WO2025003463A1[369], which highlights the versatile potential of PLO$_n$-PLP$_m$-based systems and their derivatives.

Integrating Mitochondrial Targeting Polypeptides with Molecular Motors for Advanced Biological Applications

In the second article, we extended the application of the PGA nanoconjugate developed in the first study ("**16**", here named P) to explore its integration with dynamic synthetic nanomachines for advanced biological applications. Inspired by the functional versatility of molecular machines — systems that, like biological macromolecules, can selectively respond to specific stimuli and perform specialized tasks such as membrane penetration[370] — we aimed to design a nanoconjugate incorporating a light-driven molecular motor (**MM**) for targeted functionality. We obtained the resulting nanoconjugate, **P-MM**, via site-specific click chemistry between the non-toxic, biocompatible PGA-based nanoconjugate (**P**) bearing an azide group and a propargyl-derivatized MM.

MMs represent a fascinating class of synthetic systems capable of complete 360° unidirectional rotations driven by light energy, allowing precise, repetitive motions with high spatiotemporal resolution and non-invasiveness[371–373]. Despite their potential, the biological applicability of MMs has been limited due to poor biocompatibility and solubility[373], restricting their successful integration into few publications in areas such as drug delivery[374], mechanobiology[375] and anticancer therapy[376]. To address these challenges, we selected PGA to improve the biocompatibility and solubility of MM and leverage its energy-independent uptake mechanism, as demonstrated in our earlier work.

The novelty of this study lies in demonstrating that **P-MM** retained the rotational stability of the **MM** under 405 nm light, even though the rotational speed decreased, likely due to the increased activation energy due to constraints imposed by the polypeptide structure. Importantly, light irradiation induced a structural transformation in **P-MM**, as observed by cryogenic electron

microscopy. Specifically, **P-MM** transitioned from a compact micellar form (~2–3 nm in diameter) to extended worm-like supramolecular structures (~1 × 10 nm in length) upon light activation (30 seconds at 405 nm). This conformational change significantly enhanced the cellular uptake of irradiated **P-MM** compared to its non-irradiated and control **P** forms, as quantified by high-throughput fluorescence imaging.

We achieved enhanced cellular uptake without significant cytotoxicity under the tested irradiation conditions. **P-MM** retained its mitochondrial targeting capabilities after exposure to light without substantial ROS production. These findings suggest increased uptake primarily driven by the mechanical rotation of **MM** rather than photoinduced oxidative stress; this behavior aligns more closely with recent mechanistic studies demonstrating motor-induced membrane expansion[377] and contrasts with earlier reports that employed MMs to drill holes in plasma membranes, leading to cytotoxicity and cancer cell death[376,378]. The controlled and biocompatible nature of the light-driven molecular rotation highlights the potential of **P-MM** to facilitate membrane permeabilization and cell entry without compromising cell integrity. This study positions **P-MM** as a dynamic platform integrating MMs into functional nanoconjugates, enabling precise, light-activated modulation of biological interactions. This approach offers promising opportunities for advanced applications in targeted drug delivery, paving the way to exploit dynamic molecular systems in therapeutic strategies where enhanced cytosolic delivery is required.

Engineering Multifunctional Platforms for Combined Mitochondrial Targeting and Non-Viral Gene Therapy

In the third article, we expanded the scope of polypeptide-based systems for intracellular delivery to integrate multifunctional subcellular targeting, addressing mitochondrial targeting and genetic payload delivery within a unique platform for cancer therapy using the MDA-MB-231 TNBC model. Combinatorial therapeutic approaches, which hold significant potential in enhancing treatment efficacy[379], remain underexplored in polypeptide-based systems, particularly those combining mitochondrial targeting and gene therapy. To address this, we designed a multifunctional nanoconjugate through an eight-step synthesis process with thorough characterization at each step. This nanoconjugate comprises PLO for its established endosomal escape properties, modified with PEG_{3000} to enhance steric stability and minimize non-specific interactions[380]. We conjugated PEG-modified PLO to a trivalent compound (TRV3) incorporating a triphenylphosphonium moiety (TPP) for mitochondrial targeting[381], Cy5 as a model drug payload linked via a GSH-sensitive disulfide linker

to ensure intracellular activation, and Atto488 for monitoring purposes, resulting in the final compound, **C-TRV3-A**.

C-TRV3-A demonstrated potential as a mitochondrial-targeting platform following a hierarchical delivery approach. Endosomal escape and intracellular reduction of the disulfide linker facilitated TRV3 release, enabling mitochondrial targeting. To extend its utility beyond mitochondrial delivery, we incorporated **C-TRV3-A** into polyplex formulations for gene delivery, which we formed by condensing C-TRV3-A (N) with plasmid DNA encoding luciferase (pDNA-Luc, P), then coating the complexes with the polyanionic polypeptide VLC-3 ($PSar_{100}$-b-PGA_{15}, O) (patent application ref. WO2023002014A1[382]) for enhanced polyplex stability and mitigated cytotoxic effects of C-TRV3-A's positive charges. We screened various O/N and N/P ratios and evaluated the resulting formulations for stability in physiologically relevant conditions, including complete cell medium and mouse and human plasma, while exhibiting low hemolytic activity.

We assessed transfection efficiency in conventional 2D monolayer and 3D spheroid TNBC cell culture models, with the latter providing a more physiologically relevant microenvironment due to its representation of cell-cell interactions and penetration barriers. Among the tested formulations, **Px02501** (O/P = 0.25, N/P = 1) demonstrated the highest transfection efficiency in 2D culture after 24 h; however, the transfection profiles differed between 2D and 3D cultures. Transfection efficiency failed to display dose-dependence in 2D culture, with the highest luciferase expression achieved at the lowest plasmid concentration (200 ng/mL), while 3D spheroids exhibited dose-dependent transfection, with optimal efficiency observed at 400 ng/mL but reduced efficiency observed at higher doses (600 ng/mL).

The observed differences likely reflect the unique characteristics of the two cell culture models. In 2D cultures, uniform exposure to polyplexes enables efficient cellular uptake at lower plasmid concentrations, whereas higher concentrations may promote polyplex aggregation or saturation of cellular uptake pathways[383,384]. Conversely, 3D culture introduces structural and environmental complexities, such as cell-cell interactions and 3D organization[134], which hinder polyplex penetration and uptake. These barriers require the presence of higher plasmid concentrations for effective transfection. As validated by recent literature, the distinct dose-dependent behavior observed in 3D models underscores their relevance for evaluating gene delivery systems under conditions that better mimic in vivo environments[385–387].

This multifunctional approach, combining subcellular targeting and gene delivery, highlights the versatility of polypeptide-based systems when aiming to address complex therapeutic challenges. The study underscores the importance of tailoring polypeptide design for specific applications, offering a pathway for developing advanced therapeutic platforms capable of integrating multiple functionalities within a single system.

Final Remarks

In conclusion, with this Ph.D. thesis, we developed diverse approaches for effective subcellular therapy, focusing on enhancing cytosolic delivery and precise mitochondrial targeting. The validation of our platforms, specifically at the mitochondrial level, through physical and biological assays, provides a solid foundation for understanding their therapeutic mechanisms during further preclinical translation—an aspect often overlooked in intracellular-targeted therapy development. Applying polypeptide-based polymer therapeutics in an emerging field, such as synthetic molecular machines, also represents a meaningful advancement in their biological applications. Furthermore, the engineering of platforms employing a "two birds, one stone" approach, targeting multiple intracellular sites, shows great promise for enhancing therapeutic efficacy.

Given the novelty of PLO_n-PLP_m for mitochondrial targeting, we have filed a patent (WO 2025003463A1[369]) and foresee the preclinical translation of these systems, starting with in vivo studies in MDA-MB-231 models. These systems could function as active polymers or mitochondrial targeting moieties, functionalized onto advanced delivery carriers with improved pharmacokinetic and pharmacodynamic profiles. Their use in combination with therapeutic agents as polypeptide-drug conjugates further broadens their potential. Additionally, we envision the development of a ROS-sensitive linker to conjugate polypeptide 6b with drugs, enabling drug release in oxidative stress environments, which could synergize or refine the therapeutic effects observed in our preliminary studies. Furthermore, the promising transfection efficiency of conj-α-TOS as a component in LNP formulations underscores its functional versatility in gene delivery. This aspect will be further explored in future applications within our laboratory.

For the polypeptide-molecular motor system, while the field remains nascent and its translation is challenging due to limitations in scalability, we believe our work contributes valuable insights for future advancements. This system could prove beneficial in applications requiring precise light control, acute systemic administration of biologically active agents, or scenarios where

small quantities suffice. Similarly, we foresee the translation of polyplexes for cancer therapy, potentially adapting them for different cancer types or incorporating various nucleic acid species as payloads.

Finally, while our extensive in vitro work across various models provides crucial insights into the targeting mechanisms of these platforms, we emphasize the necessity of evaluating their localization and therapeutic efficacy in vivo. Such studies are vital for bridging the gap between in vitro findings and clinical application, advancing these innovative systems toward meaningful contributions in subcellular therapy and precision medicine.

5 REFERENCES

(1) Pegoraro, C.; Domingo-Ortí, I.; Conejos-Sánchez, I.; Vicent, M. J. Unlocking the Mitochondria for Nanomedicine-Based Treatments: Overcoming Biological Barriers, Improving Designs, and Selecting Verification Techniques. *Adv. Drug Deliv. Rev.* **2024**, *207*, 115195. https://doi.org/https://doi.org/10.1016/j.addr.2024.115195.

(2) Giacomello, M.; Pyakurel, A.; Glytsou, C.; Scorrano, L. The Cell Biology of Mitochondrial Membrane Dynamics. *Nat. Rev. Mol. Cell Biol.* **2020**, *21* (4), 204–224. https://doi.org/10.1038/s41580-020-0210-7.

(3) Protasoni, M.; Zeviani, M. Mitochondrial Structure and Bioenergetics in Normal and Disease Conditions. *International Journal of Molecular Sciences*. 2021. https://doi.org/10.3390/ijms22020586.

(4) Pfanner, N.; Warscheid, B.; Wiedemann, N. Mitochondrial Proteins: From Biogenesis to Functional Networks. *Nat. Rev. Mol. Cell Biol.* **2019**, *20* (5), 267–284. https://doi.org/10.1038/s41580-018-0092-0.

(5) Kühlbrandt, W. Structure and Function of Mitochondrial Membrane Protein Complexes. *BMC Biol.* **2015**, *13* (1), 89. https://doi.org/10.1186/s12915-015-0201-x.

(6) Chandel, N. S. Mitochondria as Signaling Organelles. *BMC Biol.* **2014**, *12* (1), 34. https://doi.org/10.1186/1741-7007-12-34.

(7) Sayyed, U. M. H.; Mahalakshmi, R. Mitochondrial Protein Translocation Machinery: From TOM Structural Biogenesis to Functional Regulation. *J. Biol. Chem.* **2022**, *298* (5). https://doi.org/10.1016/j.jbc.2022.101870.

(8) Najbauer, E. E.; Becker, S.; Giller, K.; Zweckstetter, M.; Lange, A.; Steinem, C.; de Groot, B. L.; Griesinger, C.; Andreas, L. B. Structure, Gating and Interactions of the Voltage-Dependent Anion Channel. *Eur. Biophys. J.* **2021**, *50* (2), 159–172. https://doi.org/10.1007/s00249-021-01515-7.

(9) Wang, Q.; Guan, Z.; Qi, L.; Zhuang, J.; Wang, C.; Hong, S.; Yan, L.; Wu, Y.; Cao, X.; Cao, J.; Yan, J.; Zou, T.; Liu, Z.; Zhang, D.; Yan, C.; Yin, P. Structural Insight into the SAM-Mediated Assembly of the Mitochondrial TOM Core Complex. *Science (80-.).* **2021**, *373* (6561), 1377–1381. https://doi.org/10.1126/science.abh0704.

(10) Blum, T. B.; Hahn, A.; Meier, T.; Davies, K. M.; Kühlbrandt, W. Dimers of Mitochondrial ATP Synthase Induce Membrane Curvature and Self-Assemble into Rows. *Proc. Natl. Acad. Sci.* **2019**, *116* (10), 4250–4255. https://doi.org/10.1073/pnas.1816556116.

(11) Davies, K. M.; Daum, B.; Gold, V. A. M.; Mühleip, A. W.; Brandt, T.; Blum, T. B.; Mills, D. J.; Kühlbrandt, W. Visualization of ATP Synthase Dimers in Mitochondria by Electron Cryo-Tomography. *JoVE* **2014**, No. 91, e51228. https://doi.org/doi:10.3791/51228.

(12) Joubert, F.; Puff, N. Mitochondrial Cristae Architecture and Functions: Lessons from Minimal Model Systems. *Membranes*. 2021. https://doi.org/10.3390/membranes11070465.

(13) Hu, C.; Shu, L.; Huang, X.; Yu, J.; Li, liuju; Gong, L.; Yang, M.; Wu, Z.; Gao, Z.; Zhao, Y.; Chen, L.; Song, Z. OPA1 and MICOS Regulate Mitochondrial Crista Dynamics and Formation. *Cell Death Dis.* **2020**, *11* (10), 940. https://doi.org/10.1038/s41419-020-03152-y.

(14) Venkatraman, K.; Lee, C. T.; Budin, I. Setting the Curve: The Biophysical Properties of Lipids in Mitochondrial Form and Function. *J. Lipid Res.* **2024**, *65* (10). https://doi.org/10.1016/j.jlr.2024.100643.

(15) Paradies, G.; Paradies, V.; Ruggiero, F. M.; Petrosillo, G. Role of Cardiolipin in Mitochondrial Function and Dynamics in Health and Disease: Molecular and Pharmacological Aspects. *Cells*. 2019. https://doi.org/10.3390/cells8070728.

(16) Fuentes, J. M.; Morcillo, P. The Role of Cardiolipin in Mitochondrial Function and Neurodegenerative Diseases. *Cells*. 2024. https://doi.org/10.3390/cells13070609.

(17) Jiang, Z.; Shen, T.; Huynh, H.; Fang, X.; Han, Z.; Ouyang, K. Cardiolipin Regulates Mitochondrial Ultrastructure and Function in Mammalian Cells. *Genes*. 2022. https://doi.org/10.3390/genes13101889.

(18) Cogliati, S.; Enriquez, J. A.; Scorrano, L. Mitochondrial Cristae: Where Beauty Meets Functionality. *Trends Biochem. Sci.* **2016**, *41* (3), 261–273. https://doi.org/10.1016/j.tibs.2016.01.001.

(19) Bennett, C. F.; Latorre-Muro, P.; Puigserver, P. Mechanisms of Mitochondrial Respiratory Adaptation. *Nat. Rev. Mol. Cell Biol.* **2022**, *23* (12), 817–835. https://doi.org/10.1038/s41580-022-00506-6.

(20) Uzman, A. Molecular Biology of the Cell (4th Ed.): Alberts, B., Johnson, A., Lewis, J., Raff, M., Roberts, K., and Walter, P. *Biochem. Mol. Biol. Educ.* **2003**, *31* (4), 212–214. https://doi.org/https://doi.org/10.1002/bmb.2003.494031049999.

(21) Zangari, J.; Petrelli, F.; Maillot, B.; Martinou, J.-C. The Multifaceted Pyruvate Metabolism: Role of the Mitochondrial Pyruvate Carrier. *Biomolecules*. 2020. https://doi.org/10.3390/biom10071068.

(22) Yang, D.; Wang, Y.; Qi, T.; Zhang, X.; Shen, L.; Ma, J.; Pang, Z.; Lal, N. K.; McClatchy, D. B.; Seradj, S. H.; Leung, V. H.; Wang, K.; Xie, Y.; Polli, F. S.; Maximov, A.; Gonzalez, O. C.; de Lecea, L.; Cline, H. T.; Augustine, V.; Yates III, J. R.; Ye, L. Phosphorylation of Pyruvate Dehydrogenase Inversely Associates with Neuronal Activity. *Neuron* **2024**, *112* (6), 959-971.e8. https://doi.org/10.1016/j.neuron.2023.12.015.

(23) Martínez-Reyes, I.; Chandel, N. S. Mitochondrial TCA Cycle Metabolites Control Physiology and Disease. *Nat. Commun.* **2020**, *11* (1), 102. https://doi.org/10.1038/s41467-019-13668-3.

(24) Neupane, P.; Bhuju, S.; Thapa, N.; Bhattarai, H. K. ATP Synthase: Structure, Function and Inhibition. **2019**, *10* (1), 1–10. https://doi.org/doi:10.1515/bmc-2019-0001.

(25) Poburko, D.; Santo-Domingo, J.; Demaurex, N. Dynamic Regulation of the Mitochondrial Proton Gradient during Cytosolic Calcium Elevations*. *J. Biol. Chem.* **2011**, *286* (13), 11672–11684. https://doi.org/https://doi.org/10.1074/jbc.M110.159962.

(26) Zorova, L. D.; Popkov, V. A.; Plotnikov, E. Y.; Silachev, D. N.; Pevzner, I. B.; Jankauskas, S. S.; Babenko, V. A.; Zorov, S. D.; Balakireva, A. V; Juhaszova, M.; Sollott, S. J.; Zorov, D. B. Mitochondrial Membrane Potential. *Anal. Biochem.* **2018**, *552*, 50–59. https://doi.org/https://doi.org/10.1016/j.ab.2017.07.009.

(27) Divakaruni, A. S.; Jastroch, M. A Practical Guide for the Analysis, Standardization and Interpretation of Oxygen Consumption Measurements. *Nat. Metab.* **2022**, *4* (8), 978–994.

https://doi.org/10.1038/s42255-022-00619-4.

(28) Mookerjee, S. A.; Gerencser, A. A.; Nicholls, D. G.; Brand, M. D. Quantifying Intracellular Rates of Glycolytic and Oxidative ATP Production and Consumption Using Extracellular Flux Measurements. *J. Biol. Chem.* **2017**, *292* (17), 7189–7207. https://doi.org/10.1074/jbc.M116.774471.

(29) Hernansanz-Agustín, P.; Enríquez, J. A. Generation of Reactive Oxygen Species by Mitochondria. *Antioxidants*. 2021. https://doi.org/10.3390/antiox10030415.

(30) Palma, F. R.; Gantner, B. N.; Sakiyama, M. J.; Kayzuka, C.; Shukla, S.; Lacchini, R.; Cunniff, B.; Bonini, M. G. ROS Production by Mitochondria: Function or Dysfunction? *Oncogene* **2024**, *43* (5), 295–303. https://doi.org/10.1038/s41388-023-02907-z.

(31) Dominiak, K.; Galganski, L.; Budzinska, A.; Woyda-Ploszczyca, A.; Zoladz, J. A.; Jarmuszkiewicz, W. Effects of Endurance Training on the Coenzyme Q Redox State in Rat Heart, Liver, and Brain at the Tissue and Mitochondrial Levels: Implications for Reactive Oxygen Species Formation and Respiratory Chain Remodeling. *International Journal of Molecular Sciences*. 2022. https://doi.org/10.3390/ijms23020896.

(32) Glancy, B.; Kim, Y.; Katti, P.; Willingham, T. B. The Functional Impact of Mitochondrial Structure Across Subcellular Scales. *Front. Physiol.* **2020**, *11*.

(33) Mühleip, A.; Flygaard, R. K.; Baradaran, R.; Haapanen, O.; Gruhl, T.; Tobiasson, V.; Maréchal, A.; Sharma, V.; Amunts, A. Structural Basis of Mitochondrial Membrane Bending by the I–II–III2–IV2 Supercomplex. *Nature* **2023**, *615* (7954), 934–938. https://doi.org/10.1038/s41586-023-05817-y.

(34) Cogliati, S.; Frezza, C.; Soriano, M. E.; Varanita, T.; Quintana-Cabrera, R.; Corrado, M.; Cipolat, S.; Costa, V.; Casarin, A.; Gomes, L. C.; Perales-Clemente, E.; Salviati, L.; Fernandez-Silva, P.; Enriquez, J. A.; Scorrano, L. Mitochondrial Cristae Shape Determines Respiratory Chain Supercomplexes Assembly and Respiratory Efficiency. *Cell* **2013**, *155* (1), 160–171. https://doi.org/10.1016/j.cell.2013.08.032.

(35) Quintana-Cabrera, R.; Quirin, C.; Glytsou, C.; Corrado, M.; Urbani, A.; Pellattiero, A.; Calvo, E.; Vázquez, J.; Enríquez, J. A.; Gerle, C.; Soriano, M. E.; Bernardi, P.; Scorrano, L. The Cristae Modulator Optic Atrophy 1 Requires Mitochondrial ATP Synthase Oligomers to Safeguard Mitochondrial Function. *Nat. Commun.* **2018**, *9* (1), 3399. https://doi.org/10.1038/s41467-018-05655-x.

(36) Quintana-Cabrera, R.; Manjarrés-Raza, I.; Vicente-Gutiérrez, C.; Corrado, M.; Bolaños, J. P.; Scorrano, L. Opa1 Relies on Cristae Preservation and ATP Synthase to Curtail Reactive Oxygen Species Accumulation in Mitochondria. *Redox Biol.* **2021**, *41*, 101944. https://doi.org/https://doi.org/10.1016/j.redox.2021.101944.

(37) Anand, R.; Kondadi, A. K.; Meisterknecht, J.; Golombek, M.; Nortmann, O.; Riedel, J.; Peifer-Weiß, L.; Brocke-Ahmadinejad, N.; Schlütermann, D.; Stork, B.; Eichmann, T. O.; Wittig, I.; Reichert, A. S. MIC26 and MIC27 Cooperate to Regulate Cardiolipin Levels and the Landscape of OXPHOS Complexes. *Life Sci. Alliance* **2020**, *3* (10), e202000711. https://doi.org/10.26508/lsa.202000711.

(38) Acehan, D.; Malhotra, A.; Xu, Y.; Ren, M.; Stokes, D. L.; Schlame, M. Cardiolipin Affects the Supramolecular Organization of ATP Synthase In Mitochondria. *Biophys. J.* **2011**, *100*

(9), 2184–2192. https://doi.org/10.1016/j.bpj.2011.03.031.

(39) Mukherjee, I.; Ghosh, M.; Meinecke, M. MICOS and the Mitochondrial Inner Membrane Morphology – When Things Get out of Shape. *FEBS Lett.* **2021**, *595* (8), 1159–1183. https://doi.org/https://doi.org/10.1002/1873-3468.14089.

(40) Chen, W.; Zhao, H.; Li, Y. Mitochondrial Dynamics in Health and Disease: Mechanisms and Potential Targets. *Signal Transduct. Target. Ther.* **2023**, *8* (1), 333. https://doi.org/10.1038/s41392-023-01547-9.

(41) Westermann, B. Mitochondrial Fusion and Fission in Cell Life and Death. *Nat. Rev. Mol. Cell Biol.* **2010**, *11* (12), 872–884. https://doi.org/10.1038/nrm3013.

(42) Wang, S.; Long, H.; Hou, L.; Feng, B.; Ma, Z.; Wu, Y.; Zeng, Y.; Cai, J.; Zhang, D.; Zhao, G. The Mitophagy Pathway and Its Implications in Human Diseases. *Signal Transduct. Target. Ther.* **2023**, *8* (1), 304. https://doi.org/10.1038/s41392-023-01503-7.

(43) Spinelli, J. B.; Haigis, M. C. The Multifaceted Contributions of Mitochondria to Cellular Metabolism. *Nat. Cell Biol.* **2018**, *20* (7), 745–754. https://doi.org/10.1038/s41556-018-0124-1.

(44) Houten, S. M.; Wanders, R. J. A. A General Introduction to the Biochemistry of Mitochondrial Fatty Acid β-Oxidation. *J. Inherit. Metab. Dis.* **2010**, *33* (5), 469–477. https://doi.org/https://doi.org/10.1007/s10545-010-9061-2.

(45) Arnold, P. K.; Finley, L. W. S. Regulation and Function of the Mammalian Tricarboxylic Acid Cycle. *J. Biol. Chem.* **2023**, *299* (2). https://doi.org/10.1016/j.jbc.2022.102838.

(46) Gray, L. R.; Tompkins, S. C.; Taylor, E. B. Regulation of Pyruvate Metabolism and Human Disease. *Cell. Mol. Life Sci.* **2014**, *71* (14), 2577–2604. https://doi.org/10.1007/s00018-013-1539-2.

(47) Swenson, S. A.; Moore, C. M.; Marcero, J. R.; Medlock, A. E.; Reddi, A. R.; Khalimonchuk, O. From Synthesis to Utilization: The Ins and Outs of Mitochondrial Heme. *Cells*. 2020. https://doi.org/10.3390/cells9030579.

(48) Cardenas-Rodriguez, M.; Chatzi, A.; Tokatlidis, K. Iron–Sulfur Clusters: From Metals through Mitochondria Biogenesis to Disease. *JBIC J. Biol. Inorg. Chem.* **2018**, *23* (4), 509–520. https://doi.org/10.1007/s00775-018-1548-6.

(49) Lozoya, O. A.; Wang, T.; Grenet, D.; Wolfgang, T. C.; Sobhany, M.; Ganini da Silva, D.; Riadi, G.; Chandel, N.; Woychik, R. P.; Santos, J. H. Mitochondrial Acetyl-CoA Reversibly Regulates Locus-Specific Histone Acetylation and Gene Expression. *Life Sci. Alliance* **2019**, *2* (1), e201800228. https://doi.org/10.26508/lsa.201800228.

(50) Bock, F. J.; Tait, S. W. G. Mitochondria as Multifaceted Regulators of Cell Death. *Nat. Rev. Mol. Cell Biol.* **2020**, *21* (2), 85–100. https://doi.org/10.1038/s41580-019-0173-8.

(51) Czabotar, P. E.; Garcia-Saez, A. J. Mechanisms of BCL-2 Family Proteins in Mitochondrial Apoptosis. *Nat. Rev. Mol. Cell Biol.* **2023**, *24* (10), 732–748. https://doi.org/10.1038/s41580-023-00629-4.

(52) Dadsena, S.; King, L. E.; García-Sáez, A. J. Apoptosis Regulation at the Mitochondria Membrane Level. *Biochim. Biophys. Acta - Biomembr.* **2021**, *1863* (12), 183716. https://doi.org/https://doi.org/10.1016/j.bbamem.2021.183716.

(53) Morciano, G.; Naumova, N.; Koprowski, P.; Valente, S.; Sardão, V. A.; Potes, Y.; Rimessi, A.; Wieckowski, M. R.; Oliveira, P. J. The Mitochondrial Permeability Transition Pore: An Evolving Concept Critical for Cell Life and Death. *Biol. Rev.* **2021**, *96* (6), 2489–2521. https://doi.org/https://doi.org/10.1111/brv.12764.

(54) Redza-Dutordoir, M.; Averill-Bates, D. A. Activation of Apoptosis Signalling Pathways by Reactive Oxygen Species. *Biochim. Biophys. Acta - Mol. Cell Res.* **2016**, *1863* (12), 2977–2992. https://doi.org/https://doi.org/10.1016/j.bbamcr.2016.09.012.

(55) Zhang, D.; Wang, F.; Li, P.; Gao, Y. Mitochondrial Ca2+ Homeostasis: Emerging Roles and Clinical Significance in Cardiac Remodeling. *International Journal of Molecular Sciences*. 2022. https://doi.org/10.3390/ijms23063025.

(56) Giorgi, C.; Marchi, S.; Pinton, P. The Machineries, Regulation and Cellular Functions of Mitochondrial Calcium. *Nat. Rev. Mol. Cell Biol.* **2018**, *19* (11), 713–730. https://doi.org/10.1038/s41580-018-0052-8.

(57) Giorgi, C.; Agnoletto, C.; Bononi, A.; Bonora, M.; De Marchi, E.; Marchi, S.; Missiroli, S.; Patergnani, S.; Poletti, F.; Rimessi, A.; Suski, J. M.; Wieckowski, M. R.; Pinton, P. Mitochondrial Calcium Homeostasis as Potential Target for Mitochondrial Medicine. *Mitochondrion* **2012**, *12* (1), 77–85. https://doi.org/https://doi.org/10.1016/j.mito.2011.07.004.

(58) Marchi, S.; Bittremieux, M.; Missiroli, S.; Morganti, C.; Patergnani, S.; Sbano, L.; Rimessi, A.; Kerkhofs, M.; Parys, J. B.; Bultynck, G.; Giorgi, C.; Pinton, P. Endoplasmic Reticulum-Mitochondria Communication Through Ca2+ Signaling: The Importance of Mitochondria-Associated Membranes (MAMs) BT - Organelle Contact Sites: From Molecular Mechanism to Disease; Tagaya, M., Simmen, T., Eds.; Springer Singapore: Singapore, 2017; pp 49–67. https://doi.org/10.1007/978-981-10-4567-7_4.

(59) Dhaouadi, N.; Vitto, V. A. M.; Pinton, P.; Galluzzi, L.; Marchi, S. Ca2+ Signaling and Cell Death. *Cell Calcium* **2023**, *113*, 102759. https://doi.org/https://doi.org/10.1016/j.ceca.2023.102759.

(60) Brown, J. A.; Sammy, M. J.; Ballinger, S. W. An Evolutionary, or "Mitocentric" Perspective on Cellular Function and Disease. *Redox Biol.* **2020**, *36*, 101568. https://doi.org/https://doi.org/10.1016/j.redox.2020.101568.

(61) Yonova-Doing, E.; Calabrese, C.; Gomez-Duran, A.; Schon, K.; Wei, W.; Karthikeyan, S.; Chinnery, P. F.; Howson, J. M. M. An Atlas of Mitochondrial DNA Genotype–Phenotype Associations in the UK Biobank. *Nat. Genet.* **2021**, *53* (7), 982–993. https://doi.org/10.1038/s41588-021-00868-1.

(62) Meisinger, C.; Sickmann, A.; Pfanner, N. The Mitochondrial Proteome: From Inventory to Function. *Cell* **2008**, *134* (1), 22–24. https://doi.org/10.1016/j.cell.2008.06.043.

(63) Bolender, N.; Sickmann, A.; Wagner, R.; Meisinger, C.; Pfanner, N. Multiple Pathways for Sorting Mitochondrial Precursor Proteins. *EMBO Rep.* **2008**, *9* (1), 42–49. https://doi.org/https://doi.org/10.1038/sj.embor.7401126.

(64) Calvo, S. E.; Julien, O.; Clauser, K. R.; Shen, H.; Kamer, K. J.; Wells, J. A.; Mootha, V. K. Comparative Analysis of Mitochondrial N-Termini from Mouse, Human, and Yeast * . *Mol. Cell. Proteomics* **2017**, *16* (4), 512–523. https://doi.org/10.1074/mcp.M116.063818.

(65) Haastrup, M. O.; Vikramdeo, K. S.; Singh, S.; Singh, A. P.; Dasgupta, S. The Journey of

Mitochondrial Protein Import and the Roadmap to Follow. *International Journal of Molecular Sciences*. 2023. https://doi.org/10.3390/ijms24032479.

(66) Nitsch, L.; Lareau, C. A.; Ludwig, L. S. Mitochondrial Genetics through the Lens of Single-Cell Multi-Omics. *Nat. Genet.* **2024**, *56* (7), 1355–1365. https://doi.org/10.1038/s41588-024-01794-8.

(67) Moreira, J. D.; Gopal, D. M.; Kotton, D. N.; Fetterman, J. L. Gaining Insight into Mitochondrial Genetic Variation and Downstream Pathophysiology: What Can i(PSCs) Do? *Genes*. 2021. https://doi.org/10.3390/genes12111668.

(68) Wallace, D. C. Mitochondrial DNA in Evolution and Disease. *Nature* **2016**, *535* (7613), 498–500. https://doi.org/10.1038/nature18902.

(69) Serrano, I. M.; Hirose, M.; Valentine, C. C.; Roesner, S.; Schmidt, E.; Pratt, G.; Williams, L.; Salk, J.; Ibrahim, S.; Sudmant, P. H. Mitochondrial Haplotype and Mito-Nuclear Matching Drive Somatic Mutation and Selection throughout Ageing. *Nat. Ecol. Evol.* **2024**, *8* (5), 1021–1034. https://doi.org/10.1038/s41559-024-02338-3.

(70) Hudson, G.; Gomez-Duran, A.; Wilson, I. J.; Chinnery, P. F. Recent Mitochondrial DNA Mutations Increase the Risk of Developing Common Late-Onset Human Diseases. *PLOS Genet.* **2014**, *10* (5), e1004369.

(71) Filograna, R.; Mennuni, M.; Alsina, D.; Larsson, N.-G. Mitochondrial DNA Copy Number in Human Disease: The More the Better? *FEBS Lett.* **2021**, *595* (8), 976–1002. https://doi.org/https://doi.org/10.1002/1873-3468.14021.

(72) Gupta, R.; Kanai, M.; Durham, T. J.; Tsuo, K.; McCoy, J. G.; Kotrys, A. V; Zhou, W.; Chinnery, P. F.; Karczewski, K. J.; Calvo, S. E.; Neale, B. M.; Mootha, V. K. Nuclear Genetic Control of MtDNA Copy Number and Heteroplasmy in Humans. *Nature* **2023**, *620* (7975), 839–848. https://doi.org/10.1038/s41586-023-06426-5.

(73) Valenti, D.; Vacca, R. A. Primary and Secondary Mitochondrial Diseases: Etiologies and Therapeutic Strategies. *Journal of Clinical Medicine*. 2022. https://doi.org/10.3390/jcm11144209.

(74) Conti, F.; Di Martino, S.; Drago, F.; Bucolo, C.; Micale, V.; Montano, V.; Siciliano, G.; Mancuso, M.; Lopriore, P. Red Flags in Primary Mitochondrial Diseases: What Should We Recognize? *International Journal of Molecular Sciences*. 2023. https://doi.org/10.3390/ijms242316746.

(75) Kuszak, A. J.; Espey, M. G.; Falk, M. J.; Holmbeck, M. A.; Manfredi, G.; Shadel, G. S.; Vernon, H. J.; Zolkipli-Cunningham, Z. Nutritional Interventions for Mitochondrial OXPHOS Deficiencies: Mechanisms and Model Systems. *Annu. Rev. Pathol. Mech. Dis.* **2018**, *13* (Volume 13, 2018), 163–191. https://doi.org/https://doi.org/10.1146/annurev-pathol-020117-043644.

(76) Fryer, R. H.; Bain, J. M.; De Vivo, D. C. Mitochondrial Encephalomyopathy Lactic Acidosis and Stroke-Like Episodes (MELAS): A Case Report and Critical Reappraisal of Treatment Options. *Pediatr. Neurol.* **2016**, *56*, 59–61. https://doi.org/10.1016/j.pediatrneurol.2015.12.010.

(77) Rahman, S. Chapter 4 - Leigh Syndrome. In *Mitochondrial Diseases*; Horvath, R., Hirano, M., Chinnery, P. F. B. T.-H. of C. N., Eds.; Elsevier, 2023; Vol. 194, pp 43–63. https://doi.org/https://doi.org/10.1016/B978-0-12-821751-1.00015-4.

(78) Niyazov, D. M.; Kahler, S. G.; Frye, R. E. Primary Mitochondrial Disease and Secondary Mitochondrial Dysfunction: Importance of Distinction for Diagnosis and Treatment. *Mol. Syndromol.* **2016**, *7* (3), 122–137. https://doi.org/10.1159/000446586.

(79) Diaz-Vegas, A.; Sanchez-Aguilera, P.; Krycer, J. R.; Morales, P. E.; Monsalves-Alvarez, M.; Cifuentes, M.; Rothermel, B. A.; Lavandero, S. Is Mitochondrial Dysfunction a Common Root of Noncommunicable Chronic Diseases? *Endocr. Rev.* **2020**, *41* (3), bnaa005. https://doi.org/10.1210/endrev/bnaa005.

(80) Zong, Y.; Li, H.; Liao, P.; Chen, L.; Pan, Y.; Zheng, Y.; Zhang, C.; Liu, D.; Zheng, M.; Gao, J. Mitochondrial Dysfunction: Mechanisms and Advances in Therapy. *Signal Transduct. Target. Ther.* **2024**, *9* (1), 124. https://doi.org/10.1038/s41392-024-01839-8.

(81) Bhatti, J. S.; Bhatti, G. K.; Reddy, P. H. Mitochondrial Dysfunction and Oxidative Stress in Metabolic Disorders — A Step towards Mitochondria Based Therapeutic Strategies. *Biochim. Biophys. Acta - Mol. Basis Dis.* **2017**, *1863* (5), 1066–1077. https://doi.org/https://doi.org/10.1016/j.bbadis.2016.11.010.

(82) Nakamura, E.; Aoki, T.; Endo, Y.; Kazmi, J.; Hagiwara, J.; Kuschner, C. E.; Yin, T.; Kim, J.; Becker, L. B.; Hayashida, K. Organ-Specific Mitochondrial Alterations Following Ischemia–Reperfusion Injury in Post-Cardiac Arrest Syndrome: A Comprehensive Review. *Life*. 2024. https://doi.org/10.3390/life14040477.

(83) Kuznetsov, A. V; Javadov, S.; Margreiter, R.; Grimm, M.; Hagenbuchner, J.; Ausserlechner, M. J. The Role of Mitochondria in the Mechanisms of Cardiac Ischemia-Reperfusion Injury. *Antioxidants*. 2019. https://doi.org/10.3390/antiox8100454.

(84) Bouhamida, E.; Morciano, G.; Perrone, M.; Kahsay, A. E.; Della Sala, M.; Wieckowski, M. R.; Fiorica, F.; Pinton, P.; Giorgi, C.; Patergnani, S. The Interplay of Hypoxia Signaling on Mitochondrial Dysfunction and Inflammation in Cardiovascular Diseases and Cancer: From Molecular Mechanisms to Therapeutic Approaches. *Biology*. 2022. https://doi.org/10.3390/biology11020300.

(85) Liu, M.; Lv, J.; Pan, Z.; Wang, D.; Zhao, L.; Guo, X. Mitochondrial Dysfunction in Heart Failure and Its Therapeutic Implications. *Front. Cardiovasc. Med.* **2022**, *9*.

(86) Mary, A.; Eysert, F.; Checler, F.; Chami, M. Mitophagy in Alzheimer's Disease: Molecular Defects and Therapeutic Approaches. *Mol. Psychiatry* **2023**, *28* (1), 202–216. https://doi.org/10.1038/s41380-022-01631-6.

(87) Ashleigh, T.; Swerdlow, R. H.; Beal, M. F. The Role of Mitochondrial Dysfunction in Alzheimer's Disease Pathogenesis. *Alzheimer's Dement.* **2023**, *19* (1), 333–342. https://doi.org/https://doi.org/10.1002/alz.12683.

(88) Misrani, A.; Tabassum, S.; Yang, L. Mitochondrial Dysfunction and Oxidative Stress in Alzheimer's Disease. *Front. Aging Neurosci.* **2021**, *13*.

(89) Henrich, M. T.; Oertel, W. H.; Surmeier, D. J.; Geibl, F. F. Mitochondrial Dysfunction in Parkinson's Disease – a Key Disease Hallmark with Therapeutic Potential. *Mol. Neurodegener.* **2023**, *18* (1), 83. https://doi.org/10.1186/s13024-023-00676-7.

(90) Zambrano, K.; Barba, D.; Castillo, K.; Noboa, L.; Argueta-Zamora, D.; Robayo, P.; Arizaga, E.; Caicedo, A.; Gavilanes, A. W. D. Fighting Parkinson's Disease: The Return of the Mitochondria. *Mitochondrion* **2022**, *64*, 34–44. https://doi.org/https://doi.org/10.1016/j.mito.2022.02.003.

(91) She, Y.; Yu, M.; Wang, L.; Wang, Y.; Fang, P.; Zhang, Z. Emerging Protective Actions of PGC-1α in Diabetic Nephropathy. *Oxid. Med. Cell. Longev.* **2022**, *2022* (1), 6580195. https://doi.org/https://doi.org/10.1155/2022/6580195.

(92) Fan, X.; Yang, M.; Lang, Y.; Lu, S.; Kong, Z.; Gao, Y.; Shen, N.; Zhang, D.; Lv, Z. Mitochondrial Metabolic Reprogramming in Diabetic Kidney Disease. *Cell Death Dis.* **2024**, *15* (6), 442. https://doi.org/10.1038/s41419-024-06833-0.

(93) Tulen, C. B. M.; van de Wetering, C.; Schiffers, C. H. J.; Weltjens, E.; Benedikter, B. J.; Leermakers, P. A.; Boukhaled, J. H.; Drittij, M.-J.; Schmeck, B. T.; Reynaert, N. L.; Opperhuizen, A.; van Schooten, F.-J.; Remels, A. H. V. Alterations in the Molecular Control of Mitochondrial Turnover in COPD Lung and Airway Epithelial Cells. *Sci. Rep.* **2024**, *14* (1), 4821. https://doi.org/10.1038/s41598-024-55335-8.

(94) Ryter, S. W.; Rosas, I. O.; Owen, C. A.; Martinez, F. J.; Choi, M. E.; Lee, C. G.; Elias, J. A.; Choi, A. M. K. Mitochondrial Dysfunction as a Pathogenic Mediator of Chronic Obstructive Pulmonary Disease and Idiopathic Pulmonary Fibrosis. *Ann. Am. Thorac. Soc.* **2018**, *15* (Supplement_4), S266–S272. https://doi.org/10.1513/AnnalsATS.201808-585MG.

(95) de Mello, A. H.; Costa, A. B.; Engel, J. D. G.; Rezin, G. T. Mitochondrial Dysfunction in Obesity. *Life Sci.* **2018**, *192*, 26–32. https://doi.org/https://doi.org/10.1016/j.lfs.2017.11.019.

(96) Hartsoe, P.; Holguin, F.; Chu, H. W. Mitochondrial Dysfunction and Metabolic Reprogramming in Obesity and Asthma. *International Journal of Molecular Sciences*. 2024. https://doi.org/10.3390/ijms25052944.

(97) Zhao, J.; Wang, X.; Huo, Z.; Chen, Y.; Liu, J.; Zhao, Z.; Meng, F.; Su, Q.; Bao, W.; Zhang, L.; Wen, S.; Wang, X.; Liu, H.; Zhou, S. The Impact of Mitochondrial Dysfunction in Amyotrophic Lateral Sclerosis. *Cells*. 2022. https://doi.org/10.3390/cells11132049.

(98) Smith, E. F.; Shaw, P. J.; De Vos, K. J. The Role of Mitochondria in Amyotrophic Lateral Sclerosis. *Neurosci. Lett.* **2019**, *710*, 132933. https://doi.org/https://doi.org/10.1016/j.neulet.2017.06.052.

(99) Prasun, P.; Ginevic, I.; Oishi, K. Mitochondrial Dysfunction in Nonalcoholic Fatty Liver Disease and Alcohol Related Liver Disease. *Transl. Gastroenterol. Hepatol. Vol 6 (January 05, 2021) Transl. Gastroenterol. Hepatol.* **2020**.

(100) Zheng, Y.; Wang, S.; Wu, J.; Wang, Y. Mitochondrial Metabolic Dysfunction and Non-Alcoholic Fatty Liver Disease: New Insights from Pathogenic Mechanisms to Clinically Targeted Therapy. *J. Transl. Med.* **2023**, *21* (1), 510. https://doi.org/10.1186/s12967-023-04367-1.

(101) Dai, Y.; Wang, H.; Lian, A.; Li, J.; Zhao, G.; Hu, S.; Li, B. A Comprehensive Perspective of Huntington's Disease and Mitochondrial Dysfunction. *Mitochondrion* **2023**, *70*, 8–19. https://doi.org/https://doi.org/10.1016/j.mito.2023.03.001.

(102) Marino, Y.; Inferrera, F.; D'Amico, R.; Impellizzeri, D.; Cordaro, M.; Siracusa, R.; Gugliandolo, E.; Fusco, R.; Cuzzocrea, S.; Di Paola, R. Role of Mitochondrial Dysfunction and Biogenesis in Fibromyalgia Syndrome: Molecular Mechanism in Central Nervous System. *Biochim. Biophys. Acta - Mol. Basis Dis.* **2024**, *1870* (7), 167301. https://doi.org/https://doi.org/10.1016/j.bbadis.2024.167301.

(103) Braga, P. C.; Alves, M. G.; Rodrigues, A. S.; Oliveira, P. F. Mitochondrial Pathophysiology on Chronic Kidney Disease. *International Journal of Molecular Sciences*. 2022.

https://doi.org/10.3390/ijms23031776.

(104) Wang, S.-F.; Tseng, L.-M.; Lee, H.-C. Role of Mitochondrial Alterations in Human Cancer Progression and Cancer Immunity. *J. Biomed. Sci.* **2023**, *30* (1), 61. https://doi.org/10.1186/s12929-023-00956-w.

(105) Luo, Y.; Ma, J.; Lu, W. The Significance of Mitochondrial Dysfunction in Cancer. *International Journal of Molecular Sciences*. 2020. https://doi.org/10.3390/ijms21165598.

(106) Kowalczyk, P.; Sulejczak, D.; Kleczkowska, P.; Bukowska-Ośko, I.; Kucia, M.; Popiel, M.; Wietrak, E.; Kramkowski, K.; Wrzosek, K.; Kaczyńska, K. Mitochondrial Oxidative Stress—A Causative Factor and Therapeutic Target in Many Diseases. *International Journal of Molecular Sciences*. 2021. https://doi.org/10.3390/ijms222413384.

(107) Klemmensen, M. M.; Borrowman, S. H.; Pearce, C.; Pyles, B.; Chandra, B. Mitochondrial Dysfunction in Neurodegenerative Disorders. *Neurotherapeutics* **2024**, *21* (1). https://doi.org/10.1016/j.neurot.2023.10.002.

(108) Yang, D.; Ying, J.; Wang, X.; Zhao, T.; Yoon, S.; Fang, Y.; Zheng, Q.; Liu, X.; Yu, W.; Hua, F. Mitochondrial Dynamics: A Key Role in Neurodegeneration and a Potential Target for Neurodegenerative Disease. *Front. Neurosci.* **2021**, *15*.

(109) Bustamante-Barrientos, F. A.; Luque-Campos, N.; Araya, M. J.; Lara-Barba, E.; de Solminihac, J.; Pradenas, C.; Molina, L.; Herrera-Luna, Y.; Utreras-Mendoza, Y.; Elizondo-Vega, R.; Vega-Letter, A. M.; Luz-Crawford, P. Mitochondrial Dysfunction in Neurodegenerative Disorders: Potential Therapeutic Application of Mitochondrial Transfer to Central Nervous System-Residing Cells. *J. Transl. Med.* **2023**, *21* (1), 613. https://doi.org/10.1186/s12967-023-04493-w.

(110) Wallace, D. C. Mitochondria and Cancer. *Nat. Rev. Cancer* **2012**, *12* (10), 685–698. https://doi.org/10.1038/nrc3365.

(111) Liberti, M. V; Locasale, J. W. The Warburg Effect: How Does It Benefit Cancer Cells? *Trends Biochem. Sci.* **2016**, *41* (3), 211–218. https://doi.org/10.1016/j.tibs.2015.12.001.

(112) Fendt, S.-M. 100 Years of the Warburg Effect: A Cancer Metabolism Endeavor. *Cell* **2024**, *187* (15), 3824–3828. https://doi.org/10.1016/j.cell.2024.06.026.

(113) Yang, J.; Shay, C.; Saba, N. F.; Teng, Y. Cancer Metabolism and Carcinogenesis. *Exp. Hematol. Oncol.* **2024**, *13* (1), 10. https://doi.org/10.1186/s40164-024-00482-x.

(114) Shuvalov, O.; Daks, A.; Fedorova, O.; Petukhov, A.; Barlev, N. Linking Metabolic Reprogramming, Plasticity and Tumor Progression. *Cancers*. 2021. https://doi.org/10.3390/cancers13040762.

(115) Adhikary, A.; Mukherjee, A.; Banerjee, R.; Nagotu, S. DRP1: At the Crossroads of Dysregulated Mitochondrial Dynamics and Altered Cell Signaling in Cancer Cells. *ACS Omega* **2023**, *8* (48), 45208–45223. https://doi.org/10.1021/acsomega.3c06547.

(116) O'Malley, J.; Kumar, R.; Inigo, J.; Yadava, N.; Chandra, D. Mitochondrial Stress Response and Cancer. *Trends in Cancer* **2020**, *6* (8), 688–701. https://doi.org/10.1016/j.trecan.2020.04.009.

(117) Boulton, D. P.; Caino, M. C. Mitochondrial Fission and Fusion in Tumor Progression to Metastasis. *Front. Cell Dev. Biol.* **2022**, *10*.

(118) Nakamura, H.; Takada, K. Reactive Oxygen Species in Cancer: Current Findings and Future Directions. *Cancer Sci.* **2021**, *112* (10), 3945–3952. https://doi.org/https://doi.org/10.1111/cas.15068.

(119) Zhou, X.; An, B.; Lin, Y.; Ni, Y.; Zhao, X.; Liang, X. Molecular Mechanisms of ROS-Modulated Cancer Chemoresistance and Therapeutic Strategies. *Biomed. Pharmacother.* **2023**, *165*, 115036. https://doi.org/https://doi.org/10.1016/j.biopha.2023.115036.

(120) Das, P.; Chatterjee, K.; Choudhuri, T. ROS Induced Regulatory Crosstalk with Autophagy and AKT/MTOR Signaling in Cancer Cells BT - Handbook of Oxidative Stress in Cancer: Mechanistic Aspects; Chakraborti, S., Ray, B. K., Roychowdhury, S., Eds.; Springer Singapore: Singapore, 2020; pp 1–14. https://doi.org/10.1007/978-981-15-4501-6_84-1.

(121) Zhao, Y.; Xing, C.; Deng, Y.; Ye, C.; Peng, H. HIF-1α Signaling: Essential Roles in Tumorigenesis and Implications in Targeted Therapies. *Genes Dis.* **2024**, *11* (1), 234–251. https://doi.org/https://doi.org/10.1016/j.gendis.2023.02.039.

(122) Winter, J. M.; Yadav, T.; Rutter, J. Stressed to Death: Mitochondrial Stress Responses Connect Respiration and Apoptosis in Cancer. *Mol. Cell* **2022**, *82* (18), 3321–3332. https://doi.org/10.1016/j.molcel.2022.07.012.

(123) Sassano, M. L.; van Vliet, A. R.; Agostinis, P. Mitochondria-Associated Membranes As Networking Platforms and Regulators of Cancer Cell Fate. *Front. Oncol.* **2017**, *7*.

(124) Huang, A.; Xue, H.; Xie, T.; Xiang, L.; Chen, Z.; Ma, A.; Yan, H.; Yuan, J. A Review of the Pathogenesis of Mitochondria in Breast Cancer and Progress of Targeting Mitochondria for Breast Cancer Treatment. *J. Transl. Med.* **2025**, *23* (1), 70. https://doi.org/10.1186/s12967-025-06077-2.

(125) Baek, M. L.; Lee, J.; Pendleton, K. E.; Berner, M. J.; Goff, E. B.; Tan, L.; Martinez, S. A.; Mahmud, I.; Wang, T.; Meyer, M. D.; Lim, B.; Barrish, J. P.; Porter, W.; Lorenzi, P. L.; Echeverria, G. V. Mitochondrial Structure and Function Adaptation in Residual Triple Negative Breast Cancer Cells Surviving Chemotherapy Treatment. *Oncogene* **2023**, *42* (14), 1117–1131. https://doi.org/10.1038/s41388-023-02596-8.

(126) Sun, X.; Wang, M.; Wang, M.; Yu, X.; Guo, J.; Sun, T.; Li, X.; Yao, L.; Dong, H.; Xu, Y. Metabolic Reprogramming in Triple-Negative Breast Cancer. *Front. Oncol.* **2020**, *10*.

(127) Erasmo Orrantia-Borunda; Patricia Anchondo-Nuñez; Lucero Evelia Acuña-Aguilar; Francisco Octavio Gómez-Valles; Claudia Adriana Ramírez-Valdespino. Subtypes of Breast Cancer. *Breast Cancer* **2022**, 31–42.

(128) Zagami, P.; Carey, L. A. Triple Negative Breast Cancer: Pitfalls and Progress. *npj Breast Cancer* **2022**, *8* (1), 95. https://doi.org/10.1038/s41523-022-00468-0.

(129) Giaquinto, A. N.; Sung, H.; Newman, L. A.; Freedman, R. A.; Smith, R. A.; Star, J.; Jemal, A.; Siegel, R. L. Breast Cancer Statistics 2024. *CA. Cancer J. Clin.* **2024**, *74* (6), 477–495. https://doi.org/https://doi.org/10.3322/caac.21863.

(130) O'Reilly, D.; Sendi, M. Al; Kelly, C. M. Overview of Recent Advances in Metastatic Triple Negative Breast Cancer. *World J. Clin. Oncol.* **2021**, *12* (3), 164–182. https://doi.org/10.5306/wjco.v12.i3.164.

(131) Zong, Y.; Pegram, M. Research Advances and New Challenges in Overcoming Triple-Negative

Breast Cancer. *Cancer Drug Resist.* **2021**, *4* (3), 517–542. https://doi.org/10.20517/cdr.2021.04.

(132) Zhao, S.; Zuo, W.-J.; Shao, Z.-M.; Jiang, Y.-Z. Molecular Subtypes and Precision Treatment of Triple-Negative Breast Cancer. *Ann. Transl. Med. Vol 8, No 7 (April 16, 2020) Ann. Transl. Med.* **2020**.

(133) Yang, R.; Li, Y.; Wang, H.; Qin, T.; Yin, X.; Ma, X. Therapeutic Progress and Challenges for Triple Negative Breast Cancer: Targeted Therapy and Immunotherapy. *Mol. Biomed.* **2022**, *3* (1), 8. https://doi.org/10.1186/s43556-022-00071-6.

(134) Boix-Montesinos, P.; Soriano-Teruel, P. M.; Armiñán, A.; Orzáez, M.; Vicent, M. J. The Past, Present, and Future of Breast Cancer Models for Nanomedicine Development. *Adv. Drug Deliv. Rev.* **2021**, *173*, 306–330. https://doi.org/https://doi.org/10.1016/j.addr.2021.03.018.

(135) Lunetti, P.; Di Giacomo, M.; Vergara, D.; De Domenico, S.; Maffia, M.; Zara, V.; Capobianco, L.; Ferramosca, A. Metabolic Reprogramming in Breast Cancer Results in Distinct Mitochondrial Bioenergetics between Luminal and Basal Subtypes. *FEBS J.* **2019**, *286* (4), 688–709. https://doi.org/https://doi.org/10.1111/febs.14756.

(136) Wang, Z.; Jiang, Q.; Dong, C. Metabolic Reprogramming in Triple-Negative Breast Cancer. *Cancer Biol. Med.* **2020**, *17* (1), 44 LP – 59. https://doi.org/10.20892/j.issn.2095-3941.2019.0210.

(137) Shin, E.; Koo, J. S. Glucose Metabolism and Glucose Transporters in Breast Cancer. *Front. Cell Dev. Biol.* **2021**, *9*.

(138) Hay, N. Reprogramming Glucose Metabolism in Cancer: Can It Be Exploited for Cancer Therapy? *Nat. Rev. Cancer* **2016**, *16* (10), 635–649. https://doi.org/10.1038/nrc.2016.77.

(139) Quek, L.-E.; van Geldermalsen, M.; Guan, Y. F.; Wahi, K.; Mayoh, C.; Balaban, S.; Pang, A.; Wang, Q.; Cowley, M. J.; Brown, K. K.; Turner, N.; Hoy, A. J.; Holst, J. Glutamine Addiction Promotes Glucose Oxidation in Triple-Negative Breast Cancer. *Oncogene* **2022**, *41* (34), 4066–4078. https://doi.org/10.1038/s41388-022-02408-5.

(140) Jin, J.; Byun, J.-K.; Choi, Y.-K.; Park, K.-G. Targeting Glutamine Metabolism as a Therapeutic Strategy for Cancer. *Exp. Mol. Med.* **2023**, *55* (4), 706–715. https://doi.org/10.1038/s12276-023-00971-9.

(141) Li, Z.; Wang, Q.; Huang, X.; Yang, M.; Zhou, S.; Li, Z.; Fang, Z.; Tang, Y.; Chen, Q.; Hou, H.; Li, L.; Fei, F.; Wang, Q.; Wu, Y.; Gong, A. Lactate in the Tumor Microenvironment: A Rising Star for Targeted Tumor Therapy. *Front. Nutr.* **2023**, *10*.

(142) Zhang, F.; Ma, Y.; Li, D.; Wei, J.; Chen, K.; Zhang, E.; Liu, G.; Chu, X.; Liu, X.; Liu, W.; Tian, X.; Yang, Y. Cancer Associated Fibroblasts and Metabolic Reprogramming: Unraveling the Intricate Crosstalk in Tumor Evolution. *J. Hematol. Oncol.* **2024**, *17* (1), 80. https://doi.org/10.1186/s13045-024-01600-2.

(143) Dong, T.; Kang, X.; Liu, Z.; Zhao, S.; Ma, W.; Xuan, Q.; Liu, H.; Wang, Z.; Zhang, Q. Altered Glycometabolism Affects Both Clinical Features and Prognosis of Triple-Negative and Neoadjuvant Chemotherapy-Treated Breast Cancer. *Tumor Biol.* **2016**, *37* (6), 8159–8168. https://doi.org/10.1007/s13277-015-4729-8.

(144) Liu, S.; Li, Y.; Yuan, M.; Song, Q.; Liu, M. Correlation between the Warburg Effect and

Progression of Triple-Negative Breast Cancer. *Front. Oncol.* **2023**, *12*.

(145) Zhang, Y.; Wu, M.-J.; Lu, W.-C.; Li, Y.-C.; Chang, C. J.; Yang, J.-Y. Metabolic Switch Regulates Lineage Plasticity and Induces Synthetic Lethality in Triple-Negative Breast Cancer. *Cell Metab.* **2024**, *36* (1), 193-208.e8. https://doi.org/10.1016/j.cmet.2023.12.003.

(146) Tan, Z.; Zou, Y.; Zhu, M.; Luo, Z.; Wu, T.; Zheng, C.; Xie, A.; Wang, H.; Fang, S.; Liu, S.; Li, Y.; Lu, Z. Carnitine Palmitoyl Transferase 1A Is a Novel Diagnostic and Predictive Biomarker for Breast Cancer. *BMC Cancer* **2021**, *21* (1), 409. https://doi.org/10.1186/s12885-021-08134-7.

(147) Wright, H. J.; Hou, J.; Xu, B.; Cortez, M.; Potma, E. O.; Tromberg, B. J.; Razorenova, O. V. CDCP1 Drives Triple-Negative Breast Cancer Metastasis through Reduction of Lipid-Droplet Abundance and Stimulation of Fatty Acid Oxidation. *Proc. Natl. Acad. Sci.* **2017**, *114* (32), E6556–E6565. https://doi.org/10.1073/pnas.1703791114.

(148) Rawling, T.; Choucair, H.; Koolaji, N.; Bourget, K.; Allison, S. E.; Chen, Y.-J.; Dunstan, C. R.; Murray, M. A Novel Arylurea Fatty Acid That Targets the Mitochondrion and Depletes Cardiolipin To Promote Killing of Breast Cancer Cells. *J. Med. Chem.* **2017**, *60* (20), 8661–8666. https://doi.org/10.1021/acs.jmedchem.7b00701.

(149) Hardy, S.; El-Assaad, W.; Przybytkowski, E.; Joly, E.; Prentki, M.; Langelier, Y. Saturated Fatty Acid-Induced Apoptosis in MDA-MB-231 Breast Cancer Cells: A ROLE FOR CARDIOLIPIN *. *J. Biol. Chem.* **2003**, *278* (34), 31861–31870. https://doi.org/10.1074/jbc.M300190200.

(150) Terao, M.; Goracci, L.; Celestini, V.; Kurosaki, M.; Bolis, M.; Di Veroli, A.; Vallerga, A.; Fratelli, M.; Lupi, M.; Corbelli, A.; Fiordaliso, F.; Gianni, M.; Paroni, G.; Zanetti, A.; Cruciani, G.; Garattini, E. Role of Mitochondria and Cardiolipins in Growth Inhibition of Breast Cancer Cells by Retinoic Acid. *J. Exp. Clin. Cancer Res.* **2019**, *38* (1), 436. https://doi.org/10.1186/s13046-019-1438-y.

(151) Humphries, B. A.; Cutter, A. C.; Buschhaus, J. M.; Chen, Y.-C.; Qyli, T.; Palagama, D. S. W.; Eckley, S.; Robison, T. H.; Bevoor, A.; Chiang, B.; Haley, H. R.; Sahoo, S.; Spinosa, P. C.; Neale, D. B.; Boppisetti, J.; Sahoo, D.; Ghosh, P.; Lahann, J.; Ross, B. D.; Yoon, E.; Luker, K. E.; Luker, G. D. Enhanced Mitochondrial Fission Suppresses Signaling and Metastasis in Triple-Negative Breast Cancer. *Breast Cancer Res.* **2020**, *22* (1), 60. https://doi.org/10.1186/s13058-020-01301-x.

(152) Humphries, B. A.; Zhang, A.; Buschhaus, J. M.; Bevoor, A.; Farfel, A.; Rajendran, S.; Cutter, A. C.; Luker, G. D. Enhanced Mitochondrial Fission Inhibits Triple-Negative Breast Cancer Cell Migration through an ROS-Dependent Mechanism. *iScience* **2023**, *26* (6). https://doi.org/10.1016/j.isci.2023.106788.

(153) Wang, Y.; Harada-Shoji, N.; Kitamura, N.; Yamazaki, Y.; Ebata, A.; Amari, M.; Watanabe, M.; Miyashita, M.; Tada, H.; Abe, T.; Suzuki, T.; Gonda, K.; Ishida, T. Mitochondrial Dynamics as a Novel Treatment Strategy for Triple-Negative Breast Cancer. *Cancer Med.* **2024**, *13* (2), e6987. https://doi.org/https://doi.org/10.1002/cam4.6987.

(154) Kuang, J.; Liu, H.; Feng, L.; Xue, Y.; Tang, H.; Xu, P. How Mitochondrial Dynamics Imbalance Affects the Progression of Breast Cancer:A Mini Review. *Med. Oncol.* **2024**, *41* (10), 238. https://doi.org/10.1007/s12032-024-02479-2.

(155) Perillo, B.; Di Donato, M.; Pezone, A.; Di Zazzo, E.; Giovannelli, P.; Galasso, G.; Castoria, G.; Migliaccio, A. ROS in Cancer Therapy: The Bright Side of the Moon. *Exp. Mol. Med.* **2020**, *52*

(2), 192–203. https://doi.org/10.1038/s12276-020-0384-2.

(156) Glorieux, C.; Liu, S.; Trachootham, D.; Huang, P. Targeting ROS in Cancer: Rationale and Strategies. *Nat. Rev. Drug Discov.* **2024**, *23* (8), 583–606. https://doi.org/10.1038/s41573-024-00979-4.

(157) Zhi, S.; Chen, C.; Huang, H.; Zhang, Z.; Zeng, F.; Zhang, S. Hypoxia-Inducible Factor in Breast Cancer: Role and Target for Breast Cancer Treatment. *Front. Immunol.* **2024**, *15*.

(158) Koundouros, N.; Poulogiannis, G. Phosphoinositide 3-Kinase/Akt Signaling and Redox Metabolism in Cancer. *Front. Oncol.* **2018**, *8*.

(159) Li, J.; Xu, X.; Huang, H.; Li, L.; Chen, J.; Ding, Y.; Ping, J. Pink1 Promotes Cell Proliferation and Affects Glycolysis in Breast Cancer. *Exp. Biol. Med.* **2022**, *247* (12), 985–995. https://doi.org/10.1177/15353702221082613.

(160) Chen, C.; Xiang, A.; Lin, X.; Guo, J.; Liu, J.; Hu, S.; Rui, T.; Ye, Q. Mitophagy: Insights into Its Signaling Molecules, Biological Functions, and Therapeutic Potential in Breast Cancer. *Cell Death Discov.* **2024**, *10* (1), 457. https://doi.org/10.1038/s41420-024-02226-6.

(161) Singh, T.; Sharma, K.; Jena, L.; Kaur, P.; Singh, S.; Munshi, A. Mitochondrial Bioenergetics of Breast Cancer. *Mitochondrion* **2024**, *79*, 101951. https://doi.org/https://doi.org/10.1016/j.mito.2024.101951.

(162) Nocquet, L.; Roul, J.; Lefebvre, C. C.; Duarte, L.; Campone, M.; Juin, P. P.; Souazé, F. Low BCL-XL Expression in Triple-Negative Breast Cancer Cells Favors Chemotherapy Efficacy, and This Effect Is Limited by Cancer-Associated Fibroblasts. *Sci. Rep.* **2024**, *14* (1), 14177. https://doi.org/10.1038/s41598-024-64696-z.

(163) Celia, C.; Teesalu, T.; Santos, H. A. Unlocking the Potential of Nanomedicine: Advances in Precision Targeting Strategies. *Drug Deliv. Transl. Res.* **2024**, *14* (10), 2593–2597. https://doi.org/10.1007/s13346-024-01686-8.

(164) Xie, M.; Xu, Y.; Huang, J.; Li, Y.; Wang, L.; Yang, L.; Mao, H. Going Even Smaller: Engineering Sub-5 Nm Nanoparticles for Improved Delivery, Biocompatibility, and Functionality. *WIREs Nanomedicine and Nanobiotechnology* **2020**, *12* (6), e1644. https://doi.org/https://doi.org/10.1002/wnan.1644.

(165) Kaymaz, S. V.; Nobar, H. M.; Sarıgül, H.; Soylukan, C.; Akyüz, L.; Yüce, M. Nanomaterial Surface Modification Toolkit: Principles, Components, Recipes, and Applications. *Adv. Colloid Interface Sci.* **2023**, *322*, 103035. https://doi.org/https://doi.org/10.1016/j.cis.2023.103035.

(166) Zhang, C.; Yan, L.; Wang, X.; Zhu, S.; Chen, C.; Gu, Z.; Zhao, Y. Progress, Challenges, and Future of Nanomedicine. *Nano Today* **2020**, *35*, 101008. https://doi.org/https://doi.org/10.1016/j.nantod.2020.101008.

(167) Barenholz, Y. (Chezy). Doxil® — The First FDA-Approved Nano-Drug: Lessons Learned. *J. Control. Release* **2012**, *160* (2), 117–134. https://doi.org/https://doi.org/10.1016/j.jconrel.2012.03.020.

(168) Đorđević, S.; Gonzalez, M. M.; Conejos-Sánchez, I.; Carreira, B.; Pozzi, S.; Acúrcio, R. C.; Satchi-Fainaro, R.; Florindo, H. F.; Vicent, M. J. Current Hurdles to the Translation of Nanomedicines from Bench to the Clinic. *Drug Delivery and Translational Research*. 2022. https://doi.org/10.1007/s13346-021-01024-2.

(169) R., B. L.; M., E. S. H.; Brandon, E.; Karen, K.; Sharon, F.; Rick, N.; David, D.; A., S. S.; Nadine, R.; Buddy, C. C.; John, M.; Shishir, K.; Nathan, S.; Joel, S.; Adam, B.; Carlos, F.; Howard, S.; Kathleen, N.; Lawrence, C.; Peter, G.; Holly, J.; Dean, F.; Mary, M.; John, M.; Laura, P.; Julie, L.; S., G. B.; Hamilton, B.; Rolando, P.; Conor, K.; Brett, L.; Weiping, D.; Honghong, Z.; Shu, H.; Melanie, I.; Jacqueline, M.; Tal, Z. Efficacy and Safety of the MRNA-1273 SARS-CoV-2 Vaccine. *N. Engl. J. Med.* **2021**, *384* (5), 403–416. https://doi.org/10.1056/NEJMoa2035389.

(170) Shan, X.; Gong, X.; Li, J.; Wen, J.; Li, Y.; Zhang, Z. Current Approaches of Nanomedicines in the Market and Various Stage of Clinical Translation. *Acta Pharm. Sin. B* **2022**, *12* (7), 3028–3048. https://doi.org/https://doi.org/10.1016/j.apsb.2022.02.025.

(171) Subhan, M. A.; Parveen, F.; Filipczak, N.; Yalamarty, S. S.; Torchilin, V. P. Approaches to Improve EPR-Based Drug Delivery for Cancer Therapy and Diagnosis. *Journal of Personalized Medicine*. 2023. https://doi.org/10.3390/jpm13030389.

(172) Ikeda-Imafuku, M.; Wang, L. L.-W.; Rodrigues, D.; Shaha, S.; Zhao, Z.; Mitragotri, S. Strategies to Improve the EPR Effect: A Mechanistic Perspective and Clinical Translation. *J. Control. Release* **2022**, *345*, 512–536. https://doi.org/https://doi.org/10.1016/j.jconrel.2022.03.043.

(173) Zhou, Q.; Li, J.; Xiang, J.; Shao, S.; Zhou, Z.; Tang, J.; Shen, Y. Transcytosis-Enabled Active Extravasation of Tumor Nanomedicine. *Adv. Drug Deliv. Rev.* **2022**, *189*, 114480. https://doi.org/https://doi.org/10.1016/j.addr.2022.114480.

(174) Awad, N. S.; Salkho, N. M.; Abuwatfa, W. H.; Paul, V.; AlSawaftah, N. M.; Husseini, G. A. Tumor Vasculature vs Tumor Cell Targeting: Understanding the Latest Trends in Using Functional Nanoparticles for Cancer Treatment. *OpenNano* **2023**, *11*, 100136. https://doi.org/https://doi.org/10.1016/j.onano.2023.100136.

(175) Chen, Q.; Yuan, L.; Chou, W.-C.; Cheng, Y.-H.; He, C.; Monteiro-Riviere, N. A.; Riviere, J. E.; Lin, Z. Meta-Analysis of Nanoparticle Distribution in Tumors and Major Organs in Tumor-Bearing Mice. *ACS Nano* **2023**, *17* (20), 19810–19831. https://doi.org/10.1021/acsnano.3c04037.

(176) He, W.; Gao, H.; Wu, W. Nanomedicine Biointeractions during Body Trafficking. *Adv. Drug Deliv. Rev.* **2024**, *209*, 115324. https://doi.org/https://doi.org/10.1016/j.addr.2024.115324.

(177) Fu, X.; Shi, Y.; Qi, T.; Qiu, S.; Huang, Y.; Zhao, X.; Sun, Q.; Lin, G. Precise Design Strategies of Nanomedicine for Improving Cancer Therapeutic Efficacy Using Subcellular Targeting. *Signal Transduct. Target. Ther.* **2020**, *5* (1), 262. https://doi.org/10.1038/s41392-020-00342-0.

(178) Zhang, Y.-N.; Poon, W.; Tavares, A. J.; McGilvray, I. D.; Chan, W. C. W. Nanoparticle–Liver Interactions: Cellular Uptake and Hepatobiliary Elimination. *J. Control. Release* **2016**, *240*, 332–348. https://doi.org/https://doi.org/10.1016/j.jconrel.2016.01.020.

(179) Huang, W.; Xiao, G.; Zhang, Y.; Min, W. Research Progress and Application Opportunities of Nanoparticle–Protein Corona Complexes. *Biomed. Pharmacother.* **2021**, *139*, 111541. https://doi.org/https://doi.org/10.1016/j.biopha.2021.111541.

(180) Mahmoudi, M.; Landry, M. P.; Moore, A.; Coreas, R. The Protein Corona from Nanomedicine to Environmental Science. *Nat. Rev. Mater.* **2023**, *8* (7), 422–438. https://doi.org/10.1038/s41578-023-00552-2.

(181) Ren, J.; Andrikopoulos, N.; Velonia, K.; Tang, H.; Cai, R.; Ding, F.; Ke, P. C.; Chen, C. Chemical and Biophysical Signatures of the Protein Corona in Nanomedicine. *J. Am. Chem. Soc.* **2022**, *144* (21), 9184–9205. https://doi.org/10.1021/jacs.2c02277.

(182) Ilinskaya, A. N.; Dobrovolskaia, M. A. Understanding the Immunogenicity and Antigenicity of Nanomaterials: Past, Present and Future. *Toxicol. Appl. Pharmacol.* **2016**, *299*, 70–77. https://doi.org/https://doi.org/10.1016/j.taap.2016.01.005.

(183) Hoang Thi, T. T.; Pilkington, E. H.; Nguyen, D. H.; Lee, J. S.; Park, K. D.; Truong, N. P. The Importance of Poly(Ethylene Glycol) Alternatives for Overcoming PEG Immunogenicity in Drug Delivery and Bioconjugation. *Polymers*. 2020. https://doi.org/10.3390/polym12020298.

(184) Qian, H.; Wang, K.; Lv, M.; Zhao, C.; Wang, H.; Wen, S.; Huang, D.; Chen, W.; Zhong, Y. Recent Advances on next Generation of Polyzwitterion-Based Nano-Vectors for Targeted Drug Delivery. *J. Control. Release* **2022**, *343*, 492–505. https://doi.org/https://doi.org/10.1016/j.jconrel.2022.02.004.

(185) Zhang, Z.; Sun, H.; Giannino, J.; Wu, Y.; Cheng, C. Biodegradable Zwitterionic Polymers as PEG Alternatives for Drug Delivery. *J. Polym. Sci.* **2024**, *62* (10), 2231–2250. https://doi.org/https://doi.org/10.1002/pol.20230916.

(186) Yao, X.; Qi, C.; Sun, C.; Huo, F.; Jiang, X. Poly(Ethylene Glycol) Alternatives in Biomedical Applications. *Nano Today* **2023**, *48*, 101738. https://doi.org/https://doi.org/10.1016/j.nantod.2022.101738.

(187) Banskota, S.; Saha, S.; Bhattacharya, J.; Kirmani, N.; Yousefpour, P.; Dzuricky, M.; Zakharov, N.; Li, X.; Spasojevic, I.; Young, K.; Chilkoti, A. Genetically Encoded Stealth Nanoparticles of a Zwitterionic Polypeptide-Paclitaxel Conjugate Have a Wider Therapeutic Window than Abraxane in Multiple Tumor Models. *Nano Lett.* **2020**, *20* (4), 2396–2409. https://doi.org/10.1021/acs.nanolett.9b05094.

(188) Zinger, A. Unleashing the Potential of Cell Biomimetic Nanoparticles: Strategies and Challenges in Their Design and Fabrication for Therapeutic Applications. *J. Control. Release* **2023**, *358*, 591–600. https://doi.org/https://doi.org/10.1016/j.jconrel.2023.04.040.

(189) Li, J.; Huang, D.; Cheng, R.; Figueiredo, P.; Fontana, F.; Correia, A.; Wang, S.; Liu, Z.; Kemell, M.; Torrieri, G.; Mäkilä, E. M.; Salonen, J. J.; Hirvonen, J.; Gao, Y.; Li, J.; Luo, Z.; Santos, H. A.; Xia, B. Multifunctional Biomimetic Nanovaccines Based on Photothermal and Weak-Immunostimulatory Nanoparticulate Cores for the Immunotherapy of Solid Tumors. *Adv. Mater.* **2022**, *34* (9), 2108012. https://doi.org/https://doi.org/10.1002/adma.202108012.

(190) Nakamura, Y.; Mochida, A.; Choyke, P. L.; Kobayashi, H. Nanodrug Delivery: Is the Enhanced Permeability and Retention Effect Sufficient for Curing Cancer? *Bioconjug. Chem.* **2016**, *27* (10), 2225–2238. https://doi.org/10.1021/acs.bioconjchem.6b00437.

(191) Wang, Y.; Deng, T.; Liu, X.; Fang, X.; Mo, Y.; Xie, N.; Nie, G.; Zhang, B.; Fan, X. Smart Nanoplatforms Responding to the Tumor Microenvironment for Precise Drug Delivery in Cancer Therapy. *Int. J. Nanomedicine* **2024**, *19* (May), 6253–6277. https://doi.org/10.2147/IJN.S459710.

(192) Gao, J.; Jiang, X.; Lei, S.; Cheng, W.; Lai, Y.; Li, M.; Yang, L.; Liu, P.; Chen, X.; Huang, M.; Yu, H.; Xu, H.; Xu, Z. A Region-Confined PROTAC Nanoplatform for Spatiotemporally Tunable Protein Degradation and Enhanced Cancer Therapy. *Nat. Commun.* **2024**, *15* (1), 6608. https://doi.org/10.1038/s41467-024-50735-w.

(193) Xu, J.; Song, M.; Fang, Z.; Zheng, L.; Huang, X.; Liu, K. Applications and Challenges of Ultra-Small Particle Size Nanoparticles in Tumor Therapy. *J. Control. Release* **2023**, *353*, 699–712.

https://doi.org/https://doi.org/10.1016/j.jconrel.2022.12.028.

(194) Han, D.; Qi, H.; Huang, K.; Li, X.; Zhan, Q.; Zhao, J.; Hou, X.; Yang, X.; Kang, C.; Yuan, X. The Effects of Surface Charge on the Intra-Tumor Penetration of Drug Delivery Vehicles with Tumor Progression. *J. Mater. Chem. B* **2018**, *6* (20), 3331–3339. https://doi.org/10.1039/C8TB00038G.

(195) Souri, M.; Golzaryan, A.; Soltani, M. Charge-Switchable Nanoparticles to Enhance Tumor Penetration and Accumulation. *Eur. J. Pharm. Biopharm.* **2024**, *199*, 114310. https://doi.org/https://doi.org/10.1016/j.ejpb.2024.114310.

(196) Munir, M. U. Nanomedicine Penetration to Tumor: Challenges, and Advanced Strategies to Tackle This Issue. *Cancers*. 2022. https://doi.org/10.3390/cancers14122904.

(197) Deng, H.; Song, K.; Zhang, J.; Deng, L.; Dong, A.; Qin, Z. Modulating the Rigidity of Nanoparticles for Tumor Penetration. *Chem. Commun.* **2018**, *54* (24), 3014–3017. https://doi.org/10.1039/C8CC00398J.

(198) Xu, C.; Sun, Y.; Yu, Y.; Hu, M.; Yang, C.; Zhang, Z. A Sequentially Responsive and Structure-Transformable Nanoparticle with a Comprehensively Improved 'CAPIR Cascade' for Enhanced Antitumor Effect. *Nanoscale* **2019**, *11* (3), 1177–1194. https://doi.org/10.1039/C8NR08781D.

(199) Griffiths, G.; Gruenberg, J.; Marsh, M.; Wohlmann, J.; Jones, A. T.; Parton, R. G. Nanoparticle Entry into Cells; the Cell Biology Weak Link. *Adv. Drug Deliv. Rev.* **2022**, *188*, 114403. https://doi.org/https://doi.org/10.1016/j.addr.2022.114403.

(200) Rennick, J. J.; Johnston, A. P. R.; Parton, R. G. Key Principles and Methods for Studying the Endocytosis of Biological and Nanoparticle Therapeutics. *Nat. Nanotechnol.* **2021**, *16* (3), 266–276. https://doi.org/10.1038/s41565-021-00858-8.

(201) Sousa de Almeida, M.; Susnik, E.; Drasler, B.; Taladriz-Blanco, P.; Petri-Fink, A.; Rothen-Rutishauser, B. Understanding Nanoparticle Endocytosis to Improve Targeting Strategies in Nanomedicine. *Chem. Soc. Rev.* **2021**, *50* (9), 5397–5434. https://doi.org/10.1039/D0CS01127D.

(202) Cullen, P. J.; Steinberg, F. To Degrade or Not to Degrade: Mechanisms and Significance of Endocytic Recycling. *Nat. Rev. Mol. Cell Biol.* **2018**, *19* (11), 679–696. https://doi.org/10.1038/s41580-018-0053-7.

(203) McMahon, H. T.; Boucrot, E. Molecular Mechanism and Physiological Functions of Clathrin-Mediated Endocytosis. *Nat. Rev. Mol. Cell Biol.* **2011**, *12* (8), 517–533. https://doi.org/10.1038/nrm3151.

(204) Mayor, S.; Pagano, R. E. Pathways of Clathrin-Independent Endocytosis. *Nat. Rev. Mol. Cell Biol.* **2007**, *8* (8), 603–612. https://doi.org/10.1038/nrm2216.

(205) Donahue, N. D.; Acar, H.; Wilhelm, S. Concepts of Nanoparticle Cellular Uptake, Intracellular Trafficking, and Kinetics in Nanomedicine. *Adv. Drug Deliv. Rev.* **2019**, *143*, 68–96. https://doi.org/https://doi.org/10.1016/j.addr.2019.04.008.

(206) Sahay, G.; Alakhova, D. Y.; Kabanov, A. V. Endocytosis of Nanomedicines. *J. Control. Release* **2010**, *145* (3), 182–195. https://doi.org/https://doi.org/10.1016/j.jconrel.2010.01.036.

(207) Kiss, A. L.; Botos, E. Endocytosis via Caveolae: Alternative Pathway with Distinct Cellular Compartments to Avoid Lysosomal Degradation? *J. Cell. Mol. Med.* **2009**, *13* (7), 1228–1237.

https://doi.org/https://doi.org/10.1111/j.1582-4934.2009.00754.x.

(208) Choi, S.; Maeng, Y.-S.; Kim, T.; Lee, Y.; Kim, Y.-S.; Kim, E. K. Lysosomal Trafficking of TGFBIp via Caveolae-Mediated Endocytosis. *PLoS One* **2015**, *10* (4), e0119561.

(209) Hayer, A.; Stoeber, M.; Ritz, D.; Engel, S.; Meyer, H. H.; Helenius, A. Caveolin-1 Is Ubiquitinated and Targeted to Intralumenal Vesicles in Endolysosomes for Degradation. *J. Cell Biol.* **2010**, *191* (3), 615–629. https://doi.org/10.1083/jcb.201003086.

(210) Parton, R. G.; Howes, M. T. Revisiting Caveolin Trafficking: The End of the Caveosome. *J. Cell Biol.* **2010**, *191* (3), 439–441. https://doi.org/10.1083/jcb.201009093.

(211) Behzadi, S.; Serpooshan, V.; Tao, W.; Hamaly, M. A.; Alkawareek, M. Y.; Dreaden, E. C.; Brown, D.; Alkilany, A. M.; Farokhzad, O. C.; Mahmoudi, M. Cellular Uptake of Nanoparticles: Journey inside the Cell. *Chem. Soc. Rev.* **2017**, *46* (14), 4218–4244. https://doi.org/10.1039/c6cs00636a.

(212) Li, Q.; Chan, C.; Peterson, N.; Hanna, R. N.; Alfaro, A.; Allen, K. L.; Wu, H.; Dall'Acqua, W. F.; Borrok, M. J.; Santos, J. L. Engineering Caveolae-Targeted Lipid Nanoparticles To Deliver MRNA to the Lungs. *ACS Chem. Biol.* **2020**, *15* (4), 830–836. https://doi.org/10.1021/acschembio.0c00003.

(213) Pérez-Verdaguer, M.; Capera, J.; Martínez-Mármol, R.; Camps, M.; Comes, N.; Tamkun, M. M.; Felipe, A. Caveolin Interaction Governs Kv1.3 Lipid Raft Targeting. *Sci. Rep.* **2016**, *6* (1), 22453. https://doi.org/10.1038/srep22453.

(214) Qiu, Z.; Liu, W.; Zhu, Q.; Ke, K.; Zhu, Q.; Jin, W.; Yu, S.; Yang, Z.; Li, L.; Sun, X.; Ren, S.; Liu, Y.; Zhu, Z.; Zeng, J.; Huang, X.; Huang, Y.; Wei, L.; Ma, M.; Lu, J.; Chen, X.; Mou, Y.; Xie, T.; Sui, X. The Role and Therapeutic Potential of Macropinocytosis in Cancer. *Front. Pharmacol.* **2022**, *13*.

(215) Li, Y.-X.; Pang, H.-B. Macropinocytosis as a Cell Entry Route for Peptide-Functionalized and Bystander Nanoparticles. *J. Control. Release* **2021**, *329*, 1222–1230. https://doi.org/https://doi.org/10.1016/j.jconrel.2020.10.049.

(216) Means, N.; Elechalawar, C. K.; Chen, W. R.; Bhattacharya, R.; Mukherjee, P. Revealing Macropinocytosis Using Nanoparticles. *Mol. Aspects Med.* **2022**, *83*, 100993. https://doi.org/https://doi.org/10.1016/j.mam.2021.100993.

(217) Shafaq-Zadah, M.; Dransart, E.; Johannes, L. Clathrin-Independent Endocytosis, Retrograde Trafficking, and Cell Polarity. *Curr. Opin. Cell Biol.* **2020**, *65*, 112–121. https://doi.org/https://doi.org/10.1016/j.ceb.2020.05.009.

(218) Zhao, J.; Stenzel, M. H. Entry of Nanoparticles into Cells: The Importance of Nanoparticle Properties. *Polym. Chem.* **2018**, *9* (3), 259–272. https://doi.org/10.1039/C7PY01603D.

(219) Gimondi, S.; Vieira de Castro, J.; Reis, R. L.; Ferreira, H.; Neves, N. M. On the Size-Dependent Internalization of Sub-Hundred Polymeric Nanoparticles. *Colloids Surfaces B Biointerfaces* **2023**, *225*, 113245. https://doi.org/https://doi.org/10.1016/j.colsurfb.2023.113245.

(220) Wu, M.; Guo, H.; Liu, L.; Liu, Y.; Xie, L. Size-Dependent Cellular Uptake and Localization Profiles of Silver Nanoparticles. *Int. J. Nanomedicine* **2019**, *14*, 4247–4259. https://doi.org/10.2147/IJN.S201107.

(221) Francia, V.; Reker-Smit, C.; Salvati, A. Mechanisms of Uptake and Membrane Curvature

Generation for the Internalization of Silica Nanoparticles by Cells. *Nano Lett.* **2022**, *22* (7), 3118–3124. https://doi.org/10.1021/acs.nanolett.2c00537.

(222) Gupta, R.; Badhe, Y.; Mitragotri, S.; Rai, B. Permeation of Nanoparticles across the Intestinal Lipid Membrane: Dependence on Shape and Surface Chemistry Studied through Molecular Simulations. *Nanoscale* **2020**, *12* (11), 6318–6333. https://doi.org/10.1039/C9NR09947F.

(223) Xue, J.; Guan, Z.; Zhu, X.; Lin, J.; Cai, C.; Jin, X.; Li, Y.; Ye, Z.; Zhang, W.; Jiang, X. Cellular Internalization of Polypeptide-Based Nanoparticles: Effects of Size, Shape and Surface Morphology. *Biomater. Sci.* **2018**, *6* (12), 3251–3261. https://doi.org/10.1039/C8BM01163J.

(224) Liu, X.; Wu, F.; Tian, Y.; Wu, M.; Zhou, Q.; Jiang, S.; Niu, Z. Size Dependent Cellular Uptake of Rod-like Bionanoparticles with Different Aspect Ratios. *Sci. Rep.* **2016**, *6* (1), 24567. https://doi.org/10.1038/srep24567.

(225) Zhao, J.; Lu, H.; Wong, S.; Lu, M.; Xiao, P.; Stenzel, M. H. Influence of Nanoparticle Shapes on Cellular Uptake of Paclitaxel Loaded Nanoparticles in 2D and 3D Cancer Models. *Polym. Chem.* **2017**, *8* (21), 3317–3326. https://doi.org/10.1039/C7PY00385D.

(226) Yi, X.; Gao, H. Phase Diagrams and Morphological Evolution in Wrapping of Rod-Shaped Elastic Nanoparticles by Cell Membrane: A Two-Dimensional Study. *Phys. Rev. E* **2014**, *89* (6), 62712. https://doi.org/10.1103/PhysRevE.89.062712.

(227) Tay, J.; Zhao, Y.; Hedrick, J. L.; Yang, Y. Y. Elucidating the Anticancer Activities of Guanidinium-Functionalized Amphiphilic Random Copolymers by Varying the Structure and Composition in the Hydrophobic Monomer. *Theranostics* **2021**, *11* (18), 8977–8992. https://doi.org/10.7150/thno.60711.

(228) Forest, V.; Pourchez, J. Preferential Binding of Positive Nanoparticles on Cell Membranes Is Due to Electrostatic Interactions: A Too Simplistic Explanation That Does Not Take into Account the Nanoparticle Protein Corona. *Mater. Sci. Eng. C* **2017**, *70*, 889–896. https://doi.org/https://doi.org/10.1016/j.msec.2016.09.016.

(229) Evans, B. C.; Fletcher, R. B.; Kilchrist, K. V; Dailing, E. A.; Mukalel, A. J.; Colazo, J. M.; Oliver, M.; Cheung-Flynn, J.; Brophy, C. M.; Tierney, J. W.; Isenberg, J. S.; Hankenson, K. D.; Ghimire, K.; Lander, C.; Gersbach, C. A.; Duvall, C. L. An Anionic, Endosome-Escaping Polymer to Potentiate Intracellular Delivery of Cationic Peptides, Biomacromolecules, and Nanoparticles. *Nat. Commun.* **2019**, *10* (1), 5012. https://doi.org/10.1038/s41467-019-12906-y.

(230) Veider, F.; Sanchez Armengol, E.; Bernkop-Schnürch, A. Charge-Reversible Nanoparticles: Advanced Delivery Systems for Therapy and Diagnosis. *Small* **2024**, *20* (3), 2304713. https://doi.org/https://doi.org/10.1002/smll.202304713.

(231) Boix-Montesinos, P.; Medel, M.; Malfanti, A.; Đorđević, S.; Masiá, E.; Charbonnier, D.; Carrascosa-Marco, P.; Armiñán, A.; Vicent, M. J. Rational Design of a Poly-L-Glutamic Acid-Based Combination Conjugate for Hormone-Responsive Breast Cancer Treatment. *J. Control. Release* **2024**, *375*, 193–208. https://doi.org/https://doi.org/10.1016/j.jconrel.2024.09.002.

(232) Duro-Castano, A.; England, R. M.; Razola, D.; Romero, E.; Oteo-Vives, M.; Morcillo, M. A.; Vicent, M. J. Well-Defined Star-Shaped Polyglutamates with Improved Pharmacokinetic Profiles As Excellent Candidates for Biomedical Applications. *Mol. Pharm.* **2015**, *12* (10), 3639–3649. https://doi.org/10.1021/acs.molpharmaceut.5b00358.

(233) Melnyk, T.; Masiá, E.; Zagorodko, O.; Conejos-Sánchez, I.; Vicent, M. J. Rational Design of Poly-

L-Glutamic Acid-Palbociclib Conjugates for Pediatric Glioma Treatment. *J. Control. Release* **2023**, *355*, 385–394. https://doi.org/https://doi.org/10.1016/j.jconrel.2023.01.079.

(234) Duro-Castano, A.; Sousa-Herves, A.; Armiñán, A.; Charbonnier, D.; Arroyo-Crespo, J. J.; Wedepohl, S.; Calderón, M.; Vicent, M. J. Polyglutamic Acid-Based Crosslinked Doxorubicin Nanogels as an Anti-Metastatic Treatment for Triple Negative Breast Cancer. *J. Control. Release* **2021**, *332*, 10–20. https://doi.org/https://doi.org/10.1016/j.jconrel.2021.02.005.

(235) Zhang, Y.; Kim, I.; Lu, Y.; Xu, Y.; Yu, D.-G.; Song, W. Intelligent Poly(l-Histidine)-Based Nanovehicles for Controlled Drug Delivery. *J. Control. Release* **2022**, *349*, 963–982. https://doi.org/https://doi.org/10.1016/j.jconrel.2022.08.005.

(236) Olivieri, P. H.; Jesus, M. B.; Nader, H. B.; Justo, G. Z.; Sousa, A. A. Cell-Surface Glycosaminoglycans Regulate the Cellular Uptake of Charged Polystyrene Nanoparticles. *Nanoscale* **2022**, *14* (19), 7350–7363. https://doi.org/10.1039/D1NR07279J.

(237) Hui, Y.; Yi, X.; Wibowo, D.; Yang, G.; Middelberg, A. P. J.; Gao, H.; Zhao, C.-X. Nanoparticle Elasticity Regulates Phagocytosis and Cancer Cell Uptake. *Sci. Adv.* **2025**, *6* (16), eaaz4316. https://doi.org/10.1126/sciadv.aaz4316.

(238) Vicente-Ruiz, S.; Armiñán, A.; Maso, K.; Gallon, E.; Zagorodko, O.; Movellan, J.; Rodríguez-Otormín, F.; Baues, M.; May, J.-N.; De Lorenzi, F.; Lammers, T.; Vicent, M. J. Poly-l-Glutamic Acid Modification Modulates the Bio-Nano Interface of a Therapeutic Anti-IGF-1R Antibody in Prostate Cancer. *Biomaterials* **2023**, *301*, 122280. https://doi.org/https://doi.org/10.1016/j.biomaterials.2023.122280.

(239) Han, X.; Zhang, H.; Butowska, K.; Swingle, K. L.; Alameh, M.-G.; Weissman, D.; Mitchell, M. J. An Ionizable Lipid Toolbox for RNA Delivery. *Nat. Commun.* **2021**, *12* (1), 7233. https://doi.org/10.1038/s41467-021-27493-0.

(240) Chatterjee, S.; Kon, E.; Sharma, P.; Peer, D. Endosomal Escape: A Bottleneck for LNP-Mediated Therapeutics. *Proc. Natl. Acad. Sci.* **2024**, *121* (11), e2307800120. https://doi.org/10.1073/pnas.2307800120.

(241) David, A.; Alejandra, G.-D.; D., O. W.; Chih-Chao, Y.; Mitsuharu, U.; V., K. A.; Ivailo, T.; H., S. H.; Teresa, C.; L., B. J.; Kon-Ping, L.; Giuseppe, V.; Shahram, A.; Violaine, P.-B.; M., M. M.; M., C. J.; Juan, B.; H., B. T.; J., K. B.; Jeeyoung, O.; Yesim, P.; Yoshiki, S.; N., H. P.; D., S. S.; Michael, P.; J., D. P.; J., G. P.; Sunita, G.; Jihong, C.; L., S. A.; V., N. S.; T., S. M.; P., G. P.; K., V. A.; A., G. J.; B., S. O. Patisiran, an RNAi Therapeutic, for Hereditary Transthyretin Amyloidosis. *N. Engl. J. Med.* **2018**, *379* (1), 11–21. https://doi.org/10.1056/NEJMoa1716153.

(242) P., P. F.; J., T. S.; Nicholas, K.; Judith, A.; Alejandra, G.; Stephen, L.; L., P. J.; Gonzalo, P. M.; D., M. E.; Cristiano, Z.; Ruth, B.; A., S. K.; Satrajit, R.; Kenneth, K.; Ping, L.; V., K. W.; David, C.; W., F. R.; L., H. L.; Özlem, T.; Haylene, N.; Axel, S.; Serhat, Ü.; B., T. D.; Susan, M.; R., D. P.; Uğur, Ş.; U., J. K.; C., G. W. Safety and Efficacy of the BNT162b2 MRNA Covid-19 Vaccine. *N. Engl. J. Med.* **2020**, *383* (27), 2603–2615. https://doi.org/10.1056/NEJMoa2034577.

(243) Li, B.; Raji, I. O.; Gordon, A. G. R.; Sun, L.; Raimondo, T. M.; Oladimeji, F. A.; Jiang, A. Y.; Varley, A.; Langer, R. S.; Anderson, D. G. Accelerating Ionizable Lipid Discovery for MRNA Delivery Using Machine Learning and Combinatorial Chemistry. *Nat. Mater.* **2024**, *23* (7), 1002–1008. https://doi.org/10.1038/s41563-024-01867-3.

(244) Vermeulen, L. M. P.; De Smedt, S. C.; Remaut, K.; Braeckmans, K. The Proton Sponge

Hypothesis: Fable or Fact? *Eur. J. Pharm. Biopharm.* **2018**, *129*, 184–190. https://doi.org/https://doi.org/10.1016/j.ejpb.2018.05.034.

(245) Bus, T.; Traeger, A.; Schubert, U. S. The Great Escape: How Cationic Polyplexes Overcome the Endosomal Barrier. *J. Mater. Chem. B* **2018**, *6* (43), 6904–6918. https://doi.org/10.1039/C8TB00967H.

(246) Tortajada, L.; Felip-León, C.; Vicent, M. J. Polymer-Based Non-Viral Vectors for Gene Therapy in the Skin. *Polym. Chem.* **2022**, *13* (6), 718–735. https://doi.org/10.1039/D1PY01485D.

(247) Hu, W.-W.; Yeh, C.-C.; Tsai, C.-W. The Conjugation of Indolicidin to Polyethylenimine for Enhanced Gene Delivery with Reduced Cytotoxicity. *J. Mater. Chem. B* **2018**, *6* (36), 5781–5794. https://doi.org/10.1039/C8TB01408F.

(248) Zakeri, A.; Kouhbanani, M. A. J.; Beheshtkhoo, N.; Beigi, V.; Mousavi, S. M.; Hashemi, S. A. R.; Karimi Zade, A.; Amani, A. M.; Savardashtaki, A.; Mirzaei, E.; Jahandideh, S.; Movahedpour, A. Polyethylenimine-Based Nanocarriers in Co-Delivery of Drug and Gene: A Developing Horizon. *Nano Rev. Exp.* **2018**, *9* (1), 1488497. https://doi.org/10.1080/20022727.2018.1488497.

(249) Melnyk, T.; Đorđević, S.; Conejos-Sánchez, I.; Vicent, M. J. Therapeutic Potential of Polypeptide-Based Conjugates: Rational Design and Analytical Tools That Can Boost Clinical Translation. *Adv. Drug Deliv. Rev.* **2020**, *160*, 136–169. https://doi.org/https://doi.org/10.1016/j.addr.2020.10.007.

(250) Fang, H.; Guo, Z.; Lin, L.; Chen, J.; Sun, P.; Wu, J.; Xu, C.; Tian, H.; Chen, X. Molecular Strings Significantly Improved the Gene Transfection Efficiency of Polycations. *J. Am. Chem. Soc.* **2018**, *140* (38), 11992–12000. https://doi.org/10.1021/jacs.8b05341.

(251) Stefanovic, S.; McCormick, K.; Fattah, S.; Brannigan, R.; Cryan, S.-A.; Heise, A. Star-Shaped Poly(l-Lysine) with Polyester Bis-MPA Dendritic Core as Potential Degradable Nano Vectors for Gene Delivery. *Polym. Chem.* **2023**, *14* (27), 3151–3159. https://doi.org/10.1039/D3PY00346A.

(252) Barrett, S. E.; Burke, R. S.; Abrams, M. T.; Bason, C.; Busuek, M.; Carlini, E.; Carr, B. A.; Crocker, L. S.; Fan, H.; Garbaccio, R. M.; Guidry, E. N.; Heo, J. H.; Howell, B. J.; Kemp, E. A.; Kowtoniuk, R. A.; Latham, A. H.; Leone, A. M.; Lyman, M.; Parmar, R. G.; Patel, M.; Pechenov, S. Y.; Pei, T.; Pudvah, N. T.; Raab, C.; Riley, S.; Sepp-Lorenzino, L.; Smith, S.; Soli, E. D.; Staskiewicz, S.; Stern, M.; Truong, Q.; Vavrek, M.; Waldman, J. H.; Walsh, E. S.; Williams, J. M.; Young, S.; Colletti, S. L. Development of a Liver-Targeted SiRNA Delivery Platform with a Broad Therapeutic Window Utilizing Biodegradable Polypeptide-Based Polymer Conjugates. *J. Control. Release* **2014**, *183*, 124–137. https://doi.org/https://doi.org/10.1016/j.jconrel.2014.03.028.

(253) Winkeljann, B.; Keul, D. C.; Merkel, O. M. Engineering Poly- and Micelleplexes for Nucleic Acid Delivery – A Reflection on Their Endosomal Escape. *J. Control. Release* **2023**, *353*, 518–534. https://doi.org/https://doi.org/10.1016/j.jconrel.2022.12.008.

(254) Dirisala, A.; Uchida, S.; Li, J.; Van Guyse, J. F. R.; Hayashi, K.; Vummaleti, S. V. C.; Kaur, S.; Mochida, Y.; Fukushima, S.; Kataoka, K. Effective MRNA Protection by Poly(l-Ornithine) Synergizes with Endosomal Escape Functionality of a Charge-Conversion Polymer toward Maximizing MRNA Introduction Efficiency. *Macromol. Rapid Commun.* **2022**, *43* (12), 2100754. https://doi.org/https://doi.org/10.1002/marc.202100754.

(255) Mixich, L.; Boonstra, E.; Masuda, K.; Li, S.-W.; Nakashima, Y.; Meng, F.; Sakata, M.; Goda, T.; Uchida, S.; Cabral, H. Ionizable Polymeric Micelles with Phenylalanine Moieties Enhance Intracellular Delivery of Self-Replicating RNA for Long-Lasting Protein Expression In Vivo. *Biomacromolecules* **2024**, *25* (2), 1058–1067. https://doi.org/10.1021/acs.biomac.3c01102.

(256) Park, J.; Evangelopoulos, M.; Vasher, M. K.; Kudruk, S.; Ramani, N.; Mayer, V.; Solivan, A. C.; Lee, A.; Mirkin, C. A. Enhancing Endosomal Escape and Gene Regulation Activity for Spherical Nucleic Acids. *Small* **2024**, *20* (11), 2306902. https://doi.org/https://doi.org/10.1002/smll.202306902.

(257) Teo, S. L. Y.; Rennick, J. J.; Yuen, D.; Al-Wassiti, H.; Johnston, A. P. R.; Pouton, C. W. Unravelling Cytosolic Delivery of Cell Penetrating Peptides with a Quantitative Endosomal Escape Assay. *Nat. Commun.* **2021**, *12* (1), 3721. https://doi.org/10.1038/s41467-021-23997-x.

(258) Li, W.; Nicol, F.; Szoka, F. C. GALA: A Designed Synthetic PH-Responsive Amphipathic Peptide with Applications in Drug and Gene Delivery. *Adv. Drug Deliv. Rev.* **2004**, *56* (7), 967–985. https://doi.org/https://doi.org/10.1016/j.addr.2003.10.041.

(259) Hagino, Y.; Khalil, I. A.; Kimura, S.; Kusumoto, K.; Harashima, H. GALA-Modified Lipid Nanoparticles for the Targeted Delivery of Plasmid DNA to the Lungs. *Mol. Pharm.* **2021**, *18* (3), 878–888. https://doi.org/10.1021/acs.molpharmaceut.0c00854.

(260) Mai, L. D.; Wimberley, S. C.; Champion, J. A. Intracellular Delivery Strategies Using Membrane-Interacting Peptides and Proteins. *Nanoscale* **2024**, *16* (33), 15465–15480. https://doi.org/10.1039/D4NR02093F.

(261) Narum, S.; Deal, B.; Ogasawara, H.; Mancuso, J. N.; Zhang, J.; Salaita, K. An Endosomal Escape Trojan Horse Platform to Improve Cytosolic Delivery of Nucleic Acids. *ACS Nano* **2024**, *18* (8), 6186–6201. https://doi.org/10.1021/acsnano.3c09027.

(262) Wang, Z.; Zhang, J.; Wang, Y.; Zhou, J.; Jiao, X.; Han, M.; Zhang, X.; Hu, H.; Su, R.; Zhang, Y.; Qi, W. Overcoming Endosomal Escape Barriers in Gene Drug Delivery Using De Novo Designed PH-Responsive Peptides. *ACS Nano* **2024**, *18* (14), 10324–10340. https://doi.org/10.1021/acsnano.4c02400.

(263) BERG, K. Photochemical Internalization (PCI) - an Intracellular Drug Delivery Technology for Treatment of Solid Tumors. *Photodiagnosis Photodyn. Ther.* **2023**, *41*, 103453. https://doi.org/https://doi.org/10.1016/j.pdpdt.2023.103453.

(264) Ribovski, L.; Joshi, B.; Gao, J.; Zuhorn, I. Breaking Free: Endocytosis and Endosomal Escape of Extracellular Vesicles. *Extracell. Vesicles Circ. Nucleic Acids* **2023**, *4* (2), 283–305. https://doi.org/10.20517/evcna.2023.26.

(265) Joshi, B. S.; de Beer, M. A.; Giepmans, B. N. G.; Zuhorn, I. S. Endocytosis of Extracellular Vesicles and Release of Their Cargo from Endosomes. *ACS Nano* **2020**, *14* (4), 4444–4455. https://doi.org/10.1021/acsnano.9b10033.

(266) Pham, T. T.; Chen, H.; Nguyen, P. H. D.; Jayasinghe, M. K.; Le, A. H.; Le, M. T. N. Endosomal Escape of Nucleic Acids from Extracellular Vesicles Mediates Functional Therapeutic Delivery. *Pharmacol. Res.* **2023**, *188*, 106665. https://doi.org/https://doi.org/10.1016/j.phrs.2023.106665.

(267) Zhou, M.; Liu, L.; Zhou, W.; Yang, H.; Li, M.; Yin, P.; Zhou, Y. How Microbubble-Enhanced Shock Waves Promote the Delivery of Lipid-SiRNA across Neuronal Plasma Membrane: A

Computational Study. *J. Phys. Chem. B* **2024**, *128* (12), 2897–2904. https://doi.org/10.1021/acs.jpcb.3c07556.

(268) Wang, R.; Chow, Y. T.; Chen, S.; Ma, D.; Luo, T.; Tan, Y.; Sun, D. Magnetic Force-Driven in Situ Selective Intracellular Delivery. *Sci. Rep.* **2018**, *8* (1), 14205. https://doi.org/10.1038/s41598-018-32605-w.

(269) Deng, S.; Wang, S.; Xiao, Z.; Cheng, D. Unprotonatable and ROS-Sensitive Nanocarrier for NIR Spatially Activated SiRNA Therapy with Synergistic Drug Effect. *Small* **2022**, *18* (41). https://doi.org/10.1002/smll.202203823.

(270) Mo, Y.; Cheng, M. H. Y.; D'Elia, A.; Doran, K.; Ding, L.; Chen, J.; Cullis, P. R.; Zheng, G. Light-Activated SiRNA Endosomal Release (LASER) by Porphyrin Lipid Nanoparticles. *ACS Nano* **2023**, *17* (5), 4688–4703. https://doi.org/10.1021/acsnano.2c10936.

(271) Zhuo, Y.; Luo, Z.; Zhu, Z.; Wang, J.; Li, X.; Zhang, Z.; Guo, C.; Wang, B.; Nie, D.; Gan, Y.; Hu, G.; Yu, M. Direct Cytosolic Delivery of SiRNA via Cell Membrane Fusion Using Cholesterol-Enriched Exosomes. *Nat. Nanotechnol.* **2024**, *19* (12), 1858–1868. https://doi.org/10.1038/s41565-024-01785-0.

(272) Jiang, Y.; Huo, S.; Mizuhara, T.; Das, R.; Lee, Y.-W.; Hou, S.; Moyano, D. F.; Duncan, B.; Liang, X.-J.; Rotello, V. M. The Interplay of Size and Surface Functionality on the Cellular Uptake of Sub-10 Nm Gold Nanoparticles. *ACS Nano* **2015**, *9* (10), 9986–9993. https://doi.org/10.1021/acsnano.5b03521.

(273) Liu, Y.; Li, S.; Liu, X.; Sun, H.; Yue, T.; Zhang, X.; Yan, B.; Cao, D. Design of Small Nanoparticles Decorated with Amphiphilic Ligands: Self-Preservation Effect and Translocation into a Plasma Membrane. *ACS Appl. Mater. Interfaces* **2019**, *11* (27), 23822–23831. https://doi.org/10.1021/acsami.9b03638.

(274) Nakamura, H.; Watano, S. Direct Permeation of Nanoparticles across Cell Membrane: A Review. *KONA Powder Part. J.* **2018**, *35*, 49–65. https://doi.org/10.14356/kona.2018011.

(275) Ray, R.; Pal, S.; Das, S.; Jana, N. R. Direct Membrane Penetration and Cytosolic Delivery of Nanoparticles via Electrostatically Bound Amphiphiles. *ACS Appl. Mater. Interfaces* **2024**, *16* (13), 15819–15831. https://doi.org/10.1021/acsami.3c18750.

(276) Ruseska, I.; Zimmer, A. Internalization Mechanisms of Cell-Penetrating Peptides. *Beilstein J. Nanotechnol.* **2020**, *11*, 101–123. https://doi.org/10.3762/bjnano.11.10.

(277) Sahni, A.; Ritchey, J. L.; Qian, Z.; Pei, D. Cell-Penetrating Peptides Translocate across the Plasma Membrane by Inducing Vesicle Budding and Collapse. *J. Am. Chem. Soc.* **2024**, *146* (36), 25371–25382. https://doi.org/10.1021/jacs.4c10533.

(278) Kabelka, I.; Vácha, R. Advances in Molecular Understanding of α-Helical Membrane-Active Peptides. *Acc. Chem. Res.* **2021**, *54* (9), 2196–2204. https://doi.org/10.1021/acs.accounts.1c00047.

(279) Eiríksdóttir, E.; Konate, K.; Langel, Ü.; Divita, G.; Deshayes, S. Secondary Structure of Cell-Penetrating Peptides Controls Membrane Interaction and Insertion. *Biochim. Biophys. Acta - Biomembr.* **2010**, *1798* (6), 1119–1128. https://doi.org/https://doi.org/10.1016/j.bbamem.2010.03.005.

(280) Kalafatovic, D.; Giralt, E. Cell-Penetrating Peptides: Design Strategies beyond Primary

Structure and Amphipathicity. *Molecules*. 2017. https://doi.org/10.3390/molecules22111929.

(281) Zahid, M.; Robbins, P. D. Cell-Type Specific Penetrating Peptides: Therapeutic Promises and Challenges. *Molecules*. 2015, pp 13055–13070. https://doi.org/10.3390/molecules200713055.

(282) Liu, B. R.; Chiou, S.-H.; Huang, Y.-W.; Lee, H.-J. Bio-Membrane Internalization Mechanisms of Arginine-Rich Cell-Penetrating Peptides in Various Species. *Membranes*. 2022. https://doi.org/10.3390/membranes12010088.

(283) Ray, R.; Ghosh, S.; Maity, A.; Jana, N. R. Arginine Surface Density of Nanoparticles Controls Nonendocytic Cell Uptake and Autophagy Induction. *ACS Appl. Mater. Interfaces* **2024**, *16* (5), 5451–5461. https://doi.org/10.1021/acsami.3c14472.

(284) Deshayes, S.; Konate, K.; Vivès, E.; Boisguérin, P. Tips and Tools to Understand Direct Membrane Translocation of SiRNA-Loaded WRAP-Based Nanoparticles BT - Cell Penetrating Peptides: Methods and Protocols; Langel, Ü., Ed.; Springer US: New York, NY, 2022; pp 475–490. https://doi.org/10.1007/978-1-0716-1752-6_30.

(285) Pujals, S.; Giralt, E. Proline-Rich, Amphipathic Cell-Penetrating Peptides. *Adv. Drug Deliv. Rev.* **2008**, *60* (4), 473–484. https://doi.org/https://doi.org/10.1016/j.addr.2007.09.012.

(286) Jeong, Y.; Jin, S.; Palanikumar, L.; Choi, H.; Shin, E.; Go, E. M.; Keum, C.; Bang, S.; Kim, D.; Lee, S.; Kim, M.; Kim, H.; Lee, K. H.; Jana, B.; Park, M.-H.; Kwak, S. K.; Kim, C.; Ryu, J.-H. Stimuli-Responsive Adaptive Nanotoxin to Directly Penetrate the Cellular Membrane by Molecular Folding and Unfolding. *J. Am. Chem. Soc.* **2022**, *144* (12), 5503–5516. https://doi.org/10.1021/jacs.2c00084.

(287) Xia, Y.; Wu, K.; Liu, C.; Zhao, X.; Wang, J.; Cao, J.; Chen, Z.; Fang, M.; Yu, J.; Zhu, C.; Zhang, X.; Wang, Z. Filamentous-Actin-Mimicking Nanoplatform for Enhanced Cytosolic Protein Delivery. *Adv. Sci.* **2024**, *11* (10), 2305600. https://doi.org/https://doi.org/10.1002/advs.202305600.

(288) Ashford, M. B.; England, R. M.; Akhtar, N. Highway to Success—Developing Advanced Polymer Therapeutics. *Adv. Ther.* **2021**, *4* (5), 2000285. https://doi.org/https://doi.org/10.1002/adtp.202000285.

(289) Ekladious, I.; Colson, Y. L.; Grinstaff, M. W. Polymer–Drug Conjugate Therapeutics: Advances, Insights and Prospects. *Nat. Rev. Drug Discov.* **2019**, *18* (4), 273–294. https://doi.org/10.1038/s41573-018-0005-0.

(290) Đorđević, S.; Medel, M.; Hillaert, J.; Masiá, E.; Conejos-Sánchez, I.; Vicent, M. J. Critical Design Strategies Supporting Optimized Drug Release from Polymer–Drug Conjugates. *Small* **2024**, *20* (4), 2303157. https://doi.org/https://doi.org/10.1002/smll.202303157.

(291) Junyaprasert, V. B.; Thummarati, P. Innovative Design of Targeted Nanoparticles: Polymer–Drug Conjugates for Enhanced Cancer Therapy. *Pharmaceutics*. 2023. https://doi.org/10.3390/pharmaceutics15092216.

(292) Grigoletto, A.; Tedeschini, T.; Canato, E.; Pasut, G. The Evolution of Polymer Conjugation and Drug Targeting for the Delivery of Proteins and Bioactive Molecules. *WIREs Nanomedicine and Nanobiotechnology* **2021**, *13* (3), e1689. https://doi.org/https://doi.org/10.1002/wnan.1689.

(293) Sivasankaran, R. P.; Snell, K.; Kunkel, G.; Georgiou, P. G.; Puente, E. G.; Maynard, H. D. Polymer-Mediated Protein/Peptide Therapeutic Stabilization: Current Progress and Future Directions. *Prog. Polym. Sci.* **2024**, *156*, 101867. https://doi.org/https://doi.org/10.1016/j.progpolymsci.2024.101867.

(294) McLeskey, C.; Gudin, J.; Adler, J.; Rockett, C.; Jamindar, M.; Rauck, R.; Webster, L.; Mallick-Searle, T. Naloxegol (Movantik®) Provides Rapid and Sustained Improvement of Opioid-Induced Constipation Symptoms Irrespective of Opioid Dose. *Pain Manag. Nurs.* **2023**, *24* (2), 237. https://doi.org/10.1016/j.pmn.2023.02.016.

(295) Javia, A.; Vanza, J.; Bardoliwala, D.; Ghosh, S.; Misra, L. A.; Patel, M.; Thakkar, H. Polymer-Drug Conjugates: Design Principles, Emerging Synthetic Strategies and Clinical Overview. *Int. J. Pharm.* **2022**, *623*, 121863. https://doi.org/https://doi.org/10.1016/j.ijpharm.2022.121863.

(296) Thakor, P.; Bhavana, V.; Sharma, R.; Srivastava, S.; Singh, S. B.; Mehra, N. K. Polymer–Drug Conjugates: Recent Advances and Future Perspectives. *Drug Discov. Today* **2020**, *25* (9), 1718–1726. https://doi.org/https://doi.org/10.1016/j.drudis.2020.06.028.

(297) EMA. Questions and Answers on the Withdrawal of the Marketing Application for Opaxio® (Paclitaxel Poliglumex). **2009**, No. October, 1–2.

(298) Hosseini, S. M.; Mohammadnejad, J.; Salamat, S.; Beiram Zadeh, Z.; Tanhaei, M.; Ramakrishna, S. Theranostic Polymeric Nanoparticles as a New Approach in Cancer Therapy and Diagnosis: A Review. *Mater. Today Chem.* **2023**, *29*, 101400. https://doi.org/https://doi.org/10.1016/j.mtchem.2023.101400.

(299) Van Lysebetten, D.; Malfanti, A.; Deswarte, K.; Koynov, K.; Golba, B.; Ye, T.; Zhong, Z.; Kasmi, S.; Lamoot, A.; Chen, Y.; Van Herck, S.; Lambrecht, B. N.; Sanders, N. N.; Lienenklaus, S.; David, S. A.; Vicent, M. J.; De Koker, S.; De Geest, B. G. Lipid-Polyglutamate Nanoparticle Vaccine Platform. *ACS Appl. Mater. Interfaces* **2021**, *13* (5), 6011–6022. https://doi.org/10.1021/acsami.0c20607.

(300) Zagorodko, O.; Arroyo-Crespo, J. J.; Nebot, V. J.; Vicent, M. J. Polypeptide-Based Conjugates as Therapeutics: Opportunities and Challenges. *Macromol. Biosci.* **2017**, *17* (1), 1–22. https://doi.org/10.1002/mabi.201600316.

(301) Stepanova, M.; Nikiforov, A.; Tennikova, T.; Korzhikova-Vlakh, E. Polypeptide-Based Systems: From Synthesis to Application in Drug Delivery. *Pharmaceutics*. 2023. https://doi.org/10.3390/pharmaceutics15112641.

(302) Kabil, M. F.; Azzazy, H. M. E.-S.; Nasr, M. Recent Progress on PolySarcosine as an Alternative to PEGylation: Synthesis and Biomedical Applications. *Int. J. Pharm.* **2024**, *653*, 123871. https://doi.org/https://doi.org/10.1016/j.ijpharm.2024.123871.

(303) Bayraktutan, H.; Kopiasz, R. J.; Elsherbeny, A.; Martinez Espuga, M.; Gumus, N.; Oz, U. C.; Polra, K.; McKay, P. F.; Shattock, R. J.; Ordóñez-Morán, P.; Mata, A.; Alexander, C.; Gurnani, P. Polysarcosine Functionalised Cationic Polyesters Efficiently Deliver Self-Amplifying MRNA. *Polym. Chem.* **2024**, *15* (18), 1862–1876. https://doi.org/10.1039/D4PY00064A.

(304) Wan, X.; Chen, C.; Zhan, J.; Ye, S.; Li, R.; Shen, M. Dendritic Polylysine Co-Delivery of Paclitaxel and SiAXL Enhances the Sensitivity of Triple-Negative Breast Cancer Chemotherapy. *Front. Bioeng. Biotechnol.* **2024**, *12*.

(305) Yang, S.; Leong, J.; Wang, Y.; Sim, R.; Tan, K. H.; Chua, Y. H.; Tan, N.; Lee, A. L. Z.; Tay, J.; Yang, Y. Y. Drug-Free Neutrally Charged Polypeptide Nanoparticles as Anticancer Agents. *J. Control. Release* **2022**, *345*, 464–474. https://doi.org/https://doi.org/10.1016/j.jconrel.2022.03.034.

(306) Duro-Castano, A.; Nebot, V. J.; Niño-Pariente, A.; Armiñán, A.; Arroyo-Crespo, J. J.; Paul, A.; Feiner-Gracia, N.; Albertazzi, L.; Vicent, M. J. Capturing "Extraordinary" Soft-Assembled Charge-Like Polypeptides as a Strategy for Nanocarrier Design. *Adv. Mater.* **2017**, *29* (39), 1702888. https://doi.org/https://doi.org/10.1002/adma.201702888.

(307) Modica-Napolitano, J. S.; Aprille, J. R. Delocalized Lipophilic Cations Selectively Target the Mitochondria of Carcinoma Cells. *Adv. Drug Deliv. Rev.* **2001**, *49* (1), 63–70. https://doi.org/https://doi.org/10.1016/S0169-409X(01)00125-9.

(308) Wang, H.; Fang, B.; Peng, B.; Wang, L.; Xue, Y.; Bai, H.; Lu, S.; Voelcker, N. H.; Li, L.; Fu, L.; Huang, W. Recent Advances in Chemical Biology of Mitochondria Targeting . *Frontiers in Chemistry* . 2021. https://www.frontiersin.org/articles/10.3389/fchem.2021.683220.

(309) Sokolov, S.; Zyrina, A.; Akimov, S.; Knorre, D.; Severin, F. Toxic Effects of Penetrating Cations. *Membranes*. 2023. https://doi.org/10.3390/membranes13100841.

(310) Appiah Kubi, G.; Qian, Z.; Amiar, S.; Sahni, A.; Stahelin, R. V; Pei, D. Non-Peptidic Cell-Penetrating Motifs for Mitochondrion-Specific Cargo Delivery. *Angew. Chemie Int. Ed.* **2018**, *57* (52), 17183–17188. https://doi.org/https://doi.org/10.1002/anie.201811940.

(311) Yu, H.; Koilkonda, R. D.; Chou, T.-H.; Porciatti, V.; Ozdemir, S. S.; Chiodo, V.; Boye, S. L.; Boye, S. E.; Hauswirth, W. W.; Lewin, A. S.; Guy, J. Gene Delivery to Mitochondria by Targeting Modified Adenoassociated Virus Suppresses Leber's Hereditary Optic Neuropathy in a Mouse Model. *Proc. Natl. Acad. Sci.* **2012**, *109* (20), E1238–E1247. https://doi.org/10.1073/pnas.1119577109.

(312) Yoshinaga, N.; Miyamoto, T.; Odahara, M.; Takeda-Kamiya, N.; Toyooka, K.; Nara, S.; Nishimura, H.; Ling, F.; Su'etsugu, M.; Yoshida, M.; Numata, K. Design of an Artificial Peptide Inspired by Transmembrane Mitochondrial Protein for Escorting Exogenous DNA into the Mitochondria to Restore Their Functions by Simultaneous Multiple Gene Expression. *Adv. Funct. Mater.* **2024**, *34* (8), 2306070. https://doi.org/https://doi.org/10.1002/adfm.202306070.

(313) Klimpel, A.; Neundorf, I. Bifunctional Peptide Hybrids Targeting the Matrix of Mitochondria. *J. Control. Release* **2018**, *291*, 147–156. https://doi.org/https://doi.org/10.1016/j.jconrel.2018.10.029.

(314) Kang, Y. C.; Son, M.; Kang, S.; Im, S.; Piao, Y.; Lim, K. S.; Song, M.-Y.; Park, K.-S.; Kim, Y.-H.; Pak, Y. K. Cell-Penetrating Artificial Mitochondria-Targeting Peptide-Conjugated Metallothionein 1A Alleviates Mitochondrial Damage in Parkinson's Disease Models. *Exp. Mol. Med.* **2018**, *50* (8), 1–13. https://doi.org/10.1038/s12276-018-0124-z.

(315) Szeto, H. H. Cell-Permeable, Mitochondrial-Targeted, Peptide Antioxidants. *AAPS J.* **2006**, *8* (2), 32. https://doi.org/10.1007/BF02854898.

(316) Cerrato, C. P.; Kivijärvi, T.; Tozzi, R.; Lehto, T.; Gestin, M.; Langel, Ü. Intracellular Delivery of Therapeutic Antisense Oligonucleotides Targeting MRNA Coding Mitochondrial Proteins by Cell-Penetrating Peptides. *J. Mater. Chem. B* **2020**, *8* (47), 10825–10836. https://doi.org/10.1039/D0TB01106A.

(317) Cerrato, C. P.; Pirisinu, M.; Vlachos, E. N.; Langel, Ü. Novel Cell-Penetrating Peptide Targeting Mitochondria. *FASEB J.* **2015**, *29* (11), 4589–4599. https://doi.org/https://doi.org/10.1096/fj.14-269225.

(318) Shin, G.; Hyun, S.; Kim, D.; Choi, Y.; Kim, K. H.; Kim, D.; Kwon, S.; Kim, Y. S.; Yang, S. H.; Yu, J. Cyclohexylalanine-Containing α-Helical Amphipathic Peptide Targets Cardiolipin, Rescuing Mitochondrial Dysfunction in Kidney Injury. *J. Med. Chem.* **2024**, *67* (5), 3385–3399. https://doi.org/10.1021/acs.jmedchem.3c01578.

(319) Horton, K. L.; Stewart, K. M.; Fonseca, S. B.; Guo, Q.; Kelley, S. O. Mitochondria-Penetrating Peptides. *Chem. Biol.* **2008**, *15* (4), 375–382. https://doi.org/https://doi.org/10.1016/j.chembiol.2008.03.015.

(320) Yousif, L. F.; Stewart, K. M.; Horton, K. L.; Kelley, S. O. Mitochondria-Penetrating Peptides: Sequence Effects and Model Cargo Transport. *ChemBioChem* **2009**, *10* (12), 2081–2088. https://doi.org/https://doi.org/10.1002/cbic.200900017.

(321) Xiao, Q.; Dong, X.; Yang, F.; Zhou, S.; Xiang, M.; Lou, L.; Yao, S. Q.; Gao, L. Engineered Cell-Penetrating Peptides for Mitochondrion-Targeted Drug Delivery in Cancer Therapy. *Chem. – A Eur. J.* **2021**, *27* (59), 14721–14729. https://doi.org/https://doi.org/10.1002/chem.202102523.

(322) Li, L.; Geisler, I.; Chmielewski, J.; Cheng, J. X. Cationic Amphiphilic Polyproline Helix P11LRR Targets Intracellular Mitochondria. *J. Control. Release* **2010**, *142* (2), 259–266. https://doi.org/10.1016/j.jconrel.2009.10.012.

(323) Fillon, Y. A.; Anderson, J. P.; Chmielewski, J. Cell Penetrating Agents Based on a Polyproline Helix Scaffold. *J. Am. Chem. Soc.* **2005**, *127* (33), 11798–11803. https://doi.org/10.1021/ja052377g.

(324) Geisler, I. M.; Chmielewski, J. Dimeric Cationic Amphiphilic Polyproline Helices for Mitochondrial Targeting. *Pharm. Res.* **2011**, *28* (11), 2797–2807. https://doi.org/10.1007/s11095-011-0493-7.

(325) Kalafut, D.; Anderson, T. N.; Chmielewski, J. Mitochondrial Targeting of a Cationic Amphiphilic Polyproline Helix. *Bioorganic Med. Chem. Lett.* **2012**, *22* (1), 561–563. https://doi.org/10.1016/j.bmcl.2011.10.077.

(326) Jeena, M. T.; Jeong, K.; Go, E. M.; Cho, Y.; Lee, S.; Jin, S.; Hwang, S.-W.; Jang, J. H.; Kang, C. S.; Bang, W.-Y.; Lee, E.; Kwak, S. K.; Kim, S.; Ryu, J.-H. Heterochiral Assembly of Amphiphilic Peptides Inside the Mitochondria for Supramolecular Cancer Therapeutics. *ACS Nano* **2019**, *13* (10), 11022–11033. https://doi.org/10.1021/acsnano.9b02522.

(327) Woldetsadik, A. D.; Vogel, M. C.; Rabeh, W. M.; Magzoub, M. Hexokinase II–Derived Cell-Penetrating Peptide Targets Mitochondria and Triggers Apoptosis in Cancer Cells. *FASEB J.* **2017**, *31* (5), 2168–2184. https://doi.org/https://doi.org/10.1096/fj.201601173R.

(328) Kam, A.; Loo, S.; Dutta, B.; Sze, S. K.; Tam, J. P. Plant-Derived Mitochondria-Targeting Cysteine-Rich Peptide Modulates Cellular Bioenergetics. *J. Biol. Chem.* **2019**, *294* (11), 4000–4011. https://doi.org/https://doi.org/10.1074/jbc.RA118.006693.

(329) Pfeiffer, N. V; Dirndorfer, D.; Lang, S.; Resenberger, U. K.; Restelli, L. M.; Hemion, C.; Miesbauer, M.; Frank, S.; Neutzner, A.; Zimmermann, R.; Winklhofer, K. F.; Tatzelt, J. Structural Features within the Nascent Chain Regulate Alternative Targeting of Secretory

Proteins to Mitochondria. *EMBO J.* **2013**, *32* (7), 1036–1051. https://doi.org/https://doi.org/10.1038/emboj.2013.46.

(330) Yoshinaga, N.; Numata, K. Rational Designs at the Forefront of Mitochondria-Targeted Gene Delivery: Recent Progress and Future Perspectives. *ACS Biomater. Sci. Eng.* **2022**, *8* (2), 348–359. https://doi.org/10.1021/acsbiomaterials.1c01114.

(331) Deng, Y.; Jia, F.; Chen, X.; Jin, Q.; Ji, J. ATP Suppression by PH-Activated Mitochondria-Targeted Delivery of Nitric Oxide Nanoplatform for Drug Resistance Reversal and Metastasis Inhibition. *Small* **2020**, *16* (23), 2001747. https://doi.org/https://doi.org/10.1002/smll.202001747.

(332) Yang, J.; Yang, Z.; Wang, H.; Chang, Y.; Xu, J.-F.; Zhang, X. A Polymeric Nanoparticle to Co-Deliver Mitochondria-Targeting Peptides and Pt(IV) Prodrug: Toward High Loading Efficiency and Combination Efficacy. *Angew. Chemie Int. Ed.* **2024**, *63* (18), e202402291. https://doi.org/https://doi.org/10.1002/anie.202402291.

(333) Song, B.-L.; Wang, J.-Q.; Zhang, G.-X.; Yi, N.-B.; Zhang, Y.-J.; Zhou, L.; Guan, Y.-H.; Zhang, X.-H.; Zheng, W.-F.; Qiao, Z.-Y.; Wang, H. A Coupling-Induced Assembly Strategy for Constructing Artificial Shell on Mitochondria in Living Cells. *Angew. Chemie Int. Ed.* **2024**, *63* (45), e202411725. https://doi.org/https://doi.org/10.1002/anie.202411725.

(334) Ma, P.; Chen, J.; Bi, X.; Li, Z.; Gao, X.; Li, H.; Zhu, H.; Huang, Y.; Qi, J.; Zhang, Y. Overcoming Multidrug Resistance through the GLUT1-Mediated and Enzyme-Triggered Mitochondrial Targeting Conjugate with Redox-Sensitive Paclitaxel Release. *ACS Appl. Mater. Interfaces* **2018**, *10* (15), 12351–12363. https://doi.org/10.1021/acsami.7b18437.

(335) Liu, Y.; Zhou, Z.; Lin, X.; Xiong, X.; Zhou, R.; Zhou, M.; Huang, Y. Enhanced Reactive Oxygen Species Generation by Mitochondria Targeting of Anticancer Drug To Overcome Tumor Multidrug Resistance. *Biomacromolecules* **2019**, *20* (10), 3755–3766. https://doi.org/10.1021/acs.biomac.9b00800.

(336) Sharma, A.; Liaw, K.; Sharma, R.; Thomas, A. G.; Slusher, B. S.; Kannan, S.; Kannan, R. M. Targeting Mitochondria in Tumor-Associated Macrophages Using a Dendrimer-Conjugated TSPO Ligand That Stimulates Antitumor Signaling in Glioblastoma. *Biomacromolecules* **2020**, *21* (9), 3909–3922. https://doi.org/10.1021/acs.biomac.0c01033.

(337) Zhang, Y.; Zhang, H.; Zhao, F.; Jiang, Z.; Cui, Y.; Ou, M.; Mei, L.; Wang, Q. Mitochondrial-Targeted and ROS-Responsive Nanocarrier via Nose-to-Brain Pathway for Ischemic Stroke Treatment. *Acta Pharm. Sin. B* **2023**, *13* (12), 5107–5120. https://doi.org/https://doi.org/10.1016/j.apsb.2023.06.011.

(338) Li, Q.; Yang, J.; Chen, C.; Lin, X.; Zhou, M.; Zhou, Z.; Huang, Y. A Novel Mitochondrial Targeted Hybrid Peptide Modified HPMA Copolymers for Breast Cancer Metastasis Suppression. *J. Control. Release* **2020**, *325*, 38–51. https://doi.org/https://doi.org/10.1016/j.jconrel.2020.06.010.

(339) Geng, Y.; Zhong, Y.; Zhou, Q.; Chen, S.; Piao, Y.; Yin, W.; Lu, H.; Shen, Y. A Neutral Water-Soluble Mitochondria-Targeting Polymer. *Chem. Commun.* **2019**, *55* (67), 10015–10018. https://doi.org/10.1039/c9cc04291a.

(340) Jin, J.; Yuan, P.; Yu, W.; Lin, J.; Xu, A.; Xu, X.; Lou, J.; Yu, T.; Qian, C.; Liu, B.; Song, J.; Li, L.; Piao, Y.; Xie, T.; Shen, Y.; Tao, H.; Tang, J. Mitochondria-Targeting Polymer Micelle of

Dichloroacetate Induced Pyroptosis to Enhance Osteosarcoma Immunotherapy. *ACS Nano* **2022**, *16* (7), 10327–10340. https://doi.org/10.1021/acsnano.2c00192.

(341) Liu, Y.; Zhang, J.; Tu, Y.; Zhu, L. Potential-Independent Intracellular Drug Delivery and Mitochondrial Targeting. *ACS Nano* **2022**, *16* (1), 1409–1420. https://doi.org/10.1021/acsnano.1c09456.

(342) Zhang, Y.; He, X.; Zhang, Y.; Zhao, Y.; Lu, S.; Peng, Y.; Lu, L.; Hu, X.; Zhan, M. Native Mitochondria-Targeting Polymeric Nanoparticles for Mild Photothermal Therapy Rationally Potentiated with Immune Checkpoints Blockade to Inhibit Tumor Recurrence and Metastasis. *Chem. Eng. J.* **2021**, *424*, 130171. https://doi.org/https://doi.org/10.1016/j.cej.2021.130171.

(343) Cohen-Erez, I.; Issacson, C.; Lavi, Y.; Shaco-Levy, R.; Milam, J.; Laster, B.; Gheber, L. A.; Rapaport, H. Antitumor Effect of Lonidamine-Polypeptide-Peptide Nanoparticles in Breast Cancer Models. *ACS Appl. Mater. Interfaces* **2019**, *11* (36), 32670–32678. https://doi.org/10.1021/acsami.9b09886.

(344) C. Pegoraro, E. Karpova, Y. Qutbuddin, E. Masiá Sanchis, P. Dimitrijevs, C. Huck-Iriart, S. Gavrilović, P. Arsenyan, P. Schwille, C. Felip-León, A. Duro-Castaño, I. Conejos-Sánchez, M. V. Polyproline-Polyornithine Diblock Copolymers with Inherent Mitochondria Tropism. *Adv. Mater.* **2024**, *Second Rev*, Ref. adma.202411595R2.

(345) Pegoraro, C.; Guinart, A.; Masiá Sanchis, E.; Doellerer, D.; Stuart, M. C. A.; Conejos-Sánchez, I.; Feringa, B. L.; Vicent, M. J. A Light-Driven Molecular Motor-Polypeptide Conjugate Supports Controlled Cell Uptake. *J. Mater. Chem. B* **2025**. https://doi.org/10.1039/D4TB02434F.

(346) Pegoraro, C.; Masiá Sanchis, E.; Đorđević, S.; Dolz-Pérez, I.; Huck-Iriart, C.; Herrera, L.; Esteban-Pérez, S.; Conejos-Sanchez, I.; Vicent, M. J. Multifunctional Polypeptide-Based Nanoconjugates for Targeted Mitochondrial Delivery and Nonviral Gene Therapy. *Chem. Mater.* **2025**. https://doi.org/10.1021/acs.chemmater.4c02742.

(347) Wang, J.; Zhao, W.; Zhang, Z.; Liu, X.; Xie, T.; Wang, L.; Xue, Y.; Zhang, Y. A Journey of Challenges and Victories: A Bibliometric Worldview of Nanomedicine since the 21st Century. *Adv. Mater.* **2024**, *36* (15), 2308915. https://doi.org/https://doi.org/10.1002/adma.202308915.

(348) Song, Y.; Hou, W. State of the Art in Nanomedicine. In *Nanomedicine*; 2024; pp 1–48. https://doi.org/https://doi.org/10.1002/9783527830404.ch1.

(349) Duncan, R.; Vicent, M. J. Polymer Therapeutics-Prospects for 21st Century: The End of the Beginning. *Adv. Drug Deliv. Rev.* **2013**, *65* (1), 60–70. https://doi.org/https://doi.org/10.1016/j.addr.2012.08.012.

(350) Azizi, M.; Jahanban-Esfahlan, R.; Samadian, H.; Hamidi, M.; Seidi, K.; Dolatshahi-Pirouz, A.; Yazdi, A. A.; Shavandi, A.; Laurent, S.; Be Omide Hagh, M.; Kasaiyan, N.; Santos, H. A.; Shahbazi, M.-A. Multifunctional Nanostructures: Intelligent Design to Overcome Biological Barriers. *Mater. Today Bio* **2023**, *20*, 100672. https://doi.org/https://doi.org/10.1016/j.mtbio.2023.100672.

(351) Mitchell, M. J.; Billingsley, M. M.; Haley, R. M.; Wechsler, M. E.; Peppas, N. A.; Langer, R. Engineering Precision Nanoparticles for Drug Delivery. *Nat. Rev. Drug Discov.* **2021**, *20* (2), 101–124. https://doi.org/10.1038/s41573-020-0090-8.

(352) Fu, X.; Shi, Y.; Qi, T.; Qiu, S.; Huang, Y.; Zhao, X.; Sun, Q.; Lin, G. Precise Design Strategies of

Nanomedicine for Improving Cancer Therapeutic Efficacy Using Subcellular Targeting. *Signal Transduct. Target. Ther.* **2020**, *5* (1), 1–15. https://doi.org/10.1038/s41392-020-00342-0.

(353) Ye, D.; Liu, H.; Dai, E.; Fan, J.; Wu, L. Recent Advances in Nanomedicine Design Strategies for Targeting Subcellular Structures. *iScience* **2025**, *28* (1). https://doi.org/10.1016/j.isci.2024.111597.

(354) Javadov, S.; Kozlov, A. V; Camara, A. K. S. Mitochondria in Health and Diseases. *Cells*. 2020. https://doi.org/10.3390/cells9051177.

(355) Liew, S. S.; Qin, X.; Zhou, J.; Li, L.; Huang, W.; Yao, S. Q. Smart Design of Nanomaterials for Mitochondria-Targeted Nanotherapeutics. *Angew. Chemie Int. Ed.* **2021**, *60* (5), 2232–2256. https://doi.org/https://doi.org/10.1002/anie.201915826.

(356) Conejos-Sánchez, I.; Gallon, E.; Niño-Pariente, A.; Smith, J. A.; De la Fuente, A. G.; Di Canio, L.; Pluchino, S.; Franklin, R. J. M.; Vicent, M. J. Polyornithine-Based Polyplexes to Boost Effective Gene Silencing in CNS Disorders. *Nanoscale* **2020**, *12* (11), 6285–6299. https://doi.org/10.1039/C9NR06187H.

(357) Pegoraro, C.; Karpova, E.; Qutbuddin, Y.; Sanchis, E. M.; Dimitrijevs, P.; Huck-Iriart, C.; Gavrilović, S.; Arsenyan, P.; Schwille, P.; Felip-León, C.; Duro-Castano, A.; Conejos-Sanchez, I.; Vicent, M. J. Polyproline-Polyornithine Diblock Copolymers with Inherent Mitochondria Tropism. *Adv. Mater.* **2025**, *n/a* (n/a), 2411595. https://doi.org/https://doi.org/10.1002/adma.202411595.

(358) Huang, Y.; Sun, G.; Sun, X.; Li, F.; Zhao, L.; Zhong, R.; Peng, Y. The Potential of Lonidamine in Combination with Chemotherapy and Physical Therapy in Cancer Treatment. *Cancers*. 2020. https://doi.org/10.3390/cancers12113332.

(359) Nath, K.; Guo, L.; Nancolas, B.; Nelson, D. S.; Shestov, A. A.; Lee, S. C.; Roman, J.; Zhou, R.; Leeper, D. B.; Halestrap, A. P.; Blair, I. A.; Glickson, J. D. *Mechanism of Antineoplastic Activity of Lonidamine*; 2016; Vol. 1866. https://doi.org/10.1016/j.bbcan.2016.08.001.

(360) De Lena, M.; Lorusso, V.; Latorre, A.; Fanizza, G.; Gargano, G.; Caporusso, L.; Guida, M.; Catino, A.; Crucitta, E.; Sambiasi, D.; Mazzei, A. Paclitaxel, Cisplatin and Lonidamine in Advanced Ovarian Cancer. A Phase II Study. *Eur. J. Cancer* **2001**, *37* (3), 364–368. https://doi.org/https://doi.org/10.1016/S0959-8049(00)00400-7.

(361) Mansi, J. L.; de Graeff, A.; Newell, D. R.; Glaholm, J.; Button, D.; Leach, M. O.; Payne, G.; Smith, I. E. A Phase II Clinical and Pharmacokinetic Study of Lonidamine in Patients with Advanced Breast Cancer. *Br. J. Cancer* **1991**, *64* (3), 593–597. https://doi.org/10.1038/bjc.1991.356.

(362) Price, G. S.; Page, R. L.; Riviere, J. E.; Cline, J. M.; Thrall, D. E. Pharmacokinetics and Toxicity of Oral and Intravenous Lonidamine in Dogs. *Cancer Chemother. Pharmacol.* **1996**, *38* (2), 129–135. https://doi.org/10.1007/s002800050460.

(363) Cervantes-Madrid, D.; Romero, Y.; Dueñas-González, A. Reviving Lonidamine and 6-Diazo-5-Oxo-L-Norleucine to Be Used in Combination for Metabolic Cancer Therapy. *Biomed Res. Int.* **2015**, *2015* (1), 690492. https://doi.org/https://doi.org/10.1155/2015/690492.

(364) Neuzil, J.; Dong, L.-F.; Ramanathapuram, L.; Hahn, T.; Chladova, M.; Wang, X.-F.; Zobalova, R.; Prochazka, L.; Gold, M.; Freeman, R.; Turanek, J.; Akporiaye, E. T.; Dyason, J. C.; Ralph, S. J. Vitamin E Analogues as a Novel Group of Mitocans: Anti-Cancer Agents That Act by Targeting Mitochondria. *Mol. Aspects Med.* **2007**, *28* (5), 607–645.

https://doi.org/https://doi.org/10.1016/j.mam.2007.02.003.

(365) Dong, L. F.; Low, P.; Dyason, J. C.; Wang, X. F.; Prochazka, L.; Witting, P. K.; Freeman, R.; Swettenham, E.; Valis, K.; Liu, J.; Zobalova, R.; Turanek, J.; Spitz, D. R.; Domann, F. E.; Scheffler, I. E.; Ralph, S. J.; Neuzil, J. α-Tocopheryl Succinate Induces Apoptosis by Targeting Ubiquinone-Binding Sites in Mitochondrial Respiratory Complex II. *Oncogene* **2008**, *27* (31), 4324–4335. https://doi.org/10.1038/onc.2008.69.

(366) Yang, X.; Cai, X.; Yu, A.; Xi, Y.; Zhai, G. Redox-Sensitive Self-Assembled Nanoparticles Based on Alpha-Tocopherol Succinate-Modified Heparin for Intracellular Delivery of Paclitaxel. *J. Colloid Interface Sci.* **2017**, *496*, 311–326. https://doi.org/https://doi.org/10.1016/j.jcis.2017.02.033.

(367) Marathe, S.; Shadambikar, G.; Mehraj, T.; Sulochana, S. P.; Dudhipala, N.; Majumdar, S. Development of α-Tocopherol Succinate-Based Nanostructured Lipid Carriers for Delivery of Paclitaxel. *Pharmaceutics*. 2022. https://doi.org/10.3390/pharmaceutics14051034.

(368) Baer, A.; Wawra, S. E.; Bielmeier, K.; Uttinger, M. J.; Smith, D. M.; Peukert, W.; Walter, J.; Smith, A.-S. The Stokes–Einstein–Sutherland Equation at the Nanoscale Revisited. *Small* **2024**, *20* (6), 2304670. https://doi.org/https://doi.org/10.1002/smll.202304670.

(369) MJ. Vicent, I. Conejos-Sánchez, C. Pegoraro, E. Karpova, G. Sogorb, C. Felip -León, VJ. Nebot, P. Schwille, Y. Q. Polyproline-Based Block-Copolymers. WO2025003463A1. WO EP CN JP CA. Prior. 2023-06-29, Filed 2024-06-28, Publ. 2025-01-02., CIPF; PTS SL; and Max Planck Society.

(370) Tasbas, M. N.; Sahin, E.; Erbas-Cakmak, S. Bio-Inspired Molecular Machines and Their Biological Applications. *Coord. Chem. Rev.* **2021**, *443*, 214039. https://doi.org/https://doi.org/10.1016/j.ccr.2021.214039.

(371) Pooler, D. R. S.; Lubbe, A. S.; Crespi, S.; Feringa, B. L. Designing Light-Driven Rotary Molecular Motors. *Chem. Sci.* **2021**, *12* (45), 14964–14986. https://doi.org/10.1039/D1SC04781G.

(372) Brieke, C.; Rohrbach, F.; Gottschalk, A.; Mayer, G.; Heckel, A. Light-Controlled Tools. *Angew. Chemie Int. Ed.* **2012**, *51* (34), 8446–8476. https://doi.org/https://doi.org/10.1002/anie.201202134.

(373) Kistemaker, J. C. M.; Lubbe, A. S.; Feringa, B. L. Exploring Molecular Motors. *Mater. Chem. Front.* **2021**, *5* (7), 2900–2906. https://doi.org/10.1039/D0QM01091J.

(374) Guinart, A.; Korpidou, M.; Doellerer, D.; Pacella, G.; Stuart, M. C. A.; Dinu, I. A.; Portale, G.; Palivan, C.; Feringa, B. L. Synthetic Molecular Motor Activates Drug Delivery from Polymersomes. *Proc. Natl. Acad. Sci.* **2023**, *120* (27), e2301279120. https://doi.org/10.1073/pnas.2301279120.

(375) Zhou, Q.; Chen, J.; Luan, Y.; Vainikka, P. A.; Thallmair, S.; Marrink, S. J.; Feringa, B. L.; van Rijn, P. Unidirectional Rotating Molecular Motors Dynamically Interact with Adsorbed Proteins to Direct the Fate of Mesenchymal Stem Cells. *Sci. Adv.* **2025**, *6* (5), eaay2756. https://doi.org/10.1126/sciadv.aay2756.

(376) Liu, D.; García-López, V.; Gunasekera, R. S.; Greer Nilewski, L.; Alemany, L. B.; Aliyan, A.; Jin, T.; Wang, G.; Tour, J. M.; Pal, R. Near-Infrared Light Activates Molecular Nanomachines to Drill into and Kill Cells. *ACS Nano* **2019**, *13* (6), 6813–6823. https://doi.org/10.1021/acsnano.9b01556.

(377) Qutbuddin, Y.; Guinart, A.; Gavrilović, S.; Al Nahas, K.; Feringa, B. L.; Schwille, P. Light-Activated Synthetic Rotary Motors in Lipid Membranes Induce Shape Changes Through Membrane Expansion. *Adv. Mater.* **2024**, *36* (16), 2311176. https://doi.org/https://doi.org/10.1002/adma.202311176.

(378) García-López, V.; Chen, F.; Nilewski, L. G.; Duret, G.; Aliyan, A.; Kolomeisky, A. B.; Robinson, J. T.; Wang, G.; Pal, R.; Tour, J. M. Molecular Machines Open Cell Membranes. *Nature* **2017**, *548* (7669), 567–572. https://doi.org/10.1038/nature23657.

(379) Li, X.; Peng, X.; Zoulikha, M.; Boafo, G. F.; Magar, K. T.; Ju, Y.; He, W. Multifunctional Nanoparticle-Mediated Combining Therapy for Human Diseases. *Signal Transduct. Target. Ther.* **2024**, *9* (1), 1. https://doi.org/10.1038/s41392-023-01668-1.

(380) Suk, J. S.; Xu, Q.; Kim, N.; Hanes, J.; Ensign, L. M. PEGylation as a Strategy for Improving Nanoparticle-Based Drug and Gene Delivery. *Adv. Drug Deliv. Rev.* **2016**, *99*, 28–51. https://doi.org/https://doi.org/10.1016/j.addr.2015.09.012.

(381) Zielonka, J.; Joseph, J.; Sikora, A.; Hardy, M.; Ouari, O.; Vasquez-Vivar, J.; Cheng, G.; Lopez, M.; Kalyanaraman, B. Mitochondria-Targeted Triphenylphosphonium-Based Compounds: Syntheses, Mechanisms of Action, and Therapeutic and Diagnostic Applications. *Chem. Rev.* **2017**, *117* (15), 10043–10120. https://doi.org/10.1021/acs.chemrev.7b00042.

(382) Felip, C.; Dolz, I.; Esteban-Pérez, S.; Herrera-Muñoz, L. . N.-C. V. . Non-Covalent Shielding Polymers. *WO2023002014A1. WO EP CN JP CA. Prior. 2021-07-22, Filed 2022-07-22, Publ. 2023-01-26*.

(383) Pezzoli, D.; Giupponi, E.; Mantovani, D.; Candiani, G. Size Matters for in Vitro Gene Delivery: Investigating the Relationships among Complexation Protocol, Transfection Medium, Size and Sedimentation. *Sci. Rep.* **2017**, *7* (1), 44134. https://doi.org/10.1038/srep44134.

(384) Zhang, Z.; Qiu, N.; Wu, S.; Liu, X.; Zhou, Z.; Tang, J.; Liu, Y.; Zhou, R.; Shen, Y. Dose-Independent Transfection of Hydrophobized Polyplexes. *Adv. Mater.* **2021**, *33* (25), 2102219. https://doi.org/https://doi.org/10.1002/adma.202102219.

(385) Uchida, S.; Yanagihara, K.; Matsui, A.; Kataoka, K.; Itaka, K. MRNA as a Tool for Gene Transfection in 3D Cell Culture for Future Regenerative Therapy. *Micromachines*. 2020. https://doi.org/10.3390/mi11040426.

(386) Lowrey, M. K.; Day, H.; Schilling, K. J.; Huynh, K. T.; Franca, C. M.; Schutt, C. E. Remote-Controlled Gene Delivery in Coaxial 3D-Bioprinted Constructs Using Ultrasound-Responsive Bioinks. *Cell. Mol. Bioeng.* **2024**, *17* (5), 401–421. https://doi.org/10.1007/s12195-024-00818-x.

(387) Paris, J. L.; Coelho, F.; Teixeira, A.; Diéguez, L.; Silva, B. F. B.; Abalde-Cela, S. In Vitro Evaluation of Lipopolyplexes for Gene Transfection: Comparing 2D, 3D and Microdroplet-Enabled Cell Culture. *Molecules*. 2020. https://doi.org/10.3390/molecules25143277.

6 ANNEXES

The final chapter contains the summary of this doctoral thesis in Spanish and the supplementary material for the three scientific articles that form the core of this thesis. These additional details include data, figures, and methodologies that enhance and complement the results and discussions presented in Chapter 3, providing a more comprehensive understanding of the research conducted.

6.1 Annex 1: Thesis Summary in Spanish

Las mitocondrias son orgánulos fundamentales, centrales para el metabolismo energético celular, la apoptosis y la homeostasis. Las disfunciones en la dinámica mitocondrial están implicadas en una variedad de enfermedades, incluido el cáncer, donde estos orgánulos apoyan el crecimiento tumoral y la plasticidad metabólica. Esta tesis doctoral se centra en el desarrollo y la aplicación de terapias avanzadas basadas en polipéptidos, diseñadas específicamente para dirigirse a las mitocondrias en modelos de cáncer de mama triple negativo (TNBC). Al abordar desafíos como las barreras biológicas y la localización subcelular precisa, este trabajo contribuye de manera significativa a la nanomedicina de precisión.

Introducción

Las mitocondrias son orgánulos esenciales en las células eucariotas, responsables de funciones cruciales que incluyen la bioenergética celular, la señalización intracelular y la homeostasis general. Su estructura única, compuesta por una doble membrana y un ADN circular, las convierte en componentes fundamentales para la regulación metabólica y el mantenimiento celular. Su membrana interna, rica en cardiolipina, facilita la organización de los complejos de la cadena de transporte de electrones (ETC), esenciales para la fosforilación oxidativa (OXPHOS) y la generación del potencial de membrana mitocondrial (MMP). Este potencial, un gradiente electroquímico clave, no solo impulsa la producción de ATP, sino que también regula el transporte de metabolitos, el equilibrio de iones y la homeostasis celular, posicionando a las mitocondrias como centros metabólicos y de señalización críticos.

El origen endosimbionte de las mitocondrias les confiere capacidades únicas, como la producción de ROS (especies reactivas de oxígeno), que actúan como moléculas señalizadoras en concentraciones moderadas, pero que pueden causar daño celular significativo cuando están desreguladas. Este balance es particularmente relevante en patologías como el cáncer, donde las mitocondrias desempeñan un papel central en la progresión tumoral, la plasticidad metabólica y en la resistencia a terapias convencionales. En el caso del cáncer de mama triple negativo (TNBC, por sus siglas en inglés), un subtipo altamente agresivo y heterogéneo, estas características son aún más pronunciadas. Las células tumorales de TNBC presentan adaptaciones metabólicas únicas que incluyen cambios en la dinámica mitocondrial, como la fisión y la fusión, y un equilibrio funcional entre la glucólisis y la OXPHOS. Este equilibrio les permite responder a las demandas energéticas y

biosintéticas de su microambiente, facilitando su proliferación y supervivencia en entornos adversos. Estas características, junto con niveles elevados de ROS, representan tanto una ventaja para la supervivencia tumoral como una oportunidad para utilizar estrategias terapéuticas dirigidas.

Sin embargo, lograr una entrega específica de agentes terapéuticos a las mitocondrias plantea desafíos significativos. Una de las principales dificultades es superar las múltiples barreras biológicas que limitan el acceso eficiente a estos orgánulos. Estas barreras incluyen la entrada a la célula a través de la membrana plasmática, el transporte intracelular evitando la degradación en compartimentos endosomales, y finalmente, la localización precisa dentro de las mitocondrias. Además, las diferencias en el MMP entre células sanas y tumorales complican aún más la especificidad necesaria para tratamientos eficaces. Estas limitaciones no solo reducen la eficacia de los agentes terapéuticos, sino que también pueden causar efectos adversos en otros compartimentos celulares. Por lo tanto, superar estas barreras es un aspecto crítico/fundamental en el diseño de estrategias terapéuticas avanzadas dirigidas a mitocondrias.

En este contexto, la nanomedicina ha emergido como un enfoque revolucionario para superar estos obstáculos, permitiendo desarrollar plataformas terapéuticas innovadoras y efectivas. Entre ellas, los sistemas de transporte de fármacos basados en polímeros han demostrado ser especialmente prometedores. En concreto, los sistemas basados en polipéptidos destacan por ser excelentes candidatos debido a su biocompatibilidad, biodegradabilidad y capacidad para ser diseñados con alta especificidad. Estas características los convierten en herramientas versátiles para diseñar sistemas de liberación de fármaco que pueden emplear propiedades inherentes de las mitocondrias, como su alto MMP y su composición lipídica específica, para lograr dirigir agentes terapéuticos de manera precisa y eficiente.

Una de las principales ventajas de los sistemas basados en polipéptidos es su capacidad modular, que permite personalizar sus propiedades para cumplir con objetivos terapéuticos específicos. Por ejemplo, es posible diseñar polipéptidos capaces de atravesar membranas celulares evitando las rutas endosomales tradicionales y logrando un acceso directo al citoplasma. Una vez en el citoplasma, la versatilidad de estos sistemas permite su funcionalización con moléculas que reconocen características propias de las mitocondrias, como la cardiolipina o el MMP, facilitando así su acumulación específica en estos orgánulos. Este nivel de especificidad no solo mejora la eficacia terapéutica, sino que también minimiza los efectos secundarios sistémicos, una limitación común en las terapias convencionales.

Además, estos sistemas avanzados pueden integrar funcionalidades adicionales que los hacen aún más efectivos. Por ejemplo, pueden diseñarse para permitir una liberación controlada del agente(s) terapéutico(s) en respuesta a estímulos específicos del microambiente tumoral, como un pH ácido o niveles elevados de ROS. Esta capacidad de respuesta específica permite maximizar la acción terapéutica en las células tumorales mientras se preserva la funcionalidad de las células sanas. Asimismo, los polipéptidos ofrecen son plataforma apta para la creación de terapias de combinación, siendo capaces de transportar diferentes agentes terapéuticos, como quimioterápicos y terapias génicas, en un único sistema de entrega, aumentando su índice terapéutico.

A pesar de los avances significativos en el diseño de estos sistemas, sigue siendo esencial validar su eficacia y seguridad en modelos biológicos relevantes. Los estudios preclínicos desempeñan un papel fundamental en la evaluación de cómo estas plataformas interactúan con el microambiente tumoral y cómo pueden optimizarse para aplicaciones clínicas. Estos estudios no solo ayudan a cerrar la brecha entre los experimentos *in vitro* y la práctica clínica, sino que también permiten refinar el diseño de los sistemas basados en polipéptidos para abordar las complejidades específicas de enfermedades como el TNBC.

En esta línea, la revisión titulada *"Unlocking the Mitochondria for Nanomedicine-Based Treatments: Overcoming Biological Barriers, Improving Designs, and Selecting Verification Techniques"*, incluida en esta tesis, analiza en profundidad las estrategias para superar las barreras biológicas y destaca los avances recientes en el diseño de sistemas de nanomedicina dirigidos a mitocondrias. Este análisis proporciona un marco conceptual para comprender cómo los avances en nanomedicina están transformando el enfoque hacia terapias mitocondriales, desde los primeros diseños moleculares hasta las etapas avanzadas de validación preclínica.

En conclusión, las mitocondrias, con su papel central en la bioenergética, la señalización celular y la regulación metabólica, representan un objetivo terapéutico de gran relevancia. Superar las barreras biológicas que limitan el acceso a estas organelas y aprovechar sus características únicas es fundamental para desarrollar terapias más específicas y efectivas. Los sistemas basados en polipéptidos, con su capacidad para ser diseñados de manera precisa y funcionalizada, ofrecen soluciones prometedoras para estos desafíos. A través de avances en su diseño y validación, estas plataformas tienen el potencial de transformar la medicina personalizada y abrir nuevas vías en el tratamiento de enfermedades complejas como el TNBC.

Objetivos

El diseño y la evaluación de nanomedicinas basadas en polipéptidos capaces de dirigirse a las mitocondrias, ya sea mediante un tropismo inherente o la integración de elementos de direccionamiento bien caracterizados, y la evaluación de su eficacia en un modelo de cáncer de mama triple negativo (TNBC) representan los objetivos principales de esta tesis doctoral.

Dividimos este objetivo principal en los siguientes sub-objetivos:

1. **Diseño, Síntesis, Caracterización y Evaluación Biológica de Copolímeros Dibloque como Oligómeros Penetrantes de Células Dirigidos a Mitocondrias (mt-CPOs) (Artículo II)**
    - Caracterización fisicoquímica integral de una librería de copolímeros dibloque poli-L-ornitina–poli-L-prolina (PLOn-PLPm), enfocándose en la estructura secundaria, las proporciones de los bloques y la afinidad de unión a cardiolipina mediante sistemas modelo de membranas ricas en cardiolipina.
    - Investigación de la internalización celular, el direccionamiento mitocondrial y la actividad biológica de copolímeros PLOn-PLPm seleccionados en células TNBC MDA-MB-231, con un análisis comparativo de diferentes naturalezas del bloque policatiónico, proporciones del ratio n:m y líneas celulares.
    - Síntesis, caracterización fisicoquímica y evaluación biológica de PGA funcionalizado con PLO_6-PLP_{22} para su traslación clínica y aplicaciones terapéuticas.
2. **Aplicación de Nanoconjugados Basados en PGA Funcionalizados con PLO6-PLP22 en Motores Moleculares (Artículo III)**
    - Desarrollo de un motor molecular conjugado con polipéptidos (P-MM) utilizando química *click* y análisis de las propiedades de rotación impulsadas por luz y cambios conformacionales supramoleculares.
    - Estudio de la actividad inducida por luz del P-MM y su efecto en la internalización celular y localización subcelular en células TNBC MDA-MB-231.
3. **Desarrollo de Nanoconjugados Basados en Polipéptidos Funcionalizados con TPP para el Direccionamiento Mitocondrial y Aplicaciones de Terapia Génica No Viral (Artículo IV)**

- Síntesis, caracterización fisicoquímica y biológica de un transportador basado en PLO modificado con polietilenglicol (PEG) y funcionalizado con un compuesto trivalente diseñado a medida (TRV3) a través de un enlace disulfuro (C-TRV3-A).
- Formulación de poliplejos mediante la combinación del nanoconjugado catiónico C-TRV3-A con el polipéptido aniónico VLC-3 y ADN plasmídico y estudios de estabilidad.
- Investigación de la eficiencia de transfección y citotoxicidad de los poliplejos en modelos 2D y 3D de células TNBC MDA-MB-231.

4. **Síntesis y Caracterización de Nanoconjugados de Polipéptido-Fármaco Dirigidos a Mitocondrias para el Tratamiento de TNBC**
   - Síntesis y caracterización de conjugados polipéptido-fármaco basados en PLO_6-PLP_{22} y portadores de lonidamina (Loni) (conj-Loni) y α-tocoferol succinato (α-TOS) (conj-α-TOS) para el tratamiento de TNBC.
   - Evaluación de la viabilidad celular y actividad biológica de conj-Loni y conj-α-TOS en células TNBC MDA-MB-231.

Resultados y Discusión

El diseño y la evaluación de sistemas basados en polipéptidos capaces de dirigirse a mitocondria, ya sea mediante tropismo inherente o a través de la integración de elementos de direccionamiento bien caracterizados, y la evaluación de su eficacia en un modelo de TNBC, representan los objetivos principales de esta tesis doctoral. Este trabajo se llevó a cabo como un compendio de tres publicaciones científicas, cada una abordando aspectos específicos del desarrollo y la aplicación de estos sistemas terapéuticos.

1. Diseño y caracterización de copolímeros dibloque con tropismo mitocondrial inherente

El primer artículo exploró sistemáticamente el diseño y la aplicación de copolímeros dibloque basados en polipéptidos para abordar desafíos críticos en la orientación mitocondrial. Estos copolímeros estan compuestos por poli-L-ornitina (PLO), seleccionada por su naturaleza policatiónica para promover la captación celular, y poli-L-prolina (PLP), elegida por su funcionalización con residuos hidrofóbicos y/o catiónicos que permiten una orientación mitocondrial dependiente de la concentración y el potencial. Utilizando la polimerización por apertura de anillo de N-carboxianhidruros (NCA-ROP), sintetizamos una librería de copolímeros

PLOn-PLPm con diferentes proporciones del ratio n:m, longitudes de cadena y uso de otros bloques policatiónicos alternativos a la PLO, como polilisina (PLL), poli-L-arginina (PArg) y poli-L-histidina (PHis). Este enfoque sistemático permitió evaluar cómo las variaciones estructurales influyen en la eficiencia de la orientación mitocondrial, los mecanismos de captación celular y los resultados biológicos. Entre las propiedades fisicoquímicas analizadas (tamaño, propensión a la agregación, potencial zeta, composición de los bloques, conformación y estructura secundaria), la composición del bloque policatiónico surgió como un determinante significativo de la funcionalidad. Específicamente, los copolímeros PLOn-PLPm con una proporción de bloques n:m de 1:3 (n:m = 6:22 para 6b, 18:54 para 6h y 23:65 para 6i) demostraron consistentemente una captación celular independiente de energía y una orientación mitocondrial eficiente, estableciéndose como oligómeros penetrantes celulares dirigidos a mitocondrias (mt-CPOs).

Cuando reemplazamos PLO por PLL (por ejemplo, en el copolímero dibloque 7), los copolímeros resultantes exhibieron tamaños, cargas y estructuras secundarias comparables; sin embargo, el análisis NMR-DOSY reveló una distribución conformacional bimodal en solución, que se correlacionó con una captación celular ineficiente a 4°C y una orientación mitocondrial deficiente. Aunque la estructura secundaria y el potencial zeta mostraron correlaciones dependientes del contexto con la orientación mitocondrial, su importancia no fue consistente en todos los sistemas. Por ejemplo, los copolímeros PLOn-PLPm con ratios n:m alternativos mostraron un mayor potencial zeta que la proporción eficiente de 1:3, pero adoptaron una conformación aleatoria y carecían de orientación mitocondrial. De manera similar, a pesar de presentar una conformación de tipo poliprolina II, los copolímeros PLOn-PLPm con una ratio 1:2 no lograron una orientación mitocondrial efectiva. Este hallazgo sugiere que el potencial zeta y la estructura secundaria por sí solos no pueden garantizar una localización mitocondrial efectiva. Apoyando este hallazgo, la funcionalización del derivado PGA con mt-CPO 6b produjo un nanoconjugado con una conformación de bobina aleatoria, un potencial zeta negativo y una orientación mitocondrial eficiente. Estos resultados indican que la funcionalización puede superar propiedades fisicoquímicas específicas para determinar la eficiencia de la orientación mitocondrial.

Los estudios mecanísticos revelaron que la despolarización mitocondrial no afecta la capacidad de orientación de los mt-CPOs. Demostramos que el mt-CPO 6b es capaz de acumularse en las mitocondrias independientemente de la despolarización, como se evidenció mediante técnicas de imagen confocal y citometría de flujo, a diferencia de los ligandos catiónicos convencionales, como el trifosfonio, que dependen del potencial de membrana mitocondrial. Este

mecanismo independiente del potencial amplía la aplicabilidad de los mt-CPOs a patologías que implican despolarización mitocondrial, como ocurre durante fluctuaciones en la progresión de diversas enfermedades. Además, la orientación mitocondrial permaneció altamente específica para células tumorales, con una acumulación mitocondrial significativa observada en células de cáncer de mama MDA-MB-231 y MCF-7, pero no en fibroblastos BJ no cancerosos, células microgliales BV-2 ni células HepG2. Es importante destacar que el mt-CPO 6b mostró una toxicidad mínima en células no cancerosas, lo que resalta su selectividad y perfil de seguridad.

Para profundicar en los detalles del mecanismo de orientación, investigamos las interacciones de los copolímeros PLOn-PLPm con modelos de membranas artificiales y biológicas enriquecidas en cardiolipina (CL). Nuestros estudios revelaron que el bloque policatiónico es esencial para la unión a la CL, ya que los homopolímeros de PLP no mostraron afinidad medible. Mientras que los copolímeros con proporciones n:m de 1:1 y 1:2 demostraron unión a CL, solo la proporción de 1:3 indujo la formación de parches y la remodelación de membranas en regiones ricas en CL con curvatura negativa. Estos efectos mostraron especificidad para las membranas que contenían CL, pero estuvieron ausentes en membranas sin CL, lo que subraya la especificidad de estas interacciones. Además, observamos que los copolímeros PLOn-PLPm con proporción 1:3 redujeron la fluidez de la membrana, aumentaron la tensión e indujeron la ordenación de la membrana y la curvatura. La incapacidad del copolímero 7 para inducir la formación de parches enfatizó aún más el papel crítico del PLO como bloque policatiónico en la estabilización de estas interacciones. Los mecanismos físicos robustos de interacción destacan la especificidad de nuestros materiales y los diferencian de otros péptidos penetrantes mitocondriales reportados, demostrando su viabilidad para una orientación mitocondrial efectiva y selectiva.

Funcionalmente, los mt-CPOs exhibieron una potente actividad antitumoral dependiente de la concentración en células de TNBC, alterando funciones mitocondriales a concentraciones sub-IC50. Estas alteraciones incluyeron un aumento en la producción de especies reactivas de oxígeno (ROS), despolarización mitocondrial, inhibición de la fosforilación oxidativa, que específicamente redujo la actividad del complejo I y la eficiencia del acoplamiento de la cadena de transporte de electrones, e inducción de mitofagia dependiente de lisosomas. El potencial de los mt-CPOs como agentes duales de orientación y terapia representa un avance significativo en las terapias dirigidas a mitocondrias.

La escalabilidad del proceso de síntesis respaldó el potencial de la traslación clínica de esta plataforma. Utilizando una metodología robusta y rentable de NCA-ROP, escalamos la producción del mt-CPO 6b a un alto rendimiento (7,3 g, 80%) con una calidad consistente. Además, desarrollamos un nanoconjugado (compuesto 16) mediante la funcionalización de PGA lineal modificado con una corta cadena de azida-PEG con mt-CPO 6b (3,3% en peso) mediante un enlace valina-citrulina (VC), demostrando la adaptabilidad de nuestra plataforma. Este nanoconjugado retuvo una orientación mitocondrial eficiente, enfatizando la importancia de la flexibilidad del ligando y las estrategias de funcionalización. Notablemente, este derivado mejoró la viabilidad celular mientras prevenía el daño mitocondrial, destacando aún más la versatilidad de los mt-CPOs para avanzar en las terapias dirigidas a mitocondrias.

Como una extensión del trabajo publicado en el primer artículo, se sintetizaron conjugados de polipéptido-fármaco mediante la conjugación directa del mt-CPO 6b (PLO6-PLP22) con lonidamina (Loni) y α-tocoferol succinato (α-TOS), seleccionados por sus mecanismos de acción dependientes de las mitocondrias y su eficacia reportada en células de cáncer de mama triple negativo (TNBC) MDA-MB-231. Este enfoque buscó aprovechar el mt-CPO 6b como sistema de entrega para superar las limitaciones de Loni y α-TOS, mejorando su localización específica en mitocondrias, maximizando su eficacia terapéutica y minimizando los efectos no deseados.

La Loni inhibe la hexoquinasa II unida a mitocondrias, una enzima clave en la glucólisis, lo que reduce la producción de ATP e induce disfunción mitocondrial, sensibilizando a las células cancerosas a la apoptosis. Sin embargo, su desarrollo clínico se ha visto limitado por su hepatotoxicidad, pobre biodistribución y baja potencia como fármaco único. Por otro lado, el α-TOS, un derivado proapoptótico de la vitamina E, interfiere en la cadena de transporte de electrones mitocondrial en el complejo II, generando especies reactivas de oxígeno (ROS) y activando vías apoptóticas mediante la permeabilización de la membrana mitocondrial y la liberación de citocromo c.

Siguiendo un esquema de síntesis en múltiples pasos, se lograron conjugados estables entre los grupos carboxílicos de Loni y α-TOS y los grupos amino del bloque PLO del mt-CPO 6b, formando enlaces amida. Estos conjugados, denominados conj-Loni y conj-α-TOS, se caracterizaron en primer lugar mediante técnicas fisicoquímicas de los conjugados, como tamaño, potencial zeta y capacidad de carga de fármaco, se evaluaron mediante resonancia magnética nuclear (NMR) y espectroscopía UV-Vis.

A continuación, se llevaron a cabo estudios de viabilidad celular en células TNBC MDA-MB-231 que revelaron tendencias distintas entre conj-Loni y conj-α-TOS. Conj-Loni mostró una relación lineal entre el porcentaje de carga de fármaco y la disminución de la viabilidad celular. En contraste, conj-α-TOS presentó una relación no lineal, con niveles de citotoxicidad dependientes de la carga del fármaco, probablemente debido a la formación de estructuras micelares que limitan la biodisponibilidad del α-TOS a altas concentraciones. Ambos conjugados mantuvieron su capacidad de localización mitocondrial, como demostraron estudios de colocalización en células vivas mediante microscopía confocal.

Además, se observó que conj-Loni y conj-α-TOS tenían un impacto significativo en parámetros clave de la función mitocondrial, como la despolarización de la membrana mitocondrial, el aumento de ROS y la reducción en la capacidad respiratoria de reserva. Este último es un mecanismo crítico de resistencia de las células cancerosas contra la quimioterapia convencional. Los estudios realizados con el analizador Seahorse XF mostraron una disminución dependiente de la concentración en la tasa de consumo de oxígeno asociada con la producción de ATP, lo que indica una interferencia en la respiración basal y la eficiencia de la fosforilación oxidativa.

Cabe destacar que los conjugados mostraron una potencia citotóxica significativamente superior en comparación con los fármacos libres. Por ejemplo, el IC50 de Loni libre después de 24 horas fue de 446 µM, mientras que el conjugado conj-Loni 4 mostró un IC50 equivalente a 96 µM. De manera similar, el α-TOS libre tuvo un IC50 de 86 µM, mientras que conj-α-TOS 1 alcanzó un IC50 equivalente a 30 µM. Esto subraya el potencial de los conjugados polímero-fármaco para aumentar la eficacia terapéutica al mejorar la localización mitocondrial y retener la actividad del fármaco dentro de las mitocondrias.

Estos hallazgos proporcionan evidenciase preliminares prometedoras sobre los beneficios de orientar propiedades mitocondriales en células cancerosas mediante conjugados de polipéptido-fármaco y destacan la necesidad de estudios adicionales para comprender los mecanismos subyacentes. Además, en aplicaciones no terapéuticas, se exploró el potencial de conj-α-TOS en la entrega de ARN mensajero (ARNm) en colaboración con la empresa Curapath. Las formulaciones modificadas con conj-α-TOS mostraron una eficiencia de transfección significativamente mayor en células HEK293 humanas, manteniendo un perfil no tóxico, lo que amplía aún más el alcance potencial de los sistemas basados en PLOn-PLPm y sus derivados.

2. Integración de motores moleculares activados por luz con sistemas poliméricos

En el segundo artículo, ampliamos la aplicación del nanoconjugado de PGA desarrollado en el primer estudio ("16", denominado aquí como P) para explorar su integración con nanomáquinas sintéticas dinámicas en aplicaciones biológicas avanzadas. Las máquinas moleculares son sistemas versátiles que, al igual que las macromoléculas biológicas, responden selectivamente a estímulos específicos y realizan tareas especializadas como la penetración de membranas. Inspirados por esta funcionalidad, diseñamos un nanoconjugado que incorpora un motor molecular (MM) impulsado por luz para lograr una funcionalidad dirigida. El nanoconjugado resultante, P-MM, se obtuvo mediante enlace vía química *click* entre el nanoconjugado de PGA (P) portador de un grupo azida, y un MM derivatizado con propinilo.

Los motores moleculares (MMs) representan una fascinante clase de sistemas sintéticos capaces de realizar rotaciones unidireccionales completas de 360° impulsadas por energía lumínica, lo que permite movimientos precisos y repetitivos con alta resolución espaciotemporal y sin invasividad. A pesar de su potencial, la aplicabilidad biológica de los MMs ha sido limitada debido a su baja biocompatibilidad y solubilidad, lo que ha restringido su integración exitosa en áreas como la administración de fármacos, la mecanobiología y la terapia contra el cáncer. Para superar estos desafíos, seleccionamos el nanoconjugado de PGA portando nuestro mt-CPO 6b (PLO6-PLP22) como una plataforma para mejorar la biocompatibilidad y solubilidad del MM y aprovechar su mecanismo de captación independiente de energía, como se demostró en nuestro trabajo previo.

La novedad de este estudio radica en demostrar que el P-MM retuvo la estabilidad rotacional del MM bajo luz de 405 nm, aunque la velocidad de rotación disminuyó, probablemente debido al aumento de la energía de activación impuesto por la estructura del polipéptido. Es importante destacar que la irradiación lumínica indujo una transformación estructural en el P-MM, como se observó mediante microscopía electrónica criogénica. Específicamente, el P-MM pasó de una forma micelar compacta (~2–3 nm de diámetro) a estructuras supramoleculares alargadas con forma de gusano (~1 × 10 nm de longitud) tras 30 segundos de activación lumínica a 405 nm. Este cambio conformacional mejoró significativamente la internalización celular del P-MM irradiado en comparación con sus formas no irradiadas y de control, según lo cuantificado mediante imágenes de fluorescencia de alto rendimiento.

En resumen, logramos una captación celular mejorada sin citotoxicidad significativa bajo las condiciones de irradiación probadas. El P-MM mantuvo sus capacidades de orientación mitocondrial

tras la exposición a la luz, sin una producción sustancial de ROS. Estos hallazgos sugieren que el aumento en la internalización celular está impulsado principalmente por la rotación mecánica del MM en lugar del estrés oxidativo fotoinducido. Este comportamiento se alinea con estudios mecanísticos recientes que demuestran la expansión de membranas inducida por motores moleculares y contrasta con literatura previa que utilizan MMs para perforar membranas celulares, provocando citotoxicidad y muerte celular en cáncer. La naturaleza controlada y biocompatible de la rotación molecular impulsada por luz resalta el potencial de P-MM para facilitar la permeabilización de membranas y la entrada celular sin comprometer la integridad celular.

Este estudio posiciona al P-MM como una plataforma dinámica que integra MMs en nanoconjugados funcionales, permitiendo una modulación precisa y activada por luz de las interacciones biológicas. Este enfoque ofrece oportunidades prometedoras para aplicaciones avanzadas en la administración dirigida de fármacos, abriendo el camino para aprovechar sistemas moleculares dinámicos en estrategias terapéuticas que requieren una mejora para lograr una liberación citosólica eficiente.

3. Desarrollo de nanoconjugados multifuncionales para terapia génica y direccionamiento mitocondrial

En el tercer artículo, ampliamos el alcance de los sistemas basados en polipéptidos integrando una funcionalidad con múltiples capacidades para lograr una (i) internalización celular eficiente, (ii) la direccionalidad a mitocondria así como (iii) el transporte de material genético en una plataforma única para la terapia contra el cáncer, utilizando el modelo de cáncer de mama triple negativo (TNBC) MDA-MB-231. Aunque los enfoques terapéuticos combinatorios han demostrado su gran potencial para mejorar la eficacia de los tratamientos, estos permanecen poco explorados en sistemas basados en polipéptidos aunando la orientación mitocondrial y la terapia génica. Para abordar esta necesidad, diseñamos un nanoconjugado multifuncional a través de un proceso de síntesis en ocho etapas, con una caracterización fisicoquímaca exhaustiva en cada paso.

Este nanoconjugado está basado en poli-L-ornitina (PLO) por sus propiedades establecidas de escape endosomal, modificado con PEG para mejorar la estabilidad estérica y minimizar interacciones no específicas. Además, conjugamos a la PLO un compuesto trivalente (TRV3) que incluye: un grupo trifosfonio (TPP) para la orientación mitocondrial, la sonda Cy5 como fármaco modelo enlazado mediante un enlace disulfuro sensible a glutatión (GSH) para garantizar la

liberación intracelular, y la sonda Atto488 para fines de monitorización, lo que dio como resultado el compuesto final C-TRV3-A.

C-TRV3-A demostró su potencial como plataforma de orientación mitocondrial mediante un enfoque de entrega jerárquica. El escape endosomal y la reducción intracelular del enlace disulfuro facilitaron la liberación de TRV3, permitiendo su acumulación en mitocondrias. Para extender su utilidad más allá de la entrega mitocondrial, incorporamos C-TRV3-A en formulaciones de poliplejos para la entrega de material genético, formados al condensar C-TRV3-A (N) con ADN plasmídico que codifica luciferasa (pDNA-Luc, P) y recubrir los complejos con el polipéptido polianiónico VLC-3 (PSar100-b-PGA15, O) para mejorar la estabilidad del poliplejo y mitigar los efectos citotóxicos de las cargas positivas de C-TRV3-A. Evaluamos diferentes proporciones O/N y N/P para determinar la estabilidad de las formulaciones en condiciones fisiológicamente relevantes, incluyendo medio celular, plasma de ratón y humano, mostrando además una baja actividad hemolítica.

Evaluamos la eficiencia de transfección en cultivos celulares 2D convencionales y en modelos de esferoides 3D de TNBC, siendo estos últimos más relevantes fisiológicamente debido a la mejor representación de las interacciones célula-célula y barreras de penetración. Entre las formulaciones probadas, Px02501 (O/P = 0.25, N/P = 1) demostró la mayor eficiencia de transfección en cultivos 2D tras 24 horas; sin embargo, los perfiles de transfección fueron diferentes entre los cultivos 2D y 3D. En los cultivos 2D, la eficiencia de transfección no mostró dependencia de la dosis, con la mayor expresión de luciferasa lograda a la menor concentración de plasmido (200 ng/mL). En contraste, los esferoides 3D mostraron una transfección dependiente de la dosis, alcanzando una eficiencia óptima a 400 ng/mL, pero con una disminución de la eficiencia a concentraciones más altas (600 ng/mL).

Estas diferencias probablemente reflejan las características únicas de los dos modelos de cultivo celular. En los cultivos 2D, la exposición uniforme a los poliplejos permite una captación celular eficiente a concentraciones bajas de plasmido, mientras que concentraciones más altas pueden promover la agregación de poliplejos o la saturación de las vías de captación celular. En cambio, los cultivos 3D introducen complejidades estructurales y ambientales, como interacciones célula-célula y organización tridimensional, que dificultan la penetración y captación de poliplejos. Estas barreras requieren concentraciones más altas de plasmido para lograr una transfección efectiva. Como valida la literatura reciente, el comportamiento distintivo dependiente de la dosis

observado en los modelos 3D subraya su relevancia para evaluar sistemas de entrega génica en condiciones que imitan mejor los entornos *in vivo.*

Este enfoque multifuncional, que combina la orientación subcelular y la entrega génica, destaca la versatilidad de los sistemas basados en polipéptidos para abordar desafíos terapéuticos complejos. El estudio subraya la importancia de adaptar el diseño de polipéptidos a aplicaciones específicas, ofreciendo un camino para desarrollar plataformas terapéuticas avanzadas capaces de integrar múltiples funcionalidades dentro de un único sistema.

Conclusiones

En conclusión, en esta tesis doctoral hemos desarrollado diversos enfoques para terapias subcelulares efectivas, centrándonos en mejorar la entrega citosólica y en la orientación precisa hacia las mitocondrias. La validación de nuestras plataformas, específicamente a nivel mitocondrial, mediante ensayos físicos y biológicos, proporciona una base sólida para comprender sus mecanismos terapéuticos durante su futura traslación preclínica, un aspecto que a menudo se pasa por alto en el desarrollo de terapias dirigidas a nivel intracelular. La aplicación de terapias poliméricas basadas en polipéptidos en campos emergentes, como el de las máquinas moleculares sintéticas, también representa un avance significativo en sus aplicaciones biológicas. Además, la ingeniería de plataformas que emplean un enfoque de "matar dos pájaros de un tiro", dirigido a múltiples sitios intracelulares, muestra un gran potencial para aumentar la eficacia terapéutica.

Dada la novedad de los copolímeros PLOn-PLPm en la orientación mitocondrial, hemos presentado una patente (WO2025003463A1354) y prevemos la traslación preclínica de estos sistemas, comenzando con estudios *in vivo* en modelos MDA-MB-231. Estos sistemas podrían actuar como fármaco polimérico o como ligando dirigente específicamente a mitocondria. Su uso combinado con agentes terapéuticos como conjugados de polipéptidos y fármacos amplía aún más su potencial. Además, contemplamos el desarrollo de un enlace sensible a ROS para conjugar el polipéptido 6b con fármacos, lo que permitiría la liberación de estos en entornos de estrés oxidativo, pudiendo sinergizar o refinar los efectos terapéuticos observados en nuestros estudios preliminares. Asimismo, la prometedora eficiencia de transfección del conj-α-TOS como componente en formulaciones de nanopartículas lipídicas (LNP) destaca su versatilidad funcional en la entrega génica, un aspecto que se explorará más a fondo en futuras aplicaciones dentro de nuestro laboratorio.

En cuanto al sistema de motores moleculares polipeptídicos, aunque el campo aún se encuentra en una etapa incipiente y su traslación presenta desafíos debido a las limitaciones en escalabilidad, creemos que nuestro trabajo aporta conocimientos valiosos para futuros avances. Este sistema podría ser beneficioso en aplicaciones que requieran un control preciso mediante luz, administración sistémica aguda de agentes biológicamente activos o escenarios donde cantidades pequeñas sean suficientes. De manera similar, prevemos la traslación de poliplexos para terapia del cáncer, adaptándolos potencialmente a diferentes tipos de cáncer o incorporando diversas especies de ácidos nucleicos como cargas útiles.

Por último, aunque nuestro extenso trabajo *in vitro* en varios modelos proporciona información crucial sobre los mecanismos de direccionamiento de estas plataformas, creemos relevante la necesidad de evaluar su localización y eficacia terapéutica *in vivo*. Estos estudios son vitales para cerrar la brecha entre los hallazgos *in vitro* y la aplicación clínica, avanzando estos sistemas innovadores hacia contribuciones significativas en la terapia subcelular y la medicina de precisión.

6.2 Annex 2: Supplementary Material of Manuscript II

Reference scientific article I[344]: Pegoraro, C., Karpova, E., Qutbuddin, Y., Masía Sanchis, E., Dimitrijevs, P., Huck-Iriart, C., Gavrilović, S., Arsenyan, P., Schwille, P., Felip-León, C., Duro-Castano, A., Conejos-Sanchez, I., & Vicent, M. J. (2025). Polyproline-Polyornithine Diblock Copolymers with Inherent Mitochondria Tropism. Advanced Materials, 37(1), 2411595. DOI: https://doi.org/10.1002/adma.202411595.

ADVANCED MATERIALS

Supporting Information

for *Adv. Mater.*, DOI 10.1002/adma.202411595

Polyproline-Polyornithine Diblock Copolymers with Inherent Mitochondria Tropism

Camilla Pegoraro, Ekaterina Karpova, Yusuf Qutbuddin, Esther Masiá Sanchis, Pavels Dimitrijevs, Cristián Huck-Iriart, Svetozar Gavrilović, Pavel Arsenyan, Petra Schwille, Carles Felip-León, Aroa Duro-Castano, Inmaculada Conejos-Sanchez and María J. Vicent**

SUPPLEMENTARY INFORMATION

Polyproline-polyornithine diblock Copolymers with Inherent Mitochondria Tropism

Camilla Pegoraro[1], Ekaterina Karpova[2], Yusuf Qutbuddin[3], Esther Masiá Sanchis[1,4,5], Pavels Dimitrijevs[6], Cristián Huck-Iriart[7], Svetozar Gavrilović[3], Pavel Arsenyan[6], Petra Schwille[3], Carles Felip-León[2], Aroa Duro-Castano[2], Inmaculada Conejos-Sanchez[1,4], and María J. Vicent[1,4,5*]*

[1]Príncipe Felipe Research Center, Polymer Therapeutics Lab., 46012 Valencia, Spain

[2]Curapath, Av. Benjamín Franklin, 19, 46980 Paterna, Valencia, Spain

[3]Max Planck Institute of Biochemistry, Am Klopferspitz 18, 82152 Martinsried, Germany

[4]Centro de Investigación Biomédica en Red en Cáncer (CIBERONC), Instituto de Salud Carlos III, Spain

[5]Príncipe Felipe Research Center, Screening Platform., 46012 Valencia, Spain

[6]Latvian Institute of Organic Synthesis, Aizkraukles Street 21, LV-1006, Riga, Latvia

[7]ALBA Synchrotron Light Source, Experiments Division, 08209 Cerdanyola del Vallès, Spain

E-mail: iconejos@cipf.es, mjvicent@cipf.es

The supplementary information includes:

a. Materials

b. Physicochemical and Biological Methods

- Gel Permeation Chromatography in Aqueous Media
- Nuclear Magnetic Resonance Spectroscopy
- Mass spectrometry analysis
- Diffusion-ordered NMR Spectroscopy
- Circular Dichroism
- Small Angle X-ray Scattering
- Z-potential Measurements
- Ultraviolet-visible Spectroscopy
- Fluorescence Spectroscopy for Critical Aggregation Concentration Determination
- Preparation of Small Unilamellar Vesicles for Cardiolipin Affinity Studies
- Mitoplast Isolation for Cardiolipin Affinity Studies
- Atomic Force Microscopy
- Total Internal Reflection Fluorescence Microscopy
- Fluorescence Correlation Spectroscopy
- Fluorescence Lifetime Spectroscopy
- Small Unilamellar Vesicles for physical studies
- Supported Lipid Bilayers
- Zeta Potential Measurements in SUVs
- Cell Culture protocols
- Erythrocytes isolation

c. Synthetic Procedures and Physicochemical Characterization of Novel Polyproline-based Diblock Polymers

- Synthesis of PLO(Z)-b-PLP and PLL(Z)-b-PLP
- Synthesis of Phis(DNP)-b-PLP
- Synthesis of PLO(HBr)-b-PLP and PLL(HBr)-b-PLP
- Synthesis of PHis(HCl)-b-PLP
- Synthesis of PArg(HCl)-b-PLP
- Synthesis of nBuPLP
- Circular Dichroism
- Labeling with Cy5 and A488
- SAXS patterns
- Pyrene Assay

- Scaled-up synthesis of the candidate diblock copolymer by design of experiments

d. Cell Viability and Mitochondrial Colocalization of Polyproline-based Diblock Polymers

- MTS assay for Cell Viability in MDA-MB-231 cells
- Cellular Uptake Studies by Live-Cell Imaging of Cy5-Labeled Diblock Copolymers
- Cellular Internalization Studies by Flow Cytometry of Cy5-labeled Diblock Copolymers
- MTS assay for Cell Viability in Additional Cell Lines Using 6b
- Hemocompatibility assay
- Conformational Analysis of 6b vs. 7
- Quantification of Cy5-Labeled Diblock Copolymer 6b in Isolated Mitochondria
- Qualitative and Quantitative Analysis of Cy5-Labeled Diblock Copolymer 6b in Depolarized Mitochondria

e. Affinity Studies in Membrane Models of Polyproline-based Diblock Polymers

- Determination of Cardiolipin Affinity
- DPH Exclusion Assay
- Physical Studies in Cardiolipin-containing Small Unilamellar Vesicles and Supported Lipid Bilayers

f. Biological Activity of Polyproline-based Diblock Polymers in a Triple Negative Breast Cancer Model

- Mitochondria Membrane Potential Analysis
- Oxygen Consumption Rate Analysis by Oroboros
- Oxygen Consumption Rate Analysis by Seahorse Xf Analyzers
- Reactive Oxygen Species Production
- Mitochondrial Morphology

g. Synthetic Procedures, Physicochemical and Biological Characterization of the Nanoconjugate 16

- Synthesis and Characterization of Nanoconjugate 16
    - Diblock Copolymer Conjugate 6b-VC
    - Polymer 17-PD
    - Nanoconjugate 16
    - Cy5-labeling of Diblock Copolymer Conjugate 16
- MTS Assay for Cell Viability in MDA-MB-231 cells and BJ fibroblasts using 16
- Fluorescence labeling of diblock copolymer-conjugate 16 with Cy5
- Cellular Uptake Studies by Live-Cell Imaging of Cy5-Labeled Nanoconjugate 16
- Physical Studies in Cardiolipin-containing Small Unilamellar Vesicles and Supported Lipid Bilayers

a. Materials

Unless otherwise indicated, all chemicals were reagent grade and used without further purification. N-carboxyanhydride (NCAs): L-Pro-NCA, L-Orn(Z)-NCA, and His(DNP)-NCA were purchased from PMC-ISOCHEM. L-Lys(Z) NCA, 2,2,2-trifluoroethanol, and N-δ-Cbz-L-ornithine(L-ornithine(Z)) were purchased from ABCR. Triphosgene and n-butylamine were purchased from Sigma Aldrich. All solvents were anhydrous unless otherwise stated. n-hexane, ethyl acetate, chloroform, acetone, and hydrogen bromide solution 33 wt % in acetic acid were purchased from Acros. N,N-dimethylformamide (DMF), hydrochloric acid, 37%, and diethyl ether were purchased from Sharlab. Acetonitrile (amine-free) and 4 M hydrogen chloride in 1,4-dioxane were purchased from Fisher Scientific. 2-Mercaptoethanol and benzylamine were purchased from Merck. KGaA. ^{1}H-1,2,4-triazole-1-carboxamidine hydrochloride, 98%, was purchased from VWR. Cyanine5 NHS, 95% ester, and amine were purchased from Lumiprobe. Atto 488 NHS ester was purchased from ATTO-TEC GmbH. All deuterated solvents for NMR were purchased from Deutero GmbH. Ultrapure water (MilliQ) with a resistivity of 18 MΩ.cm was used in all aqueous preparations. Dialysis was performed in a Millipore ultrafiltration device fitted with a 3 kDa Molecular weight cut-off (MWCO). PD-10 desalting columns packed with Sephadex G-25 resin were purchased from Cytiva. Dulbecco's Modified Eagle's Medium F-12 Nutrient Mixture (DMEM/F-12), phosphate-buffered saline (PBS), fetal bovine serum (FBS), penicillin (P), streptomycin (S), and trypsin were provided from Gibco Life technologies. MTS/PMS systems were supplied by Promega. JC-1 was purchased from MedChemExpress.

b. Physicochemical and Biological Methods

Gel Permeation Chromatography in Aqueous Media

For size exclusion chromatography (SEC) measurements in aqueous media containing 0.1M sodium nitrate and 0.005% sodium azide as an additive, a gel permeation chromatography (GPC) max (Malvern Instruments) pump and autosampler were used with a flow rate of 0.7 mL/min at 25 ºC with TSKGel PWXL G5000 column from Tosoh Bioscience. Viscotek TDA-305 was used as an integrated detection system. The system was calibrated with polyethylene oxide (PEO) (molecular weight (Mw) = 24 kDa; PDI = 1.01) from Malvern Panalytical. For Mw determination, an integrated triple detection system was used (refractive index, light scattering (two angles: 7 and 90 º), and ultraviolet-visible detectors).

Nuclear Magnetic Resonance Spectroscopy

NMR spectra were acquired at 27 °C (300K) on a 500 MHz Bruker spectrometer equipped with a 5 mm smart broadband frequency oscillator (BBFO) probe, a triple-resonance inverse (TXI) probe, a Gradient-enhanced high-resolution magic angle spinning (g-HRMAS) probe with temperature regulation from −15 °C to 100 °C, and a temperature-regulated sample bearing and control system (BACS). Data were processed using the software Mestrenova (Bruker GmbH, Karlsruhe, Germany). Samples were prepared at the desired concentration (10-20 mg mL^{-1}) in trifluoroacetic acid-d (d-TFA) or deuterated water (D_2O).

Mass spectrometry analysis

Samples for MALDI-TOF analysis were prepared by diluting 1 µL of each compound solution (6b, 6h, and 6i in Milli-Q water) 1:10 in matrix solution. The matrix consisted of 10 mg/mL α-cyano-4-hydroxycinnamic acid (CHCA, Aldrich) in 70% acetonitrile (ACN) with 0.1% trifluoroacetic acid (TFA). The diluted samples were spotted onto a MALDI plate and air-dried at room temperature. Mass spectrometry analysis was performed using a TIMS-TOF Flex instrument (Bruker) operating in MALDI mode. Spectra were acquired in positive reflector mode over a mass range of 1000-12000 m/z, with a laser intensity set at 30%.

Diffusion-ordered NMR Spectroscopy

Two-dimensional diffusion ordered (DOSY) NMR spectroscopy was performed with a stimulated echo sequence using bipolar gradient pulses. Delay lengths were held constant at Δ = 100 ms, and 32 spectra of 64 scans were acquired with the diffusion gradient strength varying between 5 % and 95 %. 2D-DOSY-NMR data was processed using MestReNova software (Bruker GmbH, Karlsruhe, Germany). Each free induction decay in the 2D-DOSY-NMR data sets was apodized, zero-filled to xK data points, and baseline corrected with a first-order polynomial fit. Manual phase correction was performed to fine-tune the first 1D spectrum and then applied to the entire data set. The 2D DOSY-NMR data were processed using the Bayesian Transform algorithm.

Circular Dichroism

Circular dichroism (CD) spectroscopy was performed using a J-815 CD Spectrometer (JASCO Corporation), incorporating a Peltier thermostated cell holder (PTC-423, JASCO Corporation) equipped with a recirculating cooler (JULABO F250, JASCO Corporation). A nitrogen flow of approximately 1.5 L/min was directed through the spectrometer and regulated using a nitrogen flow monitor (Afriso Euro-Index). Samples were prepared using various solvents (including Milli-Q water or phosphate-buffered saline (PBS)) and different temperatures and concentrations (0.03-0.25 mg/mL). Each sample was analyzed three times (n=3) in a quartz cuvette with a 1 mm diameter.

Small Angle X-ray Scattering

Small-angle X-ray scattering (SAXS) experiments were performed at the NCD-SWEET beamline (Project ID 2022097124) at the ALBA Synchrotron Light source (Barcelona, Spain). Acquisitions were performed using X-ray energies of 12.4 and 15 keV. 2D patterns were registered using a Pilatus 1M detector (Dectris, Switzerland) with a sample-to-detector distance of 3.6 meters. As data exhibited isotropy, 1D patterns were derived following azimuthal integration with the assistance of the pyFAI library[1]. Solutions under study were contained within a sample holder designed for liquids with Kapton® windows, with an optical path length of 2.0 mm. The intensity was expressed as a function of the scattering momentum transfer, q ($q = 4\pi\sin(\theta)/\lambda$), dependent on the incoming wavelength (λ) and the scattering angle (θ). After analyzing the potential radiation damage over the samples, sixty frames of 1 s each were collected for every sample. All measurements were conducted at room temperature (RT) (22°C). Given the variations in polymerization degree and monomer composition, data

interpretation was performed using a Guinier-Porod model[2], a semi-empirical function depending on three parameters: the radius of gyration of the particle (Rg), a power law dependence at low angles (q^{-s}) for qRg << 1, and a power law dependence at high angles (q^{-d}) for qRg >> 1, where s and d represent the exponents for the Guinier and Porod regions, respectively. In the case of spherical-like particles, an s value of 0 is anticipated; however, aggregation or particle interaction factors may influence this value, thereby affecting the Rg value derived from fitting. Therefore, the results were presented considering a correlative radius ($R_{g,corr}$), which mitigates the high correlation effects[3]. For this computation, an expected d-value of 3 due to polymer branching was considered[4].

$$Rg\text{corr} = Rg * \left(\frac{3}{\sqrt{(3-s)(d-s)}}\right)$$

Z-potential Measurements

Z-potential measurements were performed at 20°C using a Malvern ZetasizerNanoZS instrument equipped with a 532nm laser using disposable folded capillary cells (Malvern Instruments Ltd., Worcestershire, UK). Polymer solutions were prepared in PBS. Z-potential was measured for each sample per n = 3 (50 scans each).

Ultraviolet-Visible spectroscopy

Ultraviolet-visible (UV-VIS) measurements were performed at 25°C using a JASCO V-630 spectrophotometer with 1.0 cm matched quartz cells and a spectral bandwidth of 0.5 nm.

Fluorescence Spectroscopy for Critical Aggregation Concentration determination

The pyrene assay was performed following an established protocol. Solutions of diblock copolymers **6b**, **h**, and **i** were prepared to encompass a broad range of polymer concentrations (0.05-2.00 mg/mL, with a dilution factor of 1.5). Subsequently, 10 µL of 0.02 mg/mL pyrene solution in acetone was added to each solution. These mixtures were then transferred to vials and incubated at 37°C for 2 h for acetone evaporation. After a 24-h storage period, measurements were taken. Emission spectra were recorded between 350-450 nm with a fixed excitation wavelength of 335 nm using a CLARIOstar fluorescent plate reader. Data was analyzed by plotting the intensity ratio I383/I73 (emission polarity index) against the polymer concentration to determine the critical aggregation concentration (CAC).

Preparation of the Small Unilamellar Vesicles for Cardiolipin affinity studies

Cardiolipin (CL)-containing small unilamellar vesicles (SUVs) were prepared using the thin film method for CL binding studies. Briefly, the desired volume of stock solutions of 1,2-dioleoyl-*sn*-glycero-3-phosphocholine (DOPC, 25 mg/ml solution in $CHCl_3$, Avanti Polar Lipids) and bovine heart CL (5 mg/ml solution in EtOH, Sigma-Aldrich) was evaporated under reduced pressure. The resulting lipid film was resuspended in HEPES buffer (20 mM, pH 6.8) to acquire a 100:300 µM CL/DOPC solution. The resultant large multilamellar vesicles were sonicated in a bath-type sonicator (Cole Parmer Ultrasonic Cleaner 8891CPX, USA) at RT for 30 min followed by extrusion (LiposoFast-Basic, Avestin) through a 100 nm polycarbonate filter (Whatman® Nuclepore™). The quality of the resulting SUVs was evaluated via dynamic light scattering (DLS) (Zetasizer Nano ZSP, Malvern Panalytical Ltd.,

UK). All SUV samples were freshly prepared before each set of experiments. CL/DOPC (250:750 μM) and DOPC (1 mM) SUVs for 1,6-diphenyl-1,3,5-hexatriene (DPH, Acros) exclusion assay were prepared in the same manner.

Mitoplasts isolation for Cardiolipin affinity studies

Mitoplasts were isolated using differential centrifugation. The heart and liver of a healthy Sprague Dawley rat* were homogenized on ice in 1:10 (w/v) medium containing 180 mM KCl, 10 mM Tris/HCl, and 1 mM EGTA (pH 7.7 at 4° C) using a Teflon glass homogenizer. The homogenate was centrifuged at 750 g for 5 min at 4° C to remove residual tissue and cell debris. The supernatant was then separated and centrifuged at 6800 g for 10 min at 4° C. The obtained mitochondrial pellet was washed once, centrifuged (10 min at 6800 g), resuspended in a hypotonic solution (5 mM sucrose, 5 mM HEPES, 1 mM EGTA, pH 7.2, v/v 1:4), and incubated on ice for 20 min to remove the outer membrane of mitochondria. To remove electrostatically bound cytochrome c, 1M KCl solution was added (final KCl concentration of 300 mM), and the mixture was centrifuged for 30 min at 14500 g at 4° C. The supernatant was discarded, and the pellet was washed with 300 mM KCl solution and centrifuged twice. The final pellet was redissolved in a buffer containing 20 mM HEPES (pH 6.8), centrifuged again for 5 min at 14500 g at 4° C to completely remove excess KCl, then resuspended in 20 mM HEPES buffer (pH 6.8) and stored at -20° C until use.

*All organs used for mitoplast isolation were collected post-mortem from healthy animals assigned to control groups in unrelated experiments. This approach aligns with the 3R principles (*Replace, Reduce, Refine*) outlined in EU actions for the protection of animals used for scientific purposes. Specifically, it adheres to the principles of *Replace* by using isolated organelles instead of live animals, and *Reduce* by maximizing the data obtained per animal to minimize the need for additional specimens. No additional animals were used specifically for this study. All experimental procedures complied with EU Directive 2010/63/EU and relevant local regulations. **Ethical approval for experiments** involving animals used for organelle isolation was obtained from the Latvian Animal Protection Ethical Committee of the Food and Veterinary Service in Riga, Latvia (Nr.132/2022).

Atomic force microscopy

Measurements were performed on a JPK Nanowizard 3 with simultaneous imaging using a Zeiss LSM800 confocal laser scanning microscope with a Zeiss C-Apochromat 20xA objective (Carl Zeiss). Diblock copolymers labeled with Atto488 were excited with a 488 nm laser, while membranes labeled with Atto655-DOPE were excited using a 633 nm He-Ne laser. Confocal microscopy was used to localize and image the areas of interest, after which atomic force microscopy (AFM) images of the same area were acquired in quantitative imaging mode using BioLever Mini BL-AC40TSC2 (Olympus) cantilevers. The nominal force was 0.3 nN, the acquisition speed was 61.1 μm s^{-1}, and the Z-range was 110 nm. Images were processed in Gwyddion (v2.58, http://gwyddion.net). Image processing included

leveling of planes, polynomial alignment of rows, scar correction, cropping of outliers above 2.5 root mean square (RMS), and conservative denoising.

Total Internal Reflection Fluorescence Microscopy

Imaging was performed on a commercial Zeiss Elyra 7 using 488nm and 641 nm laser. Laser power was maintained at 0.1% total laser power. An alpha Plan-Apochromat 63x/1.46 Oil Korr M27 Var2 (Carl Zeiss, Germany) objective was used for total internal reflection fluorescence microscopy (TIRF-M) images, which were recorded using a pco.edge sCMOS camera (pco.edge 4.2 CLHS) using an exposure time of 100 ms. Consecutive images for the Atto488 labeled diblock copolymer channel and Atto655-DOPE labeled membrane channel were acquired with different tracks to minimize fluorescence crosstalk. All images were captured at a stabilized temperature of 30° C.

Fluorescence Correlation Spectroscopy

Z-scan fluorescence correlation spectroscopy (FCS) was employed to minimize the bias introduced by the focus shift to measure the diffusion coefficient of the membrane and the diblock polymers on the membrane. Briefly, 30 s acquisitions were collected for a z-range of 2 μm with a step size of 0.2 μm. The autocorrelation curves were calculated for the entire range and fitted for diffusion times (τ_D) and the average number of particles. A Lorentzian curve was fitted to estimate the position of the membrane, and the other z positions were represented as distance from that focal plane. Parabolae were fitted for $\tau_D(z)$ and N(z) according to the following equations to calculate the diffusion coefficient, D and N_0.

$$N(z) = N * \left(1 + \frac{\lambda_0^2 z^2}{\pi^2 n^2 \omega_0^4}\right),$$

$$\tau_D(z) = \frac{\omega_0^2}{4D} * \left(1 + \frac{\lambda_0^2 z^2}{\pi^2 n^2 \omega_0^4}\right)$$

Measurements were performed on a Zeiss LSM980 laser scanning confocal microscope. 488 nm and 639 nm lasers were used to measure diblock copolymers and membranes. A C-Apochromat 40x/1.2 Korr M27-Water objective lens with a mechanized correction collar (Carl Zeiss, Germany) was used for measurements. The temperature was stabilized at 28° C for all the measurements. Custom scripts were used to correlate and fit the data.

Fluorescence Lifetime Spectroscopy

A Microtime 200 system (PicoQuant GmBH, Germany) equipped with a PicoHarp, a dual SPAD detection unit, and time-correlated single photon counting (TCSPC) were used for measurements. An inverted microscope (Olympus X1-71) was also used with a water immersion objective (UPlanApo 60x, NA 1.2, Olympus, Japan). Excitation was performed with pulsed light at a frequency of 20 MHz. Fluorescence emission was collected using the same excitation objective and carefully focused through a 50 μm pinhole. The emission was collected with an emission bandpass filter BP 605/64. Data were

fitted with the SymphoTime64 software, and the instrument response function (IRF) was auto-calculated for all the measurements.

Small Unilamellar Vesicles for physical studies

SUVs were produced using sonication. Briefly, desired lipids in chloroform were dried in a glass vial under a nitrogen stream and then left in a desiccator under vacuum to completely dry. The dried lipid film was rehydrated with respective buffers (Buffer A, 150 mM KCl, 25 mM Tris. 5 mM MgCl2, pH 7.2 for SLB production and Buffer B, 150 mM KCl, 25 mM Tris, pH 7.2 for membrane tension measurements). The solution was vortexed until the translucent lipid film on the glass vial disappeared, and the solution turned turbid. The solution was aliquoted in PCR tubes and sonicated in a bath sonicator till the solution was clear and transparent. For membrane tension measurements, 1 μm of Flipper-TR was added to the sonicated SUVs for labeling.

Supported Lipid Bilayers

Supported lipid bilayers (SLBs) were produced as previously described (cite). Briefly, #1.5 coverslips were used to stick cut Eppendorf tubes (0.5 mL) to form a manual sample holder. These sample holders were cleaned under air plasma for 1 min. SLBs were formed by fusing vesicles to the glass substrate at 45°C for 5 min. SLBs were washed with washing buffer (10x volumes of sample) and then slowly cooled to RT.

Zeta potential Measurements in Small Unilamellar Vesicles

ZetaSizer Nano (Malvern Instruments, Westborough, MA) was used to measure the electrophoretic mobility of SUVs while suspended in solution. Electrophoretic mobility was used to approximate particle surface charge and was transformed into zeta potential using the Helmholtz−Smoluchowski equation. The samples were measured at 25° C.

Cell culture protocols

HTB-26™ Basal (Triple Negative) MDA-MB-231 and HTB-22™ (human Luminal A) MCF-7 cells from ATCC® and Hep G2 from Cell Lines Service (CLS) GmbH were cultured in DMEM/F-12 medium supplemented with 10% fetal bovine serum (FBS) and 1% penicillin/streptomycin (P/S). BJ fibroblasts from LGC STANDARDS, S.L.U were cultured in EMEM medium supplemented with 10% FBS and 1% P/S. BV-2 microglial cells from CLS GmbH were cultured in RPMI medium supplemented with 10% FBS, 1% P/S, and 1% GlutaMAX™. Cells were maintained at 37°C in an atmosphere of 5% CO_2 and 95% air. The cell medium was replaced every two to three days, and passaging was performed once weekly when 80% of cell confluence was reached.

Erythrocyte Isolation

Erythrocytes were isolated from fresh mouse blood collected via cardiac puncture after being sacrificed and placed in a tube containing an anticoagulant (0.5 M EDTA; 1/10 volume) on ice. The blood was then diluted with PBS (pH 7.4) to a final volume of 10 mL and centrifuged at 3000 rpm for 10 min at 4 °C, repeating this step three times. After centrifugation, the supernatant (plasma) was carefully separated from the pellet (erythrocytes).

Animal experiments were performed in accordance with the European Communities Council Directive (86/609/ECC) and the Spanish Royal Decree 1201/2005. All procedures were approved by the Institutional Animal Care and Use Committee and carried out by accredited and trained staff, ensuring compliance with animal welfare rules. Eight-week-old female Balb/c mice, sourced from Harlan Laboratories Inc. (Spain, EU) or Envigo Laboratories Ltd. (Spain, EU), were housed in the animal facility of the Príncipe Felipe Research Center under specific-pathogen-free conditions. The facility maintained controlled temperature and humidity with a 12-hour light-dark cycle, and food pellets and water were provided ad libitum throughout the experiment. Mice were euthanized following ethical protocols using CO_2 inhalation.

c. Synthetic Procedures and Physicochemical Characterization of Novel Polyproline-based Diblock Polymers

Synthesis of PLO(Z)-b-PLP and PLL(Z)-b-PLP

Poly(N-benzyloxycarbonyl-L-ornithine)-b-poly(proline) (2a-i) and poly(N-benzyloxycarbonyl-L-Lysine)-b-poly(proline) ***(4a-i)*** *and* ***(5)***

Ornithine Z or lysine Z NCAs were added to a Schlenk tube fitted with a stirring bar and a stopper. After three cycles of vacuum/N_2, the mixture was dissolved in anhydrous DMF (C = 180 mg/ml). The initiator (n-butylamine) solution (C = 20 mg/ml) was then dispensed into flasks containing the monomer (MM) solution to obtain the desired $[MM]_0/[I]_0$. The reactions were stirred at 10 ºC for 16 h. Once NCA consumption was confirmed by IR spectroscopy, the obtained solution was added to Proline NCA, which had previously been suspended in anhydrous acetonitrile (C = 99 mg/ml). The mixture was stirred at RT for an additional 16 h. Full conversion of the monomer was detected by IR spectroscopy. Reactions were quenched with excess diethyl ether and washed three times (40 ml). The precipitate was isolated by centrifugation (4400 rpm, 4 min) and dried under a vacuum. Samples were characterized by ^{1}H-NMR to estimate the fraction of each component. nBu-PLO(Z)-*b*-PLP and nBu-PLL(Z)-*b*-PLP were collected as white powders.

4a $PLO(Z)_{10}$-*b*-PLP_5: η=94% (0.4 g)
4b $PLO(Z)_6$-*b*-PLP_{22}: η= 80% (2.6 g)
4c $PLO(Z)_{16}$-*b*-PLP_{30}: η=99% (0.38 g)
4d $PLO(Z)_{35}$-*b*-PLP_6: η=76% (0.27 g)
4e $PLO(Z)_{35}$-*b*-PLP_{15}: η=87% (0.33 g)
4f $PLO(Z)_6$-*b*-PLP_{12}: η=99% (0.30 g)
4g PLO(Z)6-b-PLP7: η=80% (0.19 g)
4h PLO(Z)15-b-PLP47: η= 93% (0.41 g)
4i PLO(Z)20-b-PLP64: η= 65% (0.43 g)
5 PLL(Z)6-b-PLP20: η= 92% (0.32 g)

nBu-PLO(Z)-b-PLP (**4a-i**)

^{1}H-NMR (500 MHz, CF_3COOD, δ): 7.43 – 7.03 (5H, Ar of PLO(Z)), 5.55 – 5.02 (2H, CH_2Ar of PLO(Z)), 4.92 – 4.34 (1H, C_α of PLP and 1H, C_a of PLO(Z)), 4.28 – 3.51 (2H, C_δ of PLP), 3.19 (2H, C_d of PLO(Z)), 2.59 – 1.24 (4H, $C_{\beta+\gamma}$ of PLP and 4H, C_{b+c} of PLO(Z) and 4H CH_2CH_2NH), 0.90 – 0.72 (m, 3H, CH_3).

nBu-PLL(Z)-b-PLP (**5**)

^{1}H NMR (300 MHz, CF_3COOD, δ): 7.60 – 7.18 (5H, Ar of PLL(Z)), 5.67 – 5.10 (2H, CH_2Ar of PLL(Z)), 5.13 – 4.57 (1H, C_α of PLP and 1H, C_a of PLL(Z)), 4.25 – 3.65 (2H, C_δ of PLP), 3.53 – 3.18 (2H, C_d of PLL(Z)), 2.89 – 1.33 (4H, $C_{\beta+\gamma}$ of PLP and 4H, C_{b+c} of PLO(Z) and 4H $\underline{CH_2CH_2}NH$), 1.03 (t, J = 7.2 Hz, 3H).

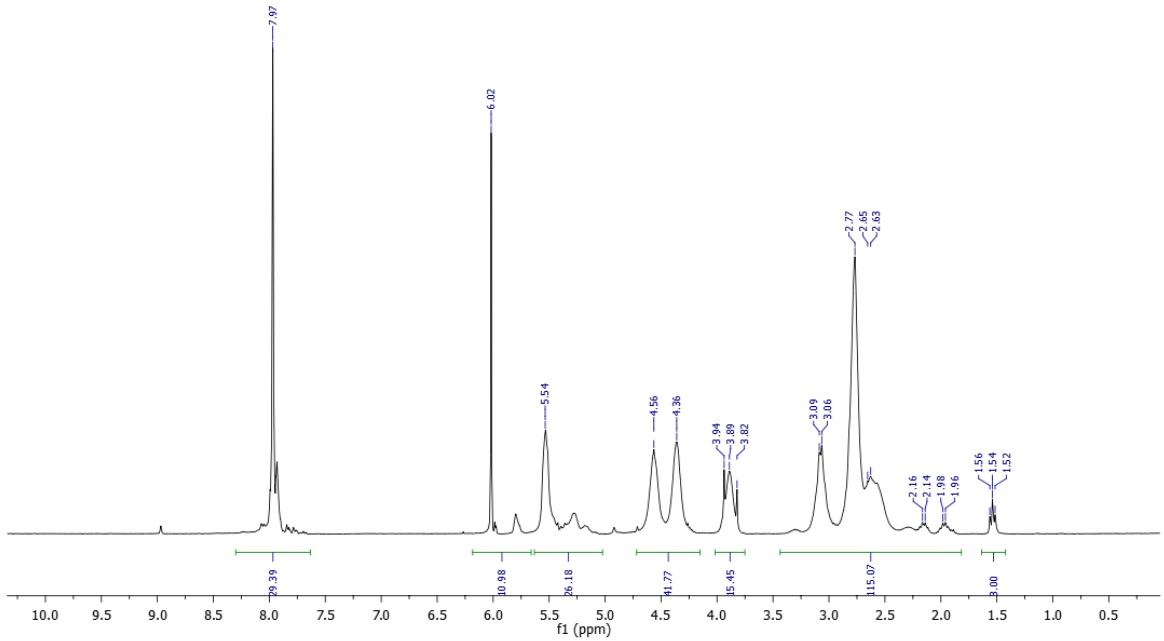


Figure S1. NMR spectra of diblock copolymer **4b** in deuterated Trifluoroacetic Acid (TFA-d_1) at 12 mg/ml

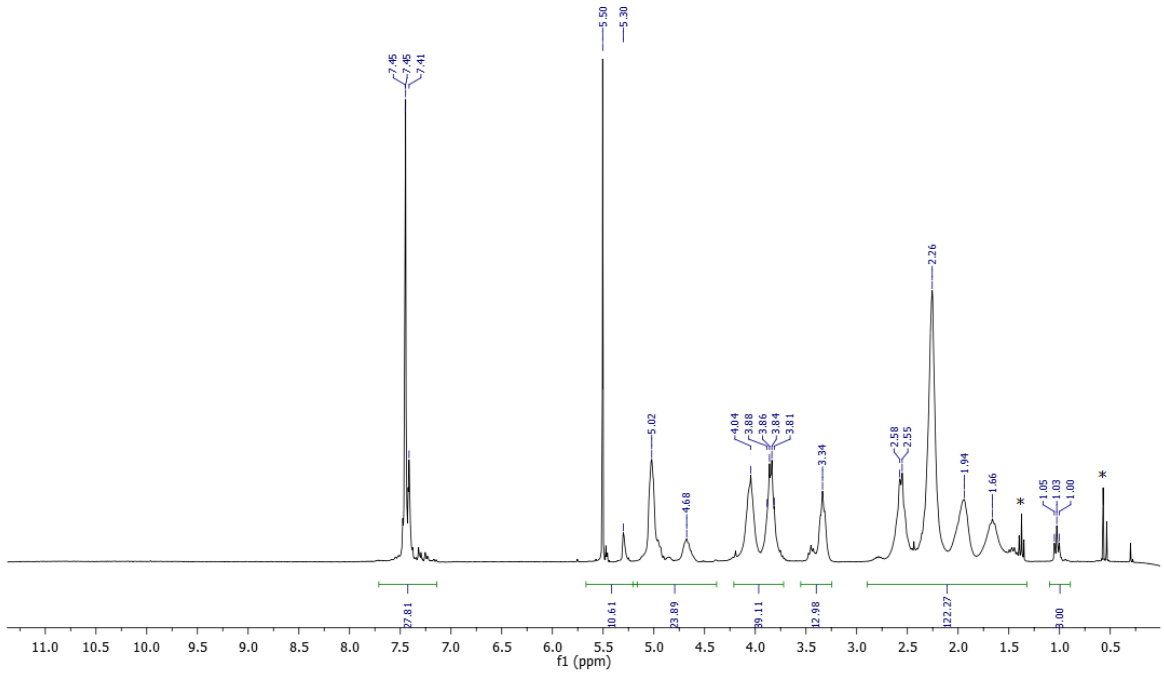
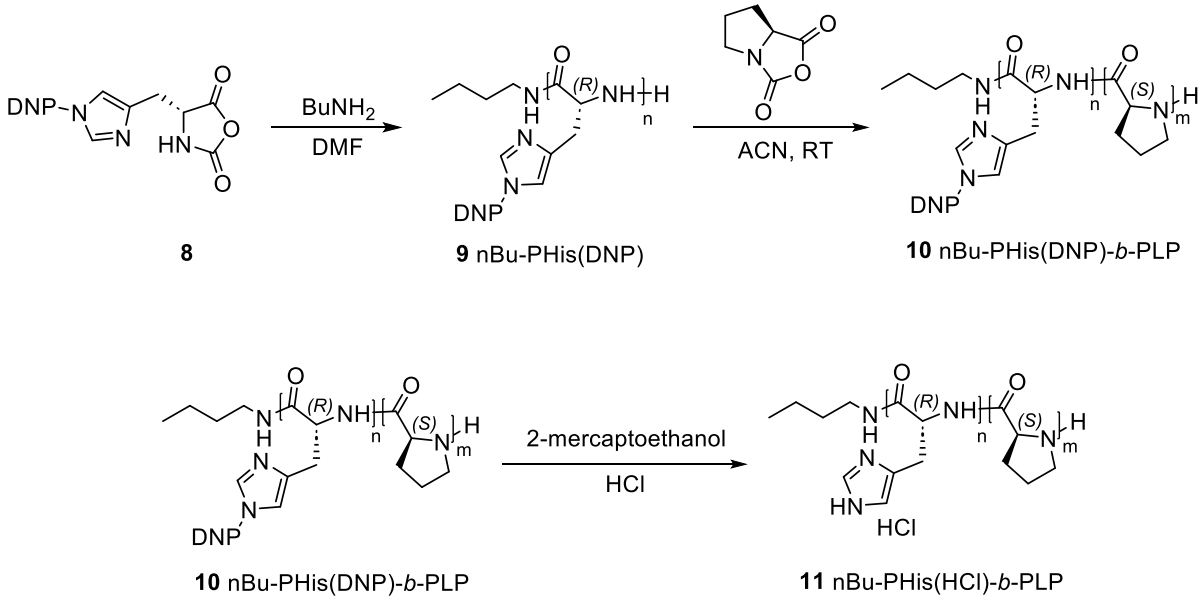


Figure S2. NMR spectra of diblock copolymer **5** in deuterated Trifluoroacetic Acid (TFA-d_1) at 12 mg/ml

Synthesis of Phis(DNP)-b-PLP



8

9 nBu-PHis(DNP)

10 nBu-PHis(DNP)-*b*-PLP

10 nBu-PHis(DNP)-*b*-PLP

11 nBu-PHis(HCl)-*b*-PLP

Scheme S1. General synthesis of the PHis-*b*-PLP diblock copolymer

*Poly(2,4-dinitrophenyl-L-histidine) (**9**)*

His(DNP) NCA was added to a Schlenk tube fitted with a stirring bar and a stopper. After three cycles of vacuum/N_2, the mixture was dissolved in anhydrous DMF (C = 180 mg/ml). The initiator (n-butylamine) solution (C = 20 mg/ml) was then dispensed into flasks containing MM solution to obtain the desired $[MM]_0/[I]_0$. The reactions were stirred at 10 ºC for 16 h. The reaction was quenched with excess diethyl ether and washed three times (40 ml). The precipitate was isolated by centrifugation (4400 rpm, 4 min) and dried under vacuum. Samples were characterized by ^{1}H NMR. nBu-PHis(DNP) was collected as an orange powder.

9 nBu-PHis(DNP): η= 99% (0.40 g)

nBu-PHis(DNP) ***(9)***

^{1}H NMR (300 MHz, CF_3COOD, δ): 9.53 – 9.28 (2H, Ar), 9.16 – 9.04 (1H, Ar), 8.43 – 8.31 (1H, *im*-CH), 8.17 – 7.91 (1H, *im*-CH), 5.76 – 5.27 (1H, C_a of PHis(DNP)), 4.24 – 3.73 (2H, CH_2-*im*), 1.96 – 1.80 (m, 2H, $CH_2\underline{CH_2}NH$), 1.77 – 1.63 (2H, $\underline{CH_2}CH_2NH$), 1.24 (t, *J* = 7.3 Hz, 3H).

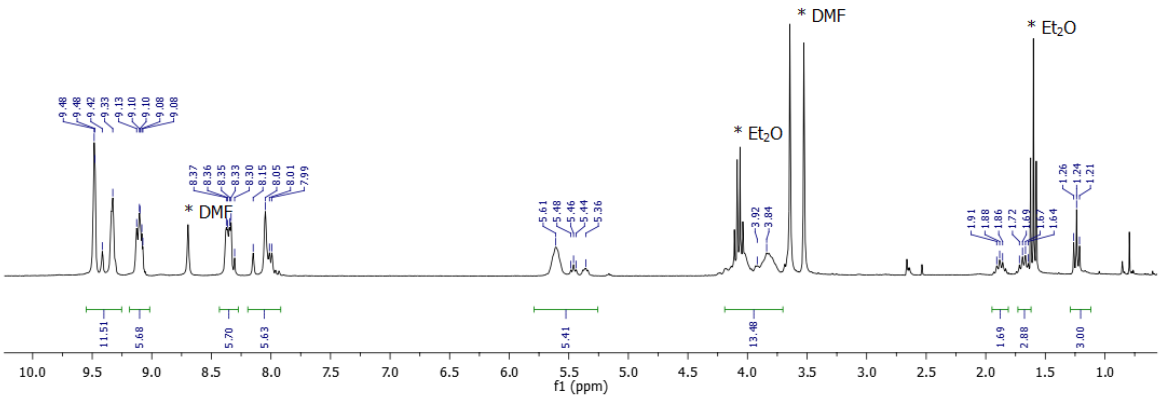


Figure S3. NMR spectra of diblock copolymer **9** in TFA-d_1 at 12 mg/ml

*Poly(2,4-dinitrophenyl-L-histidine)-b-poly(proline) **(10)***

Proline NCA was added to a Schlenk tube fitted with a stirring bar and a stopper. After three cycles of vacuum/N_2, the mixture was suspended in anhydrous acetonitrile (C = 99 mg/ml). The initiator (nBu-PHis(DNP)) was dissolved in DMF (C = 160 mg/ml), and the solution was then dispensed into flasks containing MM solution to obtain the desired $[MM]_0/[I]_0$. The reaction was stirred at RT for 16 h. Complete conversion of the monomer was detected by IR spectroscopy. The reaction was quenched with excess diethyl ether and washed three times (40 ml). The precipitate was isolated by centrifugation (4400 rpm, 4 min) and dried under vacuum. Samples were characterized by ^{1}H NMR to estimate the fraction of each component. nBu-PHis(DNP)-*b*-PLP was collected as an orange powder.

10 $PHis(DNP)_6$-*b*-PLP_{25}: η= 87% (0.21 g)

nBu-PHis(DNP)-b-PLP (**10**)

^{1}H NMR (500 MHz, TFA-d_1, δ): 9.18 (1H, Ar), 9.08 – 8.97 (1H, Ar), 8.87 – 8.75 (1H, Ar), 8.14 – 8.00 (1H, *im*-CH), 7.80 – 7.63 (1H, *im*-CH), 5.47 – 5.13 (1H, C_α of PLP), 5.05 – 4.69 (1H, C_a of PHis(DNP)), 4.21 – 3.31 (2H, C_δ of PLP and 2H, CH_2-im), 2.59 – 1.99 (4H, $C_{\beta+\gamma}$ of PLP), 1.63 – 1.54 ($CH_2CH_2CH_3$, 2H), 1.44 – 1.34 (CH_2CH_3, 2H), 0.94 (t, J = 7.3 Hz, 3H).

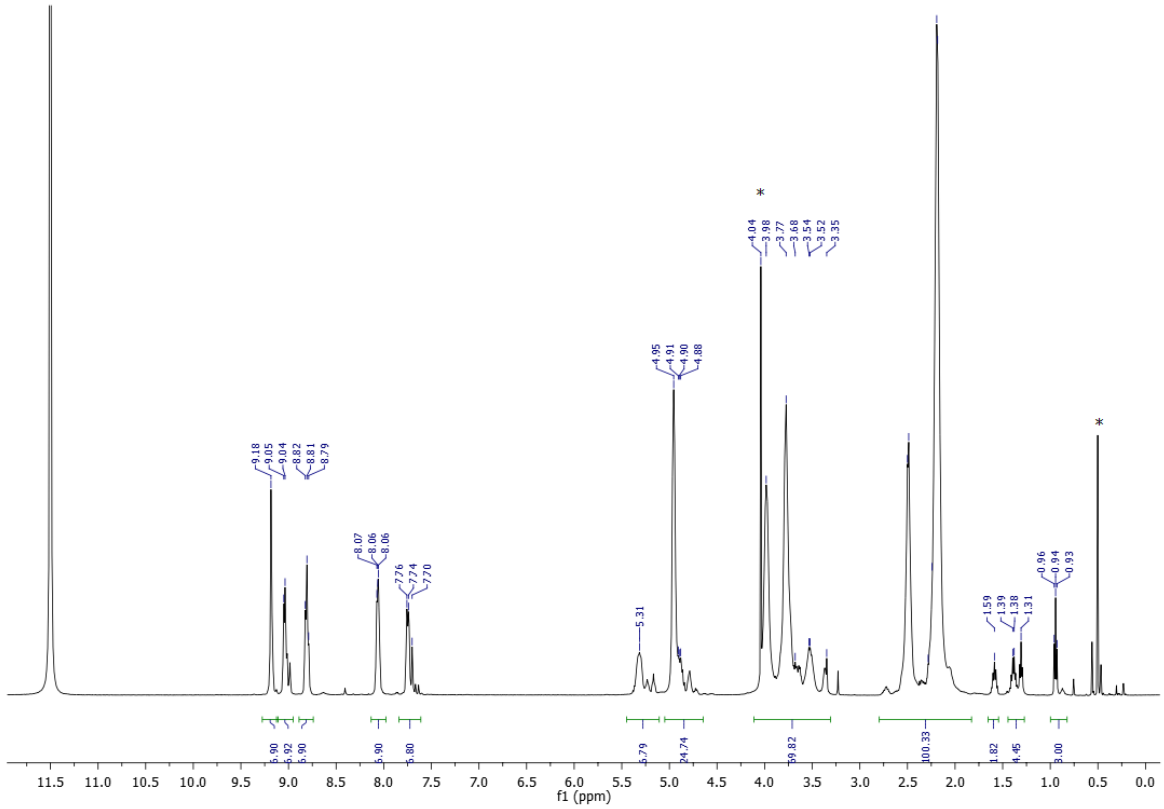


Figure S4. NMR spectra of diblock copolymer **10** in TFA-d_1 at 12 mg/ml

Synthesis of PLO(HBr)-b-PLP and PLL(HBr)-b-PLP

Poly(ornithine)hydrobromide-b-poly(proline) and poly(lysine)hydrobromide-b-poly(proline) ***(6a-i)*** *and* ***(7)***

Diblock copolymers of nBuPLO(Z)-*b*-PLP or nBuPLL(Z)-*b*-PLP were suspended in absolute chloroform at 0ºC (cooling bath applied) (50 mg/mL) and HBr in AcOH (33% wt., 240 eq.) was added dropwise. The mixture was removed from the cooling batch and stirred at RT for 3 h. The reaction was quenched with an excess of diethyl ether and washed three times. The precipitate was isolated by centrifugation (3750 rpm, 4 min) and dried under vacuum. The desired product was obtained after dialysis (Vivaspin®, 3000 MWCO Da or Spectra-Por® Float-A-Lyzer® 500-1000Da MWCO, depending on the Mw). Each sample was characterized by analytical GPC in aqueous containing 0.1M $NaNO_3$ and 0.005% NaN_3 as an additive and ^{1}H-NMR to characterize the fraction of each component. All products were collected as white powders.

6a PLO_{10}-*b*-PLP_5: η= 60% (0.17 g)

6b PLO_6-*b*-PLP_{22}: η= 70% (1.43 g)

6c $POrn_{16}$-*b*-PLP_{30}: η= 99% (0.30g)

6d $POrn_{35}$-*b*-PLP_{6}: η=62% (0.13 g)

6e $POrn_{35}$-*b*-PLP_{15}: η=72% (0.20 g)

6f PLO_{6}-*b*-PLP_{12}: η= 99% (0.21 g)

6g PLO_{6}-*b*-PLP_{7}: η= 99% (0.13 g)

6h PLO_{18}-*b*-PLP_{54}: η= 84% (0.26 g)

6i PLO_{22}-*b*-PLP_{64}: η= 74% (0.20 g)

7 PLL_{7}-*b*-PLP_{22}: η= 73% (0.17 g)

nBu-PLO(HBr)-b-PLP (**6a-i**)

^{1}H NMR (300 MHz, D_2O, δ): 4.78 – 4.71 (1H, C_α of PLP covered with D_2O), 4.51 – 4.21 (1H, C_a of PLO), 4.03 – 3.39 (2H, C_δ of PLP and CH_2 of $CH_3CH_2CH_2CH_2NH$), 3.08 (2H, C_d of PLO), 2.46 – 1.29 (4H, $C_{\beta+\gamma}$ of PLP and 4H, C_{b+c} of PLO and 4H CH_2CH_2NH), 0.92 (t, J = 7.3 Hz, 3H, CH_3).

nBu-PLL(HBr)-b-PLP (**7**)

^{1}H NMR (500 MHz, D_2O, δ): 4.77 – 4.72 (1H, C_α of PLP covered with D_2O), 4.50 – 4.13 (1H, C_a of PLL), 3.99 – 3.34 (2H, C_δ of PLP and CH_2 of $CH_3CH_2CH_2CH_2NH$), 3.30 – 2.94 (2H, C_e of PLL), 2.65 – 1.14 (4H, $C_{\beta+\gamma}$ of PLP and 4H, C_{b+c+d} of PLL and 4H CH_2CH_2NH), 0.92 (t, J = 7.3 Hz, 3H, CH_3).

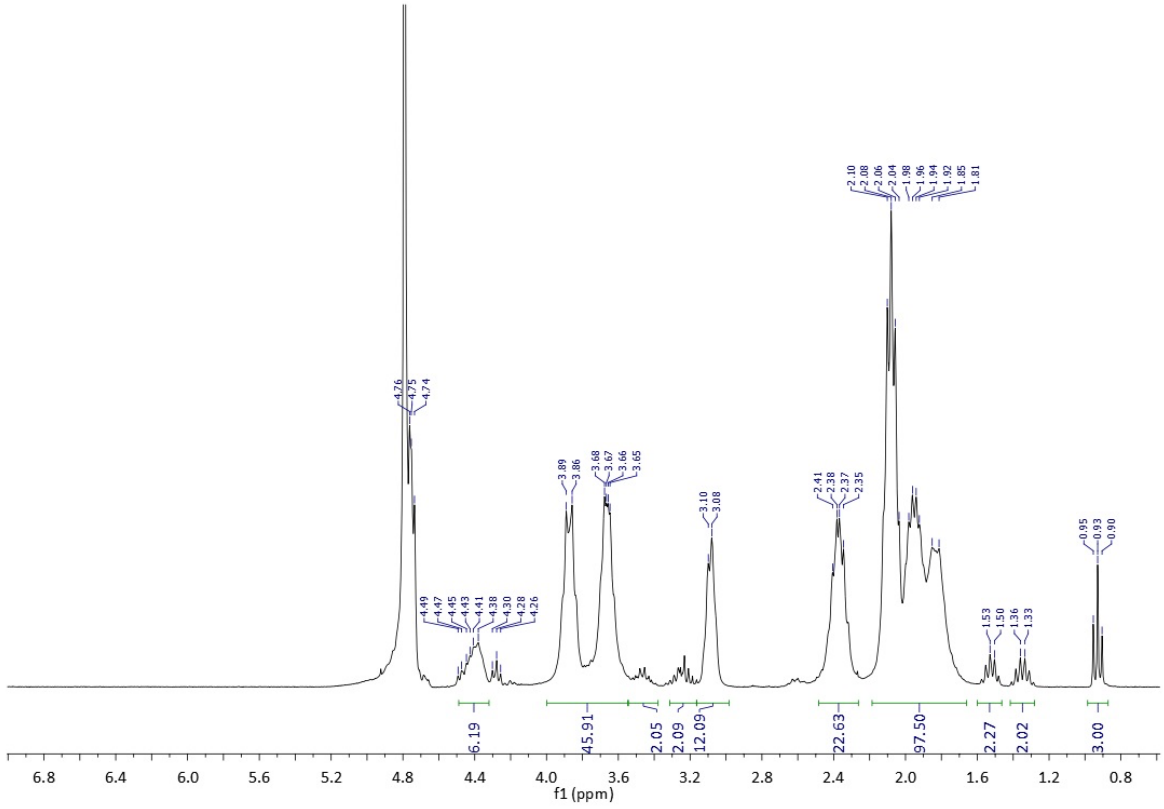


Figure S5. NMR spectra of diblock copolymer **6b** in D_2O at 12 mg/ml

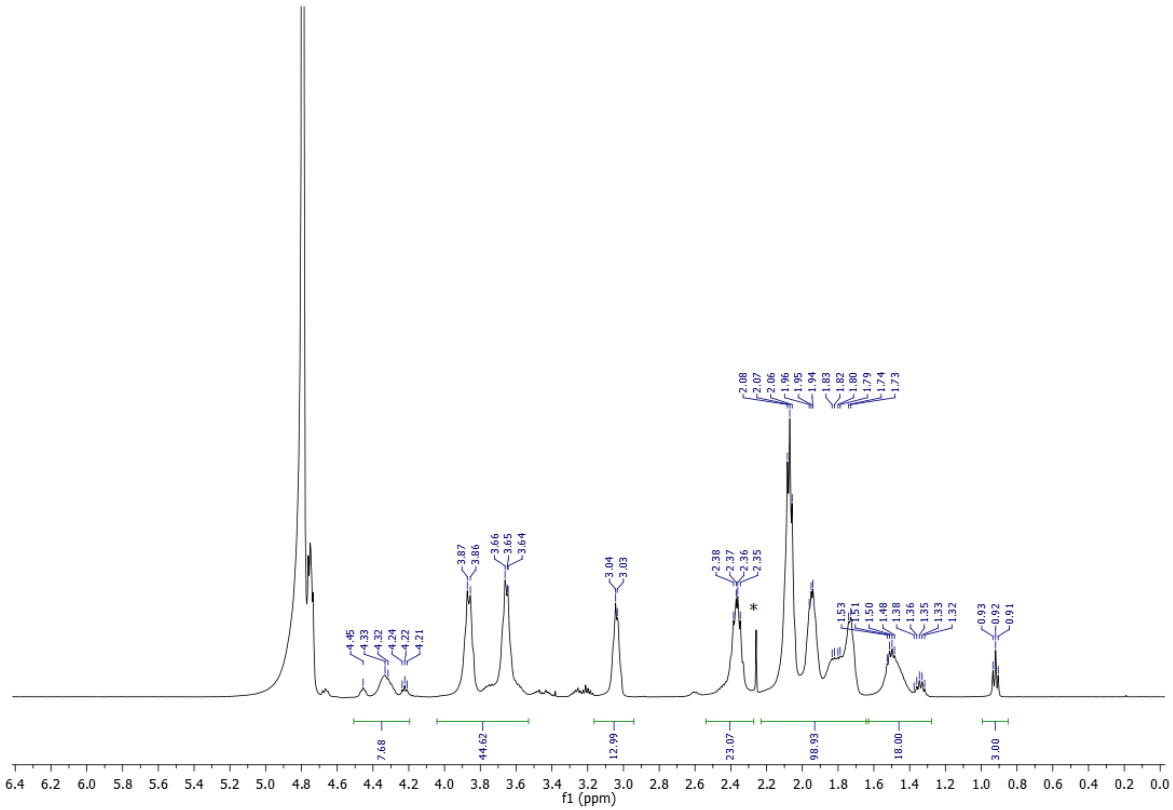


Figure S6. NMR spectra of diblock copolymer **7** in D_2O at 12 mg/ml

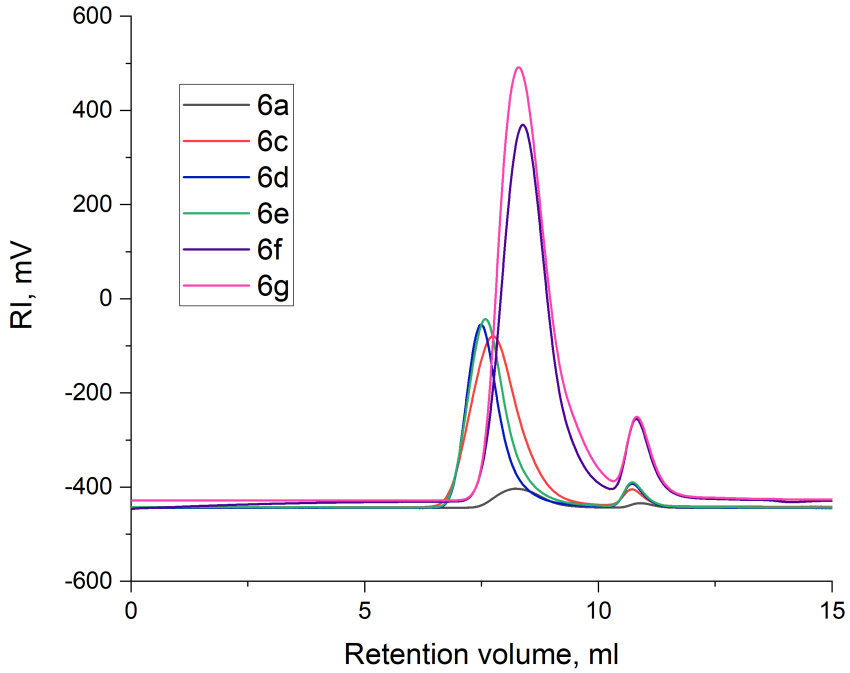


Figure S7. GPC (0.1M $NaNO_3$, 0.005% NaN_3 refractive index channel) chromatogram for diblock copolymers **6a, c, d, e, f, g**.

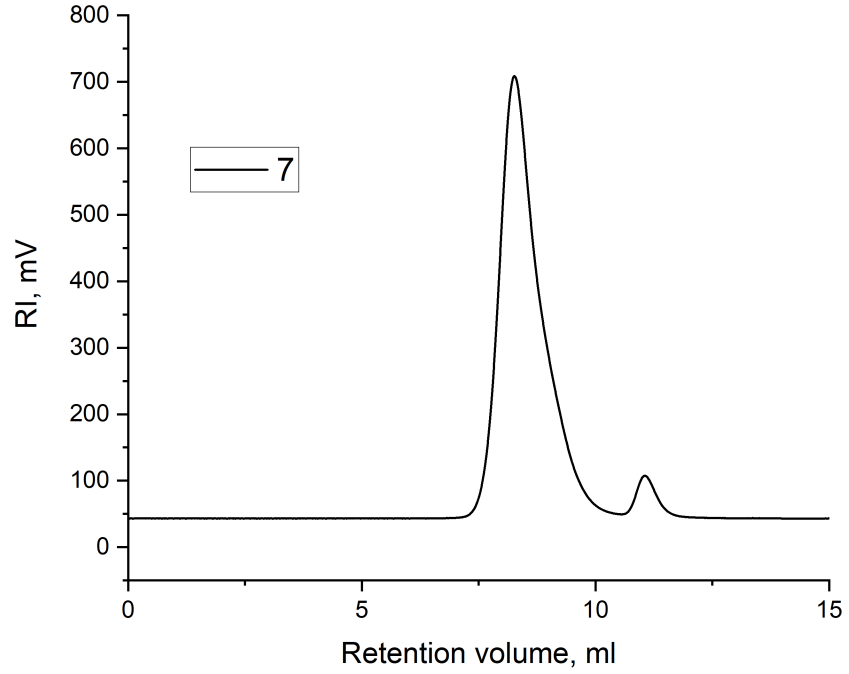


Figure S8. GPC (0.1M $NaNO_3$, 0.005% NaN_3 refractive index channel) chromatogram for diblock copolymer **7**

Synthesis of PHis(HCl)-b-PLP

Poly(histidine)hydrochloride-b-poly(proline) ***(11)***

Diblock copolymer **10** was suspended in dry DMF, and 2-mercaptoethanol (10 eq.) was added dropwise. After finishing, the mixture was stirred at RT for 16 h. The reaction mixture was precipitated in diethyl ether and washed with diethyl ether and acetone three times each. The precipitate was isolated by centrifugation (3750 rpm, 4 min) and dried under vacuum. The dry deprotected diblock copolymer was suspended in dry 1,4-dioxane in anhydrous conditions, and an excess of HCl in 1,4-dioxane was added. The reaction mixture was stirred for 3 h and poured into diethyl ether. The precipitate was isolated by centrifugation (4400 rpm, 4 min) and dried under vacuum. The desired product was purified by dialysis (100-500 MWCO Da). A yellow powder was obtained after freeze-drying.

11 $PHis_6$-*b*-PLP_{25}: η= 60% (0.15 g)

nBu-PHis(HCl)-b-PLP (**11**)

^{1}H NMR (500 MHz, TFA-d_1, δ): 8.92 – 8.53 (1H, *im*-CH), 7.80 – 7.38 (1H, *im*-CH), 5.33 – 4.77 (1H, C_a of PHis and 1H C_α of PLP), 4.24 – 3.33 (2H, C_δ of PLP and 2H, CH_2-im), 2.84 – 2.04 (4H, $C_{\beta+\gamma}$ of PLP), 1.67 – 1.57 (m, $CH_2CH_2CH_3$, 2H), 1.48 – 1.33 (m, CH_2CH_3, 2H), 1.02 (t, J = 7.3 Hz, 3H, CH_3).

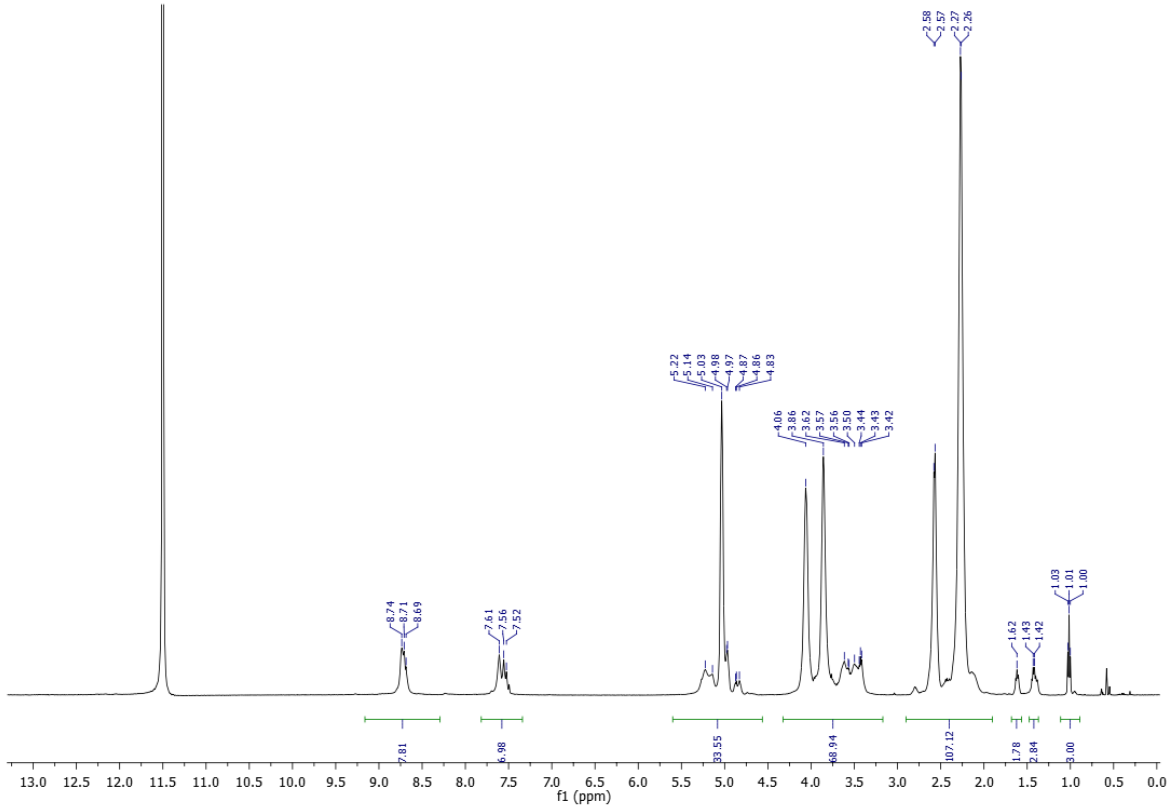
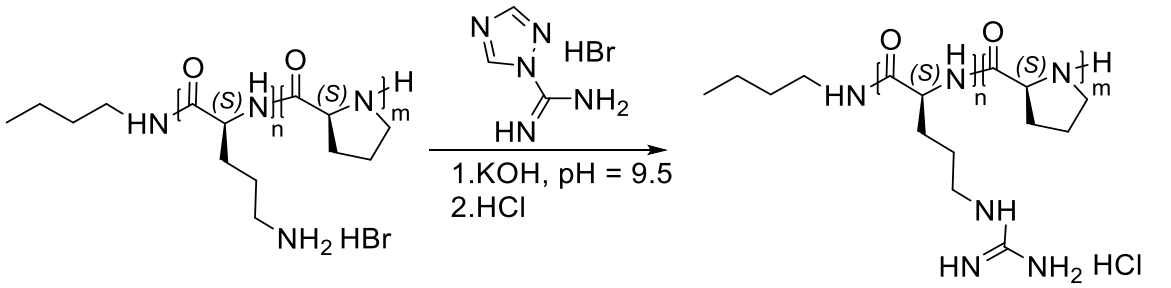


Figure S9. NMR spectra of diblock copolymer **11** in TFA-d_1 at 12 mg/ml

Synthesis of PArg(HCl)-b-PLP



6b nBu-POrn(HBr)-*b*-PLP **14** nBu-PArg(HCl)-*b*-PLP

Scheme S2. Synthesis of nBu-PArg(HCl)-*b*-PLP

Poly(arginine)hydrochloride-b-poly(proline) **(14)**

1H-1,2,4-triazole-1-carboxamidine hydrochloride (1 eq. each PLO group) was dissolved in 450 µL of Milli-Q water and basified with 5M KOH to reach pH=9.5. Separately, nBuPLO(HBr)-b-PLP was dissolved in 200 µL of Milli-Q water, and triazole solution was added. The mixture was left stirring for 16 h, terminated by adding 1M HCl to reach pH = 5. The mixture was passed through a 1.2 µL filter and purified by dialysis (Spectra-Por® Float-A-Lyzer® 500-1000Da MWCO). A white powder was obtained after freeze-drying.

14 $PArg_7$-b-PLP_{22}: η= 70% (0.09 g)

nBu-PArg(HCl)-b-PLP (**14**)

^{1}H NMR (500 MHz, D_2O, δ): 4.77 – 4.71 (1H, C_α of PLP covered with D_2O), 4.52 – 4.21 (1H, C_a of PArg), 3.93 – 3.41 (2H, C_δ of PLP and CH_2 of $CH_3CH_2CH_2CH_2NH$), 3.30 – 3.03 (2H, C_d of PArg), 2.67 – 1.21 (4H, $C_{\beta+\gamma}$ of PLP and 4H, C_{b+c} of PArg and 4H CH_2CH_2NH), 0.91 (t, J = 7.3 Hz, 3H).

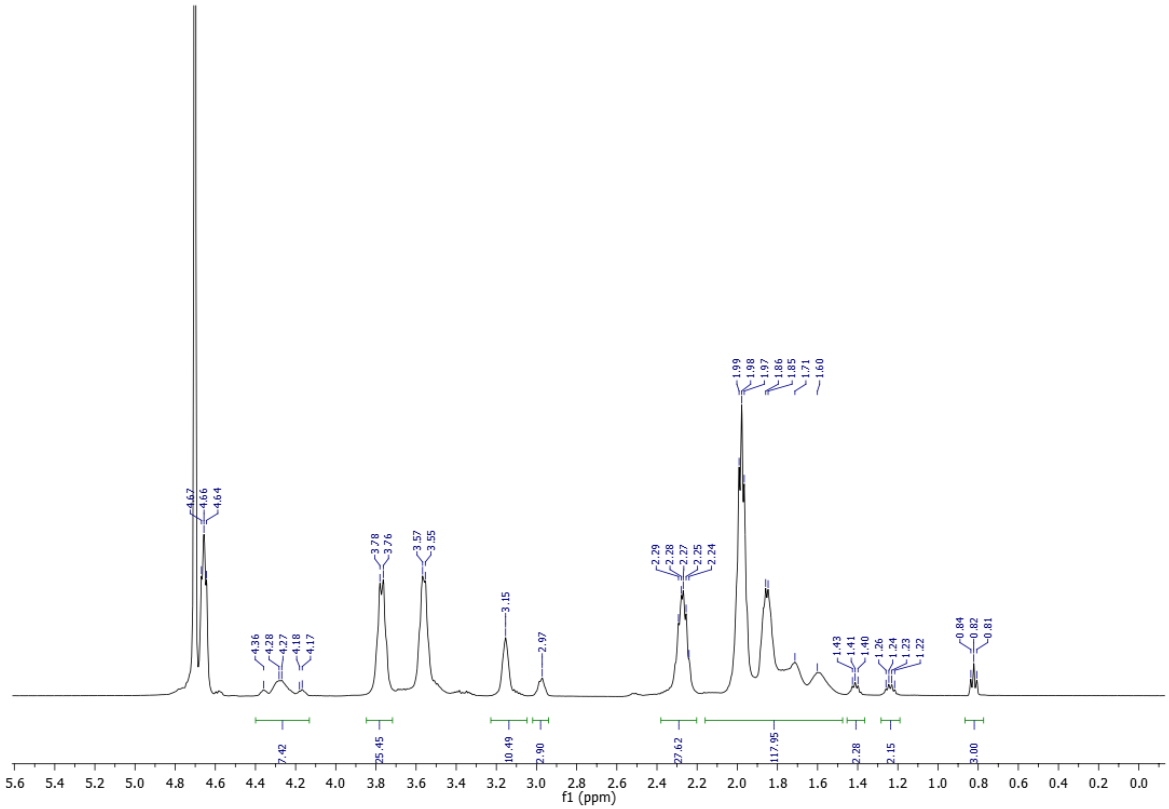


Figure S10. NMR spectra of diblock copolymer **14** in D_2O at 12 mg/ml

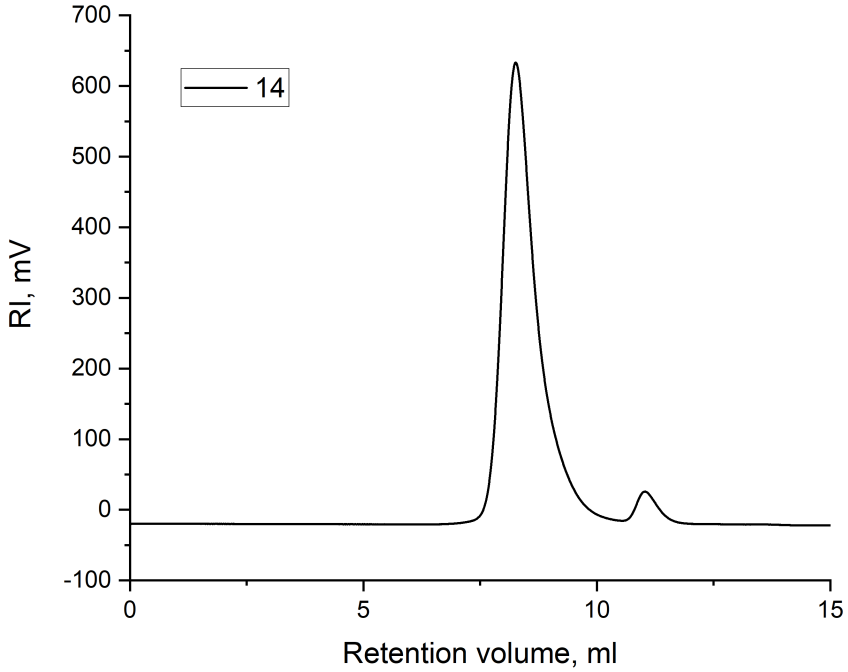
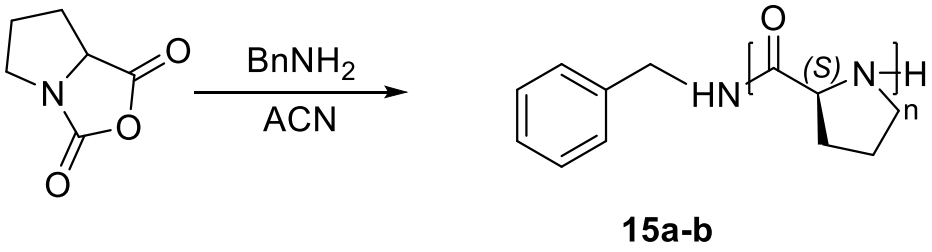


Figure S11. GPC (0.1M $NaNO_3$, 0.005% NaN_3 refractive index channel) chromatogram for diblock copolymer **14**

Synthesis of nBuPLP



15a-b

Scheme S3. Synthesis of BnPLP **(15a-b)**

Polyproline **(15a-b)**

Proline NCA was added to a Schlenk tube fitted with a stirring bar and a stopper. After three cycles of vacuum/N_2, the mixture was suspended in anhydrous acetonitrile (C = 50 mg/ml). The initiator (benzylamine) was dissolved in acetonitrile (C = 190 mg/ml), and the solution was then dispensed into flasks containing MM solution to obtain the desired $[MM]_0/[I]_0$. The reaction was stirred at RT for 16 h. Complete conversion of the monomer was detected by IR spectroscopy. The reaction was quenched with excess diethyl ether and washed three times (40 ml). The precipitate was isolated by centrifugation (4400 rpm, 4 min) and dried under vacuum. Samples were used in the next step without further characterization. Homopolyprolines were dissolved in trifluoroethanol (TFE, 2ml) and left stirring for 16 h. TFE was evaporated, and the diblock polymer redissolved in water. The desired product was

obtained after dialysis (Vivaspin®, 3000 MWCO Da, or 500-1000 MWCO Float-A-Lyzer®). A white powder was obtained after freeze-drying.

Bn-PLP

^{1}H NMR (300 MHz, D_2O, δ): 7.56 – 7.32 (5H, Ar), 3.97 – 3.58 (2H, C_δ of PLP), 2.53 – 1.92 (4H, $C_{\beta+\gamma}$ of PLP), αnH covered with D_2O.

Table S1. Analytical results summary for **Bn-PLP**

Code	DP[a](m) for Pro	MW by SEC (kDa)[b]	PDI
15a	14	2.4	1.131
15b	25	3.2	1.063

a) Estimated by NMR; b) Determined by SEC wherein the cited numbers are subject to a reasonable uncertainty within the range ±20%

The homopolyproline employed in this study was synthesized following previously reported synthetic procedures at milligram scale and characterized using ^{1}H-NMR, which agreed with the reported data[5].

Circular Dichroism

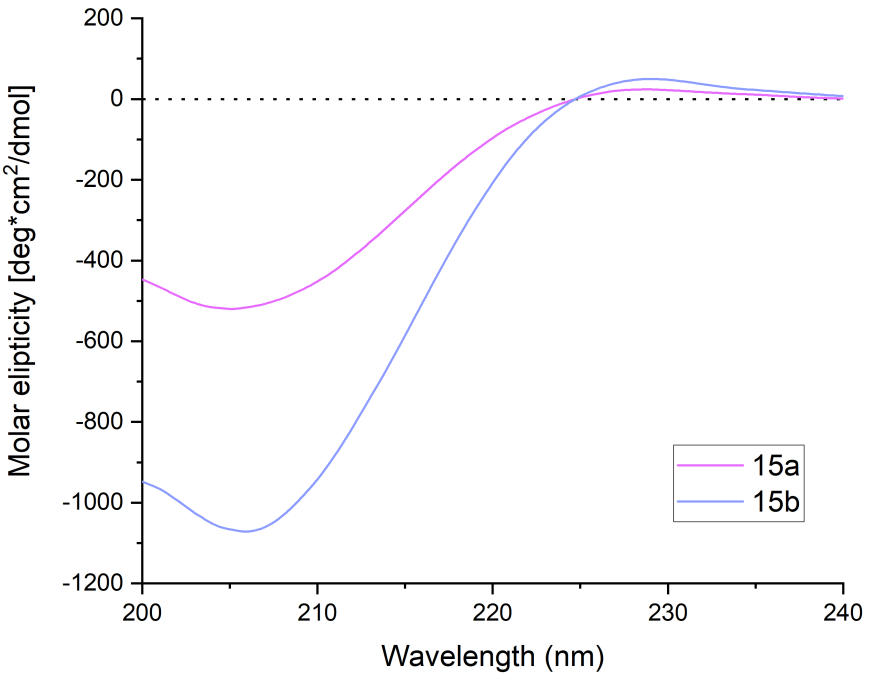


Figure S12. Circular dichroism spectra of Bn-PLP **(15a-b)** in Milli-Q water

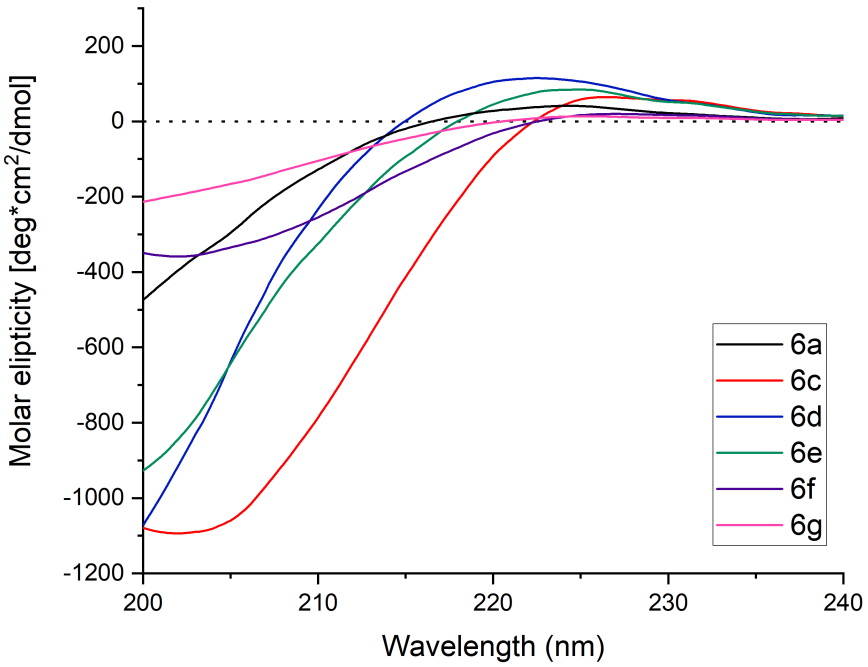


Figure S13. Circular dichroism spectra of diblock copolymers PLOn-PLPm with different n:m ratios (**6a, c, d, e, f, g**) in Milli-Q water

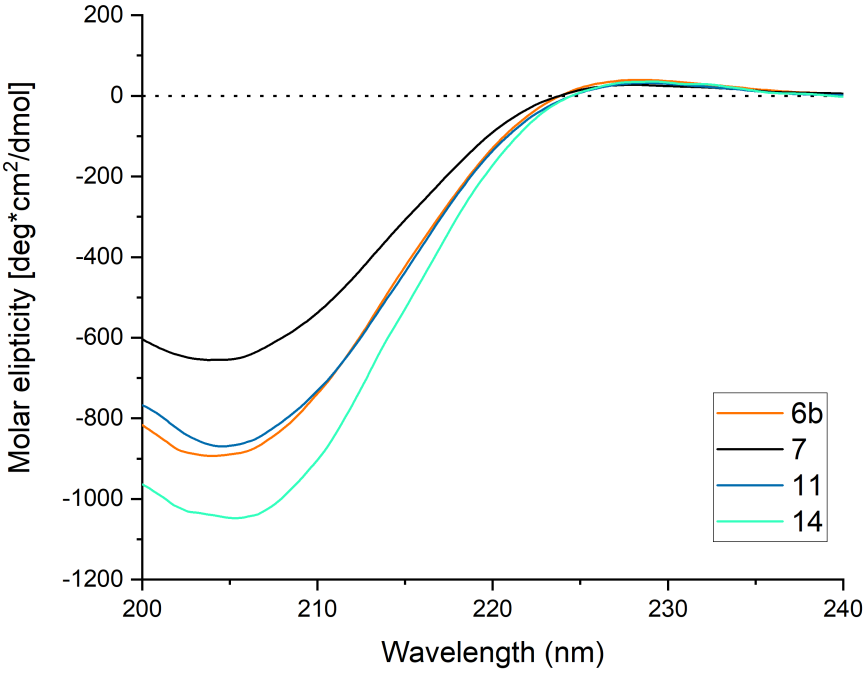


Figure S14. Circular dichroism spectra diblock copolymers with different polycationic blocks (Plys, Parg, and Phis) (**6b, 7, 11, 14**) in Milli-Q water

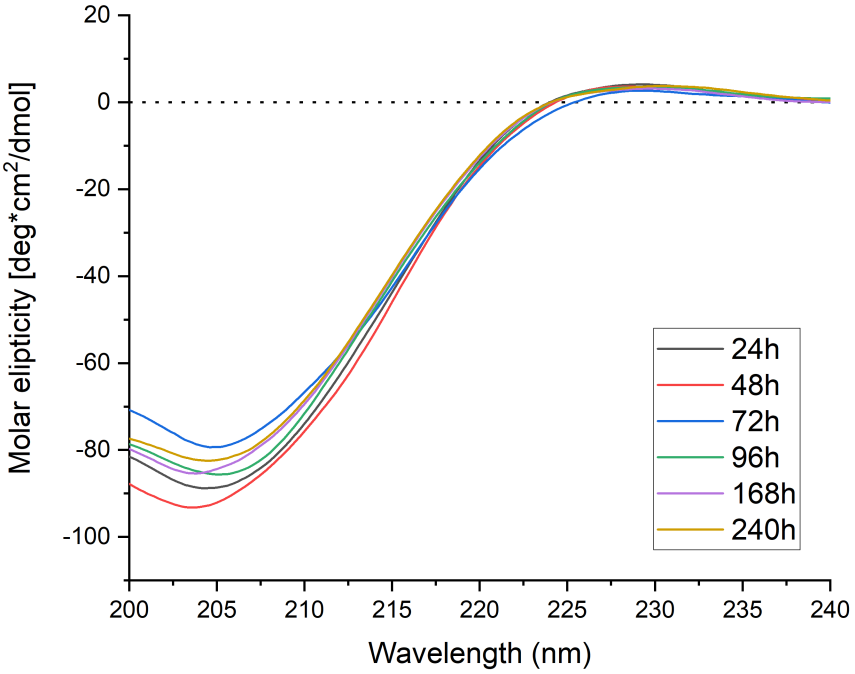


Figure S15. Circular dichroism spectra of **6b** during stability studies (freezing/defrosting) in Milli-Q water

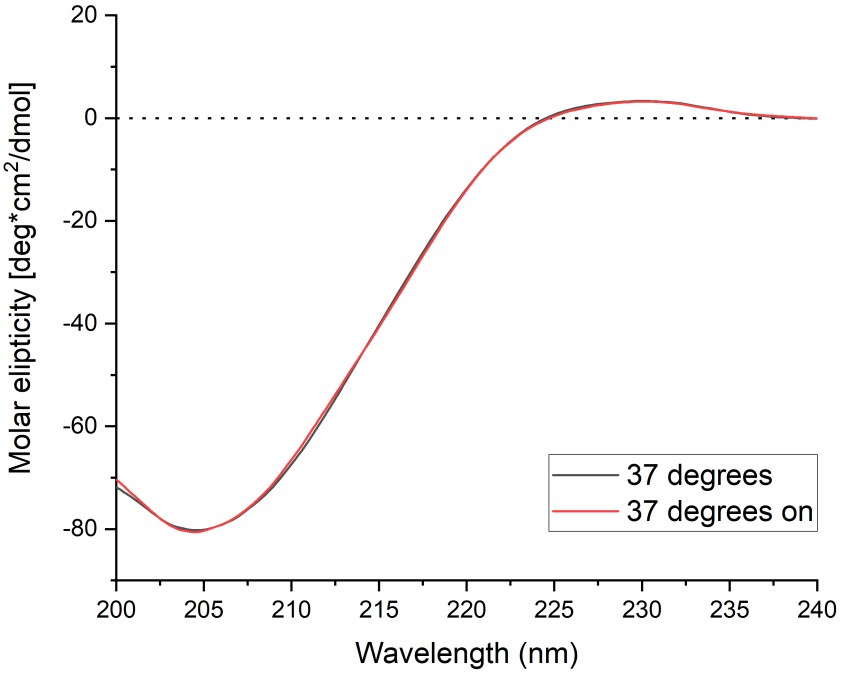


Figure S16. CD spectra of **6b** at 37 degrees (physiological temperature) and at 37 degrees after 24 h (on) in Milli-Q water

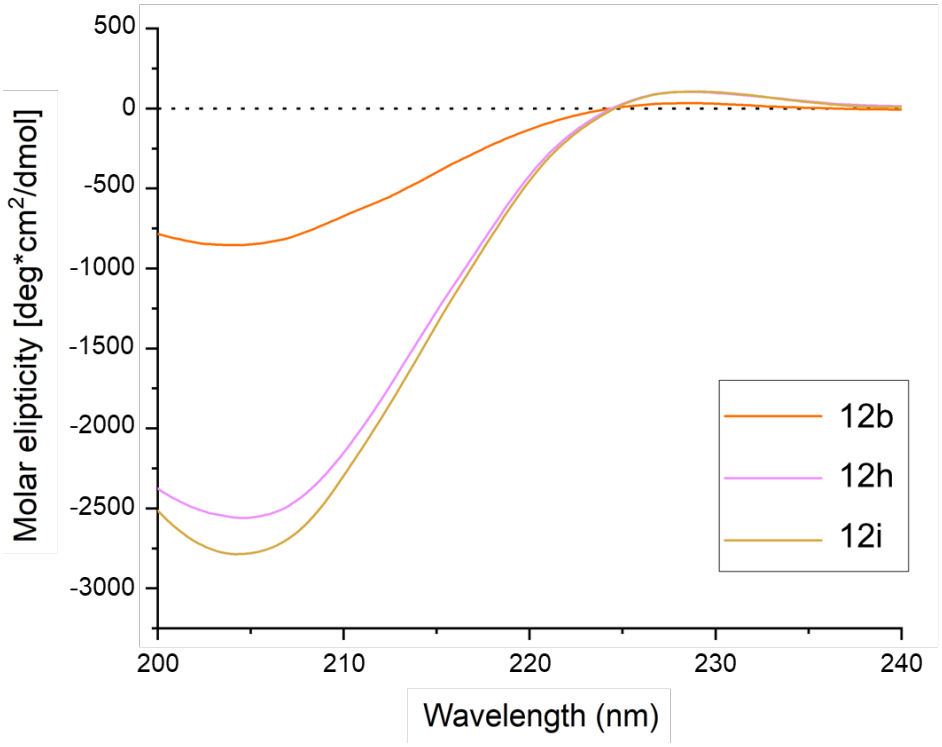


Figure S17. Circular dichroism spectra of labeled (Cy5) 6b, 6h and 6i **(12b, h, i)** in Milli-Q water

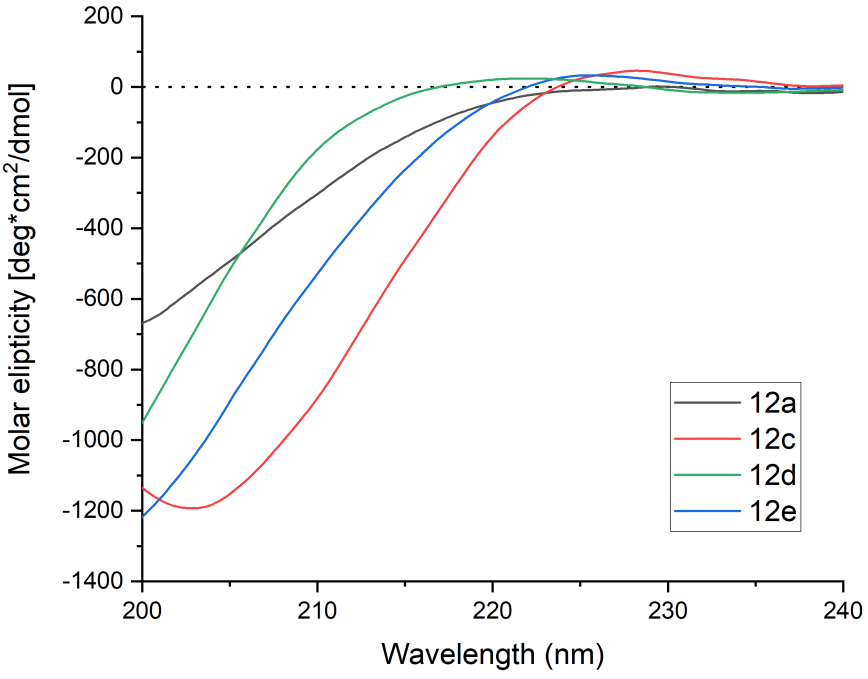


Figure S18. Circular dichroism spectra of labelled (Cy5) 6a, 6c, 6d, and 6e **(12a, c, d, e)** in Milli-Q water

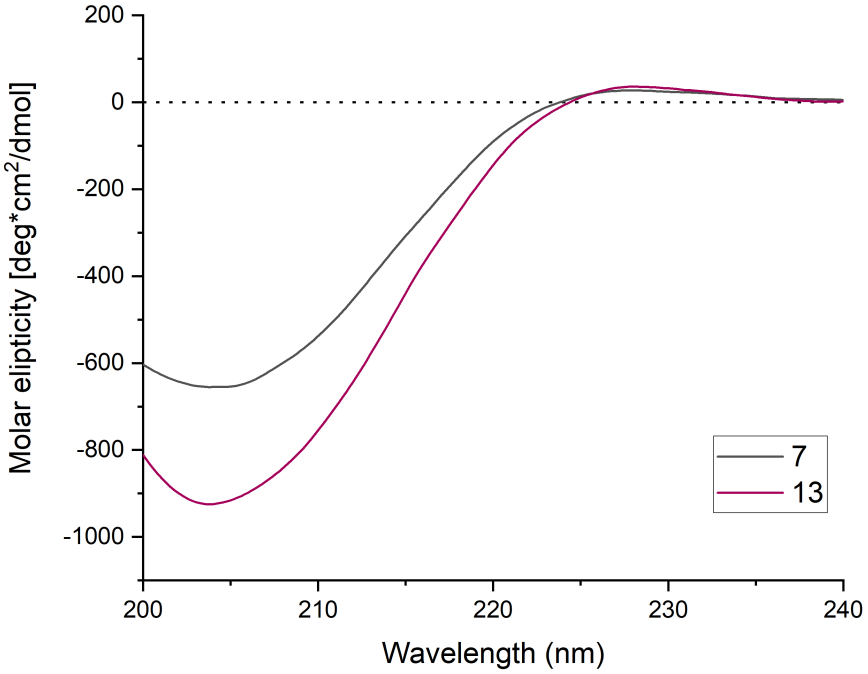
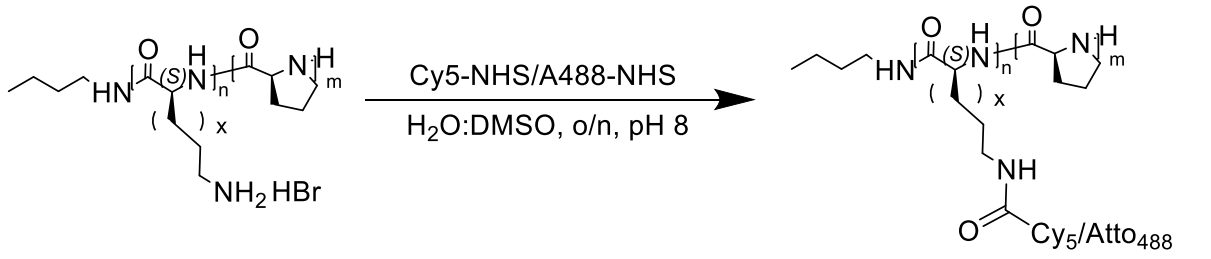


Figure S19. Circular dichroism spectra of free **(7)** and labeled **(13)** PLL(Z)$_n$-PLP$_m$ in Milli-Q water

Fluorescence labeling with Cy5 and A488



6 a-j x = 0 nBu-POrn(HBr)-b-PLP
7 x = 1 nBu-PLys(HBr)-b-PLP

12 a-j x = 0 (cy5-NHS)
13 x = 1(Cy5-NHS)
17 a-j x = 0 (A488-NHS)
18 x = 1 (A488-NHS)

Scheme S4. Labelling of nBu-PLO(HBr)-b-PLP and nBu-PLL(HBr)-b-PLP

Members of diblock copolymer families **6** and **7** were labeled with fluorophores Atto488-NHS (A488-NHS) or Cyanine5-NHS (Cy5-NHS). The diblock copolymer 6b procedure was applied to all noted diblock copolymers. In a one-neck bottom flask, diblock copolymer **6b** was dissolved in Milli-Q water (1 eq., 10 mg/mL). In a glass vial protected by light, the corresponding fluorophore was dissolved in dimethyl sulfoxide (DMSO) and added to the diblock polymer solution (0.015 eq., 1.5% mol). The pH was adjusted with 1M sodium bicarbonate (pH 8). The reaction was allowed to proceed overnight, protected by light, and checked by thin-layer chromatography (MeOH as mobile phase). After DMSO elimination using a rotavapor and freeze-drying, the product was purified by PD-10 desalting columns

packed with Sephadex G-25 resin. Dye loading was calculated by fluorescence using the CLARIOstar fluorescent plate reader. First, the corresponding free dye (DMF:H2O) calibration curve was prepared in black 96-well multiwell plates. Fluorescence was measured at λ_{ex}: 500 nm λ_{em}: 520 nm for A488-NHS and λ_{ex}: 646 nm λ_{em}: 662 nm for Cy5-NHS. Yields: 80%. Conjugation efficiency 60-100%.

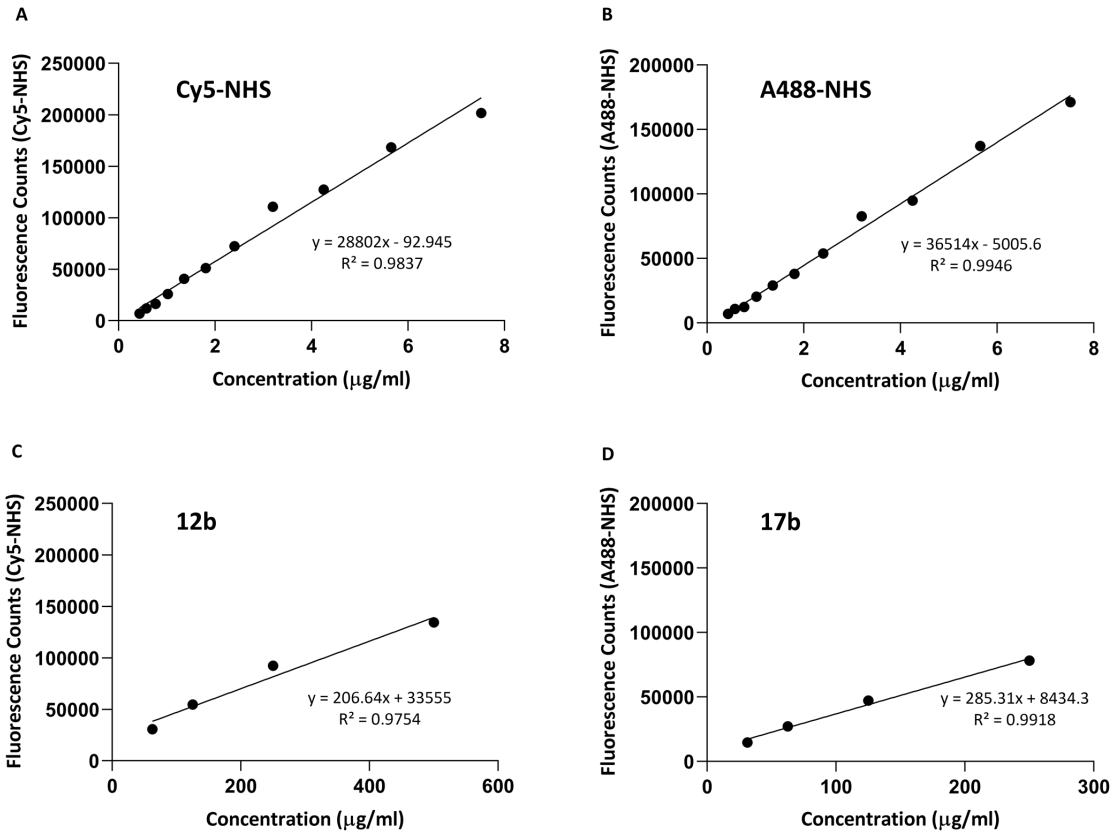


Figure S20. Fluorescence calibration curves of (**A**) Cy5-NHS and (**B**) A488-NHS fluorescence dyes and (**C**) diblock copolymers **12b** and (**D**) polymer **17b** in DMF:H_2O for quantification. % wt **12b** = 1.4 (back calculated %mol = 1.2); %wt **17b** = 1.1 (back calculated %mol = 0.7)

SAXS patterns

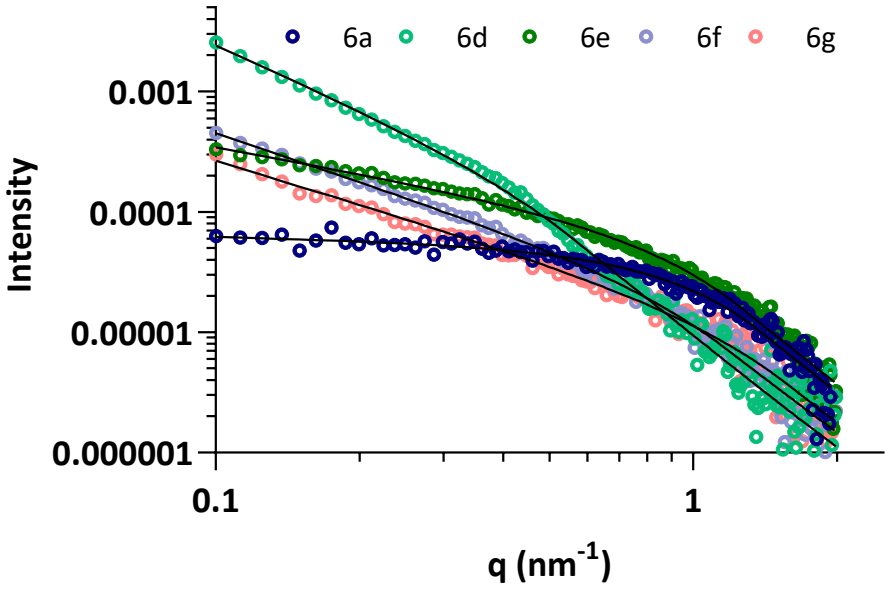


Figure S21. SAXS Scattering data for diblock copolymers **6a, d, e, f,** and **g** fitted to a partially precipitated polymer (s = 0; d = 3; with "s" the power law exponent at low angles related to the particle geometry and "d" the Porod exponent related to the interface of scatterer). Each diblock copolymer's Rg value (radius of gyration) was calculated using the semi-empirical model Guinier-Porod.

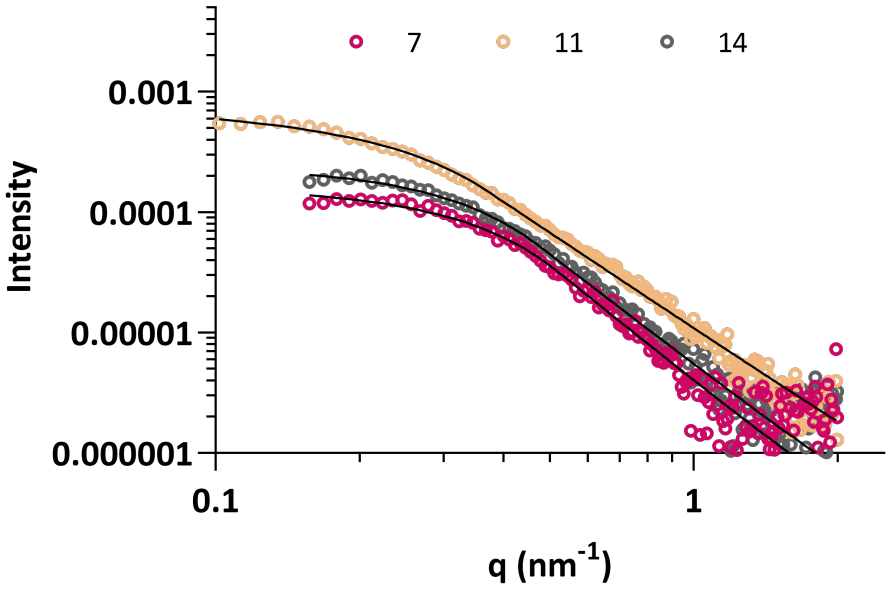


Figure S22. SAXS scattering data for diblock copolymers **7, 11,** and **14** fitted to a partially precipitated polymer (s = 0; d = 3; with "s" the power law exponent at low angles related to the particle geometry and "d" the Porod exponent related to the interface of scatterer). Each diblock copolymer's Rg value (radius of gyration) was calculated using the semi-empirical model Guinier-Porod.

Pyrene assay

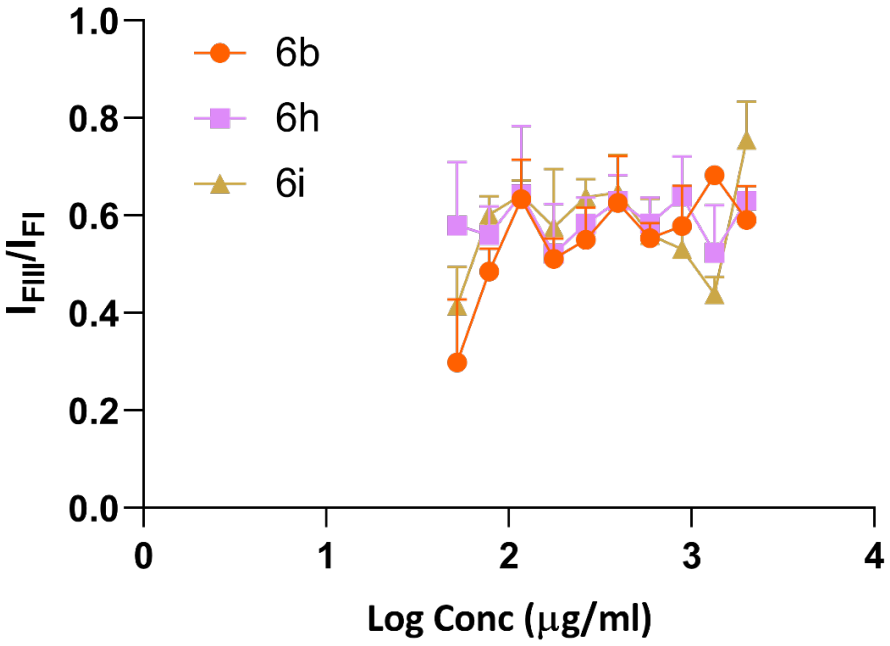


Figure S23. Evaluation of pyrene fluorescence with diblock copolymers **6b, h,** and **i**. The variation in the emission polarity index (I_{FIII}/I_{FI}) across different concentrations indicates that a consistent critical aggregation concentration (CAC) could not be identified, highlighting the dynamic nature of compact domain assembly as evidenced by SAXS analysis. This finding implies that any hydrophobic areas within the molecular assemblies cannot consistently host pyrene molecules, suggesting a transient or unstable incorporation into the assembly cavities.

Scaled-up synthesis of the candidate diblock copolymer by design of experiments

A design of experiments (DoE) approach was used to assess the effects of different variables on the process responses of interest using a minimum number of experiments and determining the interactions between parameters. Synthesizing diblock copolymer **6b** via one-pot cascade ring opening polymerization (ROP) was first focused on. Given the high interdependence of the polymerization processes in steps 1 and 2 (**Scheme 1**), a sequential process development approach was proposed, starting with PLO(Z) screening. Crucial parameters identified during polymerization were then applied to the subsequent synthetic reactions.

Screening and optimization of PLO(Z)

In the initial DOE study, three process parameters were assessed: the concentration of Orn(Z)-NCA, the concentration of the initiator n-butylamine (CNH2), and the reaction temperature (T). Monitoring the degree of polymerization (DP) of the final polymer was performed using two complementary methods – NMR and Mw analysis by GPC. The reaction was investigated with a circumscribed central composite (CCC) design with a star distance 2. The experimental matrix and dependence coefficients found are

detailed in **Table S2,** and both responses are detailed in **Figure S24**. Slight variations were observed in the model terms for both responses while maintaining the same general trend. Considering Mw measurements without workup is more statistically relevant, as including additional errors during the workup process could affect data accuracy. Limits were then set for responses so the desired area could be visible and the design space (DS) could be simulated. For DP, the desired interval is [5.0-6.7], and for MW is [1462-1700], corresponding to the DP interval. Establishing a DS was based on current regression models and estimating the probability of failure, which was set at a 5% level in the current study. DSs are shown in **Figure S25**. As evident from the DSs, the safe region for DP values was considerably broader than that of Mw. Given that the Mw region was smaller but more reliable due to workup exclusion, the Mw was explored first.

Desired Mw results were achieved at 4 ◦C and held constant when optimizing the DS. A proven acceptable range (PAR) was estimated using a dotted hypercube frame. The dotted frame in the DS Explorer plot designates the largest possible regular hypercube that can be inserted into the irregular DS volume. In the case of a fixed temperature at +4 ◦C with MODDE® simulations, the hypercube covers the area for Orn(Z)-NCA from 140-247 and CNH_2 from 23-29 mg/ml, a relatively small interval (**Fig. S26, top**). The same setpoint exploration was performed for DP to combine the two intervals (**Figure S26, bottom**).

In the case of a fixed temperature of 4◦C with MODDE® simulations, the hypercube covers the area for Orn(Z)-NCA from 182-236 mg/ml and CNH_2 from 10.7-23.4 mg/ml. Combining two intervals and taking the strictest setting for factors resulted in an interval for Orn(Z)-NCA from 182-236 mg/ml. For CNH_2, the intersection for the intervals was extremely small; therefore, setting an interval suitable for Mw aimed to solve this issue. The allowed interval for Mw was from 23-29 mg/ml, which, within the chosen interval for CNH_2, provided a probability of failure of no more than 2.5%. To decrease this probability, it was reasonable to move the NCA concentration limit to 200 mg/ml, moving deeper inside the hypercube, which was considered adequate in the current situation. The resulting interval - Orn(Z)-NCA [200 to 236] and CNH2 [23 to 29] - combines in an overall Orn(Z)-NCA concentration range from [140-170] mg/ml, which was transferred to the PLO(Z)PLP screening process.

Screening of PLO(Z)-b-PLP

In this reaction, the following factors were considered: concentration of Pro-NCA, concentration of PLO(Z) (Orn(Z)-NCA, known from the previous analysis), temperature, and stirring rate since the reaction is heterogeneous and the polymer chain grows at the liquid-solid interphase. To simplify the process, the temperature of the initiator was fixed to RT (even though PLO(Z) synthesis takes place at 4◦C).

Since polyprolines are known for their low solubility in most organic solvents, it was impossible to analyze copolymer Mw by GPC, leaving NMR as the only method of product analysis. NMR analysis was conducted in deuterated trifluoroacetic acid (TFA-d) at 12-20 mg/ml concentrations.

The desired DP interval was set to maintain a PLO(Z):PLP ratio between 3-3.9; considering the resulting DP for PLO(Z) from 5.5-6.7, the PLP DP interval used for further DS exploration was 16.5-26.

A complete factorial experiment requires 2^4 = 16 runs + 3 central runs (19 in total) as four factors vary at two levels; however, only the main factor effects were required to streamline factors for further optimization. In this scenario, a fractional factorial design with resolution IV was selected, reducing the number of experiments to eleven. **Table S3** describes the resulting experimental matrix.

As evident from the coefficient plot (**Fig. S27**), the DP is influenced by the Pro-NCA concentration, stirring, and temperature. A square term was detected; however, the current model did not provide insights into which square term is significant. A robust setpoint was identified using the same hypercube method to prepare for the next optimization design with three factors. Orn(Z)-NCA was fixed at 155 mg/ml, and considering future scale-up, the stirring rate was reduced to the interval [200 to 350], as higher speeds are not transferrable to a mechanical stirrer. **Figure S28** depicts the hypercube. The newly calculated intervals were: Pro-NCA [50 to 100] mg/ml, temperature – [10 to 20], and stirring [350 to 270].

Optimization of PLO(Z)$_n$-PLP$_m$

Parameters from the screening design were transferred into the circumscribed central composite (CCC) design model with a star distance of two. This model is well-suited for quadratic response functions, and including additional star points outside the experimental hypercube facilitates the exploration of the maximum experimental volume. **Table S4** presents the experimental matrix, while **Figure S29** presents the resultant coefficients. Surprisingly, the model did not exhibit a clear quadratic term dependence in the newly selected area. Although the square of Pro-NCA concentration has some effect, it was considered negligible compared to the temperature and concentration term. Tuning the model resulted in two meaningful coefficients and one interaction. Once again, the PAR was estimated based on the dotted hypercube frame. The estimation is centered around the robust setpoint, with stirring fixed at 155 rpm, which is even more suitable for scaling-up and meets the 5% acceptance level. **Figure 1F** (main manuscript) presents the resulting PAR. The resulting interval calculated from DS exploration is Pro-NCA [50 to 93.5] and T [10 to 22.6]. Notably, the risk of failure is less than 1% inside this interval.

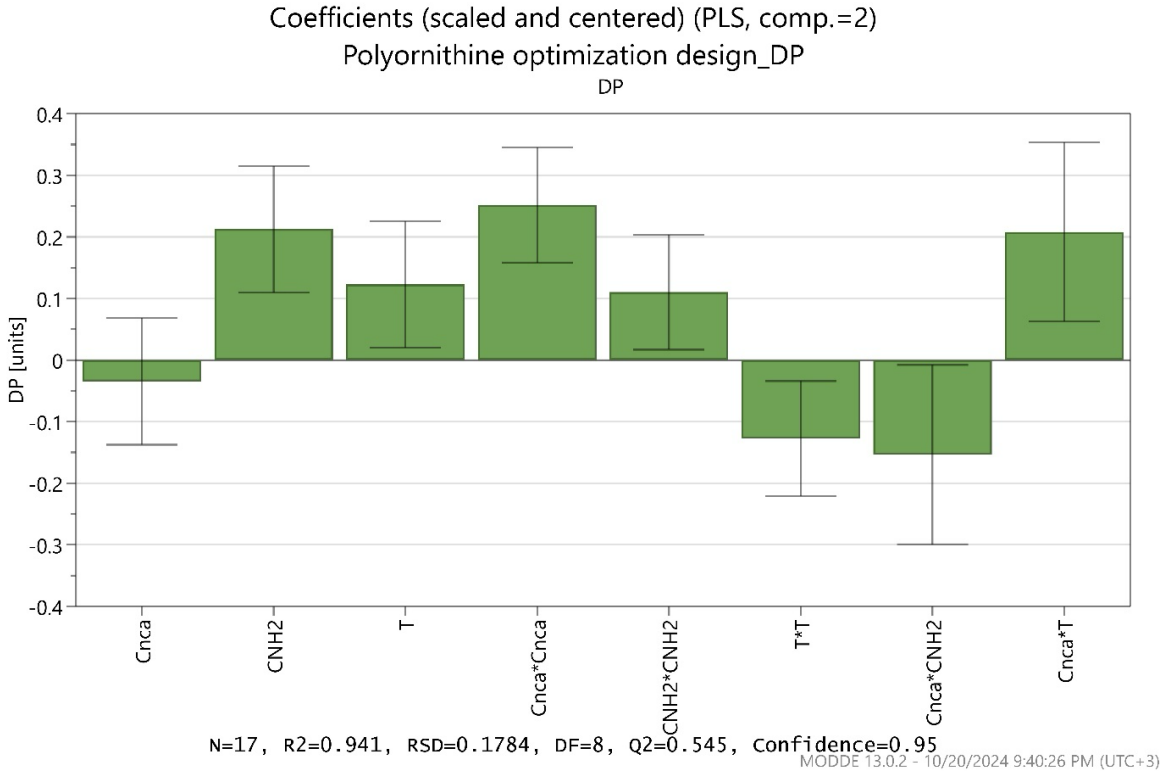
Scale-up of PLO(Z)-b-PLP

The candidate copolymer-conjugate was scaled up to 7.3 g using the estimated parameters in the sequential DoE evaluations, yielding the corresponding protected diblock copolymer with an 80% overall yield and a ratio n:m of PLO(Z)$_n$-PLP$_m$ of 6:20. **Figure S30** displays an NMR spectra of a batch. The synthesized diblock polymer was deprotected in dry chloroform using the standard conditions with HBr/CH_3COOH. **Figures S31** and **S32** present the NMR spectra and GPC analysis of the final deprotected diblock copolymer **6b**.

Table S2. The Response Surface Methodology design of experiments study parameters and results for PLO(Z)

Exp No	Exp Name	Run Order	C_{Orn}, mg/ml	C_{NH2} mg/ml	Temperature, °C	MW, Da	DP
10	N10	1	300	25	7	1987	7.55
15	N15	2	200	25	7	1679	6.58
5	N5	3	150	15	10	1845	6.43
17	N17	4	200	25	7	1635	6.68
6	N6	5	250	15	10	1828	7.08
9	N9	6	100	25	7	1880	7.71
11	N11	7	200	5	7	1714	6.5
4	N4	8	250	35	4	1827	6.47
12	N12	9	200	45	7	1974	7.6
3	N3	10	150	35	4	1783	7.15
1	N1	11	150	15	4	1550	6.73
13	N13	12	200	25	1	1489	5.8
7	N7	13	150	35	10	1841	7.04
8	N8	14	250	35	10	1759	7.06
14	N14	15	200	25	13	1649	6.35
16	N16	16	200	25	7	1624	6.25
2	N2	17	250	15	4	1699	6.55

Exp – Experiment; C_{Orn} – Concentration of Orn(Z)-NCA (ornithine (Orn) benzyloxycarbonyl (Z) in the form of N-carboxyanhydride (NCA) derivative); C_{NH2} - Concentration of n-butylamine; MW – Molecular Weight in Dalton; DP – Degree of Polymerization



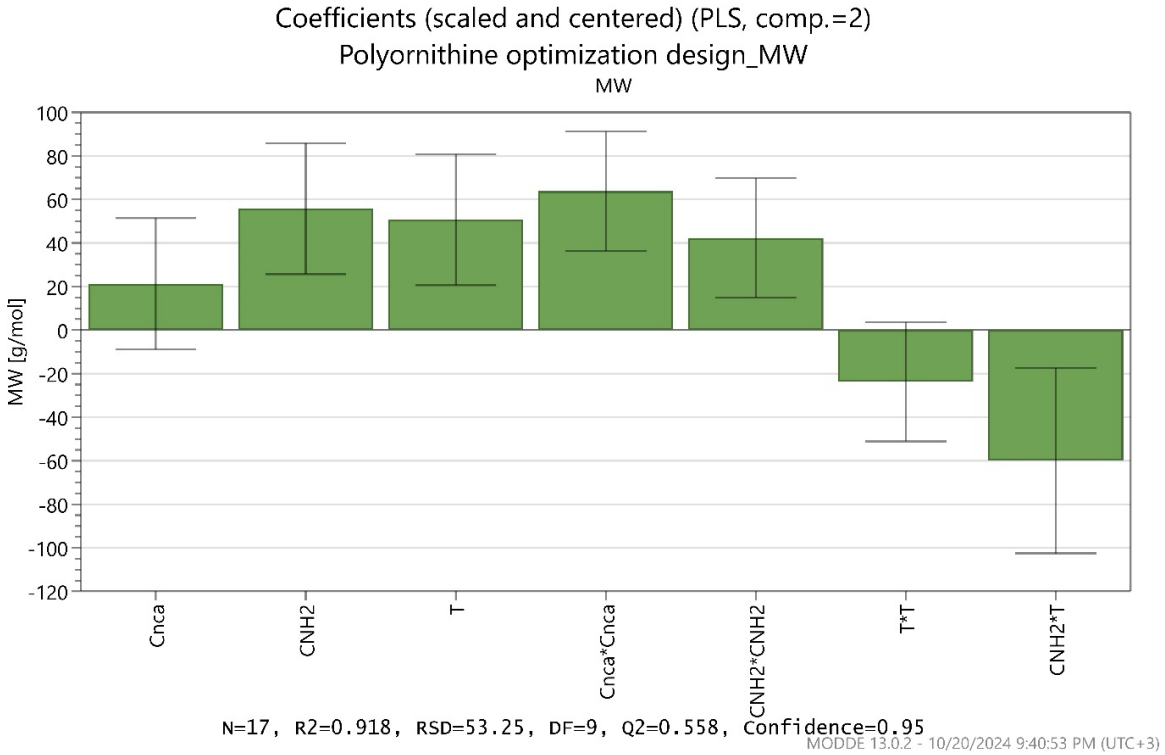


Figure S24. Coefficients plot for PLO(Z) optimization of (top) degree of polymerization and (bottom) molecular weight

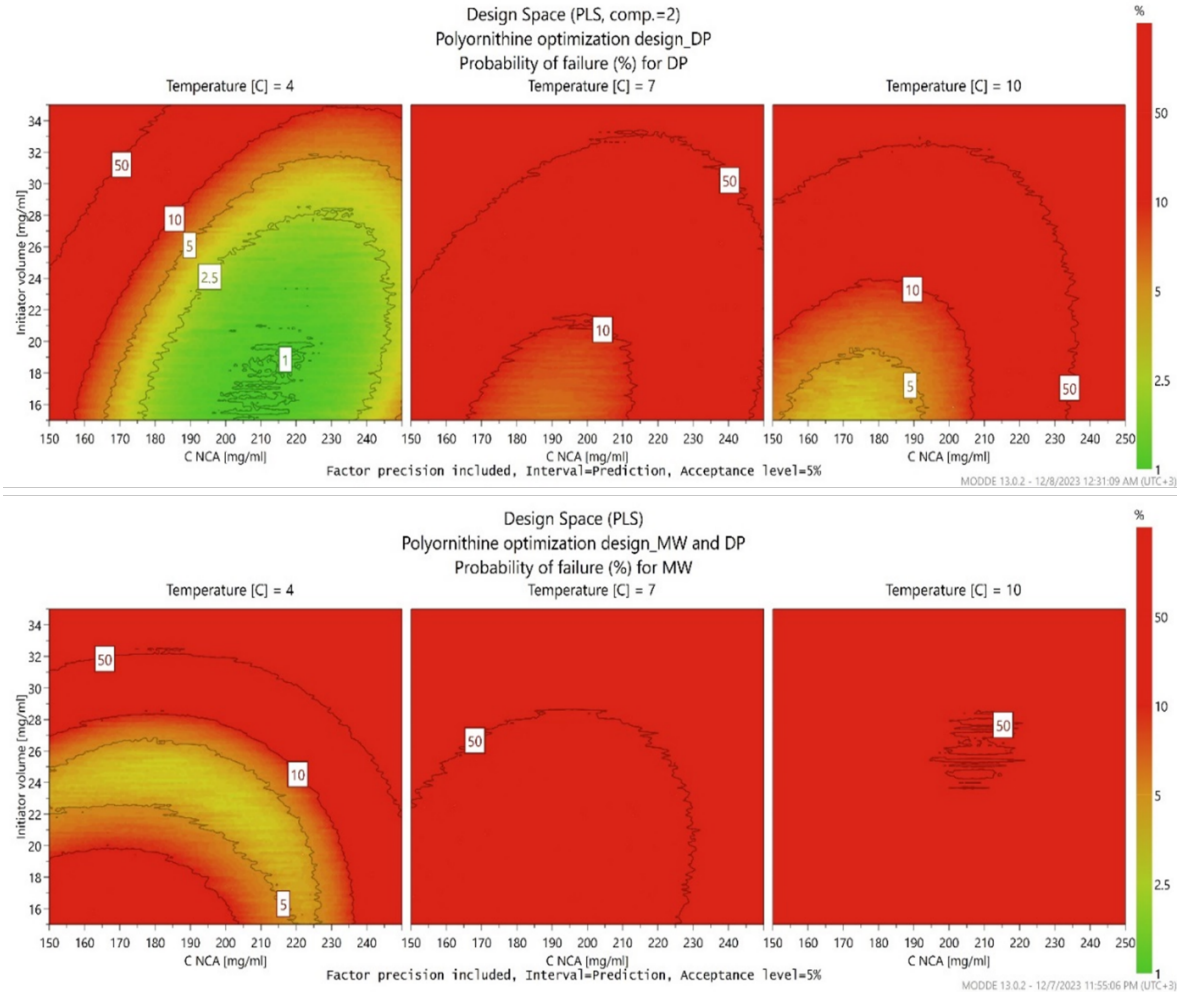


Figure S25. Design space for the (top) degree of polymerization [5 to 6.7] and (bottom) molecular weight [1462 to 1700]

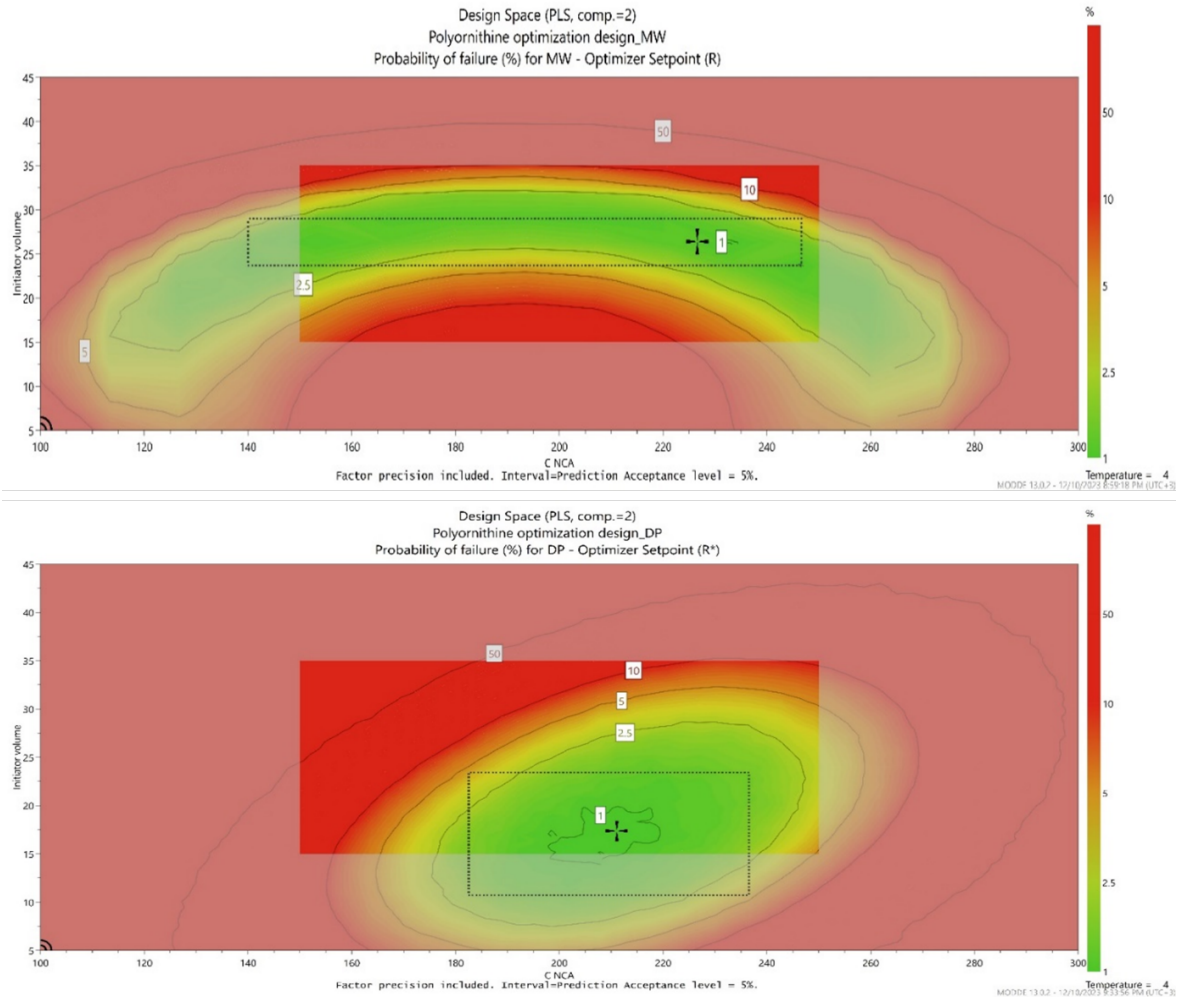


Figure S26. Design space exploration (proven acceptable range, PAR) for (top) molecular weight and (bottom) degree of polymerization

Table S3. Fractional Factorial Design of Resolution IV experiments studies parameters and results of $PLO(Z)_n$-PLP_m

Exp No	Exp Name	Run Order	C_{Pro}, mg/ml	C_{Orn}, mg/ml	Stirring rate	Temperature, °C	DP PLP
8	N8	1	150	170	500	25	18.19
10	N10	2	100	155	350	17.5	16.92
3	N3	3	50	170	200	25	18.26
4	N4	4	150	170	200	10	17.19
9	N9	5	100	155	350	17.5	16.60
11	N11	6	100	155	350	17.5	17.29
5	N5	7	50	140	500	25	19.14
6	N6	8	150	140	500	10	17.33
2	N2	9	150	140	200	25	18.00
7	N7	10	50	170	500	10	20.48
1	N1	11	50	140	200	10	19.50

Exp – Experiment; Concentration of Pro-NCA (Proline in the form of N-carboxyanhydride (NCA) derivative); C_{Orn} – Concentration of Orn(Z)-NCA (ornithine (Orn) benzyloxycarbonyl (Z) in the form of N-carboxyanhydride (NCA) derivative; DP PLP – Degree of Polymerization of Polyproline block

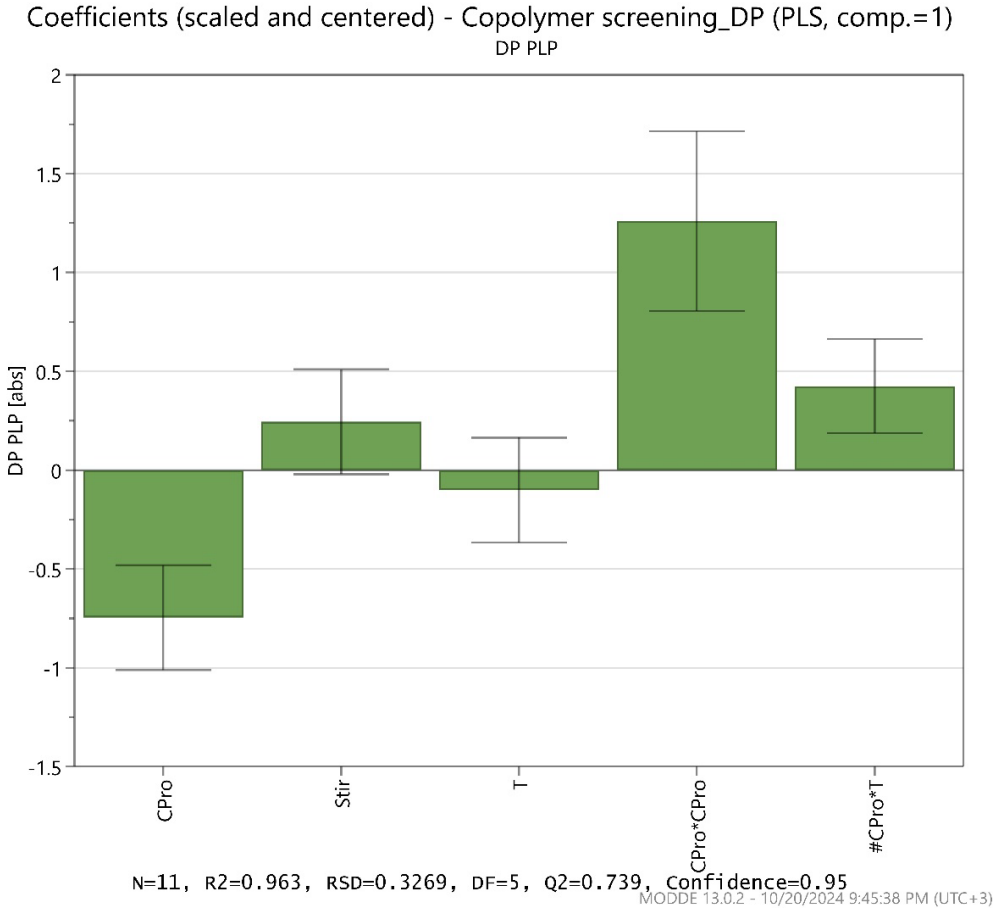


Figure S27. Coefficients plot for screening of PLO(Z)$_n$-PLP$_m$ for degree of polymerization

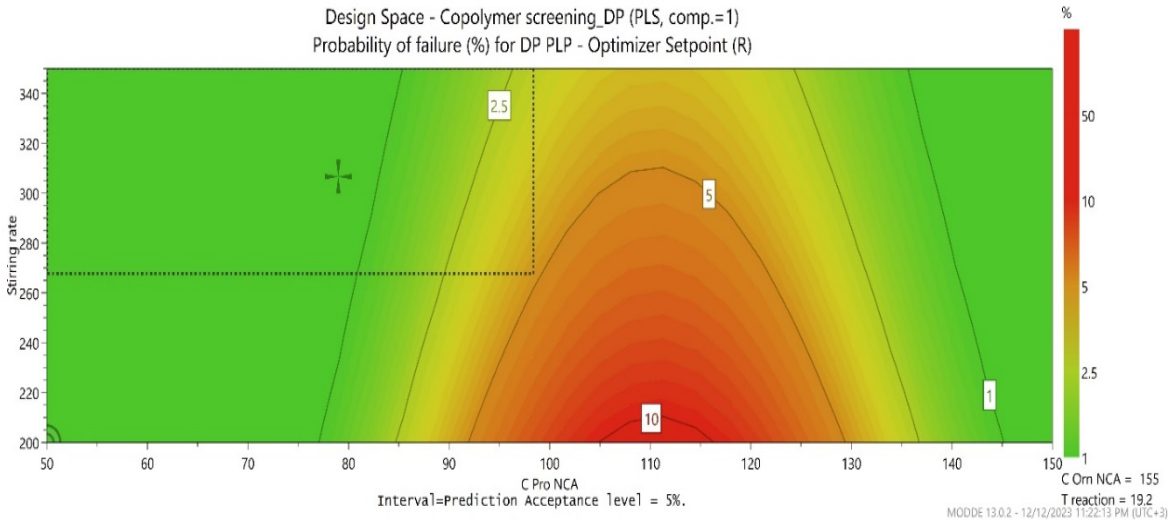
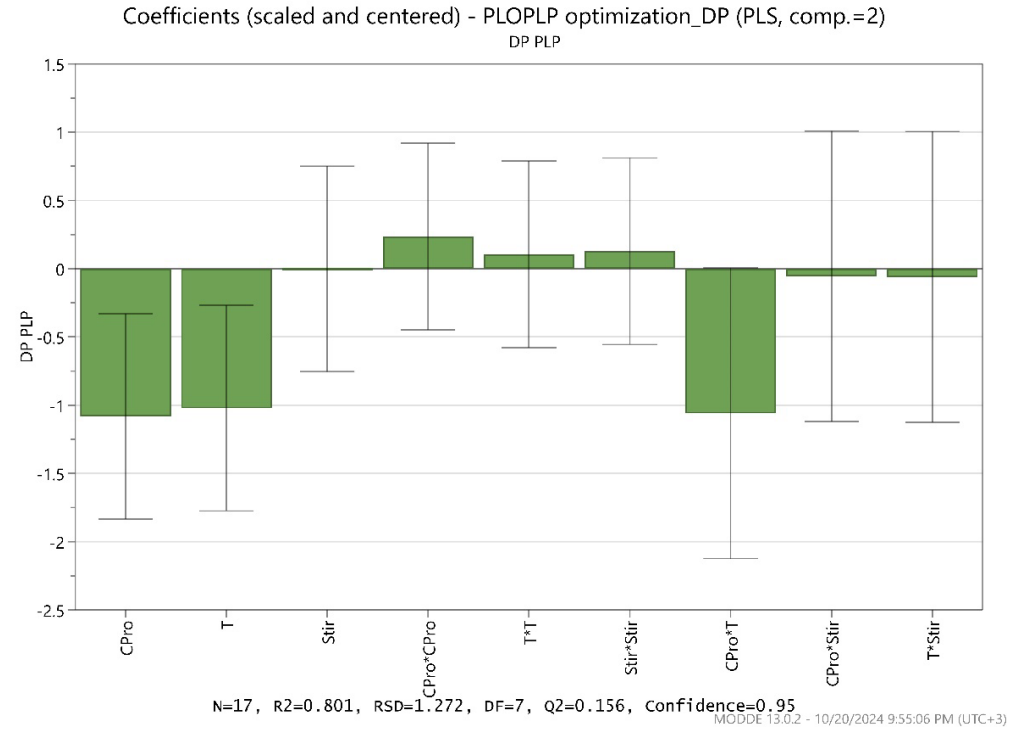


Figure S28. Design space explorer to screen PLO(Z)$_n$-PLP$_m$ for the degree of polymerization with fixed temperature

Table S4. The Response Surface Methodology (RSM) design of experiments study parameters and results for $PLO(Z)_n$-PLP_m

Exp No	Exp Name	Run Order	C_{Pro}, mg/ml	Temperature, °C	Stirring rate	DP PLP
12	N12	1	75	32.5	275	18.102
4	N4	2	100	25	200	17.972
14	N14	3	75	17.5	425	20.256
5	N5	4	50	10	350	22.206
16	N16	5	75	17.5	275	19.304
17	N17	6	75	17.5	275	20.550
6	N6	7	100	10	350	21.990
7	N7	8	50	25	350	20.974
15	N15	9	75	17.5	275	19.50
13	N13	10	75	17.5	125	20.266
1	N1	11	50	10	200	20.796
8	N8	12	100	25	350	18.922
2	N2	13	100	10	200	23.176
3	N3	14	50	25	200	22.182
10	N10	15	125	17.5	275	17.570
9	N9	16	25	17.5	275	24.110
11	N11	17	75	2.5	275	22.170

Exp – Experiment; Concentration of Pro-NCA (Proline in the form of N-carboxyanhydride (NCA) derivative); DP PLP – Degree of Polymerization of Polyproline block



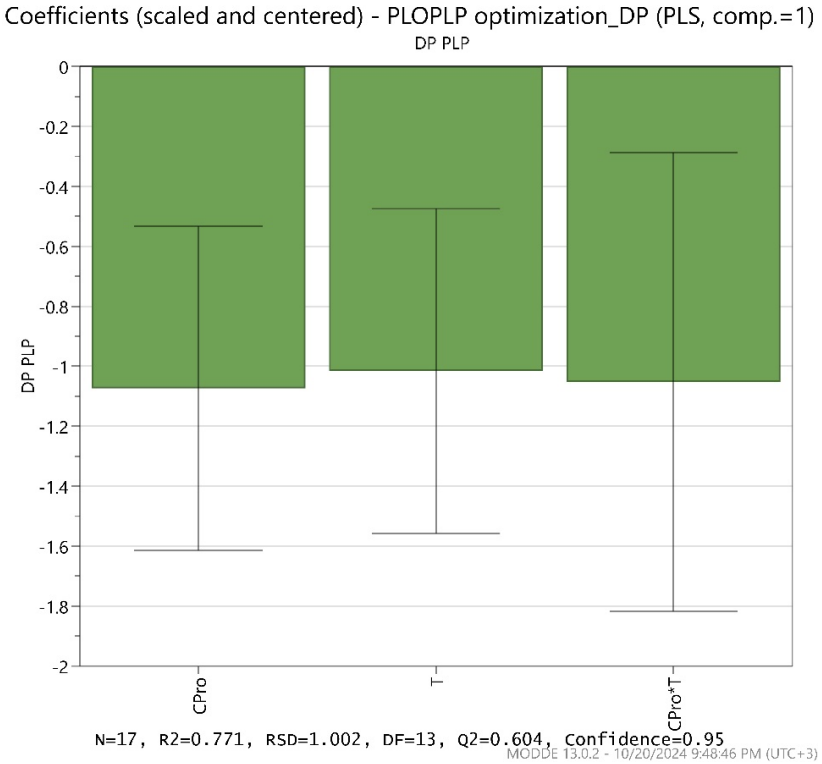


Figure S29. Coefficients plot for the degree of polymerization for optimization of PLO(Z)n-PLPm (top) before and (bottom) after model tuning

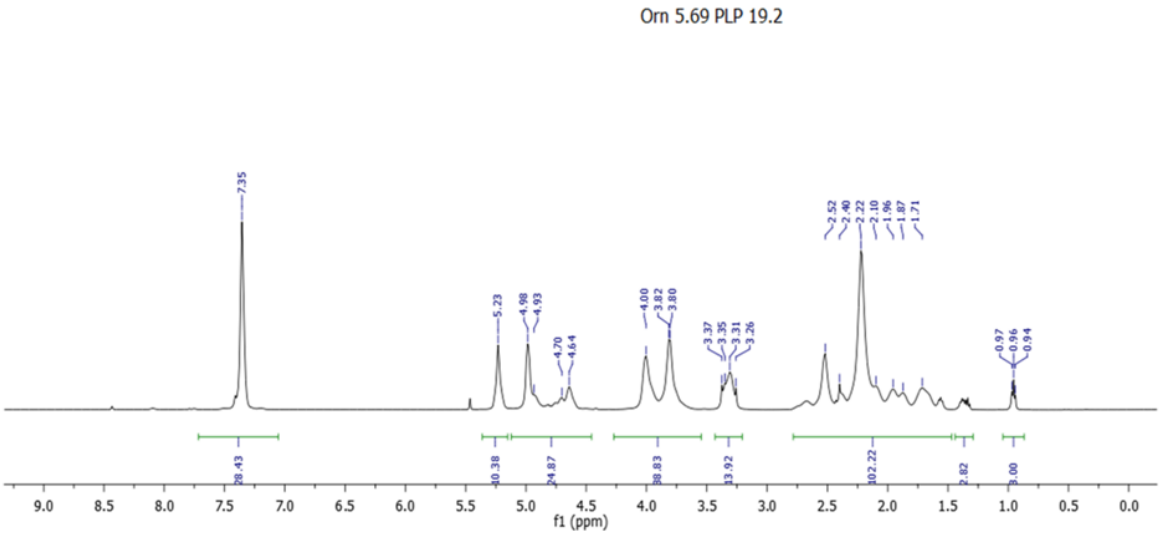


Figure S30. NMR of a scaled-up batch of $PLO(Z)_n$-PLP_m

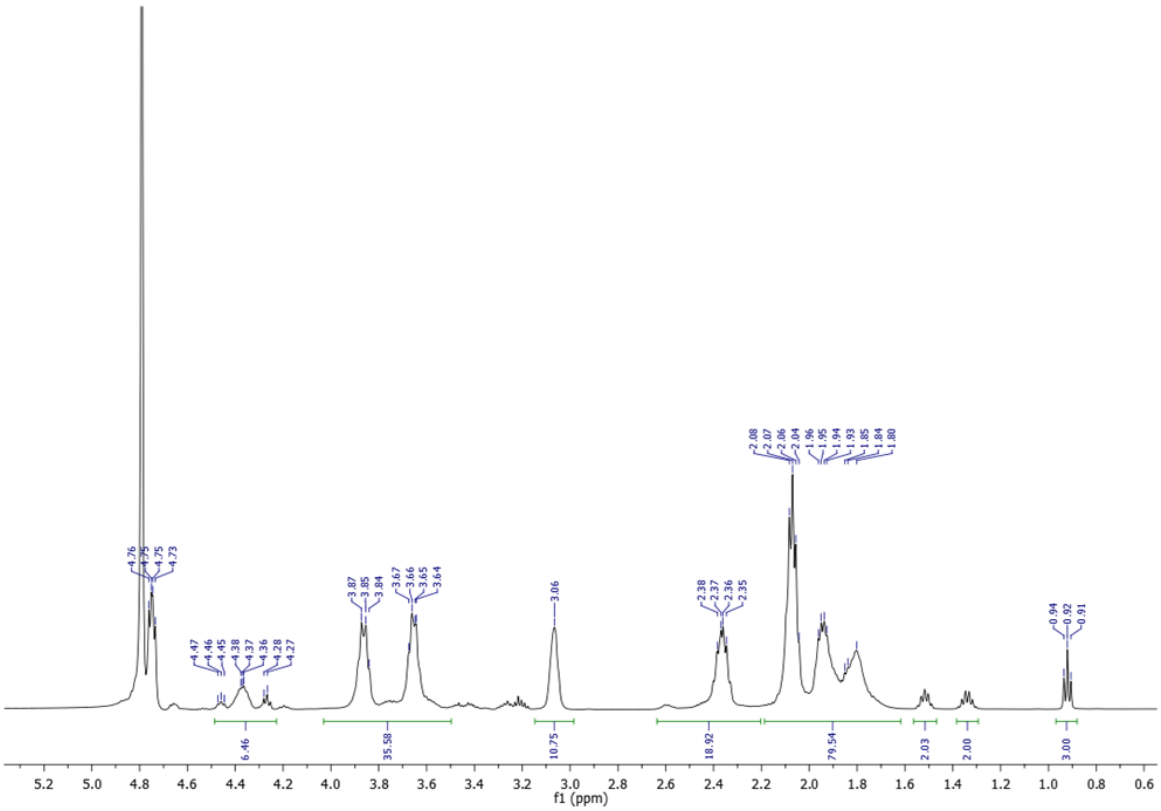


Figure S31. NMR of a scaled-up batch $PLO(HBr)_n$-PLP_m (6b)

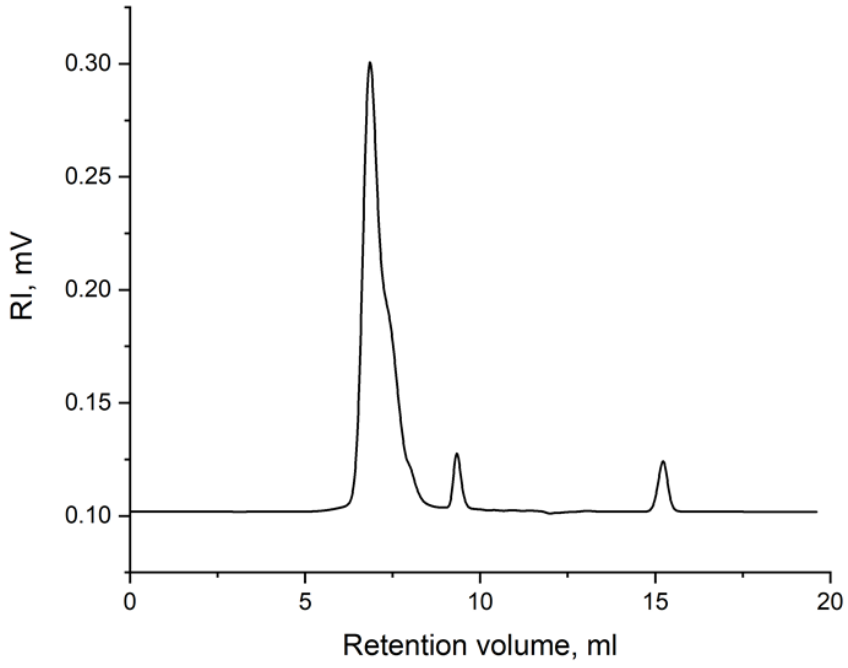


Figure S32. Gel permeation chromatogram for a scaled-up batch of PLO(HBr)$_n$-PLP$_m$ (6b)

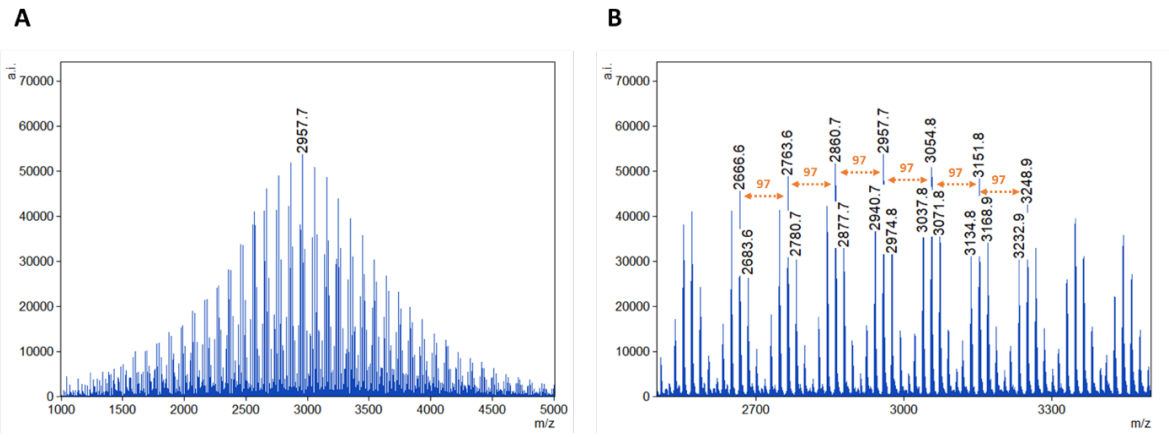


Figure S33. MALDI-TOF mass spectrometry (MS) analysis of a scaled-up batch of PLO(HBr)$_n$-PLP$_m$ (6b) displaying A) the full m/z range and B) an expanded view of a selected m/z region (right). The primary peak at 2957.7 m/z corresponds to the molecular ion of the intact polypeptide, with isotopic resolution. In the expanded view, the regular 97 Da mass intervals between adjacent peaks indicate sequential proline losses consistent with the repetitive proline-rich sequence of the polypeptide.

d. Cell Viability and Mitochondrial Colocalization of Polyproline-based Diblock Polymers

MTS assay for cell viability in MDA-MB-231 cells

MDA-MB-231 cells were seeded in 96-well microliter plates (5,000 cells/well, 0.05 ml per well) and incubated for 24 h at 37° and 5% CO_2. Concentrated stock solutions of diblock copolymers were prepared in PBS and diluted in DMEM/F-12 medium (with 10% FBS and 1% P/S). The diblock

copolymer solutions were then sterilized by passing through a 0.2 µm filter and added to give a final concentration of 0-1 mg/ml (dilution factor 1.5). After 24 or 72 h of incubation, MTS/PMS (20:1) was added, and the cells were incubated for another 4 h. The optical density of each well was measured at 490 nm using a CLARIOstar plate reader. The absorbance values were expressed as a percentage of cell viability, with 100% representing the cell viability of untreated control cells. Values represent Mean ± SD (n=3). Data are shown in **Figure 2A** of the main manuscript and **S33-35** of supporting information.

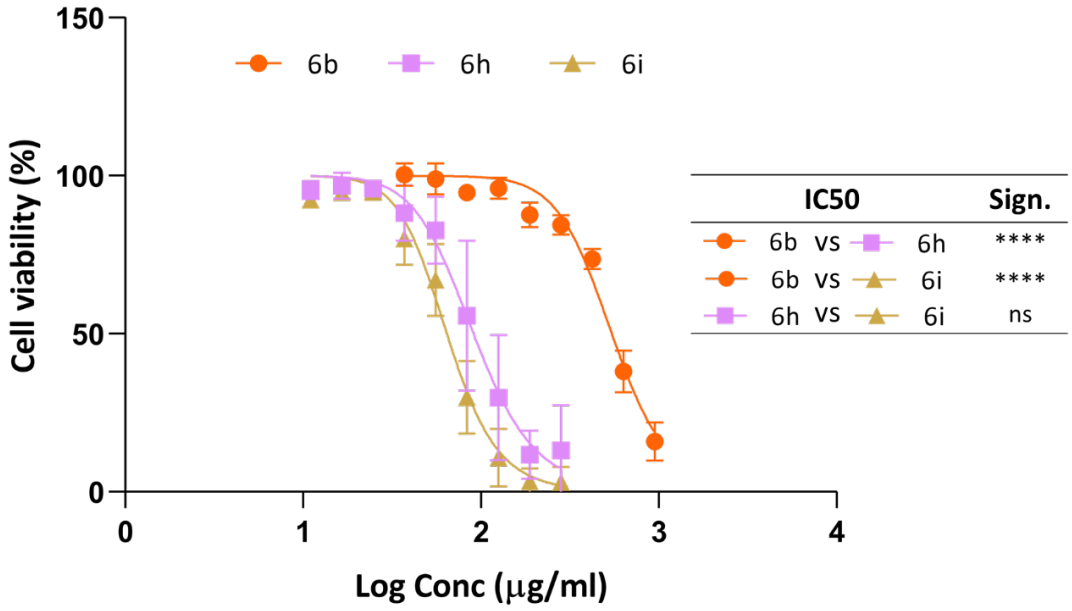


Figure S34. MDA-MB 231 cell viability by MTS assay in response to diblock copolymers **6b** (IC50 = 0.55 mg/ml) **6h** (IC50 = 0.09 mg/ml) and **6i** (IC50 = 0.06 mg/ml) (24 h, n = 3, mean ± SEM). Data was analyzed using a t-test; in all cases, differences were considered significant when p****<0.0001; p***<0.001; p**<0.01; p*<0.05 (ns: non-significant).

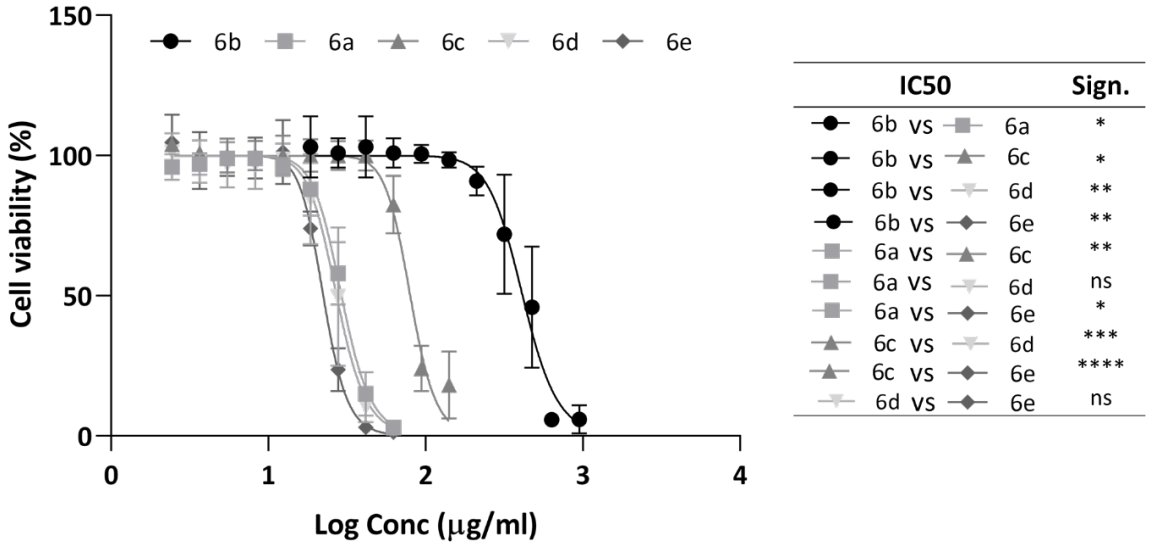


Figure S35. MDA-MB 231 cell viability by MTS assay in response to diblock copolymers **6b** (IC50 = 0.4 mg/ml), **6a** (IC50 = 0.03 mg/ml), **6c** (IC50 = 0.08 mg/ml), **6d** (IC50 = 0.03 mg/ml), and **6e** (IC50 = 0.02 mg/ml) (72 h, n = 3, mean ± SEM). Data was analyzed using a t-test; in all cases, differences were considered significant when p****<0.0001; p***<0.001; p**<0.01; p*<0.05 (ns: non-significant).

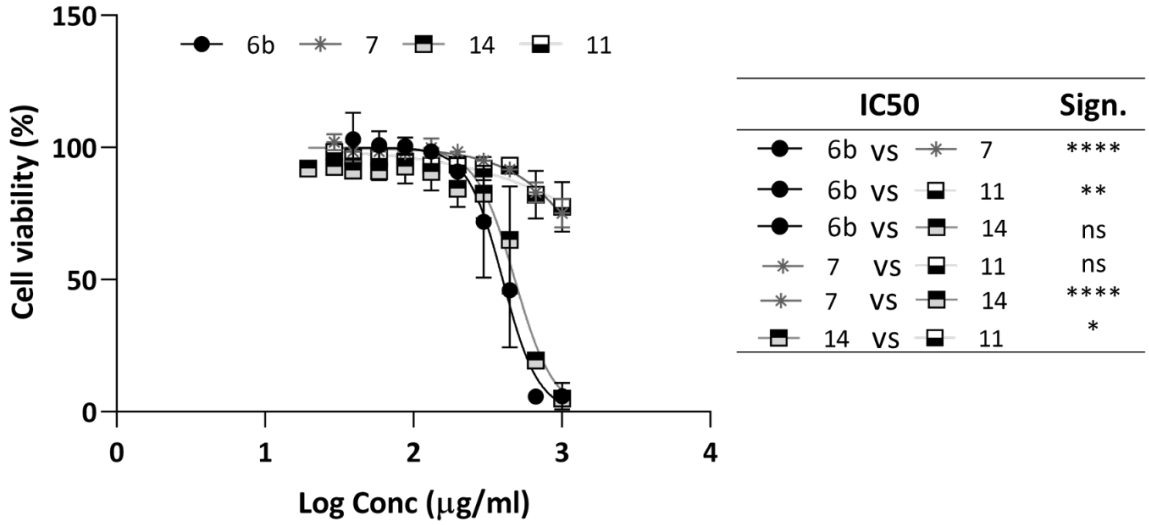


Figure S36. MDA-MB 231 cell viability by MTS assay in response to diblock copolymers **6b** (IC50 = 0.4 mg/ml), 7 (IC50>1 mg/ml), **11** (IC50>1 mg/ml), and **14** (IC50 = 0.5 mg/ml) (72 h, n = 3, mean ± SEM). Data was analyzed using a t-test; in all cases, differences were considered significant when p****<0.0001; p***<0.001; p**<0.01; p*<0.05 (ns: non-significant).

Cellular uptake studies by live-cell imaging of Cy5-labeled polymers

Uptake studies used a Leica TCS SP8 confocal microscope with a 63x 1.4NA CS2 oil immersion objective lens. Excitation wavelengths of 405, 561, and 638 nm were employed, along with four

fluorescent Photomultiplier Tubes (PMTs) and two Hybrid Detectors (HyD). The experiments were conducted under controlled levels of CO_2 and temperature. Pulse-chase and time-lapse studies were performed at non-toxic concentrations of selected diblock copolymers using specific fluorescent markers: MitoTracker™ Red CM-H2Xros M7513 (mitochondria, 100 nM), LysoTracker® Blue DND22 (lysosomes, 0.6 μM), and Cyanine5 (diblock copolymer). MDA-MB-231 cells (1,500 cells/well, 0.03 ml per well) were seeded in a 384-well black optical-bottom plate and incubated for 24 h at 37°C with 5% CO_2. For pulse-chase studies, non-toxic polymer concentrations were added at different time points (1, 2, 4, 6, 24 h), while Mitotracker and Lysotracker were added 1 h before analysis. Control cells with similar incubation times were also analyzed to establish autofluorescence levels. Time-lapse studies involved adding Mitotracker and Lysotracker 1 h before analysis, capturing images over a 20-s time range upon diblock copolymer incubation at t=0. Image processing was performed using the Leica Application Suite X (LAS X) and the Image J-JACoP plugin for Pearson r calculation. Example images are shown in **Figures 2D** and **5E** of the main manuscript (pulse-chase, 2 h). **Video S1** in supporting information represents a time-lapse study for compound **6b** for 24 hours.

Table S5. Evaluation of cell uptake through Pearson coefficient (r) analysis

	Pearson coefficient				
Diblock Copolymer	**1 h**	**2 h**	**4 h**	**6 h**	**24 h**
6b	0.17	0.59	0.53	0.43	0.14
6h	0.67	0.78	0.69	0.61	0.67
6i	0.67	0.53	0.50	0.41	0.41
6a	-	0.08	0.03	0.07	-
6c	-	0.06	0.11	0.06	-
6d	-	0.02	0.01	0.02	-
6e	-	0.01	0.03	0.04	-
7	0.01	0.40	0.39	0.43	0.10

Table S5 presents the degree of colocalization between specified diblock copolymers (labeled with Cy5) and mitochondria (stained with Mitotracker Red), determined at various times (1, 2, 4, 6, and 24 h) following pulse-chase experiments, as visualized by confocal fluorescence microscopy.

Pulse-chase studies (1, 2, 4, 6, and 24 h) were conducted using the same protocol established for MDA-MB-231 cells, with **6b** applied to BJ fibroblast (1500 cells/well, 0.03 ml per well), MCF-7 (1500 cells/well, 0.03 ml per well), Hep G2 (1500 cells/well, 0.03 ml per well), and BV-2 (1000 cells/well, 0.05 ml per well) cells.

Pearson coefficient					
Cell line	**1 h**	**2 h**	**4 h**	**6 h**	**24 h**
BJ-Fibroblast	0.02	0.02	0.08	0.10	0.24
Hep G2	0.07	0.05	0.12	0.23	0.07
MCF-7	0.01	0.53	0.45	0.51	0.60
BV-2	0.11	0.21	0.23	0.19	-

Table S6 presents the degree of colocalization between **6b** (labeled with Cy5) and mitochondria (stained with Mitotracker Red), determined at various times (1, 2, 4, 6, and 24 h) following pulse-chase experiments in BJ fibroblasts, Hep G2, MCF-7, and BV-2 cells, as visualized by confocal fluorescence microscopy.

Cellular internalization studies by flow cytometry of Cy5-labeled polymers

MDA-MB-231 cells were seeded into two 12-well plates (55,000 cells/well, 0.8 ml per well) and allowed to adhere for 24 h at 37°C with 5% CO_2. For internalization experiments conducted at 4°C, cells were pre-incubated at this temperature for 30 min before starting. Subsequently, Cy5-labeled diblock copolymers (0.15 mg/ml final concentration) were added at 0, 30, 60, and 180 mins. One plate was maintained at 37°C, while the other was stored at 4°C during the respective incubation periods. Subsequently, cells were placed on ice to inhibit energy-dependent mechanisms, washed twice with cold PBS, resuspended in 0.5 ml of DMEM/F-12 medium (with 10% FBS and 1% P/S) using a cell scraper, and then harvested into separate tubes for each condition. Cells were then incubated with propidium iodide (PI; 2 μg/ml), a marker for cell viability. Cell-associated fluorescence (CAF) was then analyzed using CytoFLEX S (Beckman-Coulter, CA, USA) flow cytometer equipped with four lasers (405 nm, 488 nm, 561 nm, and 635 nm) and thirteen fluorescence detectors. Data collection involved 10,000 counts per sample, and data were analyzed using CytExpert version 2.3 software. Data was expressed as a fold change of relative fluorescence units (RFU) to t = 0. Cells incubated without diblock copolymer were used to account for the background fluorescence. Data are shown in **Figures 2B** and **5F** of the main manuscript and **S36** of supporting information.

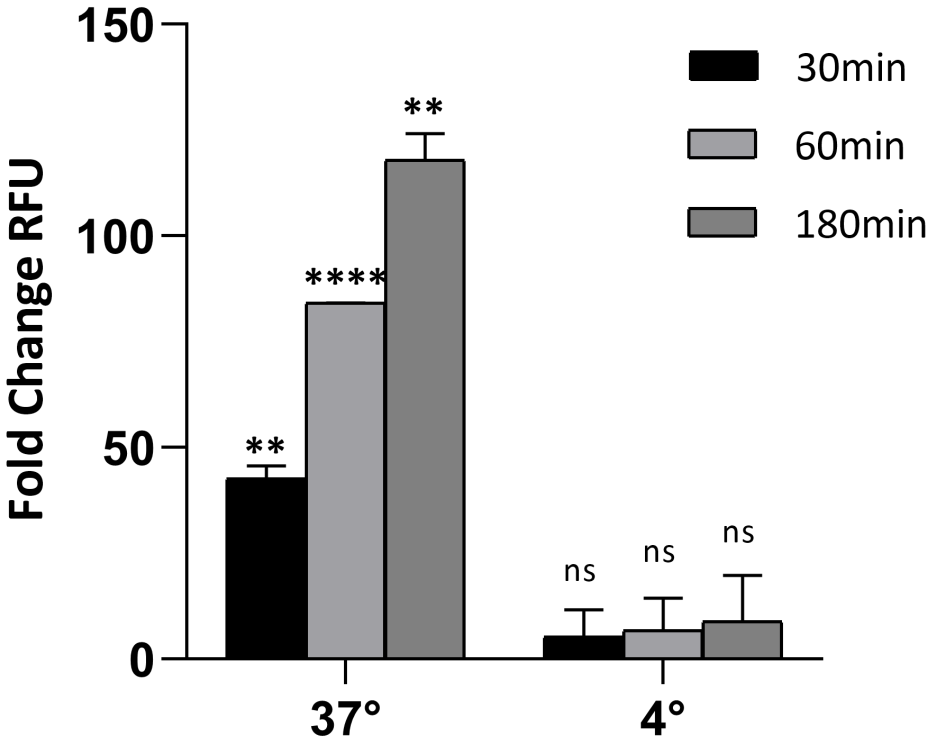
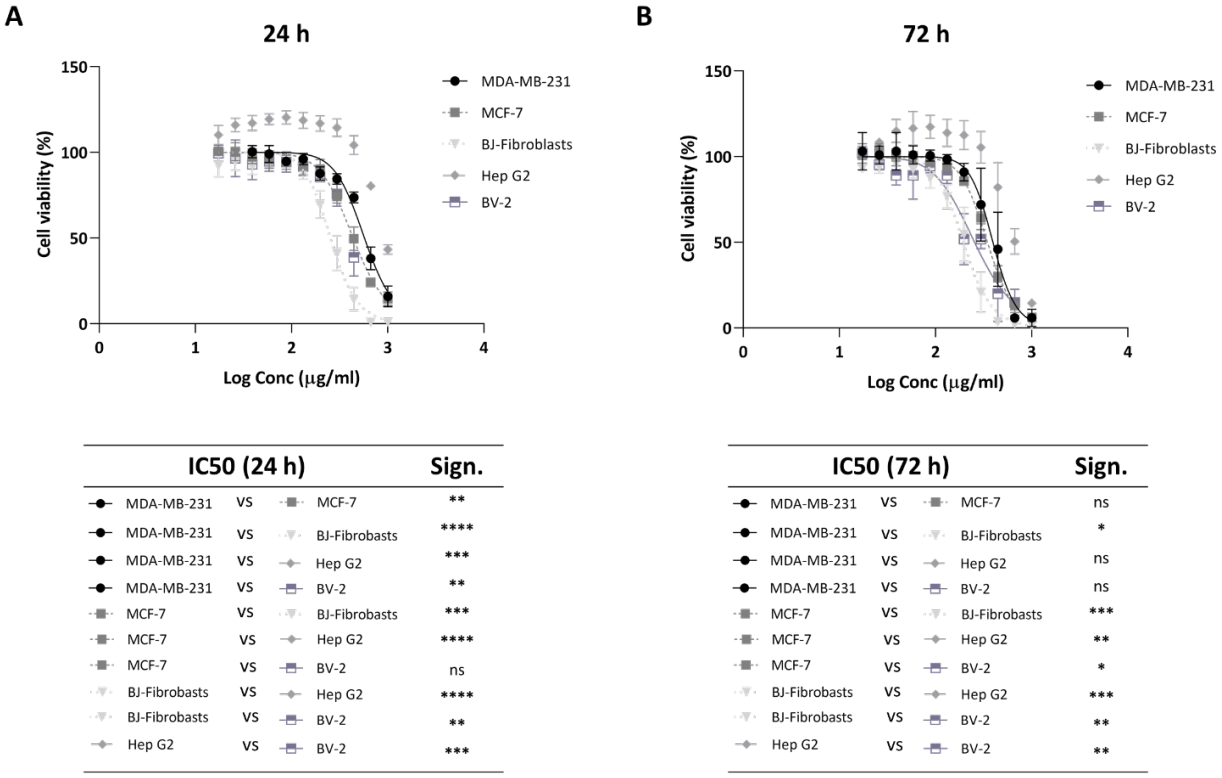


Figure S37. Cellular internalization studies performed with diblock copolymer **7** over time (30, 60, and 180 min) at 37° (endocytic-dependent pathway) and 4° (endocytic-independent pathway) by flow cytometry (t-test comparing to the control set as 100%; n = 3, mean ± SEM. Significance reported as **p ≤ 0.01, ****p ≤ 0.0001 (ns = not significant). The results demonstrate the prevalence of endocytic-dependent mechanisms of internalization.

MTS assay for Cell Viability in Additional Cell Lines Using 6b

Cell viability studies at 24 and 72 h incubation were performed for diblock copolymer **6b** in BJ fibroblast (5,000 cells/well, 0.05 ml per well), MCF-7 (5,000 cells/well, 0.05 ml per well), Hep G2 (5,000 cells/well, 0.05 ml per well) and BV-2 (2500 cells/well, 0.05 ml per well) cells following the same protocol previously described for MDA-MB-231 cells.



IC50 (24 h)			Sign.
MDA-MB-231	vs	MCF-7	**
MDA-MB-231	vs	BJ-Fibroblasts	****
MDA-MB-231	vs	Hep G2	***
MDA-MB-231	vs	BV-2	**
MCF-7	vs	BJ-Fibroblasts	***
MCF-7	vs	Hep G2	****
MCF-7	vs	BV-2	ns
BJ-Fibroblasts	vs	Hep G2	****
BJ-Fibroblasts	vs	BV-2	**
Hep G2	vs	BV-2	***

IC50 (72 h)			Sign.
MDA-MB-231	vs	MCF-7	ns
MDA-MB-231	vs	BJ-Fibroblasts	*
MDA-MB-231	vs	Hep G2	ns
MDA-MB-231	vs	BV-2	ns
MCF-7	vs	BJ-Fibroblasts	***
MCF-7	vs	Hep G2	**
MCF-7	vs	BV-2	*
BJ-Fibroblasts	vs	Hep G2	***
BJ-Fibroblasts	vs	BV-2	**
Hep G2	vs	BV-2	**

Figure S38. Cell viability by MTS assay in response to **6b** in different cell lines after A) 24 h and B) 72 h. 24 h: MDA-MB 231 (IC50 = 0.55 mg/ml), MCF-7 (IC50 = 0.45 mg/ml), BJ fibroblasts (IC50 = 0.26 mg/ml), Hep G2 (IC50 = 0.94 mg/ml), BV-2 (IC50 = 0.40 mg/ml) (24 h, n = 3, mean ± SEM). 72 h: MDA-MB 231 (IC50 = 0.40 mg/ml), MCF-7 (IC50 = 0.35 mg/ml), BJ-Fibroblasts (IC50 = 0.20 mg/ml), Hep G2 (IC50 = 0.59 mg/ml), BV-2 (IC50 = 0.31 mg/ml) (72 h, n = 3, mean ± SEM). Data was analyzed using a t-test; in all cases, differences considered significant when p****<0.0001; p***<0.001; p**<0.01; p*<0.05 (ns: non-significant).

Hemocompatibility assay

The final erythrocyte pellet was weighed and resuspended to a concentration of 2% (v/v) in sterile PBS. Solutions of **6b, 6h**, and **6i** were prepared in PBS adjusted to pH 7.4 and also citrate solution adjusted to pH 5.5. Samples were added to wells in triplicate (n = 3, 100 µL per well) at sub-IC50 final concentrations (>IC40 (C1)) and a diluted concentration (>IC15 (C2, dilution factor C1/C2 = 1.5)). Control wells contained buffer at the corresponding pH, while Triton X-100 at a concentration of 1% (w/v) served as a positive control for complete erythrocyte lysis and dextran (2 mg/ml) as a negative control. Following incubation at 37 °C for 1 h, plates were centrifuged at 3000 rpm for 10 min at room temperature, and the supernatant from each well was transferred to a new plate for hemoglobin release assessment. Hemoglobin release was quantified by measuring absorbance at 570 nm using a Clariostar plate reader, and the percentage of hemolysis for each sample was calculated relative to the 100% hemolysis obtained from Triton X-100 incubation.

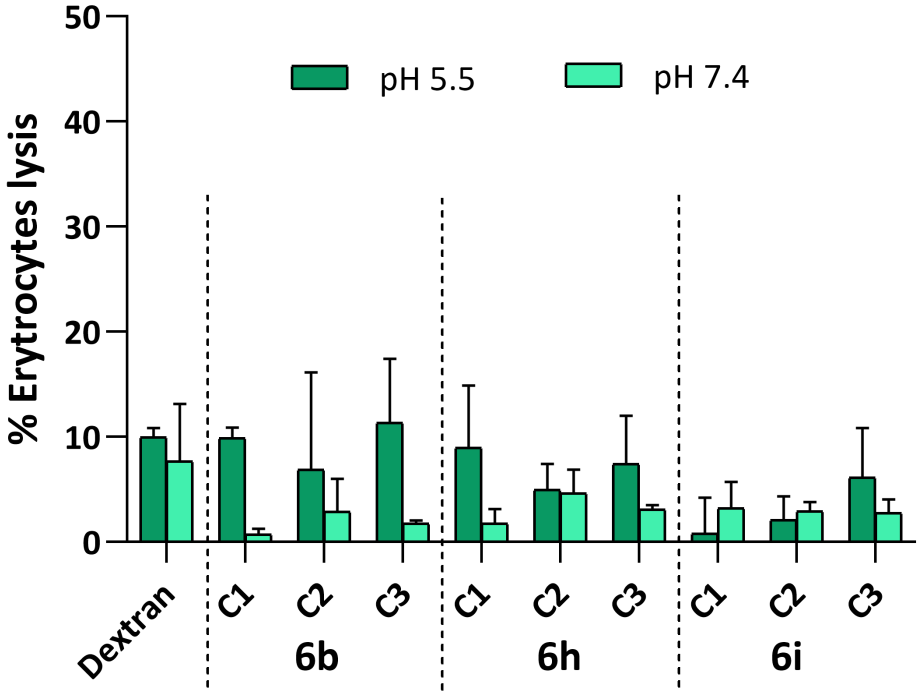


Figure S39. Erythrocyte lysis assay. **6b, 6h,** and **6i** were incubated with erythrocytes at different concentrations (>IC40 (C1)) and a diluted concentration (>IC15 (C2, dilution factor C1/C2 = 1.5)) at 37°C at physiologic pH (7.4) and lysosomal pH (5.5). Hemoglobin release was measured after 1 h. Dextran used as a negative control. Data plotted as mean ± SD, n =3. Data was analyzed using a t-test comparing each treatment group to the negative control. No statistically significant differences were observed ($p > 0.05$ for all comparisons).

Conformational Analysis of **6b** vs **7**

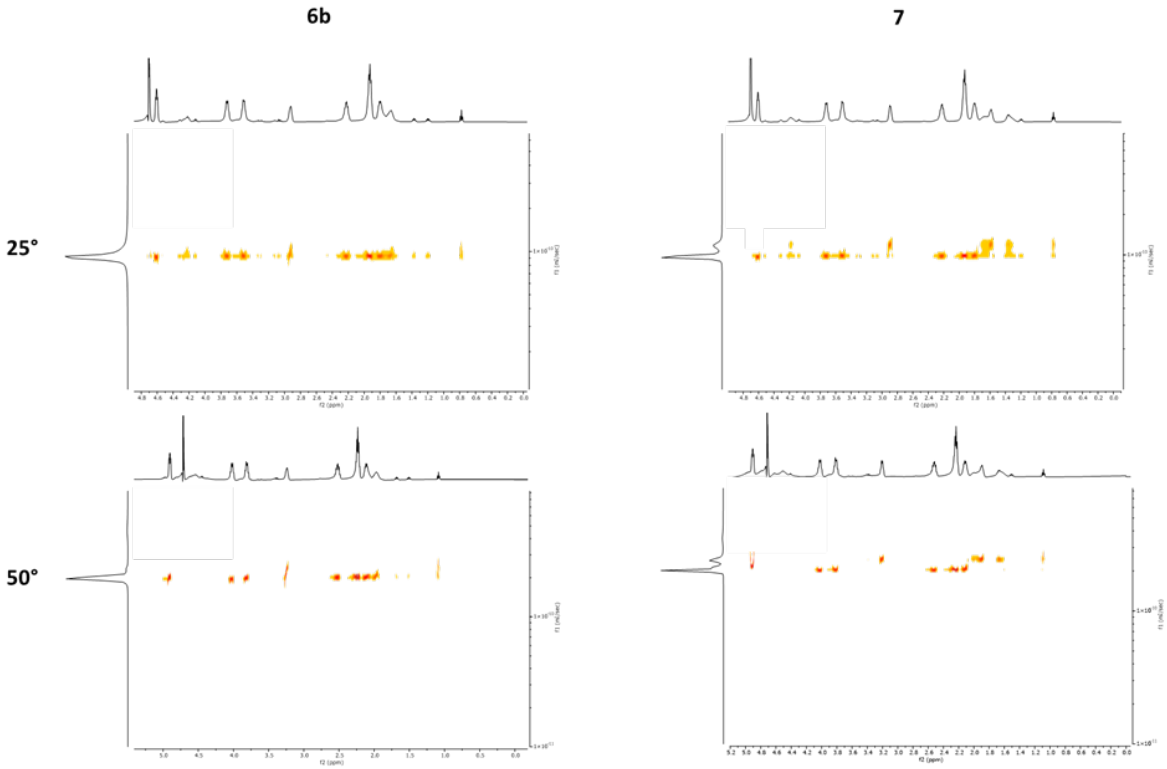


Figure S40. The bimodal profile of diblock copolymer **7** compared to diblock copolymer **6b** (attributed to a polypeptide conformational change) observed by NMR-DOSY analysis at different temperatures.

Quantification of Cy5-labeled diblock polymer 6b in isolated mitochondria

MDA-MB-231 cells were seeded into two 6-well plates (150,000/well, 2ml per well, control and treated conditions, n=2 wells for each condition) and allowed to adhere for 48 h at 37°C and 5% CO_2. 3 h prior to mitochondria isolation, a non-toxic concentration of diblock copolymer **6b** labeled with Cy5 was added to four wells (two controls and two treated with diblock copolymer **6b**). Mitochondria were isolated for each condition using the Thermo Scientific Pierce™ Mitochondria Isolation Kit for Cultured Cells (500,000 cells/condition) following the manufacturer's instructions based on serial differential centrifugation. The isolated mitochondria were resuspended in 0.5 ml PBS and incubated with MitoTracker™ Green FM M7514 (100 nM, mitochondria, 10 min incubation) and Hoechst 33342 (2 µg/ml, a marker for cell viability). The resulting samples were analyzed using flow cytometry (CytoFLEX S, Beckman-Coulter, CA, USA). Data collection involved 10,000 counts per sample, and data were analyzed using CytExpert version 2.3 software. Data are shown in **Figure 2C** of the main manuscript.

Qualitative and Quantitative Analysis of Cy5-Labeled Diblock Copolymer 6b in Depolarized Mitochondria

The qualitative analysis of diblock copolymer **6b** in polarized and depolarized mitochondria was

performed using a Leica TCS SP8 confocal microscope with a 63x 1.4NA CS2 oil immersion objective lens. Excitation wavelengths of 405, 488, 561, and 638 nm were employed, along with four fluorescent PMTs and two HyD detectors. Quantitative analysis was performed using the high-throughput imaging HCS system InCell Analyzer 2200 (Cytiva, UK) with four fluorescent channels and a 40x objective lens. The experiments, conducted under controlled levels of CO_2 and temperature, were performed at non-toxic concentrations of diblock copolymer **6b** using specific fluorescent markers: potential-dependent MitoTracker™ Red CM-H2Xros M7513 (mitochondria, 100nM), potential-independent MitoTracker™ Green FM (100 nM, mitochondria), Hoechst 33342 (nuclei, 2 µg/ml), and Cyanine5 (diblock copolymer). MDA-MB-231 cells (1,500 cells/well, 0.03 ml per well) were seeded in a 384-well black optical-bottom plate and incubated for 24 h at 37°C with 5% CO_2. 4 h prior to the analysis by confocal fluorescence microscopy, carbonyl cyanide 3-chlorophenylhydrazone (CCCP, 30 µM) was added to selected wells to induce mitochondria depolarization, while Cy5-labelled diblock copolymer **6b** was added 3 h prior to experiments. After adding markers (1 h), images were captured and processed using the Leica Application Suite X (LAS X). Control cells (to establish autofluorescence levels) and control conditions such as MitoTracker™ Red CM-H2Xros M7513 and MitoTracker™ Green FM untreated and incubated with CCCP 30 µM separately (to establish the depolarization efficiency) were also analyzed. Following the qualitative analysis, the same 384-well plate was analyzed using the InCell Analyzer 2200. For each condition (n=2), 10 regions of interest (ROI) (~ 40 live cells/ROI) were selected, and the fluorescence intensity was quantified for each channel. For the data analysis, the mean fluorescence intensity of CCCP-treated wells was normalized to CCCP-untreated controls for each channel. The diblock copolymer fluorescence intensity was determined in MitoTracker™ Green FM positive cells. Values represent Mean ± SD (n=3). Data are shown in **Figures 2E** and **2F** of the main manuscript.

e. Affinity studies in membrane models of Polyproline-based Diblock Polymers

Determination of Cardiolipin affinity

Competitive binding experiments were conducted following a procedure described by Dimitrijevs et al. [6]. Briefly, a 10 mM stock solution of 3,6-di(azetidin-1-yl)-10-(3-(trimethylsilyl)propyl)acridin-10-ium iodide (MitoCLue) was prepared in DMSO and diluted to 50 µM with 20 mM HEPES buffer (pH = 6.8). A working solution of CL/DOPC liposomes was prepared by diluting a 100:300 µM CL/DOPC stock solution to 20:60 µM in the same buffer. In a black 96-well plate (ELISA plate, flat base, Polystyrene, Medium Binding, Sarstedt), a solution of CL/DOPC liposomes (final Cardiolipin concentration of 2.5 µM) was titrated in triplicate with test compounds and gently mixed with a micropipette. CL/DOPC dilutions without a test compound were also prepared in triplicate (vehicle). A test compound without CL/DOPC liposomes was also prepared to verify the lack of a test compound-MitoCLue interaction. Cytochrome c (from equine heart, Sigma-Aldrich) was used as a positive control. A 96-well plate was then incubated on a plate shaker with a thermostat for 10 min (500 rpm, 37° C). An appropriate amount of MitoCLue stock solution was next added to wells (final MitoCLue concentration of 5 µM) and gently

mixed with a micropipette. After that, the 96-well plate was incubated for 15 min on a plate shaker (500 rpm, 37° C), and the fluorescence intensity was measured using a Tecan Infinite 1000 microplate reader (Tecan Austria GmbH, Austria) at excitation and emission wavelengths of 497 and 529 nm. Data was analyzed with GraphPad Prism® 8.0 (GraphPad, Inc., USA). The fluorescence intensity was normalized by setting CL/DOPC liposomes with MitoCLue (vehicle) as 0% and the maximal fluorescence intensity produced by adding a test compound as 100%. The normalized fluorescence intensity was plotted against the ligand concentration on a logarithmic scale and fit with a four-parameter logistic (4 PL) model to calculate the Half Maximal Effective Concentration (EC50) values. Before conducting a competitive binding experiment on isolated mitoplasts, MitoCLue was titrated with each batch to determine the optimal volume of mitoplast solution to saturate a 5 µM MitoCLue solution. The competitive binding assay was performed similarly to CL/DOPC liposomes.

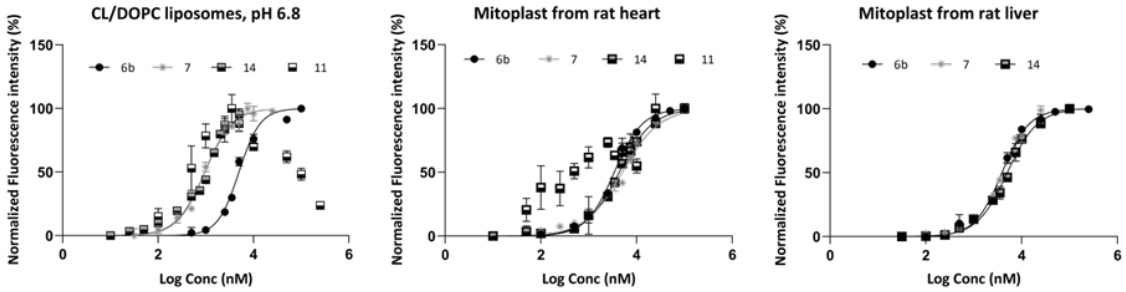


Figure S41. Using a cardiolipin-specific probe (MitoCLue), a fluorescent-based competitive binding assay was performed in different Cardiolipin-containing membranes (liposomes, mitoplasts from rat heart and liver) for diblock copolymers **6b, 7, 14,** and **11**.

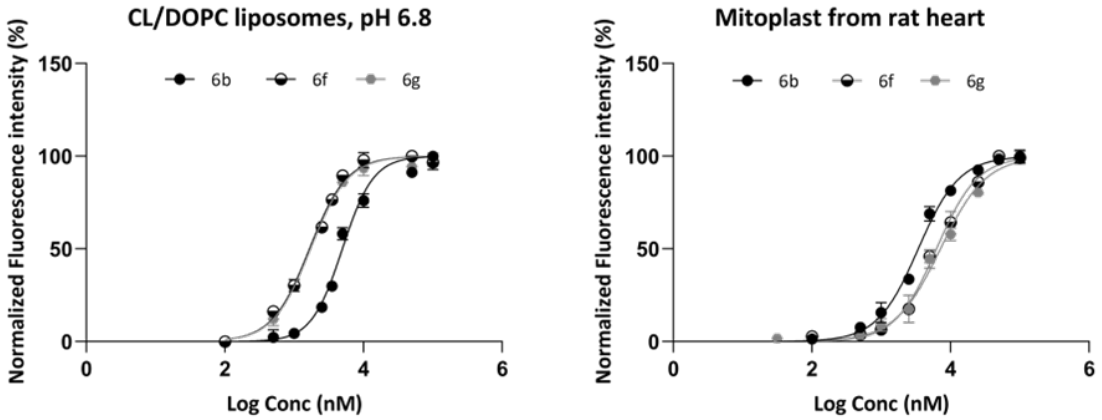


Figure S42. Using a Cardiolipin-specific probe (MitoCLue), a fluorescent-based competitive binding assay was performed in different Cardiolipin-containing membranes (liposomes, mitoplasts from rat heart and liver) for diblock copolymers **6b, f,** and **g**.

Table S7. Relative binding affinity of evaluated diblock copolymers determined by the Half Maximal Effective Concentration (EC50) values obtained from fluorescent-based competitive binding assays conducted in various Cardiolipin-containing membranes

Diblock copolymers	CL/DOPC liposomes, pH 6.8		Mitoplasts from rat heart		Mitoplasts from rat liver	
	EC50 average, μM	±SD	EC50 average, μM	±SD	EC50 average, μM	±SD
6b	1.642	0.051	3.456	0.065	3.845	0.314
7	0.960	0.114	4.998	0.619	3.911	0.144
11	n.b.	-	n.b.	-	n.b.	-
14	1.045	0.023	4.499	0.461	5.203	0.115
6g	1.705	0.122	7.092	0.600	-	-
6f	1.667	0.099	6.436	1.302	-	-
15a	>1000	-	>1000	-	-	-
15b	>1000	-	>1000	-	-	-

Cytochrome C was used as a positive control (liposomes EC_{50} average (N=3) for four experiments = 0.323 ± 0.017; mitoplast from rat heart EC_{50} average (N=3) for three experiments = 0.666 ± 0.048; mitoplast from rat liver EC_{50} average (N=3) for three experiments = 0.643 ± 0.090; n.b. = no binding; CL/DOPC - Small unilamellar vesicles or SUVs, composed of 1,2-dioleoyl-sn-glycero-3-phosphocholine (DOPC) and CL (3:1 molar ratio)

DPH exclusion assay

To evaluate the ability to intercalate into the hydrophobic region of Cardiolipin-containing and Cardiolipin-free liposomes, DPH was used as a fluorescent probe. A stock of DPH in acetone (10 mM) was freshly prepared before the experiment and stored in the dark. A working solution of DPH was prepared by diluting the stock solution to 40 μM in 20 mM HEPES buffer (pH 6.8). In a black 96-well plate, 25 μL DPH working solution was added to 50 μL 250:750 μM CL/DOPC or 1 mM DOPC solutions in duplicate and incubated on a plate shaker with a thermostat for 1 h (500 rpm, 37° C). Then, 25 μL test compound (40 and 400 μM solutions), buffer (vehicle), or nonyltriphenyl phosphonium bromide (TPP, positive control) were added. The final concentrations in the reaction mixtures were CL/DOPC (125:375 μM) or DOPC (500 μM), DPH (10 μM), test compounds (10 or 100 μM) or TPP (10 or 100 μM). The plate was then incubated for 1 h (500 rpm, 37° C), and the fluorescence was measured using a Tecan Infinite 1000 microplate reader (Tecan Austria GmbH, Austria) at excitation and emission wavelengths of 368 and 440 nm.

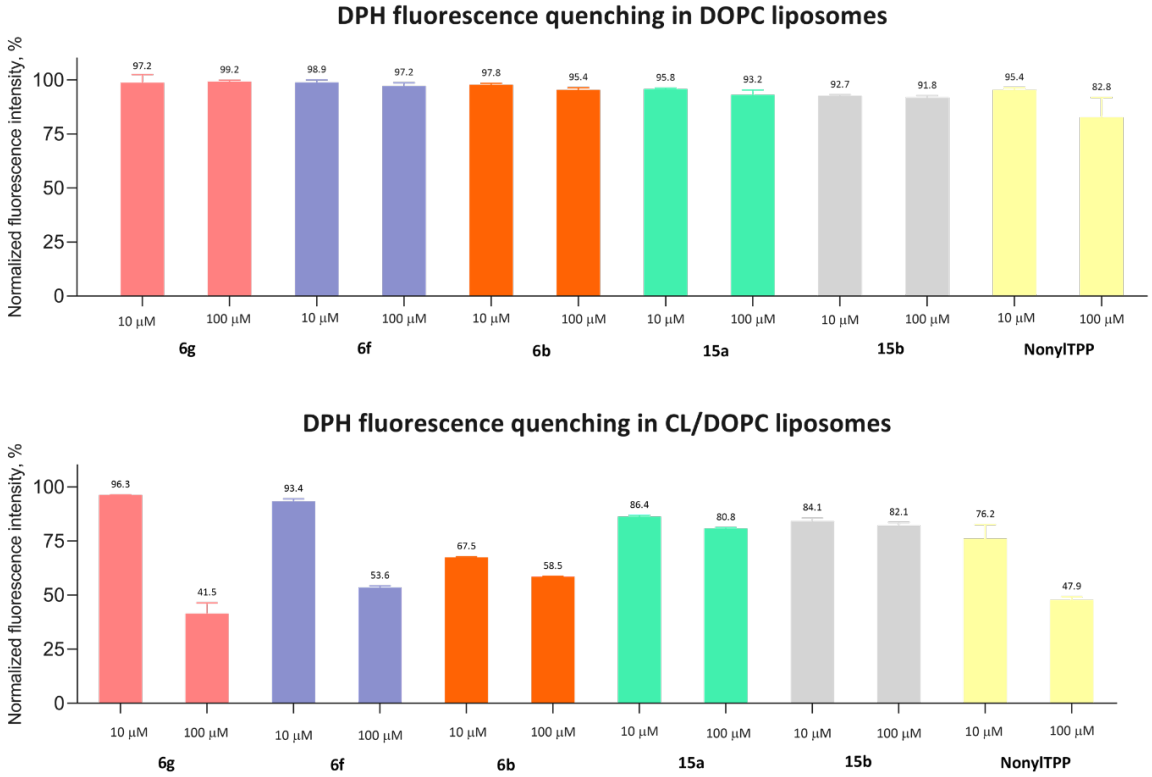


Figure S43. DPH fluorescence quenching of diblock copolymers with a polycationic block (**6g, f,** and **b**) and homopolyprolines (**15a-b**) into hydrophobic regions of DOPC and CL/DOPC small unilamellar vesicles. NonylTPP was used as a positive control.

Physical Studies in Cardiolipin-containing Small Unilamellar Vesicles and Supported Lipid Bilayers

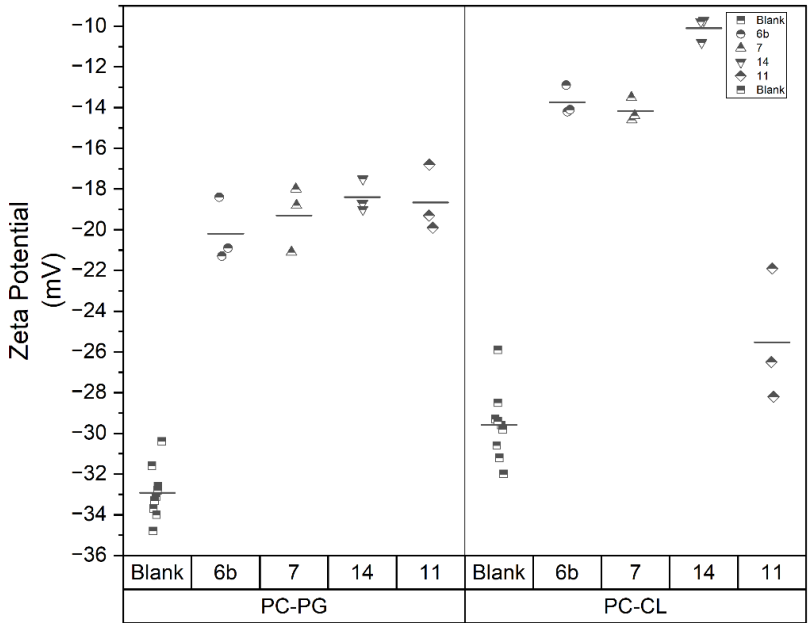


Figure S44. Zeta potential of POPC:POPG 1:1 and POPC:CL 2:1 small unilamellar vesicles after incubation with 5 μM diblock copolymers.

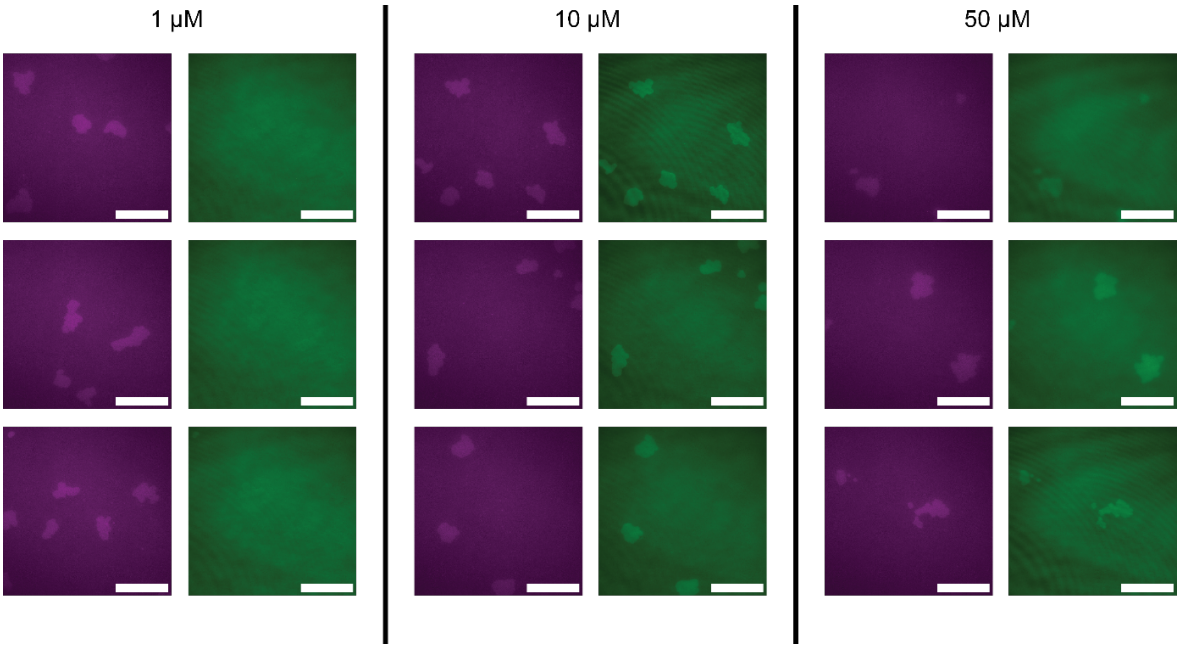


Figure S45. Concentration titration for diblock copolymer **6b** (green) on supported lipid bilayers (SLBs) of POPC and cardiolipin 1:1 labeled with 0.05 mol% Atto655-DOPE (magenta). The formation of patches is already visible with a 1 µM concentration of diblock copolymer **6b**. Increasing concentrations slightly increase the size of these patches, simultaneously reducing the number of such patches. Scale bars: 20 µm.

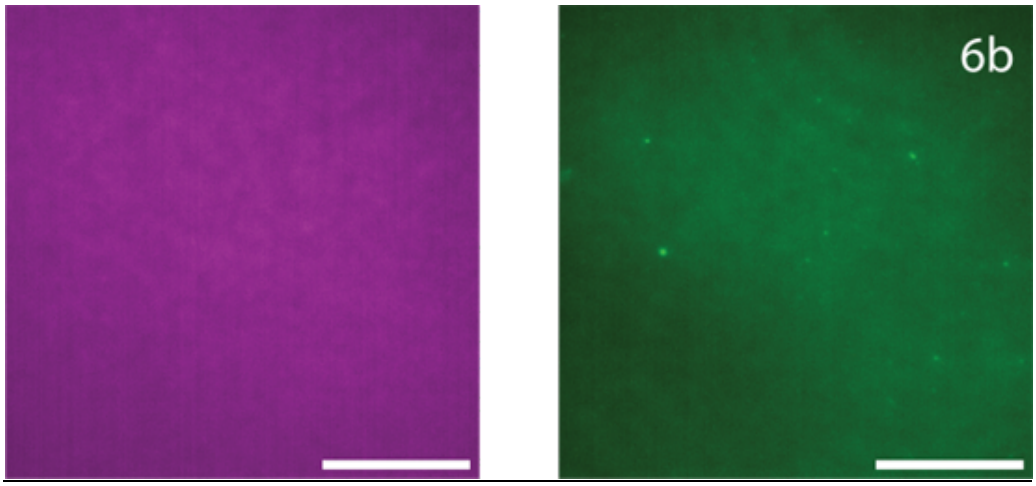


Figure S46. The addition of diblock copolymer **6b** does not induce patch formation in the case of equimolar POPC and POPG membranes. Scale bars: 20 µM.

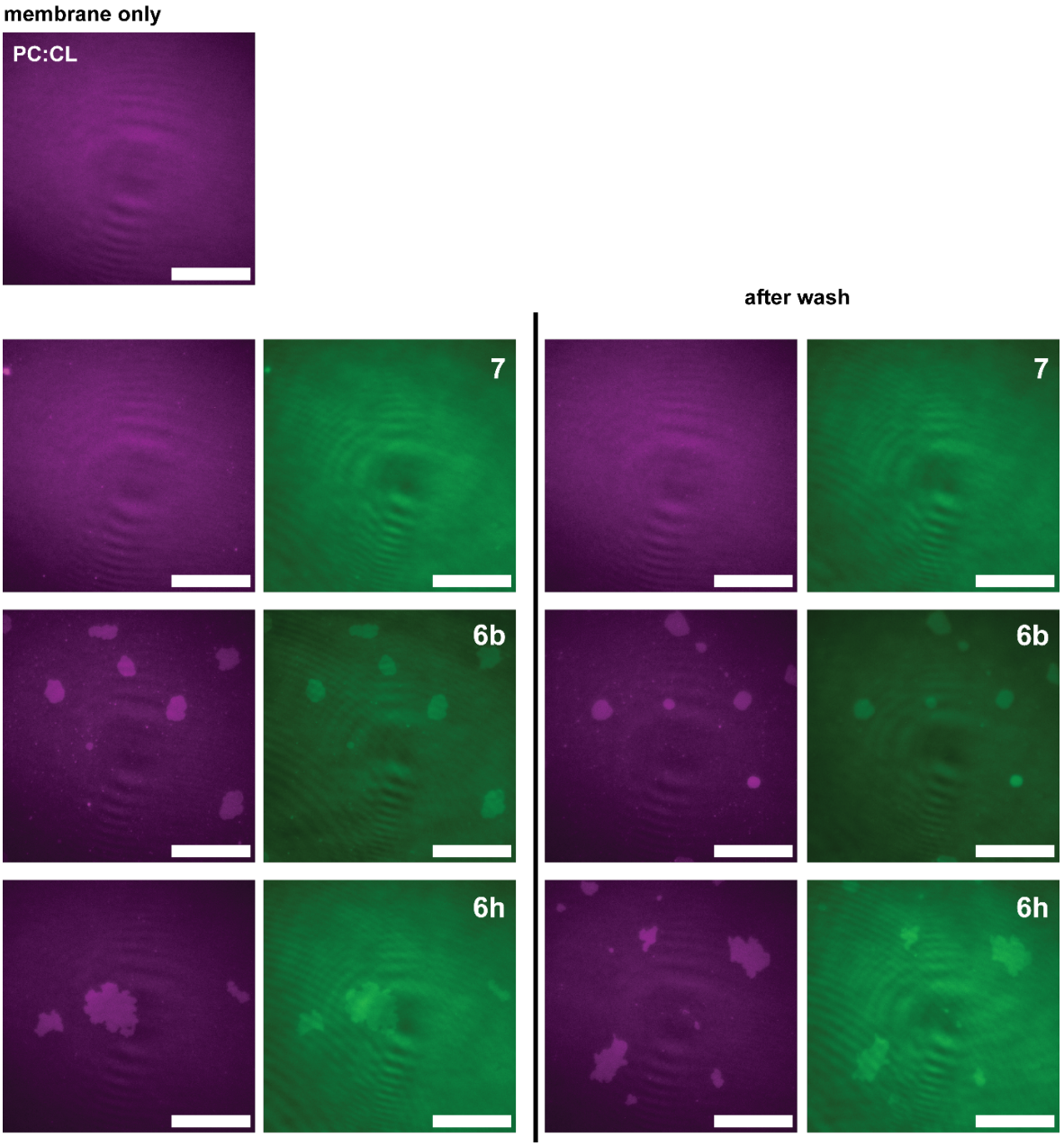


Figure S47. Total internal reflection fluorescence microscopy images of supported lipid bilayers (SLBs, POPC, and cardiolipin 1:1 labeled with 0.05 mol% Atto655-DOPE (magenta)) incubated with diblock copolymers **7**, **6b**, and **6h** at 5 μM. Magenta depicts the membrane channel, and green depicts the diblock copolymer/ diblock copolymer-conjugate channel. For a visual comparison, the contrast is set the same in all images. The left set of panels shows the supported lipid bilayers after adding 5 μM of respective diblock copolymer/diblock copolymer-conjugate without washing. The right panel set shows supported lipid bilayers after washing with 10x the sample volume. Scale bars: 20 μm.

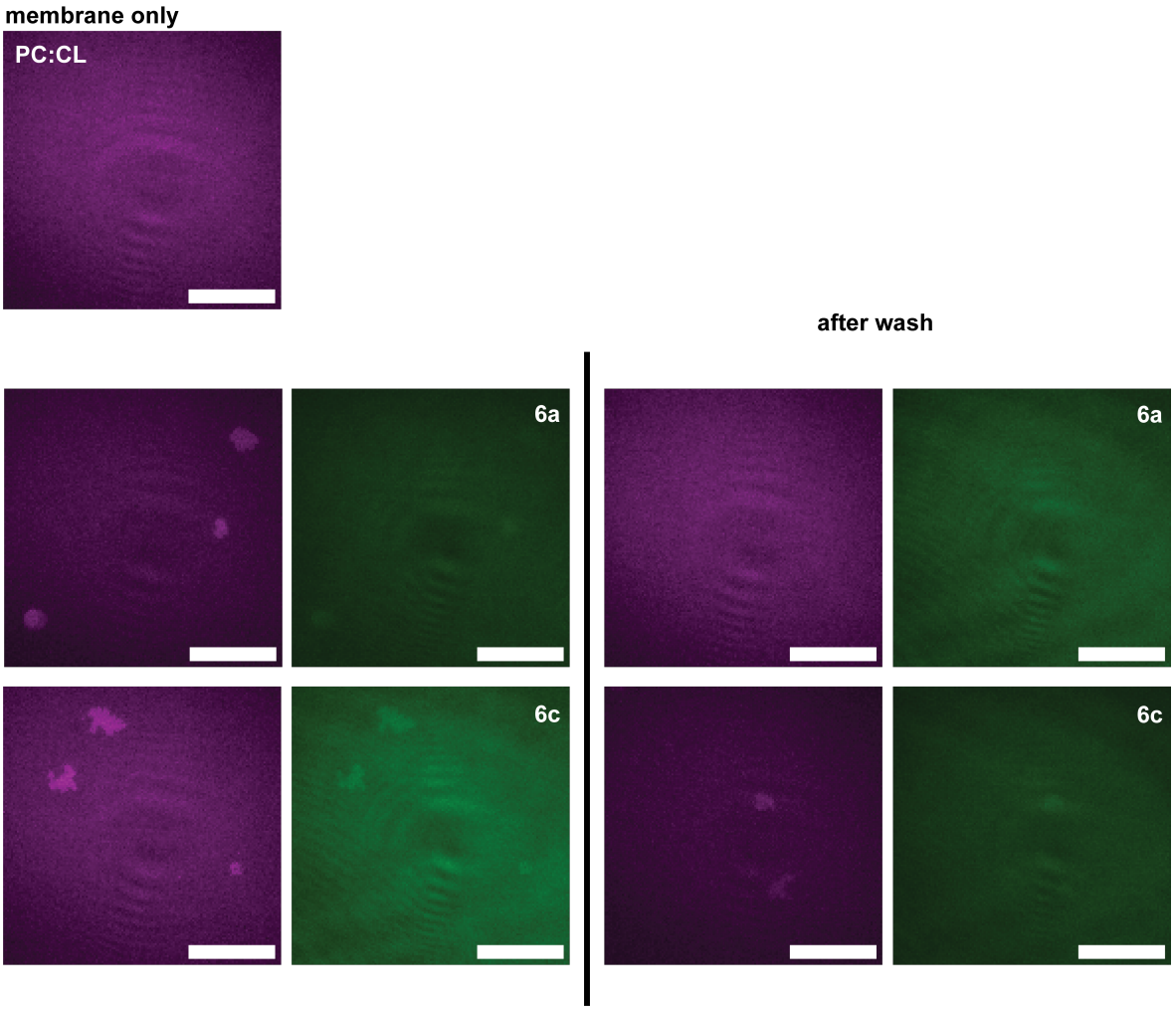


Figure S48. Total internal reflection fluorescence microscopy images of supported lipid bilayers (SLBs, POPC, and cardiolipin 1:1 labeled with 0.05 mol% Atto655-DOPE (magenta)) incubated with 5 μM diblock copolymers **6a** and **6c**. Magenta depicts the membrane channel, and green depicts the diblock copolymer channel. For a visual comparison, the contrast is set the same in all images. The left set of panels shows the supported lipid bilayers after adding 5 μM of respective diblock copolymer without washing. The right set of panels shows supported lipid bilayers after washing with 10x the sample volume. Scale bars: 20 μm.

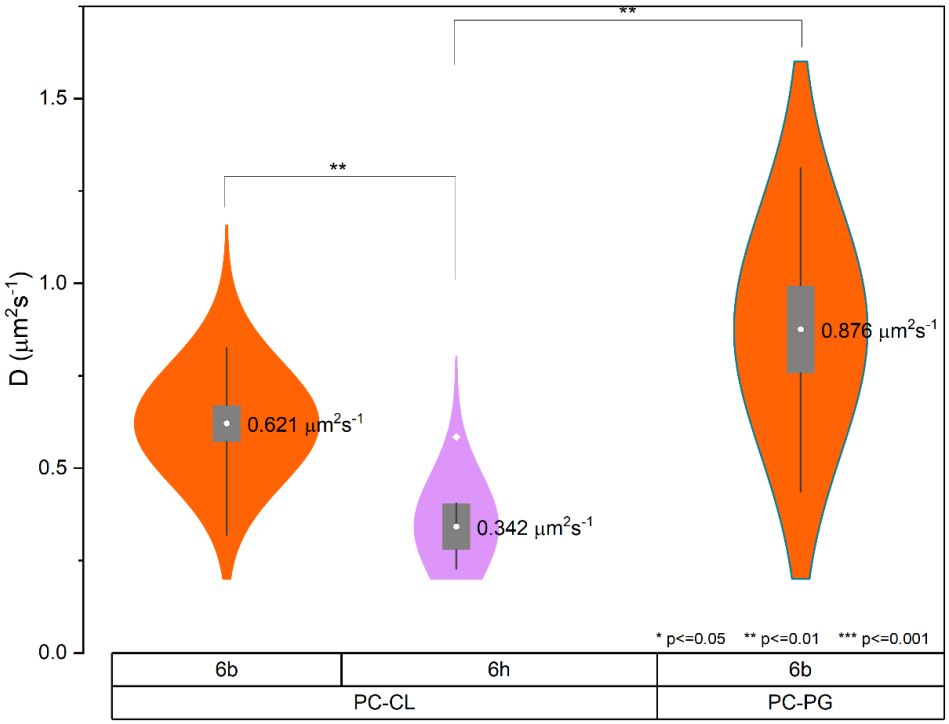


Figure S49. Diffusion coefficient of the diblock copolymers **6b** and **6h** on respective membranes (SLBs, POPC, and cardiolipin 1:1 labeled with 0.05 mol% Atto655-DOPE and equimolar POPC-POPG). Data analyzed using two-way ANOVA. Significance reported as **P ≤ 0.01 (ns = not significant).

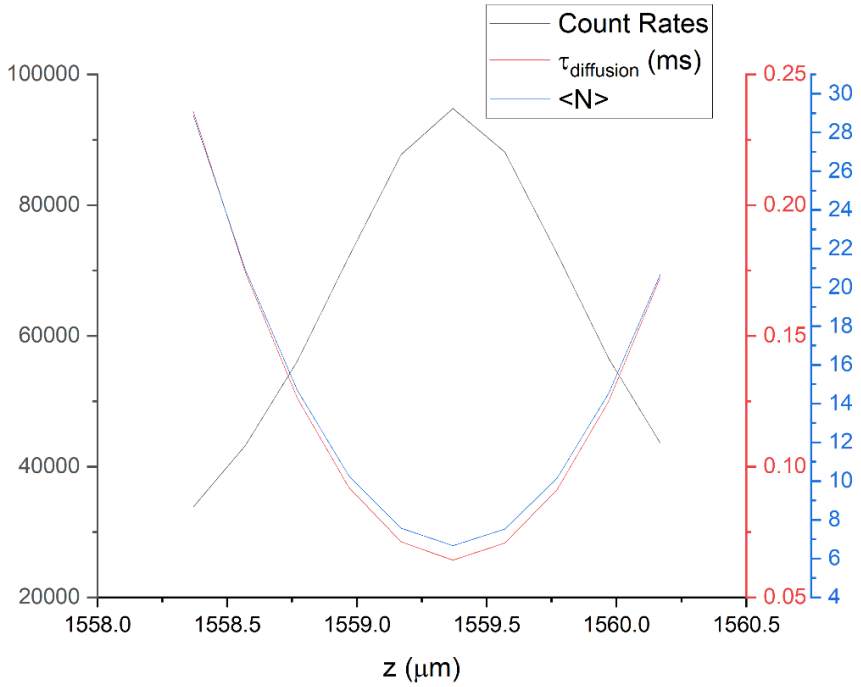


Figure S50. The representative curve for Z-scan fluorescence correlation spectroscopy with count rates, τ_D, and <N> as a function of z

f. Biological Activity of Polyproline-based Diblock Polymers in a Triple Negative Breast Cancer Model

Mitochondria membrane potential analysis

MDA-MB-231 cells were seeded in 96-well plates (5,000 cells/well, 0.05 ml per well) and incubated for 24 h at 37° and 5% CO^2. Concentrated stock solutions of diblock copolymers were prepared in PBS and diluted in DMEM/F-12 medium (with 10% FBS and 1% P/S). The diblock copolymer solutions were then sterilized by passing through a 0.2 μm filter and added to give sub-IC50 final concentrations (>IC40). Cells were treated for 2, 6, and 24 h (one plate per condition); at each time point, the medium was gently removed, cells were washed twice with PBS and incubated for 30 min with 2 μM 5,5,6,6'-tetrachloro-1,1',3,3' tetraethylbenzimidazoylcarbocyanine iodide (JC-1) solution in cell medium. CCCP was used as a positive control (50 μM, 10 min). Finally, the JC-1 solution was removed, and cells were washed twice with PBS. The fluorescence was simultaneously measured at abs/em 550/605 (red) and 484/528 nm (green) using a CLARIOstar plate reader. For data analysis, the red/green fluorescence ratio was considered after each time and normalized to untreated controls (set as 100%). Values represent Mean ± SD (n=3). Data are shown in **Figure 4A** of the main manuscript.

Oxygen Consumption rate Analysis by Oroboros

High-resolution respirometry was performed using the Oxygraph-O2k system (OROBOROS INSTRUMENTS, Austria). All experiments were carried out at 37° C in MiR05 medium (110 mM sucrose, 60 mM K-lactobionate, 0.5 mM EGTA, 3 mM $MgCl_2$, 20 mM taurine, 0.1% bovine serum albumin (BSA) essentially fatty acid-free, 10 mM KH_2PO_4, 20 mM HEPES, pH 7.1). The medium was reoxygenated when the oxygen concentration dropped to 90-100 μM.

First, a suspension of MDA-MB-231 cells (1×10^6/ml final concentration) was placed into a chamber and permeabilized with saponin (25 μg/ml, Sigma-Aldrich) for 10 min. Diblock copolymer **6b** (sub-IC50 final concentrations (>IC40 (C1) and diluted concentration C2 (C1/C2 = 2) and C3 (C2/C3 = 5)) or an equivalent volume of PBS (control chamber) was added to the permeabilized cells. Next, pyruvate (5 mM, Sigma-Aldrich) and malate (2 mM, Sigma-Aldrich) were used to determine complex I (CI)-linked LEAK (non-phosphorylating resting state) respiration. Subsequently, ADP (5 mM, Calbiochem) was added to determine the oxidative phosphorylation-dependent respiration (OXPHOS state). Glutamate (10 mM, Sigma-Aldrich) was added to support CI-dependent respiration. After that, succinate, a complex II (CII) substrate (10 mM, Sigma-Aldrich), was added to assess CI-II-linked respiration.

To determine electron transfer capacity, the CCCP uncoupler was titrated in 1 μM steps until the maximum respiration rate (4 μM final concentration). Then, rotenone (0.5 μM, an inhibitor of CI, Sigma-Aldrich) and antimycin A (2.5 μM, an inhibitor of complex III, Sigma-Aldrich) were added to determine CII-linked electron transfer capacity and the residual oxygen consumption, respectively. Flux control factors were calculated as described by Gnaiger et al. [7]. The substrate-dependent flux control factors were calculated as follows:

$$1 - \frac{\text{Resp. rate before the addition of a substrate}}{\text{Resp. rate after the addition of a substrate}}$$

The rotenone effect was calculated as follows:

$$1 - \frac{\text{Resp. rate after the addition of rotenone}}{\text{Resp. rate before the addition of rotenone}}$$

Elaborated Data are shown in **Figure 4D** of the main manuscript.

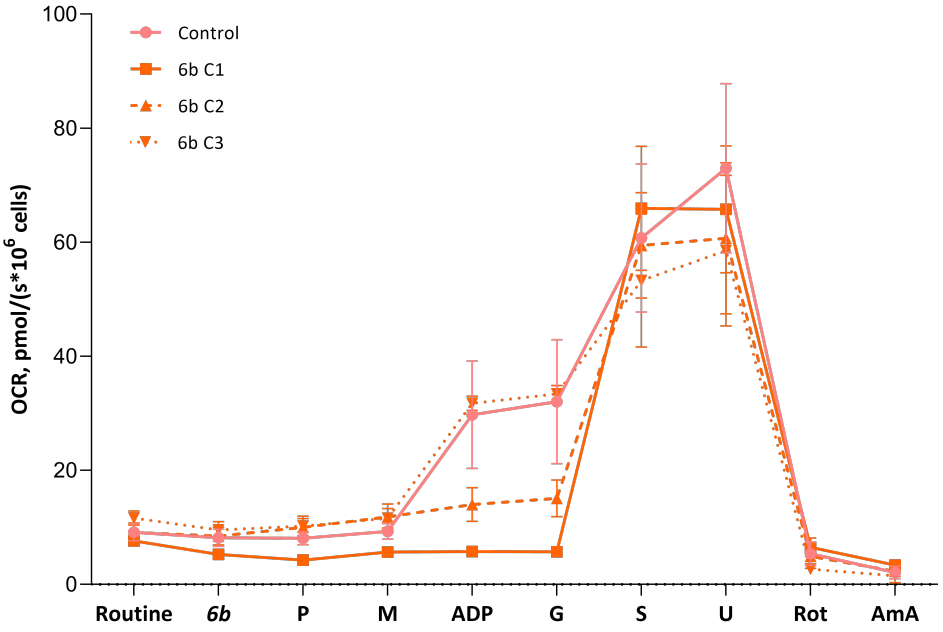


Figure S51. Oxygen consumption rate (OCR) profile upon treatment with diblock copolymer **6b** compared to control cells. P- pyruvate, M – malate, G – glutamate, S – succinate, U – uncoupler, CCCP, Rot – rotenone, AmA – Antimycin A. The results demonstrate a concentration-dependent mechanism of action of diblock copolymer **6b**, which acts as an inhibitor of mitochondria complex I and uncoupler of oxidative phosphorylation from the electron transport chain.

Oxygen Consumption Rate Analysis by Seahorse XF Analyzers

The Agilent Seahorse XF Mitostress Test measures critical parameters of mitochondrial function by directly measuring the OCR of cells after adding modulators of respiration, which include oligomycin, an inhibitor of the ATP synthase; carbonyl cyanide-p-trifluoromethoxyphenylhydrazone (FCCP), an uncoupling agent that collapses the proton gradient; and rotenone/antimycin (Rot/AA), inhibitors of complex I and III.

For our experiment, cells were seeded in 96-well plates (20,000 cells/well, 0.05 ml per well) and incubated at 37° and 5% CO_2. Concentrated stock solutions of diblock copolymers were prepared in PBS and diluted in DMEM/F-12 medium (with 10% FBS and 1% P/S). The diblock copolymer solutions were then sterilized by passing through a 0.2 μm filter and added to give sub-IC50 final concentrations

(>IC40 (C1) and diluted concentration C2 (C1/C2 = 1.5)). After 24 h, their culture medium was replaced with DMEM XF medium (with 1 mM pyruvate, 2 mM glutamine, and 10 mM glucose). The inhibitors were loaded into the injection ports of the XFe96 Sensor Cartridge, previously hydrated for 24 h with the XF calibrant solution (final concentrations of 1.5 µM oligomycin, 1 µM FCCP, and 0.5 µM Rot/AA). Analysis was performed using an Agilent Seahorse XF Pro analyzer. Results were normalized using Hoechst 3342 staining (1.5 µg/ml), a marker for cell viability. OCR was measured in pmol/min/2x10^4 cells. Data were normalized to the control set as 100%. Values represent Mean ± SD (n=3). Data are shown in **Figures 4C** and **5J** of the main manuscript and **S49** of supporting information.

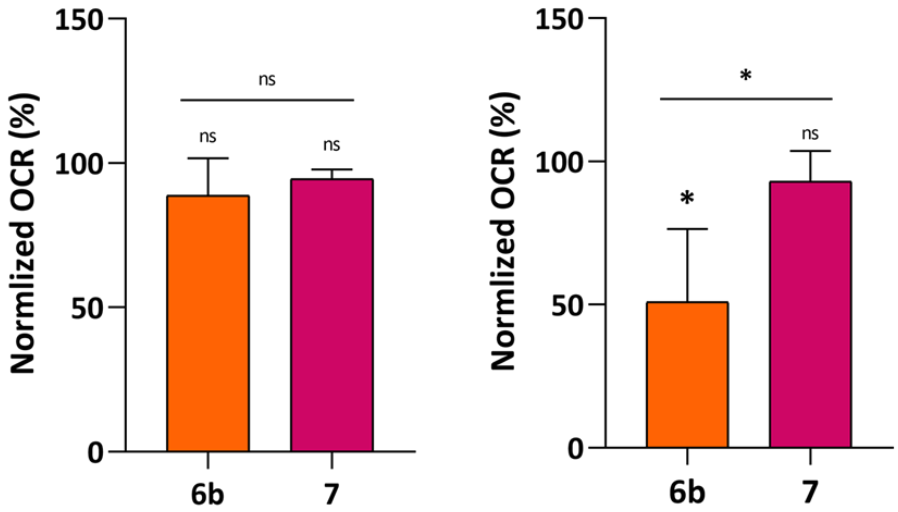


Figure S52. Oxygen consumption rate (OCR) related to the (**left**) spare respiration capacity and (**right**) ATP-production coupled respiration analysis by Seahorse XF after a 24-h treatment with diblock copolymer **7** at an equivalent concentration of diblock copolymer **6b** (~IC40). OCR was measured in pmol/min/2x10^4 cells, with the control set as 100%; n = 3, mean ± SEM. Data was analyzed using a t-test. Differences were considered significant when p*<0.05 (ns: non-significant).

Reactive Oxygen Species Production

MDA-MB-231 cells were seeded into a 6-well plate (150,000/well, 2 ml per well) and allowed to adhere for 24 h at 37°C and 5% CO_2. Concentrated stock solutions of diblock copolymers were prepared in PBS diluted in DMEM/F-12 medium (with 10% FBS and 1% P/S). The diblock copolymer solutions were then sterilized by passing through a 0.2µm filter and added to give a sub-IC50 final concentration (>IC40). After 24 h, cells were washed with PBS, trypsinized, and centrifuged to obtain cell pellets resuspended in fresh DMEM/F-12 medium (with 10% FBS and 1% P/S). Cells were then incubated with 5 µg/ml of 2,7-dichlorodihydrofluorescein (DCFH) for 30 min at 37°C and 5% CO_2. Subsequently, propidium iodide (2 µg/ml), a marker for cell viability, was added, and the resulting samples were analyzed using flow cytometry (CytoFLEX S, Beckman-Coulter, CA, USA). Data collection involved 10,000 counts per sample, and data were analyzed using CytExpert version 2.3 software. Data were

normalized to the control set as 100%. Values represent Mean ± SD (n=3). Data are shown in **Figures 4B** and **4I** of the main manuscript.

Mitochondrial morphology

MDA-MB-231 cells were seeded into an 8-well Permanox® chamber (12,500 cells/well, 0.3 ml per well) and allowed to adhere for 24 h at 37°C and 5% CO_2. Subsequently, sub-IC50 final concentrations (>IC40) of each selected compound were added at 6, 24, and 48 h. After washing with PBS, 3% glutaraldehyde was added for 10 min at 37°C for pre-fixation, removed, and added for 1 h at RT. The fixative was removed, and the cells were washed with 0.1 M PB buffer five times (each for 10 min) and stored at 4°C. The samples were post-fixed in 2% OsO4 for 60 min at RT, then stained in 2% uranyl acetate in the dark for 2 h at 4°C.

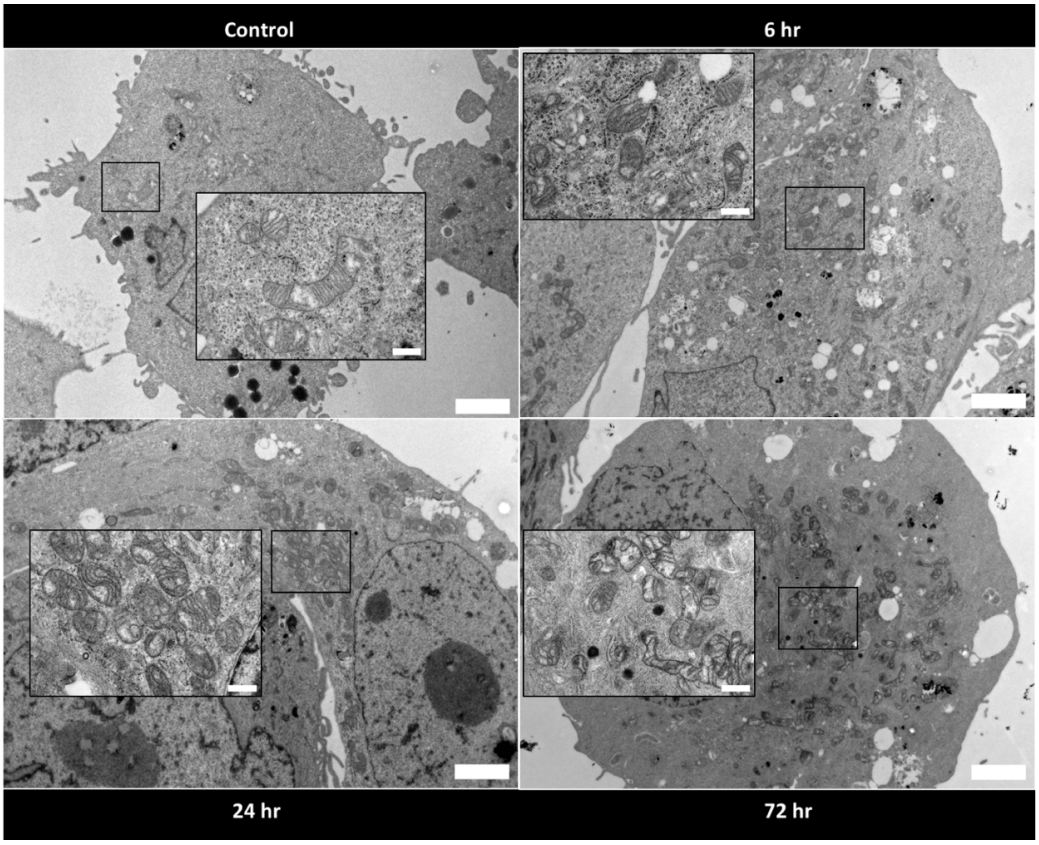


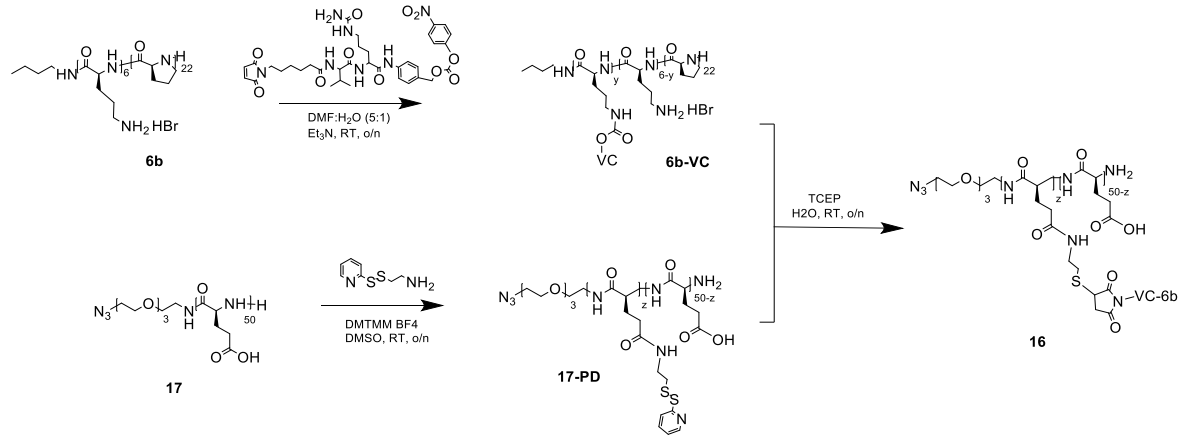
Figure S53. Mitochondria morphological studies by transmission electron microscopy after treatment with diblock copolymer **7** at equivalent diblock copolymer 6b (~IC40) concentrations at different times (6, 24, 72 h; n = 3, mean ± SEM). Scale bar main images: 20 μm; scale bar inset images: 500 nm.

Subsequently, the samples were rinsed in distilled water, dehydrated in ethanol, and left to embed overnight in Durcupan resin (Sigma-Aldrich, USA). After polymerization, the embedded cultures were detached from the wells and affixed to Durcupan blocks. Finally, ultrathin sections (0.08 μm) were sliced using an Ultracut UC-6 (Leica Microsystems, Germany) and stained with lead citrate (Reynold's

solution). Finally, samples were examined with an FEI Tecnai Spirit BioTwin transmission electron microscope (ThermoFisher Scientific, USA) and a Morada digital camera (EMSIS GmbH, Germany). Twenty images of ten distinct cells were captured for each sample, with one set at 1900x magnification and another at 11000x magnification. Data are shown in **Figures 4E** and **5H** of the main manuscript.

g. Synthetic Procedures, Physicochemical and Biological Characterization of the Diblock Copolymer Conjugate 16

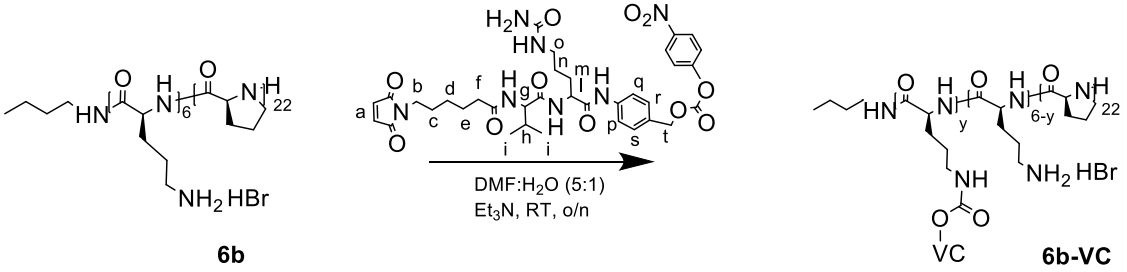
Synthesis and characterization of diblock copolymer-conjugate 16



Scheme S5. Convergent synthetic procedure for the synthesis of diblock copolymer-conjugate **16**

Diblock copolymer-conjugate **16** was synthesized through a convergent process, initially involving the separate synthesis of diblock copolymer **6b-VC** and polymer **17-PD**.

Diblock copolymer 6b-VC



Scheme S6. Synthetic procedure for the preparation of diblock copolymer **6b-VC**

In a two-neck bottom flask, 6b was dissolved in 5:1 DMF:H_2O (1 eq, 10 mg/mL). In a glass vial, the valine-citrulline linker derivative (maleimidocaproyl-L-valine-L-citrulline-p-aminobenzyl alcohol p-nitrophenyl carbonate, VC) was dissolved in 1 mL DMF (i.e. 0.03 eq for 3% mol VC modification) and added to the diblock copolymer solution, followed by triethylamine (Et_3N; 0.03 eq). The reaction was incubated for 24 h. After DMF elimination using a rotavapor and freeze-drying, the product was purified by PD-10 desalting columns packed with Sephadex G-25 resin and Vivaspin®, 2000 MWCO Da.
Yield: 70%. Conjugation efficiency >90%.

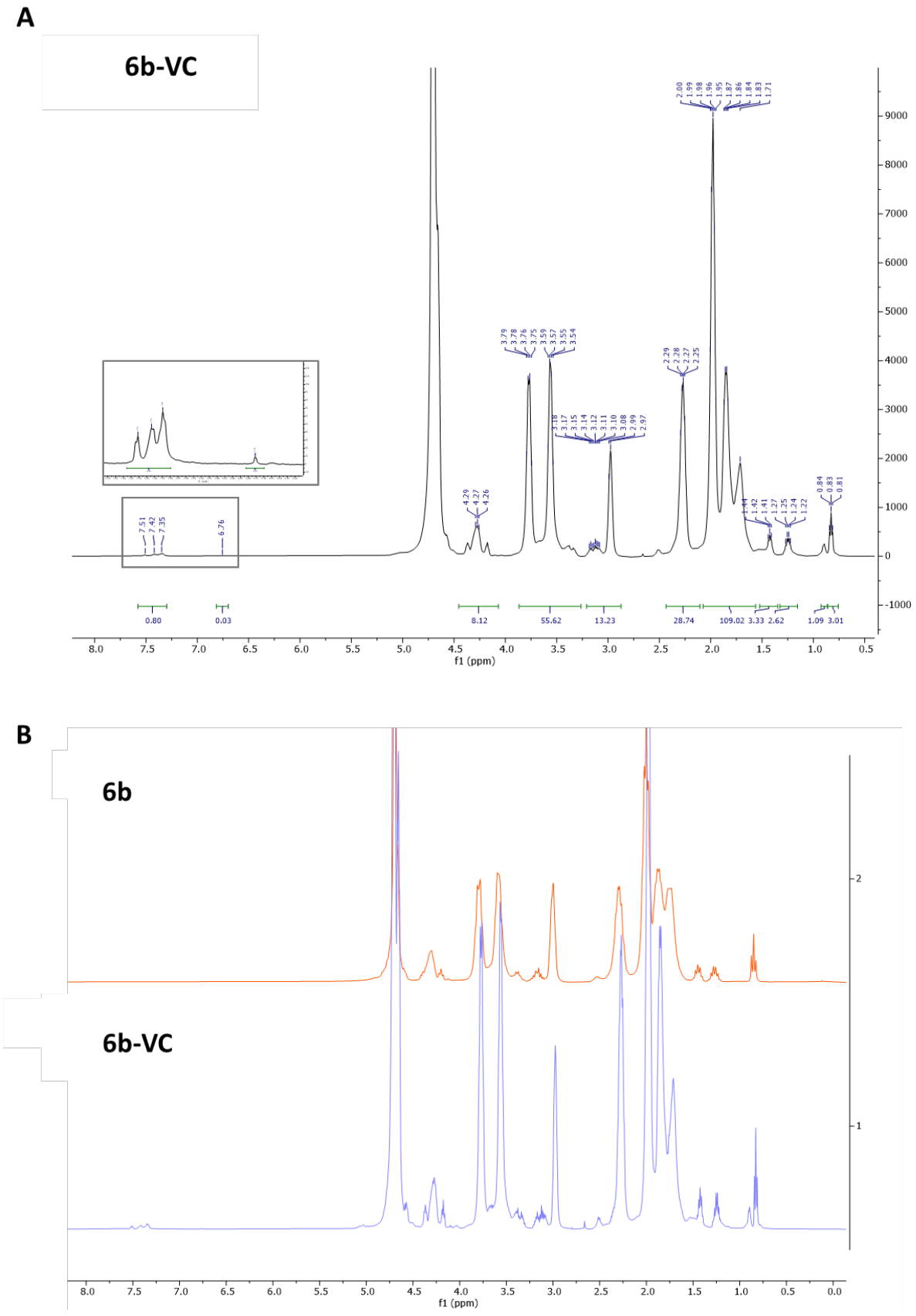


Figure S54. A) NMR spectra of diblock copolymer **6b-VC** in D2O (10 mg/ml). **B)** Comparison of stacked NMR spectra of diblock copolymers **6b** and **6b-VC.**

^{1}H NMR (500 MHz, D2O, 25 °C) δ 7.6-7.3 (m, 4H p,q,r,s), 6.8 (s, 2H, a), 4.77 – 4.71 (m, 1H, Cα of PLP; 1H g covered with D2O;), 4.50 – 4.20 (m, 1H, Cα of PLO; 1H l; 2H t), 3.96 – 3.30 (m, 2H, Cδ of PLP; CH2 of CH3CH2CH2CH2NH and 2H b), 3.24 -3.06 (m, 2H, Cδ of PLO and 2H o), 2.51 – 1.23 (m, 4H CH2CH2CH3, 4H Cβ+γ of PLP; 4H Cβ+γ of PLO; 13H c,d,e,f,h,m,n), 0.9 (s, 6H, i) 0.82 (t, J = 7.3 Hz, 3H, CH2CH2CH3).

VC functionalization was calculated by ultraviolet/visible spectroscopy (% wt) after the preparation of the free VC (DMF:H_2O) calibration curve and matrix effect adjustment (defined as the naked diblock polymer's influence on conjugate absorbance). Measurements were performed using ultraviolet/visible spectroscopy (JASCO V-630 spectrophotometer), considering VC absorbance at 250 nm. Diblock copolymer **6b-VC** functionalization could not be determined by ^{1}H-NMR analysis due to the overlap of the PLO Cα and the VC l,t peaks, which hindered the selection of a reference peak. The %mol was back-calculated from the %wt.

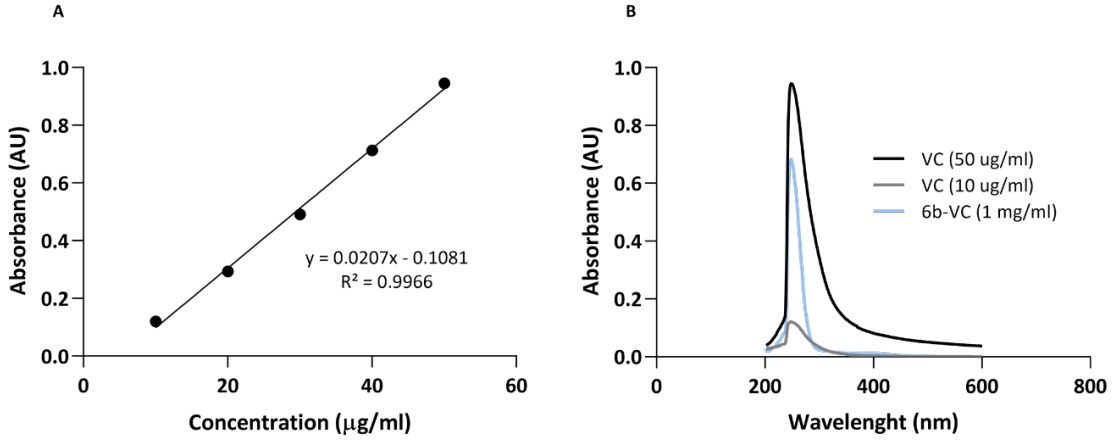
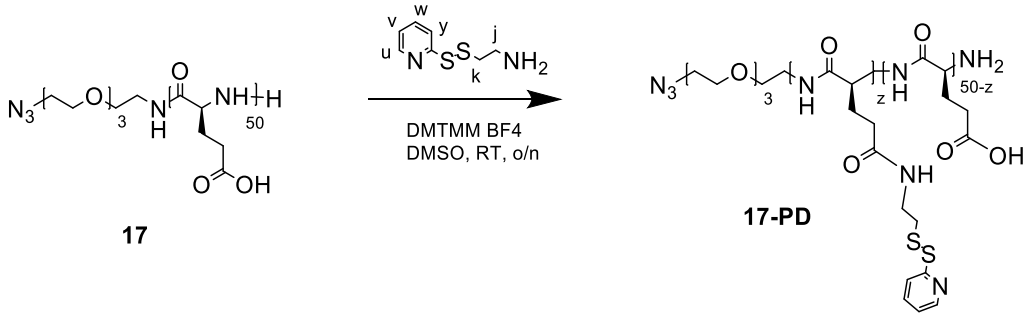


Figure S55. A) Calibration curve of VC (DMF:H_2O 9:1) for quantification. **(B)** Absorption spectra of VC (max and minimum concentration of the calibration curve) and diblock copolymer **6b-VC**. % wt VC = 3.8 (back calculated %mol = 2.8).

Polymer 17-PD



Scheme S7. Synthetic procedure for the preparation of polymer **17-PD**

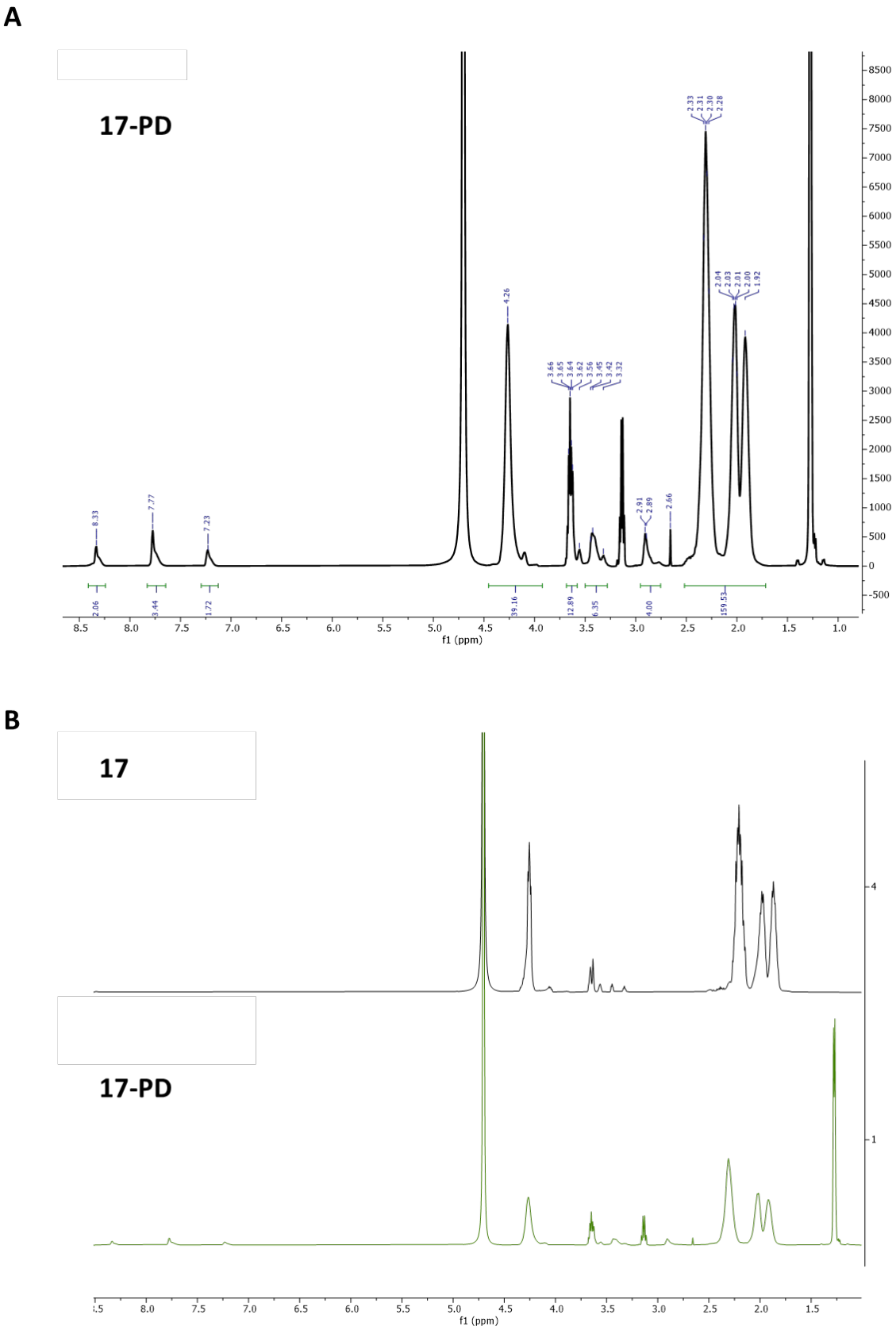


Figure S56. A) NMR spectra of polymer **17-PD** in D_2O (10 mg/ml). **B)** Comparison of stacked NMR spectra of polymers **17** and **17-PD**.

^{1}H NMR (500 MHz, D2O, 25 °C) δ 8.40 (d, 1H, u), 7.80 (m, 2H, v,x), 7.25 (d, 1H, y), 4.40 – 4.20 (m, 1H, Cα of PGA), 3.80 – 3.30 (m, 12H, N3(CH2CH2)$_3$O; 4H OCH2CH2NH), 3.17 -2.66 (m, 4H, k,j) 2.51 – 1.66 (m, 4H Cβ+γ of PGA).

In a two-neck bottom flask, polymer **17** (N_3-PEG_3-PGA_{50}, Curapath) was dissolved in anhydrous DMSO (1 eq., 10 mg/mL), while the carboxylic group was activated with DMTMM BF4 (i.e., 0.1 eq. for 5% mol PD-NH_2 modification) dissolved in 0.5 mL anhydrous DMSO. The activation was allowed to proceed for 20 min. (S)-2-Pyridylthio cysteamine hydrochloride (PD-NH2, i.e., 0.05 eq for 5% mol modification) solution was added to the diblock copolymer solution. The pH was adjusted with 1M sodium bicarbonate solution (pH 8). The reaction was left to proceed for 48 h. The product was precipitated in cold diethyl ether while stirring, then incubated at -20° for 1 h, centrifuged, and the pellet lyophilized overnight. To convert the product to its salt form, 1M sodium bicarbonate solution was added dropwise while mixing at RT until pH 7/8 and the total dissolution was reached. The product was then purified by Vivaspin®, 3000 MWCO Da.
Yield: 60%. Conjugation efficiency: 90%.

PD functionalization was calculated by ^{1}H-NMR analysis (mol %) and ultraviolet/visible spectroscopy (% wt) after preparation of the calibration curve for free PD-NH_2 and matrix effect adjustment (defined as the naked diblock copolymer's influence on conjugate absorbance. Measurements were performed by ultraviolet/visible spectroscopy (JASCO V-630 spectrophotometer), considering PD-NH_2 absorbance at 280 nm.

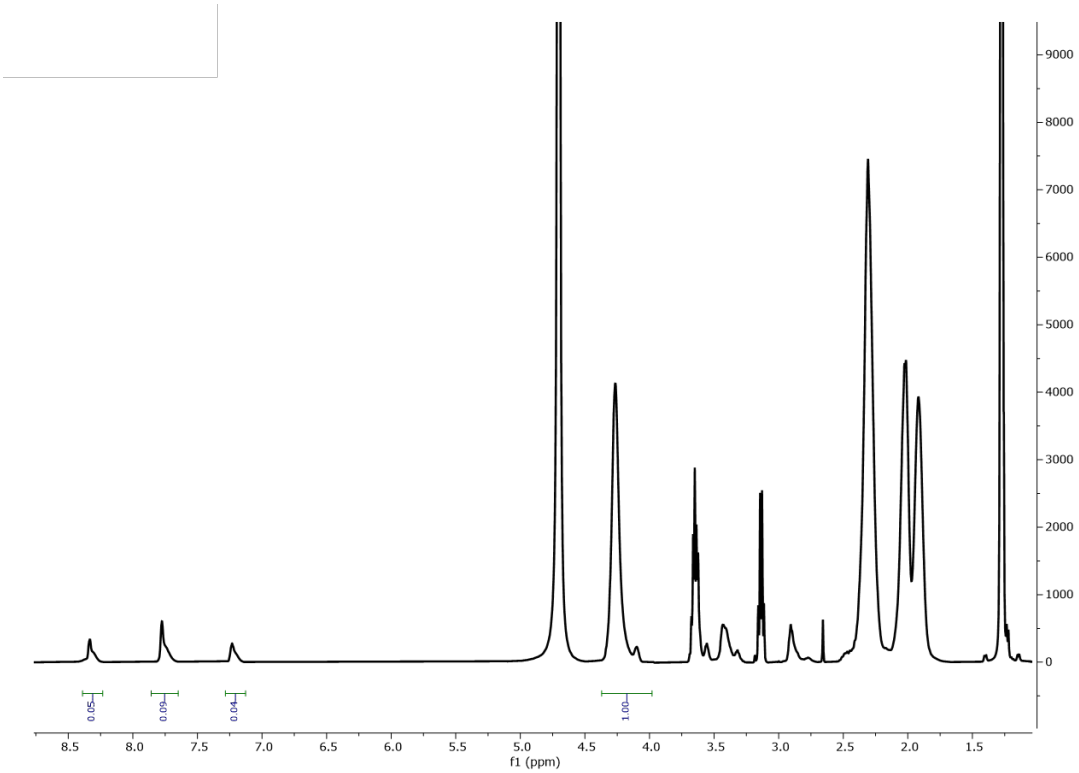


Figure S57. A) NMR spectra of polymer **17-PD** in D_2O (10 mg/ml) used to calculate the %mol of PD-NH_2 (%mol PD-NH2 = 4.5)

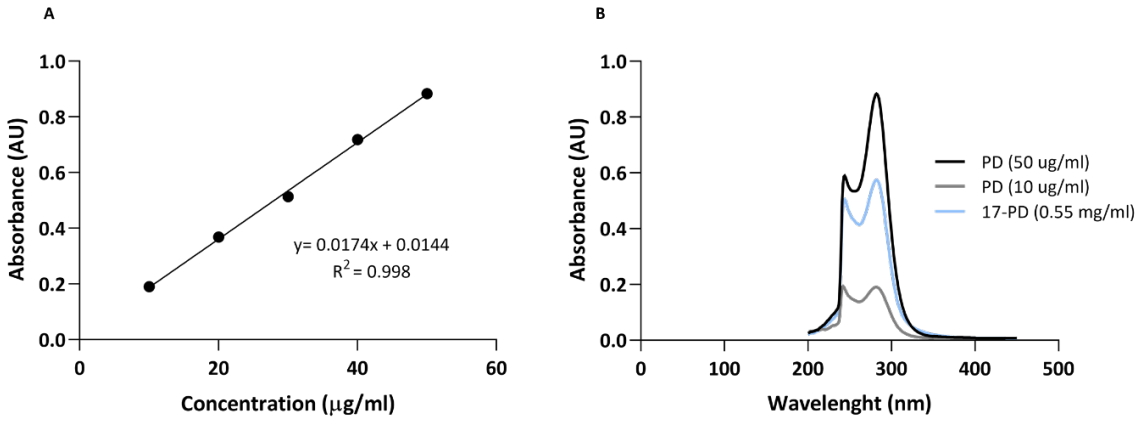


Figure S58. A) Calibration curve of PD (DMF:H_2O 9:1) for quantification. **(B)** Absorption spectra of PD (max and minimum concentration of the calibration curve) and polymer **17-PD**. % wt PD = 5.8.

Nanoconjugate 16

In a one-neck bottom flask, polymer **17-PD** was dissolved in Milli-Q water (1 eq., 10 mg/ml). In a glass vial, copolymer **6b-VC** (i.e., 0.02 eq. for 2% mol **6b-VC** modification) was dissolved in 0.5 mL Milli-Q water and added to the **17-PD** solution, followed by the reducing agent tris(2-carboxyethyl)phosphine (TCEP; 0.0025 eq. for 2% mol **6b-VC** modification). The reaction was left to proceed for 48 h, and the product was purified using PD-10 desalting columns packed with Sephadex G-25 resin.

Yield: 50 %. Conjugation efficiency: 80-90%

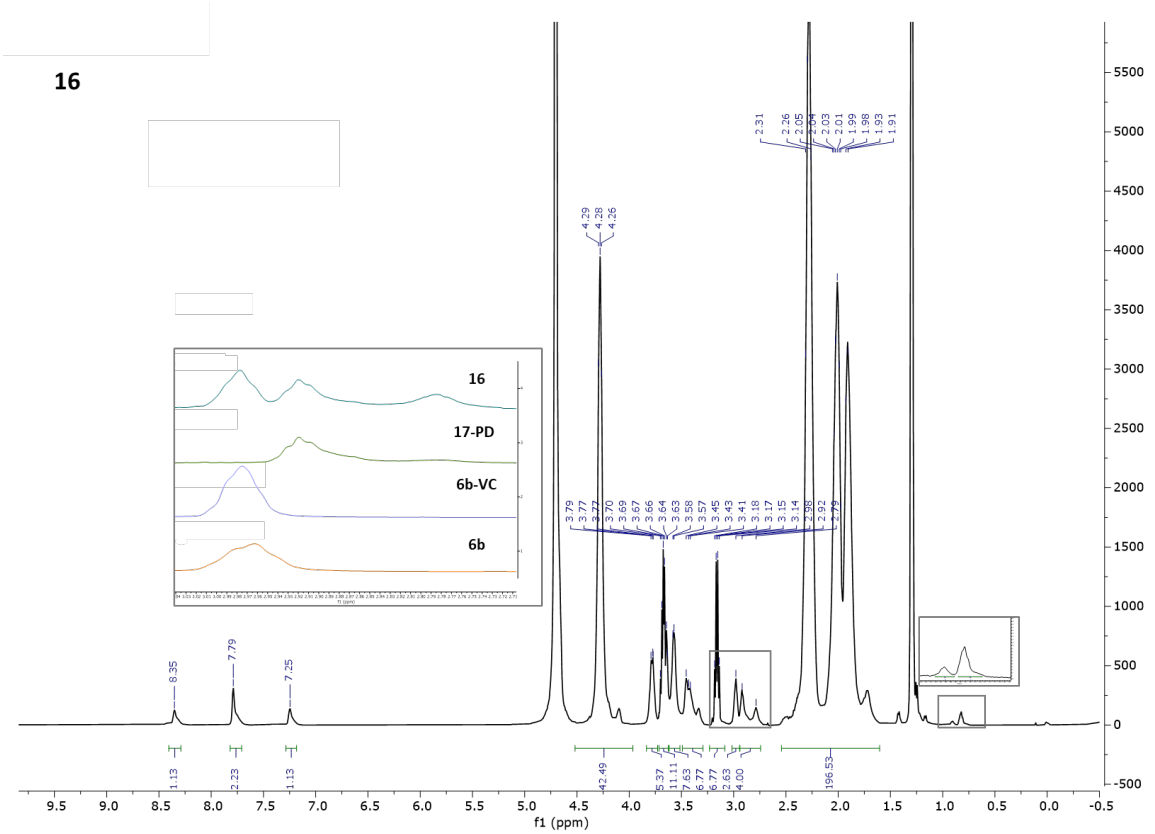


Figure S59. NMR spectra of Nanoconjugate **16** in D_2O (10 mg/ml)

^{1}H NMR (500 MHz, D2O, 25 °C) δ 8.40 (d, 1H, u), 7.80 (m, 2H, v,x), 7.25 (d, 1H, y), 4.77 – 4.71 (m, 1H, Cα of PLP; 1H g covered with D2O), 4.40 – 4.20 (m, 1H, Cα of PGA, 1H, Cα of PLO; 1H l; 2H t), 3.83 – 3.30 (12H, N3(CH2CH2)$_3$O, 4H OCH2CH2NH, 2H, Cδ of PLP; CH2 of CH3CH2CH2CH2NH and 2H b), 3.20 -2.66 (2H, Cδ of PLO, 2H o and 4H, k,j) 2.51 – 1.66 (4H Cβ+γ of PGA, 4H CH2CH2CH3, 4H Cβ+γ of PLP; 4H Cβ+γ of PLO; 13H c,d,e,f,h,m,n), 0.9 (s, 6H, i) 0.82 (t, J = 7.3 Hz, 3H, CH2CH2CH3).

Diblock copolymer **6b-VC** functionalization could not be determined by ^{1}H-NMR analysis due to the overlapping of PGA, PLO, and VC alpha-carbons, which hindered the selection of a reference peak. Instead, the functionalization of diblock copolymer **6b-VC** was back-calculated from the difference between the % wt of PD-NH_2 in polymer **17-PD** and the % wt of PD-NH_2 in diblock copolymer **16** (PD-NH2 abs at 280nm), obtained by ultraviolet/visible spectroscopy.

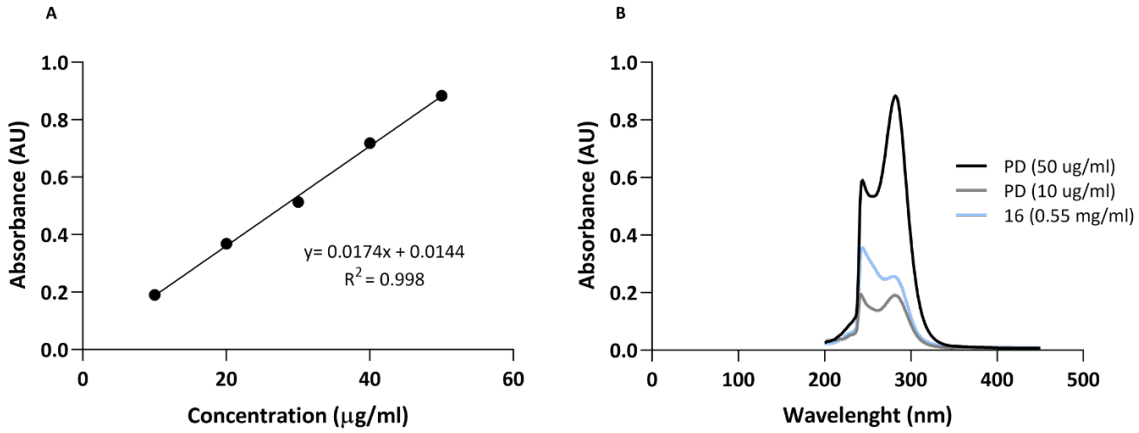


Figure S60. A) Calibration curve of PD (DMF:H_2O 9:1) for quantification. **(B)** Absorption spectra of PD (max and minimum concentration of the calibration curve) and nanoconjugate **16**. % wt PD = 2.5 (% wt **6b-VC** back calculated = 3.3).

MTS Assay for Cell Viability in MDA-MB-231 cells and BJ Fibroblasts using 16

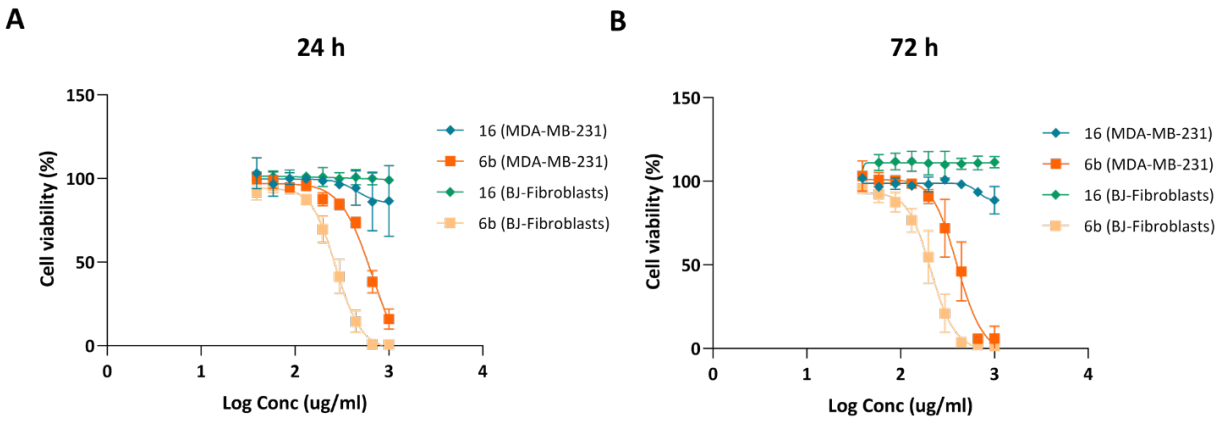
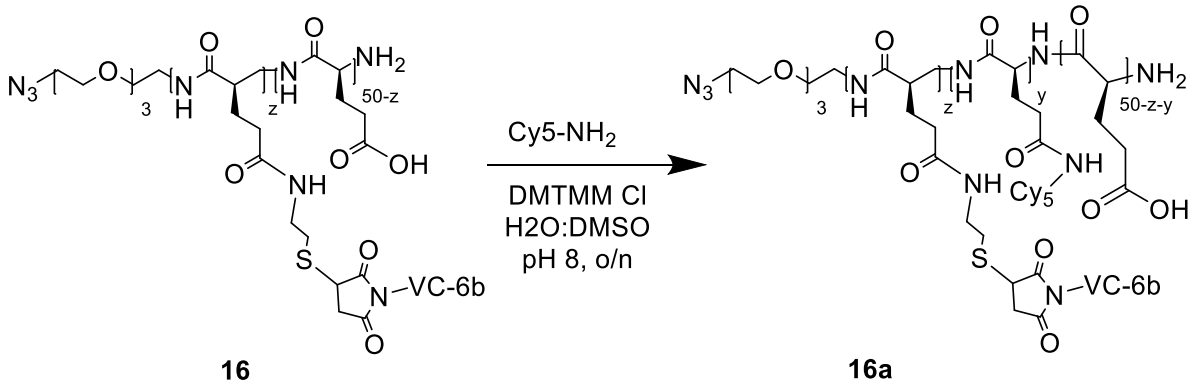


Figure S61. Cell viability by MTS assay after exposure to **16** (compared to 6b) in different cell lines after A) 24 h and B) 72 h. 24 h: MDA-MB 231 cells and BJ fibroblasts (IC50 > 1 mg/ml) (24 h, n = 3, mean ± SEM). 72 h: MDA-MB 231 cells and BJ fibroblasts (IC50 > 1 mg/ml) (72 h, n = 3, mean ± SEM).

Fluorescence labeling of diblock copolymer-conjugate 16 with Cy5



Scheme S8. Labeling of nanoconjugate **16** with Cy5-NH_2

In a one-neck bottom flask, **16** was dissolved in Milli-Q water (1 eq., 10 mg/mL), and the carboxylic group activated with DMTMM BF4 (0.03 eq. for 1.5% mol Cy5-NH_2) dissolved in 0.5 mL Milli-Q water. In a glass vial protected by light, Cy5-NH_2 was dissolved in DMSO and added to the diblock copolymer-conjugate solution (0.015 eq, 1.5% mol). The pH was adjusted with 1M sodium bicarbonate (pH 8). The reaction was allowed to proceed overnight, protected from the light, and evaluated by thin-layer chromatography (using MeOH as the mobile phase). After DMSO elimination using a rotavapor and freeze-drying, the product was purified by PD-10 desalting columns packed with Sephadex G-25 resin. Dye loading was calculated by fluorescence using the CLARIOstar fluorescent plate reader.
The corresponding free dye (DMF:H2O) calibration curve was prepared in dark 96-Well multiwell plates. Fluorescence was measured at λ_{ex}: 632 nm λ_{em}: 684 nm for Cy5-NH_2. Yields: 80%. Conjugation efficiency 60-100%.

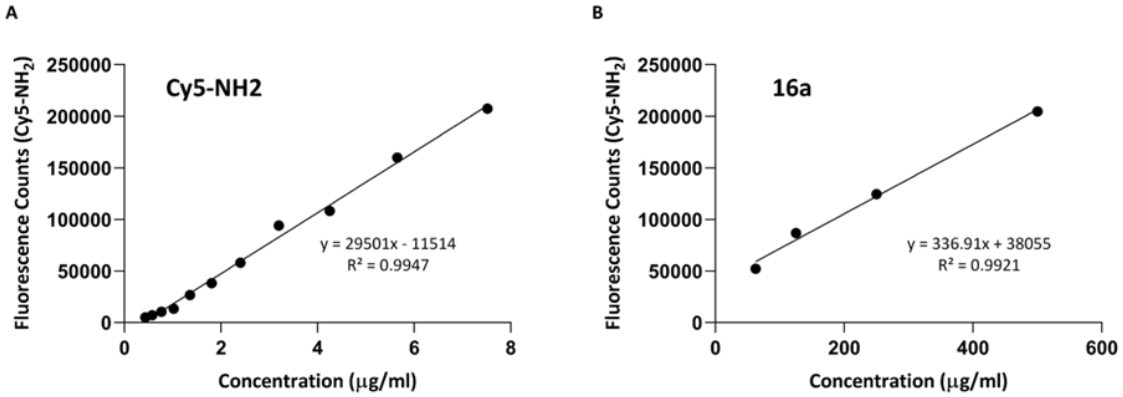


Figure S62. Fluorescence calibration curves of (**A**) Cy5-NH_2 and (**B**) nanoconjugate **16a** in DMF:H_2O for quantifications. % wt **16a** = 1.8 (back calculated %mol = 1.5)

Cellular Uptake Studies by Live-Cell Imaging of Cy5-Labeled Diblock Copolymer Conjugate 16

Table S8. Evaluation of cell uptake through Pearson coefficient (r) analysis

Pearson coefficient					
30 min	**1 h**	**2 h**	**4 h**	**6 h**	**24 h**
0.53	0.62	0.59	0.62	0.40	0.16

Physical Studies in Cardiolipin-containing Small Unilamellar Vesicles and Supported Lipid Bilayers

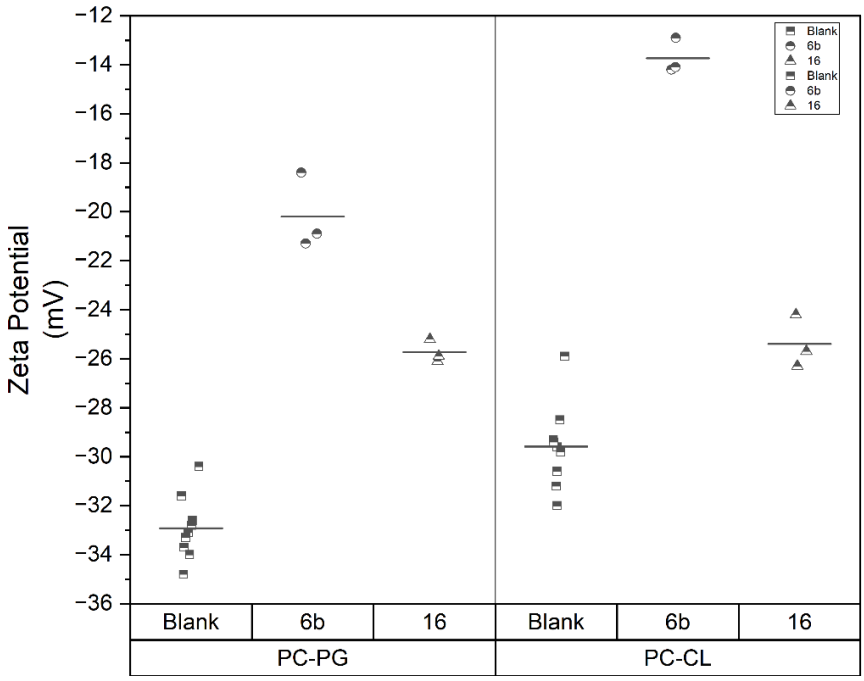


Figure S63. Zeta potential of POPC:POPG 1:1 and POPC:CL 2:1 small unilamellar vesicles after incubation with 5 μM **16** and **6b**

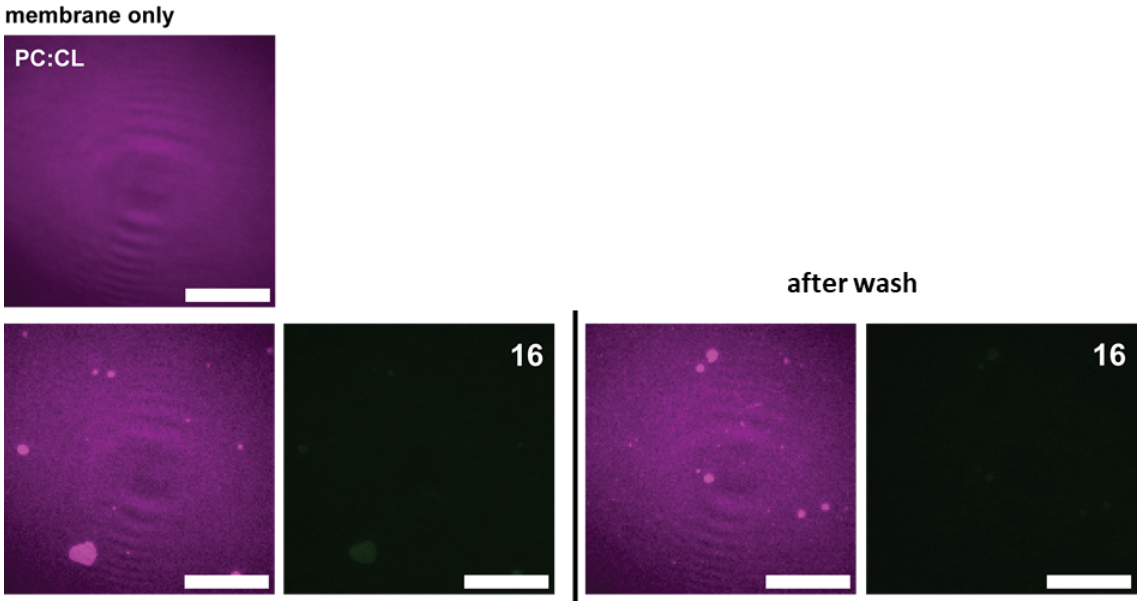


Figure S64. Total internal reflection fluorescence microscopy images of supported lipid bilayers (SLBs, POPC, and cardiolipin 1:1 labeled with 0.05 mol% Atto655-DOPE (magenta)) incubated with 5 µM **16**. Magenta depicts the membrane channel, and green depicts the diblock copolymer channel. For a visual comparison, the contrast is set the same in all images. The left set of panels shows the supported lipid bilayers after adding 5 µM of respective diblock copolymer without washing. The right set of panels shows supported lipid bilayers after washing with 10x the sample volume. Scale bars: 20 µm.

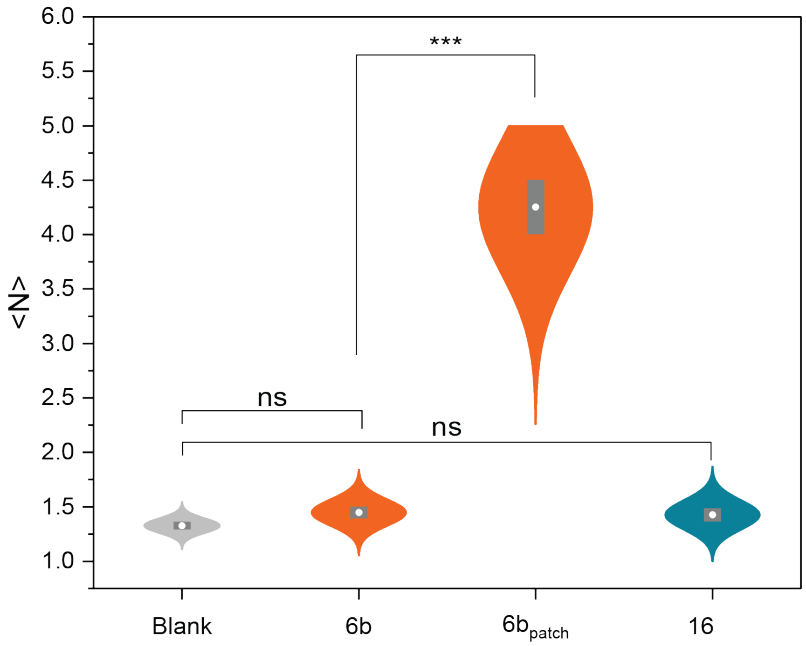


Figure S65. Average number of A655-DOPE particles (<N> A655-DOPE, number of membrane particles) for cardiolipin-rich membranes incubated with diblock copolymers at patch-containing (**6b**$_{patch}$ and **6h**$_{patch}$) and patch-lacking (**6b** and **6h** and **16**) regions acquired through fluorescence correlation spectroscopy. Data analyzed using two-way ANOVA. Significance reported following American Psychological Association (APA) guidelines (*P ≤ 0.05, **P ≤ 0.01, ***P ≤ 0.001, ns = not significant).

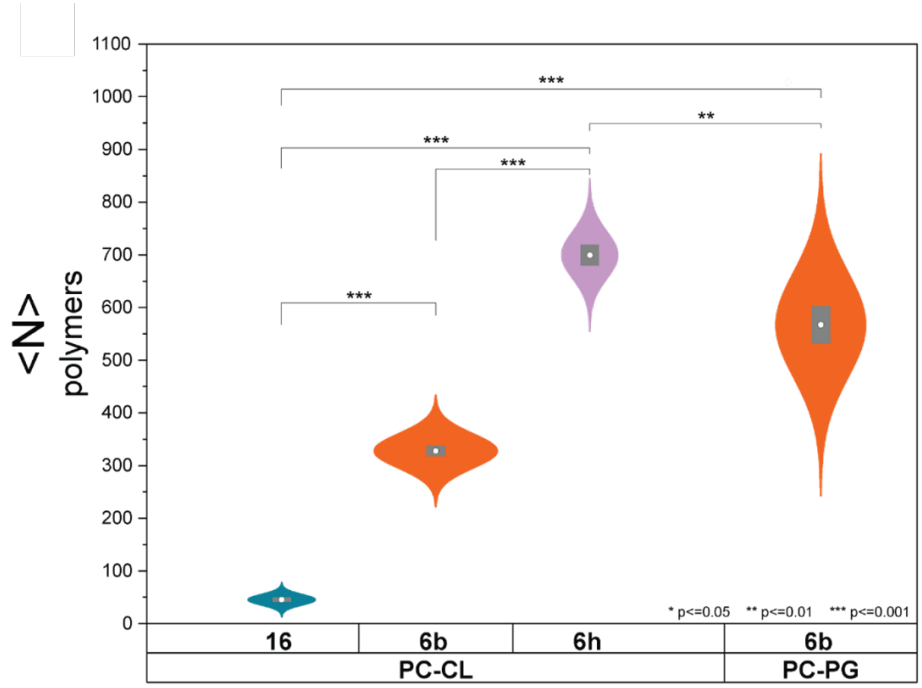


Figure S66. The average number of diblock copolymer particles (<N> polymer) bound to cardiolipin-rich membranes acquired through fluorescence correlation spectroscopy of labeled diblock copolymers **6b** and **6h** and nanoconjugate **16.** Data analyzed using two-way ANOVA. Significance reported as **P ≤ 0.01, ***P ≤ 0.001).

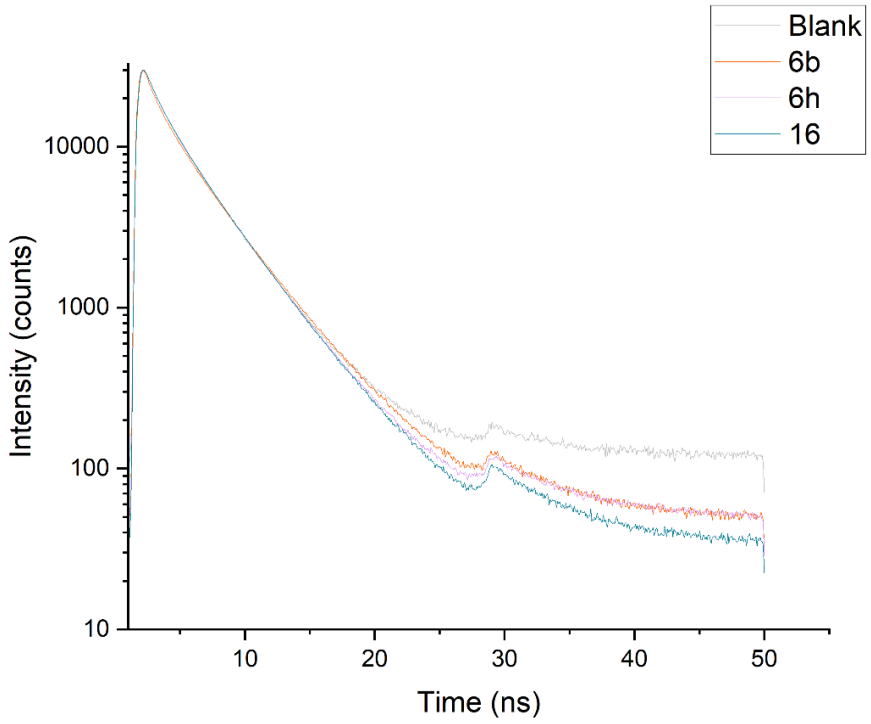


Figure S67. Representative curves for the time-correlated single photon counting (TCSPC) histograms for the membrane tension/order measurement with the Flipper-TR dye

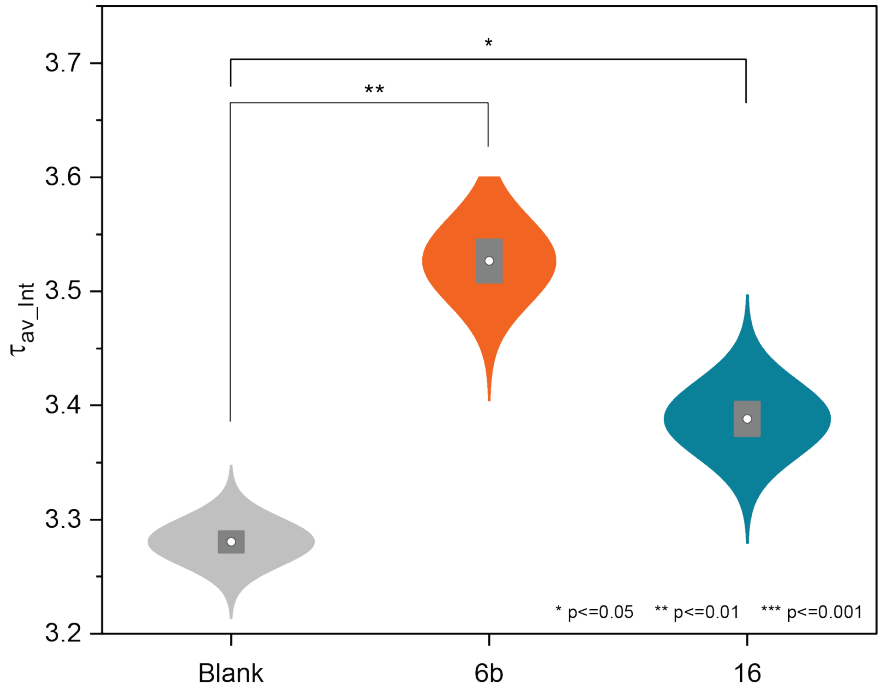


Figure S68. The intensity-averaged fluorescence lifetime of Flipper-TR-stained small unilamellar vesicles (τ_{av_Int}) incubated with diblock copolymers **6b** and **6h** and nanoconjugate **16.** Data analyzed using two-way ANOVA. Significance reported as *p ≤ 0.05, **p ≤ 0.01, ***p ≤ 0.001 (ns = not significant).

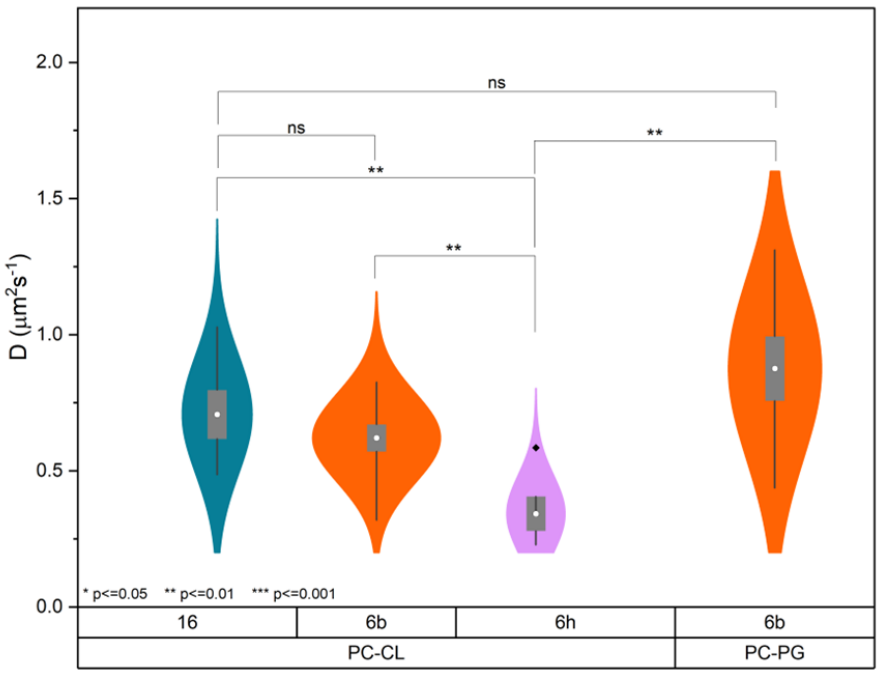


Figure S69. Diffusion coefficient of the diblock copolymers **6b** and **6h** and nanoconjugate **16** on respective membranes (SLBs, POPC, and cardiolipin 1:1 labeled with 0.05 mol% Atto655-DOPE and equimolar POPC-POPG). Data analyzed using two-way ANOVA. Significance reported as **p ≤ 0.01 (ns = not significant).

References

[1] G. Ashiotis, A. Deschildre, Z. Nawaz, J. P. Wright, D. Karkoulis, F. E. Picca, J. Kieffer, *J. Appl. Crystallogr.* **2015**, *48*, 510.

[2] B. Hammouda, *J. Appl. Crystallogr.* **2010**, *43*, 716.

[3] H.-I. C. Quintero-Marquina G, Segovia G, Oestreicher V, Lamas D, *ChemRxiv.* **2024**

[4] B. Hammouda, *Macromol. Theory Simulations* **2012**, *21*, 372.

[5] M. Gkikas, R. K. Avery, B. D. Olsen, *Biomacromolecules* **2016**, *17*, 399.

[6] P. Dimitrijevs, P. Arsenyan, *Sensors Actuators B Chem.* **2021**, *346*, 130537.

[7] E. Gnaiger, *5th ed. Bioenerg Commun **2020**.2.*

6.3 Annex 3: Supplementary Material of Manuscript III

Reference scientific article II[345]: Pegoraro, C.; Guinart, A.; Masiá Sanchis, E.; Doellerer, D.; Stuart, M. C. A.; Conejos-Sánchez, I.; Feringa, B. L.; Vicent, M. J. A Light-Driven Molecular Motor-Polypeptide Conjugate Supports Controlled Cell Uptake. *J. Mater. Chem. B* **2025**. DOI: 10.1039/D4TB02434F.

Supplementary Information (SI) for Journal of Materials Chemistry B.
This journal is © The Royal Society of Chemistry 2024

Supporting Information

A Light-driven Molecular Motor-Polypeptide Conjugate Supports Controlled Cell Uptake

Camilla Pegoraro[1,#], Ainoa Guinart[2,#], Esther Masiá Sanchis[1,3,4], Daniel Doellerer[2], Marc C. A. Stuart[2]

Inmaculada Conejos-Sánchez[1,3], Ben L. Feringa[2*], and María J. Vicent[1,3,4*]*

[1]Príncipe Felipe Research Center, Polymer Therapeutics Lab., 46012 Valencia, Spain

[2]Stratingh Institute for Chemistry, University of Groningen, Groningen 9747 AG, The Netherlands

[3]Centro de Investigación Biomédica en Red en Cáncer (CIBERONC), Instituto de Salud Carlos III, Spain

[4]Príncipe Felipe Research Center, Screening Platform., 46012 Valencia, Spain

*Co-corresponding Authors E-mail: iconejos@cipf.es, b.l.feringa@rug.nl, mjvicent@cipf.es

[#]Authors with equal contributions

1. Materials

All reactions involving oxygen-sensitive reagents were performed under a nitrogen atmosphere. Reagents purchased from Sigma-Aldrich, Acros Organics, or TCI Europe were used as received. Reagent-grade solvents were used without prior water removal unless otherwise indicated. Maleimidocaproyl-L-valine-L-citrulline-p-aminobenzyl alcohol p-nitrophenyl carbonate (VC linker) was purchased from MedChemExpress, pyridylthio-cysteamine hydrochloride (PD-NH2) from ABCR, and triethylamine and tris(2-carboxyethyl)phosphine from Thermo Fisher. N_3-PEG_3-PGA_{50} was kindly provided by Curapath. Diblock copolymer polyornithine-polyproline (PLO_6-PLP_{22}, **PP**) was synthesized as previously reported[14,15]. Anhydrous solvents were obtained using either an MBraun SPS-800 solvent purification system or from Acros Organics. Solvents were degassed by purging with nitrogen for at least 30 min/three freeze-pump-thaw cycles. Flash column chromatography used silica gels (Merck, type 9385, 230 to 400 mesh) or a Büchi Reveleris purification system using silica cartridges. Thin-layer chromatography used aluminum sheets coated with silica gel 60F254 (Merck). Compounds were visualized with a UV lamp and/or by staining with $KMnO_4$, cerium ammonium molybdate, or vanillin. ^1H and ^{13}C NMR spectra were recorded on a Varian Mercury Plus 400 or a Bruker AVANCE 600 NMR spectrometer at 298 K unless otherwise indicated. Photostationary state (PSS) studies were performed on a Varian Unity Plus 500 NMR spectrometer. Chemical shifts are shown as parts per million relative to the residual solvent signal ($CDCl_3$ = δ 7.26 for ^1H, δ 77.2 for ^{13}C; CD_2Cl_2 = δ 5.32 for ^1H, δ 53.8 for ^{13}C). Multiplets in ^1H NMR spectra are designated as s (singlet), d (doublet), t (triplet), q (quartet), p (pentet), m (multiplet), or br (broad). High-resolution mass spectrometry used an LTQ Orbitrap XL spectrometer.

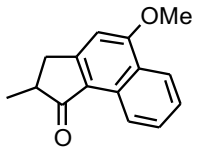
Vivaspin® 2000 and 3000 Da molecular weight cut-off (MWCO) and PD-10 desalting columns packed with Sephadex G-25 resin were purchased from Sartorius and Cytiva. VC and PD-NH_2 content were quantified by UV-vis (JASCO V-630 spectrophotometer). ^1H NMR spectra were acquired at 27°C (300K) on a 500 MHz Bruker NMR spectrometer. Cyanine5 amine (Cy5) was purchased from Lumiprobe.

Further details on N_3-PEG_3-PGA_{50}-VC-PP (**P**) physicochemical and biological characterization can be found in [14,15].

2. Preparation and characterization of the molecular motor

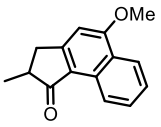
2.1. Synthetic procedure for preparing the upper half of MM

5-methoxy-2-methyl-2,3-dihydro-1H-cyclopenta[a]naphthalen-1-one (**S1**)

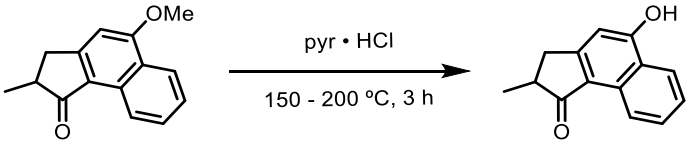


S1

Ketone **S1** was synthesized according to a previously described procedure[16].



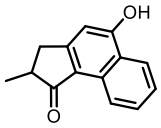
^{1}H NMR (600 MHz, $CDCl_3$) δ 9.13 (d, J = 8.3 Hz, 1H), 8.25 (d, J = 8.4 Hz, 1H), 7.70 – 7.63 (m, 1H), 7.52 (t, J = 7.7 Hz, 1H), 6.77 (s, 1H), 4.08 (s, 3H), 3.47 – 3.37 (m, 1H), 2.82 – 2.72 (m, 2H), 1.36 (d, J = 7.3 Hz, 3H). **^{13}C NMR** (151 MHz, $CDCl_3$) δ 211.0, 164.3, 161.8, 133.3, 131.9, 128.6, 127.8, 126.5, 126.1, 125.1, 104.1, 80.0, 79.7, 79.3, 58.6, 44.8, 38.5, 19.6.



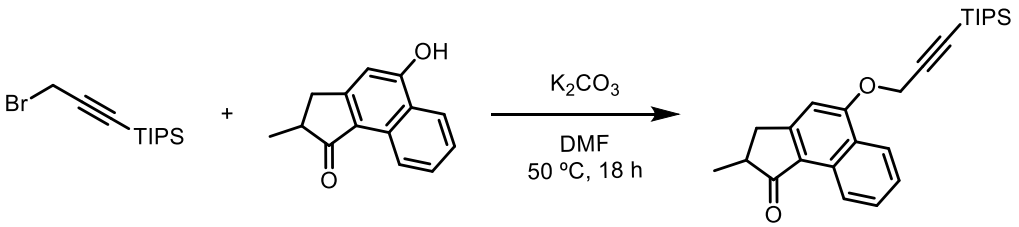
S1 **S2**

5-hydroxy-2-methyl-2,3-dihydro-1H-cyclopenta[a]naphthalen-1-one (**S2**).

Pyridine hydrochloride (14.700 g, 0.127 mol, 30.0 eq) was melted in a vial at 150°C before addition to an oven-dried vial charged with **S1** (0.963 g, 0.004 mol, 1.0 eq). The mixture was heated to 200°C for 3 h and then cooled to room temperature. The solid was partitioned between water and EtOAc. The organic layer was washed with aq. 0.5 M HCl, water, and brine before drying over $MgSO_4$, followed by undergoing filtration and finally the samples concentrated. The residue was purified by flash column chromatography to produce a light orange solid (0.765 g, 0.004 mol, 85%). NMR data in accordance with those in previous reports[17].



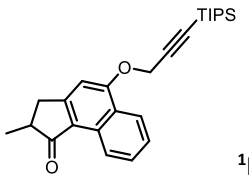
^{1}H NMR (400 MHz, DMSO-d6) δ 11.41 (s, 1H), 8.96 (d, J = 8.3 Hz, 1H), 8.20 (d, J = 8.4 Hz, 1H), 7.67 (t, J = 7.5 Hz, 1H), 7.53 (t, J = 7.7 Hz, 1H), 6.92 (s, 1H), 3.37 (dd, J = 18.4, 8.3 Hz, 1H), 2.80 – 2.61 (m, 2H), 1.21 (d, J = 7.2 Hz, 3H). **^{13}C NMR** (101 MHz, DMSO-d6) δ 207.0, 160.4, 159.8, 130.5, 129.1, 125.4, 124.1, 122.9, 122.8, 121.1, 105.6, 41.4, 34.9, 16.6.



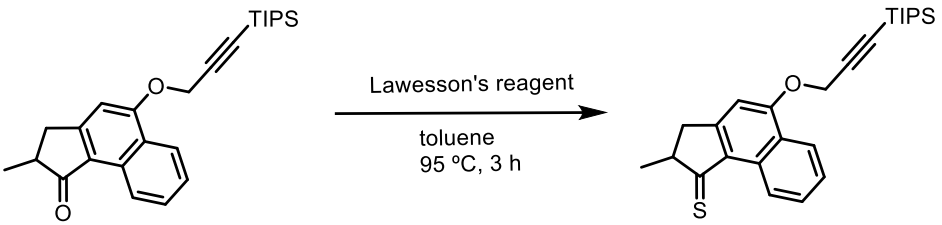
S3 **S2** **S4**

2-methyl-5-((3-(triisopropylsilyl)prop-2-yn-1-yl)oxy)-2,3-dihydro-1H-cyclopenta[a]naphthalen-1-one (**S5**).

An oven-dried vial was charged with **S2** (0.544 g, 2.563 mmol, 1.0 eq.) and K_2CO_3 (1.416 g, 10.249 mmol, 4.0 eq.). Dimethylformamide (DMF) (30 mL, 0.085 M) was then added, followed by 3-bromoprop-1-yn-1-yl)triisopropylsilane (**S3**) addition (0.919 g, 3.154 mmol, 1.2 eq.). **S3** was synthesized following a previously described procedure[17]. The resulting mixture was heated to 50°C for 18 h and then cooled to room temperature, and water and dichloromethane (DCM) were added. The mixture was extracted with DCM, and the combined organic layers were dried over Na_2SO_4 and concentrated in vacuo. Flash column chromatography (SiO_2, dry load on celite, 5% EtOAc in pentane) gave **S4** (0.763 g, 1.805 mmol, 70%) as a light-yellow oil.



^{1}H NMR (400 MHz, $CDCl_3$) δ 9.13 (d, J = 8.4 Hz, 1H), 8.27 (d, J = 8.4 Hz, 1H), 7.67 (t, J = 8.3 Hz, 1H), 7.58 – 7.50 (m, 1H), 7.03 (s, 1H), 5.02 (s, 2H), 3.46 – 3.36 (m, 1H), 2.81 – 2.72 (m, 2H), 1.36 (d, J = 7.3 Hz, 3H), 1.04 (s, 22H). **^{13}C NMR** (151 MHz, $CDCl_3$) δ 208.6, 159.6, 158.8, 130.8, 129.4, 126.1, 125.4, 124.0, 124.0, 122.7, 103.7, 100.9, 90.9, 57.4, 42.4, 36.0, 18.6, 17.1, 11.2. **HRMS** (ESI pos) m/z calcd for $C_{26}H_{35}O_2Si$ $[M+H]^+$ 407.24008, found 407.24036.

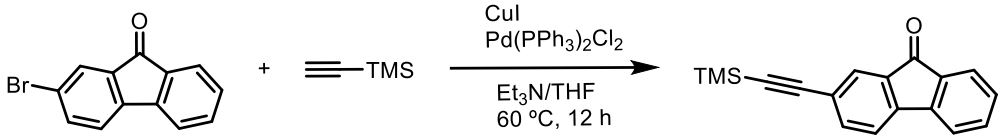


S4 **S5**

2-methyl-5-((3-(triisopropylsilyl)prop-2-yn-1-yl)oxy)-2,3-dihydro-1H-cyclopenta[a]naphthalene-1-thione (**S5**).

A mixture of **S4** (0.793 g, 0.002 mol, 1.0 eq.) and Lawesson's reagent (0.485 g, 1.200 mmol, 6.0 eq.) in anhydrous toluene (41 mL, 0.06 M) was heated at 95°C. After 6 h, toluene was removed in vacuo, and the resulting thioketone intermediate **S5** was purified by flash column chromatography (SiO_2, 10% DCM in pentane) and used without further isolation.

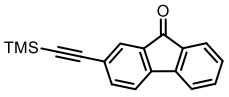
2.2. Synthetic procedure for preparing the bottom half of the MM



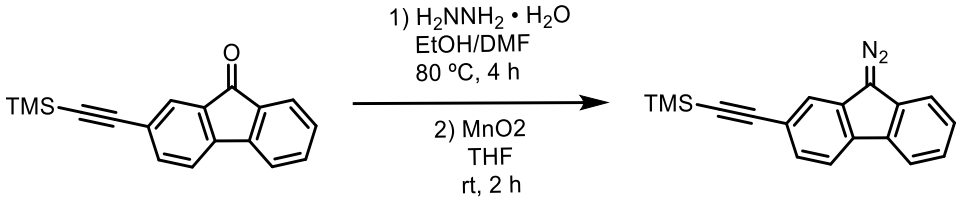
S6 **S7**

2-((trimethylsilyl)ethynyl)-9H-fluoren-9-one (**S7**).

The corresponding aryl halide **S6** (2-bromo-9H-fluoren-9-one, 0.500 g, 1.930 mmol, 1.0 eq.) was obtained commercially and loaded into a glass vial together with CuI (0.018 g, 0.096 mmol, 0.05 eq.) and $Pd(PPh_3)_2Cl_2$ (0.067 g, 0.096 mmol, 0.05 eq.). Tetramethylsilane (TMS, 0.284 g, 2.895 mmol, 1.5 eq.) was mixed with tetrahydrofuran (THF, 16 mL, 0.12 M) and triethylamine (Et_3N, 3 mL, 0.64 M) in another vial and degassed by nitrogen bubbling for 15 min. After degassing, the resulting mixture was added to the solids and the mixture stirred at 60°C overnight. After 12 h, the product solution was cooled to room temperature, filtered over a silica plug, which was flushed with DCM. The remaining solvent was evaporated, and the residue was purified by flash column chromatography to yield **S7** as an off-white solid (0.498 g, 1.802 mmol, 93%).



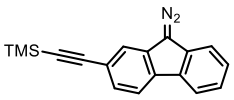
^{1}H NMR (400 MHz, $CDCl_3$) δ 7.62 (s, 1H), 7.54 (d, J = 7.3 Hz, 1H), 7.48 (d, J = 7.7 Hz, 1H), 7.41 – 7.34 (m, 2H), 7.31 (d, J = 7.7 Hz, 1H), 7.20 (t, J = 7.9 Hz, 1H), 0.25 (s, 9H). **^{13}C NMR** (151 MHz, $CDCl_3$) δ 192.9, 143.8, 137.9, 134.8, 134.3, 134.0, 129.3, 127.7, 124.4, 124.0, 120.6, 120.1, 104.0, 96.2, -0.0. **HRMS** (ESI pos) m/z calcd for $C_{18}H_{16}OSi$ $[M+H]^+$ 277.10000, found 277.18349.



S7 **S8**

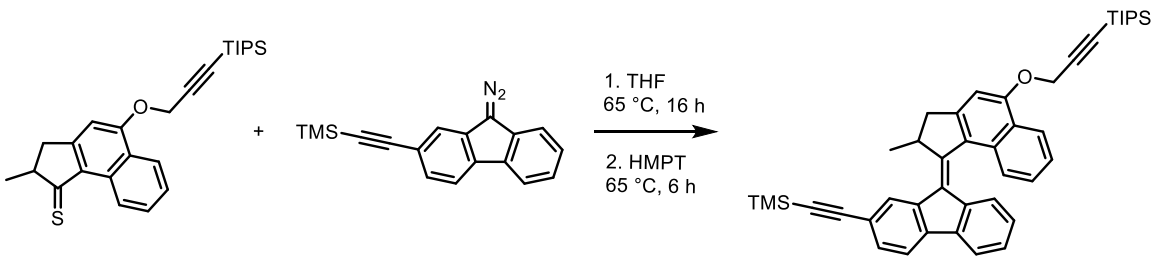
((9-diazo-9H-fluoren-2-yl)ethynyl)trimethylsilane (**S8**).

Hydrazine monohydrate (50-60% in H_2O, 1.6 mL, 32.411 mmol, 18.0 eq.) was added to a mixture of **S7** (0.500 g, 1.809 mmol, 1.0 eq) and EtOH (21 mL, 0.086 M) and the resulting suspension was heated at 80°C. After 4 h, the mixture was allowed to cool to room temperature, and H_2O was added. A precipitate appeared almost immediately and was placed in the freezer at -18°C to crystallize overnight. The resultant solid was collected the following day, yielding a pale-yellow solid being the corresponding hydrazone (0.393 g, 1.353 mmol, 75%). The crude hydrazone was dissolved in anhydrous THF (22.4 mL, 0.06 M), and MnO_2 (2.712 g, 31.200 mmol, 23.0 eq.) was added. The resultant black solution was stirred at room temperature for 2 h and filtered over a celite plug. The product solution was concentrated in vacuo to yield a yellow solid (0.210 g, 0.728 mmol, 54%), which was used immediately in the next step.



^{1}H NMR (400 MHz, $CDCl_3$) δ 10.22 – 10.14 (m, 1H), 8.33 (dd, J = 8.4, 1.4 Hz, 1H), 7.74 (ddd, J = 8.5, 6.9, 1.4 Hz, 1H), 7.56 (ddd, J = 8.3, 6.9, 1.3 Hz, 1H), 7.18 (d, J = 2.8 Hz, 1H), 7.08 (s, 1H), 7.02 – 6.90 (m, 1H), 1.05 (s, 9H).

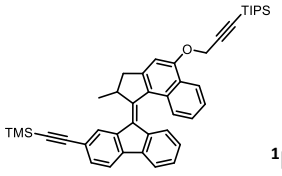
2.3. Synthetic procedure for preparing the final MM



S5 **S8** **S9**

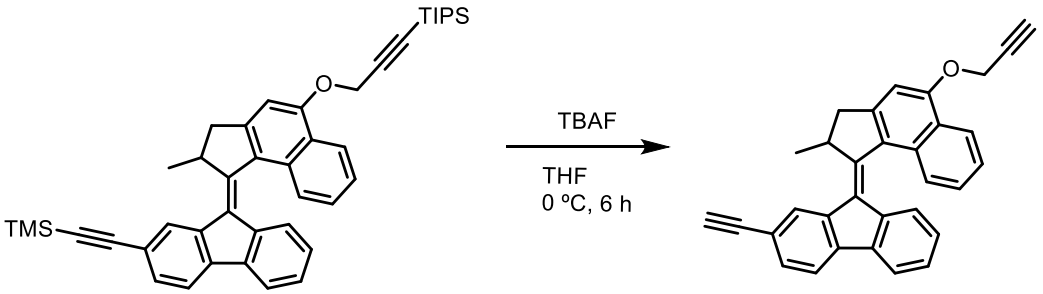
(E)-Triisopropyl(3-((2-methyl-1-(2-((trimethylsilyl)ethynyl)-9H-fluoren-9-ylidene)-2,3-dihydro-1H-cyclopenta[a]naphthalen-5-yl)oxy)prop-1-yn-1-yl)silane (**S9**).

An oven-dried vial was charged with **S6** (830 mg, 1.964 mmol, 1.1 eq.) and **S7** (510 mg, 1.768 mmol, 1.0 eq.), and oxygen was removed. THF (15 mL) was added, and the mixture was stirred overnight at 65°C. After 16 h, hexamethylphosphoramide (HMPT, 1.8 mL) was added, and the mixture was stirred for another 6 h at 65°C. The resulting crude product was concentrated in vacuo. Flash column chromatography (SiO_2, dry load on celite, 1% DCM in pentane) provided **S9** as a yellow solid (226 mg, 0.347 mmol, 20%). The product was isolated as a mixture of the two isomers, *E* could be isolated as a small amount (> 2 mg) using high-performance liquid chromatography (HPLC) (0-0.5% DCM in heptane); however, due to the technical difficulties involved in the separation process, the procedure was continued with a racemic mixture of the compound.



^{1}H NMR (400 MHz, $CDCl_3$) δ 8.34 (d, J = 8.7 Hz, 1H), 7.98 (d, J = 7.9 Hz, 1H), 7.86 (d, J = 7.4 Hz, 1H), 7.72 (d, J = 7.7 Hz, 1H), 7.60 (d, J = 8.7 Hz, 1H), 7.48 (d, J = 10.6 Hz, 2H), 7.43 – 7.40 (m, 2H), 7.32 (d, J = 8.1 Hz, 1H), 7.05 (s, 1H), 6.75 (s, 1H), 4.30 (s, 1H), 3.50 (d, J = 9.8 Hz, 1H), 2.72 (d, J = 15.3 Hz, 1H), 1.20 (s, 2H), 1.02 (d, J = 6.8 Hz, 22H), 0.07 (s, 9H). **^{13}C NMR** (151 MHz, $CDCl_3$) δ 155.8, 152.6, 149.0, 140.0, 138.7, 138.1, 130.3, 130.0, 129.8, 129.4, 127.3, 127.1, 127.0, 126.7, 126.2, 126.1, 125.5, 124.7, 124.6, 123.5, 122.7, 119.7, 119.2, 104.6, 104.5, 90.0, 77.2, 76.8, 76.5, 75.7, 57.0, 50.3,

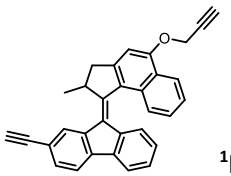
45.0, 42.2, 19.4, 19.3, 18.3, 10.8, 0.2, 0.4. **HRMS** (ESI pos) m/z calcd for $C_{44}H_{50}OSi_2$ $[M+H]^+$ 651.34000, found 650.99802.



S9 **MM**

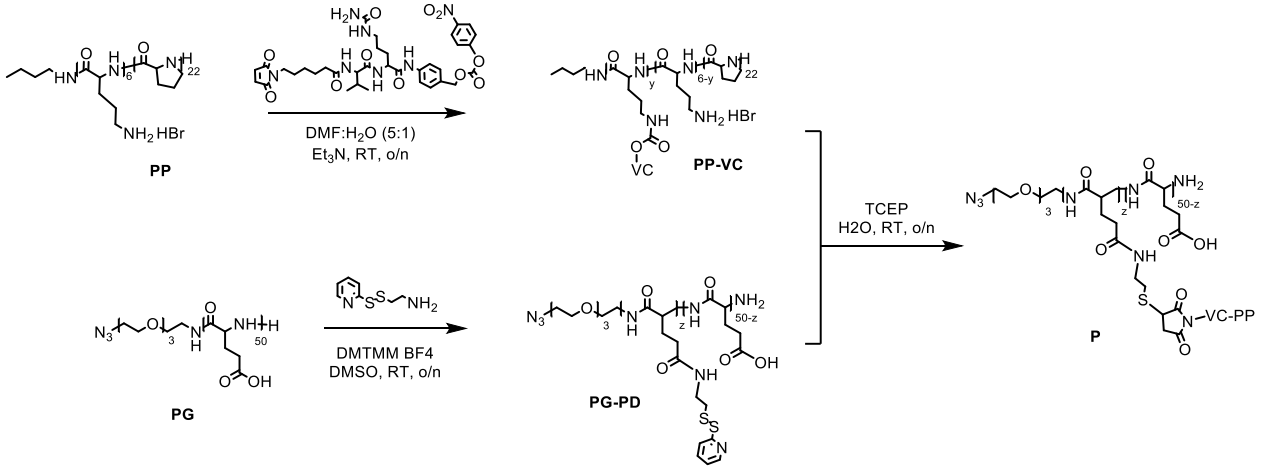
2-ethynyl-9-(2-methyl-5-(prop-2-yn-1-yloxy)-2,3-dihydro-1H-cyclopenta[a]naphthalen-1-ylidene)-9H-fluorene (**MM**).

In a Schlenk tube under a nitrogen atmosphere, tetra-n-butylammonium fluoride (TBAF, 21.1 mg, 0.081 mmol, 2.1 eq.) was added dropwise to a solution of **S9** (25 mg, 0.038 mmol, 1.0 eq.) in thiourea (THI, 1.7 mL) at 0°C. The mixture was left to stir for 6 h, quenched with ammonium chloride (1 M, 0.5 ml), and subsequently separated between water and DCM. The aqueous layer was extracted with DCM, and the combined organic layers were dried over Mg_2SO_4 and concentrated in vacuo. Flash column chromatography (SiO_2, dry load on celite, 5% DCM in pentane) gave the final molecular motor (**MM**) as a yellow solid. The product was isolated as a mixture of the two isomers, and all attempts to separate them by HPLC failed due to the low polarity of the compound.



^{1}H NMR (400 MHz, $CDCl_3$) δ 8.58 – 8.53 (m, 1H), 7.92 (d, J = 1.9 Hz, 1H), 7.83 (s, 1H), 7.69 (d, J = 8.4 Hz, 1H), 7.57 (ddd, J = 8.2, 6.8, 1.2 Hz, 1H), 7.53 – 7.52 (m, 1H), 7.38 (ddd, J = 8.3, 6.7, 1.3 Hz, 1H), 7.31 (d, J = 1.2 Hz, 1H), 6.92 (dd, J = 8.5, 1.9 Hz, 1H), 6.53 (d, J = 8.5 Hz, 1H), 5.30 (s, 2H), 4.24 (p, J = 6.6 Hz, 1H), 3.59 – 3.53 (m, 1H), 2.78 (d, J = 15.0 Hz, 1H), 1.38 (d, J = 6.7 Hz, 4H), 1.26 (s, 3H), 0.89 – 0.86 (m, 3H). **^{13}C NMR** (151 MHz, $CDCl_3$) δ 152.7, 148.7, 147.4, 141.0, 140.5, 138.9, 136.5, 136.2, 133.1, 130.7, 129.8, 129.6, 128.1, 127.7, 126.7, 125.7, 125.5, 124.7, 124.1, 123.5, 122.7, 122.5, 121.4, 116.0, 97.6, 87.7, 67.5, 67.4, 53.8, 45.6, 42.0, 19.7. **HRMS** (ESI pos) m/z calcd for $C_{32}H_{22}O$ $[M+H]^+$ 423.17000, found 423.17022.

3. Preparation and characterization of the polypeptide-based nanocarrier, P



Scheme S1. The general convergent synthetic procedure for synthesizing compound N_3-PEG_3-PGA_{50}-VC-PP (polypeptide, **P**) initially involved the synthesis of PP-VC and PG-PD separately. Adapted from Pegoraro et al.[14].

The detailed synthesis of N_3-PEG_3-PGA_{50}-VC-PP (polypeptide, **P**) is described in Pegoraro et al.[14] (reported as compound 16). Briefly, the convergent synthesis involved the synthesis of PP-VC and PG-PD separately. For the synthesis of PP-VC (described in Pegoraro et al.[14] as 6b), a reaction between PP, dissolved in 5:1 DMF:H2O (1 eq, 10 mg/mL), and a VC linker (i.e., 0.03 eq for 3% mol VC modification), dissolved in DMF, followed by Et_3N, was left stirring 24 h. The product was purified by PD-10 columns, yielding a 70% product with over 90% conjugation efficiency. VC functionalization was quantified using UV-vis spectroscopy. Separately, PG (described in e Pegorarot al.[14] as 17) was dissolved in anhydrous DMSO (1 eq., 10 mg/mL), activated with 4-(4,6-dimethoxy-1,3,5-triazin-2-yl)-4-methylmorpholinium tetrafluoroborate (DMTMM BF4 i.e., 0.1 eq for 5% mol PD-NH2 modification), and reacted with PD-NH2 (i.e., 0.05 eq. for 5% mol modification). After pH adjustment, the reaction proceeded for 48 h, and the product was purified by Vivaspin®, 3000 MWCO Da (after conversion to its salt form), achieving a 60% yield and 90% conjugation efficiency. PD functionalization was determined using both ^{1}H-NMR and UV-vis spectroscopy. Finally, PG-PD (1 eq., 10 mg/ml) was dissolved in water and reacted with PP-VC (i.e., 0.02 eq. for 2% mol PP-VC modification) followed by the reducing agent tris(2-carboxyethyl)phosphine (TCEP, i.e., 0.0025 eq. for 2% mol PP-VC modification). **P** was purified using PD-10 columns, resulting in a 50% yield and 80-90% conjugation efficiency. The functionalization of PP-VC was indirectly calculated by comparing the % wt of PD-NH_2 in PG-PD and P, using UV-vis analysis, resulting in 3.3 % wt of PP-VC.

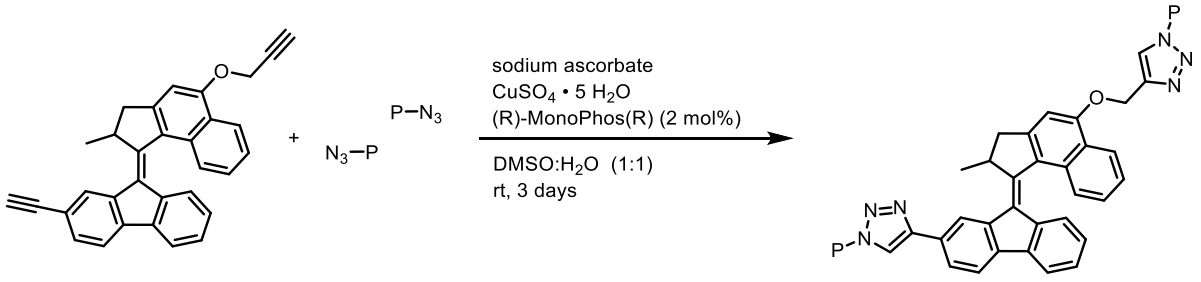
PP-VC: ^{1}H NMR (500 MHz, D_2O, 25°C) δ 7.6-7.3 (m, 4H, p, q, r, s), 6.8 (s, 2H, a), 4.77 – 4.71 (m, 1H, Cα of PLP; 1H g covered with D_2O), 4.50 – 4.20 (m, 1H, Cα of PLO; 1H l; 2H t), 3.96 – 3.30 (m, 2H, Cδ of PLP; CH_2 of $CH_3CH_2CH_2CH_2NH$ and 2H b), 3.24 – 3.06 (m, 2H, Cδ of PLO and 2H o), 2.51 – 1.23 (m, 4H, $CH_2CH_2CH_3$, 4H Cβ + Cγ of PLP; 4H Cβ + Cγ of PLO; 13H c, d, e, f, h, m, n), 0.9 (s, 6H, i), 0.82 (t, J = 7.3 Hz, 3H, $CH_2CH_2CH_3$).

PG-PD: 1H NMR (500 MHz, D_2O, 25°C) δ 8.40 (d, 1H, u), 7.80 (m, 2H, v, x), 7.25 (d, 1H, y), 4.40 – 4.20 (m, 1H, Cα of poly-L-glutamic acid (PGA)), 3.80 – 3.30 (m, 12H, $N_3(CH_2CH_2)_3O$; 4H OCH_2CH_2NH), 3.17 - 2.66 (m, 4H, k, j), 2.51 – 1.66 (m, 4H, Cβ + Cγ of PGA).

P: ^{1}H NMR (500 MHz, D_2O, 25°C) δ 8.40 (d, 1H, u), 7.80 (m, 2H, v, x), 7.25 (d, 1H, y), 4.77 – 4.71 (m, 1H, Cα of PLP; 1H g covered with D_2O), 4.40 – 4.20 (m, 1H, Cα of PGA, 1H, Cα of PLO; 1H l; 2H t), 3.83 – 3.30 (12H, $N_3(CH_2CH_2)_3O$, 4H OCH_2CH_2NH, 2H Cδ of PLP; CH_2 of $CH_3CH_2CH_2CH_2NH$ and 2H b), 3.20 – 2.66 (2H, Cδ of PLO, 2H o and 4H k, j), 2.51 – 1.66 (4H Cβ + Cγ of PGA, 4H $CH_2CH_2CH_3$, 4H Cβ + Cγ of PLP; 4H Cβ + Cγ of PLO; 13H c, d, e, f, h, m, n), 0.9 (s, 6H, i), 0.82 (t, J = 7.3 Hz, 3H, $CH_2CH_2CH_3$).

The detailed physicochemical and biological characterization of **P** is provided in Pegoraro et al. [14]. Briefly, **P** revealed a branched structure with a compact core (5.0 ± 0.3 nm) as determined by small-angle x-ray scattering (SAXS), similar to parental polymer PP. Due to PGA, Zeta potential measurements revealed a negatively charged surface (-15.7 ± 0.2 mV). **P** demonstrated excellent biocompatibility with over 80% cell viability across all tested concentrations. Flow cytometry analysis showed significant cell internalization via an energy-independent mechanism due to its small size and flexible structure. Importantly, **P** maintained its mitochondrial colocalization capability, with a high Pearson r value (>0.6) after 30 min of incubation in MDA-MB-231 cells. In membrane interaction studies, **P** formed selective patches in cardiolipin-rich supported lipid bilayers, confirming cardiolipin-specific interaction while preserving membrane physical properties. Activity studies verified a safer biological profile than PP, with no significant alterations in reactive oxygen species (ROS) production, mitochondrial morphology, or respiration.

4. Preparation of the polypeptide-molecular motor conjugate



MM **P-MM**

Scheme S2. Synthetic procedure for **P-MM** preparation.

An oven-dried vial was charged with **MM** (1.2 mg, 2.8 µmol, 0.5 eq.) and **P** (40 mg, 5.6 µmol, 1.0 eq.) in a mixture of DMSO:H_2O (1:1). Sodium ascorbate (40 mg, 5.5 µmol, 5.0 eq.), copper sulfate pentahydrate (1.4 mg, 5.6 µmol, 1.0 eq, and ligand (*R*)-MonoPhos(*R*) (0.04 mg, 0.112 µmol, 0.02 eq.) were added to the mixture. The reaction mixture was stirred for three days at room temperature. After DMSO elimination using a rotavapor and freeze-drying, the product was purified by PD-10 desalting columns packed with Sephadex G-25 resin.

*Note on characterization of **P-MM**: The final compound could not be characterized by NMR spectroscopy due to the low prevalence of the molecular motor peaks in the peptide signal. Proofs of the obtain compound come from the change in color of the product; **MM** as an intense yellow, **P** as a soft white solid, gave **P-MM** as a soft solid with an intense yellow color after purification. Raman spectroscopy (see section below), confirmed the complete disappearance of alkyne signals (around 2120 cm^{-1}) present in **MM** after conjugation to **P**, confirming that no free alkynes are present in the resulting structure. IR spectroscopy (see section below) further corroborated the conjugation via the disappearance of P's azide peaks (around 2110 cm^{-1}). Changes in the supramolecular conformation of **P-MM** after light irradiation (see Cryo-TEM section) also give undirect proof of molecular motor attachment. Attempts with MALDI-TOF spectroscopy were not successful.*

5. Raman spectroscopy

Steady-state non-resonant Raman spectra of **P, MM,** and **P-MM** were recorded using an excitation laser at 785 nm. The Raman data was baseline corrected using Spectragryph.

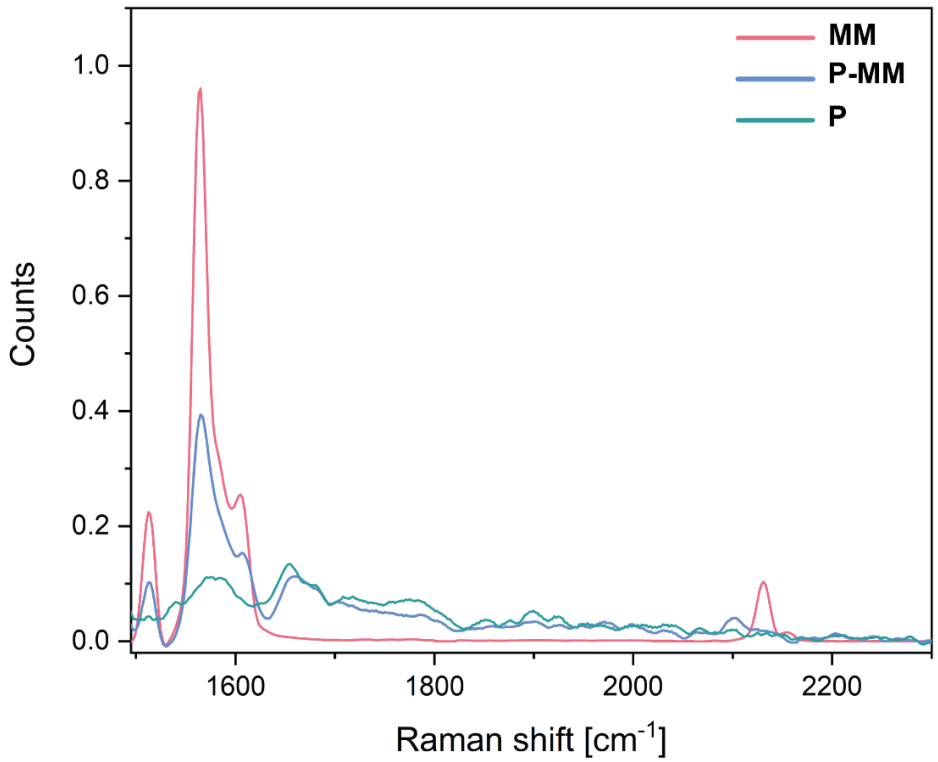


Figure S1. Raman spectra of **MM** (red), **P-MM** (blue) and **P** (green) superposed.

6. InfraRed spectroscopy

Infrared spectrometry (IR) of **P** and **P-MM** was carried out with Spectrum Two FT_IR Spectrometer (PerkinElmer) in the solid state.

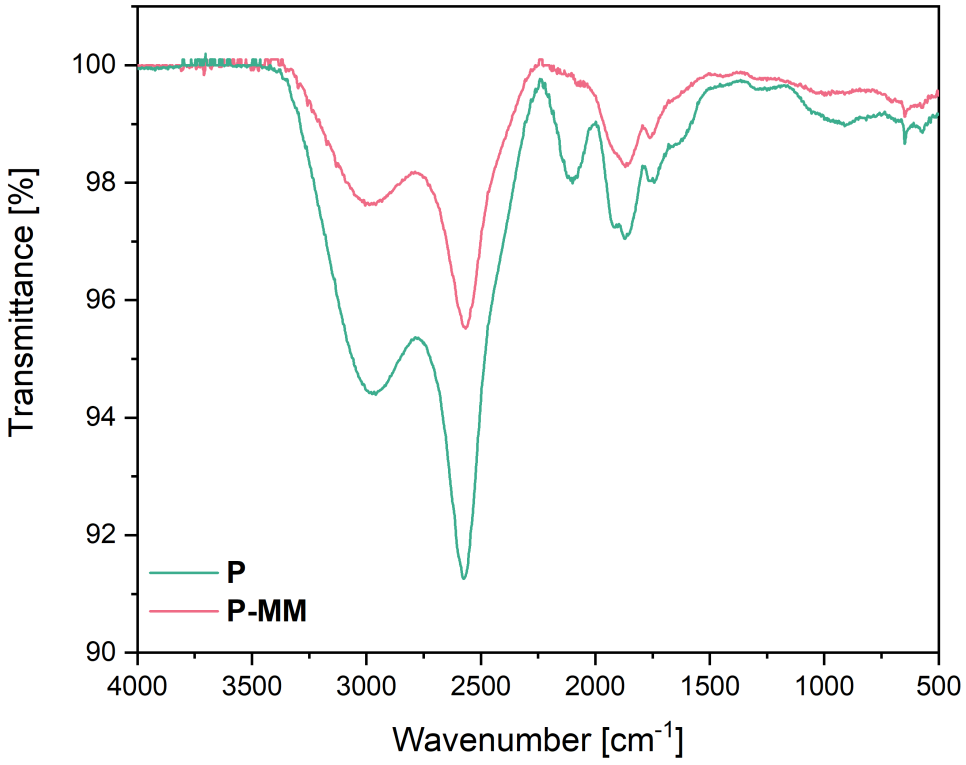
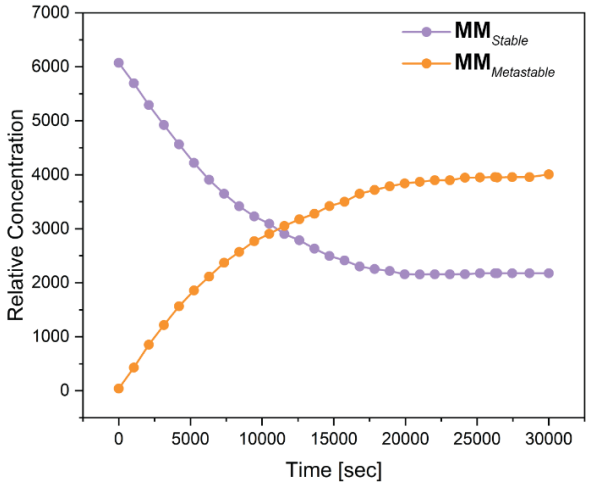


Figure S2. InfraRed spectra of **P** (green) and **P-MM** (red) superposed.

7. NMR studies of 'MM's rotation cycle

A 1 mM solution of **MM** in its stable form (**MM_{Stable}**) was prepared in $CDCl_3$ and transferred into an NMR tube fitted with a glass optic fiber for *in situ* irradiation studies. The sample was placed in a Varian Unity Plus 500MHz NMR and cooled to -15°C. ^1H NMR spectra were recorded before irradiation while irradiating at 405 nm until the PSS was reached and during the THI step until completion.

A



B

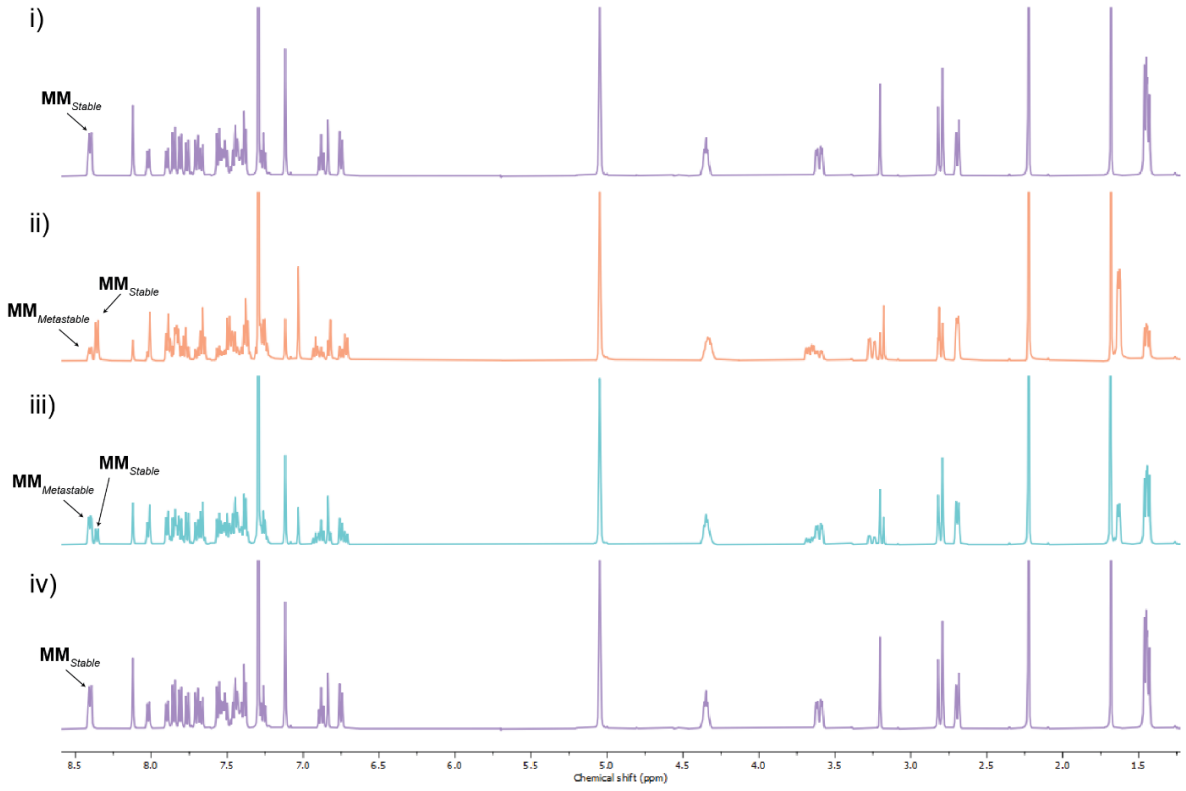


Figure S3. A) ^{1}H-NMR irradiation studies of **MM** in its stable form in $CDCl_3$ (c = 5 mM) at 5°C. **B**) Kinetics of distinct species of **MM**$_{Stable}$ ^{1}H-NMR spectra change under irradiation. i) **MM**$_{Stable}$ before irradiation, ii) after 1 h of irradiation at 405 nm, iii) 7 h of irradiation reaching PSS, iv) no irradiation THI, after 12 h in the dark.

8. UV-vis

UV–vis spectroscopy was used to evaluate **MM** and **P-MM** isomerization and for thermodynamic studies using an Agilent 8453 UV–vis Diode Array System equipped with a Quantum Northwest Peltier controller. Unless specified, irradiations were conducted using a built-in setup coupled to an LED. Solutions were prepared and measured using a 10 mm quartz cuvette. The same procedure was used for UV-Vis controls on **P**.

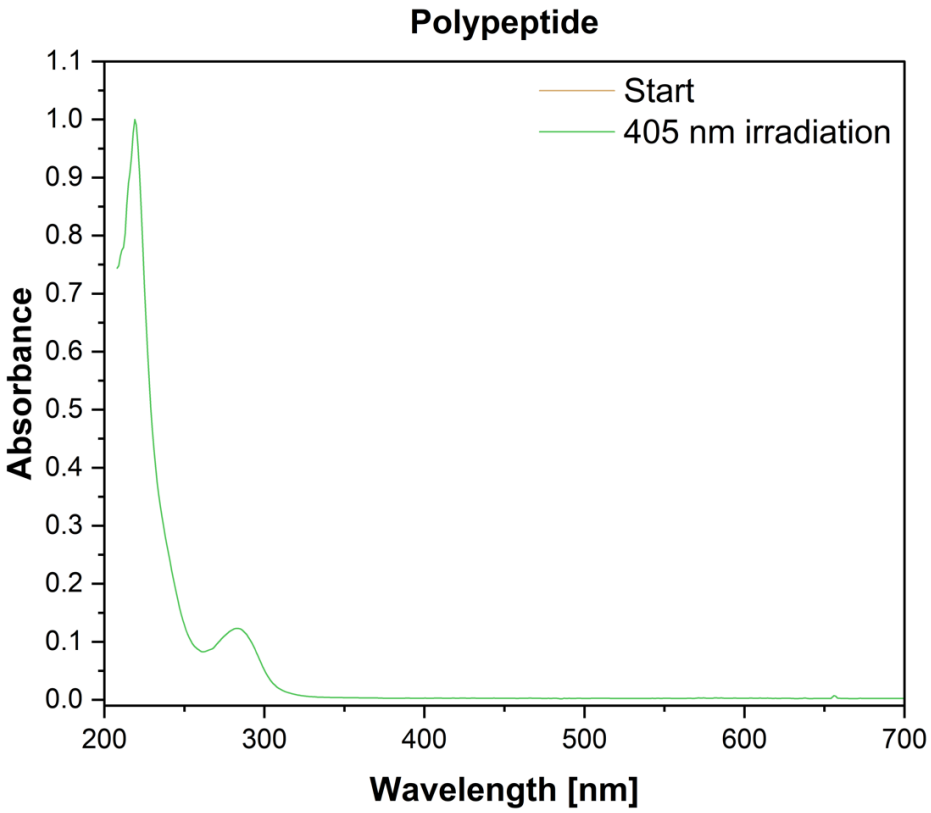


Figure S4. Absorption spectra of **P** under light irradiation (in PBS, 37°C). The orange line is not visible due to the complete overlap of the two spectra.

9. Thermodynamics - Eyring analysis

50 µM solutions of **MM** and **P-MM** were prepared in a 10 mm quartz cuvette and irradiated with 405 nm light until the PSS was reached. An Eyring plot analysis of the thermal isomerization processes in different environments was performed by monitoring the decrease in absorption of a UV-Vis sample over time at five different temperatures. Rate constants, (k), as changes of absorbance over time were

determined by fitting a first-order decay and plotted to determine the thermodynamic parameters of the thermal helix inversions using Origin 2023 software and a least squares analysis was performed on the Eyring equation to retrieve the ΔG ‡. The activation parameters at 25°C for the metastable → stable process can be determined and are displayed in **Table S1**. Eyring plots and half-live times at 25°C for the studied environments are shown in **Figure S4**.

Table S1. Activation parameters of **MM** and **P-MM** at 37°C.

Compound	$\Delta G^{\ddagger}$ $[kcal/mol]$	$\Delta H^{\ddagger}$ $[kcal/mol]$	$\Delta S^{\ddagger}$ $[kcal/mol]$	$t_{1/2}$ $[sec]$
MM	18.953±0.027	18.944	-0.0272	2.43
P-MM	22.136±0.051	7.822	-46.151	425.38

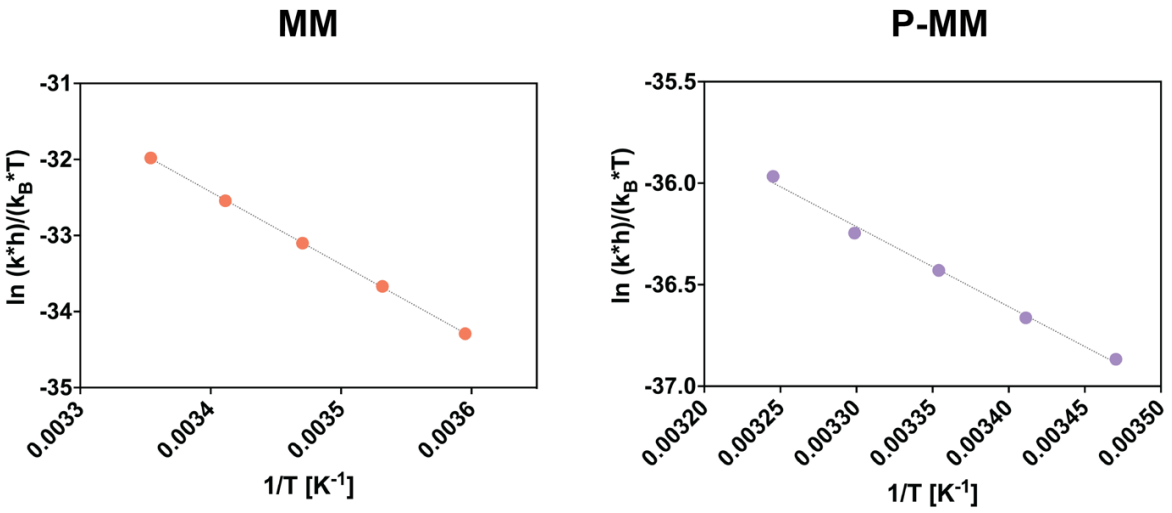


Figure S5. Eyring plot analysis of the **MM** and **P-MM** monitoring the decrease in absorption at 425 nm at five different temperatures.

10. Circular Dichroism

Circular dichroism (CD) spectroscopy was conducted utilizing a J-815 CD Spectrometer from JASCO Corporation, incorporating a Peltier thermostated cell holder (PTC-423, JASCO Corporation) equipped with a recirculating cooler (JULABO F250, JASCO Corporation). A nitrogen flow of approximately 1.5 L/min was directed through the spectrometer and regulated using a nitrogen flow monitor from Afriso Euro-Index. The samples were prepared in PBS buffer at 0.25 mg/mL. Each sample was analyzed three times (n=3) in a quartz cuvette with a 1 mm diameter.

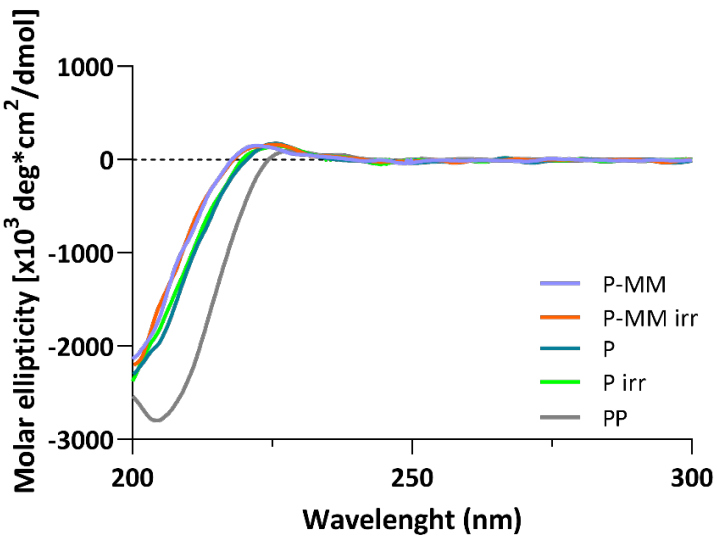


Figure S6. Circular dichroism spectra of irradiated (irr) and non-irradiated **P-MM** and **P** (random coil) compared to the diblock copolymer PP (PPII).

11. Critical Aggregation Concentration Studies

The differential self-assembly of the **P-MM** after irradiation was assessed by incorporation of the hydrophobic solvatochromic probe Nile Red (9-diethylamino-5-benzo[α]phenoxazinone), which exhibits a blue shift emission upon inclusion in hydrophobic environments. Starting from a 2 mg/ml **P-MM** solution, 1:2 dilutions were prepared in PBS. Nile Red (0.5 mM in ethanol) was added to each **P-MM** solution to a final concentration of 375 nM. Using a JASCO FP6200 fluorometer, the solutions were excited at 550 nm, and the spectra were recorded over a wavelength range of 580–750 nm. After 5-10 min of irradiation at 405 nm of each solution, the measurements were repeated under the same conditions. Blue shifts were calculated by subtracting the emission wavelength of Nile Red in buffer solutions (PBS) from the emission wavelength of the sample. Blue shifts were plotted against concentrations (log. Conc in ug/ml) to determine the critical aggregation concentration (CAC) value.

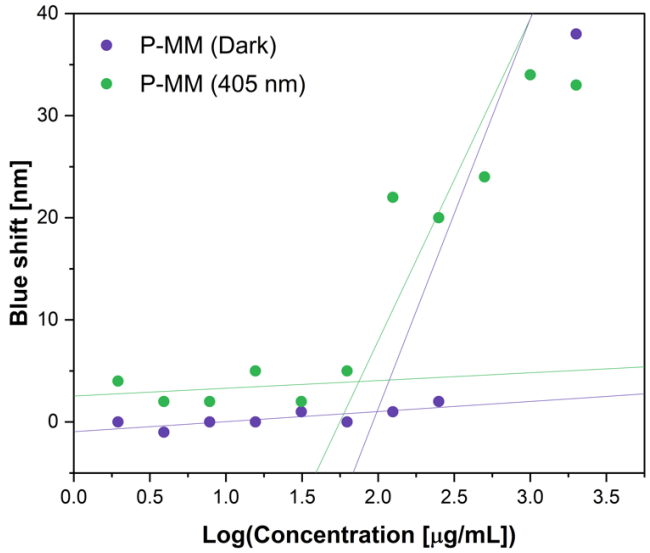


Figure S7. Blue shift in Nile Red maxima absorbance peak with increasing concentrations of non-irradiated (purple) and irradiated (green) **P-MM** in aqueous solution.

Table S2. CAC values obtained for **P-MM** with/without irradiation at 405 nm.

P-MM	Before irradiation	**59.4 μM**
	5 min at 405 nm	**25.9 μM**

12. Cryo-TEM

2.5 µL (2 mM) samples were placed on a glow-discharged hollow carbon-coated grid (Quantifoil 3.5/1, QUANTIFOIL Micro Tools GmbH). After blotting, the corresponding grid was rapidly frozen in liquid ethane (Vitrobot, FEI) and kept in liquid nitrogen until measurement. The grids were observed with a Gatan model 626 cryostage in a Tecnai T20 Field Electron and Ion Company (FEI) cryo-electron microscope operating at 200 keV. Cryo-TEM images were recorded on a slow-scan charge-coupled device (CCD) camera under low-dose conditions. All processes were performed in the dark. The same procedure was used with a quartz cuvette for irradiated samples immediately before freezing.

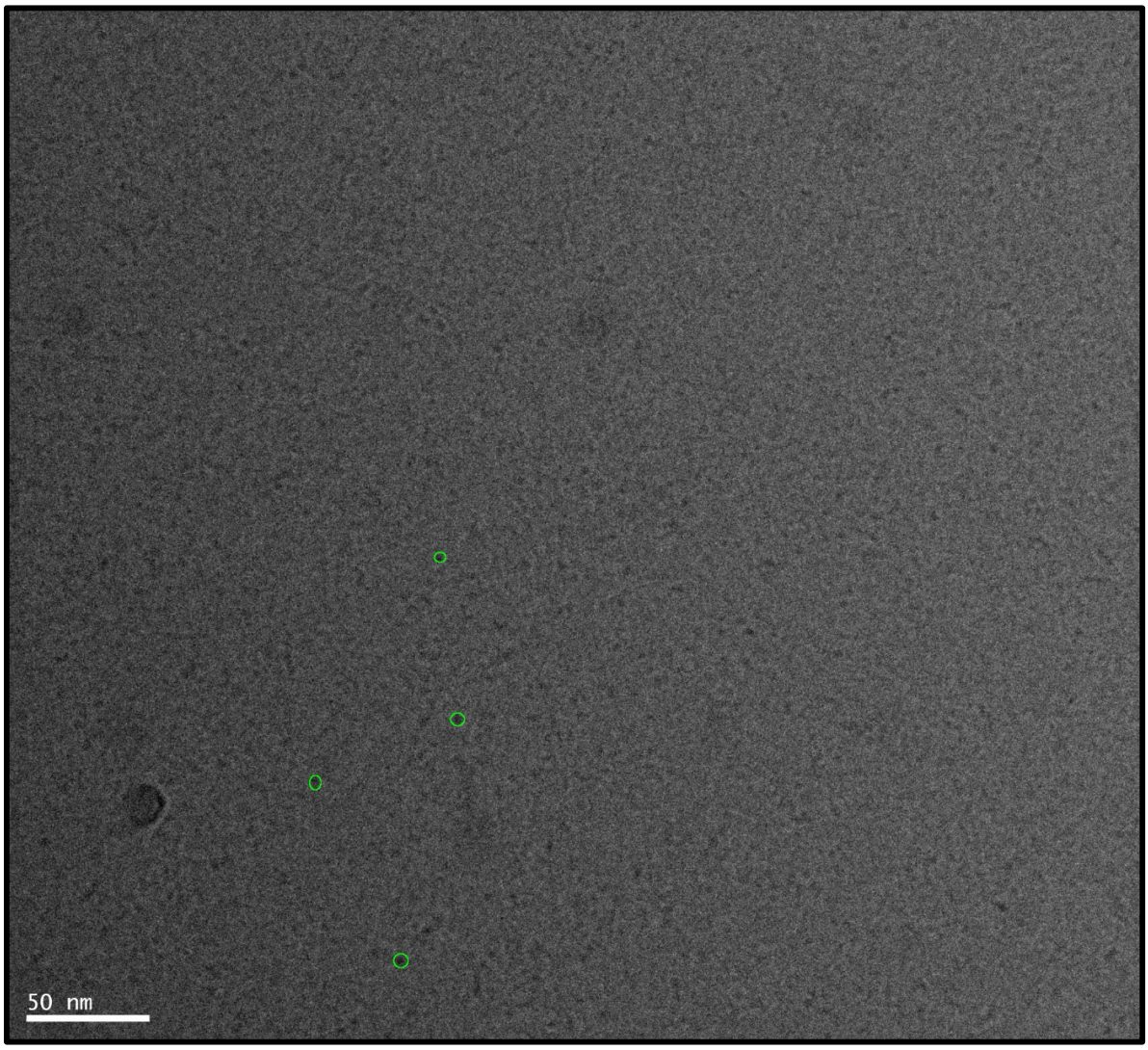


Figure S8. Cryo_EM picture of P-MM (in PBS solution) before irradiation.

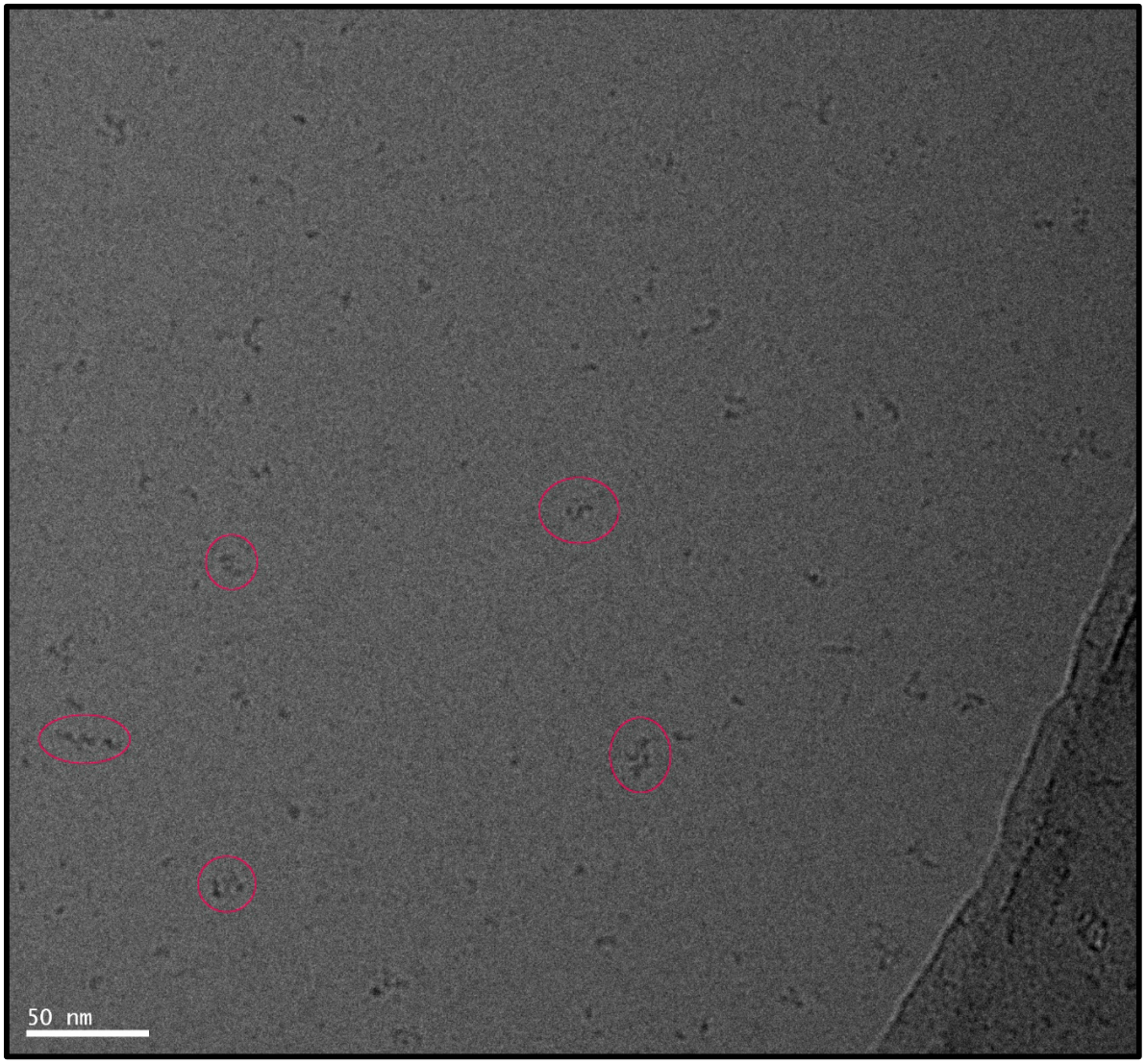


Figure S9. Cryo-EM picture of **P-MM** after irradiation (5 min, 405 nm LED, PBS solution).

13. Cell viability studies

Cell viability was assessed after treatment with the **P** and **P-MM**. MDA-MB-231 cells were seeded in 96-well microlitre plates (5,000 cells/well, 0.05 ml per well) and incubated for 24 h at 37° and 5% CO^2. Concentrated stock solutions of P and P-MM were prepared in PBS buffer and diluted in DMEM/F-12 medium (with 10% fetal bovine serum (FBS) and 1% penicillin/streptomycin (P/S). P and P-MM solutions were sterilized using a 0.2 µm filter and added to give a final concentration of 0-1 mg/ml (dilution factor 1.5). After 24/72 h of incubation, the CellTiter-Glo® 2.0 Cell Viability Assay was performed to determine cell viability. Following 20 min of incubation, ATP luminescence was measured

spectrophotometrically using a CLARIOstar plate reader. The luminescence values were expressed as a percentage of cell viability, with 100% representing the cell viability of untreated control cells. Value's represent mean ± SD (n=3).

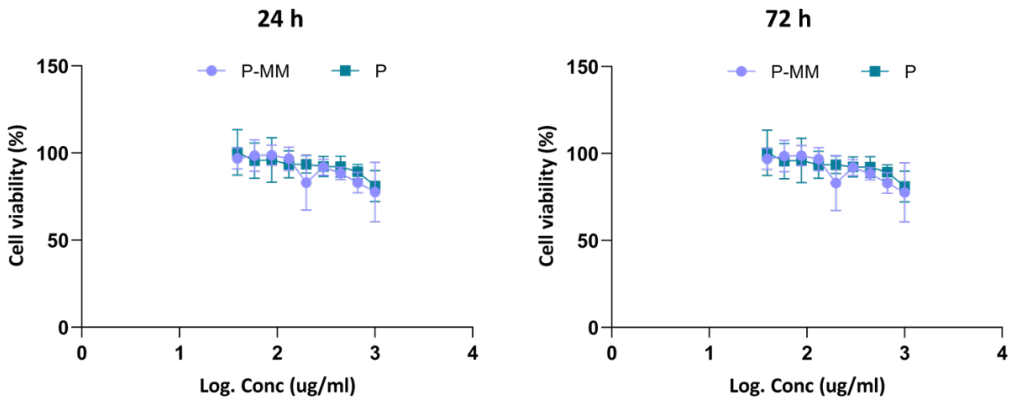


Figure S10. MDA-MB 231 cell viability CellTiter-Glo® 2.0 Cell Viability Assay in response to **P-MM** and **P** treatment (24 and 72 h, n = 3, mean ± SEM).

Cell viability studies were performed using MTS assays at various exposure times to determine the optimal non-toxic irradiation time at 405 nm for further biological investigations. MDA-MB-231 cells were seeded in 96-well microlitre plates (5,000 cells/well, 0.05 ml per well) and incubated for 24 h at 37° and 5% CO_2. The cells were then irradiated using a Lumidox® II 96-Well LED Arrays (lens mat/solid base) (UV wavelength of 405 nm) powered by the Lumidox® II LED Controller (LUM2CON) with customizable power light/well and irradiation time control. After irradiation, the CellTiter-Glo® 2.0 Cell Viability Assay was performed to determine cell viability. Following 20 min of incubation, ATP luminescence was measured spectrophotometrically using a CLARIOstar plate reader. The luminescence values were expressed as a percentage of cell viability, with 100% representing the cell viability of untreated control cells. Values represent mean ± SD (n=3). Among the tested exposure times, 30 s was selected as the optimal condition for further experiments.

Table S3. Laser power per well at varying irradiation times at 405 nm

Irradiation 405nm - 65mW/well (355 mW/cm^2 = 0.355 J/cm^2 x sec)	
Time (sec)	Laser Power (J/cm^2)
0	0
30	10.65
60	21.3
120	42.6

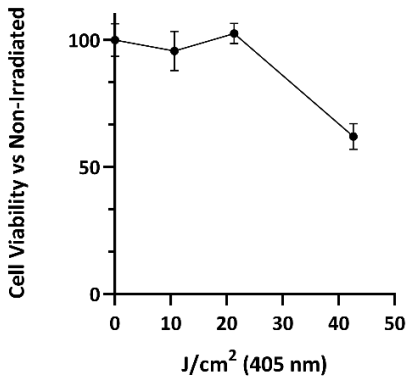
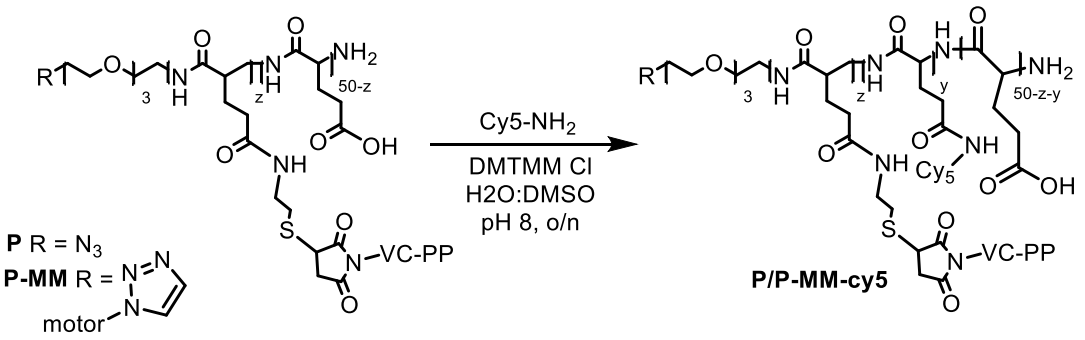


Figure S11. MDA-MB 231 cell viability CellTiter-Glo® 2.0 Cell Viability Assay in response to different irradiation times at 405nm (n = 3, mean ± SEM).

Cell viability was then assessed after treatment with the **P** and **P-MM** after 30 s of irradiation at 405 nm. MDA-MB-231 cells were seeded in 96-well microlitre plates (5,000 cells/well, 0.05 ml per well) and incubated for 24 h at 37° and 5% CO_2. Concentrated stock solutions of **P** and **P-MM** were prepared in PBS and diluted in DMEM/F-12 medium (with 10% FBS and 1% P/S). **P** and **P-MM** solutions were then sterilized using a 0.2 µm filter and added to give a final concentration of 0-1 mg/ml (dilution factor 1.5). Immediately after addition, cells were irradiated using a Lumidox® II 96-Well LED Arrays (lens mat/solid base) (UV wavelength of 405 nm) powered by the Lumidox® II LED Controller (LUM2CON) for 30 sec. After 3/24 h, CellTiter-Glo® 2.0 Cell Viability Assay was performed to determine cell viability. Following 20 min of incubation, ATP luminescence was measured spectrophotometrically using a CLARIOstar plate reader. The luminescence values were expressed as a percentage of cell viability, with 100% representing the cell viability of untreated control cells. Values represent mean ± SD (n=3).

14. Fluorescence labeling of P and P-MM with Cy5



Scheme S3. Labeling of **P** and **P-MM** with Cy5-NH_2.

In a one-neck bottom flask, **P** or **P-MM** was dissolved in Milli-Q water (1 eq., 10 mg/mL), and the carboxylic group was activated with DMTMM Chloride (i.e., 0.03 eq. for 1.5% mol Cy5-NH_2) dissolved in 0.5 mL of Milli-Q water. In a glass vial protected by light, Cy5-NH_2 was dissolved in DMSO and added to the solution (0.015 eq., 1.5% mol). The pH was adjusted with sodium bicarbonate (1M, pH 8). The reaction was allowed to proceed overnight, the mixture protected from light, and evaluated by thin-layer chromatography (MeOH as mobile phase). After DMSO elimination on the rotavapor and by freeze-drying, the product was purified using PD-10 desalting columns packed with Sephadex G-25 resin. Dye loading was calculated by fluorescence using the fluorescent plate reader CLARIOstar. First, the corresponding free dye (DMF:H2O) calibration curve was prepared in dark 96-well multiwell plates. Fluorescence was measured at λex: 632 nm λem: 684 nm for Cy5-NH2. Yields: 80%. Conjugation efficiency 60-100%.

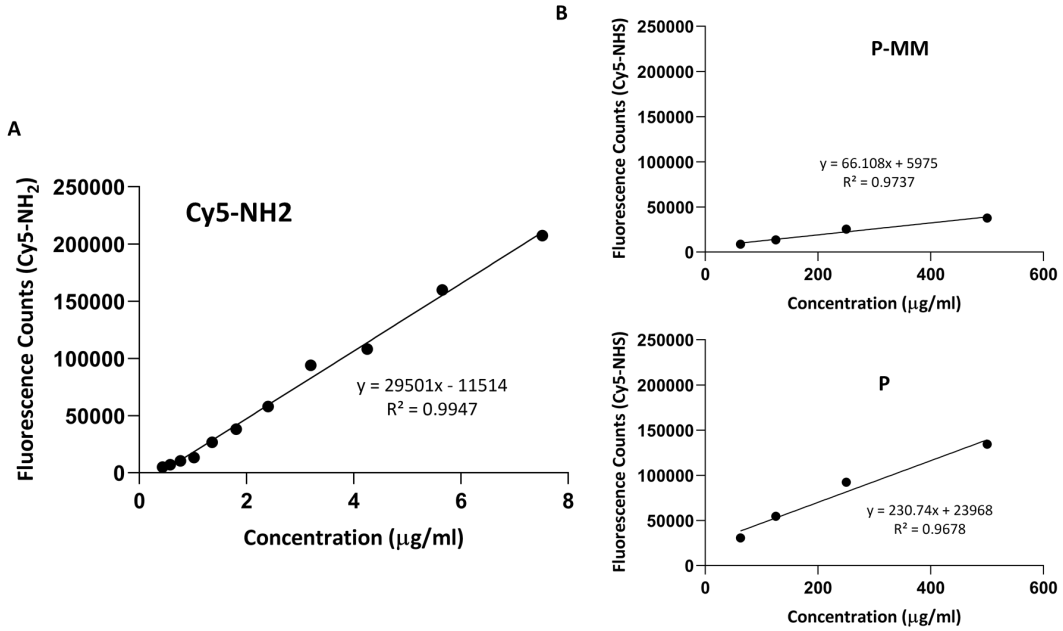


Figure S12. Fluorescence calibration curves of **(A)** Cy5-NH2 and **(B)** P-MM (**upper**) and P (**lower**) in DMF:H_2O for quantifications. % wt **P-MM** = 0.5 and **P** = 1.8.

15. Cell Uptake studies

Cell uptake of **P** and **P-MM** with/without irradiation at 405 nm was quantitatively analyzed using the high-throughput In Cell Analyzer 2200 (Cytiva, UK) system with four fluorescent channels and a 40x objective. The experiments, conducted under controlled CO_2 and temperature conditions, were performed using specific fluorescent markers: Invitrogen™ CellTracker™ Red CMTPX Dye (cytosol, 0.5 μM, ex. 575/25 em. 620/30), Helix NP™ Green (nuclei, 50 nM, ex. 475/28 em. 525/48), and Cyanine5 (Cy5, **P** and **P-MM**, 0.2 mg/ml, ex. 632/22 em. 684/25). MDA-MB-231 cells (5,000 cells/well, 0.05 ml per well) were seeded in a 96-well black optical-bottom plate and incubated for 24 h at 37°C with 5% CO_2. DMEM/F-12 medium (with 10% FBS and 1% P/S) was removed and substituted with DMEM/F-12 medium (1% P/S, without FBS), followed by a 1-h incubation with Invitrogen™ CellTracker™ Red CMTPX Dye. **P** and **P-MM** were added (0.2 mg/ml) to reach a final volume of 100 μl per well, and the plate was rapidly irradiated using a Lumidox® II 96-Well LED Arrays (lens mat/solid base) (UV wavelength of 405 nm) powered by the Lumidox® II LED Controller (LUM2CON) for 30 s. Non-irradiated treated cells with **P** and **P-MM**, control cells (to establish autofluorescence levels), and control conditions (Invitrogen™ CellTracker™ Red CMTPX Dye (cytosol, 0.5 μM) and Helix NP™ Green) were also analyzed. For each condition (n=3), 7 regions of interest (ROIs) (~ 60 live cells/ROI) were selected, and the fluorescence

intensity was quantified for each channel every 20 min for 6 h.

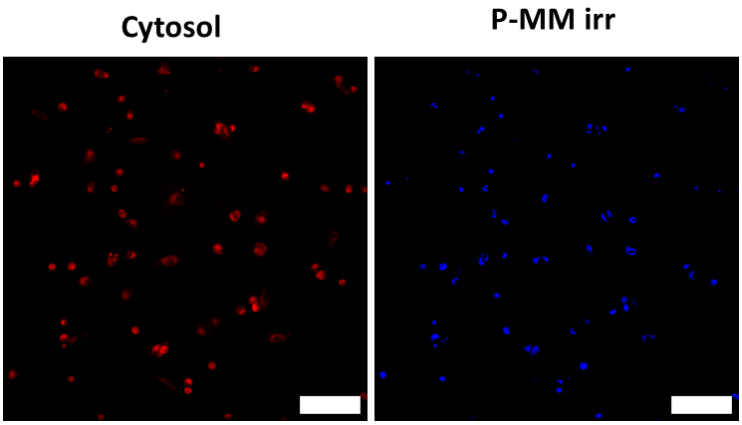


Figure S13. Representative ROI of irradiated (irrr) **P-MM** 20 min post-irradiation at 405 nm (right). CellTracker™ Red CMTPX Dye used to label the cell cytosol (left). For each condition (n=3), 7 ROI (~ 60 live cells/ROI) were analyzed using the InCell Analyzer 2200. Scale bar: 200 μm.

For the data analysis, the mean fluorescence intensity of the **P** and **P-MM**-treated wells was normalized to the % of Cy5 for each treatment. The Cy5 fluorescence intensity was adjusted to account for the quenching effect caused by irradiation at 405 nm for 30 s. To determine the quenching conversion factors, the fluorescence intensity of **P** and **P-MM** was monitored at 20-min intervals over 6 h in both irradiated and non-irradiated states using a CLARIOstar plate reader, replicating the conditions of an InCell experiment without cells. The quenching conversion factors, calculated as the ratio of Cy5 fluorescence intensity between non-irradiated and irradiated samples, were 2.3 (± 0.03) for **P-MM** and 2.15 (± 0.02) for **P**. The Cy5 fluorescence intensity was determined in CellTracker™ Red CMTPX Dye positive cells. Values represent mean ± SD (n=3).

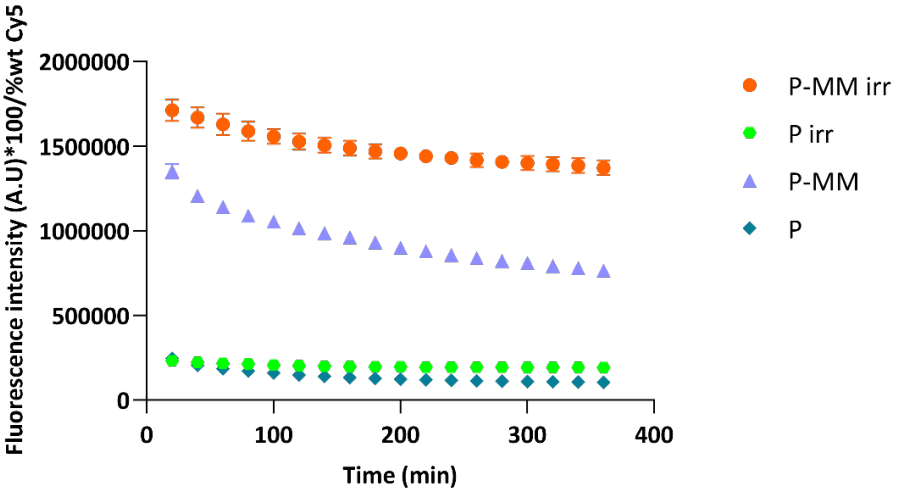


Figure S14. Cy5 fluorescence intensity of **P and P-MM** (non-irradiated and irradiated [irr] at 405 nm for 30 s) after cell segmentation every 20 min for 6 h. The slight decrease in Cy5 fluorescence intensity over time for **P-MM** is due to the quenching effect of **MM**, which acts as an effective Förster resonance energy transfer (FRET) acceptor when they are close to molecular dyes such as Cy5. The same effect was not observed for **P**.

The cellular uptake of **P-MM** with/without irradiation at 405 nm was qualitatively analyzed by confocal fluorescence microscopy (live-cell imaging) using a Leica TCS SP8 confocal microscope with a 63x 1.4NA CS2 oil immersion objective. Excitation at 488 nm, 561 nm, and 638 nm was employed, along with four fluorescent photomultiplier tubes (PMTs) and two hybrid Detectors (HyD). The experiments were conducted under controlled CO_2 and temperature conditions. Pulse-chase studies (n=3) were performed using specific fluorescent markers: MitoTracker™ Red CM-H2Xros M7513 (mitochondria, 100nM), LysoTracker™ Green DND-26 (lysosomes, 100nM), and Cyanine5 (P-MM). MDA-MB-231 cells (1,500 cells/well, 0.03 ml per well) were seeded in a 384-well black optical-bottom plate and incubated for 24 h at 37°C with 5% CO_2. For pulse-chase studies, **P-MM** was added at different time points (20, 40, 80,120, 160, and 200 min), immediately followed by irradiation (in case of irradiated conditions) using a Lumidox® II 96-Well LED Arrays (lens mat/solid base) (UV wavelength of 405 nm) powered by the Lumidox® II LED Controller (LUM2CON) for 30 s. Mitotracker and Lysotracker were added 1 h before analysis. Control cells with similar incubation times were also analyzed to establish autofluorescence levels. Image processing was conducted using Leica Application Suite X (LAS X) and the Image J-JACoP plugin for Pearson r calculation.

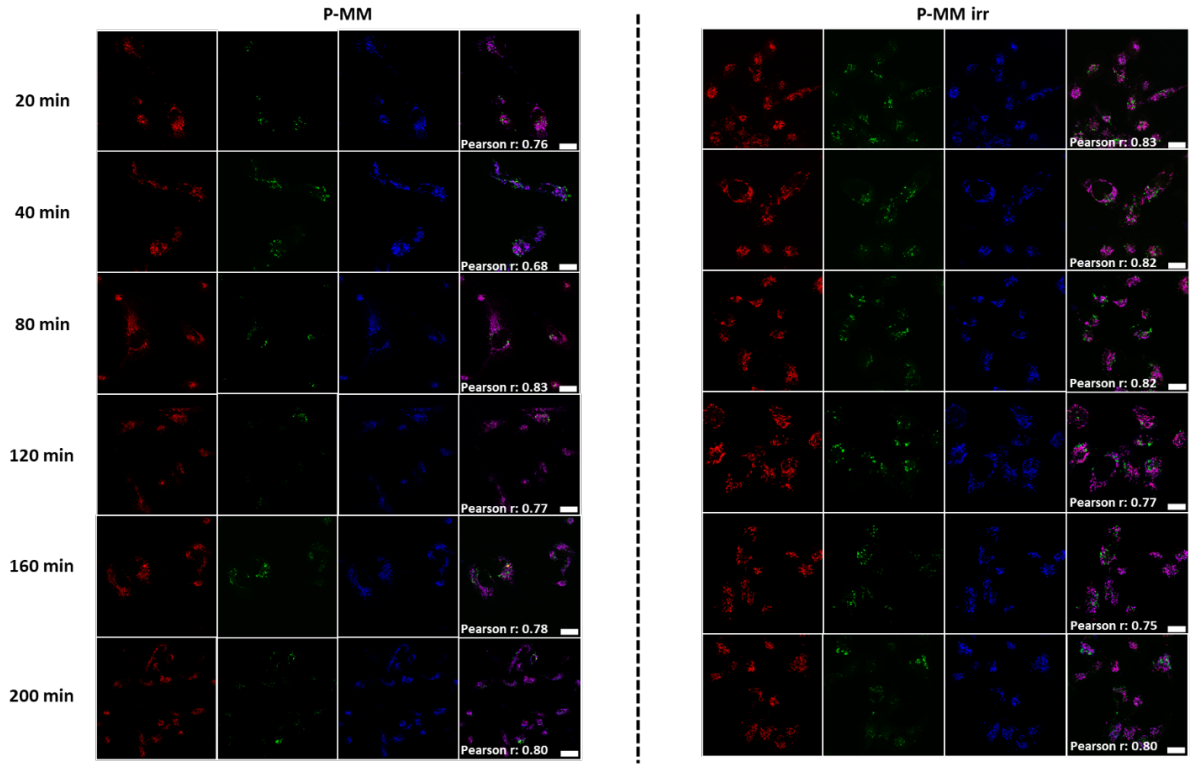


Figure S15. Confocal images of **P-MM** uptake at different times post-treatment and irradiation (405 nm, 30 s for P-MM irr) in MDA-MB-231 cells following a pulse-chase experiment (Figure SXX) (Red – MitoTracker™ Red CM-H2Xros for mitochondria; Green – LysoTracker® Green for lysosomes; Blue – Cy5 for P-MM and P-MM irr). Colocalization of **P-MM and P-MM irr** with Mitotracker Red shown in the merged image (in purple). The Pearson r value was calculated using the ImageJ – JACoP plugin. Scale bar: 10 μm.

16. Reactive oxygen species production

MDA-MB-231 cells were seeded into a 6-well plate (150,000/well, 2 ml per well) and allowed to adhere for 24 h at 37°C and 5% CO_2. P-MM and P (labeled with Cy5) were added to give a final concentration of 0.2 mg/ml (same concentration used for the uptake studies), immediately followed by irradiation (in case of irradiated conditions) using a Lumidox® II 96-Well LED Arrays (lens mat/solid base) (UV wavelength of 405 nm) powered by the Lumidox® II LED Controller (LUM2CON) for 30 s. After 3/24 h, cells were washed with PBS, trypsinized, and centrifuged to obtain cell pellets resuspended in fresh DMEM/F-12 medium (with 10% FBS and 1% P/S). Cells were then incubated with 5 μg/ml of 2,7-dichlorodihydrofluorescein (DCFH) for 30 min at 37°C and 5% CO_2. Subsequently, propidium iodide (2 μg/ml), a marker for cell viability, was added, and the resulting samples were analyzed using flow

cytometry (CytoFLEX S, Beckman-Coulter, CA, USA). Data collection involved 10,000 counts per sample, and data were analyzed using CytExpert version 2.3 software. Data were normalized to the control set as 100%. Control cells with the same irradiation times (with/without **P** and **P-MM**) were also analyzed to establish autofluorescence levels. Values represent mean ± SD (n=3).

17. NMR spectra

The ^{1}H and ^{13}C NMR spectra of newly reported compounds are reported here.

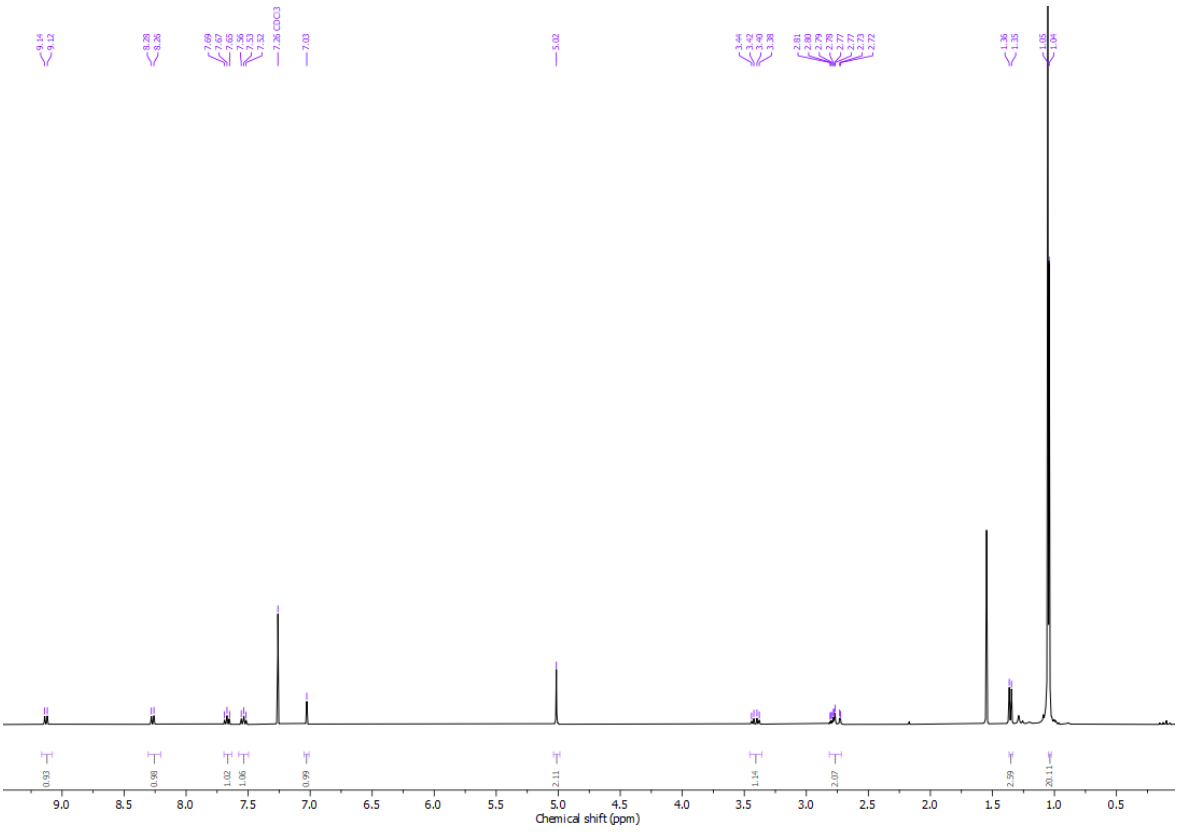


Figure S16. ^{1}H-NMR spectra of **S5**.

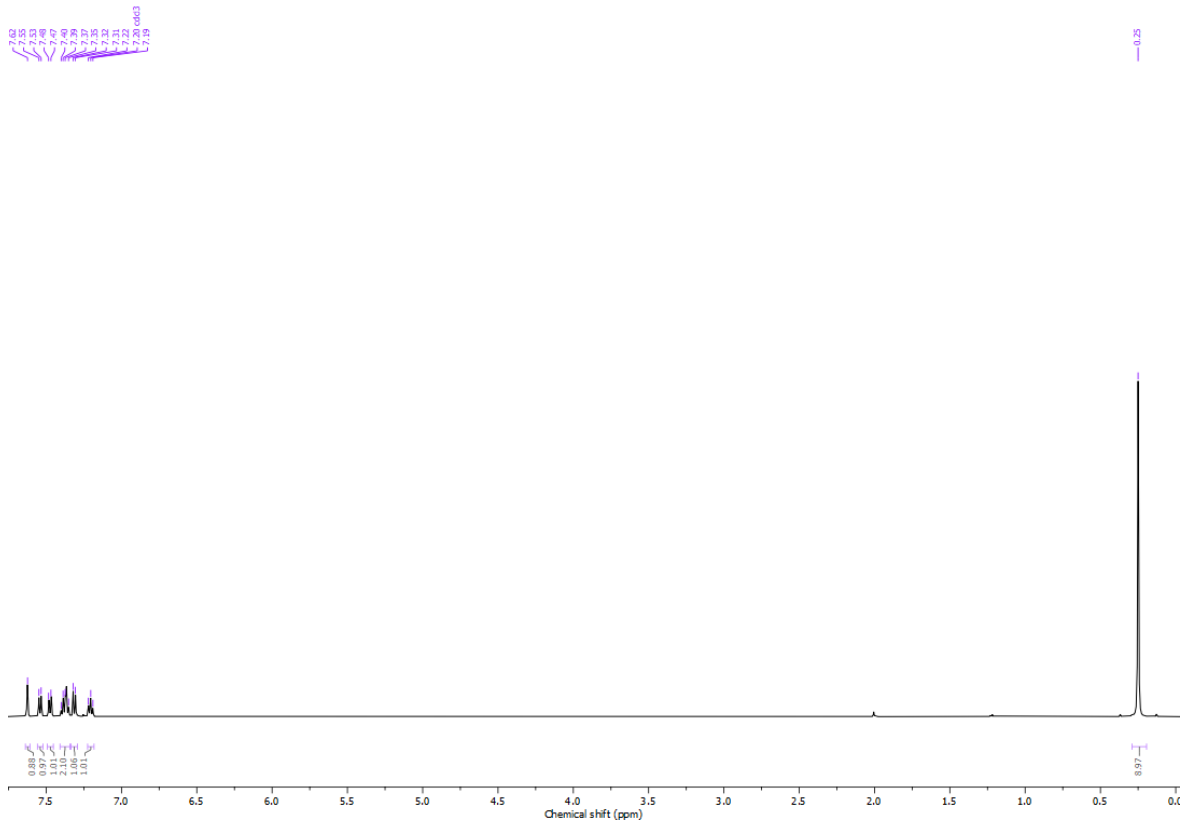


Figure S17. ^{1}H-NMR spectra of **S6**.

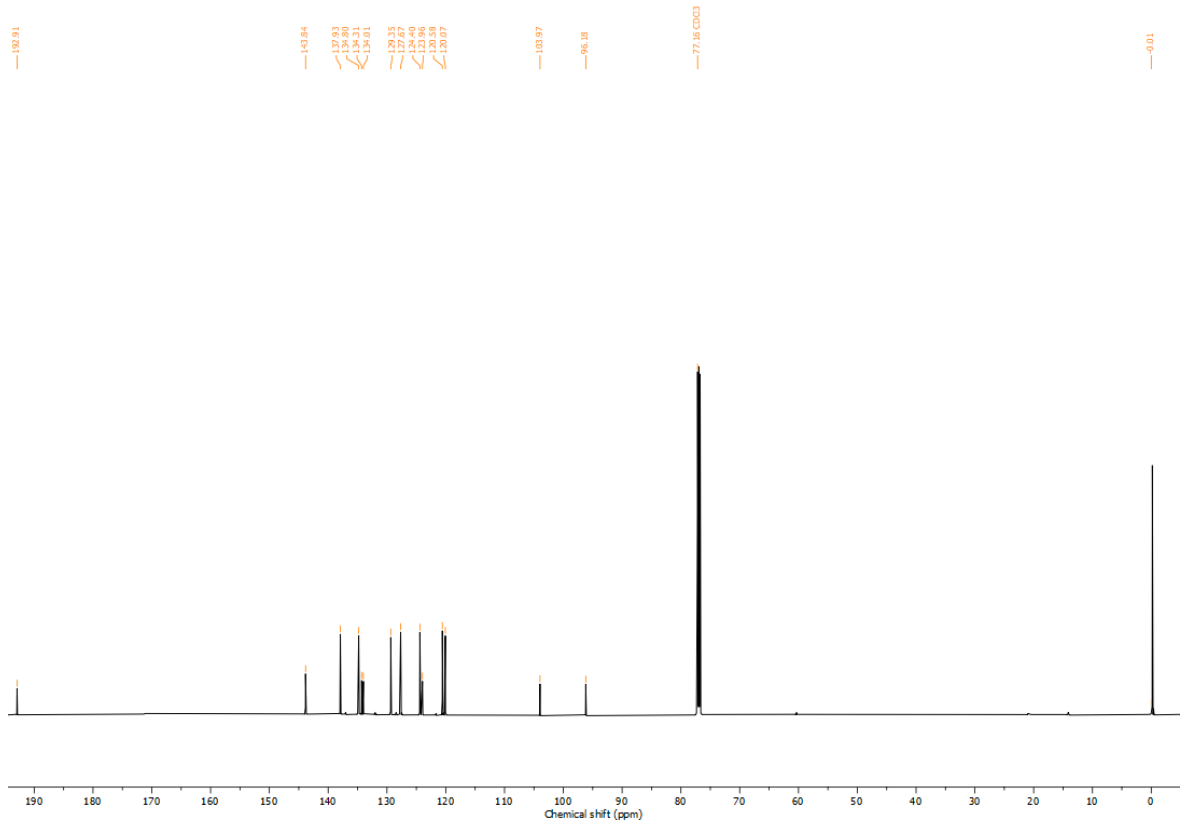


Figure S18. ^{13}C-NMR spectra of **S6**.

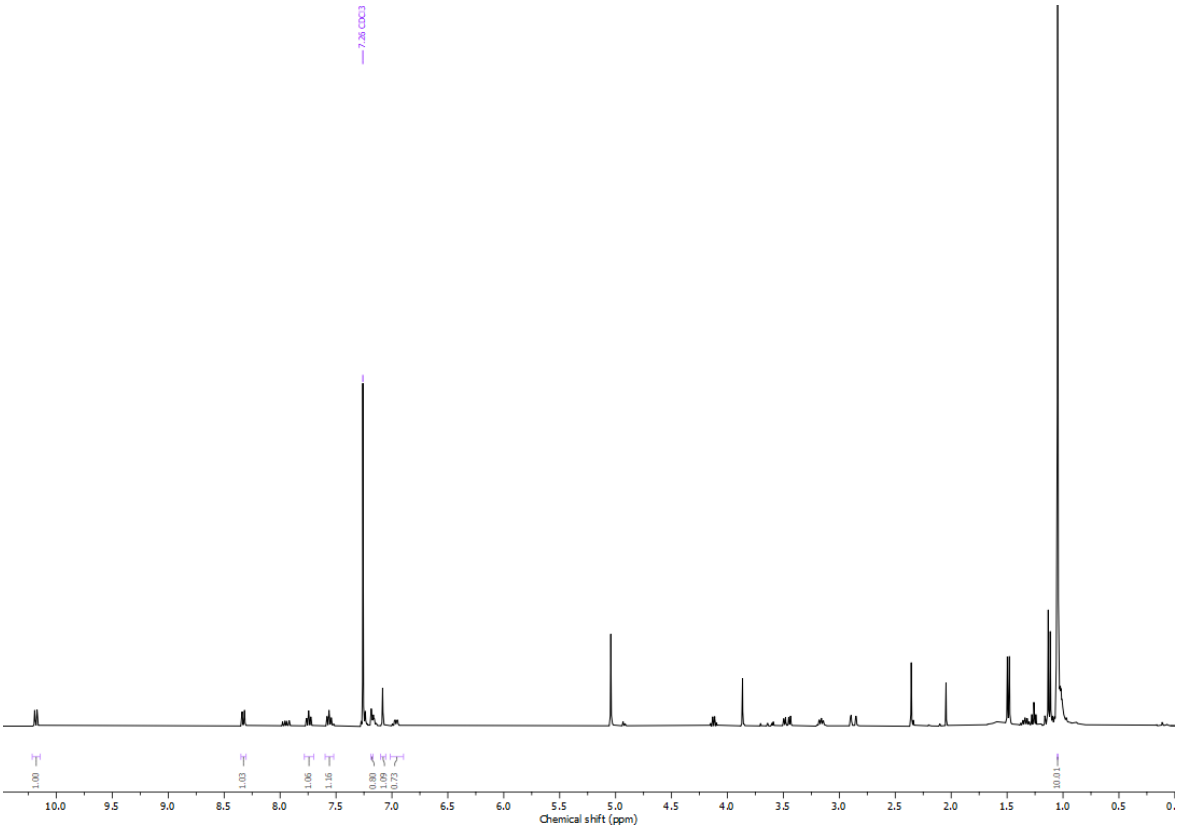


Figure S19. ^{1}H-NMR spectra of **S7**.

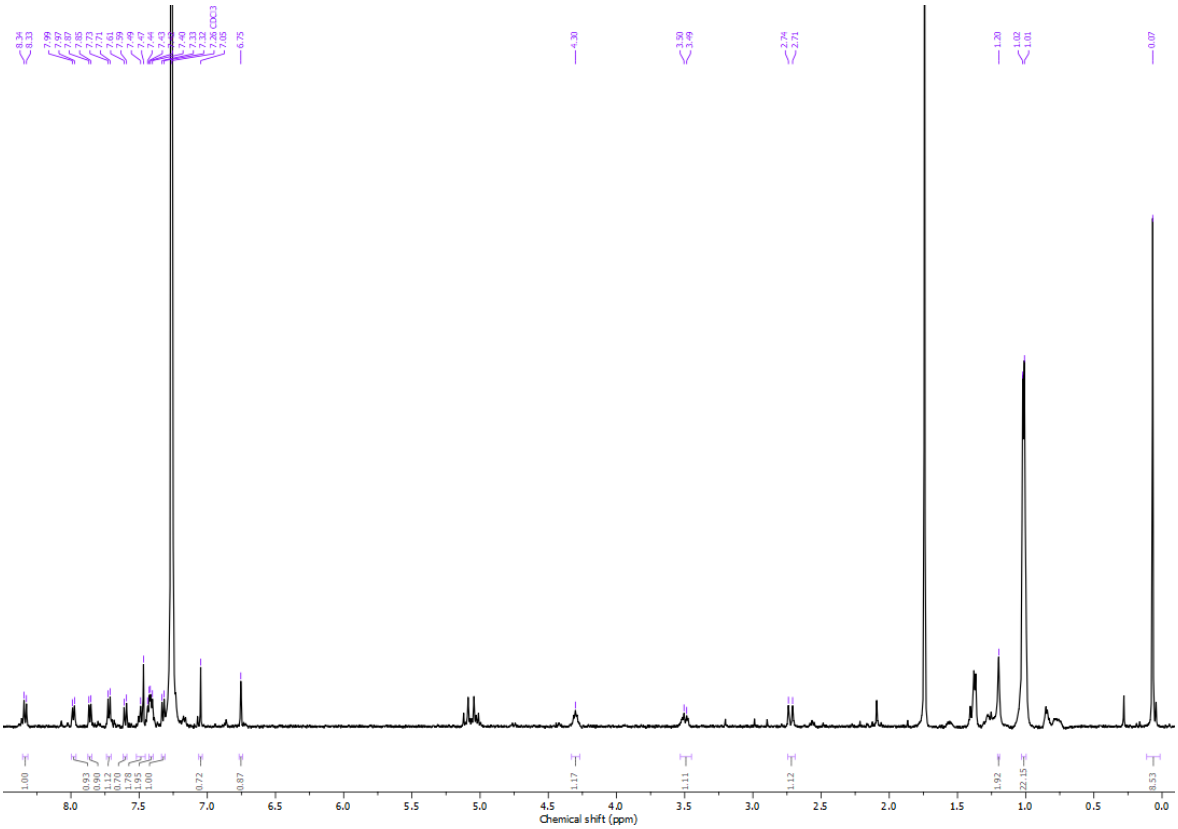


Figure S20. ^{1}H-NMR spectra of **S9**.

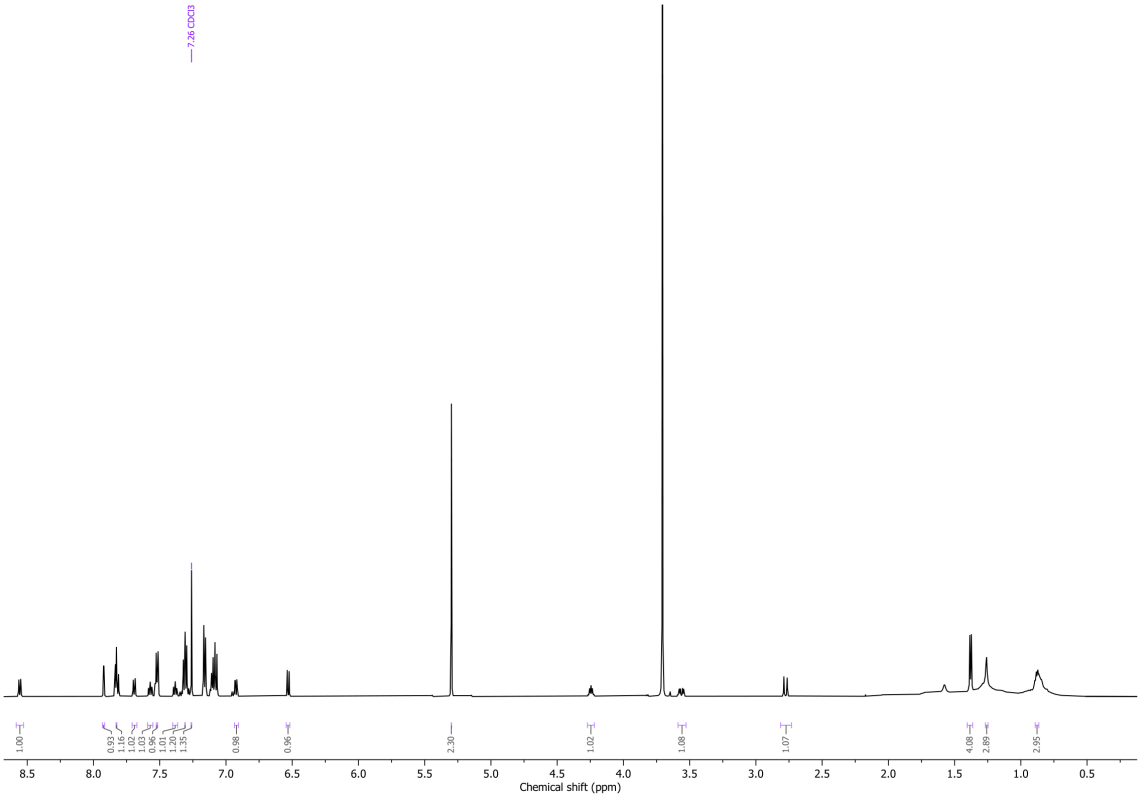


Figure S21. ^{1}H-NMR spectra of **MM**.

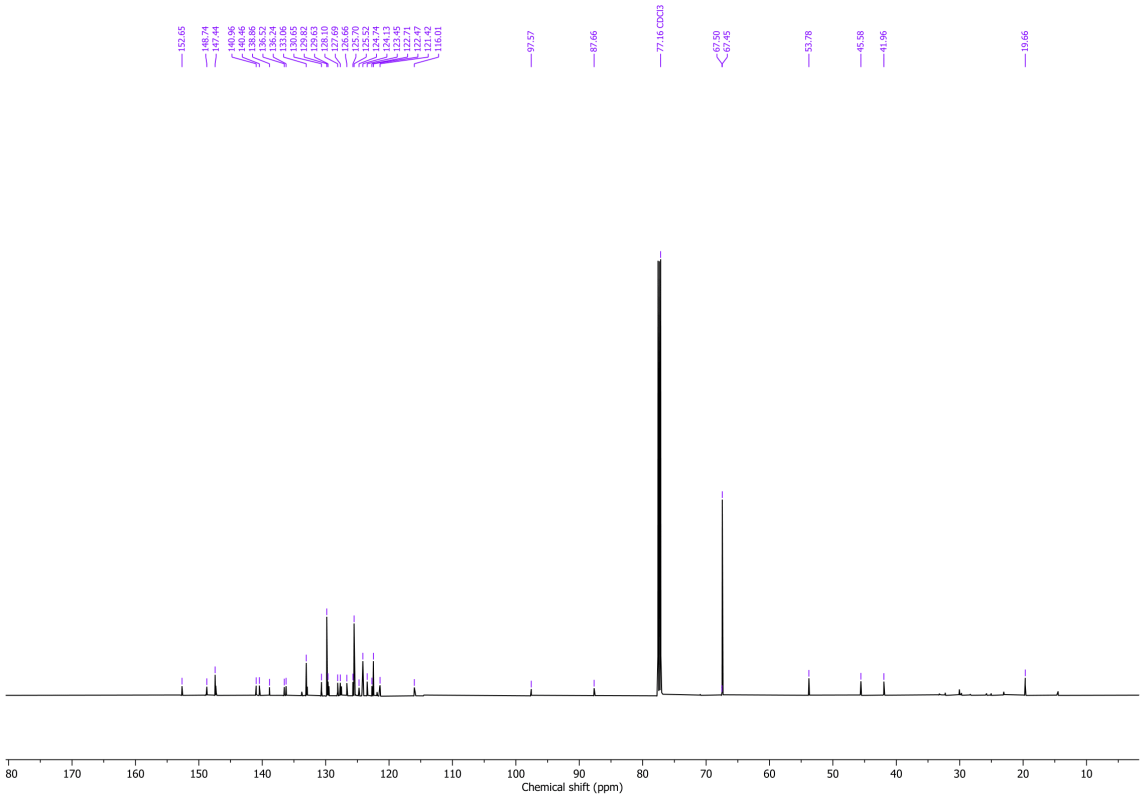


Figure S22. ^{13}C-NMR spectra of **MM**.

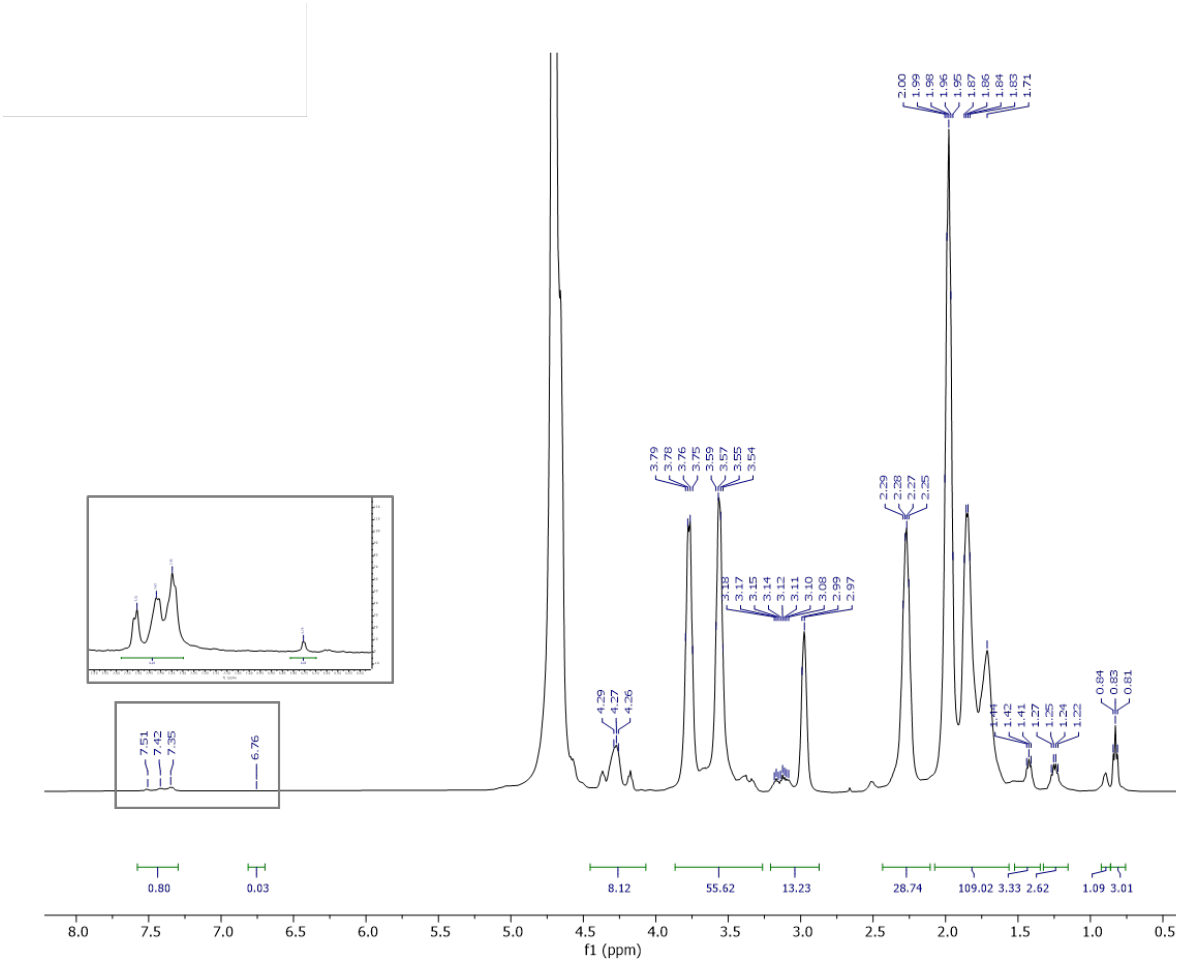


Figure S23. ^{1}H-NMR spectra of **PP-VC.** Adapted from Pegoraro et al. [14].

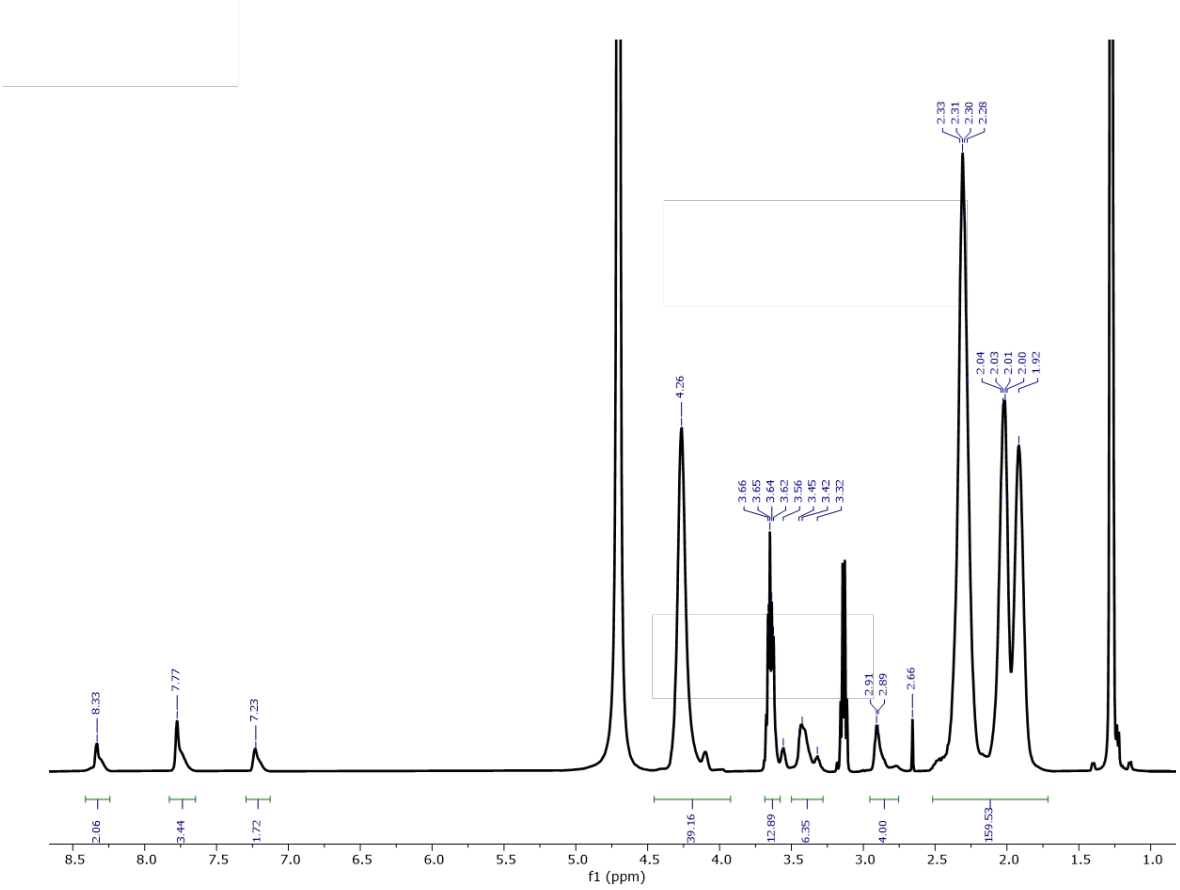


Figure S24. ^{1}H-NMR spectra of **PG-PD.** Adapted from Pegoraro et al. [14].

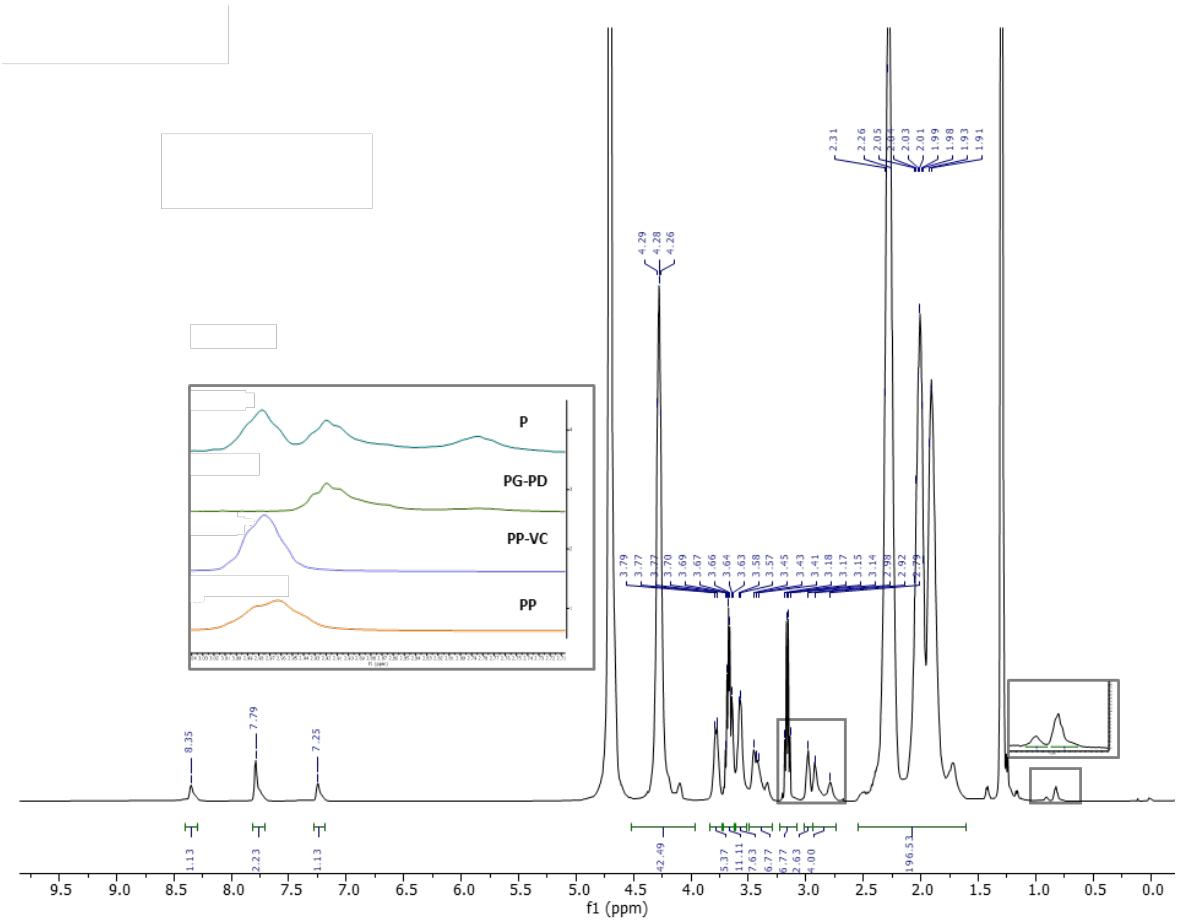


Figure S25. ^{1}H-NMR spectra of **P.** Adapted from Pegoraro et al. [14].

18. Statistical Analysis

Data from the experiments was analyzed using a t-test. We considered differences significant in all cases when p****<0.0001; p***<0.001; p**<0.01; p*<0.05; ns: not significant.

6.4 Annex 4: Supplementary Material of Manuscript IV

Reference scientific article III[346]: Pegoraro, C.; Masiá Sanchis, E.; Đorđević, S.; Dolz-Pérez, I.; Huck-Iriart, C.; Herrera, L.; Esteban-Pérez, S.; Conejos-Sanchez, I.; Vicent, M. J. Multifunctional Polypeptide-Based Nanoconjugates for Targeted Mitochondrial Delivery and Nonviral Gene Therapy. *Chem. Mater.* **2025**. DOI: 10.1021/acs.chemmater.4c02742.

Supporting information

Multifunctional Polypeptide-Based Nanoconjugates for Targeted Mitochondrial Delivery and Non-Viral Gene Therapy

Camilla Pegoraro[1], Esther Masiá Sanchis[1,2,3], Snežana Đorđević[1,2#], Irene Dolz-Pérez[5], Cristián Huck-Iriart[4], Lidia Herrera[5], Sergio Esteban-Pérez[5], Inmaculada Conejos-Sanchez[1,2], and María J. Vicent[1,2,3*]*

[1]Príncipe Felipe Research Center, Polymer Therapeutics Lab., 46012 Valencia, Spain

[2]Centro de Investigación Biomédica en Red en Cáncer (CIBERONC), Instituto de Salud Carlos III, Spain

[3]Príncipe Felipe Research Center, Screening Platform., 46012 Valencia, Spain

[4]ALBA Synchrotron Light Source, Experiments Division, 08209 Cerdanyola del Vallès, Spain

[5] Curapath, Av. Benjamin Franklin 19, 46980, Paterna, Valencia, Spain

*Co-corresponding Authors: Dr Inmaculada Conejos-Sánchez E-mail: iconejos@cipf.es and Prof. María J. Vicent, E-mail: mjvicent@cipf.es

KEYWORDS: mitochondrial targeting, gene therapy, nanoconjugate, polypeptides cytosolic delivery, endosomal escape

1. Materials and General Procedures

All reactions involving oxygen-sensitive reagents were performed under a nitrogen atmosphere. Poly-L-ornithine (PLO, 5700 g mol^{-1}, n = 50) was provided by Curapath (Valencia, Spain). 4-(4,6-dimethoxy-1,3,5-triazin-2-yl)-4-methylmorpholinium tetrafluoroborate salt (DMTMM BF4) was synthesized according to Kamiński et al.[1]. All other chemicals were reagent grade and used without further purification. The heterobifunctional poly(ethylene glycol) (PEG) derivative MeO-PEG_{3000}-NHS (3023 g mol−1; NHS = N-hydroxysuccinimide and MeO = methoxy) was purchased from Biopharma PEG (USA). (3-carboxypropyl)triphenylphosphonium bromide (CTPB), N,N-dimethyl aminopyridine (DMAP), diisopropylethylamine (DIEA), anhydrous dimethylformamide (DMF), dimethylsulfoxide (DMSO), and methanol (MeOH) were purchased from Sigma Aldrich (USA). The fluorophores $Atto_{488}$-NHS and cyanine5-NH_2 (Cy5-NH_2) were purchased from ATTO-TEC GmbH (Germany) and Lumiprobe GmbH (Germany). Dichloromethane (DCM) was purchased from Acros Organics (Belgium). Diethyl ether (Et_2O) and deuterated solvents such as D_2O and $CDCl_3$ were purchased from VWR Chemicals (USA). Trifluoroacetic acid (TFA) was purchased from Tokyo Chemical Industry (Japan). Piperidine was purchased from Merck Schuchardt OHG (Germany). Fmoc-L-Nw-boc-β-homolysine (Lys) and 3,3'-dithiopropionic acid di(N-succinimidyl ester) (S-S linker derivative) were purchased from ABCR GmbH (Germany). Acetonitrile (liquid chromatography-mass spectrometry (LC-MS) grade) was obtained from AppliChemGmbh. Water and formic acid (FA) (LC-MS grade) were purchased from Fisher Scientific (USA). Thin-layer chromatography used aluminum sheets coated with silica gel 60F254 (Merck). Compounds were visualized with an ultraviolet (UV) lamp. Vivaspin® 2000 Da molecular weight cut-off (MWCO) and PD-10 desalting columns packed with Sephadex G-25 resin were purchased from Sartorius (Germany) and Cytiva (Sweden). Solid-phase extraction (SPE) cartridges (Silica; 1 g/6 mL) were purchased from Led Techno (Netherlands).

Dulbecco's Modified Eagle's Medium F-12 Nutrient Mixture (DMEM/F-12), high glucose DMEM, high glucose/no phenol red DMEM, phosphate-buffered saline (PBS), fetal bovine serum (FBS), penicillin (P), streptomycin (S), and trypsin were purchased from Gibco Life Technologies (USA). 3-(4,5-dimethylthiazol-2-yl)-5-(3-carboxymethoxyphenyl)-2-(4-sulfophenyl)-2H-tetrazolium (MTS) and phenazine methosulfate (PMS) (MTS/PMS) and Bright-Glo Luciferase Assay kits were purchased from Promega (Spain). The pCMV-Luc (pDNA-Luc) plasmid was purchased from Plasmid Factory (Germany). The intercalating agent GelRed was purchased from VWR (USA). 6X Orange DNA Loading Dye, B-27™ Supplement (50X) minus vitamin A (B27 – vitamin A), agarose (Molecular Biology Grade), and Hoechst 33342 were purchased from ThermoFisher Scientific (USA). Human epidermal growth factor (EGF) was purchased from Sigma Aldrich. Tris(hydroxymethyl)aminomethane (Tris base), acetic acid, and ethylenediaminetetraacetic acid (EDTA) were purchased from Sigma Aldrich (USA). JetPEI® was purchased from Sartorius (Germany).

^{1}H-NMR experiments. NMR spectra were acquired at 27 ˚C (298 K) on a 300 MHz Bruker spectrometer with a broadband 5 mm broadband fluorine observe (BBFO) probe and 60-sample automation system. Data were processed using the software Mestrenova (Bruker GmbH, Karlsruhe, Germany). Samples were prepared at the desired concentration (10-20 mg/mL) in deuterated chloroform ($CDCl_3$) or deuterated water (D_2O). Chemical shifts shown as parts per million relative to the residual solvent signal. Multiplets in ^{1}H NMR spectra are designated as s (singlet), d (doublet), t (triplet), dd (doublet of doublet), or m (multiplet).

Direct mass spectrometry scan (Q1 MS SCAN). Analysis was performed using an ExionLC system comprising a pump, AC autosampler, AC Column oven, and AB Sciex QTRAP 4500 (Sciex, Singapore). Eluent A was H_2O with 0.1% FA, and eluent B was acetonitrile. All Q1 MS scans were performed with a 20 µL injection volume, 1 min scanning time, 0.5 ml/min flow rate, 50% eluent B, oven temperature 40˚C, 250˚C electrospray ionization (ESI) source temperature, 20 V curtain gas, ionization spray voltage of 5500 V, declustering potential 62 V, entrance potential 2 V, and exit potential 5 V. Data were analyzed using Analyst software (Sciex, Singapore).

Dynamic light scattering (DLS). Measurements were performed at 25˚C using a Malvern ZetaSizer NanoZS instrument with a 532 nm laser at a fixed scattering angle of 173˚. Polyplex solutions (in PBS, at C-TRV3-A = 0.02 mg/ml) were measured in disposable plastic cuvettes (Waters, Wyatt Technology, USA), assessing

size distribution by number (hydrodynamic diameter (Dh) in nm). Measurements were conducted with n > 3 for each sample. Automatic optimization of beam focusing and attenuation was applied. Zeta potential was measured using disposable folded capillary cells (Malvern Instruments Ltd., UK) under the same conditions, with 50 sub-runs of 10 seconds each at 25 ˚C (n = 3).

Transmission electron microscopy (TEM). Samples were examined with an FEI Tecnai Spirit BioTwin transmission electron microscope (TEM; ThermoFisher Scientific, USA) and a Morada digital camera (EMSIS GmbH, Germany). Twenty images of ten distinct cells were captured for each sample, with one set at 1900x magnification and another at 11000x magnification. Samples dissolved in PBS were deposited onto carbon-coated 200 mesh copper grids. Any excess sample was removed via capillary action using filter paper. The grids were then immediately negatively stained with 2% (w/v) uranyl acetate solution for 30 s. Excess stain was similarly removed by capillary action. The prepared grids were allowed to air dry before imaging.

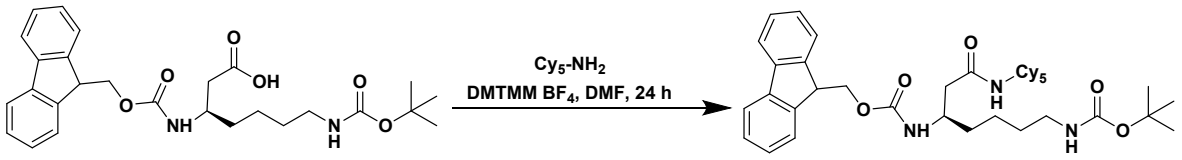
Small-angle X-ray Scattering. Small-angle X-ray Scattering (SAXS) measurements were performed at the NCD-SWEET beamline at the ALBA synchrotron (Barcelona, Spain; project ID 2022097124). The sample-to-detector distance was set to 6.57 m with an incident beam energy of 12.4 keV. A Pilatus 1M detector (Dectris, Switzerland) was employed for data collection. Polymer solutions (2 mg/mL) were prepared and placed in a custom-built sample holder for liquid samples. The total exposure time per sample was approximately 1 min, following careful exclusion of any radiation damage effects. Azimuthal integration of the SAXS patterns was performed using the pyFAI software package[2], resulting in one-dimensional (1D) scattering profiles. The scattering intensity (I) was plotted as a function of the momentum transfer vector q, where $q = 4\pi \sin(\theta)/\lambda$ with θ representing the scattering angle and λ the wavelength of the incident X-rays. A fractal coil model[3], incorporating an excluded volume parameter of 1/3, was applied to interpret the scattering data from the high-qq region (Porod region), where a linear slope in the log-log plot was observed.

Isolation of plasma and red blood cells. Red blood cells and plasma were isolated from fresh mouse blood collected via cardiac puncture after death and placed in a tube containing an anticoagulant (0.5 M EDTA at a 1/10 volume) on ice. The blood was then diluted with PBS (pH 7.4) to a final volume of 10 mL and subjected to centrifugation at 3000 rpm for 10 min at 4 ˚C, repeating this step three times. After

centrifugation, the supernatant (plasma) was carefully separated from the pellet (red blood cells) and used separately for polyplex stability and hemocompatibility experiments. Animal experiments were performed in accordance with the European Communities Council Directive (86/609/ECC) guidelines and by the Spanish Royal Decree 1201/2005 and were approved by the Institutional Animal Care and Use Committee, and accomplished by accredited and trained staff, meeting the animal care rules. The animals were maintained in a specific-pathogen-free facility, with controlled temperature and humidity, using a 12-h light-dark cycle. Food pellets and water were provided as ad-libitum during the whole experiment. Eight-week-old female Balb/c mice were used for blood extractions. All the experimental procedures were purchased from Harlan Laboratories Inc. (Spain, EU) or Envigo Laboratories Ltd. (Spain, EU) and housed in the animal facility of the Príncipe Felipe Research Center. Mice were euthanized according to ethical protocols. For the isolation of human plasma, samples 3622 and 3387 (patient (pt) 2 and 3) were obtained from Columbus Explorer/Tyris, while sample 9928 (patient (pt) 1) was isolated in our laboratory. The protocol for the latter is referenced as REF: DICTAMEN CEI 20220128_04, approved by the Research Ethics Committee of the General Directorate of Public Health and the Superior Center for Public Health Research (CEI DGSP-CSISP).

2. Preparation of C-TRV3-A

2.1. Synthetic procedure for TRV3 preparation



Scheme S1. Synthetic procedure for preparing Lys-Cy5 (S2)

In a two-neck bottom flask, Fmoc-L-Nw-boc-β-homolysine (Lys, **S1**) was dissolved in anhydrous DMF (35.4 mg, 1.20 eq., 5 mg/mL), while the carboxylic group was activated with DMTMM BF4 (48.2 mg, 2.40

eq) dissolved in 0.5 mL anhydrous DMF. Activation proceeded for 20 min. Cy5-NH_2 (40 mg, 1 eq., 10 mg/mL) solution in anhydrous DMF was added to the previous solution. The pH was adjusted (pH 8) with DIEA. The reaction was left to proceed for 24 h at room temperature and protected from light. The solvent was removed under reduced pressure, and the product (**S2**) was directly collected for the following reactions and analyzed via NMR and a Q1 MS scan.

^{1}H NMR (300 MHz, CDCl3, 25˚C) δ 9.3 (NH amide, 2H), 7.9 (NH amide, 1H), 7.7 (d, 2H, a), 7.6 (d, 2H, d), 7.4-7.2 (m, 12H, b, c, y, z, a_1, b_1, j_1, k_1, l_1, m_1), 7.1 (t, 1H, f_1), 6.74 (dd, 2H, d_1, h_1), 6.22 (dd, 2H, g_1, e_1), 4.3 (dd, 2H, f), 3.76-3.52 (m, 4H, e, g, x) 3.30 – 3.0 (m, 6H, k, n, s), 2.51-2.27 (m, 2H, m), 1.60-1.20 (m, 43H, h, i, j, l, o, p, q, r, u, t, v, w, c_1, i_1).

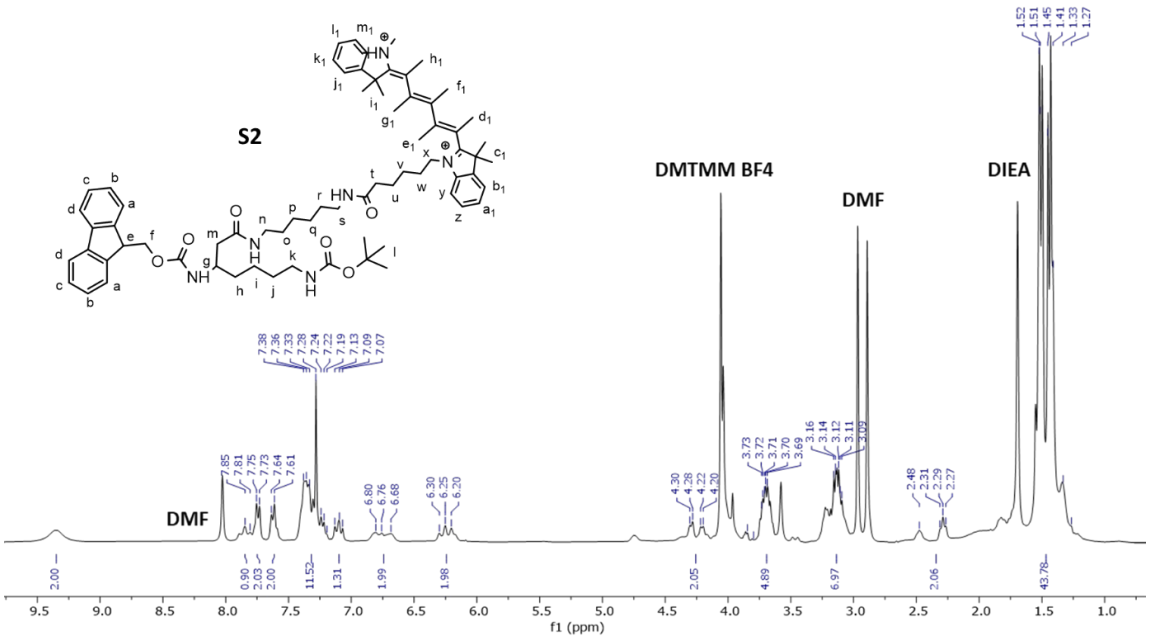


Figure S1. ^{1}H-NMR spectra of S2 in $CDCl_3$

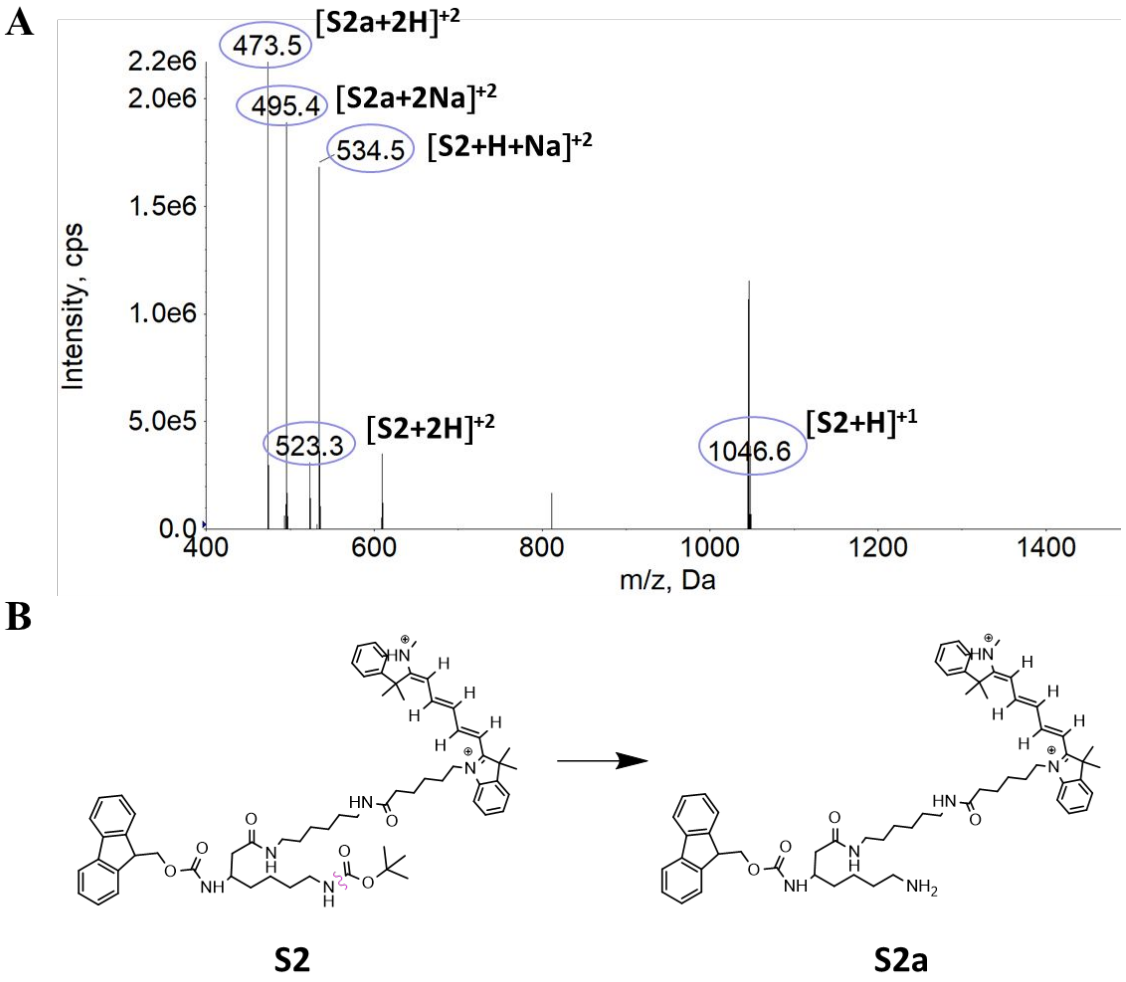
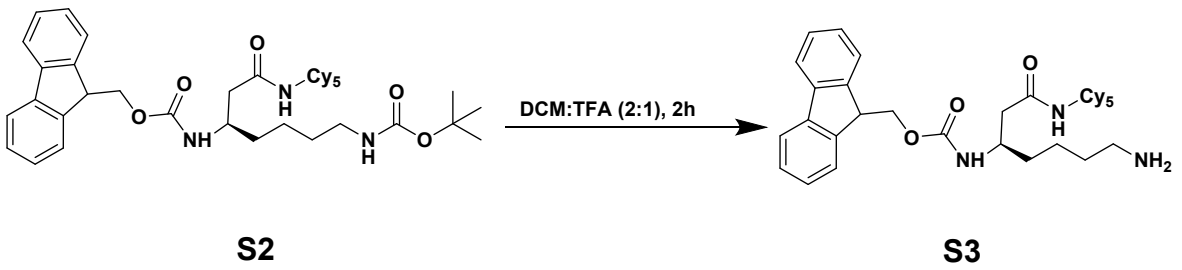


Figure S2. Qualitative analysis of S2. Direct MS analysis enabled the **A**) identification according to the MS/MS spectra of **S2** (centroid m/z values and background subtracted spectra) and **B**) the fragmentation mechanism



Scheme S2. Synthetic procedure for Boc deprotection of S2 to obtain S3

S2 (theoretical yield: 68.4 mg) was dissolved in a 2:1 mixture of DCM and TFA, left stirring at room temperature, and protected from light for 2 h. The Boc-deprotected product (**S3**) was precipitated in cold Et_2O while stirring, then incubated at -20˚ for 1 h, centrifuged, and the pellet lyophilized overnight. The purified product **S3** was analyzed via ^{1}H NMR and a Q1 MS scan. Yield: 85% (58.1 mg).

^{1}H NMR (300 MHz, $CDCl_3$, 25˚C) δ 9.3 (NH amide, 1H, NH_2, 2H, traces of TFA), 7.9 (NH amide, 1H), 7.7 (d, 2H, a), 7.6 (d, 2H, d), 7.4-7.2 (m, 12H, b, c, y, z, a_1, b_1, j_1, k_1, l_1, m_1), 4.3 (dd, 2H, f), 3.76-3.52 (m, 4H, e, g, x, traces of Et_2O) 3.30 – 3.0 (m, 6H, k, n, s), 2.51-2.27 (m, 2H, m), 1.60-1.20 (m, 34H, h, i, j, o, p, q, r, u, t, v, w, c_1, i_1).

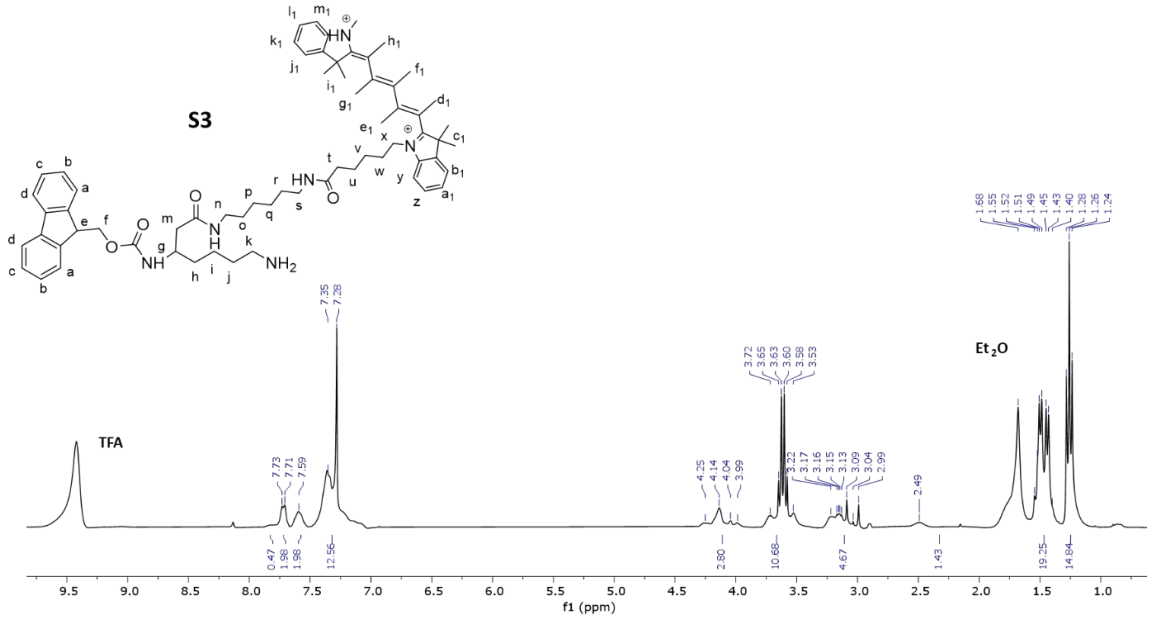


Figure S3. ^{1}H-NMR spectra of S3 in $CDCl_3$

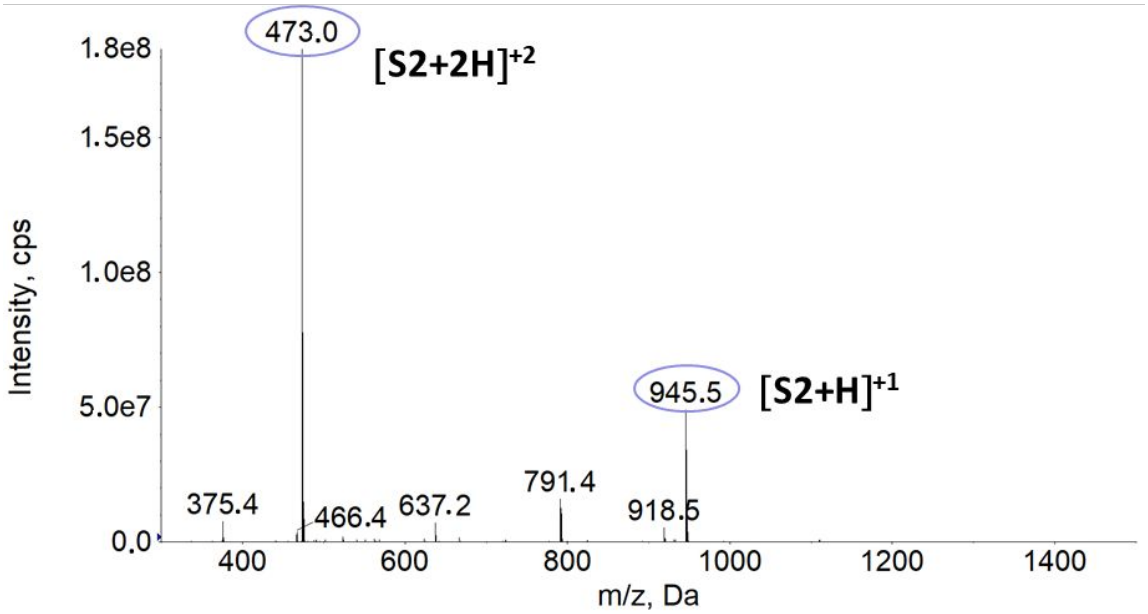
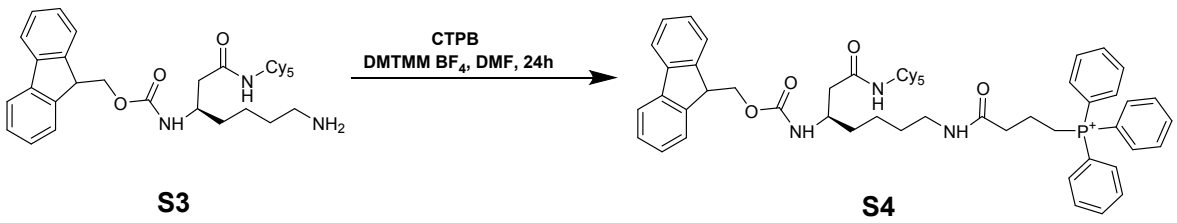


Figure S4. Qualitative analysis of S3. Direct MS analysis enabled the identification according to the MS/MS spectra of S3 (centroid m/z values and background subtracted spectra).



Scheme S3. Synthetic procedure for preparing Lys-Cy5-TPP (S4)

In a two-neck bottom flask, **S3** was dissolved in anhydrous DMF (58.1 mg, 1 eq., 7 mg/mL). CTPB (TPP derivative, 31.6 mg, 1.20 eq., 4 mg/mL) was dissolved in anhydrous DMF, and the carboxylic group was activated with DMTMM BF4 (48.3 mg, 2.4 eq.) dissolved in 0.5 mL anhydrous DMF. The activation proceeded for 20 min. The solution was then added to the **S3** solution. The pH was adjusted (pH 8) with DIEA. The reaction proceeded for 24 h at room temperature and protected from light. The product (**S4**) was

precipitated in cold Et_2O while stirring, then incubated at -20˚ for 1 h, centrifuged, and the pellet lyophilized overnight. The purified product **S4** was analyzed via ^{1}H NMR and a Q1 MS scan.

^{1}H NMR (300 MHz, $CDCl_3$, 25˚C) δ 9.3 (NH amide, 2H), 7.9-7.5 (m, 20H, NH amide, a, d, q_1), 7.4-7.2 (m, 13H, b, c, y, z, a_1, b_1, j_1, k_1, l_1, m_1, f_1), 6.74 (dd, 2H, d_1, h_1), 6.22 (dd, 2H, g_1, e_1), 4.3 (dd, 2H, f), 3.76-3.52 (m, 4H, e, g, x) 3.30 – 3.0 (m, 6H, k, n, s), 2.51-2.27 (m, 2H, m), 1.60-1.20 (m, 40H, h, i, j, o, p, q, r, u, t, v, w, c_1, i_1, n_1, o_1, p_1).

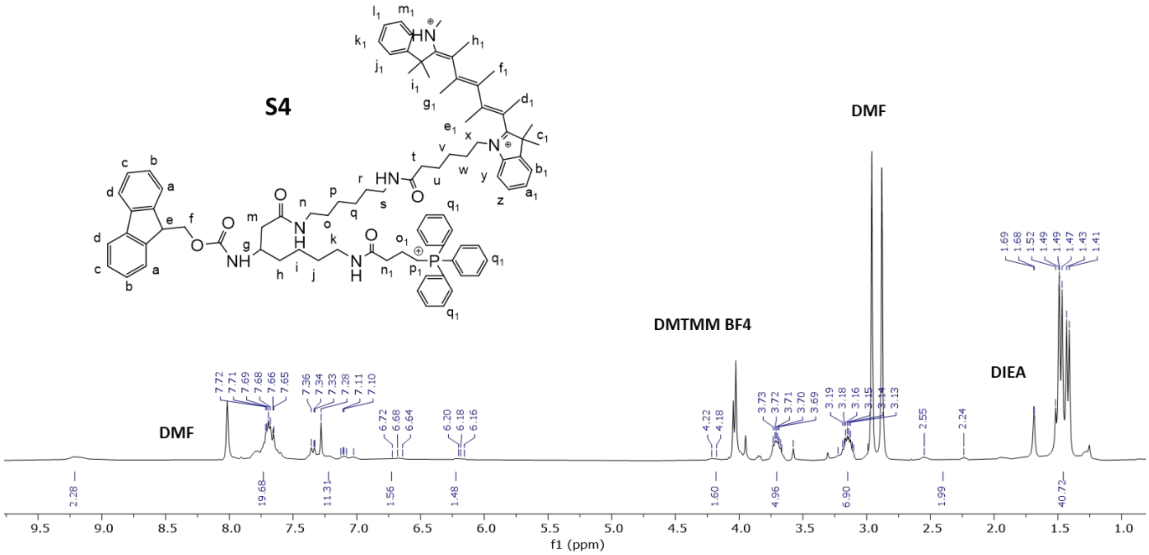


Figure S5. ^{1}H-NMR spectra of S4 in $CDCl_3$

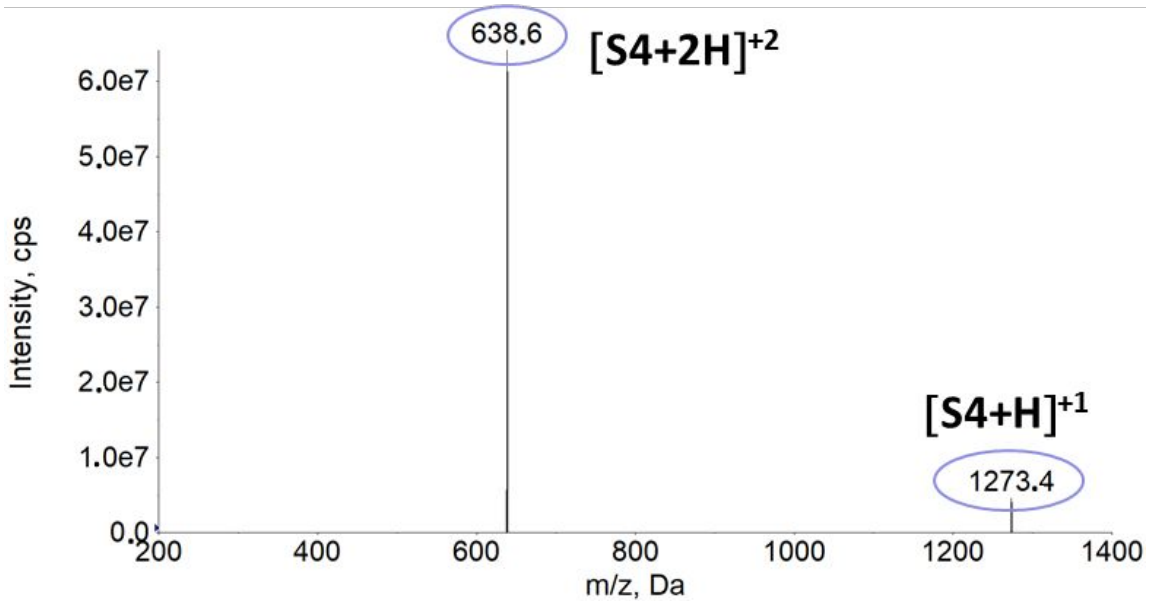
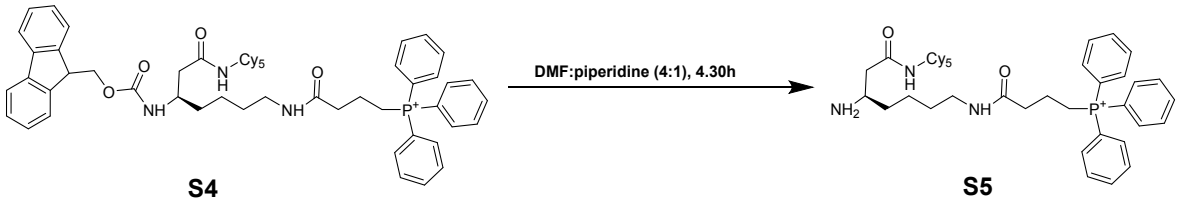


Figure S6. Qualitative analysis of S4. Direct MS analysis enabled the identification according to the MS/MS spectra of S4 (centroid m/z values and background subtracted spectra).



Scheme S4. Synthetic procedure for Fmoc deprotection of S4 to obtain S5

S4 (theoretical yield: 83.4 mg) was dissolved in a 4:1 mixture of DMF and piperidine, left stirring at room temperature, and protected from light for 4.5 h. Fmoc deprotection was monitored over time (30, 75, 120, 180, and 240 min) by MS until complete reaction. The Fmoc-deprotected product (**S5**) was precipitated in cold Et_2O while stirring, then incubated at -20˚ for 1 h, centrifuged, and the pellet lyophilized overnight. The purified product **S5** was analyzed via ^1H NMR and a Q1 MS scan. Yield: 78% (65 mg).

^{1}H NMR (300 MHz, $CDCl_3$, 25°C) δ 7.9-7.5 (m, 16H, NH amide, q_1), 7.4-7.2 (m, 9H, y, z, a_1, b_1, j_1, k_1, l_1, m_1, f_1), 6.74 (dd, 2H, d_1, h_1), 6.22 (dd, 2H, g_1, e_1), 3.35 – 3.0 (m, 9H, g, x, k, n, s), 2.51-2.27 (m, 2H, m), 1.60-1.20 (m, 40H, h, i, j, o, p, q, r, u, t, v, w, c_1, i_1, n_1, o_1, p_1)

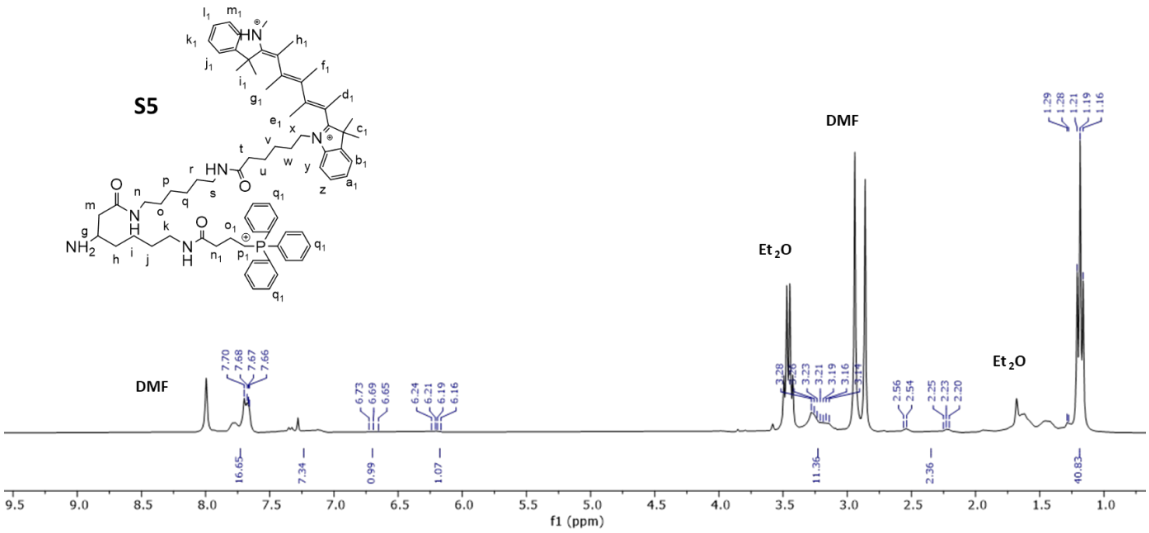


Figure S7. ^{1}H-NMR spectra of S5 in $CDCl_3$

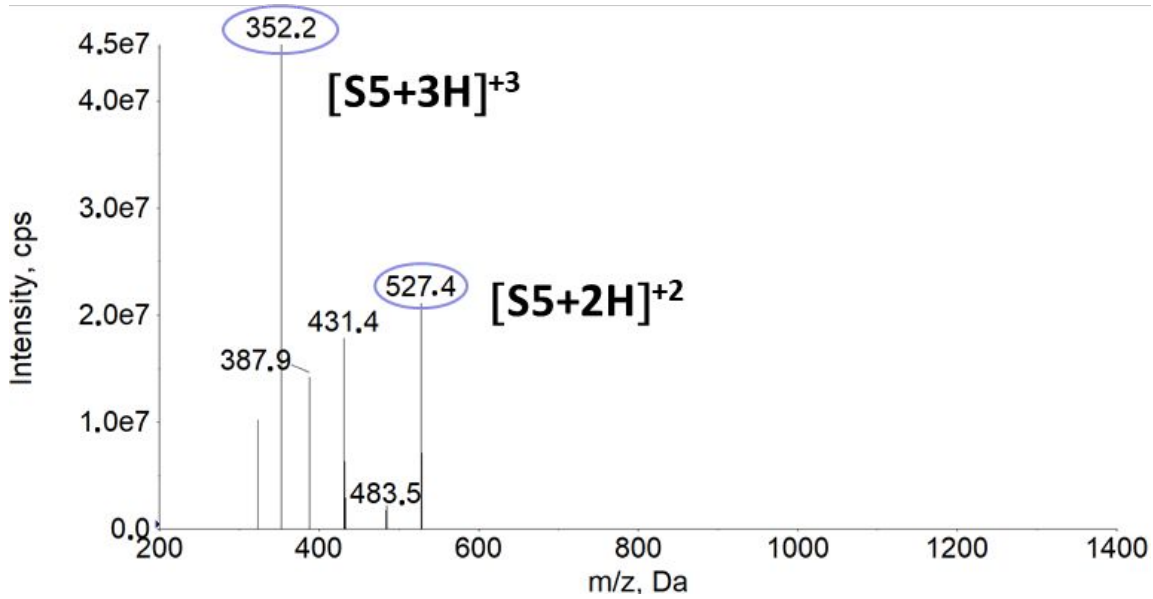
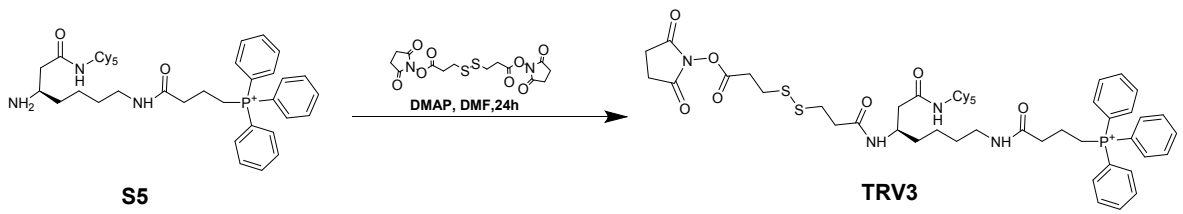


Figure S8. Qualitative analysis of S5. Direct MS analysis enabled the identification according to the MS/MS spectra of S5 (centroid m/z values and background subtracted spectra).



Scheme S5. Synthetic procedure for preparing TRV3

In a two-neck bottom flask, **S5** was dissolved in anhydrous DMF (65 mg, 1 eq., 7 mg/mL). In a glass vial, the S-S linker derivative was dissolved in 1 mL anhydrous DMF (50.1 mg, 2 eq., 5 mg/mL) and added to the previous solution, followed by a catalytic amount of DMAP. The pH was adjusted (pH 8) with DIEA. The reaction was left to proceed for 24 h at room temperature and protected from light. The product (**TRV3**) was purified using SPE with silica cartridges (1 g/6 mL). Elution was performed using a gradient mobile phase of DCM and MeOH. The purified product **TRV3** was analyzed via ^{1}H NMR and a Q1 MS scan. Yield: 70% (57.9 mg).

^{1}H NMR (300 MHz, $CDCl_3$, 25°C) δ 7.9-7.5 (m, 16H, NH amide, q_1), 7.4-7.2 (m, 9H, y, z, a_1, b_1, j_1, k_1, l_1, m_1, f_1), 6.74 (dd, 2H, d_1, h_1), 6.22 (dd, 2H, g_1, e_1), 3.70 – 3.0 (m, 9H, g, x, k, n, s), 2.67 (s, 4H, v_1), 2.57-1.90 (m, 10H, m), 1.60-1.20 (m, 40H, h, i, j, o, p, q, r, u, t, v, w, c_1, i_1, n_1, o_1, p_1).

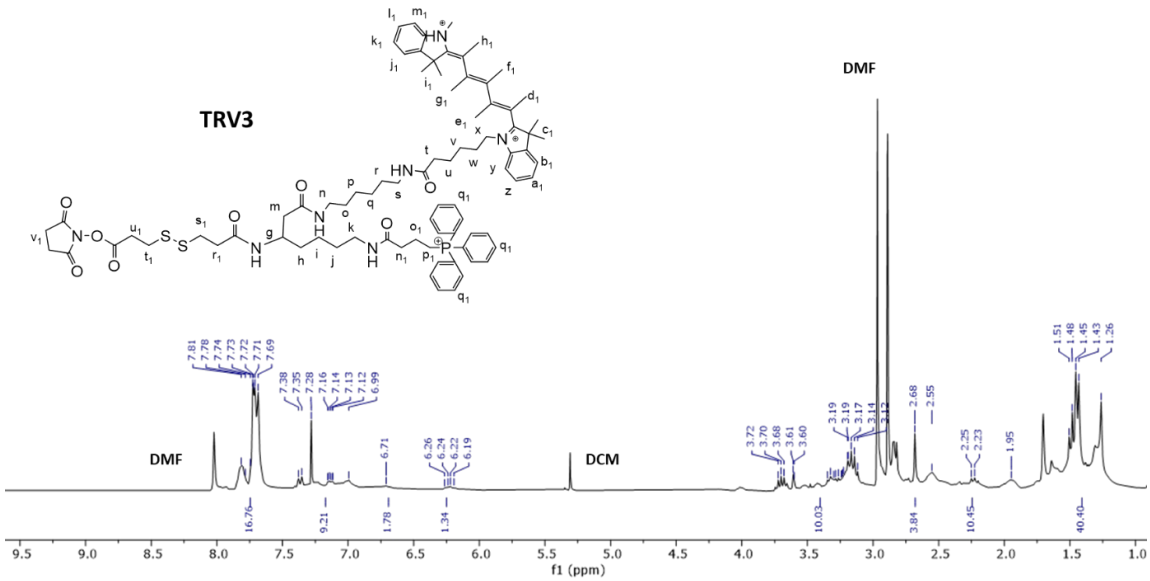


Figure S9. ^{1}H-NMR spectra of TRV3 in $CDCl_3$

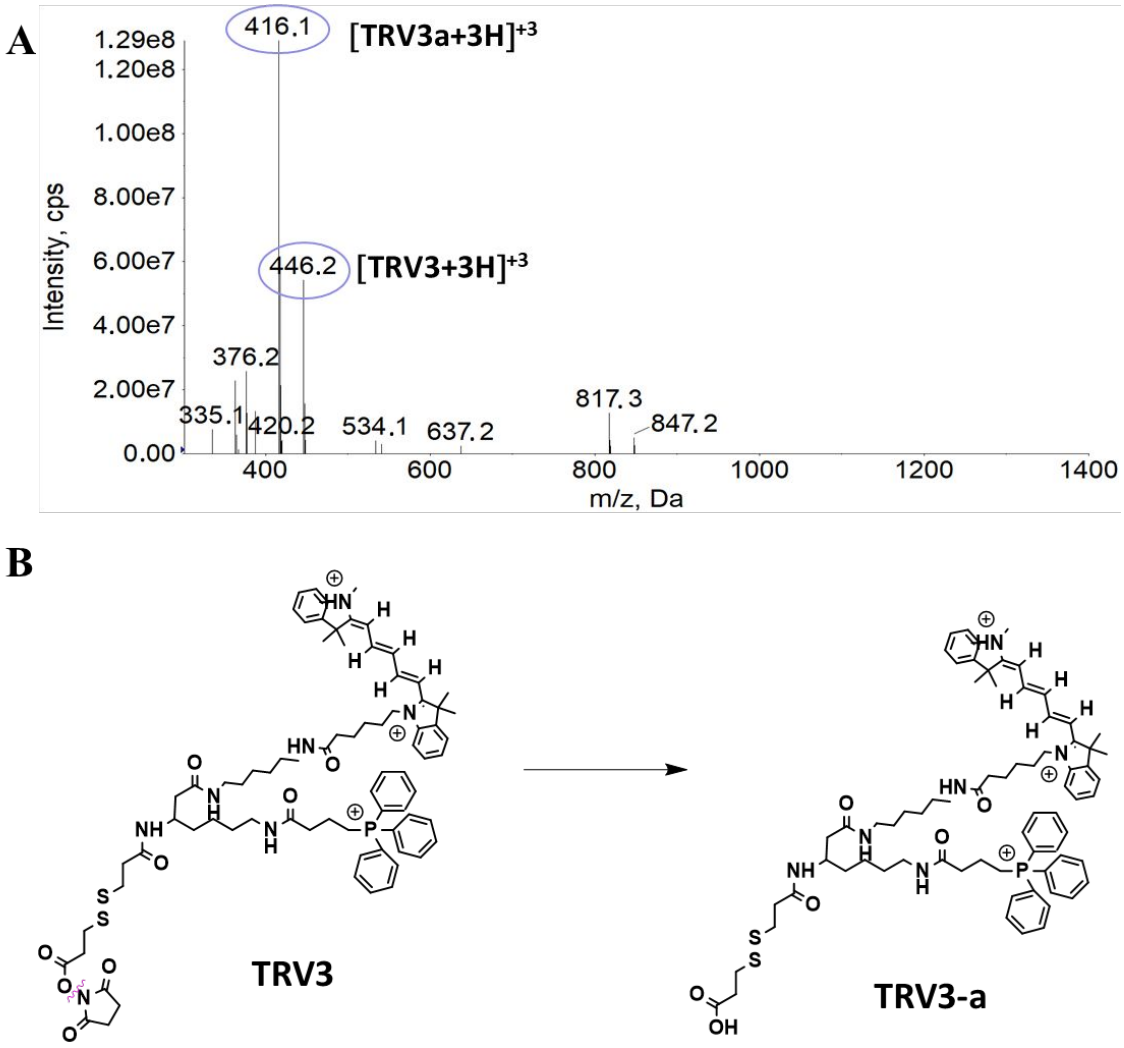
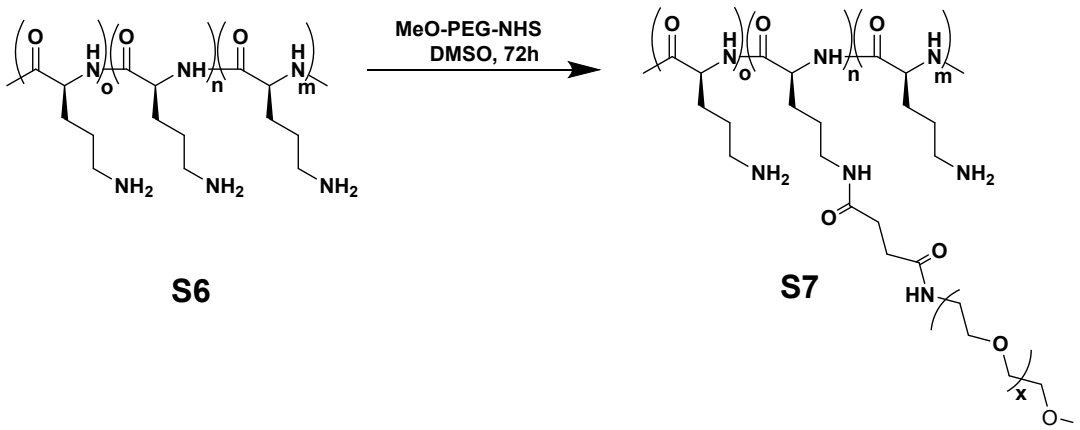


Figure S10. Qualitative analysis of TRV3. Direct MS analysis enabled the **A**) identification according to the MS/MS spectra of TRV3 (centroid m/z values and background subtracted spectra) and **B**) the fragmentation mechanism

2.2. Synthetic procedure for PLO-PEG preparation



Scheme S6. Synthetic procedure for preparing PLO-PEG (S7)

In a two-neck bottom flask, PLO was dissolved in anhydrous DMSO (200 mg, 1 eq., 20 mg/mL). In a glass vial, MeO-PEG_{3000}-NHS was dissolved in 1 mL anhydrous DMSO (i.e., 123 mg, 0.04 eq. for 4% mol PEG modification) and added to the previous solution, followed by a catalytic amount of DMAP. The pH was adjusted (pH 8) with DIEA. The reaction was left to proceed for 72 h at room temperature. The solvent was removed under reduced pressure, and the product (**S7**) was resuspended in 300 µL Milli-Q water and purified by size exclusion chromatography (PD-10 desalting columns packed with Sephadex G-25). The purified product **S7** was analyzed via ^{1}H NMR. PEG functionalization was calculated by ^{1}H-NMR analysis (mol %), resulting in 3.6 % mol functionalization. Conjugation efficiency = 90%

^{1}H NMR (300 MHz, $CDCl_3$, 25˚C) 4.40 – 4.30 (m, 1H, Cα of PLO), 3.66 (m, 4H, NHCH2CH2O) 3.05 - 2.98 (m, 2H, Cδ of PLO; 4H CH2 of CH2CH2O), 1.88 – 1.69 (m, 4H Cβ+γ of PLO; 4H NHOCH2CH2ONH).

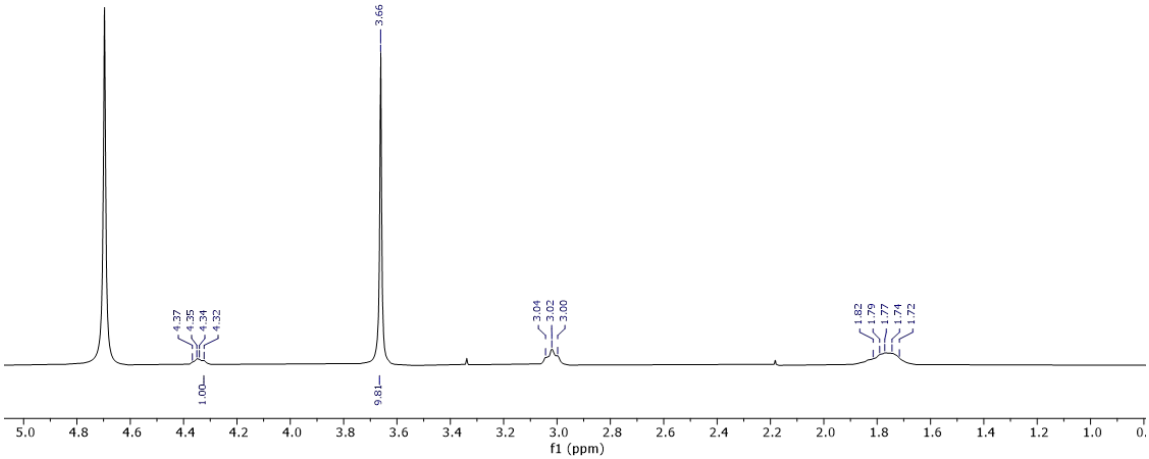
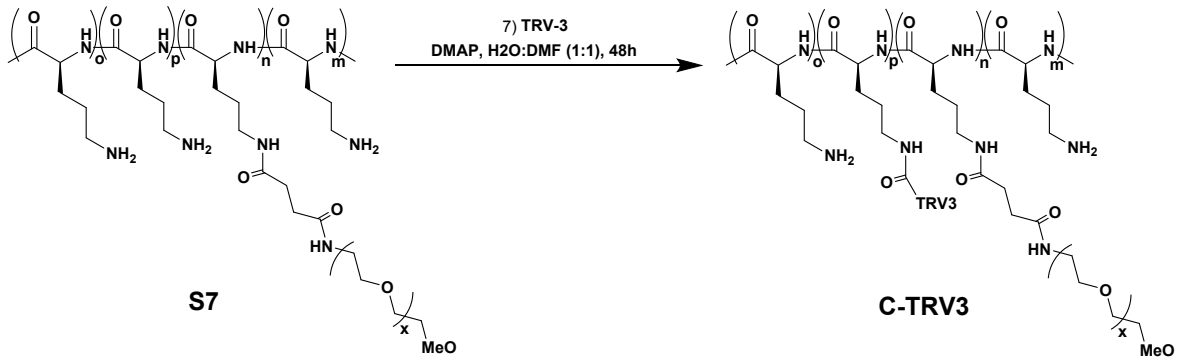


Figure S11. ^{1}H-NMR spectra of S7 in D_2O. The peaks of Cα of PLO and NHCH2CH2O (4H) were used to calculate the %mol of PEG functionalization.

2.3. Synthetic procedure for preparing C-TRV3



Scheme S7. Synthetic procedure for preparing C-TRV3

In a two-neck bottom flask, **S7** was dissolved in anhydrous DMSO (100 mg, 1 eq., 4 mg/mL). In a glass vial, **TRV3** was dissolved in 1 mL anhydrous DMF (i.e., 53.7 mg, 0.10 eq for 10% mol TRV3 modification) and added to the previous solution, followed by DMAP (cat.). The pH was adjusted (pH 8) with DIEA. The

reaction was left to proceed for 24 h at room temperature and protected from light. The solvent was removed under reduced pressure. The product (**C-TRV3**) was resuspended in 300 µL Milli-Q water and purified by size exclusion chromatography (PD-10 desalting columns packed with Sephadex G-25) and Vivaspin®, 2000 MWCO Da. The purified product **C-TRV3** was analyzed via ^{1}H NMR. **TRV3** functionalization was calculated by ^{1}H-NMR analysis (mol %), resulting in 4 % mol. Moreover, to quantify the presence of Cy5 in the final product **C-TRV3**, Cy5 loading was calculated by fluorescence using the CLARIOstar fluorescent plate reader. The corresponding free dye (DMF:H2O) calibration curve was prepared in dark 96-Well multiwell plates. Fluorescence was measured at λ_{ex}: 632 nm λ_{em}: 684 nm for Cy5-NH2. The % wt of Cy5 < 1%. Conjugation efficiency = 40%.

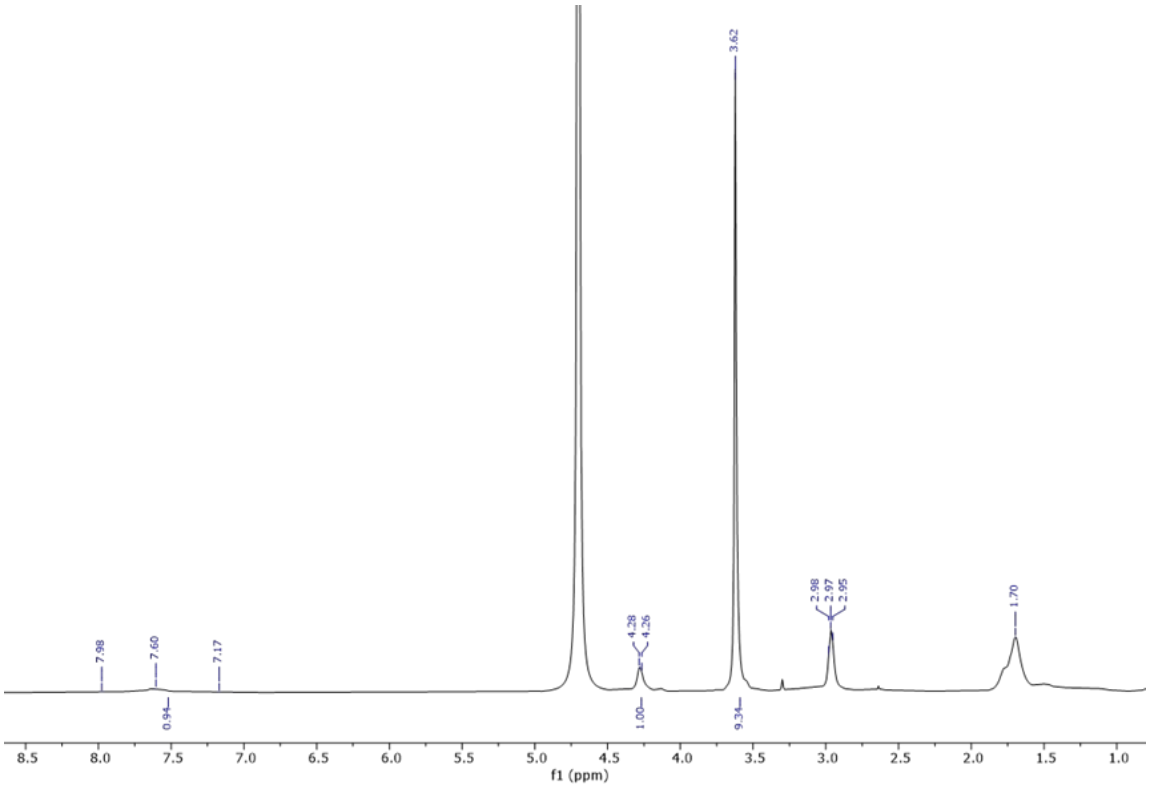


Figure S12. ^{1}H-NMR spectra of C-TRV3 in D_2O. The peaks of Cα of PLO and the aromatic peaks of TRV3 (m, 23Hy, z, a_1, b_1, j_1, k_1, l_1, m_1, q_1) were used to calculate the %mol of TRV3 functionalization.

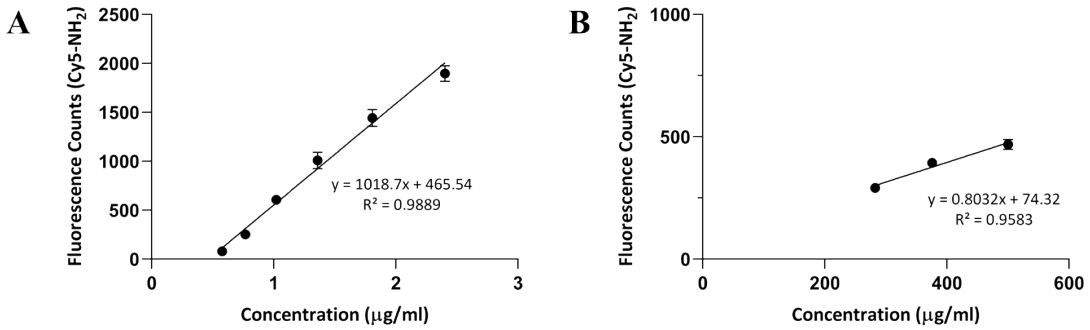
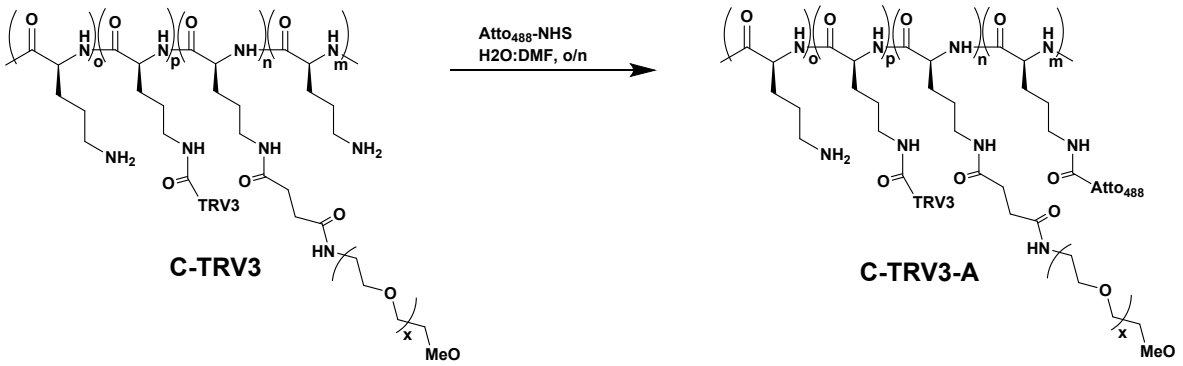


Figure S13. Fluorescence calibration curves of (**A**) Cy5-NH2 and (**B**) **C-TRV3** in DMF:H_2O for dye quantification. % wt Cy5 in **C-TRV3** = 0.03%.

2.4. Fluorescence labeling of C-TRV3 with $Atto_{488}$-NHS



Scheme S8. Labeling of C-TRV3 with $Atto_{488}$ to obtain C-TRV3-A

In a one-neck bottom flask, **C-TRV3** was dissolved in Milli-Q water (1 eq., 10 mg/mL). In a glass vial protected from light, $Atto_{488}$-NHS was dissolved in DMSO and added to C-TRV3 (0.010 eq., 1.0% mol). The pH was adjusted with 1M sodium bicarbonate (pH 8). The reaction was allowed to proceed overnight, protected from light, and analyzed via thin-layer chromatography (MeOH as mobile phase). After DMSO

elimination using a rotavapor and freeze-drying, the product was purified by size exclusion chromatography (PD-10 desalting columns packed with Sephadex G-25). Dye loading was calculated by fluorescence using the CLARIOstar fluorescent plate reader. First, the corresponding free dye (DMF:H_2O) calibration curve was prepared in black 96-well multiwell plates. Fluorescence was measured at λ_{ex}: 500 nm λ_{em}: 520 nm for A488-NHS. Conjugation efficiency = 90-100%.

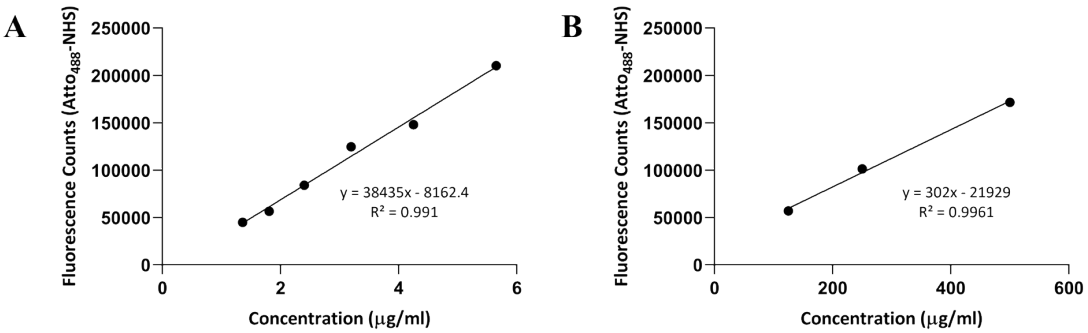


Figure S14. Fluorescence calibration curves of (**A**) $Atto_{488}$-NHS and (**B**) C-TRV3-A in DMF:H_2O for dye quantification. % wt $Atto_{488}$ in **C-TRV3-A** = 1%.

3. Biological characterization of C-TRV3-A

3.1. MTS assay for cell viability

MDA-MB-231 cells were seeded in 96-well microliter plates (5,000 cells/well, 0.05 ml per well) and incubated for 24 h at 37˚ and 5% CO_2. Concentrated stock solutions of **C-TRV3-A** were prepared in PBS and diluted in DMEM/F-12 medium (with 10% FBS and 1% P/S). A **C-TRV3-A** solution was sterilized by passing through a 0.2 µm filter and added to give a final concentration of 0.04-1 mg/mL (dilution factor 1.5). After a 72-h incubation, MTS/PMS (20:1) was added, and the cells were incubated for another 4 h. The optical density of each well was measured at 490 nm using a CLARIOstar plate reader. The absorbance values were expressed as a percentage of cell viability, with 100% representing the cell viability of untreated control cells. Values represent mean ± SD (n=3).

3.2. Cellular uptake studies of C-TRV3-A by live-cell imaging

C-TRV3-A uptake studies used a Leica TCS SP8 confocal microscope with a 63x 1.4NA CS2 oil immersion objective lens. Excitation wavelengths of 405 nm, 488 nm, 561 nm, and 638 nm were employed, along with four fluorescent Photomultiplier Tubes (PMTs) and two Hybrid Detectors (HyD). The experiments were conducted under controlled levels of CO_2 and temperature. Pulse-chase and time-lapse studies were performed at non-toxic concentrations of **C-TRV3-A** using specific fluorescent markers: MitoTracker™ Red CM-H2Xros M7513 (mitochondria, 100 nM), LysoTracker® Blue DND22 (lysosomes, 0.6 μM), Cy5 and $Atto_{488}$ (C-TRV3-A). MDA-MB-231 cells (1,500 cells/well, 0.03 ml per well) were seeded in a 384-well black optical-bottom plate and incubated for 24 h at 37˚C with 5% CO_2. Non-toxic nanoconjugate concentration was added at different time points (1, 2, 4, and 6 h), while Mitotracker and Lysotracker were added 1 h before analysis. Control cells with similar incubation times were also analyzed to establish autofluorescence levels. Time-lapse studies involved adding Mitotracker and Lysotracker 1 h before analysis, capturing images over a 20-s time range upon a 20-min 20min incubation with **C-TRV3**. Image processing was performed using the Leica Application Suite X (LAS X) and the Image J-JACoP plugin for Pearson r calculation. **Video S1** represents a time-lapse study for compound C-TRV3-A for 10 h.

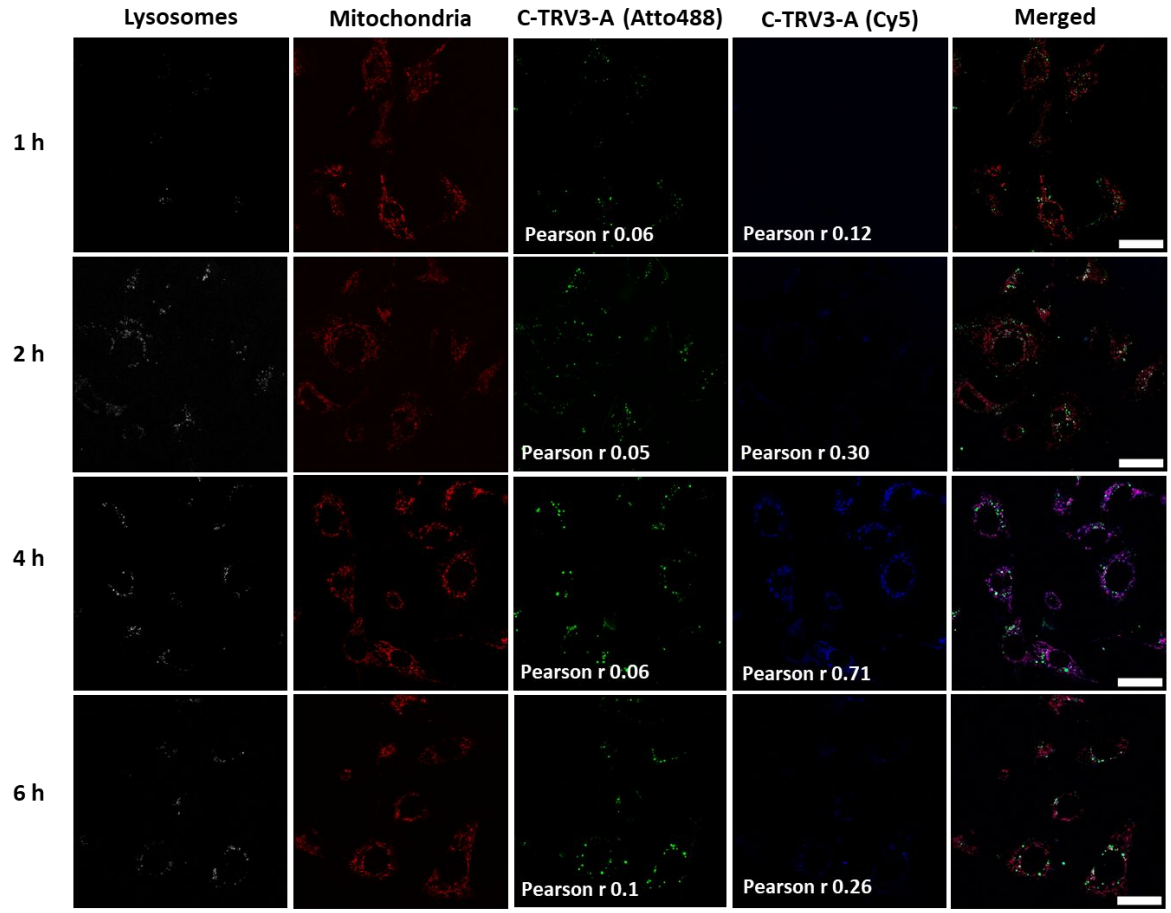
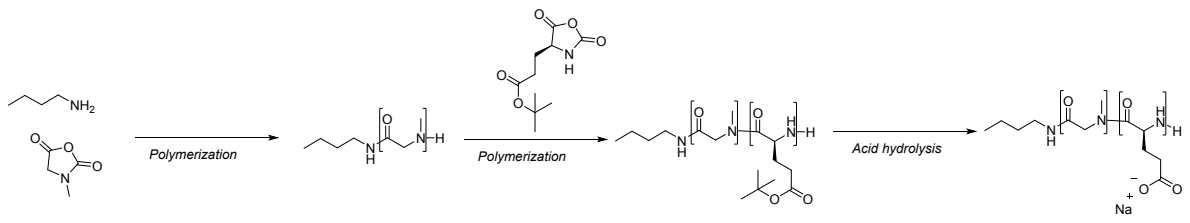


Figure S15. Confocal images of C-TRV3-A uptake over time in MDA-MB-231 cells following a pulse-chase experiment. White - LysoTracker® Blue Red – MitoTracker™ Red CM-H2Xros for mitochondria; Blue and Green – Cy5 and $Atto_{488}$ of **C-TRV3-A**). **TRV3** (Cy5) colocalization with Mitotracker Red shown in the merged image (in purple). The Pearson r value was calculated for **TRV3** (Cy5) and PLO-PEG (**S7**, labeled with $Atto_{488}$) using the ImageJ – JACoP plugin. Scale bar: 10 μm.

4. Polyplex preparation and characterization

4.1. Synthesis of a non-covalent shielding polyanion PSar-b-PGlu block copolymer (VLC-3)



Scheme S9. Complete synthetic procedure for $PSar_{100}$-*b*-PGA_{15} block copolymer (VLC-3) preparation

VLC-3 was synthesized as follows: Sarcosine N-carboxyanhydride (Sar NCA) was added to a Schlenk tube fitted with a stirring bar and a stopper. After 3 cycles of vacuum/N_2, the mixture was dissolved in anhydrous DMF. Then, the initiator n-butylamine diluted in DMF (2 mL) was added to the reaction mixture, which was stirred at 10 °C overnight. Upon completion, the reaction mixture became clear and full conversion of the monomer could be detected by IR. Next, the Glutamic acid t-tert butyl ester NCA was added to the reaction mixture dissolved in anhydrous DMF. The mixture was stirred at 10 °C overnight. Upon completion, the reaction mixture was poured into diethyl ether to precipitate the product. The precipitate was isolated by centrifugation and dried under vacuum. The block copolymer was isolated as a white solid. Yield: 70-90%.

Next, the block copolymer of $PSar_{100}$-*b*-$PGA_{15}OtBu$ was dissolved in trifluoroacetic acid at 0°C, and the mixture was stirred at 5 °C for 1 hour. The reaction mixture was poured into diethyl ether to precipitate the product. The precipitate was isolated by centrifugation and dried under vacuum. The deprotected $PSar_{100}$-*b*-PGA_{15} block copolymer was isolated as a white solid. Yield: 95%. The product was characterized by NMR (D_2O) and size exclusion chromatography (SEC), obtaining a Mw 9.2 KDa (Mw Salt), PDI: 1.09. Specific information on synthesis and purification methodologies are detailed in the corresponding patent[4].

^{1}H NMR (300 MHz, CDCl3, 25°C) δ 4.45- 4.36 (s, -CH_2-, 2H, e), 4.16 (t, CH, 1H, g), 3.05-2.91 (s, CH_3, 3H, f; t, CH_2, 2H, d), 2.25 (t, -CH_2-, 2H, i), 1.99 (dd, -CH_2-, 2H, h), 1.45 (m, CH_2, 2H, c), 1.28 (m, CH_2, 2H, b), 0.85 (t, CH_3, 3H, a).

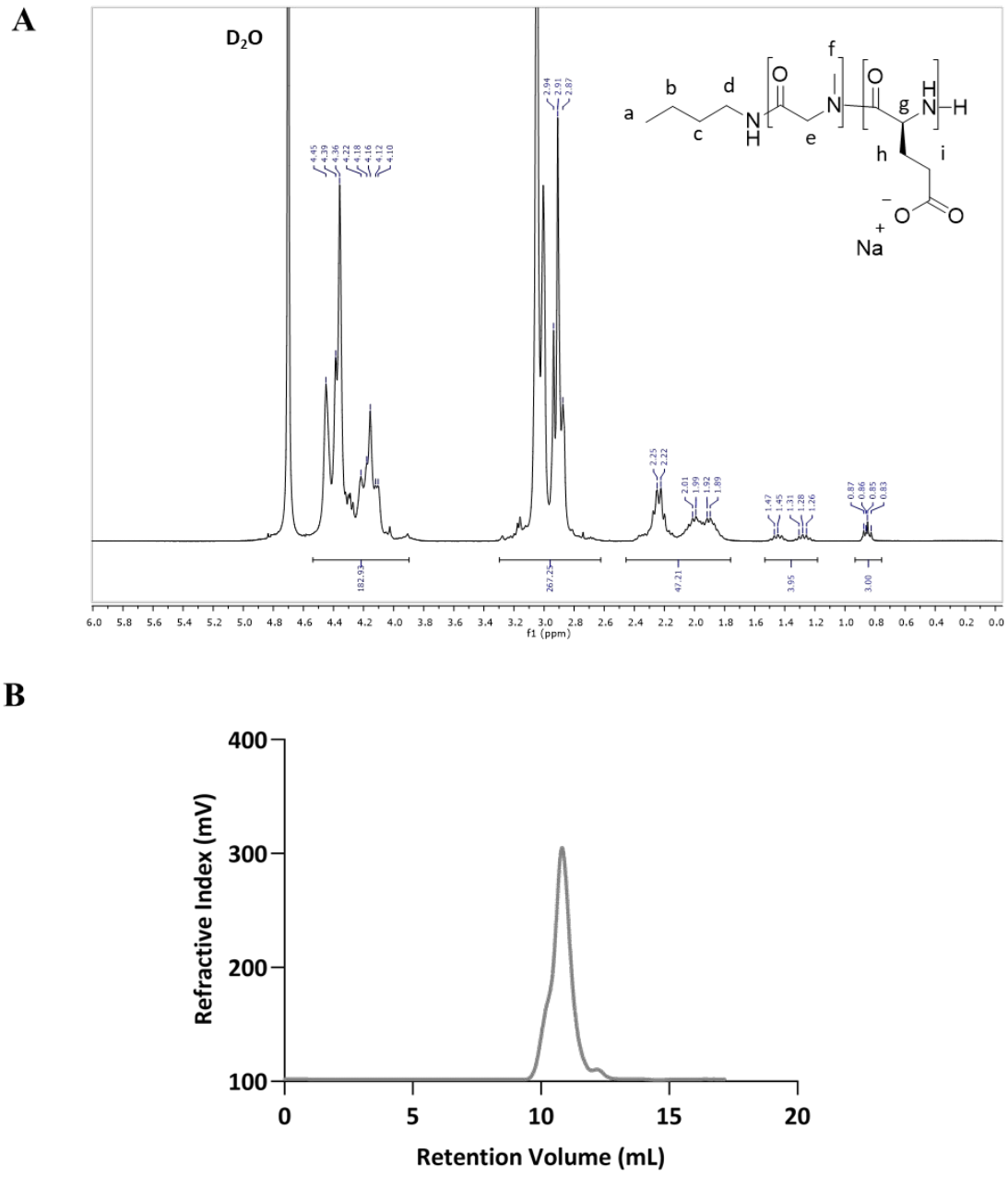


Figure S16. Characterization of $PSar_{100}$-*b*-PGA_{15} block copolymer (VLC-3). A) ^{1}H-NMR spectra of VLC-3 in D_2O **B)** Representative SEC chromatogram (0.1M sodium nitrate ($NaNO_3$), 0.005% (w/w) sodium azide (NaN_3); refractive index channel) for VLC-3

4.2. Polyplex formation

Polyplexes (C-TRV3-A-px) were prepared using pDNA-Luc (P, 200 ng), **C-TRV3-A** (N, cationic polymer), and **VLC-3** (O, anionic shielding polymer) at specified amine to phosphate (N/P) and oxygen to amine (O/N) ratios. Each component was diluted in separate tubes with Milli-Q water. N/P calculations considered only protonable nitrogens (excluding amide nitrogens) and account for PLO functionalization with PEG (3.6 mol%), **TRV3** (4 mol%), and Atto488 (1% wt).

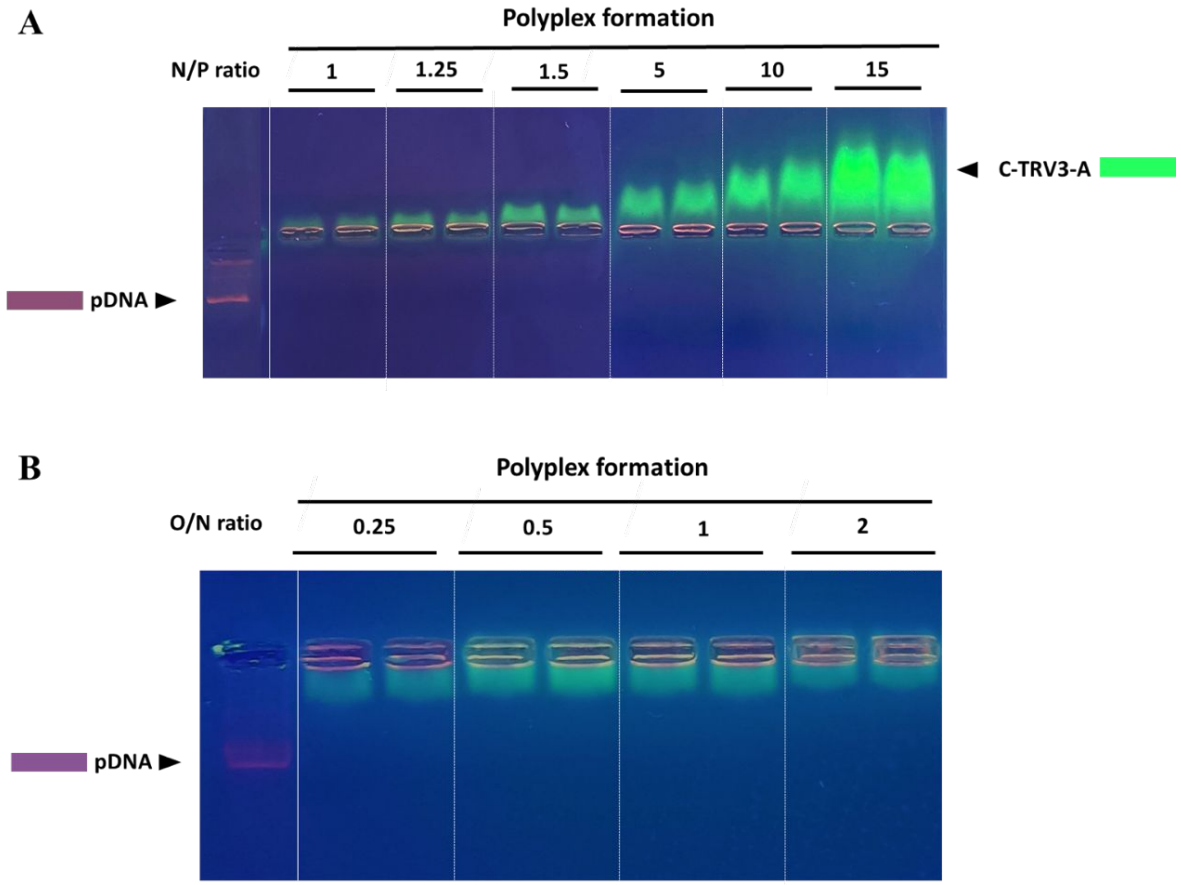


Figure S17. Shift-gel assays of polyplexes (C-TRV3-A-px) prepared using pDNA-Luc (P, 200 ng), **C-TRV3-A** (N, cationic polymer), and **VLC-3** (O, anionic shielding polymer) in PBS, varying **A**) the N/P ratio, while keeping a constant O/N = 1 ratio and **B**) varying the O/N ratio, while keeping constant N/P = 1. pDNA in purple, C-**TRV3-A** in green, VLC-3 not visible by UV lamp.

Complexation was achieved by mixing pDNA-Luc with **VLC-3**, followed by **C-TRV3-A** addition, with vigorous pipetting and 20-min incubation at room temperature. Electrophoresis assays were conducted to ensure C-TRV3-A-px formation. A 1.25% (w/v) agarose gel was prepared by dissolving agarose in TAE buffer (Tris base, acetic acid, and EDTA) and boiling at 100 ˚C. After cooling to 50 ˚C and adding GelRed, the agarose gel was set in an electrophoresis unit. Polyplexes containing 200 ng of pDNA-Luc in PBS and loading buffer were loaded into the sample wells. Electrophoresis was performed at 120 V for 45 min.

4.3. Polyplex stability

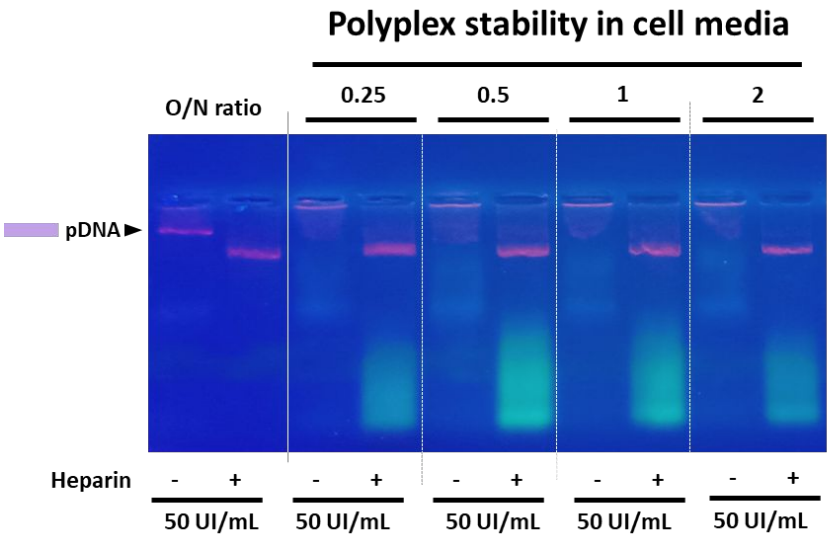


Figure S18. Shift-gel assays of polyplexes (C-TRV3-A-px) prepared using pDNA-Luc (P, 200 ng), **C-TRV3-A** (N, cationic polymer), and **VLC-3** (O, anionic shielding polymer) in PBS (varying the O/N ratio while keeping constant N/P = 1) and their stability after their dilution in cell media (DMEM high glucose medium (with 10% FBS and 1% P/S)) and 1 h incubation at 37 ˚C. 50 IU/ml heparin was added after 1 h at 37 ˚C incubation to disassemble the polyplex and verify the presence of the pDNA-Luc in the complex. pDNA in purple, C-TRV3-A in green, and VLC-3 not visible by UV lamp.

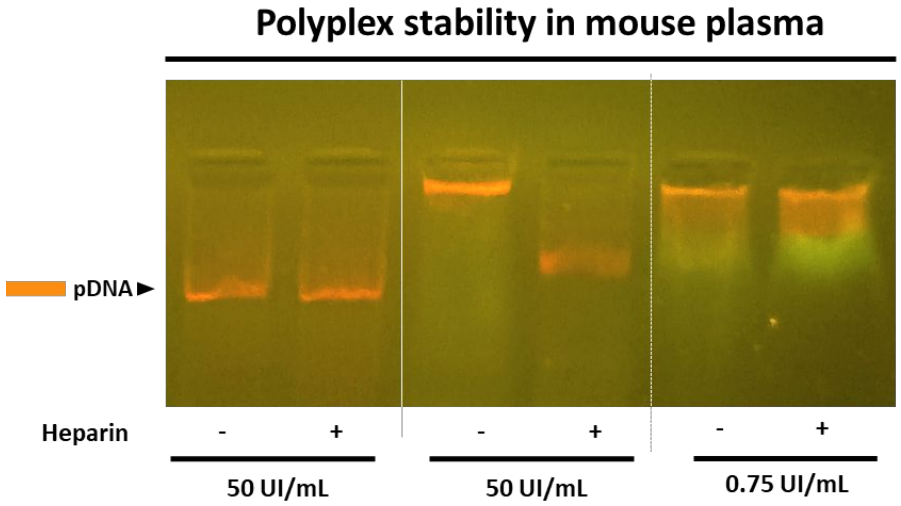


Figure S19. Shift-gel assays of **Px02501** prepared using pDNA-Luc (P, 200 ng), **C-TRV3-A** (N, cationic polymer), and **VLC-3** (O, anionic shielding polymer) in PBS (O/N = 0.25, N/P = 1) and their stability in mouse plasma. **Px02501** were incubated for 1 h at 37 ˚C before heparin addition. A high heparin concentration (50 IU/ml) was used to disassemble **Px02501** and verify pDNA-Luc presence. A low heparin concentration (0.75 IU/ml, equivalent to 75 IU per 100 mL) assessed **Px02501** stability at supra-physiological plasma heparin levels (average human plasma levels: 15 IU per 100 mL). pDNA in brown, C-TRV3-A in green, and VLC-3 not visible by UV lamp. A UV filter was applied to enhance the gel visualization.

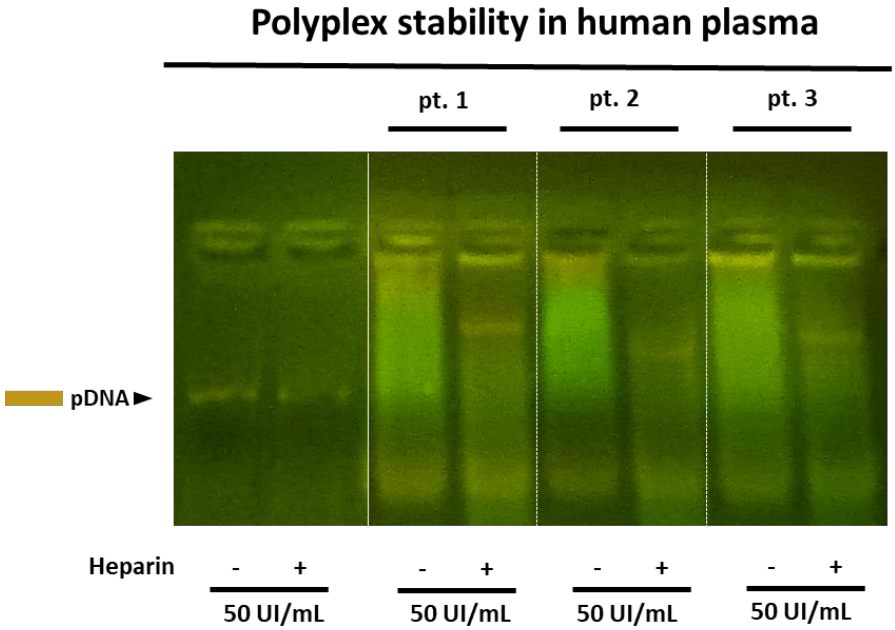


Figure S20. Shift-gel assays of **Px02501** prepared using pDNA-Luc (P, 200 ng), **C-TRV3-A** (N, cationic polymer), and **VLC-3** (O, anionic shielding polymer) in PBS (O/N = 0.25, N/P = 1) and their stability in human plasma (3 patient samples, pt. 1, 2, and 3) and 1 h incubation at 37 ˚C. 50 IU/ml heparin was added after 1 h at 37 ˚C incubation to disassemble **Px02501** and verify the presence of the pDNA-Luc in the complex. pDNA in brown, **C-TRV3-A** in green, and **VLC-3** not visible by UV lamp. A UV filter was applied to enhance the gel visualization. pt = patient.

4.4. Polyplex hemocompatibility assay

Erythrocytes were isolated from fresh mouse blood collected via cardiac puncture after death and placed in a tube containing an anticoagulant (0.5 M EDTA at a 1/10 volume) on ice. The blood was then diluted with PBS (pH 7.4) to a final volume of 10 mL and subjected to centrifugation at 3000 rpm for 10 minutes at 4 ˚C, repeating this step three times. After each centrifugation, the supernatant was carefully removed, and the cells were resuspended in sterile PBS. The final erythrocyte pellet was weighed and resuspended to a concentration of 2% (v/v) in sterile PBS. Solutions of **C-TRV3-A** and **Px02501** (O/N 0.25, N/P 1) were prepared in PBS adjusted to pH 7.4. Samples were added to wells in triplicate (n = 3, 100 µL per well) at

concentrations of 0.08, 0.04, and 0.01). Control wells contained buffer at the corresponding pH, while Triton X-100 at a concentration of 1% (w/v) served as a positive control for complete erythrocyte lysis. Following incubation at 37 ˚C for 1 h, plates were centrifuged at 3000 rpm for 10 min at room temperature, and the supernatant from each well was transferred to a new plate for hemoglobin release assessment. Hemoglobin release was quantified by measuring absorbance at 570 nm using a Clariostar plate reader, and the percentage of hemolysis for each sample was calculated relative to the 100% hemolysis obtained from Triton X-100 incubation.

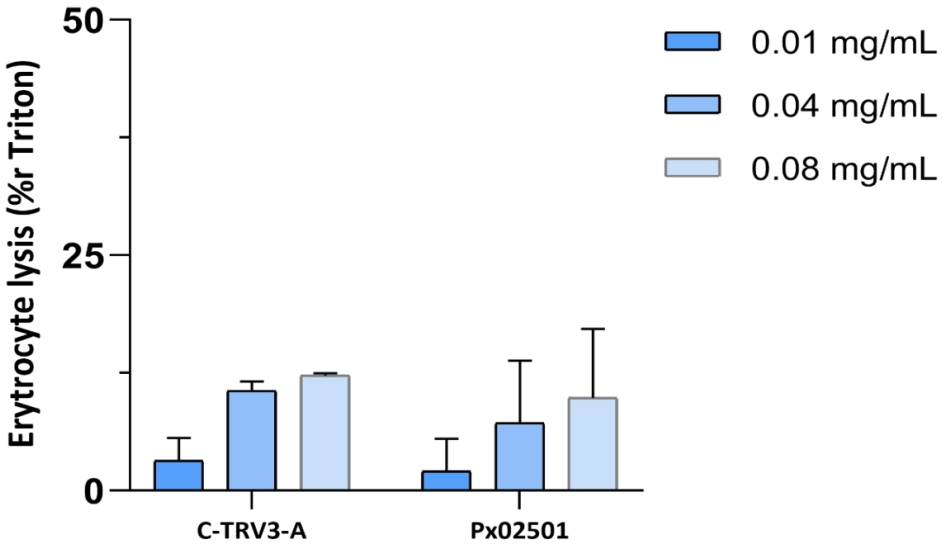


Figure S21. Erythrocyte lysis assay. C-TRV3-A and **Px02501** (O/N 0.25, N/P 1) were incubated with erythrocytes at different concentrations at 37˚C at physiologic pH. Hemoglobin release was measured after 1 h. Data are plotted as mean ± SD, n =3.

5. Biological characterization of polyplexes

5.1. 3D breast cancer cell spheroid culture

MDA-MB-231 2D cultures were maintained in DMEM high glucose medium (10% FBS/1% P/S) at 37˚ and 5% CO_2. For 3D cell culture experiments, cell monolayers were detached using trypsin, centrifuged,

and resuspended in fresh high glucose/no phenol red DMEM medium supplemented with 2% B27 – vitamin A, 0.002 % EGF (100 µg/ml), 2% exosome-free FBS, and 1% P/S. Irregular spheroid formations were obtained after a 24-h incubation after seeding in ultra-low attachment plates (ULA P96 ref. 3474, Corning) at 37˚ and 5% CO_2[5].

5.2. Cell viability in 2D and 3D in vitro breast cancer cell models

For 2D cultures, MDA-MB-231 cells were seeded in white OptiPlate 96-well plates in high glucose/no phenol red DMEM medium (10% FBS and 1% P/S; 5,000 cells/well, 0.08 ml per well) and incubated for 24 h at 37˚ and 5% CO_2. C-TRV3-A-px were prepared in PBS as described in section 2.2.3.1 of the manuscript, and after a 20-min incubation, 20 µl was added to each well. After 24, 48, or 72 h of incubation, Hoechst 33342 was added (1 µg/ml) and incubated for 30 min at 37˚. Cell confluency was quantified and visualized using an EnSight™ Multimode Plate Reader, measuring fluorescence at 450 nm. Fluorescence values were expressed as a percentage of cell viability, with 100% representing the cell viability of untreated control cells. Values represent mean ± SEM (n > 3).

For 3D cultures, MDA-MB-231 cells were seeded in 96-well ultra-low attachment plates in high glucose/no phenol red DMEM medium (2% B27 – vitamin A, 0.002 %, EGF (100 µg/ml), 2% exosome-free FBS, and 1% P/S; 10,000 cells/well, 0.08 ml per well) and incubated for 24 h at 37˚ and 5% CO_2. **Px02501** were prepared in PBS as described in section 2.2.3.1 of the manuscript, and after a 20-min incubation, 20 µl was added to each well. After 24 h of incubation, MTS/PMS (20:1) was added, and the spheroids were incubated for another 4 h. The optical density of each well was measured at 490 nm using a CLARIOstar plate reader. The absorbance values were expressed as a percentage of cell viability, with 100% representing the cell viability of untreated control cells. Values represent mean ± SEM (n > 3). JetPEI (PEI, N/P = 1) was used as a positive control, while non-formulated pDNA-Luc was used as a negative control (CTRL -).

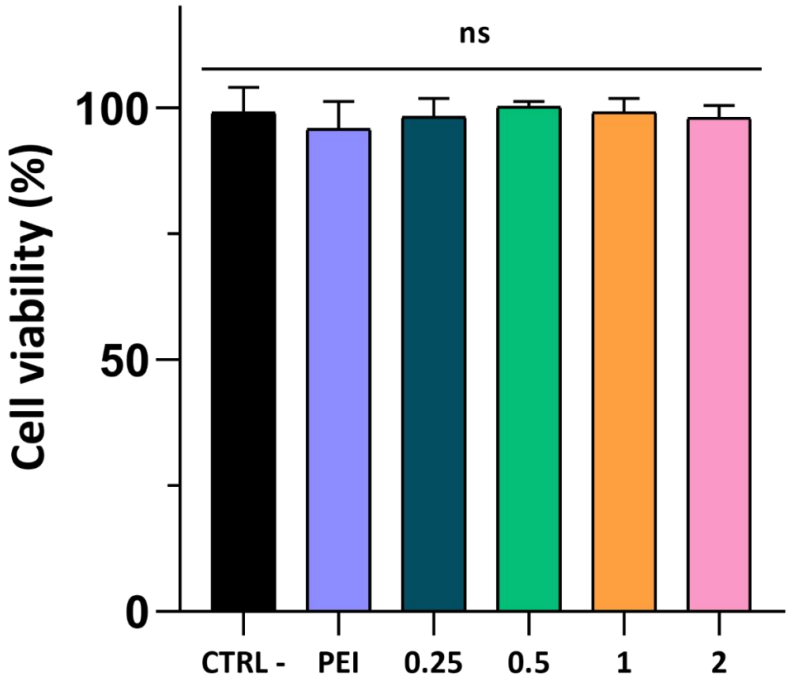


Figure S22. MDA-MB-231 cell viability by Hoechst fluorescence intensity after C-TRV3-A-px exposure (constant N/P =1, O/N = 0.25, 0.5, 1, 2; 24 h, n > 3, mean ± SEM). PEI (N/P = 1) used as a positive control, while non-formulated pDNA-Luc used as a negative control (CTRL -). Values normalized to cell viability of untreated control cells (100%).

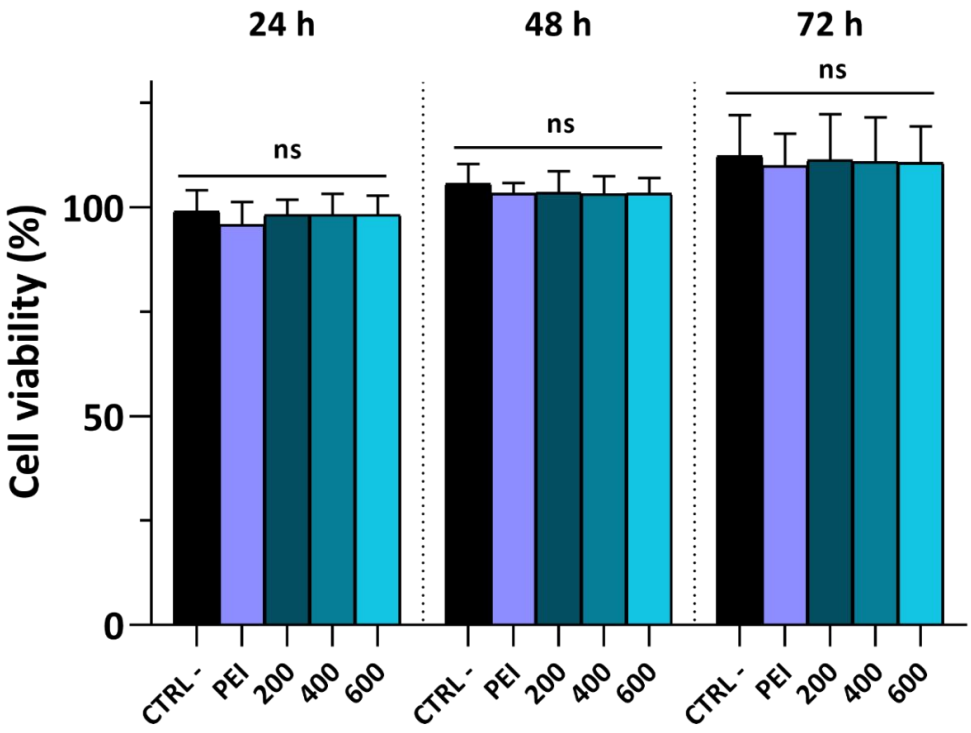


Figure S23. MDA-MB-231 cell viability by Hoechst fluorescence intensity after **Px02501** exposure (N/P =1, O/N = 0.25) at various times (24, 48, and 72 h) and pDNA-Luc concentration (200, 400, and 600 ng/ml). PEI (N/P = 1) used as a positive control; non-formulated pDNA-Luc used as a negative control (CTRL -). Values normalized to cell viability of untreated control cells (100%). n > 3, mean ± SEM.

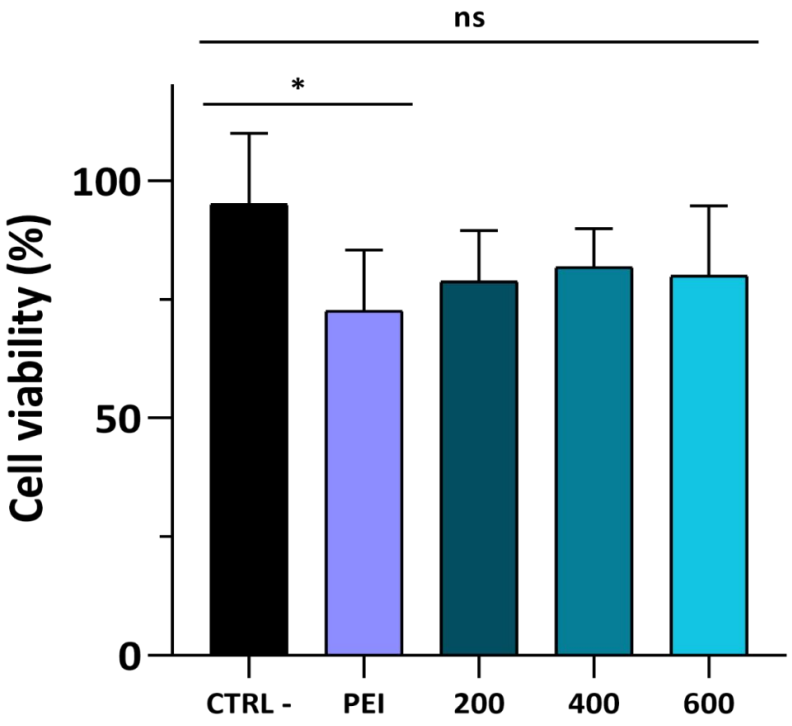


Figure S24. MDA-MB-231 spheroid viability by MTS assay after Px02501 polyplex exposure (N/P =1, O/N = 0.25) at different pDNA-Luc concentrations (200, 400, 600 ng/ml; 24 h, n > 3, mean ± SEM). PEI (N/P = 1) used as a positive control; non-formulated pDNA-Luc used as a negative control (CTRL -). Values normalized to cell viability of untreated control spheroids (100%).

5.3. Transfection in 2D and 3D in vitro cell models

For 2D cultures, MDA-MB-231 cells were seeded in white OptiPlate 96-well plates in high glucose/no phenol red DMEM medium (10% FBS/1% P/S; 5,000 cells/well, 0.08 ml per well) and incubated for 24 h at 37˚ and 5% CO2. C-TRV3-A-px were prepared in PBS as described in section 2.2.3.1 of the manuscript, and after a 20-min incubation, 20 µl was added to each well. After 24, 48, or 72 h of incubation, cells were treated with 20 µL of Bright-Glo reagent (2 min, room temperature). Luciferase (Luc) activity was quantified by EnSight™ Multimode Plate Reader, measuring luminescence at 535 nm. Luminescence values were expressed as a percentage of relative luciferase expression, normalized to cell viability for each

condition (as detailed in section 5.2, where 100% corresponds to the cell viability of untreated control cells) and adjusted by subtracting the background luminescence from non-seeded wells treated with each condition. Values represent mean ± SEM (n > 3).

For 3D cultures, MDA-MB-231 cells were seeded in 96-well ultra-low attachment plates in high glucose/no phenol red DMEM medium (2% B27 – vitamin A, 0.002 %, EGF (100 μg/ml), 2% FBS exosome free, 1% P/S; 10,000 cells/well, 0.08 ml per well) and incubated for 24 h at 37˚ and 5% CO_2. **Px02501** were prepared in PBS as described in section 2.2.3.1 of the manuscript and after a 20-min incubation, 20 μl was added to each well. After 24 h of incubation, spheroids were treated with 20 μL of Bright-Glo reagent (2 min, room temperature). The volume of each well was transferred to a white OptiPlate 96-well plate, and the Luc activity was quantified by EnSight™ Multimode Plate Reader, measuring luminescence at 535 nm. Luminescence values were expressed as a percentage of relative luciferase expression, normalized to cell viability for each condition (as detailed in section 5.2, where 100% corresponds to the cell viability of untreated control cells) and adjusted by subtracting the background luminescence from non-seeded wells treated with each condition. Values represent mean ± SEM (n > 3). PEI (N/P = 1) used as a positive control; non-formulated pDNA-Luc used as a negative control (CTRL -).

6. Statistical analysis

Data were analyzed using a t-test, with differences considered significant when p****<0.0001; p***<0.001; p**<0.01; p*<0.05 (ns: not significant).

REFERENCES

(1) Kamiński, Z. J.; Kolesińska, B.; Kolesińska, J.; Sabatino, G.; Chelli, M.; Rovero, P.; Błaszczyk, M.; Główka, M. L.; Papini, A. M. N-Triazinylammonium Tetrafluoroborates. A New Generation of Efficient Coupling Reagents Useful for Peptide Synthesis. *J. Am. Chem. Soc.* **2005**, *127* (48), 16912–16920. https://doi.org/10.1021/ja054260y.

(2) Ashiotis, G.; Deschildre, A.; Nawaz, Z.; Wright, J. P.; Karkoulis, D.; Picca, F. E.; Kieffer, J. The Fast Azimuthal Integration Python Library: PyFAI. *J. Appl. Crystallogr.* **2015**, *48*, 510–519.

https://doi.org/10.1107/S1600576715004306.

(3) Hammouda, B. Small-Angle Scattering From Branched Polymers. *Macromol. Theory Simulations* **2012**, *21* (6), 372–381. https://doi.org/https://doi.org/10.1002/mats.201100111.

(4) Felip, C.; Dolz, I.; Esteban-Pérez, S.; Herrera-Muñoz, L. . N.-C. V. . Non-Covalent Shielding Polymers. *WO2023002014A1. WO EP CN JP CA. Prior. 2021-07-22, Filed 2022-07-22, Publ. 2023-01-26*.

(5) Đorđević, S.; Medel, M.; Hillaert, J.; Masiá, E.; Conejos-Sánchez, I.; Vicent, M. J. Critical Design Strategies Supporting Optimized Drug Release from Polymer–Drug Conjugates. *Small* **2024**, *20* (4), 2303157. https://doi.org/https://doi.org/10.1002/smll.202303157.